Geochemical investigations of submarine groundwater discharge, river outflow, and benthic diagenesis in the coastal Baltic Sea

I n a u g u r a l d i s s e r t a t i o n

zur

Erlangung des akademischen Grades eines

Doktors der Naturwissenschaften (Dr. rer. nat.)

der

Mathematisch-Naturwissenschaftlichen Fakultät

der

Universität Greifswald

vorgelegt von

CÁTIA MILENE EHLERT VON AHN

Greifswald, 16.12.2022

Dekan: Prof. Dr. Gerald Kerth

1. Gutachter: Prof. Dr. Michael Ernst Böttcher

2. Gutachter: Prof. Dr.-Ing. Michael Kersten

Tag der Promotion: 01.06.2023

This thesis was printed/published with support from the German Academic Exchange Service (DAAD).

Table of Contents:

Abstract

The exchange of water and dissolved elements between the continents and the oceans occurs via different routes in the hydrological cycle, such as rivers, atmospheric exchange, and submarine groundwater discharge (SGD). In addition, the elemental fluxes in the coastal waters may strongly depend on benthic water-solid-microbe interactions close to the sediment-water interface. It is becoming increasingly recognized that SGD can impact diagenesis and act as a source of water and dissolved substances for coastal ecosystems. The qualitative and quantitative assessment of SGD is still challenging as it requires the identification of suitable geochemical tracers for the complex hydrological and biogeochemical processes in the subterranean estuary. In this study, geochemical analyses were combined with geophysical, hydrological, and biological investigations to gain insights into the mechanisms driving SGD in coastal waters. In addition, onshore ground and surface waters were evaluated to identify the processes controlling the potential end member. The surveys were performed along the Baltic Sea coast: Warnow River and Wismar Bay in Germany, the Gulf of Gdańsk and Puck Bay in Poland, and Hanko Bay in Finland. The results suggest that the analyzed surface water system was strongly impacted by seasonal variations, while SGD displayed a much more stable composition throughout the year. New areas of SGD were also identified along the Baltic Sea. It was also observed that anthropogenic coastal infrastructures could promote SGD affecting the water balance and the benthic fluxes. At other sites, the SGD was associated with natural structures such as pockmarks. The stable isotopic composition of the fresh component of SGD was close to the meteoric water at most sites; however, old groundwaters from distinct aquifers were identified. Combining all sites, SGD showed high variability, ranging from near 0 to up to 300 L m^{-2} d^{-1}, and the saline SGD was more dominant than the fresh component. The fluxes obtained at one site were even higher than the surface runoff. SGD was higher on sandy sediments, but the elemental fluxes were relatively low. Despite low SGD at muddy sites, interfacial elemental fluxes, enhanced by intense diagenesis in the top sediments, resulted in higher chemical fluxes to the water column. The sediment porewater gradients at the SGD impacted sites suggest that the advective upward flow of groundwater increased the elemental fluxes across the sediment-water interface. Therefore, the dissolved substances of SGD are partly impacted by the processes in the soil zone and aquifer during groundwater development, and partly impacted by the early diagenetic process in the surface sediments. Overall, this study shows the importance of SGD for the biogeochemical cycles of coastal waters. Moreover,

it can be concluded that a combination of interdisciplinary approaches can provide a better understanding and assessment of SGD in a specific environment. Although all the studies presented here are local, the methodology and results presented in this thesis can be replicated and thus provide assistance in other coastal areas.

Zusammenfassung

Der Austausch von Wasser und gelösten Elementen zwischen den Kontinenten und den Ozeanen läuft über verschiedene Wege im Wasserkreislauf, z. B. über Flüsse, den Austausch über die Atmosphäre und über den submarinen Grundwasserabfluss (SGD). Zusätzlich können die Elementflüsse in den Küstengewässern stark von benthischen Wasser-Feststoff-Mikroben-Interaktionen nahe der Sediment-Wasser-Grenzfläche abhängen. Es wird immer mehr erkannt, dass SGD die Diagenese beeinflussen und als Quelle von Wasser und gelösten Stoffen für Küstenökosysteme agieren können. Die qualitativen und quantitativen Untersuchungen von SGD sind nach wie vor eine große Herausforderung, da sie die Bestimmung geochemischer Tracer für die komplexen hydrologischen und biogeochemischen Prozesse im unterirdischen Ästuar erfordern. Geochemische Analysen wurden mit Untersuchungen zur Geophysik, Hydrologie und Biologie kombiniert, um Einblicke in die Mechanismen zu bekommen, die SGD in die Küstengewässer bringen. Zusätzlich wurden die Grund- und Oberflächengewässer an Land untersucht, um die Prozesse zu identifizieren, die potenzielle Endglieder kontrollieren. Die Untersuchungen wurden an den Küsten der Ostsee durchgeführt: Die Warnow und die Wismarer Bucht in Deutschland, der Golf von Danzig und die Puck-Bucht in Polen sowie die Hanko-Bucht in Finnland. Die Oberflächenwassersysteme waren stark von jahreszeitlichen Variationen beeinflusst, während der SGD eine wesentlich stabilere Komposition über das ganze Jahr hatten. Neue Bereiche mit SGD wurden innerhalb der Ostsee identifiziert. Es wurde auch festgestellt, dass anthropogene Küsteninfrastrukturen SGD verstärken können, was sich auf den Wasserkreislauf und die benthischen Stoffflüsse auswirkt. An einigen anderen Stellen war der SGD mit natürlichen Strukturen wie Pockmarks assoziiert. Die stabile Isotopenkomposition der Süßwasserkomponente des SGD war in den meisten Gebieten nahe am Meteorwasser; es wurden jedoch auch alte Grundwässer aus verschiedenen Aquiferen gefunden. Bei der Zusammenfassung aller Gebiete zeigte die SGD eine enorme Variabilität von nahe 0 bis zu 300 l m^{-2} d^{-1}, wobei der salzhaltige SGD dominanter war als die Süßwasserkomponente. Die an einee Stelle gemessenen Flüsse waren sogar höher als der Oberflächenabfluss. Der SGD war auf sandigen Sedimenten höher, aber die

Elementflüsse waren relativ niedrig. Trotz des niedrigen SGD an schlickigen Sedimenten kam es zu höheren Elementenflüssen an den Grenzflächen, die durch die intensive Diagenese in den oberen Sedimenten verstärkt wurden und zu höheren Elementflüssen in die Wassersäule führten. Die sedimentären Porenwassergradienten an den SGD-beeinflussten Stellen legen nahe, dass der advektive Fluss des Grundwassers nach oben die Elementflüsse über die Sediment-Wasser-Grenzfläche erhöht hat. Deshalb sind die gelösten Stoffe zum Teil auf Prozesse in der Bodenzone und im Aquifer während der Grundwasserentwicklung zurückzuführen, zum großen Teil aber auch auf den diagenetischen Prozess in den Oberflächensedimenten. Insgesamt zeigt diese Studie die große Bedeutung von SGD für die biogeochemischen Kreisläufe von Küstengewässern. Darüber hinaus lässt sich ableiten, dass eine Kombination von interdisziplinären Ansätzen ein besseres Verständnis und eine bessere Bewertung von SGD in einer bestimmten Umgebung ermöglichen kann. Obwohl alle hier vorgestellten Studien auf lokaler Ebene durchgeführt wurden, können die in dieser Arbeit vorgestellten Methoden und Ergebnisse auf andere Küstengebiete übertragen werden und somit auch dort unterstützen.

Chapter 1. Introduction

1.1 General introduction

Water is the most abundant substance on the Earth's surface. About 96% is stored in the oceans, and the remaining 4% is either on the continents or in the atmosphere. The water does not remain in any reservoir but is constantly moving from one place to another within the hydrological cycle (Figure 1). Water evaporates from the oceans and land into the atmosphere and falls again back to the earth`s surface as rain. Part of it runs off in rivers, accumulates temporarily in lakes, and some run underground merging later in rivers, lakes, and oceans (Berner and Berner 1996).

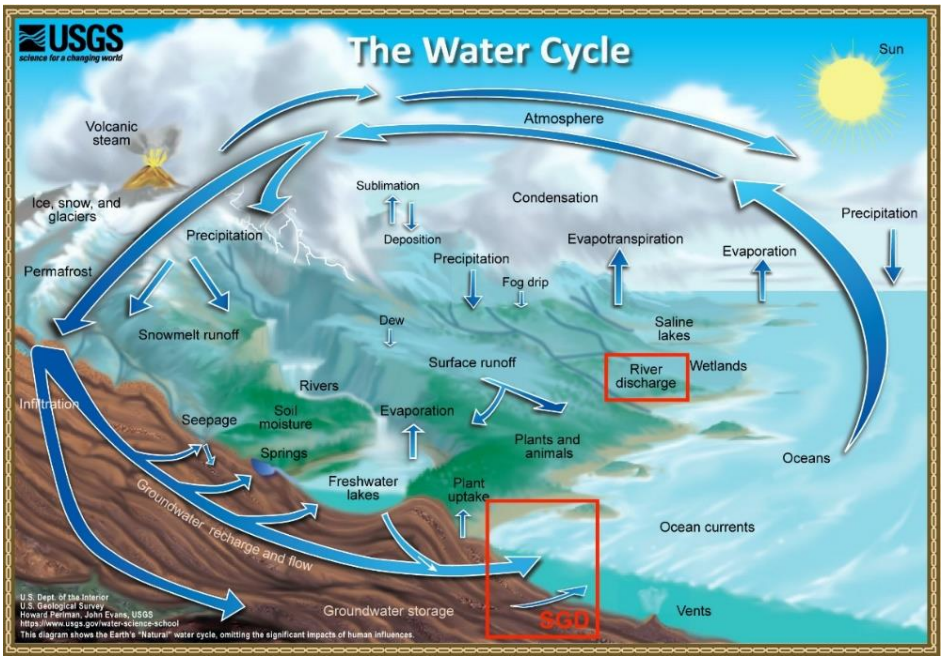

Figure 1 - The natural water cycle emphasizing the contribution from SGD. Modified from USGS (credits: Howard Perlman, USGS, and John Evans, USGS)

When in contact with rocks (and derived soils), the water reacts with primary minerals. The minerals dissolve to varying extents and react with each other to form new secondary minerals. Dissolution of newly formed minerals is mainly induced by acid from plants and by bacterial metabolism called chemical weathering, aided by physical weathering through fracturing of the rocks (Berner & Berner, 1996). The availability of the elements for mobilization and transport is, therefore, strongly dependent on geology of the catchment area (Chester, 2000).

The land-ocean interface is the area where water, substances, and energy are exchanged. This interface is critical since it influences the hydro-physical, chemical, and biological processes in both realms. To understand marine geochemistry, it is necessary to assess the composition, flux rate, and subsequent fate of the terrestrial material delivered to the ocean (Chester, 2000). Rivers disperse most of the terrestrial material mobilized by crustal weathering and anthropogenic activities. They are the major routes by which continental rain and the products of continental weathering reach the oceans (Degens et al., 1991; Hartmann et al., 2014). The underground route, submarine groundwater discharge (Figure 1), is now recognized as an important route for water within the hydrologic cycle, which in some locations can be compared to river discharge (Church 1996; Moore 1996).

1.2 Composition and dynamic of coastal regions

At the land-ocean interface, the continental margins occupy less than 20% of the surface area of the world's oceans; however, one-third of the pelagic primary production occurs in these regions, which therefore play a significant role in the global biogeochemical cycles (Walsh, 1991; Bauer et al., 2013). High productivity is caused to a large extent by riverine and groundwater input of nutrients and organic matter from continents. Around 90% of the organic matter is already remineralized in the sediments of the coastal areas before reaching open waters (Wollast, 1991).

Sediments are the main location for modification and accumulation of particulate matter. The prevalent sediment type/size at a particular location depends largely on local depositional conditions (Rullkötter, 2006). Also, organic matter loading is often associated with sedimentary mud fractions, and it is potentially used as a proxy for sedimentation conditions (Kei et al., 1994, Böttcher et al., 1998). Molecular diffusion dominates solute transport processes in fine-grained muddy sediments (e.g., Böttcher et al., 2000; Hyacinthe et al., 2001). In contrast, advection porewater flow is more important in permeable sandy sediments. Although the latter are organic-poor, biogeochemical rates can be as high as in organic-rich muddy sediments (e.g., Santos et al., 2012; Reckhardt et al., 2017). Vertical fluid flow processes can, in specific cases, result on pockmarks

structures on the seafloor, which are like creater depressions allowing sites of preferential discharge to be recognized (Hovland and Judd, 1988).

The biogeochemical processes at the sediment-water interface usually depend on sediment properties but also on benthic fauna, and physical processes. Moreover, they are influenced by dynamic physical boundary conditions such as light intensity, temperature, hydrodynamics, oxygen penetration, organic matter load, and salinity (Boudreau & Jørgensen, 2001).

Sediments consist of a framework for the biogeochemical reactions during early diagenesis. Once the organic matter is incorporated into the sediments, biogeochemical processes driven by microbial degradation occur in the pore spaces. The remineralization of organic matter is coupled to various processes (Figure 2) such as consumption of electron acceptors, release of mineralized products, and production of metabolites which are reflected in the solid phase and porewater gradients (Reeburgh, 1983; Rullkötter, 2006). Figure 2 only considers the unidirectional processes; however, more abiotic and biotic interactions between different solid and dissolved species occur (e.g. Jørgensen, 2006).

Oxygen is the most favorable terminal electron acceptor. Below the oxic zone, in the suboxic zone, anaerobic bacteria uses different electron acceptors to degrade the organic matter, such as nitrate, manganese, and iron oxides. In the anoxic zone, microbial sulphate reduction is the dominant process, especially because of the availability of sulfate derived from seawater (Jørgensen, 1982). When all the other electron acceptors are depleted, methanogenesis and fermentation processes begin (Jørgensen & Kasten, 2006). Since organic matter contains carbon, nitrogen, and phosphorus the diagenetic oxidation releases dissolved inorganic carbon, nitrogen, and phosphorus into the porewaters, and subsequent reactions of produced metabolites such as sulfide, dissolved iron, and manganese take place (Reeburgh, 1983; Froelich et al., 1979; Thamdrup et al., 1994; Schulz, 2006; Jørgensen, 2006). Besides authigenic mineral formation, like carbonate and phosphate minerals (e.g. Schulz, 2006), net accumulating substances in the porewater may be liberated into the bottom water and, thereby, recycled and further impacting the pelagic biogeochemistry.

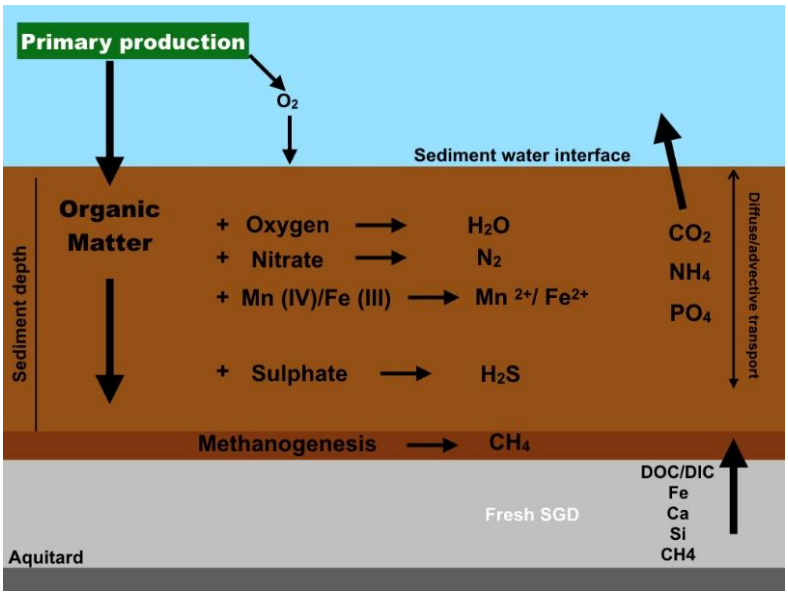

Figure 2 - Conceptual model of the most relevant biogeochemical processes on surface sediments (modified from Jørgensen (2006) and the possible contribution of elements from groundwater.

Identifying, characterizing, and quantifying water and dissolved element fluxes throughout the continental shelf is a challenge because the physical, chemical, and biological impacts on these systems are highly complex and variable in temporal and spatial scales (Moore, 2000).

Furthermore, as coastal areas are directly connected to the land, they are under impact by anthropogenic activity such as eutrophication, ocean acidification, fishering activity, or port operations. Anthropogenic activities potentially disturb the coastal sediments impacting the organic matter pathways, and can negatively influence the carbon cycle and other major and trace elements (Bauer et al., 2013; van de Velde et al., 2018).

Submarine groundwater discharge (hereafter SGD) has been recognized as an essential contribution of water, particularly dissolved constituents, to the coastal waters (Church, 1996; Knee et al., 2010; Böttcher et al., 2023). Nutrients supplied via SGD to surface waters can also impact biogeochemical cycles, benthic fluxes, and pelagic zones (Valiela et al., 1990; Church, 2006; Moore, 2010; Rodellas et al., 2015; Santos et al., 2021).

1.3 Submarine groundwater discharge (SGD)

Aquifers are lithological geological structures with interconnected porosity and permeability that allow the movement of water under a hydraulic gradient. Usually, groundwater flows from areas of high to areas of low hydraulic gradient under the force of gravity. In coastal aquifers, the hydraulic gradients generally point toward the sea leading to groundwater discharge to the coastal waters (Glover, 1959). These aquifers are complex due to the combined influences of oceanic and inland forces.

The connection between seawater and freshwater can result in the formation of a mixing zone, which can be called as subterranean estuary, representing a zone of intense physic-chemical reactions (e.g., mineral precipitation, adsorption, microbial activity) with the same importance as the surface estuaries (Moore, 1999; Beck et al., 2007).

Although not visually apparent as river discharge, continental groundwater also discharges directly to the oceans whenever a coastal aquifer is connected to the sea (Burnett et al., 2003).

SGD is defined in this study as the mixture of seawater and freshwater that discharges to the coastal water at scales of meters to kilometers, regardless of fluid composition or driving force (Figure 3), moreover SGD is ubiquitous in sandy, muddy, and rocky shorelines and is composed of fresh and saline groundwater (e.g. Burnett et al., 2003; Moore, 2010).

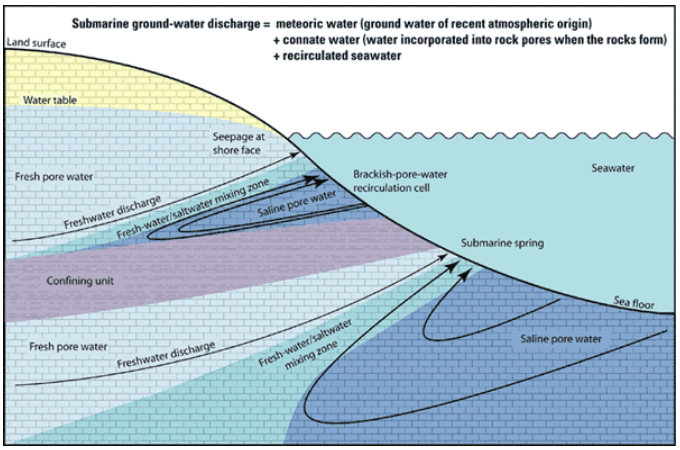

Figure 3 - Schematic drawing of submarine groundwater discharge (SGD) that includes direct input of fresh groundwater into the coastal sea and recirculated seawater. Both processes constitute transport pathways for chemical elements into the coast. Source: USGS – Submarine Groundwater Discharge.

The investigation of SGD on different scales is challenging due to the spatial variability and different physical processes which control its fluxes (Figure 4). Although measurements of SGD are complex (Figure 4), many studies using various approaches have successfully started to quantify the magnitude of fresh groundwater fluxes and recirculated saline SGD (Burnett et al., 2006; Taniguchi et al., 2019). The main methods used are remote sensing (e.g., Mallast & Siebert, 2019; Bejannin et al., 2020), hydrological modeling (e.g., Thompson et al., 2007; Schafmeister & Darsow, 2014), direct seepage measurements (e.g., Lee, 1977; Cable et al., 1997; Taniguchi et al., 2003), geophysical tracers such as groundwater temperature or electrical tomography and acoustic imaging (e.g., Schlüter et al., 2004; Viso et al., 2010), and geochemical tracers (Moore, 2006; Povinec et al., 2008).

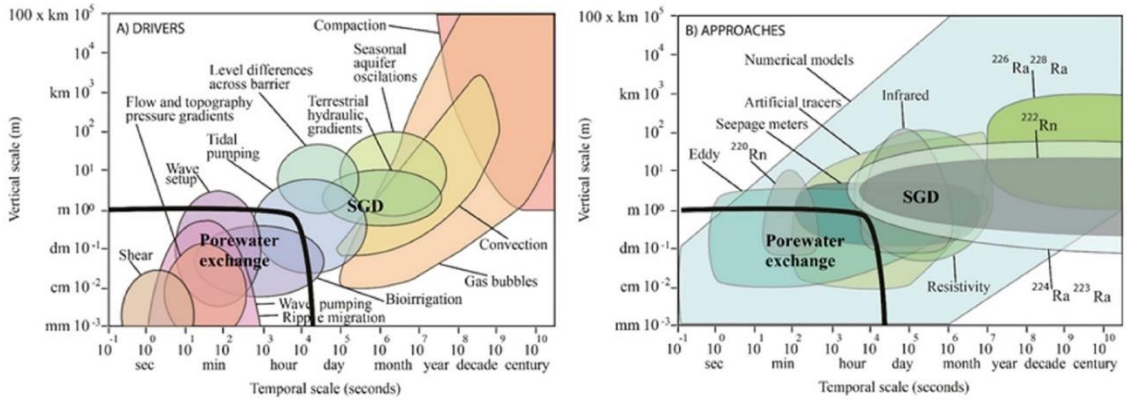

Figure 4 - Physical processes driving porewater exchange and SGD in coastal systems. The black line separates the porewater exchange from the SGD (A). Approaches used to quantify SGD often capture different drivers, making it difficult to quantify individual processes (B). SOURCE: Taniguchi et al., 2019.

Many studies make use of chemical tracers that are characteristic of, and ideally restricted to discharge fluids and relatively unreactive in coastal waters. High concentrations of such tracers in the coastal ocean provide evidence that coastal aquifers are freely connected to the sea and that fluid exchange in these systems is substantial (Moore et al., 2006).

Among the chemical tracers, radium (Ra) isotopes are used to differentiate the SGD inflow from different matrices by the ratio among the uranium (^{223}Ra and ^{226}Ra) and

thorium (^{224}Ra and ^{228}Ra). The relative difference in ingrowth rates can result in the groundwater being enriched in shorter-lived Ra isotopes relative to the longer-lived ones, depending on the flushing frequency (e.g., Moore, 2008; Rodellas et al., 2017; Cho et al., 2018). Stable isotopes of water (δ^2H_{H2O} and $\delta^{18}O_{H2O}$) are well established tracers in hydro(geo)logical studies for identifying physical impacts on surface waters (e.g. evaporation, condensation) and in general mixing processes, since meteoric waters such as precipitation and terrestrial groundwater usually have an isotopic composition that is lighter than seawater (e.g., Povinec et al., 2012; Rocha et al., 2018). Carbon isotopes of DIC, DOC, and CH_4 are useful variables for obtaining information on the sources and transformation of organic matter in transition zones (Zetsche et al., 2011; Pain et al., 2019). Recently, isotopes of Li, S, and Sr in were evaluated by Ikonen et al. (2022), and different behaviors, as expected for conservative mixing, were found in the subterranean estuary.

Globally, the amount of fresh SGD entering the oceans has been estimated to be up to 10% of river discharge (Taniguchi et al., 2002); other studies estimated that the total flux of SGD, including saline water, is estimated to be higher (Church, 1996; Kwon et al., 2014). The fresh component of SGD would only represent up to 0.2% of the total SGD flux (Luijendijk et al., 2020).

Coastal groundwater discharge displays a high variability. However, in some locations it can be close to riverine discharge (Figure 5), and leading to a high solute loads to coastal waters (Luijendijk et al., 2020). In particular, for the biogeochemistry of coastal ecosystems, SGD may have substantial effects on local and regional scales that are still under investigation in many coastal areas.

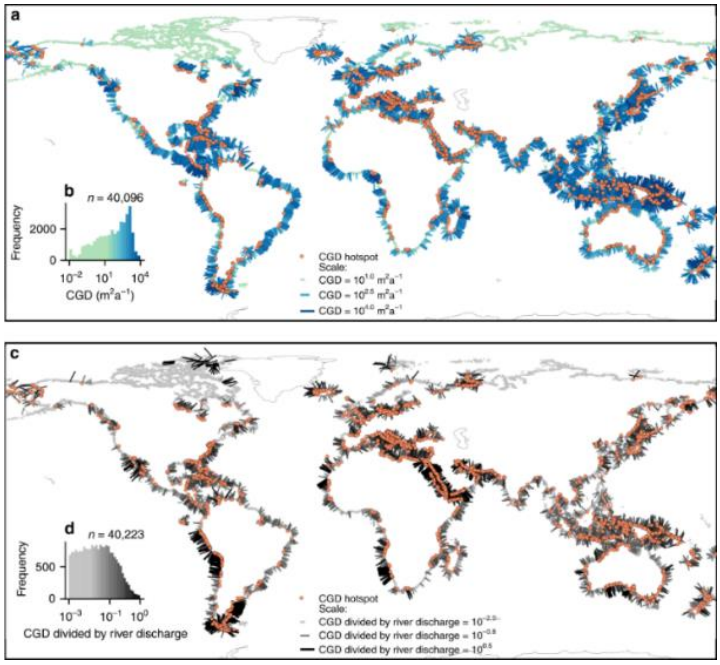

Figure 5 - Global maps of coastal groundwater discharge and comparison with surface water discharge. Source: Luijendijk et al., 2020.

The distinction between fresh and saline SGD is important when estimating elemental fluxes to the coastal ocean (Church, 1996). Fresh SGD is a source of both new water and dissolved elements, while the saline SGD often flushes out the recycled elements generated by organic matter mineralization (Santos et al., 2021).

Due to the many reactions in coastal aquifers, specifically in the subterranean estuary, the SGD becomes element-enriched and significantly impacts the chemical composition of coastal waters (Knee & Paytan, 2011; Luijendijk et al., 2020; Santos et al., 2021). For example, SGD can act as a source of metals (Mayfield et al., 2021; Chakrabarti et al., 2018) and dissolved inorganic carbon (Qian Liu et al., 2014; Chen et al., 2018). Some other elements, such as organic and inorganic pollutants, may also have other (deleterious) impacts on the biogeochemistry of coastal ecosystems (McKenzie et al., 2020; Brookfield et al., 2021). Furthermore, the development of different physicochemical gradients may affect the benthic organism communities (Kotwicki et al., 2014; Lecher & Mackey et al., 2018).

There are examples around the world where SGD is even associated with a commercial value. There are areas where SGD can be used as a source of potable and domestic water

for the population (Duarte et al., 2010). Furthermore, there are SGD locations strongly associated with social and historical perspectives (Moosdorf & Oehlert, 2017).

Although there is already clear evidence of the importance of SGD as a source for coastal nutrients, this has not yet been considered in legislation and major initiatives such as the EU Water Framework Directive and the EU Marine Strategy Framework Directive. At the same time, an even better understanding of the role of SGD in ecological, economic, and social contexts is needed to make management policies and legislation become more effective (Santos et al., 2021).

A recent literature review on SGD (Santos et al., 2021) compiled 239 SGD studies from 31 countries, and revealed a wide but uneven distribution of SGD studies worldwide. Few studies have been carried out in the Baltic Sea, although the occurrence of SGD on the water balance has been already recognized in the early 1990's (Piekarek-Jankowska, 1996; Falkowska and Piekarek- Jankowska, 1999).

1.4 Studies on submarine groundwater discharge into the Baltic Sea

Coastal areas of the southern Baltic Sea offer an excellent opportunity to investigate the role of freshwater inputs. The drainage basin composition of the Baltic Sea is diverse, dominated by limestone in the south and granite in the northern parts (Figure 6), which could potentially provide distinct fluxes to the coastal waters. Besides surface water discharge, SGD has been observed in different locations.

Although the groundwater discharging directly to the Baltic Sea represents only 1% of the river discharge, local contributions can be significantly higher from a small-scale perspective (Peltonen, 2003).

In general, the fluxes of fresh SGD stay in the range below 1 L m^{-2} d^{-1} (see Table 1). In contrast, when considering the fresh plus the saline components of SGD, the fluxes can reach up to 242 L m^{-2} d^{-1}, which can have a significant impact on the material budget of the Baltic Sea. In addition, all presented studies emphasized the impact of SGD on the geochemical aspects of the coastal waters.

In the Eckernförde Bay, Germany (Figure 6 – Site A), for example, studies focusing mainly on pockmarks have shown that CH_4 fluxes and SGD impact the water column

(e.g., Whiticar and Werner, 1981; Whiticar et al., 2002; Schlüter et al., 2004; Hoffmann et al., 2020). Also, the groundwater supply to the bay is attributed to aquifers of different geological ages (Bussmann & Suess, 1998; Marczinek & Piotrowski, 2002; Withicar, 2002). More specifically, the impact of freshwater in some pockmarks has lowered the initial amount of sulfate available for bacterial sulfate reduction (Whiticar, 2002), thereby impacting diagenetic processes.

To the east of Eckernförde Bay, near to Wismar Bay (Figure 6 – Site B), the coastal groundwater discharge was estimated by numerical modeling based on a water balance. It was found that 14.3% of the total recharge was discharged into the Baltic Sea (Schafmeister and Darsow, 2004). In Meschendorf, also near Wismar Bay (Figure 5- Site B), iron-rich groundwaters are emerging at the shoreline, which may be considered as a window of the SGD escaping further at the Baltic Sea seafloor (Lipka et al., 2018).

Table 1 – Summary of some of the SGD studies along the coastal Baltic Sea. The locations are displayed in Figure 5.

Location - Figure 6	**Location**	**Reference**	**Highlights**	**Fluxes [L m^{-2} d^{-1}]**
Site A	Eckernförde Bay, Germany	Whiticar & Werner 1981	pockmark associated SGD methane	
Site A	Eckernförde Bay, Germany	Bussmann & Suess 1998	pockmark associated SGD and methane	
Site A	Eckernförde Bay, Germany	Bussmann et al.,1999	pockmark associated SGD and bacteria activity	
Site A	Eckernförde Bay, Germany	Whiticar 2002	pockmark associated SGD and methane	
Site A	Eckernförde Bay, Germany	Kaleris et al., 2002	SGD modeling	0.1 (FW)
Site A	Eckernförde Bay, Germany	Marczinek & Piotrowski 2002	source of groundwater	
Site A	Eckernförde Bay, Germany	Schlüter & Sauter, 2004	pockmarks SGD budget Rn	0-3 (FW)
Site A	Eckernförde Bay, Germany	Hoffman et al., 2020	pockmarks associated SGD methane	
Site B	Wismar Bay, Germany	Schafmeister & Darsow, 2004	groundwater modeling	0.2 (FW)
Site B	Meschendorf, Germany	Lipka et al., 2018	Springs at beach rich in Iron	
Site C	Hütelmoor, Germany	Schreiber et al., 2021	groundwater modeling	
Site C	Hütelmoor, Germany	Racasa et al., 2021	SGD associated Peatland	
Site D	Gulf of Gdańsk, Poland	Falkowska & Piekarek-Jankowska 1999	Anomalies in the water column	
Site D	Gulf of Gdańsk, Poland	Idczak et al., 2020	Pockmark-associated SGD and methane	
Site D	Puck Bay, Poland	Piekarek-Jankowska 2016	SGD fluxes and composition, water isotopes	0.4 (FW)
Site D	Puck Bay, Poland	Szymczycha et al., 2012	SGD associated nutrients fluxes	3-22 (FW + SW)
Site D	Puck Bay, Poland	Szymczycha et al., 2013	SGD-associated mercury fluxes	
Site D	Puck Bay, Poland	Szymczycha et al., 2014	SGD-associated carbon fluxes	

Site D	Puck Bay, Poland	Szymczycha et al., 2016	SGD-associated metal fluxes	
Site D	Puck Bay, Poland	Szymczycha et al., 2020	SGD associated nutrients and farma-ceuticals fluxes	
Site D	Puck Bay, Poland	Kotwicki et al., 2014	SGD impact on the meiofauna	10-150 (FW + SW)
Site D	Puck Bay, Poland	Donis et al., 2017	SGD impact on biogeochemistry porewaters	86 ±16 (FW + SW)
Site D	Puck Bay, Poland	Kłostowska et al., 2019	SGD fluxes and hydrochemistry	156-242 (FW + SW)
Site D	Puck Bay, Poland	Matciak et al., 2015	Salinity anomalies water column	
Site E	Gulf of Finland	Viventsova & Voronov 2003	Groundwater discharge and quality	0.1 (FW)
Site E	Hanko Bay, Finland	Virtasalo et al., 2019	pockmarks associated SGD	
Site E	Hanko Bay, Finland	Luoma et al., 2021	groundwater flow model	
Site E	Hanko Bay, Finland	Ikonen et al., 2022	SGD impact mixing processes stable isotopes	
Site F	Forsmark, Sweden	Krall et al., 2017	SGD fluxes - Ra mass balance	0.3-5.9 (FW + SW)

The contribution of SGD has also been investigated in a coastal peatland in Germany, Hütelmoor (Figure 5 – Site C) (Jurasinski et al., 2018; Racasa et al., 2021; Schreiber et al., 2021). Fluids originating from peatlands are typically enriched in dissolved organic matter, which can affect the geochemical budgets of the Baltic Sea coastal waters (Racasa et al., 2021).

In Puck Bay (Figure 6 – Site D), a lowered bottom water salinity was observed almost across the whole of Puck Bay, indicating an extended impact by SGD (Matciak et al., 2015). Measurements of SGD and their associated chemical fluxes were estimated for different areas in Puck Bay. Considering the recirculated SGD in the Puck Bay, the discharge can be higher than the river runoff (Kłostowska et al., 2019). As further observed by direct measurements of SGD, even at low flow rates of fresh SGD an impact on the material budgets in the Baltic Sea was detected (Szymczycha et al., 2012, 2016, 2020). Additionally, an impact of SGD on the meiofauna community was observed by Kotwicki et al. (2014). Donis et al. (2017) evaluated the impact of SGD on the porewater gradients of the sandy sediments. In the Gulf of Gdańsk, a pockmark associated with SGD was recently assessed by Idczak et al. (2020).

In the northern region of the Baltic Sea, groundwater discharge to the Gulf of Finland (Figure 6 – Site 5) was estimated by Viventsova & Voronov (2003). Pockmarks showing

different degrees of SGD were found in Hanko bay, southern Finland (Figure 5-Site E), impacting the geochemical aspects of the marine sediments (Virtasalo et al., 2019; Ikonen et al., 2022). In the Gulf of Bothnia (Figure 6 – Site F), one study quantified the fresh and saline SGD based on a Ra isotope mass balance (Krall et al., 2017).

1.5 Open research questions

SGD itself is a complex component at the land-ocean interface. First, SGD is most of the time not visually apparent, such as river; therefore, measuring SGD is still challenging even with modern analytical techniques available. Second, coastal aquifers, mixing zones, and surface sediments are chemically reactive; therefore, the transport behavior through these systems differs from the one predicted by a simple fresh-seawater mixing process. For example, processes such as ion exchange, redox reactions, mineral dissolution and precipitation mostly under impact by biological catalysis may have to be considered.

The catchment area of the Baltic Sea (Figure 6), and the coastal zone have a heterogeneous hydrogeological composition. Moreover, especially in the southern Baltic Sea, mud and sand sediments overlay the aquifers, and diagenesis influences the overall composition of the water entering the coastal zone. Therefore, a better understanding of the chemical reactions within the subterranean estuary and the benthic-pelagic coupling is needed to quantify the SGD-chemical fluxes into coastal waters. Furthermore, the salinity gradient between surface waters and (fresh) groundwaters is less pronounced compared to, for instance, the North Sea (Seibert et al., 2021), in particular, in the northern part of the Baltic Sea.

Theoretically, the amount of water from rivers is much higher; however, the discharge of chemical elements from SGD can be comparable to or even higher than that from river discharge (Kwon et al., 2014; Luijendijk et al., 2020). A conceptual understanding of the processes controlling the hydrochemistry of SGD and their stability is necessary to characterize the spatial-temporal dynamic of fluxes in coastal waters.

Last, compared to other areas of the world only a few SGD studies have been carried in the Baltic Sea area (Figure 6, Table 1). However, SGD would be expected to occur wherever a positive hydraulic gradient between groundwater and sea exists, and it is

important to place the Baltic Sea on the overall picture of SGD contribution/influence to the oceans.

1.6 Aims of the present study

A leading hypothesis of this study is that ***the contribution of SGD to coastal waters in the Baltic Sea is influenced by hydrogeochemical processes in the mixing zone that result on regionally distinct SGD signatures from each other, and differs from landbase groundwaters and surface waters entering the coastal zone.*** In order to test the hypothesis, SGD was evaluated in different coastal regions along the Baltic Sea where the presence of SGD has been previously recognized. This study focuses on the potential impact on surface sediments and water columns and compares the interfacial zones with the open Baltic Sea, regional groundwaters, and rivers entering the coast.

The objectives of this study are in more detail as follows:

- To identify and estimate potential SGD fluxes using (isotopic) geochemical tracers;
- To estimate the composition of SGD and compare it with potential fresh water sources;
- To evaluate how aquifer lithology and coastal sedimentology can impact water-microbe-rock interactions modifying the SGD composition;
- To evaluate the impact of SGD on sedimentary porewater gradients;
- To investigate the role of early diagenesis on the composition of SGD finally discharging into the coastal bottom waters;
- To infer the consequences of chemical fluxes associated with SGD for coastal waters of the Baltic Sea.

1.7 Study sites

The present study explores different sites along the coastal Baltic Sea: Wismar Bay and Warnow River, located on the coastline of Germany; Hanko Bay, located on the coastline

of Finland; and the Gulf of Gdańsk/Puck Bay, located on the coastline of Poland (Figure 6).

The Baltic Sea is a young shelf sea in northern Europe and the largest brackish water basin in the world. It has been connected to the North Sea and the North Atlantic since the Litorina transgression about 8000 years ago (Harff et al., 2011; Jurasinski et al., 2018).

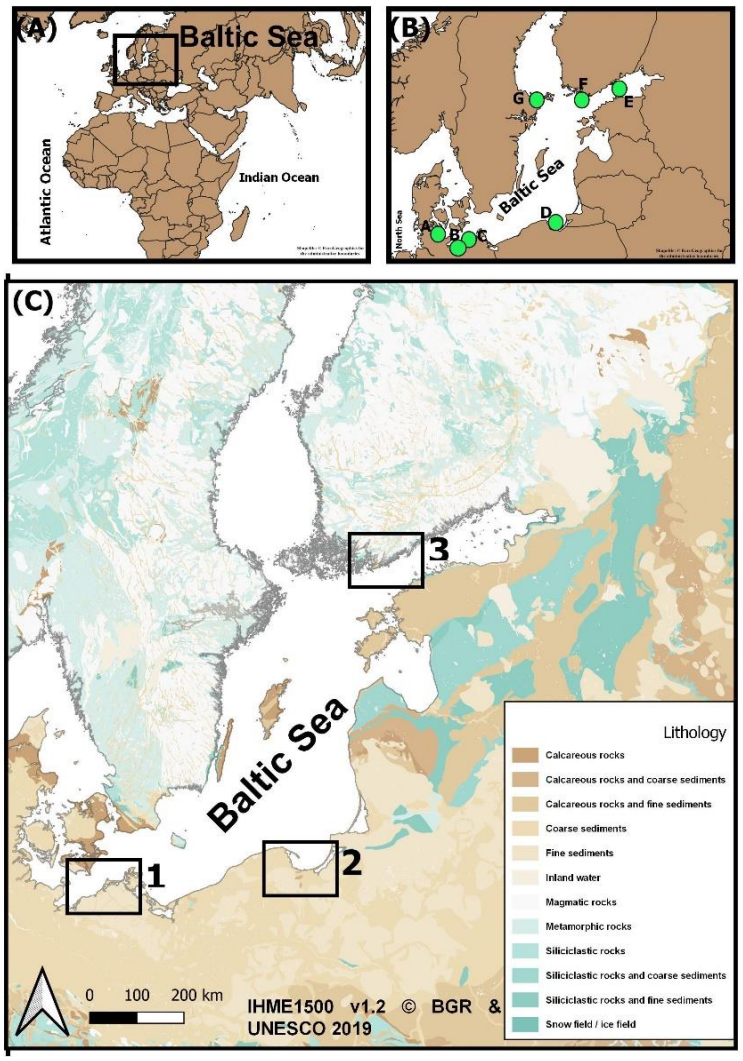

Figure 6 – (A) Map showing the location of the Baltic Sea. (B) Map of the Baltic Sea showing some of the SGD sites which are explained in detail in the Table 1. (C) Map of the Baltic Sea showing the lithology and the study locations. Source shapefiles:(A, B) @EuroGeographics (C)UHME1500 v1.2 BGR UNESCO 2019.

The Baltic Sea is a tideless inland sea covering almost 420.000 km^2, and a coastline of 8.000 km. Its drainage area is about four times its surface area (HELCOM, 2018; Carstensen et al., 2020). The mean river runoff is 15609 m^3 s^{-1} (Donnelly et al., 2014),

constituting about 2% of the total water volume of the Baltic Sea. Moreover, the drainage area of the Baltic Sea is densely populated, industrialized, and is subject to intense anthropogenic activities (Rana et al., 2021), thus eutrophication is one of the most evident pollution problems in the Baltic Sea (Struck et al., 2000).

The Warnow River, located in the southern Baltic Sea (Figure 6-Site 1), has a length of 155 km and has a drainage area of about 3280 km^2, with a long-term average discharge of 12.3 m^{-3} s^{-1}. It is characterized by a high load of nutrients (Pagenkopf, 2001; Bitschofsky & Nausch, 2019).

Wismar Bay is a coastal embayment in the southern Baltic Sea (Figure 4-Site 1) composed of Quaternary glaciofluvial sands and intercalated tills (Prena, 1995; Schafmeister & Darsow, 2004). The maximum water depth is 10 m, where muddy sediments are prevalent, while the shallow parts are dominated by sandy sediments (Prena, 1995). A port is located on the eastern side of the bay, in the town of Wismar, and ship navigation to the open Baltic Sea via an about 27 km long channel has been artificially created (VSW, 2018).

The Gulf of Gdańsk, Poland, is also located in the southern part of the Baltic Sea (Figure 6 - Site 2). The surface area of the Gulf is 4940 $km^{2,}$ and the mean depth is 59 m. The surface sediments are dominated by clays, fine-grained sands, silt fraction, and clayey silty (Idczak et al., 2020). In the western part of the Gulf of Gdańsk, the Polish Hel Peninsula forms a semi-enclosed basin called Puck Bay. The Hel Peninsula, which developed during the Holocene, separates Puck Bay from the sea. The bay has a total area of 359.2 $km^{2,}$ and it is divided into two parts: the outer Puck Bay, with an average depth of 20.5 m, and the inner bay, with an average depth of 3.1 m, which is also called the Puck Lagoon (Matciak, et al., 2015). The outer Puck bay comprises diverse sediments from fine sands to clay cliffs. In contrast, the inner Puck Bay has a relatively constant grain-size distribution dominated by fine and medium-grained sands (Kłostowska et al., 2019).

Hanko Bay, Finland, is located in the Gulf of Finland (Figure 6 – Site 3), and the study site is characterized by a sandy beach and a sandy shore platform that extends 100-250 m

seaward. Approximately twenty pockmarks (including those impacted by SGD) have been identified in the area (Virtasalo et al., 2019).

1.8 Methodological approach

The different methodological approaches explored in this thesis vary from small to larger scales, and include a range of approaches wrt. sampling techniques and both *in situ* and laboratory based measurements. The studies in Chapters 2- 4 provide a qualitative and quantitative interpretation of mineralization processes by analyzing solid sedimentary phases and porewaters gradients. The chosen sites were in areas generally known to be under SGD impact (Table 1), and sites with different degrees of SGD impact were included. To determine the biogeochemical processes on early diagenesis without modulation by SGD, reference sites were investigated using the same set of methods. Surface waters were evaluated to identify and quantify the impact of SGD on a regional scale and provide a quantitative estimate based on Ra isotope distribution. Surface waters at the land-sea boundary were also studied as potential fresh water endmembers via estuaries to the coastal waters.

In the Wismar Bay (Figure 6 – Site 1), the fieldwork took place during the spring and summer of the year 2019, and surface water samples were obtained from 47 stations across the bay. Furthermore, short sediment cores (n=6) were retrieved from different areas, including the major ship channel. Along the beachline, porewater samples were collected at five different sites. In addition, four fresh water streams draining into the Wismar Bay were sampled in the FW-SW mixing zone.

In the Gulf of Gdańsk and the Puck Bay (Figure 6 – site 2), a ship-based campaign took place in October 2019, and 40 water samples were collected. In addition, sediment cores (n=6) were retrieved. In the inner Puck Bay, an additional campaign was carried out in June 2021, focusing on SGD-impacted nearshore sites. Additionally, groundwater from wells and rivers were also sampled. In this study, the newly collected data were combined with data from earlier investigations between 2009 and 2011.

In Hanko Bay, Finland (Figure 6 – Site 3), seawater, sediment, and porewater samples were collected in September 2019. At that time, two groundwater wells were also sampled.

In the Warnow River (Figure 6 – Site 1), 25 sites from its source until it reaches the estuary were sampled in April 2019. Moreover, monthly campaigns (2018-2021) were carried out at the boundary between the fresh water part and the estuary under impact of mixing with the brackish Baltic Sea. The newly collected data from this study were combined with data derived within a MSc project (Rach, 2018) from 2017.

At each campaign on the coastal site, surface water was collected via submersible pumps and Niskin bottles. Water aliquots were immediately filtered (0.45 µm membrane filters), transferred into different tubes, and adequately conditioned for further laboratory analyses. Surface water from the rivers was collected using buckets and telescopic samplers. Groundwater was sampled in collaboration with the groundwater supply company. Additional shallow groundwater was sampled by pumping water from permanent piezometers. Porewater was extracted from shoreline sites using a push point sampler (MHE products) and a peristaltic pump. Sediment cores were collected with a Gemax corer. The sediment cores were sliced for the solid phases, and a parallel core was used for porewater extraction.

Table 2 presents the data generated during this study between 2018-2022 for the respective study site and briefly explains the methodology. A more detailed explanation of the methods can be found in the respective chapter.

Table 2 - Short overview of the parameters and their methodology obtained during this study.

Parameter		Measurement	Study site
Physico chemical parameters	water	Hand held devices (Hach, Schott)	Wismar Bay, Puck Bay, Hanko Bay and Warnow River
Major elements	water	ICP-OES 6400	Wismar Bay, Puck Bay, Warnow River
Trace elements	water	ICP-OES 6400	Wismar Bay, Puck Bay, Warnow River
Nutrients	water	QuAAtro nutrient ana-lyzer (SEAL Analytical)	Puck Bay, Warnow River, Hanko Bay
H_2S	water	Photometry	Wismar Bay and Puck Bay,
DIC	water	CF-irmMS	Wismar Bay, Puck Bay, Hanko Bay, Warnow River
δ^{13}C-DIC	water	CF-irmMS	Wismar Bay, Puck Bay, Hanko Bay, Warnow River

δ^{34}S-SO4	water	CF-irmMS	Warnow River
δ^{18}O-SO4	water	CF-irmMS	Warnow River
δ^{18}O-H2O	water	Picarro	Wismar Bay, Puck Bay, Warnow River
δ^{2}H-H2O	water	Picarro	Wismar Bay, Puck Bay, Warnow River
Ra isotopes	water	RaDeCC	Wismar Bay, Puck Bay, Warnow River
Water content	sediment		Wismar Bay
Grain sise	sediment	Mastersizer 3,000	Wismar Bay
Total carbon	sediment	Elemental Analyser EuroEA 3052	Wismar Bay, Puck Bay
Total nitrogen	sediment	Elemental Analyser EuroEA 3052	Wismar Bay, Puck Bay
Total sulfur	sediment	Elemental Analyser EuroEA 3052	Wismar Bay, Puck Bay
Total inorganic carbon	sediment	Elemental Analyser EuroEA 3052	Wismar Bay, Puck Bay
Total Mercury	sediment	DMA-80 analyzer	Wismar Bay, Puck Bay
Extractable Fe	sediment	HCl extraction ICP-OES 6400	Wismar Bay
Extractable Mn	sediment	HCl extraction ICP-OES 6400	Wismar Bay
Extractable Pb	sediment	HCl extraction ICP-OES 6400	Wismar Bay

1.9 Main results from the enclosed published papers and submitted manuscripts.

Chapter 2 shows freshwater sources for the Wismar Bay in the southern part of the Baltic Sea, Germany. The development of gradients of different elements, water isotopes, and higher radium activities towards the open Baltic Sea indicates the leaking of fresh groundwater along the shoreline. In the central part of Wismar Bay, freshening was found at 50 cmbsf for selected sediment pore waters. The upward transport of ground water impacted the development of chemical gradients and potentially increased benthic fluxes. In addition, the study shows that the SGD site is located in the major artificial channel prepared for ship movement. This emphasizes that the coastal aquifer is shallow and that anthropogenic activities in the coastal areas can impact the benthic-pelagic coupling, especially through SGD. Dredging activity also had an impact on porewater gradients and organic matter mineralization due to the remobilization of sediments. The acoustic images suggested the potential for many other sites with different routes for SGD throughout the bay.

Chapter 3 presents the results from surface water gradients and acoustic imagery that SGD is a common phenomenon in the whole bay and is also associated with pockmarks structures. Estimated water fluxes were highly variable, ranging from 0 up to 301 L m^2 $d^{-1,}$ including both saline and fresh water. Based on seepage meter applications, the fresh component of SGD would represent a maximum of 20% of the total flux of SGD. The fresh water composition of SGD was characterized and comparable to nearby rivers and groundwaters. Moreover, it was observed that SGD is a mixture of groundwater of different ages and originating from different geological periods. When comparing different lithologies, higher SGD fluxes were found for sandy sediments when compared to muddy sediments. In contrast, benthic fluxes were higher on muddy sediments. This is related to the relative importance of diagenesis on the surface sediments in supplying chemical elements to the surface waters. Gradients of $\delta^{13}C_{DIC}$ responded to different processes on the sandy sites, such as remineralization, mixing, methanogenesis, and methane oxidation. On sites dominated by sandy sediments, SGD was much more pronounced, and it was observed that the upward groundwater flow increased the fluxes of elements at the sediment-water interface, when compared to sites not impacted by SGD.

Chapter 4 shows the impact of SGD on both geochemical and microbial processes in pockmarks. Pockmarks had a strong upward flow of freshwater, which pushed the elements to the surface of the sediments. Apparently, SGD prevented organic matter accumulation on pockmarks, resulting in a low accumulation of nutrients and DIC in the sediment porewater compared to a pockmark not impacted by SGD. The lack of SGD allowed fast organic matter deposition and, therefore, a higher accumulation of products from remineralization of organic matter. Therefore, although there was no SGD impact, the higher integrated depth fluxes of elements were higher in these pockmarks not impacted by SGD. However, the fluxes from the non-SGD impacted pockmark represent internal cycling of elements, while the fluxes from the SGD impacted pockmarks represent external new element fluxes into the coastal waters. Groundwater influenced the microbial community structure of the active pockmarks, where populations of groundwater origin were found.

Chapter 5 shows that in a surface water system (Warnow River) the composition is controlled by in situ processes, exchange with the atmosphere, diffuse groundwater, contribution from tributaries, and internal processes. On a seasonal trend the composition was strongly impacted by the blooms during spring. The Warnow River was shown to be a source of different elements to the estuarine waters, especially DIC, and the fluxes seem to vary with the season, due to changing biological pelagic and benthic activity.

Chapter 6, a review paper, focuses on the aspects of subterranean estuaries on a regional scale, displaying the importance of defining the local composition to estimate the real effects of their products on coastal systems. Groundwater from land undergoes chemical reactions within the subterranean estuary, influencing the groundwater water (SGD) finally discharging into the coastal waters. Further current methodologies encompassing geochemical tracers, biological indicators, geophysical methods, hydrological modeling and remote sensing are described. In the end the review highlights that the research is at the stage where it is necessary to focus on an interdisciplinary study to understand the local and regional processes for advancing our knowledge of the land-sea interface. The review is the perfect foundation for the importance of the previous chapters, which are focusing on local studies, applying a multi-method approach.

Thesis outline and personal contributions of the cumulative dissertation

(Eigenanteil bei kumulativen Dissertationen)

This dissertation is organized into seven chapters. **Chapter 1** is a general introduction to the subject and gives a general context for the scientific investigations. It summarize the main results obtained in the combined scientific publications and manuscripts. **Chapter 2** represents a first-author paper. **Chapters 3 and 5** were submitted to international scientific journals (therefore, following the review process, their final published version may differ from the manuscripts presented here as chapters). The publications given in **Chapters 4 and 6** were published with contributions from the candidate as a co-author. **Chapter 7** summarizes the most important results and conclusions of the submitted dissertation, and future research directions are formulated as an outlook.

The chapters are followed by Declaration/ Erklärung, the candidate's CV, a list of publications, and presentations on international scientific conferences and workshops during the time of the doctoral study, acknowledgments, funding information, and an appendix close this PhD thesis.

Chapter 2 A Multi-Tracer Study of Fresh Water Sources for a Temperate Urbanized Coastal Bay (Southern Baltic Sea)

By Cátia Milene Ehlert von Ahn, Jan C. Scholten, Christoph Malik, Peter Feldens, Bo Liu, Olaf Dellwig, Anna-Kathrina Jenner, Svenja Papenmeier, Iris Schmiedinger, Mary A. Zeller and Michael Ernst Böttcher

Published on 15 October 2021 in Frontiers in Environmental Science (Section Biogeochemical Dynamics)

doi: 10.3389/fenvs.2021.642346

The doctoral candidate prepared together with the supervisor (MEB) and JCS the concept and design of the study, carrying out field campaigns (with JCS and PF), part of the analytical measurements, and provided data visualization and interpretation. The first draft of the manuscript was written by the PhD candidate with minor contributions from MEB, and later edited by all co-authors.

Chapter 3 Submarine groundwater discharge into a semi-protected coastal bay of the southern Baltic Sea: A multi-method approach

by Cátia Milene Ehlert von Ahn, Olaf Dellwig, Beata Szymczycha, Lech Kotwicki, Jurjen Rooze, Rudolf Endler, Peter Escher, Iris Schmiedinger, Jürgen Sültenfuß, Magdalena Diak, Matthias Gehre, Ulrich Struck, Susan Vogler and Michael Ernst Böttcher

This manuscript was submitted to Science of the Total Environment in November 2022.

The original concept of the study (leading to field and analytical results in 2009-2011) was formulated by MEB and field work as geochemical analysis of these data were carried out by some of the co-authors (OD, MEB, BS, SV, RE, US). The PhD candidate prepared together with MEB the concept of the sampling campaings in 2019 and 2021, carrying out the sampling during the field campaings and later part of the analytical measurements in 2019-2021. The PhD candidate combined the existing previous data set and carried out formal analysis, and visualization and interpretatiob of all data. The first draft of the manuscript was written by the PhD candidate with minor contributions from MEB. The text was later edited by all co-authors.

Chapter 4 Impact of submarine groundwater discharge on biogeochemistry and microbial communities in pockmarks

by Lotta Purkamo, Cátia Milene Ehlert von Ahn, Tom Jilbert, Muhammad Muniruzzaman, Hermann W. Bange, Anna-Kathrina Jenner, Michael Ernst Böttcher, and Joonas J. Virtasalo

Published on 21 July 2022 in Geochimica et Cosmochimica Acta.

doi.org/10.1016/j.gca.2022.06.040

The PhD candidate was invited to participate in the field campaign, carried out part of the analytical measurements, and contributed to the manuscript's first draft, focusing on the biogeochemical aspects.

Chapter 5 Spatial and temporal variations in the isotope hydrobiogeochemistry of a managed river draining towards the southern Baltic Sea

by Cátia Milene Ehlert von Ahn, Michael Ernst Böttcher, Christoph Malik, Benjamin Rach, Julia Westphal, Carla Nantke, Anna-Kathrina Jenner, Rhodelyn Saban, Iris Schmiedinger

This manuscript was submitted to Geochemistry in December 2022.

The PhD candidate contributed to the study's conceptualization based on an original concept by MEB and JW. The PhD candidate carried out the field campaings between 2018 and 2022, and part of the analytical measurements of samples taken during these campaings. The PhD candidate combined the new data with the previous measurements carried out within a MSc thesis (BR) in years 2017 and 2018, and a BSc thesis (CM) in year 2019, and carried out formal analysis, data visualization and interpretation. The first draft of the manuscript was done by MEB and the PhD candidate and edited by all co-authors.

Chapter 6 A State-Of-The-Art Perspective on the Characterization of Subterranean Estuaries at the Regional Scale

Nils Moosdorf, Michael Ernst Böttcher, Dini Adyasari, Ercan Erkul, Benjamin S. Gilfedder, Janek Greskowiak, Anna-Kathrina Jenner, Lech Kotwicki, Gudrun Massmann, Mike Müller-Petke, Till Oehler, Vincent Post, Ralf Prien, Jan Scholten, Bernhard Siemon, Cátia Milene Ehlert von Ahn, Marc Walther, Hannelore Waska, Tina Wunderlich and Ulf Mallast

Published on 14 May 2021 in Frontiers in Environmental Science (Biogeochemical Dynamics section).

The original concept of this review article was set up by NM and UM with an initial revision by all co-authors. The PhD candidate contributed a chapter to the biogeochemical part in the section ob geochemical tracers.

_____ _____

Cátia Milene Ehlert von Ahn Prof. Dr. Michael Ernst Böttcher

Chapter 2. A multi-tracer study of fresh water sources for a temperate urbanized coastal bay (southern Baltic Sea).

frontiers in Environmental Science

ORIGINAL RESEARCH
published: 15 October 2021
doi: 10.3389/fenvs.2021.642346

A Multi-Tracer Study of Fresh Water Sources for a Temperate Urbanized Coastal Bay (Southern Baltic Sea)

Cátia Milene Ehlert von Ahn[1], Jan C. Scholten[2], Christoph Malik[1,3], Peter Feldens[4], Bo Liu[5], Olaf Dellwig[1], Anna-Kathrina Jenner[1], Svenja Papenmeier[4], Iris Schmiedinger[1], Mary A. Zeller[1] and Michael Ernst Böttcher[1,6,7]**

[1]Geochemistry and Isotope Biogeochemistry Group, Leibniz Institute for Baltic Sea Research (IOW), Warnemünde, Germany, [2]Institute of Geosciences, Kiel University, Kiel, Germany, [3]Department of Hydrogeology, UmweltPlan GmbH Stralsund, Stralsund, Germany, [4]Marine Geophysics Group, Leibniz Institute for Baltic Sea Research (IOW), Warnemünde, Germany, [5]Section of Marine Geochemistry, Alfred Wegener Institute Helmholtz Centre for Polar and Marine Research, Bremerhaven, Germany, [6]Marine Geochemistry, University of Greifswald, Greifswald, Germany, [7]Maritime Systems, Interdisciplinary Faculty, University of Rostock, Rostock, Germany

OPEN ACCESS

Edited by:
Henry Bokuniewicz,
The State University of New York (SUNY), United States

Reviewed by:
Aaron J. Beck,
GEOMAR Helmholtz Center for Ocean Research Kiel, Germany
Olivier Radakovitch,
Institut de Radioprotection et de Sûreté Nucléaire, France

***Correspondence:**
Cátia Milene Ehlert von Ahn
catia.vonahn@io-warnemuende.de
Michael Ernst Böttcher
michael.boettcher@io-warnemuende.de

Specialty section:
This article was submitted to Biogeochemical Dynamics, a section of the journal Frontiers in Environmental Science

Received: 15 December 2020
Accepted: 03 September 2021
Published: 15 October 2021

Citation:
von Ahn CME, Scholten JC, Malik C, Feldens P, Liu B, Dellwig O, Jenner A-K Papenmeier S, Schmiedinger I, Zeller MA and Böttcher ME (2021) A Multi-Tracer Study of Fresh Water Sources for a Temperate Urbanized Coastal Bay (Southern Baltic Sea). Front. Environ. Sci. 9:642346. doi: 10.3389/fenvs.2021.642346

Terrestrial surface waters and submarine ground water discharge (SGD) act as a source of dissolved substances for coastal systems. Solute fluxes of SGD depend on the ground water composition and the water-solid-microbe interactions close to the sediment-water interface. Thus, this study aims to characterize and evaluate the hydrogeochemical gradients developing in the fresh-salt water mixing zone of the Wismar Bay (WB), southern Baltic Sea, Germany. Sampling campaigns covering the WB, the fresh-salt water mixing zone at the beach of the WB shoreline, terrestrial surface and ground waters near the WB as well sediments pore water were carried out. In these different waters, the distribution of dissolved inorganic carbon, nutrients, major ions, trace elements, stable isotopes (H, O, C, S), and radium isotopes have been investigated. Enhanced concentrations of radium isotopes together with dissolved manganese, barium in the surface waters of the eastern WB indicated benthic-pelagic coupling via the exchange between pore water and the water column. Salinity, stable isotopes, and major ions in sediment pore water profiles identified the presence of fresh ground water below about 40 cmbsf in the central part of the bay. Geophysical acoustic techniques revealed the local impact of anthropogenic sediment excavation, which reduced the thickness of a sediment layer between the coastal aquifer and the bottom water, causing, therefore, a ground water upward flow close to the top sediments. The fresh impacted pore water stable isotope composition ($\delta^{18}O$, $\delta^{2}H$) plot close to the regional meteoric water line indicating a relatively modern ground water source. The calculated organic matter mineralization rates and the dissolved inorganic carbon sediment-water fluxes were much higher at the fresh impacted site when compared to other unimpacted sediments. Therefore, this study reveals that different fresh water sources contribute to the water balance of WB including a SGD source.

Keywords: urbanized coastal bay, submarine ground water discharge, subterranean estuary, hydrogeochemistry, stable isotope, radium isotope, acoustic survey, Wismar Bay

INTRODUCTION

Coastal regions are great of interest because they receive water and elements from the continents. Water drains the watershed towards the sea through surface water flow like rivers, coastal lagoons, and streams. In addition, ground waters may act as a further transport route for land-derived dissolved matter via submarine ground water discharge (SGD) (e.g., Johannes, 1980; Church, 1996; Burnett et al., 2003, Burnett et al., 2006; Moore 2010; Jurasinski et al., 2018).

A combination of the enhanced material transport and high pelagic productivity in coastal regions lead to an intensive benthic biogeochemical element recycling (Jørgensen and Kasten, 2006) and steep pore water gradients of, e.g., dissolved carbon species, nutrients, and major and trace elements to surface waters. SGD has been found to contribute to the overall oceanic water and element budget (e.g., Burnett et al., 2003; Santos et al., 2012), however, processes impacting the flux and associated solutes along the land-ocean continuum are considered as one of the unsolved problems in hydrology (Blöschl et al., 2019).

In contrast to rivers, where water discharge and their compositional variations are known in sufficient resolution and precision, the quantification of SGD entering coastal waters remains a challenge (e.g., Stieglitz et al., 2008; Rodellas et al., 2012; Douglas et al., 2020; Moosdorf et al., 2021). Therefore, more studies are needed combining different techniques to understand the dynamics in SGD and its role for water and element transfer on different scales (Burnett et al., 2006; Taniguchi, et al., 2019; Moosdorf et al., 2021; Rocha et al., 2021).

Common approaches to calculate SGD fluxes often rely on measurements of dissolved constituents in riverine and nearshore fresh ground water as endmembers, and assume conservative behavior of dissolved constituents across the mixing zone (Oberdorfer et al., 1990; Burnett et al., 2008; Rodellas et al., 2015; de Souza et al., 2021). However, due to the complexity of coastal aquifer mixing zones between ground water and sea water, it is a challenge to characterize the actual composition of solutions that finally discharge to the marine bottom waters (Cerdà-Domènech et al., 2017; Bejannin et al., 2020). This challenge is fostered by biogeochemical and associated physicochemical processes (e.g., mineralization of organic matter, ionic ad/desorption, mineral dissolution/precipitation) between fresh and saline pore water within the aquifer mixing zone that may lead to substantial changes in the composition of SGD-born element fluxes (e.g., Beck et al., 2007; Donis et al., 2017). These mostly redox-dependent processes in the subterranean estuary are more pronounced than those taking place in the oxic mixing zone of surface water estuaries (e.g., Moosdorf et al., 2021).

In many coastal areas, anthropogenic interventions may impact flow conditions and water balance (Stieglitz et al., 2007; Stegmann et al., 2011). For instance, dredging of canals in coastal areas may reduce the sediment cover on top of unconfined aquifers, thereby, enhancing the discharge of SGD and associated substances (Santos et al., 2008; Macklin et al., 2014; Teatini et al., 2017), or may promote salt water intrusions into aquifers (Moore, 1996). Moreover, an enhancement of coastal ground water exchange, e.g., caused by anthropogenic activities, may lead to an indirect enhancement of dissolved nutrient and carbon loads reflecting in changes in the biogeochemistry of surface waters (Lee et al., 2009).

Coastal areas of the southern Baltic Sea (BS) offer great opportunities to investigate the role of different fresh water inputs. Besides surface water inflows, SGD has been observed, for instance, in the Eckernförde Bay in the south-western BS (Whiticar and Werner, 1981; Schlüter et al., 2004). Other studies are focusing on the Puck Bay, in the southern BS (Jankowska et al., 1994; Szymczycha et al., 2012, 2020; Kotwicki et al., 2014; Donis et al., 2017; Böttcher et al., 2021) where significant discharge has been observed. The hydrogeology in these areas differs from those in the northwestern part of the BS, where multiple submarine fresh water sources were described that are only under minor impact by human activities (Krall et al., 2017; Virtasalo et al., 2019).

In the present study, investigations were conducted in the urbanized Wismar Bay (WB), southern BS (**Figure 1**). During a first survey carried out in 2012 along parts of the southern BS coastline comparably higher ^{224}Radium (^{224}Ra) activities were observed in surface waters of the WB (**Figure 2**). This suggested an enhancement of benthic-pelagic coupling, likely driven by SGD, which would agree with a tentative water balance for the WB (Schafmeister and Darsow, 2004). Moreover, the semi-enclosed WB is an interesting site to investigate inputs of water and substances, since the bay is under multiple anthropogenic impacts including port activities (VSW, 2018), making it similar to other modern coastal areas.

We combined a multi-isotope hydrochemical approach including a geophysical characterization of sedimentary structures to improve our understanding of fresh water sources into the WB. In addition, the biogeochemical processes taking place in the top sediments were modeled and investigated to understand the impact of SGD on their release of elements. The results show that different fresh water sources exist for the WB. SGD takes place at different areas through the bay, e.g., near the coastline, and in the central part of the bay. Anthropogenic activities, such as the creation of a navigation channel may cause a connection to unconfined aquifers and, therefore, promoting the exchange of water and associated elements with the WB bottom water.

METHODS

Study Area

The north-eastern part of Germany is characterized by a generally flat topography consisting of unconsolidated glacial sediments, humid climate conditions, urbanized cities, and often agricultural land use in the catchment basin. The present study was carried out in the WB (**Figure 1**), which is a coastal embayment in the southern BS, separated from the open BS by two shallow banks (Prena, 1995). Sediments in the bay are composed of quaternary glaciofluvial sands and intercalated tills (Schafmeister and Darsow, 2004). Maximum water depths of 10 m are in the western part of WB where muddy sediments are found, with

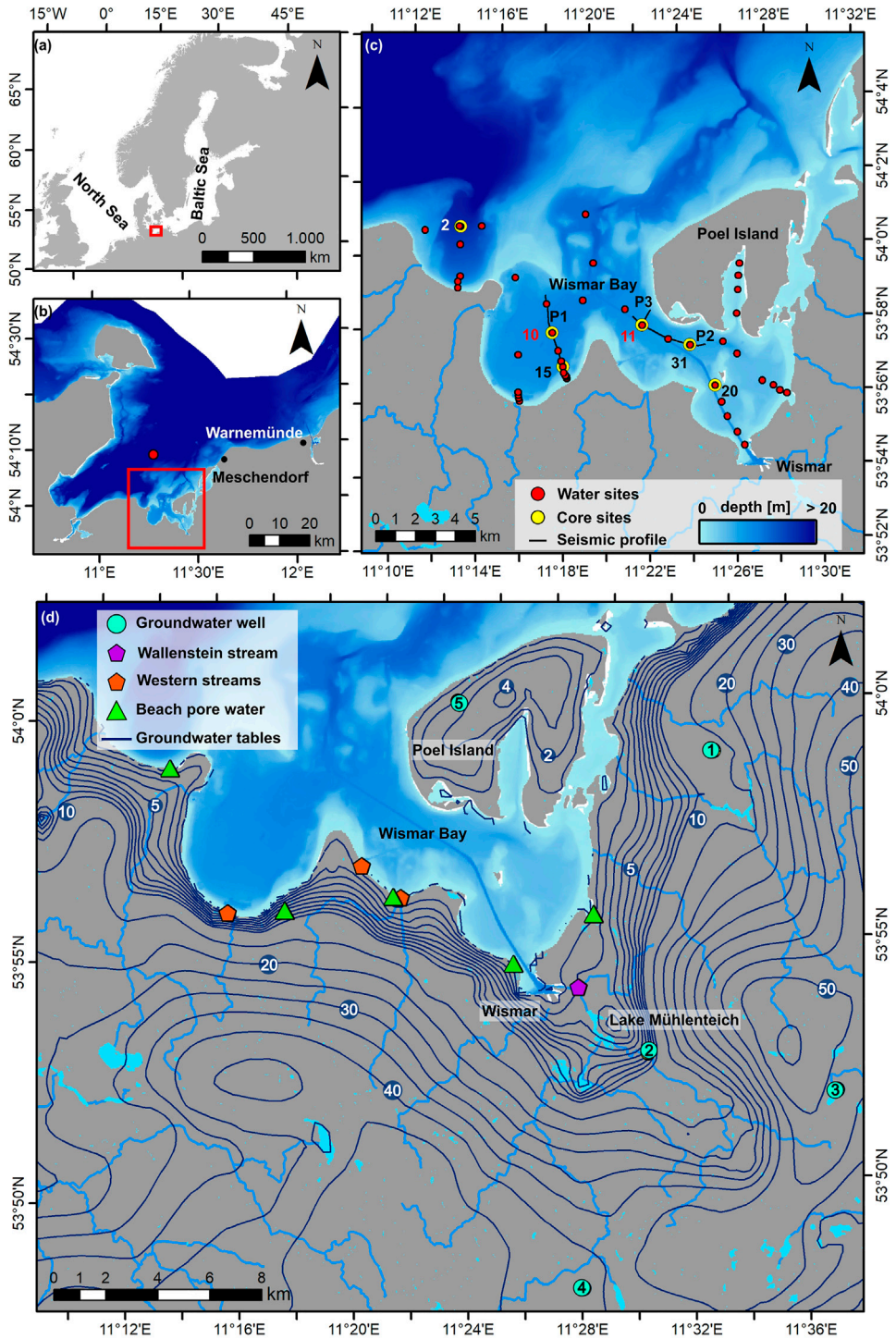

FIGURE 1 | Map of Baltic Sea and North Sea showing the location of the Wismar Bay **(A)**. Southern Baltic Sea, Germany shoreline showing the location of the Wismar Bay, including the adjacent investigated areas: Meschendorf, Warnemünde and, the surface water site at open Baltic Sea waters (red dot). Map of Wismar Bay with the sampling sites: surface water (red dots), sediment cores (yellow dots), the tracks of the seismic profiles (black line). The sediment cores are labeled, and the red numbers are the locations where SGD was found. **(C)**. Map of Wismar Bay and surrounding showing the ground water table (m), the streams discharging into the bay, and the lakes, as well as the ground water wells (cyan circles) also labeled, the sites at the western streams (orange diamond), Wallenstein stream (purple diamond), and the beach pore water sites (green triangle). The bathymetry highlighted the location of the navigation channel in the Wismar Bay. SOURCE: BSH, LUNG.

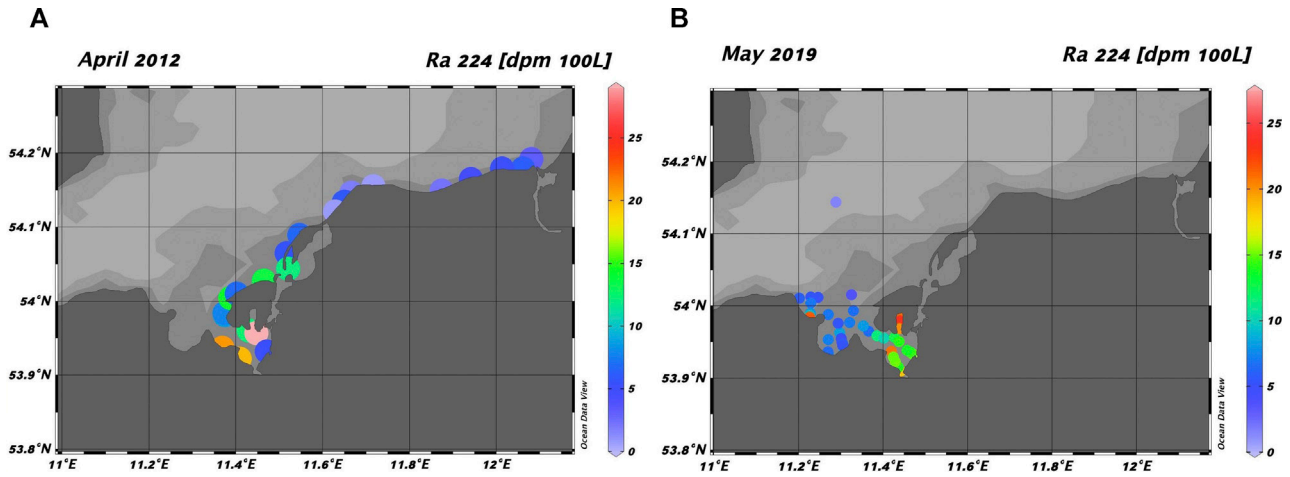

FIGURE 2 | Map of Germany coastline from WB to Warnemünde showing the activities of $^{224}Ra_{ex}$ in surface water from WB until Warnemünde carried out on April 2012 **(A)** and $^{224}Ra_{ex}$ in WB from the present study **(B)**.

sedimentary organic matter of up to 10% (Prena, 1995). Sandy sediments occur in the shallower areas.

The port of the town of Wismar is located on the east side of the bay, and ship navigation to the open BS is via an about 27 km long channel (**Figure 1**) (VSW, 2018).

The surrounding area of WB has three, each approximately 10 m thick aquifers in glaciofluvial sands of Saalian and Weichselian ages. The uppermost and partly phreatic aquifer is separated from the deeper aquifer by up to 20 m thick glacial till layers, which locally pinch out. Hydraulic gradients of up to 0.5% are slightly steeper than reported for other NE German areas (**Figure 1**, Schafmeister and Darsow, 2004, Jordan and Weder, 1995; Jurasinski et al., 2018).

Based on the regional flow dynamics, ground water is entering the WB area from 3 hydraulic height maxima, situated at least 10 km away from the WB (Hennig and Hilgert, 2007). Within the catchment area (about 200 km^2), a lake Mühlenteich and other small streams act as routes of surface water flow into the WB.

The Mecklenburg Western-Pomeranian mean annual ground water recharge is about 123 mm/a, estimated by Hilgert (2009) and Hennig and Hilgert (2007). In combination with a mass balance approach, this leads to a rough daily SGD estimation of 60.000 m^3 to the WB (Schafmeister and Darsow, 2004). Ground water recharge rates in the western part of the WB are lower compared to the SE part (Hilgert, 2009; LUNG, 2009).

Ship and boat based fieldwork took place during the spring and summer of 2019. Meteoric water inputs to WB during this period made up 6% of the annual precipitation 548 mm - Germany Weather Station - Wismar (DWD, 2020).

No large rivers drain into WB, but streams such as the Wallenstein located in the eastern part of the coast and the Tarnewitzer on the western part contribute to the fresh water inputs. The average discharge of both streams based on 10-years data are 0.76 and 0.39 $m^3\ s^{-1}$ respectively (Stalu-MV, 2019). In addition to these streams, smaller ones are also present, however, no hydrologic data are available for them.

Sampling Strategy

Sampling in the WB was performed using RV LITTORINA (L19-06) between 20 and 25 May, 2019. Surface water samples were collected at 47 sites spanning the whole bay (**Figure 1**), and additional bottom water samples at four sites (**Supplementary Figure S1**). For sampling in shallow waters (<5 m) a rubber boat was used (20 sites). At six sites, short sediment cores were retrieved for pore water and sediment analyses (**Figure 1**). The coordinates of all sites in the WB are compiled in **Supplementary Table S1**.

At sites exceeding water depths >3 m, CTD profiles were obtained and surface water samples (1 m) were sampled using a submersible pump. The water was pumped through a filter cartridge (1 µm pore size) into 100 L barrels. Water subsamples were taken via syringe and filtered (0.45 µm, cellulose acetate disposable filters, Carl Roth) for analyses of major and trace elements, dissolved inorganic carbon (DIC), $\delta^{13}C_{DIC}$, and stable isotopes of water ($\delta^{18}O$ and $\delta^{2}H$). Samples for DIC and $\delta^{13}C_{DIC}$ were filled without headspace into 12 ml Exetainer® tubes, previously cleaned with 2% HNO_3 washed, dried, and pre-filled with 100 µl saturated $HgCl_2$ solution. Samples for major and trace element analysis were filled into acid cleaned 2 ml reaction tubes and acidified with concentrated HNO_3 to 2 vol.% and samples for $\delta^{18}O$ and $\delta^{2}H$ analyses were collected in 1.5 ml vials glass sealed with a PTFE-coated septum cap. All samples were stored dark and cool until further analyses.

Water samples in the barrels were pumped, using a submersible pump through manganese-coated acrylic fibers at a flow rate of 1 L min^{-1} to quantitatively extract radium (Ra) isotopes. The fibers were washed to remove salts and partly dried for further measurements.

Short sediment cores were collected at six different sites in the WB (**Figure 1**) using a Rumohr-Lot (60 cm length, inner diameter: 10 cm). For pore water sampling, Rhizons (Rhizosphere Research Products, 0.12 µm pore size (Seeberg-Elverfeldt et al., 2005)) were inserted in pre-drilled holes of the plastic liner and attached to 10 ml plastic syringes. Salinity and pH of pore waters were

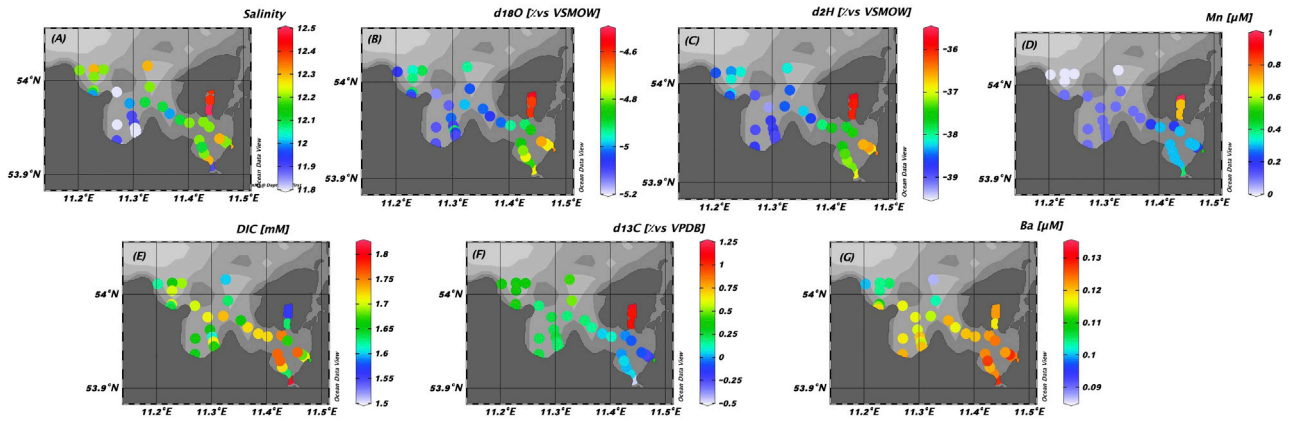

FIGURE 3 | Areal distribution of selected variables in surface waters of the Wismar Bay. Salinity **(A)**, $\delta^{18}O_{H2O}$ **(B)**, $\delta^{2}H_{H2O}$ **(C)** of water, dissolved Mn **(D)**, DIC **(E)**, $\delta^{13}C_{DIC}$ **(F)**, and Ba **(G)**.

measured immediately after recovery using a refractometer and hand-held pH meter (Schott handylab pH meter 11—calibrated with Mettler Toledo Buffer solutions), respectively. Pore water was fixed with 5% Zn-acetate solution for later analysis of total sulphide (H_2S) concentrations. Additional pore water samples were taken for major and trace elements, DIC, $\delta^{18}O$, and $\delta^{2}H$ of water, and preserved and stored as described above. Parallel sediment cores were (sites 10, 11, 15, 20, and 31), sliced at 2–4 cm intervals for geochemical analyses of sediments. Sediments at site 2 were sampled on the same core after pore water extraction. Sediment aliquots were transferred into 50 ml centrifuge tubes (Sarstedt) and kept frozen (−20°C) until further preparation.

Between July and August 2019 along the shoreline pore water samples were collected at five different sites in 0.4–1.8 m depth using push-point lances (MHE products) (**Figure 1**). In addition, four streams draining to the WB were sampled at the mixing zone with BS water. For major and trace elements, and stable isotopes analyses using the same methods as described for surface water of WB. In addition, samples for chloride (Cl) analysis were filled into 500 ml plastic bottles. pH, conductivity, and temperature were measured *in situ* using Schott handylab pH 11 and Schott handylab LF 11 devices. For Ra isotope measurements, 25 L of pore water was collected using a peristaltic pump, while 60 L of stream surface waters were collected and filtered through a 25 µm filter into pre-cleaned gallon containers for further filtration through the Mn fibers.

To identify the potential impact of SGD on coastal waters a pre-survey of Ra isotope distribution in surface water was carried in April 2021 along the shoreline between WB and Warnemünde (~50 km east of WB, **Figure 3**). Water samples for Ra measurements were taken at 23 sites, with 6 sites within WB and the remainder between WB and further east along the coastline (**Figure 3**). The sampling method is the same as described above.

The isotope-hydrochemical composition of ground waters emerging on a nearby coastal beach (Site Meschendorf–**Figure 1**) was considered for comparative purposes in the discussion of this study. The sampling was conducted in the same way as for the surface water campaign in the WB and took place in September 2018.

In addition, fresh ground water samples collected from monitoring wells located adjacent to the WB are presented for comparison purposes. Ground water sampling was carried out in 2014 and followed the protocol described by Jenner (2018). The ground water well at Poel Island (**Figure 1**) and the ground water well 2 are located in a confined aquifer with more than 10 m of soil layer above the filter screen. The other 3 ground water wells (1, 3, and 4) are located in an unconfined aquifer with sampling depths less than 5 m below the surface (Jenner, 2018).

Geophysical acoustic investigations of the subsurface sediments were carried out from July 29th to 31st 2019 using an Innomar SES96 parametric echo sounder mounted on the IOW research catamaran Klaashahn. Seismic data were collected at three frequencies, of which only the 8 kHz dataset is presented here. Results were corrected for ship movements using a motion sensor during data acquisition. The processing of the seismic data was done using Seismic Unix, which involved threefold stacking of the data for the signal to noise ratio improvement, and application of a time-varied gain. The time-depth conversion was calculated using a constant sound velocity of 1,500 m s^{-1}.

Analytical Methods

Water contents of the sediment samples were determined gravimetrically after freeze-drying (considering the water loss due to pore water extractions at Site 2). About 1 g of each sediment sample was pre-treated for grain size analysis by removing carbonate and organic matter using hydrochloric acid (HCl) and hydrogen peroxide, respectively to prevent the binding of the small particles. Grain size measurements in the range from 0.01 to 3.500 µm were performed using a Mastersizer 3,000 with a wet dispersion unit (Hydro EV; Malvern Panalytical). Grain size statistics (including the first mode) were calculated using the program GRADISTAT (Blott and Pye, 2001), applying the volume percentage data and a geometric graphical method modified after Folk and Ward (1957).

Freeze-dried sediments were analyzed for total carbon (TC), total nitrogen (TN), and total sulphur (TS) content with a CHNS Elemental Analyzer (Euro Vector EuroEA 3,052). The

combustion was catalyzed by V_2O_5, the resulting gaseous products were chromatographically separated and quantified via infrared spectrophotometry. Total inorganic carbon (TIC) was determined with an Elemental Analyzer multi-EA (Analytik Jena) after reaction with phosphoric acid 40% followed infrared spectrophotometry quantification of CO_2. The precision of the method were ±3, ±10, ±7.6, and ±4.3% for TC, TN, TS, and TIC respectively, using MBSS- (CNS) and OBSS-$CaCO_3$ (TIC) as in-house standards. The content of total organic carbon (TOC) was calculated from the difference of TC and TIC. The contents of total Mercury (Hg) were analyzed using a DMA-80 analyzer with a detection limit of about 0.15 μg kg^{-1}, as described by Leipe et al. (2013). The precision and accuracy of the measurement were ±8 and ±1.3%, respectively. The calibration was carried out with the 142R MBSS standards.

For the analysis of the acid extractable fraction of several metals (identified in the text with *) about 200 mg of freeze-dried and homogenized sediment was treated with 10 ml 0.5 M HCl agitated for 1 h (Kostka and Luther, 1994). The extracts were filtered with 0.45 μm disposable surfactant-free cellulose acetate membrane filters (Carl Roth), and analyzed by inductively coupled plasma optical emission spectrometry, ICP-OES (Thermo, iCAP, 7,400 Duo Thermo Fischer Scientific), after 10-fold dilution with 2% HNO_3 using external calibration and Sc as an internal standard. The international reference material SGR-1b (USGS) revealed precision and accuracy of better than 2.1 and 3.8%, respectively (Dellwig et al., 2019).

Major ions (Na, Mg, Ca, K, S) and trace elements (Ba, Fe, Li, Mn, Sr) in the water samples were analyzed by ICP-OES using matrix-matched external calibration (diluted OSIL Atlantic Sea water standard spiked with Ba, Fe, Li, Mn, and Sr) and Sc as internal standard. Precision and accuracy were checked with spiked SLEW-3 (NRCC) and were better than 4.7 and 7.6%, respectively.

Concentrations of H_2S were determined by the methylene blue method (Cline, 1969) using a Spekord 40 spectrophotometer (Analytik Jena). The chloride concentration of the water samples was determined by an electric potentiometric precipitation titration (Schott instruments), which utilizes the changing electrical potential difference of the solution by quantitative precipitation of Cl ions due to titration with 0.05 M $AgNO_3$. Analytical accuracy was constantly checked with the international reference standard OSIL Atlantic Seawater 35.

$\delta^{13}C_{DIC}$ values were determined as described by Winde et al. (2014) by means of continuous-flow isotope-ratio-monitoring mass spectrometry (CF-irmMS) using a Thermo Finnigan MAT253 gas mass spectrometer attached to a Thermo Electron Gas Bench II via a Thermo Electron Conflo IV split interface. Solutions were allowed to react for at least 18 h at room temperature before introduction into the mass spectrometer. The international calibration materials IAEA Ca carbonate standard and Solnhofer Plattenkalk were used for calibration of measured isotope ratios towards the V-PDB scale. $\delta^{18}O$ and $\delta^{2}H$ values of water were analysed with a CRDS system (laser cavity-ring-down-spectroscopy; Picarro L2140-I; Böttcher and Schmiedinger, 2021). The reference materials SLAP and VSMOW were used for calibration of measured isotope ratios towards the V-SMOW scale. All stable isotope results are giving in the δ-notation. The given '‰' values are equivalent to mUr (milli Urey; Brand and Coplen, 2012).

Ra isotopes (^{223}Ra, $t_{1/2}$ = 11.4d, and ^{224}Ra $t_{1/2}$ = 3.7d) were measured with radium-delayed coincidence counters (RaDeCC) (Moore and Arnold, 1996) within 3 days after sampling. After about a month, a further measurement was conducted for the determination of ^{224}Ra supported by ^{228}Th ($t_{1/2}$:1.9 years), this measurement is then subtracted from the initial ^{224}Ra to obtain the excess of ^{224}Ra activities ($^{224}Ra_{ex}$). Activities of ^{223}Ra, ^{224}Ra, and $^{224}Ra_{ex}$ were calculated and the expected error of the measurement is 12 and 7% for ^{223}Ra and ^{224}Ra respectively (Garcia-Solsona et al., 2008). The calibration of the detectors is done once a month using ^{232}Th with certificate activities. In this study, we do not discuss ^{223}Ra, but the data can be found in the **Supplementary Table S2**.

The isotope-hydrochemical analysis of the ground water from the wells was carried out by the department of "Strahlen und Umweltschutz" at the "Landesamt für Umwelt, Naturschutz und Geologie". As for methods used, all methods and DIN standards are given in **Supplementary Table S3**. The data was kindly provided by LUNG Güstrow and further details can be found at Jenner (2018).

Numerical Model

Steady-state modeling of pore water profiles was performed to assess the transport mechanism, i.e., diffusive or advective fluxes. The model further evaluates the essential geochemical reactions and the transformations rates. Net-release of a solute into the bottom water leads to positive transformation rates while net consumption results in negative transformation rates (Schultz, 2006).

Pore water sulphates (SO_4) and DIC concentration profiles were computed as a function of sedimentation rate, organic matter degradation, and diffusion rates using the reactive transport model described in (Meister et al., 2013). The following general equation was used:

$$\frac{\partial(\varphi C)}{\partial t} = -\frac{\partial(\omega\varphi c)}{\partial z} + \frac{\partial}{\partial z}\left(\frac{D_0}{\tau^2}\varphi\frac{\partial C}{\partial Z}\right) + \varphi\sum R_i \qquad (1)$$

where C is the concentration, t is time, ω is the sedimentation rate, z is the depth below seafloor, φ is the porosity, and D_0 is the diffusion coefficients corrected by tortuosity (τ^2), which was calculated according to Boudreau (1997) as $\tau^2 = 1–2\cdot\ln\varphi$. The mean sedimentation rate ω was taken as 2 mm yr^{-1} (Lampe et al., 2013) and an average porosity was taken as 0.88 derived from the sediment water content. The diffusion coefficients for SO_4 and DIC were calculated as 0.0236 and 0.0257 $m^2\,yr^{-1}$ respectively, based on the average temperature of 12°C and an average salinity of 13 (Boudreau, 1997).

Sources and sinks of SO_4 and DIC are stoichiometrically coupled to rates of organic carbon decay via the following simplified reaction for organoclastic sulphate reduction:

$$SO_4^{2-} + 2CH_2O \rightarrow HS^- + 2HCO_3^- + H^+ \qquad (2)$$

The organic matter decay rate R_G was followed by the reactive continuum (RC) model of Boudreau and Ruddick (1991).

$$R_G(t) = -\nu(a+t)^{-1}G(t) = -\frac{\nu a^{\nu}}{(a+t)^{\nu+1}}\frac{\rho_s(1-\varphi)G_0}{100\varphi M_C} \quad (3)$$

where the free parameters and a ν determine the shape of the initial distribution of organic matter reactivity. The parameter a describes the average life-time of the more reactive components of the spectrum whereas ν defines the shape of the distribution. The dry density of the sediment is ρ_s (ρ_s = 2.6 g cm^{-3}), M_C is the molecular weight of carbon (M_C = 12) and G_0 is the initial TOC upon sedimentation (wt%). Thus, the SO_4 reduction and DIC production rate can be given by $0.5R_G$ and R_G, respectively.

The isotopic composition was calculated from the measured ratios R and referred to the VPDB according to Hoefs (2018):

$$\delta^{13}C = \left(\frac{Rsample}{R_{VPDB}} - 1\right) \cdot 1000 \quad (4)$$

The absolute concentrations of [^{13}DIC] and [^{12}DIC] were computed by separated reaction-transport equations (**Eq. 1**) for each isotope. Negligible carbon isotope fractionation was assumed during organoclastic sulphate reduction (cf. Claypool and Kaplan, 1974). Therefore, this source of inorganic carbon was assumed to show the same isotopic composition as the organic source.

Initial conditions were 0 mM SO_4 and DIC at all depths. The computer domain was set to be 50 cm. The Dirichlet boundary condition was applied at both the sediment/water interface (z = 0 cm) and bottom (z = 50 cm) according to the observed data. All parameters used in the model are listed in **Supplementary Table S4**.

Data Presentation

The figures presenting the vertical profiles were created using Sigma Plot 10.0 software (Systat Software, Inc., United States). The concentration maps were plotted using Ocean Data View (Schlitzer, 2001). The study area map was created using the Qgis development Team.

RESULTS

Results of all chemical elements measured in the Wallenstein stream, western streams, beach pore water, fresh ground water from the wells, fresh surface water from springs in Meschendorf are listed in **Table 1**. To place these data in a context, the data of surface water and pore water from the WB were also compiled in this table. The parameters of these different waters were plotted against salinity to assess the behavior of the parameter along the salinity gradient and the contribution of mixing and biogeochemical processes (**Supplementary Figure S2**).

Water Composition

Surface Waters in the Wismar Bay

The salinity of the WB surface waters ranged between 11.8 and 12.5 (**Figures 3A**), which is in the range of previously observed (Prena, 1995). The WB water column was well mixed, showing a slight salinity increase in bottom waters at some sites (**Supplementary Figure S3**). All conservative elements followed expected trends by covarying with salinity.

The δ^2H_{H2O} and $\delta^{18}O_{H2O}$ varied between −35.7 and −39.3‰ and between −4.5 and −5.2‰, respectively. Heavier isotopic compositions were found in the sheltered eastern part of the bay, mainly near Poel Island. Towards the western part of the WB, the isotope values were lighter, but show a trend of decreasing values close to the coastline (**Figures 3B,C**).

In surface waters, DIC ranged from 1.5 to 1.8 mM (**Figure 3E**) and $\delta^{13}C_{DIC}$ varied between -0.5 and 1.1‰ (**Figure 3F**). We found a W-E trend increasing concentrations in DIC and an inverse relationship between concentrations and its stable isotope composition. Only the waters close to Poel Island showed the lowest concentrations and the highest $\delta^{13}C_{DIC.}$

The concentrations of manganese (Mn) and barium (Ba) varied between 0.03 and 0.1, 0.07, and 0.1 μM, respectively, (**Figure 3D,G**). The eastern area was characterized by higher concentrations of Mn and Ba compared to the western parts (**Figure 3E**).

The activities of $^{224}Ra_{ex}$ ranged between 3 and 28 dpm 100 L^{-1} with an average of 7 L dpm 100 L^{-1}, presenting also higher activities in the eastern area. The site located in open BS waters presented a ^{224}Ra activity of 1.5 dpm 100 L^{-1} (**Figure 2**).

Streams

The Wallenstein stream discharges into the eastern part of the bay and showed $\delta^{18}O_{H2O}$ and δ^2H_{H2O} values of −4.0‰ and −33.2‰, respectively, which were heavier than the other streams in the western part of the WB. All isotopic compositions plot below Local Meteoric Water Line (LMWL) established for the southern BS at Warnemünde (**Figure 4**) in contrast with the results for ground waters in the WB region that fall on LMWL (**Table 1**; **Figure 4**).

For a general characterization, the hydrochemical composition of the investigated waters is compiled in a Piper diagram (Piper, 1944) (**Figure 5**). Most of the streams can be characterized as Na-Cl, and one of them as CaMg-HCO_3 waters (**Figure 5**), with the Na-Cl type being impacted by mixing with BS water at the sampling site.

The western streams were enriched in DIC compared to the Wallenstein stream. The DIC concentration in the western streams reached 5.8 mM and the $\delta^{13}C_{DIC}$ values were around −13.2‰ whereas the Wallenstein stream had a concentration of 2.5 mM and a $\delta^{13}C_{DIC}$ value of 6.5‰.

The activities of $^{224}Ra_{ex}$ in the western streams (salinities 0.1–1.8) discharging to the western WB ranged from 7 to 24 dpm 100 L^{-1}, which is within the range of the activities measured in the WB surface waters. The activities for the Wallenstein stream were found to be slightly higher (36 dpm 100 L^{-1}).

Ground Water

Ground waters from the WB catchment are characterized by a water isotopic composition ranging from −8.6 to −8.3‰ ($\delta^{18}O_{H2O}$) and −58.8 to −56.7‰ (δ^2H_{H2O}), similar to the composition of the ground water escaping at the Site Meschendorf, which showed average values of −8.5 and 58‰ respectively (**Table 1**- springs; **Figure 4**).

TABLE 1 | Average, minimum, maximum, and number of samples of the WB surface water (WB), Wallenstein stream, small streams, beach pore water (PW), ground water (GW) from the wells near Wismar, GW from a well in Poel Island, springs located close to Wismar, sediment pore water (PW). The pore waters from the beach and from Wismar were extrapolated to 1 mM Na, which is the concentrations found in the fresh ground waters, and termed as central SGD and beach SGD.

Variables	Unit	WB	Wallenstein stream	Small streams	Beach pore water	GW well 1	GW well 2	GW well 3	GW well 4	GW well 5	Springs Meschendorf	PW st. 10 and 11	PW st. 2, 15, 20 and 31	Central SGD	Beach SGD
Salinity		12.1	7.2	1.7	5.5						0.1	13	14		
		11.8/ 12.6 (46)	(1)	0.1/1.8 (3)	3.1/10.2 (5)						0.1/0.3 (6)	1/15 (30)	12–17 (57)		
Cond.	mS. cm^{-1}		12.6	1.4	9.7	0.8	0.7	0.7	1.0	0.7	0.8				
			(1)	0.8/3.6 (3)	5.7/17.4 (5)	(1)	(1)	(1)	(1)	(1)	0.6/1.1 (6)				
pH		8.3	7.9	8.2	7.38	7.2	7.4	7.3	7.0	7.3	7.3	7.7	7.5		
		8.2/9.0 (17)	(1)	8.1/8.7 (3)	7.1/7.8 (5)	(1)	(1)	(1)	(1)	(1)	7.1/7.4 (6)	7.0/8.2 (30)	7.1/8.3 (57)		
Temp.	°C	14.2	23.7	21.0	20.3	10.2	10.2	10.2	10.9	10.0					
		11.7/20.0 (46)	(1)	16.5/23.5 (3)	19.9/24.7 (5)	(1)	(1)	(1)	(1)	(1)					
DIC	mM	1.67	2.5	4.9	8.6		6.1	5.5		5.4	6.1	7.1	3.5	6.4	13.4
		1.51/1.80 (49)	(1)	4.3/5.8 (3)	4.0/9.4 (5)	(1)	(1)	(1)	(1)	(1)	5.50/6.70 (6)	1.49/ 16.38 (29)	1.51/13.57 (55)	(1)	13.30/13.39 (2)
$\delta^{13}C_{DIC}$	‰ VPDB	0.21	-6.46	–13.23	–15.34	–13.77		–13.79	–14.24		–13.75	–9.29	–6.59	–6.63	–26.30
		–0.46/1.15 (49)	(1)	–13.92/ –10.95 (3)	–17.52/ –8.56 (5)	(1)	(1)	(1)	(1)	(1)	–14.4/–13.61 (2)	=–14.4/ 0.1 (29)	–13.4/0.2 (55)	(1)	–26.50/–26.10 (2)
$\delta^{18}O_{H2O}$	‰ VSMOW	–5.0	–4.0	–7.4	–6.1	–8.4	–8.3	–6.7	–8.4	–8.6	–8.5	–4.9	–4.78	–8.5	–7.14
		–5.2 /–4.5 (49)	(1)	–7.3/ –8.1 (3)	– 7.2/–5.2 (5)	(1)	(1)	(1)	(1)	(1)	–8.7/– 8.4 (4)	–7.2/–4.4 (29)	–5.15/–3.9 (55)	(1)	–8.34/6.26 (5)
$\delta^{2}H_{H2O}$	‰ VSMOW	–38.2	–33.2	–52.3	–43.8	–58.0	–56.7	–48.9	–57.3	–58.8	–57.7	–37.7	–36.4	–56.6	–49.4
		–39.3/–35.7 (49)	(1)	–55.4/ –51.5 (3)	–49.4/–39.3 (5)	(1)	(1)	(1)	(1)	(1)	–58.8/–57.2 (4)	–50.2/ 33.8 (29)	–39.5/–29.5 (55)	(1)	–55.35/–44.74 (5)
Cl	mM		124.5	25.1	74.3	1.21	1.30	0.79	0.99	1.32	0.53				
			(1)	1.45/26.30 (3)	39.40/ 165.09 (5)	(1)	(1)	(1)	(1)	(1)	0/0.66 (3)				
Na	mM	162.2	98.4	23.50	66.9	0.7	2.2	1.0	0.8	0.83	1.03	165.6	176.7	1.0	1.0
		150.5/169.2 (49)	(1)	1.35/36.5 (3)	23.7/142.4 (5)	(1)	(1)	(1)	(1)	(1)	0.9/1.1 (5)	30.9/ 207.4 (23)	148.7/244.2 (55)	(1)	(5)
Mg	mM	18.3	11.4	2.9	9.2	0.5	0.6	0.4	0.6	0.7	0.7	18.64	19.0	0.0	0.3
		17.1/19.9 (49)	(1)	0.7/5.6 (3)	3.0/16.9 (5)	(1)	(1)	(1)	(1)	(1)	0.6/0.9 (5)	2.4/21.8 (23)	16.7/24.2 (55)	–1	0/7.6(5)
Ca	mM	4.0	3.3	2.9	8.0	3.7	2.1	2.5	4.0	3.1	3.5	4.2	4.5	2.4	10.1
		3.7/4.1 (49)	(1)	2.6/3.1 (3)	2.8/14.2 (49)	(1)	(1)	(1)	(1)	(1)	2.7/4.8	3.0/5.3 (23)	3.7/5.6 (55)	(1)	2.6/38.9 (4)
K	mM	3.5	2.2	0.9	1.7	0.0	0.1	0.3	0.3	0.1	0.1	3.7	3.87	0.6	0.3
		3.3/3.7 (49)	(1)	0.1/2.2 (3)	0.6/3.4 (5)	(1)	(1)	(1)	(1)	(1)	0.1/ 0.2 (5)	1.2/4.2 (23)	3.3/5.4 (55)	(1)	0/2.7 (5)
SO_4	mM	9.9	5.8	0.7	4.4	0.6	0.2	0.5	2.3	1.0	1.5	0.0	10.0	0.0	1.0
		9.2/10.4 (49)	(1)	0.6/2.2 (3)	0.8/8.9 (5)	(1)	(1)	(1)	(1)	(1)	1.1/2.7 (5)	0/10.25 (23)	5.3/12.1 (55)	(1)	0/3.4 (5)
Si	µM	6.1	0.1	0.4	0.4						0.4	622.3	258.5	887.3	0.0
		4.4/10.6 (49)	(1)	0.2/0.5 (3)	0.1/0.5 (5)						0.3/0.4 (5)	6.8/ 756.28 (23)	6.2/685.5 (55)	(1)	(3)
P	µM	0	9.9	13.5	11.3						4.2	76.8	38.8	22.0	13.7
		0.0/0.0 (49)	(1)	6.6/284.7 (3)	4.1/22.6 (5)						2.3/5.3 (5)	1.7/269.4 (20)	4.2/89.2 (55)	(1)	4.9/185.0 (5)
Ba	µM	0.1	0.4	0.2	1.1	0.3	0.8	0.3	0.5	0.9	1.1	0.3	0.2	1.4	1.1
		0.1/0.1 (49)	(1)	0.2/0.6 (3)	0.2/2.9 (5)	(1)	(1)	(1)	(1)	(1)	0.8/2.0 (5)	0.12/1.79 (24)	0.1/1.3 (55)	(1)	0.4/7.7(5)
Fe	µM	0.1	1.6	1.1	1.3						55.6	0.7	0.3	10.2	2.1
		0.1/1.8	(1)	0.4/2.1 (3)	0.2/2.1						44.7/124.1 (5)	0.1/624.2 (23)	0.0–5.2 (55)	(1)	1.1/3.5 (5)
Li	µM	8.6	6.4	2.9	8.3						2.0	9.2	9.9100	5.8	4.8
		8.2/9.1 (46)	(1)	2.1/3.0 (3)	2.3/9.9 (5)						1.5/2.1 (5)	6.9/11.5 (23)	8.4/ 13.2 (55)	(1)	2.4/13.0 (5)
Mn	µM	0.1	3.5	2.6	12.0	0.0	0.0	0.0	0.0	0.0	3.0	2.3	1.9	4.2	17.4
		0.0/1.5 (46)	(1)	0.7/4.3 (3)	1.5/24.4	(1)	(1)	(1)	(1)	(1)	2.8/4.6 (5)	0.2/58.2 (23)	0.1/9.5 (55)	(1)	1.7/44.5 (5)
Sr	µM	32.0	21.6	9	28.7						5.6	34.2	35.6	6.9	9.9
		29.9/33.3 (49)	(1)	6.4/13.9 (3)	8.4/34.0 (5)						5.0/9.7 (5)	14.01/ 40.7 (23)	31.0/ 44.3 (55)	(1)	4.6/39.0 (5)
^{224}Ra	dpm $100L^{-1}$	8.01	36.2	15.6	362.2										
		2.8/27.4 (49)	(1)	6.8/24.3 (3)	25.8/ 547.1 (5)										
^{223}Ra	dpm $100L^{-1}$	0.9	0.9	0.4	10.6										
		0/1.7 (26)	(1)	01/0.6 (3)	0.5/18.0 (5)										
$^{224}Ra_{ex}$	dpm $100L^{-1}$	7.3	34.9	15.4	350.6										
		2.3/26.5 (49)	(1)	6.3/23.7 (3)	17.6/530.0 (5)										

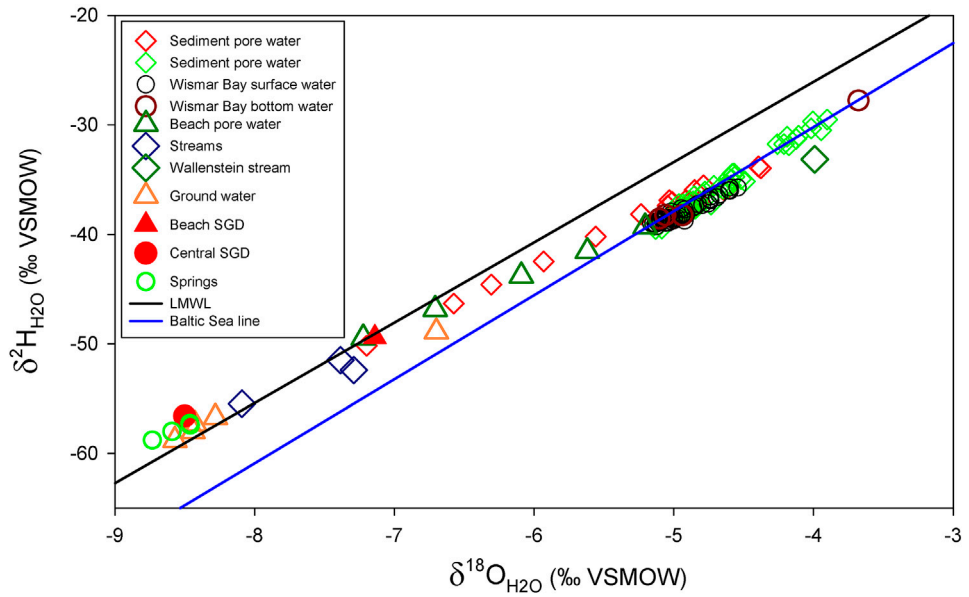

FIGURE 4 | Scatter plot of δ^2H_{H2O} versus $\delta^{18}O_{H2O}$ for sediment porewaters, both impacted (red diamonds) and non-impacted by SGD (green diamonds), Wismar Bay surface (black circles) and bottom (brown circles) waters, beach porewater (green triangles), streams (blue diamond), river (large dark green diamond), ground water (yellow triangle), Beach porewater extrapolated to 1 mM Na called Beach SGD (filled red triangle). The Local Meteoric Water line (LMWL) and the Baltic Sea surface water line from (Böttcher et al., 2020) are also presented.

The hydrogeochemical ground water composition in the region around the WB and of Meschendorf can be classified as Ca-Mg-HCO_3 type (**Figure 5**). Based on the classification scheme by Löffler et al. (2010) it can be further characterized as a relatively young confined ground water.

Sediment Pore Water at the Beachline of Wismar Bay

Salinities of beach pore waters ranged between 3 and 10 (**Table 1**), representing different relative mixtures between fresh (salinities <1) and brackish waters (salinities of the WB: 11.8–12.5). Metabolites were enhanced when compared with the composition of the WB surface water, streams, and fresh ground waters around the WB (**Supplementary Figure S2**).

The water isotope data varied from −7.2 to −5.2 ($\delta^{18}O_{H2O}$) and −49.4 to −39.3‰ (δ^2H_{H2O}), reflecting also a mixture between two different endmembers (**Figure 4**).

The average $^{224}Ra_{ex}$ activity was 351 ± 188 dpm 100 L^{-1} (n = 5), which is one order of magnitude higher than those found in the surface waters from either WB or in the streams (**Table 1**).

Sediment Pore Water in the Wismar Bay

The downcore variation in the pore waters composition from six sediment sites in the WB is presented in **Figure 6** as a function of sediment depths. Sites 2, 15, 20, and 31 are presented separately from sites 10 and 11.

Sediments at sites 2, 15, 20, and 31 showed pore water profiles with constant salinity, except for a slight maximum at around 6 to 15 cmbsf, (**Figure 6A**). At Site 10 and in particular Site 11 (**Figure 1**), a strong downcore decrease in salinity was found. Relative to the bottom water conditions, the pore water salinities at Site 10 decreased by about 30% at 40 cmbsf. At the same depth, the salinity gradient at Site 11 reached essentially fresh water conditions (**Figure 6A-2**). In agreement with the salinity changes, the other conservative elements (Na, Mg, and K) also decreased with depth.

The δ^2H_{H2O} and $\delta^{18}O_{H2O}$ isotope values of the pore water at sites 2, 15, 20, and 31 varied from −39.5 to −29.5‰ and −5.1 and −3.9‰ respectively (**Figures 6B,C**). Due to the freshening by ground water at depth, the down core variations at sites 10 and Site 11 are much more pronounced, −50.2 and −36.9‰ (δ^2H_{H2O}) and −7.2 and −4.9‰ ($\delta^{18}O_{H2O}$), and at 40 cmbsf at sites 11 and 10, respectively (**Figures 6B-2,C-2**).

All pore waters were enriched in metabolites when compared to the bottom waters (**Table 1**), with increase concentrations at depth. A pronounced maximum concentration in the top 10 cmbsf was found at Site 11 (**Figures 6K-2–M-2, O-2**).

Pore water concentrations of SO_4 at the sediment-water interface were between 8 and 12 mM and decreased with depth, reaching 2 mM at most sites, and reaching even complete depletion at the base of Sites 10 and 11 (fresh water influenced sites) (**Figure 6I-2**). H_2S was determined at all sites showing net accumulation below about 16 cmbsf. At site 11, no H_2S accumulation was observed (**Figure 6J-2**).

The concentrations of DIC increased with depth up to 16 mM at all sites except for Site 11 where again a maximum was found in 10 cmbsf (**Figure 6-O2**). The increase in DIC concentrations was associated with a decrease in $\delta^{13}C_{DIC}$ values (**Figure 6P-2**).

Results from the modeling downcore profiles of SO_4, DIC, and $\delta^{13}C_{DIC}$ were indicated by dashed lines in the panels I, I-2, O, O-2, P, P-2 of **Figure 6**. The corresponding fluxes and accumulated mineralization rates in depth intervals of 10 cm are given in

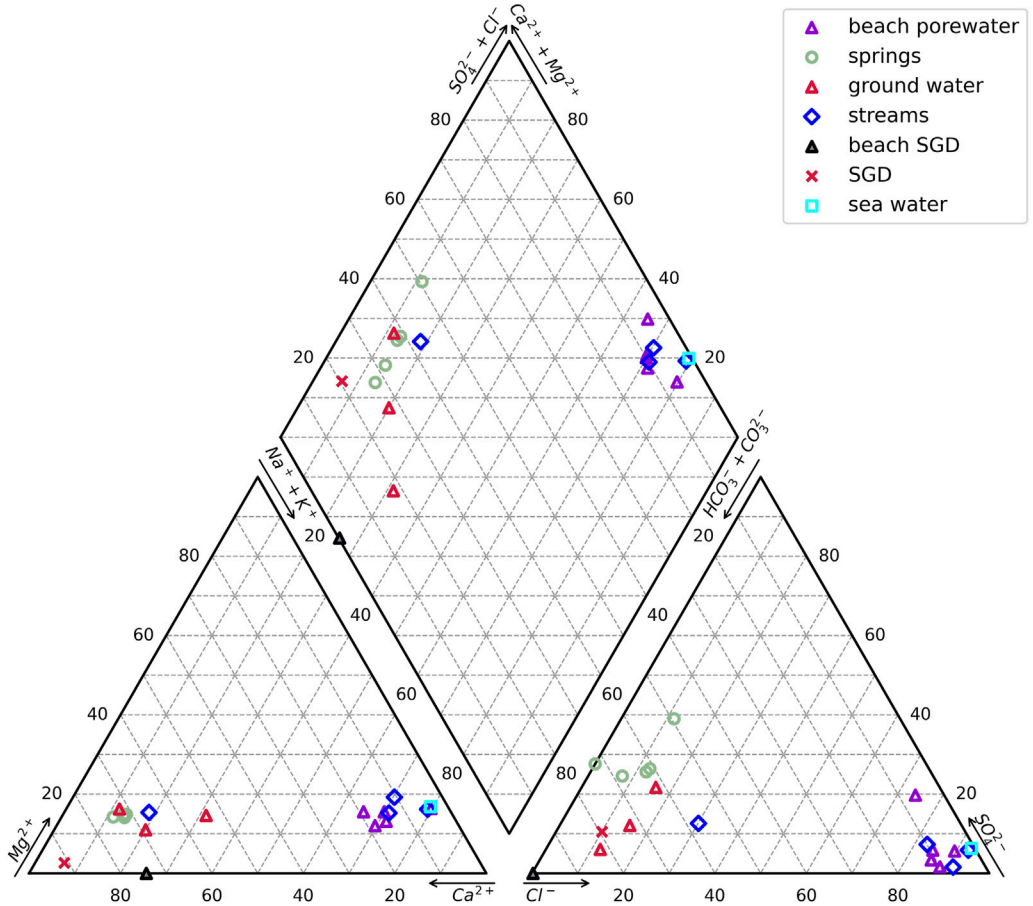

FIGURE 5 | Piper diagram of the major ions of the Wallenstein stream and western streams (blue diamond), springs (green circle), fresh ground water (red triangle), beach porewater (purple diamond) and sea water of Wismar Bay (turquoise square), extrapolated beach porewater (beach SGD—black triangle) and porewater of site 11 (SGD—red cross) to 1 mM Na.

Table 2. The modeled SO_4 fluxes both in the top and bottom sediment are positive and similar at all the sites. In contrast, the modeled DIC fluxes are negative, except at Site 11 which shows positive fluxes. In addition, the results of the model show that in the first 10 cmbsf of the majority of the sites there is a high OM accumulation, especially in Site 11, which is caused by a reactive metal oxide other than sulphate reduction. To verify the additional OM mineralization rate by reactive metal oxide on this site, different mineralization rates at 6–10 cm were tested (**Supplementary Figure S4**). It becomes obvious that an enhanced OM mineralization rate is required to fit the $^{13}C_{DIC}$ values.

Sediment Composition

Sediment Geochemistry

All sediment cores comprised a dark gray to black color with muddy texture covered by a brown fluffy layer on top.

Grain-size analyses show an uni-to bimodal distribution in the upper sediment. The vertical grain-size characteristics represented here by the first mode are given in **Supplementary Figure S5**. The samples first mode ranges between 8 and 100 µm. Fine to medium silt dominate at sites 10 and 11 (<40 µm) and at the surface of site 2 (subsurface), while sites 15 and 31 consist of coarse silt with a second mode around 8 µm. At site 20, in the southeastern part of WB, sediments consist of very fine sand. At sites 10 and 11 grain-size becomes finer with depth, whereas the mean grain-size increases at the other sites. The water content of the sediments ranged between 44 and 87% and generally decreased with sediment depth (**Supplementary Figure S5**).

The total organic carbon (TOC) contents ranged from 1 to 8% dwt. Organic matter-rich sediments (TOC >4 %wt.) were found at sites 10, 11, and 31, whereas sediments at other sites contained less TOC (**Figure 7C**). The molar TOC/TN ratios varied between 6 and 12 (**Figure 7D**) with increasing ratios with sediment depth. Total sulphur (TS) contents ranged from 0.3 to 2.4 wt. % (**Figure 7B**), typical for marine sediments (**Figure 8**) (Berner and Raiswell, 1983). Reactive Fe and Mn were generally pronounced in the top layers and mostly decreased at larger depths (**Figure 9**). Site 11 was characterized by the relatively highest values.

In brackish-marine sediments, microbial sulphate reduction limited by the availability of OM (Berner, 1980) which may be reflected by a positive co-variation of TOC with pyrite sulphur as found for Holocene sediments (Berner, 1982). The TS contents (taken here as a measure for pyrite sulphur) found in the shallow sediments of WB are positioned on or below the relationship

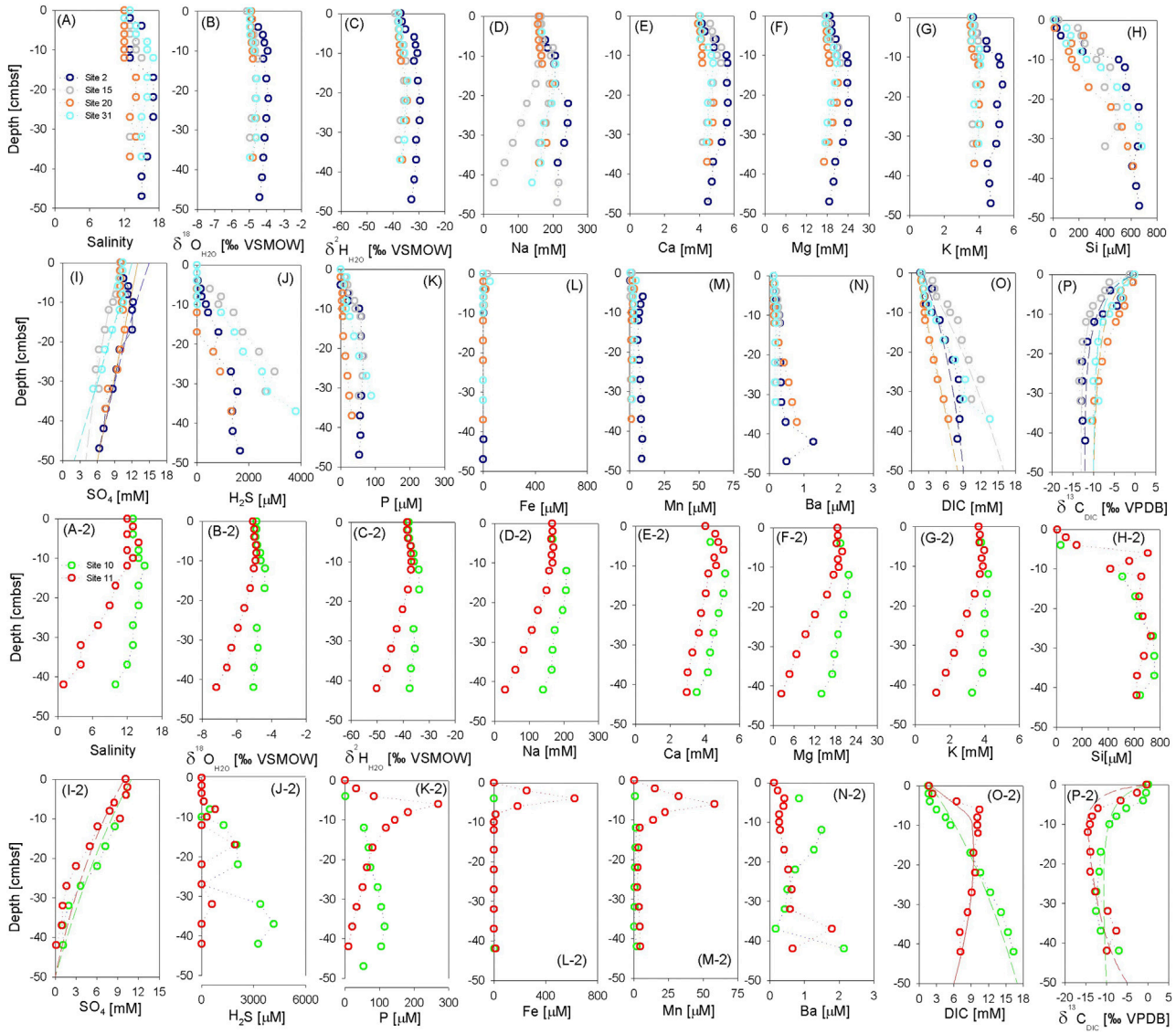

FIGURE 6 | Pore water profiles in sediment cores from WB showing salinity **(A)**, $^{18}O_{H2O}$ **(B)**, $^{2}H_{H2O}$ **(C)**, and different dissolved components Na **(D)**, Ca **(E)**, Mg **(F)**, K **(G)**, Si **(H)**, SO_4 **(I)**, H_2S **(J)**, P **(K)**, Fe **(L)**, Mn **(M)**, Ba **(N)**, DIC **(O)**, $^{13}C_{DIC}$ **(P)**, of sites 2, 15, 20, and 31. The sites impacted by freshening at depth are presented in the panels: salinity **(A-2)**, $^{18}O_{H2O}$ **(B-2)**, $^{2}H_{H2O}$ **(C-2)**, and different dissolved components Na **(D-2)**, Ca **(E-2)**, Mg **(F-2)**, K **(G-2)**, Si **(H-2)**, SO_4 **(I-2)**, H_2S **(J-2)**, P **(K-2)**, Fe **(L-2)**, Mn **(M-2)**, Ba **(N-2)**, DIC **(O-2)**, $^{13}C_{DIC}$ **(P-2)**. The additional dashed lines in the panels I, I-2, O, O-2, P, P-2 are the diagenetic modeling results.

proposed for siliciclastic sediments deposited beneath an oxygenated water column (**Figure 8**) (Berner, 1982).

The typical anthropogenic contaminants as Hg and acid-extractable lead (Pb*), showed pronounced variations reaching maximum contents of 156 µg kg^{-1} and 60 mg kg^{-1}, respectively, mostly in the shallower part of the cores (**Figure 9**). Here, relatively similar concentrations may be related to bioturbation, probably caused by different activities of macrozoobenthos (Lipka et al., 2018b; Gogina et al., 2018). At Site 11, lateral sediment supply from the flanks of the channel, sediment redistribution caused by the channel excavation, and fresh water flow from below may have cause relative constant concentrations. At Site 11, both Hg and Pb* concentrations show no trend with depth.

Geophysical Characterization

The position of transects within WB are displayed in (**Figure 1**) and the results of the acoustic measurements are presented in **Figures 10**, **11**. In the western transect, a steep drop in the bathymetry from less than 3 m water depth to approximately 9 m water depth is observed (**Figure 10**). In shallow waters of 3 m water depth and less no subsurface structures can be recognized in the seismic data.

Directly below the seafloor at the base of the steep drop (near site 15), mostly acoustically transparent sediments with weak horizontal internal layering are deposited (S2). Within this unit, gas fronts prohibited further penetration of the acoustic signal, and are recognized along the profile by high acoustic turbidity. At

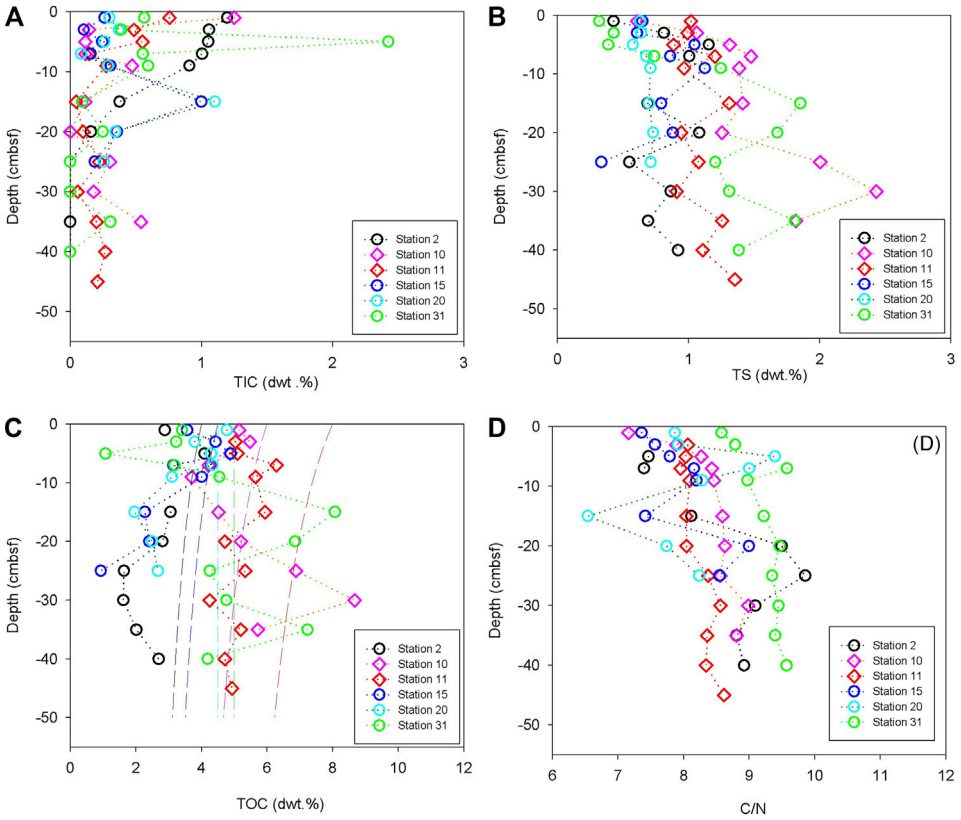

FIGURE 7 | Vertical profiles of the bulk geochemical parameters TIC **(A)**, TS **(B)**, TOC **(C)**, and C/N **(D)** ratios in sediments cores from the WB. The dashed lines in panel C (TOC) display the results from the diagenesis transport model (see discussion).

two locations (Site 13 and between sites 13 and 14), chimneys rise from the gas front to the seafloor. Between sites 13 and 15, the gas front was penetrated and the seismic units S3 and S4 can be observed. A distinct reflector is forming a low angle unconformable boundary of S3 with the overlying unit S2. Within unit S3, a faint and distorted internal lamination is observed. Unit S3 is separated from unit S4 by an unconformable high-amplitude reflector that is strongly undulating. Unit S4 is acoustically transparent and forms the base of acoustic penetration, corresponding to the onset of glacial deposits.

In the central WB, a channel dredged for ship traffic to approx. 10 m water depth is visible (**Figure 11**). At the flank of this artificial depression, seismic unit S1 is observed in the top meter of the subsurface. Based on the acoustic measurement, the unit has a chaotic texture but may be separates into sub-units by an unconformity (near site 31). A medium to high amplitude reflector separated unit S1 from S2, which again shows a weak, horizontal internal lamination with a thickness of up to 3 m. Along the majority of the profile, free gas fronts are observed at a depth of approx. 9 m. Near site 30, a gas chimney reaches the seafloor. Closer to the channel and on a perpendicular profile, unit S3 occurs with a thickness of approx. 1 m. Seismic unit S4, separated from the overlying units by a marked unconformity, forms the base of acoustic penetration.

DISCUSSION

Fresh Water in the Catchment Area and Inlets at the Margins of Wismar Bay

Fresh ground waters from the catchment in the southern part of the WB and from a well on Poel Island (**Figure 1**) display a water isotope composition positioned on the LMWL of Warnemünde (**Table 1**; **Figure 4**). These data are also close to the composition of ground waters escaping at beach spring in Meschendorf (**Figure 1**), which has been shown water of age about 30 years (Lipka et al., 2018a). The hydrogeochemical ground water composition of the majority of investigated wells and the springs fall into the field for relatively "young" ground waters (**Figure 5**).

The Wallenstein stream and the other western streams carry different isotope-hydrochemical signatures, thus representing different surface waters sources entering the southern WB.

The western streams showed a water isotopic composition and $\delta^{13}C_{DIC}$ signatures similar to those found in the well waters of the catchment area (**Table 1**). The slight shift towards heavier isotope values is likely the result of an impact by evaporation and CO_2 degassing when stream waters get in contact with the atmosphere (Michaelis et al., 1985; Clark and Fritz, 1997).

The Wallenstein stream, on the other hand, is enriched in heavy water isotopes and dissolved ions when compared to well waters

TABLE 2 | Modeled diffusive and advective fluxes of DIC and SO_4 and the accumulated OM mineralization rate for all the 6 sediment core sites. The fluxes and the rates are given in mmol m^{-2} d^{-1}.

	Advective and diffusion fluxes					
Sites	**2**	**10**	**11**	**15**	**20**	**31**
			Top (z= 0 cm)			
			SO4 flux			
Advective flux	0.07	0.05	0.05	0.05	0.06	0.06
Diffusive flux	1.18	1.55	1.66	1.66	0.62	0.89
Total flux	1.25	1.60	1.70	1.70	0.68	0.94
			DIC flux			
Advective flux	0.01	0.01	0.01	0.01	0.00	0.00
Diffusive flux	−1.46	−2.62	−4.30	−2.24	−0.68	−1.36
Total flux	−1.45	−2.61	−4.29	−2.22	−0.68	−1.36
			Bottom (z= 50 cm)			
			SO4 flux			
Advective flux	0.03	0.00	0	0.02	0.03	0.01
Diffusive flux	0.60	0.66	0.44	0.29	0.65	0.93
Total flux	0.63	0.66	0.45	0.31	0.68	0.94
			DIC flux			
Advective flux	0.04	0.08	0.03	0.08	0.04	0.07
Diffusive flux	−0.23	−0.81	1.01	−0.89	−0.72	−1.43
Total flux	−0.19	−0.73	1.04	−0.81	−0.68	−1.36
			Accumulated OM mineralization rate			
0-10 cm	0.44	0.66	3.70	0.49	0.00	0.00
10-20 cm	0.29	0.44	0.59	0.33	0.00	0.00
20-30 cm	0.22	0.32	0.43	0.24	0.00	0.00
30-40 cm	0.17	0.26	0.34	0.19	0.00	0.00
40-50 cm	0.14	0.21	0.28	0.16	0.00	0.00
0-50 cm	1.26	1.89	5.34	1.42	0.00	0.00

and western streams (**Figure 4**; **Table 1**). Besides the mixing with BS surface waters during the time of sampling, this could also be the result of surface water evaporation (e.g., Gat, 1996; Clark and Fritz, 1997) that took place during the origin of this stream in Lake Schwerin and a further crossing through Lake Mühlenteich before reaching the WB coastline (**Figure 1**).

The impact of stream waters on the composition of the WB surface waters is most pronounced in the western part of the bay. There the water isotopic composition decreased towards the coastline (**Figures 3B,C**), due to mixing between open BS water, containing heavier isotopes, and a fresh water component characterized by lighter isotopes. In addition, higher concentrations of DIC together with the depleted $\delta^{13}C_{DIC}$ found near the western coastline (**Figures 3E**) are probably related to fresh water sources (Winde et al., 2014). The surface water of the WB in the western part showed water isotopes values decreasing close to the coastline (**Figures 3B,C**), probably due to mixing between open BS water containing heavier isotopes, and a fresh water component characterized by lighter isotopes coming from the small streams located in this region. These streams showed a water isotopic composition similar to those found in the ground water recovered from wells near Wismar (**Table 1**, GW) and fresh water springs at Meschendorf (**Table 1**–springs). The slight trend to heavier isotopes is likely the result of an impact by evaporation and CO_2 degassing when stream waters become in contact with the atmosphere (Clark and Fritz, 1997). The $^{13}C_{DIC}$ isotopic signatures of the western streams are similar to the values in the ground water as well, which reinforces the idea that the streams are supplied by ground water from unconfined aquifers.

Within the western part of the WB, ^{224}Ra activities showed a decrease towards the open BS (**Figure 2B**). Since the ^{224}Ra activities in the streams were comparable to those measured in the surface water of the WB (**Figure 2**; **Table 1**), further sources may are contributing to the observed spatial patterns. Besides the ground water below the central part of the bay (see 4.3), which has not been analyzed for ^{224}Ra, the permeable sediments along the bay may act as a further fresh water and ^{224}Ra source to the WB. The pore water at the beach showed average $^{224}Ra_{ex}$ activities that were about one order of magnitude higher than the activities found in the surface water of WB. These findings, therefore, suggest, that SGD can enter the WB from the boundaries and contributing as a further source to the water balance of the WB.

Beach pore water consist of a mixture between fresh water and a brackish water component. To estimate the fresh water endmember the beach pore water compositions were extrapolated based on actual measurements and using Na as conservative mixing tracer (boundary conditions: average WB and 1 mM for the fresh water, which is the mean concentration found in the ground water wells). These values can be found in **Table 1**—Beach SGD. For the majority of the dissolved compounds a composition close to ground waters was found (**Table 1**). Only some non-conservative constituents, like DIC and Ca were enhanced in the estimated fresh water component, likely due to corrosion processes of carbonates present in the coastal sands (e.g., Smellie et al., 2008).

Although a ^{224}Ra gradient was not established in the eastern part of the WB (**Figure 2**), the generally higher activities in this part may indicate a source of ^{224}Ra. This source may originate from the exchange with pore water or resuspended sedimentary particles or SGD, besides the Wallenstein stream. Moreover, enhancement of Mn and Ba compared to the open BS surface water confirms strong benthic pelagic fluxes.

Tentative Radium Mass Balance for Wismar Bay

A mass balance is constructed, based on Rodellas et al. (2021), to estimate SGD in the WB. The Ra mass balance relies on the assumption that the most important Ra sources and sinks are in steady state, and then SGD can be evaluated by the difference of supply and removal according **Eq. 5**.

$$F_{SGD} * A_{SGD} + Q_{str}C_{str} + F_{sed} * A_{WB} = \lambda VC + Q_{out}C \qquad (5)$$

Where V and A_{WB} are the water volume (m^3) and surface area (m^2) of where samples were collected (**Figure 1**). We assume for the balance that SGD is taking place at 27 km of the shoreline and 10 m offshore (A_{SGD}). Q_{str} is the discharge from streams (m^3 d^{-}). We consider here the Wallenstein stream and the three western streams. Q_{out} is the water outflow to the open BS (m^3 d^{-1}) determined by using the water mass ages, the activity difference between WB and open-sea water and the volume of the study area. The water ager was calculated following (Moore and de Oliveira, 2008). C is the weighted average of $^{224}Ra_{ex}$ of the WB, determined by the $^{224}Ra_{ex}$ inventory. C_{str} are the mean concentrations of $^{224}Ra_{ex}$ in the surface water inlets (Bq m^{-3}). F_{sed} is the $^{224}Ra_{ex}$ diffusion from sediments. λ is the radioactive decay constant of ^{224}Ra. F_{SGD} is the fluxes of $^{224}Ra_{ex}$ per unit area associated with SGD (Bq m^{-2} d^{-1}), respectively. Terms used in the mass balance together with the units are summarized in **Table 3**.

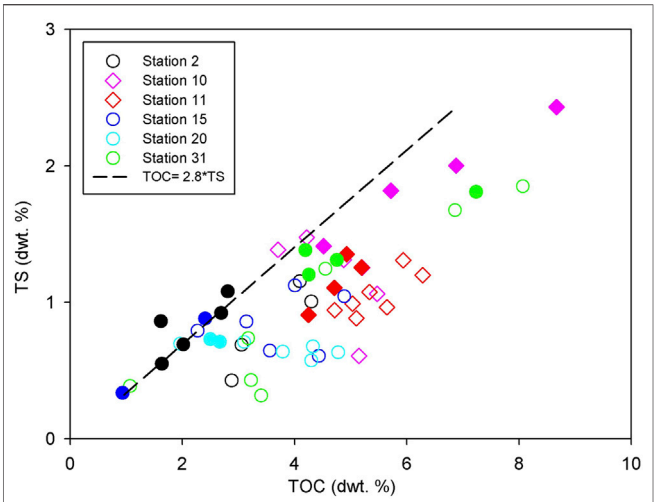

FIGURE 8 | Covariations of TS versus TOC including the relationship suggested for Holocene siliciclastic sediments (Berner, 1982). It is assumed that TS essentially consists in the investigated samples essentially of pyrite sulfur. Surface sediments <20 cmbsf are open symbols and >20 cmbsf are filled symbols.

Solving **Eq. 5** a $^{224}Ra_{ex}$ flux from SGD (F_{SGD}—**Table 3**) of 261.7 Bq m^{-2} d^{-1} was obtained.

This flux was converted into a water flow by dividing it by the $^{224}Ra_{ex}$ activities in different endmembers which were derived from four beach pore water samples with activities of 51, 65, 84, and 88 Bq m^{-3}. The resulting estimated volumetric SGD flow is 3.8 ± 0.7 cm d^{-1} (**Table 3**).

The estimated flow is higher compared to the flow obtained by (Schafmeister and Darsow, 2004). These authors applied a numeric ground water flow model (about 0.02 cm d^{-1}). This is due to the model only considering the fresh water component, whereas the Ra mass balance applied in the present study includes recirculated sea water. However, the SGD rate from WB is considered low when comparing to other SGD rates from different regions in the world, where SGD rates can reach up to 280 cm d^{-1} (Santos et al., 2021).

Benthic Processes and Submarine Fresh Water Source in the Central Wismar Bay

The composition of sediments investigated in the WB is typical for silty/muddy deposits along the North-German coastline

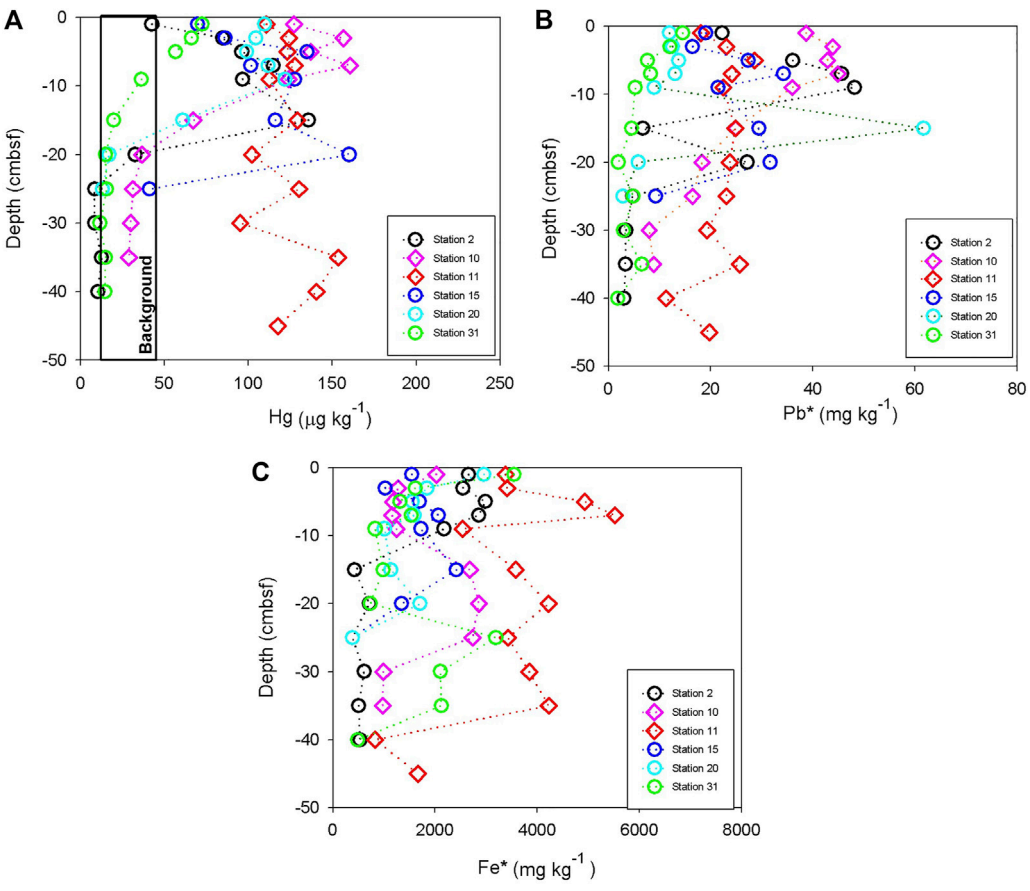

FIGURE 9 | Vertical profiles of the contents of total Hg, **(A)**, including the background level for Baltic Sea (Leipe et al., 2013), and Pb **(B)** and Fe **(C)** of sediment cores from WB. *HCl extractable fraction.

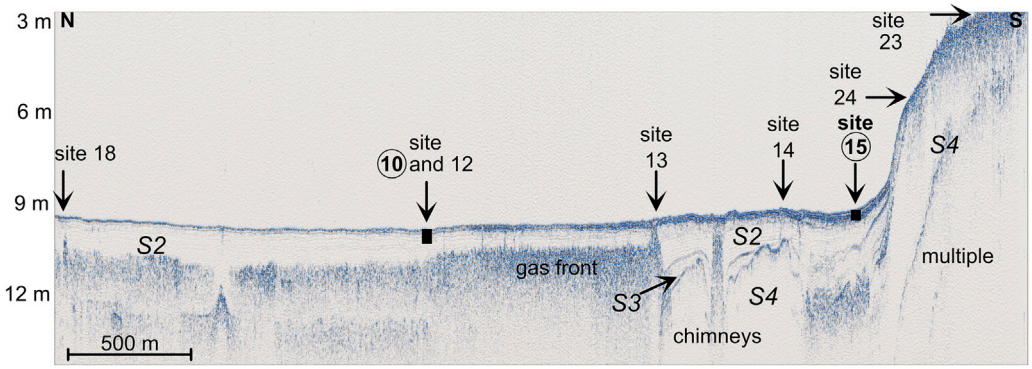

FIGURE 10 | Sediment acoustic profile of the western N-S transect in WB. The cores are represented as a circle around the site number, and the length of each core is indicated by the black bar.

(e.g., Böttcher et al., 2000; Al-Raei et al., 2009; Lipka et al., 2018b).

Except for sites 10 and 11 (**Figure 1**), pore water salinities in the WB sediments were characterized by relatively constant values (**Figures 6A**). Slight maxima around 10 to 15 cmbsf were observed at all sites and are due to past changes of bottom water salinities which are consequence of intrusion of salty North Sea water intrusions into the southern BS (Matthäus and Lass, 1995; Mohrholz, 2018).

Pore water salinities at Site 10 and in particular at Site 11 show a different pattern. Below the surface maxima, they decrease, and at Site 11 the values even reach fresh water conditions at the lowermost depth (salinity of about 1). It suggests that the sediments below the surface muds may host an aquifer containing fresh water, situated above glacial deposits and potentially part of seismic unit 3 (**Figure 11**). The pore water gradients of Site 11 (**Figure 6A-2**) result from mixing between endmembers (e.g., ground water and BS), superimposed by diagenetic reactions leading to further accumulation of some elements in the top sediments.

The pore waters at sites not impacted by freshening (sites 2, 15, 20, and 31) are characterized by a continuous increase in metabolite concentrations and a decrease in SO_4 and $\delta^{13}C_{DIC}$ values (**Figures 6J–O**). These vertical profiles are shaped by intense OM mineralization catalyzed by microorganisms using in particular SO_4 as terminal electron acceptors (Froelich et al., 1979; Jørgensen, 1982).

The maxima in Si, P, DIC, Mn, and Fe concentrations at Site 11 at around 10 cmbsf are in agreement with higher loads of top sediments in metabolizable organic matter leading to enhanced mineralization when compared to the other sites (**Figures 6K-2–M-2,O-2**). These observations also demonstrate that the fresh ground water is not substantially enriched in those substances. The pore water at Site 11 is depleted in SO_4 due to both, microbial sulphate reduction in the upper part of the sediment, but in particular due to the dilution with the underlying ground water that is free of SO_4.

The high dissolved Fe and Mn concentrations observed in the top sediments (**Figures 6L-2,M-2**) may accumulate due to the chemical reaction of metal ox (yhydrox)ides by biogenic sulphide

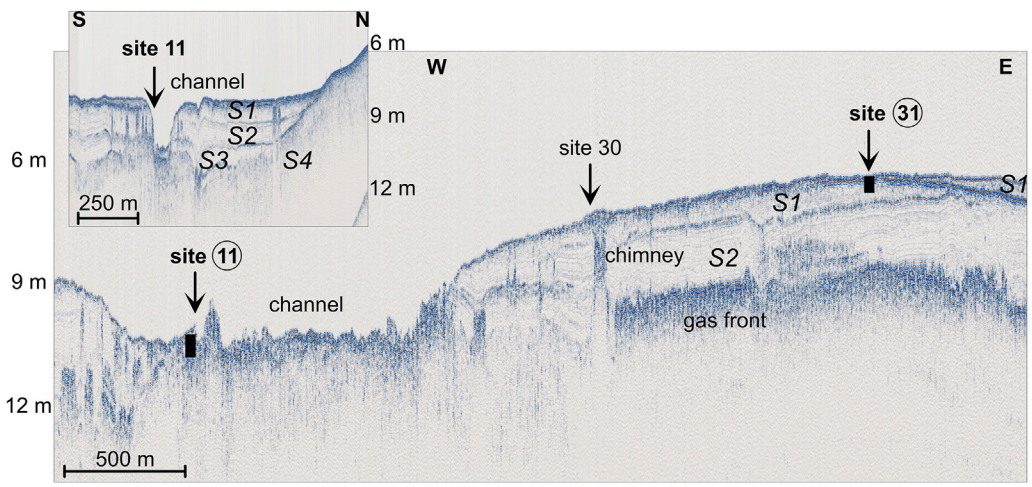

FIGURE 11 | Sediment acoustic profile of the eastern W-E transect. The cores are marked as a circle around the site number, and the length of each core is denoted by the black bar. Inset: perpendicular S-N transect highlighting site 11.

TABLE 3 | Summary of the terms used in the Ra mass balance.

Term	Definition	Value	±	Units	Source
A_{WB}	WB surface area–study area	81,472,500		m^2	Calculated from the bathymetry (GDI-BSH, 2020)
A_{WB}	assumed area where SGD take place	270,000		m^2	
V	WB volume - study area	430,812,610		m^3	Calculated from the bathymetry (GDI-BSH, 2020)
h	average depht of the bay	5		m	V/A_{WB}
Q_{str}	Discharge for the 3 western streams	1,515		$m^3\ d^{-1}$	Because there were no hydrologic data available for these streams, the value was taken from another stream close to area (LUNG, 2020)
Q_{str}	Discharge from Wallenstein stream	26,524		$m^3\ d^{-1}$	LUNG, (2021)
WA	Water age	5	1	d	(ln ($^{224}Ra/^{223}Ra$)WB–ln ($^{224}Ra/^{223}Ra$)beach pore water)/λ223 - λ223
Q_{out}	Water outflow	0.3		Bq d^{-1}	($^{224}Ra_{WB}$–$^{224}Ra_{offshore}$) *v/RT
C_{str}	$^{224}Ra_{ex}$ concentration in Wallenstein stream	5.8		Bq m^{-3}	this study–**Table 1**
C_{str}	$^{224}Ra_{ex}$ concentration in the western stream	1.1		Bq m^{-3}	this study–**Table 1**
C_{str}	$^{224}Ra_{ex}$ concentration in the western stream	2.6		Bq m^{-3}	this study–**Table 1**
C_{str}	$^{224}Ra_{ex}$ concentration in the western stream	4.1		Bq m^{-3}	this study–**Table 1**
$C_{offshore}$	$^{224}Ra_{ex}$ concentration in the open BS (Site 1)	0.2		Bq m^{-3}	this study
C	Average of ^{224}Ra inventory concentration in the WB	1.4	0.8	Bq m^{-3}	this study
λ	$^{224}Ra_{ex}$ decay constant	0.189		d^{-1}	
F_{sed}	Sediment diffusion from seabed	0.5	0.03	Bq $m^{-2}\ d^{-1}$	Krall et al. (2017)
F_{SGD}	$^{224}Ra_{ex}$ inputs from pore water fluxes	261.7		Bq $m^{-2}\ d^{-1}$	this study–**Table 1**
$C_{endmember}$	$^{224}Ra_{ex}$ of beach pore water (endmember)	51		Bq m^{-3}	this study–**Table 1**
$C_{endmember}$	$^{224}Ra_{ex}$ of beach pore water (endmember)	65		Bq m^{-3}	this study–**Table 1**
$C_{endmember}$	$^{224}Ra_{ex}$ of beach pore water (endmember)	84		Bq m^{-3}	this study–**Table 1**
$C_{endmember}$	$^{224}Ra_{ex}$ of beach pore water (endmember)	88		Bq m^{-3}	this study–**Table 1**
V_{SGD}	Volumetric SGD flow	3.8	0.7	cm d^{-1}	$F_{SGD}/C_{endmember}$

(e.g., Moeslund et al., 1994; Thamdrup et al., 1994; Böttcher et al., 2000). At the sediment-water interface, Fe and in part Mn may are oxidized by NO_3 and/or O_2, whereas in deeper sediment layers Fe and Mn may react with H_2S and DIC to form Fe sulphides and MnCa carbonate solid-solutions, respectively (Froelich et al., 1979; Berner, 1980; Huckriede and Meischner, 1996; Böttcher and Dietzel, 2010). The observed near-surface maximum in dissolved P at Site 11 is due to the parallel release from OM and reduction of Fe ox(yhydrox)ides that acted previously as sorption substrate for P (e.g., Haese, 2006).

The surface sediments at all sites are low in accumulating TS (considered to reflect essentially pyrite contents) when compared to the predicted Holocene saturation line (**Figure 8**), indicating the impact of sulphate-independent mineralization processes in the top sediments and the impact of bioturbation-driven-re-oxidation of sedimentary sulphur species (e.g., Jørgensen and Kasten, 2006). This is in line with previous observations (Mossmann et al., 1991; Böttcher et al., 2000) that gave evidence that for modern sediments some burial at depth and associated time is necessary to establish a constant TOC/S ratio. However, the freshening of pore water at Site 11 establishes SO_4 limited conditions and caused the TOC/TS ratio to remain below 2.8 (**Figure 8**).

Overall, the modeled mineralization rates at the WB are at the lower end when compared to measured gross sulphate reduction rates in muddy sediments from German coastal areas (Böttcher et al., 2000; Llobet-Brossa et al., 2002; Al-Raei et al., 2009; Lipka et al., 2018b) which is likely due to some H_2S reoxidation by metal oxy (hydrox)ides taken place in the surface sediments (Jørgensen, 1982). The highest net anaerobic mineralization rates are found at Site 11 (**Table 2**). The excavation of sediment (**Figure 11**) formed a local sediment trap and led to a fast accumulation of sediments as reflected by the homogeneous distribution of sedimentary organic matter, reactive metals like Fe and Mn, and anthropogenic tracers (Hg, Pb*) (**Figure 9**). This accumulation further leads to enhanced availability of fresh organic matter fostering microbial activity (Aller and Blair, 1996; Jørgensen and Kasten, 2006), and therefore, higher diagenetic element fluxes across the sediment-water interface (**Table 2**).

Moreover, the modeled fluxes indicate that advective and diffuse components are taking place, however, the last one has been more pronounced. DIC is liberated from deeper sediments to the bottom waters, especially at Site 11 (**Table 2**). The pore water at Site 11 was physicochemically evaluated by the Phreeq-C package (Parkhurst and Appelo, 1999). Assuming an equilibrium with

calcite at depth (Morse and Mackenzie, 1990) all solutions are characterized by an enhanced CO_2 partial pressure higher than atmospheric pressure. Therefore, the impact of fresh water at Site 11 on the bottom water of WB will enhance the capability of surface water to act as a potential CO_2 source for the atmosphere.

An Anthropogenic Bottle Opener for SGD?

A stronger decrease in salinity, and therefore an indication of fresh water occurrence is observed at Site 11 compared to the other sites (**Figure 6A-2**). The main morphological difference between this sites is the presence of an excavated navigation channel. This is an about 3–4 m deep artificial sedimentary depression (**Figure 11**) which was built for ship navigation channel between the open BS and the port of Wismar (VSW, 2018).

Based on the geophysical profiles, the dredging removed the previously overlying muddy sediments (units S1 and S2), thereby touching the underlying aquifer in unit 3 (**Figure 11**). The removal of the mud cover at Site 11 promotes the exchange of solutes and water between the aquifer and the bottom water. A more continued excavation this structure in the future, may enhance the direct impact of SGD on the WB. On the other hand, depending on the hydrographic boundary conditions, the artificial channel may also temporarily allow brackish water to penetrate the aquifer.

CONCLUSION AND OUTLOOK

The multi-tracer approach used in the present study demonstrated the impact of different fresh water sources on the Wismar Bay (WB), southern Baltic Sea, and in particular to prove the occurrence of SGD at the center of the bay. In addition, the change in the radium gradient towards the open sea suggests potential ground water leaking from the coastal borders in agreement with direct observations at the shoreline.

The sediment cores retrieved from the central part of the bay together with the acoustic survey discovered fresh water discharge at the sea bottom in the central part of the bay. The discovered SGD site (Site 11) is located in a navigation channel, which demonstrates that the dredging activity may have caused a change in the pressure gradient, thereby allowing ground water to penetrate the sediments overlying the aquifer and the bottom waters of the WB, respectively. Using a tentative Ra mass balance, we estimate a potential contribution from SGD to the WB of about 3.8 ± 0.7 cm d^{-1}.

Diagenesis in the surface sediments results in the enhancement of metabolites in the pore waters at depth. At Site 11, however, enhanced concentrations of metabolites were found in the top sediments which may also be related to the remineralization of fresh organic matter added by dredging in the past that lead to higher mineralization rates.

From the geochemical profiles it can be inferred that SGD is not just limited to the central part of, but can also occur in other places of the WB, which may or may not be associated with dredging activities. Therefore, explorations to determine the number of SGD sites are necessary.

Possible future engineering to impact the WB benthic structure may have impacts on benthic-pelagic coupling and, thereby, change the element fluxes into the bottom waters. Further studies, however, are required to investigate the potential impact of local sediment properties as a source for nutrients and dissolved carbon species for the WB water column.

DATA AVAILABILITY STATEMENT

The raw data supporting the conclusions of this article will be made available by the authors, and graphically presented data will be stored in the PANGEA data base.

AUTHOR CONTRIBUTIONS

MB, CVA, and JS developed the scientific concept and design of the study. CVA, JS, and PF, conducted the field campaigns and on-site measurements. IS, CVA, OD, SP, and PF carried out the analytical data measurements and processing. BL performed the reaction-transport modeling. CM and A-KJ contributed to the groundwater hydrogeochemistry and -geology and MZ was involved in data discussion. CVA and MB wrote the article with contributions and revisions from all co-authors. All authors agreed about the submission of the final version.

FUNDING

The study was supported by the German Academic Exchange Service (DAAD) via a PhD stipend for CvA to work in the Geochemistry & Isotope Biogeochemistry Group at IOW (project no. 57381412), and the Deutsche Forschungsgemeinschaft (DFG) to MB and A-KJ within the framework of the Research Training Group 'Baltic TRANSCOAST' funded by under grant number GRK 2000. This is Baltic TRANSCOAST publication no. GRK2000/0046. It is also supported by DFG to MB and JS within the KiSNet project. JS was further supported by the BONUS SEAMOUNT project funded jointly by the EU and the Federal Ministry of Education and Research of Germany (BMDF, grant no. 03F0771B) and by a FP7 EU Marie Curie Career Integration Grant (grant PCIG09-GA-2011-293499). MZ is supported by BMBF during DAM-MGF. BL acknowledges additional support from the Helmholtz Association (Alfred Wegener Institute Helmholtz Centre for Polar and Marine Research). We acknowledge financial support by Leibniz IOW for Open Access Publishing.

ACKNOWLEDGMENTS

The authors wish to thank the crew and captain of RV LITTORINA and M. Staniek for their expert technical on-board support, and S.

Plewe for his expert support during the field campaigns. We also wish to thank A. Köhler for expert ICP-OES support and I. Scherff for further laboratory assistance, B. Schnetger for providing a Th Standard, and J. Deepen (Stalu-MV) for providing the hydrological data. Aaron J. Beck and Olivier Radakovitch for the careful reviews that helped to improve the manuscript, and Henry Bokuniewicz for the editorial handling. MB further wishes to thank H.-J. H. Dohrenkamp, C.S. Henn, and The United Jazz + Rock ensemble for their culinary and musical inspirations during manuscript preparation. He dedicates this publication to the memory of T.G.P. Jones, C. Reiner, and U. Steinfurth, who recently passed away, for their inspiring and vital sense of humor.

SUPPLEMENTARY MATERIAL

The Supplementary Material for this article can be found online at: https://www.frontiersin.org/articles/10.3389/fenvs.2021.642346/full#supplementary-material

REFERENCES

Al-Raei, A. M., Bosselmann, K., Böttcher, M. E., Hespenheide, B., and Tauber, F. (2009). Seasonal Dynamics of Microbial Sulfate Reduction in Temperate Intertidal Surface Sediments: Controls by Temperature and Organic Matter. *Ocean Dyn.* 59, 351–370. doi:10.1007/s10236-009-0186-5

Aller, R. C., and Blair, N. E. (1996). Sulfur Diagenesis and Burial on the Amazon Shelf: Major Control by Physical Sedimentation Processes. *Geo-Marine Lett.* 16, 3–10. doi:10.1007/bf01218830

Beck, A. J., Tsukamoto, Y., Tovar-Sanchez, A., Huerta-Diaz, M., Bokuniewicz, H. J., and Sañudo-Wilhelmy, S. A. (2007). Importance of Geochemical Transformations in Determining Submarine Groundwater Discharge-Derived Trace Metal and Nutrient Fluxes. *Appl. Geochem.* 22, 477–490. doi:10.1016/j.apgeochem.2006.10.005

Bejannin, S., Tamborski, J. J., van Beek, P., Souhaut, M., Stieglitz, T., Radakovitch, O., et al. (2020). Nutrient Fluxes Associated with Submarine Groundwater Discharge from Karstic Coastal Aquifers (Côte Bleue, French Mediterranean Coastline). *Front. Environ. Sci.* 7, 205. doi:10.3389/fenvs.2019.00205

Berner, R. A. (1982). Burial of Organic Carbon and Pyrite Sulfur in the Modern Ocean; its Geochemical and Environmental Significance. *Am. J. Sci.* 282, 451–473. doi:10.2475/ajs.282.4.451

Berner, R. A. (1980). *Early Diagenesis: A Theoretical Approach*. Princeton, NJ: Princeton University Press.

Berner, R. A., and Raiswell, R. (1983). Burial of Organic Carbon and Pyrite Sulfur in Sediments over Phanerozoic Time: a New Theory. *Geochimica et Cosmochimica Acta* 47 (5), 855–862. doi:10.1016/0016-7037(83)90151-5

Blöschl, G., Bierkens, M. F. P., Chambel, A., Cudennec, C., Destouni, G., Fiori, A., et al. (2019). Twenty-three Unsolved Problems in Hydrology (UPH) – a Community Perspective. *J. Hydrol. Sci.* 64, 1141–1158.

Blott, S. J., and Pye, K. (2001). GRADISTAT: a Grain Size Distribution and Statistics Package for the Analysis of Unconsolidated Sediments. *Earth Surf. Process. Landforms* 26, 1237–1248. doi:10.1002/esp.261

Böttcher, M. E., and Dietzel, M. (2010). Metal-ion Partitioning during Low-Temperature Precipitation and Dissolution of Anhydrous Carbonates and Sulphates. *EMU Notes in Mineralogy* 10 (4), 139–187.

Böttcher, M. E., Hespenheide, B., Llobet-Brossa, E., Beardsley, C., Larsen, O., Schramm, A., et al. (2000). The Biogeochemistry, Stable Isotope Geochemistry, and Microbial Community Structure of a Temperate Intertidal Mudflat: an Integrated Study. *Continental Shelf Res.* 20, 1749–1769. doi:10.1016/s0278-4343(00)00046-7

Böttcher, M. E., Mallast, U., Massmann, G., Moosdorf, N., Mueller-Pethke, M., and Waska, H. (2021). "Coastal-Groundwater Interfaces (Submarine Groundwater Discharge)," in *Ecohydrological Interfaces*. Editors S. Krause, D. M. Hannah, and N. Grimm (New York, NY: Wiley & Sons).

Böttcher, M. E., and Schmiedinger, I. (2021). The Impact of Temperature on the Water Isotope ($^{2}H/^{1}H$, $^{17}O/^{16}O$, $^{18}O/^{16}O$) Fractionation upon Transport through a Low-Density Polyethylene Membrane. *Isotopes Environ. Health Stud.* 57, 183–192. doi:10.1080/10256016.2020.1845668

Boudreau, B. P., and Ruddick, B. R. (1991). On a Reactive Continuum Representation of Organic Matter Diagenesis. *Am. J. Sci.* 291, 507–538. doi:10.2475/ajs.291.5.507

Boudreau, B. P. (1997). *Diagenetic Models and Their Implementation: Modelling Transport and Reactions in Aquatic Sediments*. New York: Springer.

Brand, W. A., and Coplen, T. B. (2012). Stable Isotope Deltas: Tiny, yet Robust Signatures in Nature. *Isotopes Environ. Health Stud.* 48, 393–409. doi:10.1080/10256016.2012.666977

Burnett, W. C., Aggarwal, P. K., Aureli, A., Bokuniewicz, H., Cable, J. E., Charette, M. A., et al. (2006). Quantifying Submarine Groundwater Discharge in the Coastal Zone via Multiple Methods. *Sci. Total Environ.* 367, 498–543. doi:10.1016/j.scitotenv.2006.05.009

Burnett, W. C., Bokuniewicz, H., Huettel, M., Moore, W. S., and Taniguchi, M. (2003). Groundwater and Pore Water Inputs to the Coastal Zone. *Biogeochemistry* 66, 3–33. doi:10.1023/b:biog.0000006066.21240.53

Burnett, W. C., Peterson, R., Moore, W. S., and Oliveira, J. (2008). Radon and Radium Isotopes as Tracers of Submarine Groundwater Discharge – Results from the Ubatuba, Brazil SGD Assessment Intercomparison. *Est., Coast., Shelf Sci.* 76, 501–511. doi:10.1016/j.ecss.2007.07.027

Cerdà-Domènech, M., Rodellas, V., Folch, A., and Garcia-Orellana, J. (2017). Constraining the Temporal Variations of Ra Isotopes and Rn in the Groundwater End-Member: Implications for Derived SGD Estimates. *Sci. Total Environ.* 595, 849–857. doi:10.1016/j.scitotenv.2017.03.005

Church, T. M. (1996). An Underground Route for the Water Cycle. *Nature* 380, 579–580. doi:10.1038/380579a0

Clark, I., and Fritz, P. (1997). *Environmental Isotopes in Hydrogeology*. Boca Raton: Lewis Publishers, 138–140.

Claypool, G. E., and Kaplan, I. R. (1974). "The Origin and Distribution of Methane in Marine Sediments," in *Natural Gases in Marine Sediments*. Editor I. R. Kaplan (New York: Plenum Press), 99–140. doi:10.1007/978-1-4684-2757-8_8

Cline, J. D. (1969). Spectrophotometric Determination of Hydrogen Sulfide in Natural Waters. *Limnol. Oceanogr.* 14, 454–458. doi:10.4319/lo.1969.14.3.0454

de Souza, G. K., von Ahn, C. M. E., Niencheski, L. F. H., and de Andrade, C. F. F. (2021). Effects of Coastal Lagoon Water Level on Groundwater Fluxes of Nutrients to the Coastal Zone of Southern Brazil. *J. Mar. Sys.* 213, 103459. doi:10.1016/j.jmarsys.2020.103459

Dellwig, O., Wegwerth, A., Schnetger, B., Schulz, H., and Arz, H. W. (2019). Dissimilar Behaviors of the Geochemical Twins W and Mo in Hypoxic-Euxinic Marine Basins. *Earth-sci. Rev.* 193, 1–23. doi:10.1016/j.earscirev.2019.03.017

DWD (2020). Deutscher Wetterdienst 2019. Climate Data Germany – Wismar Station. Available at: https://cdc.dwd.de/portal/ (Accessed January 10, 2020).

Donis, D., Janssen, F., Liu, B., Wenzhöferö, F., Dellwig, O., Escher, P., et al. (2017). Biogeochemical Impact of Submarine Groundwater Discharge on Coastal Surface Sands of the Southern Baltic Sea. *Est., Coast., Shelf Sci.* 189, 131–142. doi:10.1016/j.ecss.2017.03.003

Douglas, A. R., Murgulet, D., and Peterson, R. N. (2020). Submarine Groundwater Discharge in an Anthropogenically Disturbed, Semiarid Estuary. *J. Hydrol.* 124369, 124369. doi:10.1016/j.jhydrol.2019.124369

Folk, R. L., and Ward, W. C. (1957). Brazos River Bar: a Study in the Significance of Grain Size Parameters. *J. Sed. Petrol.* 27, 3–26. doi:10.1306/74d70646-2b21-11d7-8648000102c1865d

Froelich, P. N., Klinkhammer, G. P., Bender, M. L., Luedtke, N. A., Heath, G. R., Cullen, D., et al. (1979). Early Oxidation of Organic Matter in Pelagic Sediments of the Eastern Equatorial Atlantic: Suboxic Diagenesis. *Geochim Cosmochim Acta* 43, 1075–1090. doi:10.1016/0016-7037(79)90095-4

Garcia-Solsona, E., Garcia-Orellana, J., Masqué, P., and Dulaiova, H. (2008). Uncertainties Associated with ^{223}Ra and ^{224}Ra Measurements in Water via a Delayed Coincidence Counter (RaDeCC). *Mar. Chem.* 109, 198–219. doi:10.1016/j.marchem.2007.11.006

Gat, J. (1996). Oxygen and Hydrogen Isotopes in the Hydrological Cycle. *Annu. Rev. Earth Planet. Sci.* 24, 225–262. doi:10.1146/annurev.earth.24.1.225

Gdi-Bsh (2020). GeoSeaPortal. Bundesamt fürfur Seeschiffahrt und Hydrographie. Available at: www.geoseaportal.de.

Gogina, M., Lipka, M., Woelfel, J., Liu, B., Morys, C., Böttcher, M. E., et al. (2018). In Search of a Field/based Relantioship between Benthic Macrofauna and Biogeochemistry in a Modern Brackish Coastal Sea. *Front. Mar. Sci.* 5, 489. doi:10.3389/fmars.2018.00489

Haese, R. R. (2006). in *The Biogeochemistry of Iron. Marine Geochemistry*. Editors H. D. Schulz and M. Zabel (Berlin: Springer-Verlag), 207–240.

Hennig, H., and Hilgert, T. (2007). Dränabflüsse – Der Schlüssel zur Wasserbilanzierung im nordostdeutschen Tiefland. – *Hydrologie und Wasserbewirtschaftung* 51 (6), 248–257.

Hilgert, T. (2009). Grundwasserneubildung Mecklenburg-Vorpommern-Aktualisierung und ergänzende Beschreibung, internal project report.

Hoefs, J. (2018). *Stable Isotope Geochemistry*. Springer-Nature, Science Ltd.

Huckriede, H., and Meischner, D. (1996). Origin and Environment of Manganese-Rich Sediments within Black-Shale Basins. *Geochimica et Cosmochimica Act* 8, 1399–1413. doi:10.1016/0016-7037(96)00008-7

Jankowska, H., Matciak, M., and Nowacki, J. (1994). Salinity Variations as an Effect of Groundwater Seepage through the Seabed (Puck Bay, Poland). *Oceanologia* 36, 33–46.

Jenner, A-K. (2018). Ground Water Development in North-Eastern Germany as Deduced from the Hydrogeochemical and Stable Isotopic Composition of Selected Drinking Waters. Griefswald: University of Greifswald and Leibniz IOW. [MSc thesis].

Johannes, R. E. (1980). The Ecological Significance of the Submarine Discharge of Groundwater. *Mar. Ecol. Prog. Ser.* 3, 365–373. doi:10.3354/meps003365

Jordan, H., and Weder, H. J. (1995). *Hydrogeologie – Grundlagen und Methoden und Regionale Hydrogeologie: Mecklenburg-Vorpommern, Brandenburg und Berlin, Sachsen-Anhalt, Sachsen, Thüringen*. Stuttgart: Enke Verlag, 603.

Jørgensen, B. B., and Kasten, S. (2006). in *Sulfur Cycling and Methane Oxidation. Marine Geochemistry*. Editors H. D. Schulz and M. Zabel (Springer), 271–309.

Jørgensen, B. B. (1982). Mineralization of Organic Matter in the Sea Bed: the Role of Sulphate Reduction. *Nature* 296, 643–645.

Jurasinski, G., Janssen, M., Voss, M., Böttcher, M. E., Brede, M., Burchard, H., et al. (2018). Understanding the Coastal Ecocline: Assessing Sea-Land-Interactions at Non-tidal, Low-Lying Coasts through Interdisciplinary Research. *Front. Mar. Sci.* 5 (342), 1–22. doi:10.3389/fmars.2018.00342

Kostka, J. E., and Luther, G. W. (1994). Partitioning and Speciation of Solid Phase Iron in Saltmarsh Sediments. *Geochim. Cosmochim. Acta* 58, 1701–1710. doi:10.1016/0016-7037(94)90531-2

Kotwicki, L., Grzelak, K., Czub, M., Dellwig, O., Gentz, T., Szymczycha, B., et al. (2014). Submarine Groundwater Discharge to the Baltic Coastal Zone: Impacts on the Meiofaunal Community. *J. Mar. Sys.* 129, 118–126. doi:10.1016/j.jmarsys.2013.06.009

Krall, L., Garcia-Orellana, J., Trezzi, G., and Rodellas, V. (2017). Submarine Groundwater Discharge at Forsmark, Gulf of Bothnia, provided by Ra Isotopes. *Mar. Chem.* 162, 162–172. doi:10.1016/j.marchem.2017.09.003

Lampe, R., Luebke, H., Endtmann, E., and Harff, J. (2013). A New Relative Sea-Level Curve for the Wismar Bay, N-German Baltic Coast. *Meyniana* 57, 5–35.

Lee, Y. W., Hwang, D-W., Kim, G., Lee, W-C., and Oh, H-T. (2009). Nutrient Inputs from Submarine Groundwater Discharge (SGD) in Masan Bay, an Embayment Surrounded by Heavily Industrialized Cities, Korea. *Sci. Tot. Env.* 407, 3181–3188. doi:10.1016/j.scitotenv.2008.04.013

Leipe, T., Moros, M., Kotilainen, A., Vallius, H., Kabel, K., Endler, M., et al. (2013). Mercury in Baltic Sea Sediments – Natural Background and Anthropogenic Impact. *Chem. der Erde* 73, 249–259. doi:10.1016/j.chemer.2013.06.005

Lipka, M., Böttcher, M. E., Wu, Z., Sültenfuß, J., Jenner, A-K., Westphal, J., et al. (2018a). Ferruginous Groundwaters as a Source of P, Fe, and DIC for Coastal Waters of the Southern Baltic Sea: (Isotope) Hydrobiogeochemistry and the Role of an Iron Curtain. *E3s Web Conf.* 54, 1–5. doi:10.1051/e3sconf/20185400019

Lipka, M., Woelfel, J., Gogina, M., Kallmeyer, J., Liu, B., Morys, C., et al. (2018b). Solute Reservoirs Reflects Variability of Early Diagenetic Processes in Temperate Brackish Surface Sediments. *Front. Mar. Sci.* 5, 413. doi:10.3389/fmars.2018.00413

Llobet-Brossa, E., Rabus, R., Böttcher, M. E., Könneke, M., Finke, N., Schramm, A., et al. (2002). Community Structure and Activity of Sulfate-Reducing Bacteria in an Intertidal Surface Sediment: A Multi-Method Approach. *Aquat. Microb. Ecol.* 29, 211–226. doi:10.3354/ame029211

Löffler, H., Adam, C. G. B., Brinschwitz, D., Gieseler, W., Ginzel, G., Grunske, K.-A., et al. (2010). Hydrochemische Typisierung für Grundwasser im Lockergesteinsbereich des norddeutschen Flachlandes. *Schriftenreihe für Geowissenschaften.* 18, 369–399. doi:10.1787/9789282102701-13-fr

Lung, M. V. (2009). Landesamt für Umwelt, Naturschutz und Geologie Mecklenburg-Vorpommern. Map of groundwater recharge, German: "Grundwasserneubildung", gwn.shp. Available at: https://www.umweltkarten.mv-regierung.de/script/ (Accessed December 14, 2019).

Lung, M. V. (2020). Landesamt für Umwelt, Naturschutz, und Geologie Mecklenburg-VorpommernKartenportal Umwelt Mecklenburg-Vorpommern. Data set "Grundwasserhöhengleichen". Available at: https://www.umweltkarten.mv-regierung.de/atlas/script/index.php (Accessed December 15, 2020).

Lung, M. V. (2021). Landesamt für Umwelt, Naturschutz, und Geologie Mecklenburg-Vorpommern. Lake Network Map of Mecklenburg Western-Pomerania: Gewässernetz M-V: Standgewässer: Seen, dlm25w_sg_seen.shp. Available at: https://www.umweltkarten.mv-regierung.de/atlas/script/index.php (Accessed December 14, 2020).

Macklin, P. A., Damien, T. M., and Santos, I. R. (2014). Estuarine Canal Estate Waters: Hotspots of CO_2 Outgassing Driven by Enhanced Groundwater Discharge? *Mar. Chem.* 167, 82–92. doi:10.1016/j.marchem.2014.08.002

Matthäus, W., and Lass, H. U. (1995). The Recent Salt Inflow into the Baltic Sea. *J. Phys. Oceanograph.* 25, 280–286. doi:10.1175/1520-0485(1995)025<0280:trsiit>2.0.co;2

Meister, P., Liu, B., Ferdelman, T. G., Jørgensen, B. B., and Khalili, A. (2013). Control of Sulphate and Methane Distributions in Marine Sediments by Organic Matter Reactivity. *Geochim. Cosmochim. Acta* 104, 183–193. doi:10.1016/j.gca.2012.11.011

Michaelis, J., Usdowski, E., and Menschel, G. (1985). Partitioning of ^{13}C and ^{12}C on the Degassing of CO_2 and the Precipitation of Calcite Rayleigh-type Fractionation and a Kinetic Model. *Am. J. Sci.* 285, 318–327. doi:10.2475/ajs.285.4.318

Moeslund, L., Thamdrup, B., and Jørgensen, B. B. (1994). Sulfur and Iron Cycling in a Coastal Sediment: Radiotracer Studies and Seasonal Dynamics. *Biogeochemistry* 27, 129–152. doi:10.1007/bf00002815

Mohrholz, V. (2018). Major Baltic Inflow Statistic – Revised. *Front. Mar. Sci.* 5, 384. doi:10.3389/fmars.2018.00384

Moore, W. S. (1996). Large Groundwater Inputs to Coastal Waters Revealed by ^{226}Ra Enrichments. *Nature* 380, 612–614. doi:10.1038/380612a0

Moore, W. S., and Arnold, R. (1996). Measurement of ^{223}Ra and ^{224}Ra in Coastal Waters Using a Delayed Coincidence Counter. *J. Geophys. Res.* 101, 1321–1329. doi:10.1029/95jc03139

Moore, W. S., and de Oliveira, J. (2008). Determination of Residence Time and Mixing Processes of the Ubatuba, Brazil, Inner Shelf Waters Using Natural Ra Isotopes. *Est.Coast. Shelf Sci.* 76, 512e521. doi:10.1016/j.ecss.2007.07.042

Moore, W. S. (2010). The Effect of Submarine Groundwater Discharge on the Ocean. *Annu. Rev. Mar. Sci.* 2, 59–88. doi:10.1146/annurev-marine-120308-081019

Moosdorf, N., Böttcher, M. E., Adyasari, D., Erkul, E., Gilfedder, B., Greskowiak, J., et al. (2021). A State-Of-The-Art Perspective on the Characterization of Subterranean Estuaries at the Regional Scale. *Front. Earth Sci.* 9, 601293.

Morse, J., and Mackenzie, F. T. (1990). *Geochemistry of Sedimentary Carbonates*. New York: Elsevier, 707.

Mossmann, J-R., Aplin, A. C., Curtis, C. D., and Coleman, M. L. (1991). Geochemistry of Inorganic and Organic sulphur in Organic-Rich Sediments from the Peru Margin. *Geochim. Cosmochim. Acta* 55, 3581. doi:10.1016/0016-7037(91)90057-c

Oberdorfer, J. A., Valentino, M. A., and Smith, S. V. V. (1990). Groundwater Contribution to the Nutrient Budget of Tomales Bay, California. *Biogeochemistry* 10, 199–216. doi:10.1007/bf00003144

Parkhurst, D., and Appelo, C. (1999). User's Guide to PHREEQC (Version 2): A Computer Program for Speciation, Batch-Reaction, One-Dimensional Transport, and Inverse Geochemical Calculations. *Water-Resources Invest. Rep.*, 99–4259. doi:10.3133/wri994259

Piper, A. (1944). A Graphic Procedure in the Geochemical Interpretation of Water Analyses. *Eos, Trans. Am. Geophys. Union* 25, 914–928. doi:10.1029/tr025i006p00914

Prena, J. (1995). Temporal Irregularities in the Macrobenthic Community and Deep-Water Advection in Wismar Bay (Western Baltic Sea). Estuarine. *Coastal Shelf Sci.* 41, 705–717. doi:10.1006/ecss.1995.0085

Rocha, C., Robinson, C. E., Waska, H., Holly, M. A., and Bokuniewicz, H. (2021). A Place for Subterranean Estuaries in Coastal Zone. Estuarine. *Coastal Shelf Sci.* 250, 107167. doi:10.1016/j.ecss.2021.107167

Rodellas, V., Garcia Orellana, J., Garcia-Solsona, E., Masque, P., Dominguez, J. A., Ballesteros, B. J., et al. (2012). Quantifying Groundwater Discharge from Different Sources into a Mediterranean Wetlandwetland by Using ^{222}Rn and Ra Isotopes. *J. Hydrol.* 466-467, 11–22. doi:10.1016/j.jhydrol.2012.07.005

Rodellas, V., Garcia-Orellana, J., Masqué, P., Feldman, M., and Weinstein, Y. (2015). Submarine Groundwater Discharge as a Major Source of Nutrients to the Mediterranean Sea. *PNAS March* 112 (13), 3926–3930. doi:10.1073/pnas.1419049112

Rodellas, V., Stieglitz, T. C., Tamborski, J. J., van Beek, P., Andrisoa, A., and Cook, P. G. (2021). Conceptual Uncertainties in Groundwater and Porewater Fluxes Estimated by Radon and Radium Mass Balances. *Limnol. Oceanogr.* 9999, 1–19. doi:10.1002/lno.11678

Santos, I. R., Chen, X., Lecher, A. L., Sawyer, A. H., Moosdorf, N., Rodellas, V., et al. (2021). Submarine Groundwater Discharge Impacts on Coastal Nutrient Biogeochemistry. *Nat. Rev. Earth Environ.* 2, 307–323. doi:10.1038/s43017-021-00152-0

Santos, I. R., Eyre, B. D., and Huettel, M. (2012). The Driving Forces of Porewater and Groundwater Flow in Permeable Coastal Sediments: A Review. *Estuarine, Coastal Shelf Sci.* 98, 1–15. doi:10.1016/j.ecss.2011.10.024

Santos, I. R., Niencheski, F., Burnett, W., Peterson, R., Chanton, J., Andrade, C. F. F., et al. (2008). Tracing Anthropogenically Driven Groundwater Discharge into a Coastal Lagoon from Southern Brazil. *J. Hydrol.* 353, 275–293. doi:10.1016/j.jhydrol.2008.02.010

Schafmeister, M-T., and Darsow, A. (2004). "Potential Change in Groundwater Discharge as Response to Varying Climatic Conditions – an Experimental Model Study at Catchment Scale," in *The Baltic Sea Basin*. Editors J. Harff and S. Bjorck (Springer), 449.

Schlitzer, R. (2001). Ocean Data View. Availableat: http://www.awi-bremerhaven.de/GEO/ODV.

Schlüter, M., Sauter, E., Andersen, C. E., Dahlgaard, H., and Dando, P. R. (2004). Spatial Distribution and Budget for Submarine Groundwater Discharge in Eckernförde Bay (Western Baltic Sea). *Limnol. Oceanogr.* 49 (1), 157–167. doi:10.4319/lo.2004.49.1.0157

Schultz, H. D. (2006). "Quantification of Early Diagenesis: Dissolved Constituents in Marine Pore Water," in *Mar. Geoch.* Editors H. D. Schulz and M. Zabel (Berlin, Heidelberg: Springer-Verlag).

Seeberg-Elverfelds, J., Schlüter, M., Feseker, T., and Kölling, M. (2005). Rhizon Sampling of Porewaters Near the Sediment-Water Interface of Aquitic Systems. *Limnol. Oceanogr.: Methods* 3, 361–371. doi:10.1002/lom3.v3.11

Smellie, J., Tullborg, E -L., Nilsson, A. C., Sandström, B., Waber, N., Gimeno, M., et al. (2008). *Explorative Analysis of Major Components and Isotopes—SDM-Site Forsmark*. SKB R- 08-84. Stockholm, Sweden: SKB.

Stegmann, S., Sultan, N., Kopf, A., Apprioual, R., and Pelleau, P. (2011). Hydrogeology and Ist Effect on Slope Stability along the Coastal Aquifer of Nice, France. *Mar. Geology* 280, 168–181. doi:10.1016/j.margeo.2010.12.009

Stieglitz, T. C., Rapaglia, J., and Kruoa, S. C. (2007). An Effect of Pier Pillings on Nearshore Submarine Groundwater Discharge from a (Partially) Confined Aquifer. *Estuaries and Coasts* 30 (3), 543–550. doi:10.1007/bf03036520

Stieglitz, T., Taniguchi, M., and Skyler, N. (2008). Spatial Variability of Submarine Groundwater Discharge. *Ubatuba, Brazil. Estuarine Coastal Shelf Science* 76, 493–500. doi:10.1016/j.ecss.2007.07.038

Szymczycha, B., Klostowska, Z., Lengier, M., and Dzierzbicka-Glowacka, L. (2020). Significance of Nutrients Fluxes via Submarine Groundwater Discharge in the Bay of Puck, Southern Baltic Sea. *Oceanologia* 62, 117–125. doi:10.1016/j.oceano.2019.12.004

Szymczycha, B., Vogler, S., and Pempkowiak, J. (2012). Nutrient Fluxes via Submarine Groundwater Discharge to the Bay of Puck, Southern Baltic Sea. *Sci. Total. Environ.* 438, 86–93. doi:10.1016/j.scitotenv.2012.08.058

Taniguchi, M., Dulaim, H., Burnett, K. M., Santos, I. R., Sugimoto, R., Stieglitz, T., et al. (2019). Submarine Groundwater Discharge Updates on its Measurement Techniques, Geophysical Drivers, Magnitudes, and Effects. *Front. Environ. Sci.* 7, 141. doi:10.3389/fenvs.2019.00141

Teatini, P., Isotton, G., Nardean, S., Ferronato, M., Mazzia, A., Da Lio, C., et al. (2017). Hydrogeological Effects of Dredging Navigable Channels Canals through Lagoon Shallows. A Case Study in Venice. *Hydrol. Earth Syst. Sci.* 21, 5627–5646. doi:10.5194/hess-21-5627-2017

Thamdrup, B., Fossing, H., and Jørgensen, B. B. (1994). Manganese, Iron, and Sulfur Cycling in a Coastal Marine Sediment, Aarhus Bay, Denmark. *Geochim. Cosmochim. Acta* 58, 5115–5129. doi:10.1016/0016-7037(94)90298-4

Virtasalo, J. J., Schroeder, J. F., Luoma, S., Majaniemi, J., Mursu, J., and Scholten, J. (2019). Submarine Groundwater Discharge Site in the First Salpausselkä Ice-Marginal Formation, South Finland. *Solid Earth-EGU* 10, 405–432. doi:10.5194/se-10-405-2019

VSW (2018). Wasserstrassen und Schiffahrtsverwaltung des Bundes. Anpassung der seewaertigen Zufahrt zum Seehafen Wismar. Availableat: https://www.gdws.wsv.bund.de/SharedDocs/Downloads/DE/Planfeststellungsverfahren/100_Anpassung_Wismar/Scopingunterlage.pdf?__blob=publicationFile&v=2 (Accessed July 10, 2020).

Whiticar, M. J., and Werner, F. (1981). Pockmarks: Submarine Vents of Natural Gas or Freshwater Seeps? *Geo-Marine Lett.* 1, 193–199. doi:10.1007/bf02462433

Winde, V., Böttcher, M. E., Escher, P., Böning, P., Beck, M., Liebezeit, G., et al. (2014). Tidal and Spatial Variations of DI^{13}C and Aquatic Chemistry in a Temperate Tidal basin during winter Time. *J. Mar. Syst.* 129, 394–402. doi:10.1016/j.jmarsys.2013.08.005

Conflict of Interest: The authors declare that the research was conducted in the absence of any commercial or financial relationships that could be construed as a potential conflict of interest.

The reviewer (AB) declared a past co-authorship with one of the authors (JS) to the handling Editor.

Publisher's Note: All claims expressed in this article are solely those of the authors and do not necessarily represent those of their affiliated organizations, or those of the publisher, the editors and the reviewers. Any product that may be evaluated in this article, or claim that may be made by its manufacturer, is not guaranteed or endorsed by the publisher.

Chapter 3. Submarine groundwater discharge into a semi-protected coastal bay of the southern Baltic Sea: A multi-method approach

Graphical Abstract

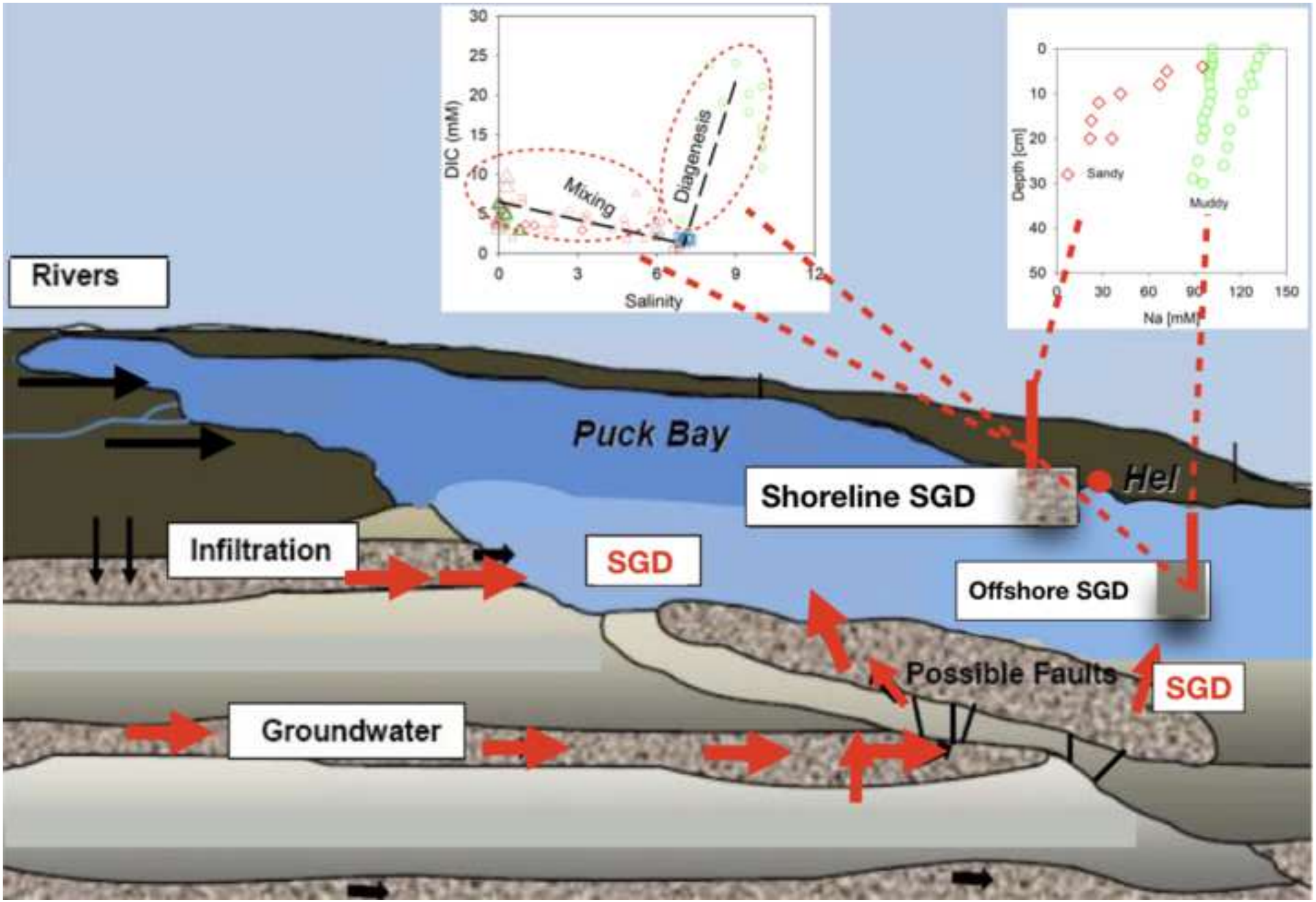

Highlights

- Submarine groundwater discharge (SGD) was assessed using a multi-method approach.
- Estimates of SGD were based on local and regional approaches.
- A greater degree of SGD was observed in the sandy sediments compared to the muddy sediments.
- SGD impacts benthic diagenetic processes.
- SGD increases the element fluxes at the sediment-water interface.
- SGD is a mixing between groundwater originating from different aquifers.

Submarine groundwater discharge into a semi-enclosed coastal bay of the southern Baltic Sea: A multi-method approach

Cátia Milene Ehlert von Ahn[1*], Olaf Dellwig[1], Beata Szymczycha[2], Lech Kotwicki[2], Jurjen Rooze[1], Rudolf Endler[3], Peter Escher[1,4], Iris Schmiedinger[1], Jürgen Sültenfuß[5], Magdalena Diak[2], Matthias Gehre[6], Ulrich Struck[7], Susan Vogler[1] and Michael Ernst Böttcher[1,8,9*]

[1]Geochemistry & Isotope Biogeochemistry, Leibniz Institute for Baltic Sea Research (IOW), Warnemünde, Germany.
[2] Institute of Oceanology, Polish Academy of Sciences (IOPAN), Sopot, Poland.
[3]Marine Geophysics, Leibniz Institute for Baltic Sea Research (IOW), Warnemünde, Germany.
[4]current address: Ecoandmore Freiburg, Germany.
[5]Institute of Environmental Physics, University of Bremen, Bremen, Germany.
[6]Department of Isotope Biogeochemistry, Helmholtz Centre for Environmental Research (UFZ), Leipzig-Halle, Germany.
[7]Free University Museum for Natural History, Berlin, Germany.
[8]Marine Geochemistry, University of Greifswald, Greifswald, Germany.
[9]Interdisciplinary Faculty, University of Rostock, Rostock, Germany.
*michael.boettcher@io-warnemuende.de
*catia.vonahn@io-warnemuende.de

Abstract

The present study aims to understand the impact of submarine groundwater discharge (SGD) on a coastal area with different lithology and degrees of SGD. The sampling campaigns took place on Puck Bay and the Gulf of Gdańsk, southern Baltic Sea encompassing the years between 2009 and 2021. The methodological approach combined geophysical characterization of the surface sediments with detailed spatial and temporal (isotope) biogeochemical investigations of pore and surface waters. The isotope hydrochemical composition of the freshwater component supplying SGD sites is characterized and compared to nearby-coastal groundwater and rivers around the bay. The composition of porewater gradients and differences in the bay's surface waters show that SGD is a common phenomenon in the study area. The acoustic investigations have identified areas of surface sediment disturbances that may indicate zones of preferential occurrence of SGD. Regional SGD was estimated through a radium mass balance. The estimated volumetric SGD into Puck Bay is of the same order of magnitude as river discharge. Local estimation of SGD based on porewater profiles indicated the highest SGD fluxes on the sandy shoreline sediments; however, relatively low element fluxes. In

contrast, at the shoreline muddy sites, SGD was low. However, the interfacial elements fluxes, enhanced by intense diagenesis in the top sediments, lead to the liberation of higher nutrients and dissolved carbon to the open water column. This combination of different techniques in the study area demonstrated that SGD may result from different freshwater endmembers and that diagenesis in surface sediments essentially modifies the composition of the mixed solutions, finally discharging to the coastal waters.

Keywords: Stable isotopes, Radium isotopes, Acoustic survey, Diagenesis, Gulf of Gdańsk, Puck Bay.

1. Introduction

Coastal regions are ecosystems subjected to intense and dynamic water and element fluxes, and nowadays, under increasing anthropogenic pressure. Often high nutrient loads lead to enhanced primary productivity and organic carbon remineralization, thereby having a trigger function for carbon cycling. The processes are typically associated with other elements, such as sulfur species and metals (e.g., Froelich et al., 1979; Jørgensen, 2006). Depending on the lithological and sedimentological boundary conditions, physicochemical and biogeochemical processes are promoted upon mixing between fresh and salty waters and further superimposed by diagenetic processes, thereby modifying the concentrations of reactive species. Whereas surface estuaries provide essentially oxygenated waters to the ocean, submarine groundwater discharge (SGD) may also add anoxic waters to the coastal environment (Church, 1996; Slomp & van Cappelen, 2004; Paytan et at., 2006; Moosdorf et al., 2021; Santos et al., 2021).

The role of SGD acting as a potential source and carrier of dissolved substances in the coastal ocean has increasingly attracted the interest of the scientific community over the last decades (Zektzer et al., 1963; Moore, 1996; Taniguchi et al., 2002; Moore 2010; Santos et al., 2021; Böttcher et al., 2023). Element fluxes through SGD have been documented to impact coastal

waters in a way that fresh SGD provides new dissolved constituents, while saline SGD, after modification by diagenesis, releases recycled nutrients to coastal waters (Sadat-Noori et al., 2016; Santos et al., 2021; Purkamo et al., 2022). Furthermore, the importance of SGD for the water and element balance may differ enormously on local, regional and global scales (Moosdorf et al., 2021), and the processes controlling those fluxes at the land-sea interface remain an open question in hydrology (Blöschl et al., 2019).

The fresh and saline components of SGD are usually well mixed, making the quantification and their impact on coastal waters complex (Sadat-Noori et al., 2016). Detection and estimation of SGD have been carried out through different approaches (Burnett et al., 2006; Taniguchi et al., 2019; Böttcher et al., 2023). For example, geophysical techniques identified fluid/gas flows across surface sediments (e.g., Hoffmann et al., 2020; Idczak et al., 2020); direct measurements based on piezometers and seepage meters evaluated porewater gradients, and quantified SGD and the associated chemical fluxes (e.g., Oberdorfer et al., 2008; Donis et al., 2017; Tamborski et al., 2018).

Among the geochemical tracers, radium, radon, methane, silica, and stable isotopes have been applied in the majority of SGD studies and the results are promising both for detecting, evaluating and quantifying SGD. For example, water isotopes quantified mixing processes since groundwater is depleted in heavier isotopes than seawater (Gat, 1996; Povinec et al., 2008). The concentrations and stable carbon isotope composition of DIC, DOC, and CH_4 are powerful tracers for accessing the biogeochemical process within the subterranean estuary (Böttcher et al., 2014; Winde et al., 2014; Sadat-Nouri et al., 2016; Donis et al., 2017). Radium and radon isotopes are generally enriched in groundwater compared to the surface water and, therefore, can provide quantitative and qualitative information on the regional occurrence of SGD (Moore, 1996; Top et al., 2001; Moore, 2006; Beck et al., 2007b; Moore et al., 2011; Rodellas et al., 2017; Taniguchi et al., 2019; von Ahn et al., 2021).

Most studies about water and element fluxes associated with SGD derive from the characterization of endmembers (e.g., groundwater, rivers, and surface seawater) with less work investigating the mixing zone. However, the processes taking place in the subterranean estuary, and particularly in the sediments overlying the aquifers, being the interface towards the surface, are impacted by biotic and abiotic transformations that result in sources and sink for reactive elements (Huettel et al., 1998; Moore, 1999, Charette et al., 2005; Moosdorf et al., 2021, Böttcher et al., 2023; Goyetche et al., 2022). Ion sorption, mineral dissolution, precipitation, and remineralization of organic matter are among the processes occurring in the aquifers and throughout the flow path of SGD (Moore, 1999; Moosdorf et al., 2021). Additionally, the substrate availability, the aquifer rock composition, and groundwater residence time are also of great importance. Therefore, the controls of non-conservative behavior must be understood and considered when estimating SGD element fluxes to coastal waters (Beck et al., 2007a; Cerdà-Domènech et al., 2017; Donis et al., 2017; von Ahn et al., 2021).

Studies on SGD have been carried out in the Baltic Sea (e.g., Peltonen 2002, Viventsowa and Voronow, 2003; Purkl & Eisenhauer, 2004; Schlüter et al., 2004; Krall et al., 2017; Virtasalo et al., 2020; von Ahn et al., 2021, Purkamo et al., 2022), particularly in the Gulf of Gdańsk and the Puck Bay, already since the 90s (e.g., Piekarek-Jankowska, 1996; Falkowska and Piekarek-Jankowska, 1999). Different occurrences of SGD have been identified throughout the Gulf of Gdańsk and Puck Bay, which act as hot spots for localized SGD to the surface waters impacting in different degrees the coastal water balance and the biogeochemical cycles within the coastal waters. For example, based on seepage meters, measurement fluxes of SGD and their associated chemical fluxes were estimated for different areas in Puck Bay (Szymczycha et al., 2012, 2016). Furthermore, the impact of SGD on the meiofaunal community was investigated by Kotwicki et al. (2014). Donis et al. (2017) evaluated the impact of SGD on the sandy

sediments of Hel Bight, Puck Bay. The impact of pharmaceuticals and caffeine via SGD on the Puck Bay surface waters was also evaluated (Szymczycha et al., 2020). A pockmark associated with SGD in the Gulf of Gdańsk was assessed by Idczak et al. (2020). Moreover, a lowered bottom water salinity was observed almost across Puck Bay, indicating an extended impact by SGD (Matciak et al., 2015).

Due to the high number of SGD sites along the Polish coastline and their changing dynamic, the goals of the present study are 1) to evaluate the impact of SGD on the chemical gradients in surface sediments taking into consideration lithology, 2) to estimate the (isotope) hydrochemical composition of the fresh water component entering the Puck Bay via SGD compared to groundwater and river around Puck Bay, and 3) to estimate the contribution of SGD to the Puck Bay based on local porewater gradients, seepage meters, and regionally, using a Ra isotope balance.

The potential physical pathways and indicators for SGD in central Puck Bay were characterized using acoustic methods. The investigation was further supplemented by a sedimentological and geochemical characterization of the sediments under different degrees of SGD impact. Water column and porewater samples were analyzed for major and trace elements, nutrients, sulfide, total alkalinity, dissolved inorganic carbon (DIC), $\delta^{13}C_{DIC}$, methane (CH_4), $\delta^{13}C_{CH4}$, $\delta^{2}H_{CH4}$, $\delta^{2}H_{H2O}$, $\delta^{18}O_{H2O,}$ radium isotopes (^{223}Ra and $^{224}Ra_{ex}$), tritium (^{3}H) and helium (He) isotopes. This multi-method approach highlights the role of SGD in the local and regional water and elemental budget for coastal waters of the Baltic Sea. Finally, it provides a basis for future estimates of the hydrological and ecosystem consequences of coastal areas affected by climate change.

2. Methods

2.1 Study area

133 The Gulf of Gdańsk is located in the southern Baltic Sea (Figure 1). The maximum water depth
134 is approximately 118 m, and the surface and bottom layer salinity are about 8 and 12,
135 respectively. Because the tidal influence is minimal in the southern Baltic Sea, small changes
136 in the dynamic of the bay are mainly due to wind and the river plume front of the Vistula River
137 (Dippner et al., 2019). The shallower sediments of the central gulf are covered with clays that,
138 in some places, contain fine-grained sand and silt, whereas the deepest part is dominated by
139 clayey silt (Idczak et al., 2020; Majewski, 1990. Figure 1).

140 In the eastern part of the Gulf of Gdańsk, the Hel peninsula forms a semi-enclosed basin called
141 Puck Bay. The bay has a total area of 359.2 km^2. It is divided into two parts: the outer bay,
142 with an average depth of 20.5 m, and the inner bay, a markedly shallower part, called the Puck
143 Lagoon, with an average depth of 3.1 m (Matciak et al. 2011), which has an area of 104 km^2
144 (Kramarska et al., 1995).

145 The outer Puck Bay comprises diverse sediments with coarse-grained sands dominating a depth
146 of about 20 m. Fine sands, silt, silt-clay, and sand-silt-clay are the composition in the deepest
147 parts, and some sandy beaches, gravel beds, stony outcrops, clay cliffs, and vegetated river
148 mouths (see Kłostowska et al., 2019 and references therein, Figure 1). Sediments in the inner
149 part of Puck Bay have a relatively constant grain distribution dominated by fine and medium-
150 grained sands (Figure 1).

151 Puck Bay is the major drainage area of Cretaceous, Tertiary, and Quaternary aquifers. It affects
152 the direction of the groundwater flow, thereby modeling the groundwater regime of the
153 piezometric groundwater surface. The groundwater flows into the bay occurs mainly via
154 seepage through the seabed. The Hel Peninsula also receives groundwater from Holocene
155 aquifers; however, those flow directly to the Baltic Sea (see Piekarek-Jankowska 1996 and
156 references therein).

Different areas along the Puck Bay shoreline show impact by SGD (e.g., Szymczycha et al., 2012, 2020; Kotwicki et al., 2014; Donis et al., 2017; Kłostowska et al., 2019), and the present study is a continuation of these studies as well. The investigated SGD sites are Hel, Chałupy, Swarzewo, and Osłonino (Figure 1)

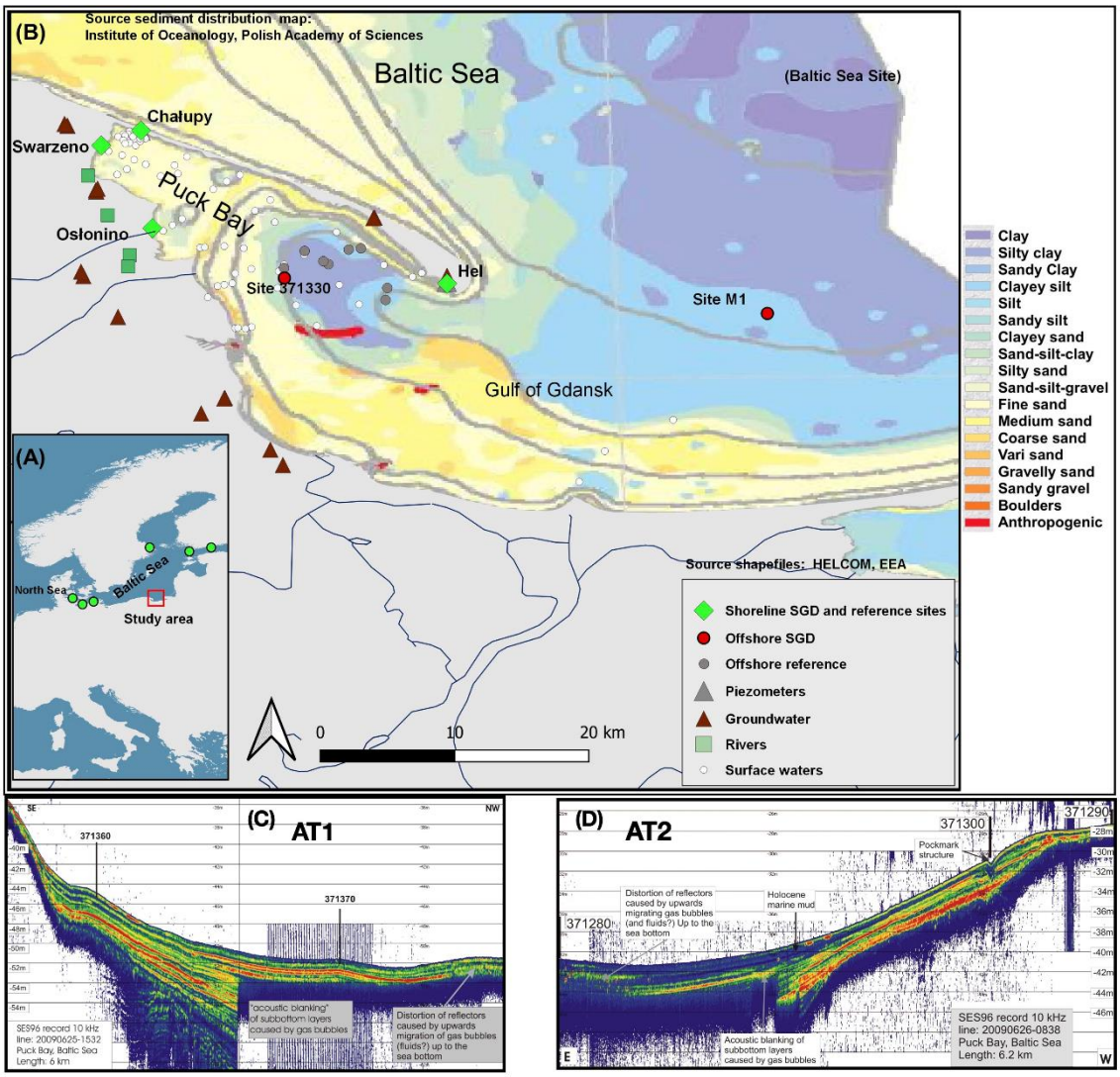

Figure 1 - (A) Map showing the location of the study area (red dot) and some of the SGD investigated sites along the Baltic Sea (Viventsova and Voronov, 2003; Schlüter et al., 2004; Krall et al., 2017; Jurasinski et al., 2018; Racasa et al., 2021; Virtasalo et al., 2020; von Ahn et al., 2021, Purkamo et al., 2022, green dots). (B) Map of the study area in the Gulf of Gdańsk/Puck Bay showing the different sampling sites (surface waters, porewater, groundwaters, and rivers). Source of the shapefiles European Environmental Agency and HELCOM database. Atlas of Polish marine area bottom habitats. Environmental valorization of marine habitats. 2009 Institute of Oceanology PAS. (C) Acoustic transect AT1 (E) and AT2 (Böttcher et al., 2023) in the Outer Puck Bay from the campaign in 2009. NOTE: The sediment distribution map (modified) was added as a background for a rough overview of the sediment composition of the study area. The map is not georeferenced to the sampled sites.

2.2 Materials and methods

2.2.1 Sampling and sample preparation

The sampling campaigns took place in 2009-2011, 2019, and 2021. Fresh groundwater from wells and piezometers, river waters, porewater, sediments, and surface waters from the Puck Bay, the Gulf of Gdańsk, and the coastal Baltic Sea were sampled. Figure 1 shows the sampling sites. Additional information on sampling sites is given in supplementary Table 1.

The outer Puck Bay water column was sampled at 16 sites in June 2009 onboard the RV Professor Albrecht Penck (07PE0919) using a conventional CTD with bottle rosette as well as a Pump-CTD system (Strady et al., 2008). In October 2019, onboard the RV Oceania, surface waters were sampled at 40 sites (0.5 m), including the central Gulf of Gdańsk and the coastal Baltic Sea, using a pump attached to the vessel. Additionally, the bottom waters at four sites were sampled using Niskin bottles.

Surface water sampling in the inner Puck Bay was carried out in October 2019 using a rubber boat and in June 2021 using a sailing boat. The water samples were taken via PE syringes and filtered with 0.45 μm cellulose acetate disposable filters (Carl Roth, Karlsruhe, Germany). For Ra isotopes, 100-150 liters of surface water were pumped into barrels through a 1 μm filter. From the barrels, the filtered water was pumped again using a submersible pump through manganese-coated acrylic fibers (Mn-fiber) at a flow rate of around 1 L min^{-1} to extract the Ra isotopes quantitatively. The fibers were washed to remove salt and were partly dried for measurements (Garcia-Solsona et al., 2008).

During the cruise in June 2009, sediment cores from five sites were retrieved by a multi-corer device (Sites: 371370, 371290, 371330, 37160, 371270), and in October 2019, four sediment cores were retrieved using a GEMAX corer (sites M2, 12M, 15M, 13M) in the outer Puck Bay (Figure 1). Additionally, one sediment core was taken in the central Gulf of Gdańsk in 2019 (Site M1). These sites are named in this study as offshore sites.

196 Sediment cores were sectionized and frozen for further geochemical analyses. Porewater was
197 extracted from a parallel core via 0.2 μm rhizons (Rhizosphere Research - Wageningen, The
198 Netherlands; Seeberg-Elverfeldt et al., 2005) and stored in cold or frozen for geochemical
199 analyses. Salinity and pH were measured in situ using a refractometer and hand-held pH meter.

200 The sampling campaigns along the shoreline at Hel took place in September and November
201 2009, March, May, and October 2010, and June 2021. Chałupy, Swarzewo, and Osłonino, were
202 sampled only in June 2021. These sites are named in this study as shoreline sites.

203 Along the shoreline of Puck Bay, porewaters were extracted via pre-established porewater
204 samplers (Donis et al., 2017) during the campaigns between 2009 and 2011. During the 2019
205 and 2021 campaigns, the porewater was extracted by push point lances (MHE products) using
206 PE syringes and filtered with 0.45 μm cellulose acetate disposable filters (Carl Roth, Karlsruhe,
207 Germany). For Ra isotopes, 5-10 liters of porewater were transferred into canisters without
208 filtration by a peristaltic pump. From the canister, the sample was filtered through Mn-fiber, as
209 explained for the surface water samples from the Puck Bay cruises. Additionally, sediment
210 cores were taken and sliced for further analysis.

211 Seepage meters were used to measure seepage water fluxes and collect samples for further
212 chemical analysis from sites in Hel, Chałupy, and Swarzewo during the campaign in 2021. The
213 seepage meter consists of a PE chamber with a surface of 0.785 m^2 connected to a PE bag at
214 the end. The seepage flux rate was calculated from the water volume change in the bag as a
215 function of time.

216 Groundwater from 17 wells and two piezometers from depths varying between 2 to 180 m was
217 sampled. Six groundwater wells and two piezometers located on the peninsula, and 11
218 groundwater wells located on the land site. The sampling campaigns were carried out in April
219 2009 and June 2021. River water samples were collected in April 2011 and June 2021: the

Reda (0.6 km inland from the mouth), the Zagórska Struga (0.1 km inland from the mouth), the Plutnica (0.2 km inland from the mouth), and Gizdepka (0.2 km inland from the mouth). Samples were taken via PE syringe and filtered using 0.45 μm SFCA disposable filters (Carl Roth, Karlsruhe, Germany). For Ra isotopes, 60 L of river water was pumped through a 1 μm filter into barrels, and 20 L of groundwater was transferred without filtration into canisters. The sampled water was filtered from the barrels/canisters through an Mn-fiber as described above.

For determination of total carbon (TC), total nitrogen (TN), total sulphur (TS), total inorganic carbon (TIC), and mercury total (Hg), the sediment aliquots were stored in centrifuge tubes (Sarstedt) and kept frozen until freeze-drying and homogenization using an agate ball mill.

Filtrated water samples for major and trace element analysis were filled into acid-cleaned PE bottles and acidified with concentrated HNO_3 to 2 vol. %. Nutrient water samples were filled into pre-cleaned PE bottles. Samples for dissolved sulfide (H_2S) water samples were filled into PE bottles pre-filled with ZnAc 5%. Porewater samples for total alkalinity (TA) were collected in PE vials pre-filled with 0.1M HCl. Water samples for dissolved inorganic carbon (DIC) and $\delta^{13}C_{DIC}$ were filled without headspace into Exetainer® tubes pre-filled with saturated $HgCl_2$ solution. Samples for $\delta^{13}C_{CH4}$ and $\delta^{2}H_{CH4}$ were kept closed in glass containers closed with a butyl septum (black) and preserved with NaOH solution (Jørgensen et al., 2004). Samples for $\delta^{18}O_{H2O}$ and $\delta^{2}H_{H2O}$ analyses were collected in 1.5 mL glass vials (Zinser) sealed with a PTFE-coated septum cap. Samples for ^{3}H were stored in PE bottles. For helium isotopes, samples were allowed to flow through and finally stored in head-space-free copper tubes. All samples were stored in dark cool or frozen until further analyses.

The diffused Ra flux from the bottom sediments of Puck Bay was quantified following the approach outlined by Rodellas et al. (2012) using sediment from the Osłonino Site (Figure 1). The sediments were composed mostly by sand. The sediments were placed in a glass 3L beaker,

and the overlying water was extracted and replaced with Ra-free Puck Bay surface water from Puck Bay (2 L). A closed loop system was assembled, and the water was continuously circulated through the tubing and the Mn-Fiber. The Mn-fibers were replaced after 12, 24, 36, and 48 h. Overlying water was constantly aerated to prevent changes in redox conditions. The diffusion rate was calculated from the slope of the accumulated $^{224}Ra_{ex}$ activity (in Bq) per incubation time (h) (Supplementary Figure 2).

2.2.2 Geophysical investigations

High-resolution sub-bottom profiling using an INNOMAR SES96 Standard parametric sediment echo sounder was performed during a cruise with RV Professor Penck in 2009. A motion reference unit was used to steer/keep the acoustic beam in the vertical direction to correct the ship's vertical movements. The track plots of the acoustic profiles are depicted in (Supplementary Figure 1). Detailed descriptions of the SES96 echo sounder system are available at *www.innomar.com.* During the acoustic survey, the parametric echo sounder transmitted acoustic pulses in a very narrow sound beam with virtually no side lobes and a narrow opening angle of 4 degrees. This resulted in a sonified seafloor area of about four m² at a water depth of 30 m. The acoustic pulses were built up by a primary frequency component of 100 kHz and a selectable secondary frequency component ranging from 5-15 kHz. Only the secondary low-frequency components penetrated the sub-bottom because the seafloor sediments strongly attenuated the primary high-frequency parts of the acoustic pulses. Depending on the selected secondary frequency, a vertical resolution of sediment layers in the range of 0.2-0.5 m was obtained.

2.2.3 Geochemical analyses

Freeze-dried and homogenized sediments were analyzed for their TC, TN, and TS content with a CHNS Elemental Analyzer (Euro Vector EuroEA 3052). The combustion was catalyzed by

V_2O_5, and the resulting gaseous products were chromatographically separated and quantified via infrared spectrophotometry. Total inorganic carbon (TIC) was determined with Elemental Analyzer multi-EA (Analytik Jena) after a reaction with 40% phosphoric acid followed by infrared spectrophotometry quantification of CO_2. The precision of the method for the samples from 2019-21 was about 13, 6, 14, and 6%, and accuracy was about 2, 12, 8, and 1% for TC, TN, TS, and TIC, respectively, using MBSS- (CNS) and OBSS (TIC) in-house reference materials. The content of TOC was calculated from the difference between TC and TIC. Total mercury was analyzed using a DMA-80 analyzer with a detection limit of about 0.15 µg kg^{-1} (Leipe et al. 2013), and a calibration carried out with 142R and MBSS reference materials precision and accuracy of the measurement for 2019-21 was better than ± 4.5 and ±0.6%, respectively.

In the water samples, the major ions (Na, Mg, Ca, K, S) and trace elements (Ba, Fe, Mn) were analyzed by inductively coupled plasma optical emission spectrometry (ICP-OES; iCAP 6400 (before 2016), Duo/iCAP 7400, Thermo Fischer Scientific) using matrix-matched external calibration and Sc as internal standard. Precision and accuracy were checked with spiked CASS-4 and SLEW-3 (NRCC) and were better than 4 and 5% for CASS-4, and 7 and 7% for SLEW-3, respectively. In all water samples, the measured total dissolved S is considered to consist essentially of SO_4.

Concentrations of H_2S were determined by the methylene blue method (Cline, 1969) using a Spekord 40 spectrophotometer (Analytik Jena). Nutrients were analyzed using QuAAtro autoanalyzer system (Seal Analytical, Southampton, UK) following Grasshoff et al. (2009).

Total alkalinity (TA) was measured by potentiometric titration (Van den Berg and Rogers, 1987). Dissolved inorganic carbon (DIC) and $\delta^{13}C_{DIC}$ values were determined as described by Winde et al. (2014) by means of continuous-flow isotope-ratio mass spectrometry (CF-IRMS)

using a Thermo Finnigan MAT253 gas mass spectrometer attached to a Thermo Electron Gas Bench II via a Thermo Electron Conflo IV split interface. Solutions were allowed to react for at least 18 h at room temperature before introduction into the mass spectrometer. The international NBS19 standard, a carbonate from Solnhofer Platternkalk, and in-house $NaHCO_3$ were used to calibrate measured isotope ratios towards the V-PDB scale. Concentrations of DIC from 2009-2011 were determined based on pH and TA values.

Values of $\delta^{18}O_{H2O}$ and $\delta^{2}H_{H2O}$ were analyzed by a laser cavity-ring-down-spectroscopy (LCRDS) system Picarro L1102-I (2009-2011 data); Picarro L2140-I (2019-2021 data); Gupta et al., 2009; Böttcher and Schmiedinger, 2021). Six replicate injections were performed for each sample, and arithmetic averages and standard deviations (1 sigma) were calculated. The reproducibility of replicate measurements was generally better than 0.7‰ and 0.6‰ (2009-2011 data) and better than 0.06 mUr and 0.3 mUr (2019-2021 data) for oxygen and hydrogen, respectively. The reference materials SLAP, and VSMOW were used to calibrate measured isotope ratios towards the V-SMOW scale. The stable isotope composition of dissolved porewater methane was carried out at the Centre of Environmental Research (UFZ) (Tamisier et al., 2022). The given '‰' values are equivalent to mUr (Milli Urey; Brand and Coplen, 2012).

^{3}H and He isotopes were measured as described by Sültenfuß et al. (2009). Short-lived Ra isotopes (^{223}Ra, $t_{1/2}$ = 11.4 d, and ^{224}Ra $t_{1/2}$ = 3.7 d) were measured with a radium-delayed coincidence counter (RaDeCC) (Moore and Arnold, 1996) within 3 and 7 days after sampling. After about a month, a further measurement was conducted to determine ^{224}Ra supported by ^{228}Th ($t_{1/2}$ = 1.9 years). This measurement is then subtracted from the initial ^{224}Ra to obtain the excess of ^{224}Ra activities ($^{224}Ra_{ex}$). Activities of ^{223}Ra, ^{224}Ra, and $^{224}Ra_{ex}$ were calculated, and the expected error of the measurement is 12 and 7% for ^{223}Ra and ^{224}Ra, respectively (Garcia-

316 Solsona et al., 2008). The calibration of the detectors is done once a month using ^{232}Th with
317 certificate activities.

318 2.2.3 Flux calculations

319 Exchange fluxes between sediment and the overlying water were estimated based on measured
320 porewater profiles. To constrain the upward porewater velocity, the salinity gradient formed
321 by mixing fresh groundwater with seawater near the sediment-water interface was fitted. The
322 partial differential equation

323 $$0 = \frac{d}{dx}\left[\emptyset\left(\frac{D_m}{\theta^2} + D_e\right)\frac{dC}{dx} - \emptyset uC\right] \quad (1)$$

324 describes the concentration profile of sodium, where u is the upward flow velocity, C is the
325 concentration, D_m is the ionic diffusion coefficient, which was corrected for temperature and
326 salinity, θ2 is the tortuosity, and φ is the porosity (Boudreau, 1997), which was set to a constant
327 value, based on measurements or else the type of sediment substrate. Here, we used D_e to
328 account for additional mixing near the sediment-water interface, which may result from
329 currents and groundwater recirculation (Qian et al., 2009; Donis et al., 2017).
330 It was implemented as functions with the highest mixing in a surficial layer with a thickness
331 varying between 0 and 7 cm before decaying exponentially over depth. Our approach was to
332 set D_e to zero when mixing in the top was not apparent and generally use low values, leading
333 to conservative estimates of the upward porewater velocities and submarine groundwater
334 discharge. The bottom-water sodium concentration was used as the upper boundary condition.
335 A zero concentration was imposed as lower boundary condition, except in cases where there
336 was no gradient at depth, i.e., at sites with no clear SGD, a non-zero concentration was imposed.
337 The equation was solved both numerically with the ReacTran package in R (Soetaert &
338 Meysman, 2012; R Core Team, 2022) and analytically. For the latter, the concentration was
339 assumed to be constant in the upper mixing zone if present, and D_e was set to 0. The analytical
340 solution was used to check if the domain depth was sufficiently long so that it did not affect

the outcome. The numerical and analytical solutions only differed significantly in cases with weak mixing in the top layer, and then the numerical solution was preferred.

Using the constrained upward porewater velocity and additional mixing coefficient, fluxes of chemicals were estimated by

$$F = -\emptyset \frac{D_m}{\emptyset^2} \frac{dC}{dx} - \emptyset D_e \frac{dC}{dx} + \emptyset u C \quad (2)$$

where the first, second, and third terms on the right-hand side represent the diffusive, additional mixing, and advective fluxes. Linear regression was used to fit the concentration gradient dC/dx either through points near the sediment-water interface or, in cases with strong mixing at the top, the depth from where a clear gradient was visible.

3. Results

The results of the (isotope) hydrochemical measurements of the surface water of the open Baltic Sea, surface and porewaters of the Gulf of Gdańsk and Puck Bay, fresh groundwater, and rivers are summarized in Table 1.

354

355 Table 1 – Chemical average, minimum, maximum and number of samples of the Baltic Sea, Gulf of Gdańsk, outer Puck Bay, inner Puck Bay, rivers, groundwater from wells, groundwater from
356 piezometers, offshore porewaters, shoreline porewaters, the estimated fresh component of SGD, and the seepage meter sample.

Variables	Unit	Baltic Sea	Gdansk Bay	PB outer	PB inner	Rivers	GW_Well Deep	GW piazometer shallow	Offshore SGD impacted PW	Offshore reference PW	Shoreline SGD impacted PW	Shoreline reference PW	Fresh SGD component	Seepage meters
Years		2019	2019	2009 and 2019	2019 and 2021	2011 and 2021	2009 and 2021	2009 to 2021	2009 and 2019	2009 and 2019	2009 to 2021	2009 to 2021	2009 to 2021	2021
Salinity			6.8	6.9	6.8	0.2	0.1	0.3	8	8	3.3	6.4		6.5
			(1)	6.1/7.6 (26)	5.8/7.3 (68)	0.2/0.3 (4)	0.1/0.3 (17)	0.0/0.8 (6)	6/10 (26)	6/9 (83)	0.4/7.2 (103)	5.1-7.3 (27)		5.8/6.9 (4)
pH		8.0	7.8	7.9	8.1	7.7	7.5	7.1	7.3	7.4	7.2	7.3	6.9	7.9
		(1)	7.8 (4)	7.7/8.2 (31)	6.6/8.8 (66)	7.3/8.4 (8)	7.2/8.4 (25)	6.3/7.5 (5)	7.0/7.5 (13)	6.9/7.7 (51)	6.2/8.3 (80)	6.4-8.0 (27)	5.8/8.2 (6)	7.2/8.9 (4)
TA	mM			1.7						4.9	3.8	2.2	5.1	
				(2)						0.4-15.0 (54)	0.8/7.2 (80)	0.4/7.8 (27)	2.5/7.1 (6)	
DIC	mM	1.6	1.7	1.6	1.8	4.0		4.6	11	4.7	3.6	2.5	5.7	1.9
		(1)	1.6/1.8 (4)	0.7/1.7 (41)	1.6/2.3 (49)	3.6/4.4 (2)	3.1/9.6 (19)	2.9/6.2 (3)	1.3/24.1 (20)	1.4/13.1 (38)	0.5/8.4 (31)	0.5-7.6 (21)	3.2/8.8 (4)	1.5/2.6 (4)
$\delta^{13}C_{DIC}$	‰ VPDB	0	-0.8	-0.5	-0.8	-12.3	-11.8	-20.1	-3.6	-10.4	-9.7	-8.0	-13.6	-8.4
		(1)	-2.5/0.0 (4)	-1.7/-0.1 (32)	-7/0.8 (59)	-13/-11 (2)	-19/-8 (20)	-24/-13 (3)	-14/14 (26)	-18/-1.6 (55)	-26/2.9 (47)	-12/-3.5 (9)	-32.8/-0.6 (5)	-15.5/-5.1 (4)
$\delta^{13}C_{CH4}$	‰ VPDB										-60			
											-63-(-48) (7)			
$\delta^{2}H_{CH4}$	‰ VSMOW										-222			
											-248-(-132) (6)			
$\delta^{18}O_{H2O}$	‰ VSMOW	-6.4	-6.5	-6.4	-6.3	-9.7	-10.6	-9.6	-6.1	-6.4	-8.7	-6.2	-9.7	-6.7
		(1)	-6.5/-6.4 (4)	-6.7/-6.2 (42)	-7/-5 (53)	-10.2/-9.2 (6)	-13.7/-9.8 (20)	-11.0/-9.1 (6)	-6.6/-5.7 (11)	-6.6/-6.0 (28)	-10.4-(-6.1) (32)	-7.0-5.4 (9)	-10.9/-7.8 (5)	-7.3/-5.8 (4)
$\delta^{2}H_{H2O}$	‰ VSMOW	-48.8	-48.7	-48.3	-48.0	-67.2	-74.1	-67.8	-45.8	-48.3	-64.0	-48.3	-69.4	-51.2
		(1)	-49.2/-48.5 (4)	-47.1/-52.6 (42)	-56/-42 (41)	-69.8/-65.3 (6)	-102.2/-66.9 (20)	-80.0/-62.0) (6)	-49.5/-43.1 (11)	-49.2/-47.6 (28)	-76.2-(-47.5) (32)	-51.7-44.0 (9)	-78.4/-56.7 (5)	-54.7/-46.1 (4)
Na	mM			101	92	0.6	2.3	3.2	107	103	47.2	87.1	3.2	84.4
				84/126 (9)	76/104 (39)	0.2/1.2 (6)	0.2/7.2 (25)	2.8/3.6 (4)	89/135 (26)	87/112 (93)	4-102 (93)	70/103 (24)	0/14 (6)	74/90 (4)

Mg	mM			11.6	10.7	0.3	0.4	0.3	12.3	11.4	5.2	9.9	0.5	9.9
				10.1/13.6 (9)	8.3/11.8 (39)	0.3/0.4 (6)	0.0/0.7 (25)	0.2/0.4 (4)	9.6/16.0 (26)	9.6/13.7 (93)	0.5-11.5 (93)	8.1/11.7 (24)	0/0.9 (6)	8.7/10.3 (4)
Ca	mM			2.8	2.7	2.0	1.8	2.3	3.1	2.8	2.6	2.9	1.9	2.8
				2.7/3.2 (9)	2.3/3.0 (39)	1.8/2.4 (6)	1.1/3.4 (25)	2.0/2.6 (4)	2.5-3.7 (26)	2.4-3.1 (93)	1.0-8.4 (93)	2.3/4.1(24)	0.7/3.0 (6)	2.7/2.9 (4)
K	mM			2.1	2.1	0.1	0.1	0.5	2.6	2.4	1.1	1.9	0.4	2.0
				1.8/2.6 (9)	1.6/2.8 (39)	0.0/0.1 (6)	0.0/0.5 (25)	0.4/0.5 (4)	2.1/3.3 (26)	2.0/2.7 (93)	0.2-2.2 (93)	1.3/2.2 (24)	0.1/1.4 (6)	1.8/2.0 (4)
SO_4	mM				6.0	0.4	0.7	0.3	3.6	4.2	2.7	4.9	0.1	5.4
					5.1/6.6 (39)	0.3/0.6 (6)	0.0/2.4 (25)	0.2/0.4 (4)	0.2/6.3 (26)	0.3/7.1 (92)	0.0-6.0 (86)	2.6-6.1 (24)	0/0.6 (6)	4.6/5.8 (4)
H_2S	µM								345	327	87	185		0.5
									0/2041 (26)	0/1683	0-1585 (87)	0-1248 (24)		0/1.0 (4)
Si	mM			0	0.1	1.1	0.4	0.4	0.5	0.5	0.2	0.1	3.1	0
				(7)	0-0.7 (39)	0.1/1.9 (6)	0.2/0.6 (14)	0.3/0.4 (2)	0.0-0.9 (26)	0.0-0.8 (82)	0/0.6 (44)	0/0.3 (12)	0.2/6.3 (6)	0/0.1 (4)
P	µM			0.4	1.4	1.6	2.2	43.5	266	112	40	18.0	49.2	3.9
				0.2/1.3 (9)	0.3/9.9 (39)	0.4/3,5 (6)	0.1/5.9 (20)	41.0/46.2 (4)	1.0-668.2 (26)	1.4-310 (93)	0.5/113 (93)	0.6/54.4 (24)	1.8/64.6 (6)	1.5/10.1 (4)
Ba	µM			0.1	0.1	0.6	0.1	0.2	0.7	0.3	0.1	0.2	0.4	0.2
				0.1/0.2 (9)	0.1-0.2 (39)	0.1/1.3 (6)	0.1/0.7 (25)	0.0/0.5 (4)	0.1-1.7 (26)	0.1-0.5 (93)	0/1.4 (91)	0.1/0.3 (24)	0/2.3 (6)	0.1/0.2 (4)
Fe	µM			0	0.2	2.2	15	1.5	69	24	48	116	54.8	2.4
				(9)	0/1.3 (39)	1.0/3.9 (6)	0.2/52 (25)	0.1/2.5(4)	0.1-317 (26)	0.0-193 (93)	0/1032(92)	0/795 (24)	0.7/324 (6)	0.4/5.8 (4)
Mn	µM			0	0.1	1.4	1.8	0.7	8.2	2.6	1.9	1.3	4.2	0.8
				0/0.1 (9)	0.0/0.1 (39)	0.3/3.2 (6)	0.0/4.1 (25)	0.2/1.1 (4)	0.5-21.1 (26)	0-13.5 (93)	0/9.9 (91)	0/6.6 (24)	0.2/15.3 (6)	0.1/2.1 (4)
NH_4	µM				0.0	3.7	35	25	1134	200	244	131		7.1
					0.0/0.7 (18)	1.5/5.5 (4)	1.1/170 (15)	15.0/43 (4)	0-4103.0 (25)	53/635 (17)	0/1068 (91)	0.8/974 (27)		1.3/16.2 (4)
^{224}Ra	Bq m^{-3}	0.3	0.6	0.5	2	0.8	5	21			50			36
		(1)	0.2/1.3 (8)	0.1/0.9 (32)	0.9/10 (28)	0.6/1.2 (4)	0.4/13 (14)	6/49 (3)			10/86 (4)			12/64 (3)
^{223}Ra	Bq m^{-3}	0	0	0	0	0.1	0.1	1			1.2			1
		(1)	(8)	(30)	0.0/1 (28)	0/0.2 (4)	0/0.4 (13)	0/1 32)			0.5-2.4 (3)			0/2 (2)
$^{224}Ra_{ex}$	Bq m^{-3}	0.3	0.5	0.4	2	1	5	20			45			30
		(1)	0.1/1.2 (8)	0.1/0.8 (32)	0.8/10 (24)	0.5/1.0 (4)	0.4/13 (14)	6/48 (3)			10/79 (4)			6/54 (3)

357

3.1 Surface waters composition

The Puck Bay surface waters salinity ranged between 5.8 and 7.6, with slightly lower values in the inner part (Table 1). The water isotope composition varied from -7 to -5‰ and -56 to -42‰ for $\delta^{18}O$ and $\delta^{2}H$, respectively (Table 1), with the inner part of the Puck Bay showing heavier values (Figure 2). The Gulf of Gdańsk and the Baltic Sea composition were in the same range (Table 1).

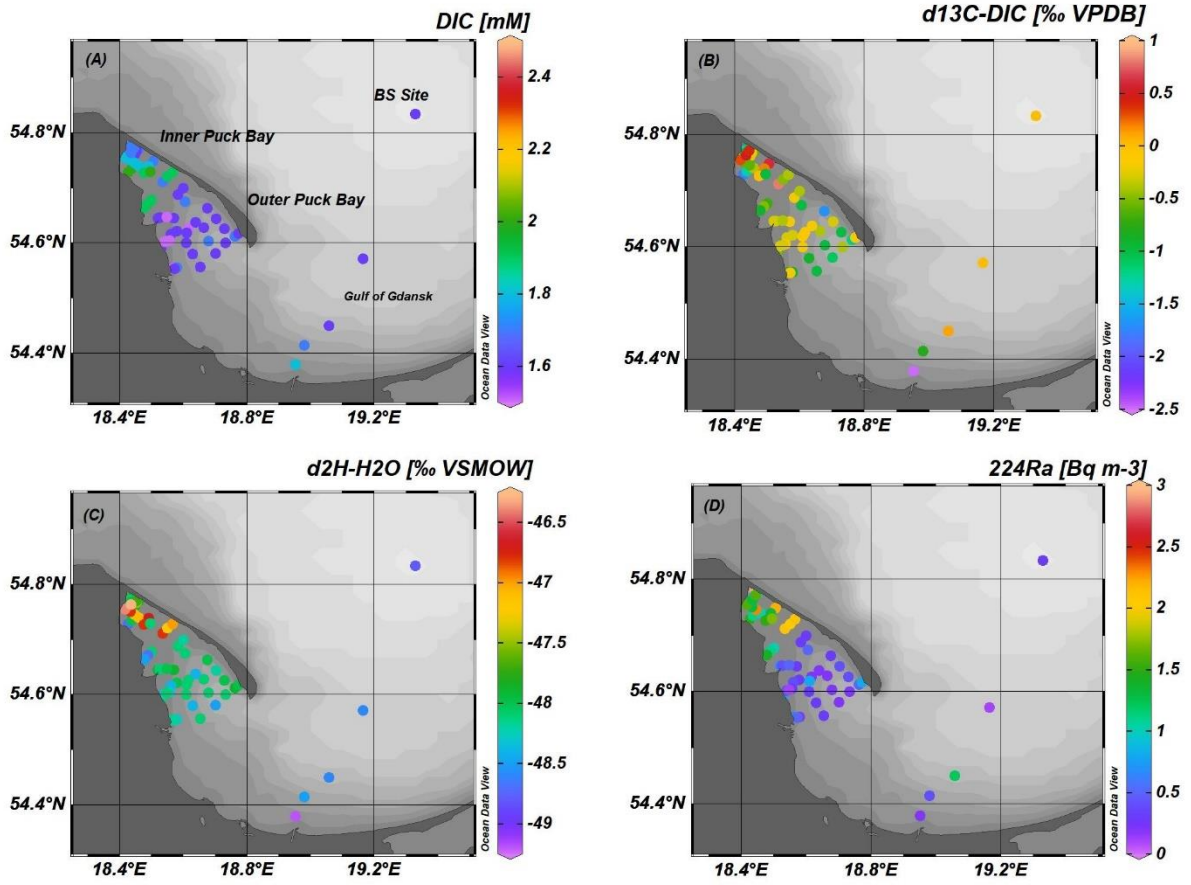

Figure 2 - Variation of (A) dissolved inorganic carbon (DIC), (B) $\delta^{13}C$-DIC, (C) $\delta^{2}H$-H2O, (D) ^{224}Radium. Data of the outer Puck Bay corresponds to the campaign in 2019. Data of the inner Puck Bay correspond to the campaigns in 2019 and 2021. The concentration maps were plotted using Ocean Data View (Schlitzer, 2001). The shoreline sites are not presented in the figures.

The surface water of the outer Puck Bay showed pH values ranging from of 7.7 and 8.2, while the inner part had values between 6.6 and 8.8 (Table 1). Gulf of Gdańsk and the open Baltic Sea, had values of 7.8 and 8.0, respectively. The DIC concentrations in the Puck Bay surface

372 waters ranged between 0.7 to 2.3 mM, with slightly higher concentrations in the inner part of
373 the bay (Figure 2). The Gulf of Gdańsk and the Baltic Sea showed similar DIC concentrations
374 of around 1.7 mM. The $\delta^{13}C_{DIC}$ signatures ranged from -1.7 to 0.8‰. At sites near the shoreline
375 where SGD has been observed, the signatures reached -6‰. The Gulf of Gdańsk showed
376 $\delta^{13}C_{DIC}$ values between -2.4 and 0.1‰, with the isotopically lightest value being close to the
377 coastline and probably affected by the Vistula River discharge (Figure 2). The Baltic Sea Site
378 had an isotope signature during sampling of about 0‰.

379 The $^{224}Ra_{ex}$ activities in the surface waters varied between 0.1 and 3 Bq m^{-3} (Table 1, Figure 2).
380 The average activities in the Baltic Sea, Gulf of Gdańsk, and outer Puck Bay were 0.2, 0.5, and
381 0.4 Bq m^{-3}, respectively, while the inner part showed a much higher level up to 3 Bq m^{-3}.
382 Activities of ^{223}Ra showed a similar behavior as $^{224}Ra_{ex,}$ with values ranging between near 0 to
383 0.2 Bq m^{-3} (Table 1).

384 Bottom water $^{224}Ra_{ex}$ activities measured at three sites in the outer Puck Bay showed slightly
385 higher values of 0.3, 0.3, and 0.6 Bq m^{-3} than the surface water activities of 0.2, 0.2, and 0.4
386 Bq $m^{-3,}$ respectively. In contrast, a much more significant difference appeared in the Gulf of
387 Gdańsk, which bottom and surface water $^{224}Ra_{ex}$ activities of 4 and 0.1 Bq $m^{-3,}$ respectively.

388 In addition, the investigated shoreline sites Hel, Chałupy, Swarzewo, and Osłonino (Figures 1
389 and 2) revealed particularly high Ra activities in surface waters, and the activities of $^{224}Ra_{ex}$
390 were 2, 9, 9, and 3 Bq m^{-3}, and ^{223}Ra activities were 0.1, 0.3, 0.5, and 0 Bq m^{-3}, respectively.

391 **3.2 Geophysical characterization of sediments of the outer Puck Bay**

392 Acoustic sub-bottom images from the muddy central part of the outer Puck Bay are displayed
393 in Figure 1 – C, D. In both images, the sea bottom echo is weak, indicating a low contrast in
394 acoustic impedance between water and bottom sediments, a typical feature for soft mud

sediments. The thickness of this nearly acoustic transparent mud layer is about 1 m in the central part of the bay and thins out towards the SE slope of the basin. Moreover, it is possible to observe that the deposits below are well stratified and reflect the different stages of the Holocene's marine, brackish and limnic periods. Some of the deepest reflections may come from late Pleistocene deposits.

The well-stratified sub-bottom images in both transects are suddenly interrupted in the center of the bay at a depth of about 2.5 m below the seafloor. This is caused by tiny gas bubbles present in the pore space of the sediments. Depending on the frequency-gas bubble size ratio, these bubbly layers can act as an acoustic shield, absorbing, scattering acoustic energy, and hiding deeper structures. Gas bubbles (mainly CH_4) may originate from the decomposition of organic matter in the underlying deposits. The absence of gas bubbles in the uppermost sediments is likely caused by anaerobic CH_4 oxidation (Iversen & Jørgensen, 1985; Whiticar and Faber, 1986).

Towards the NW-end transect (Figure 1, D), the acoustic image of the uppermost mud layer changes to a more diffuse appearance. This might indicate additional diffusive fluid flow from deeper sources toward the sea bottom, transporting small amounts of gas bubbles. These gas bubbles act as acoustic scatters, masking the sedimentary structure. Moreover, related diagenetic changes of the solid phase, e.g., by precipitation, may produce dispersive distributed acoustic scatters.

While pockmarks were found, no indications of gas bubbles were observed in the sediment or the water column. Fluid flow along permeable, fractured zones in the sub-bottom may cause these pockmark structures.

3.3 Sediment geochemistry

The site in the Gulf of Gdańsk (Site M1) had the highest TOC contents reaching 9% dwt in the top sediments. The contents of TOC at the sites of the outer Puck Bay ranged from 2 to 8% dwt, with values decreasing with depth (Figure 3-A). In contrast, the surface sediments at the sandy sites at the shoreline were characterized by distinctly lower TOC contents (< 1% dwt., Figure 3-G), except for one site located in the inner part of the bay (Osłonino), which showed a maximum of 2% dwt. at seven cmbsf.

The molar TOC/TN ratio at Site M1 ranged between 8 and 10 (Figure 3-E), with the high TOC indicating a more significant proportion of marine organic matter. The sites at the outer Puck Bay showed values between 8 and 13.

Contents of TS at the site in the Gulf of Gdańsk and the outer bay sites varied between near zero and 2% dwt. without apparent differences between the sites (Figure 3 –B). Total sulfur (TS) further displayed a positive correlation with the TOC content, typical for brackish-marine sediments that are limited by the availability of organic matter (Berner & Raiswell, 1983) (Figure 3 – F). The TS content was very low at all sandy sites (Figure 3-H).

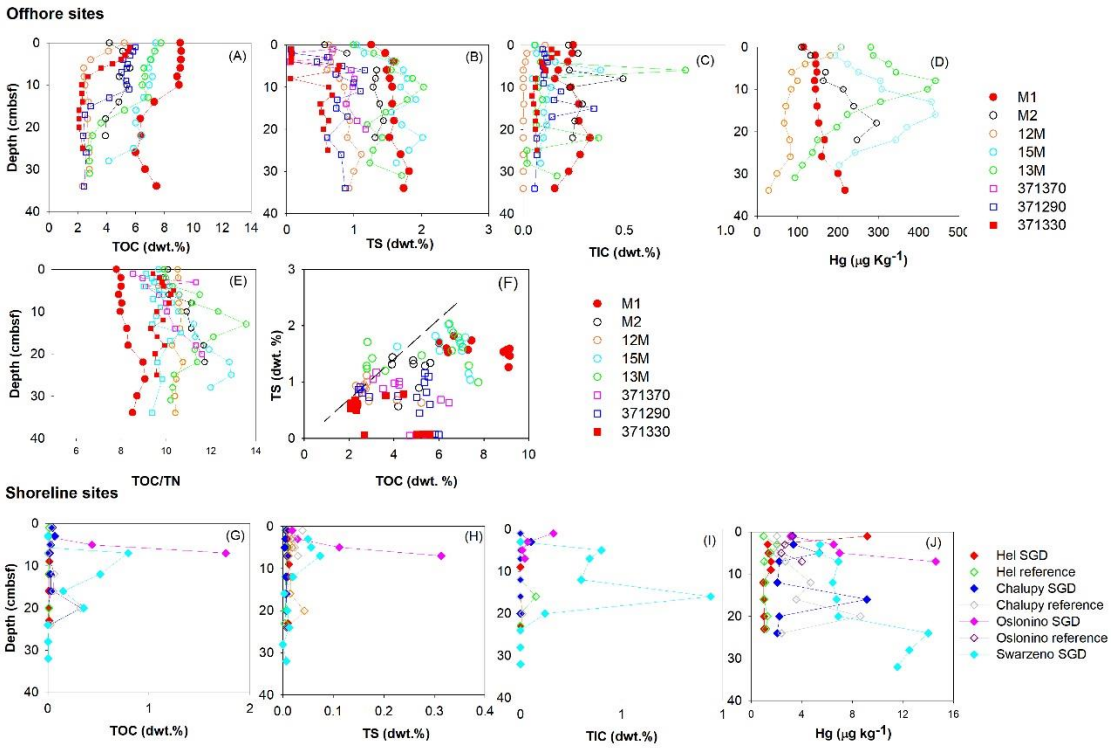

Figure 3 - Vertical profiles of bulk geochemical parameters in the sediments from muddy sites (A-F), data from 2009-2019, and sandy sites (G-J) from 2021. Sediment profiles of TOC/TN at the muddy sites (A). Dashed line marks in panel F mean the relationship suggested for Holocene siliciclastic sediments (Berner, 1982). Note: The original definition of (B), (F), and (H) are based on the reducible sulfur (TRIS) content.

Vertical profiles of Hg contents (Figure 3 - D) partly indicated the zone of surface sediments deposited during times of high anthropogenic impact (Leipe et al., 2013). However, some profiles are superimposed by physical disturbance, like sediment resuspension, ripple movement, and bioturbation (e.g., Huettel et al., 1998). Pronounced differences were observed in the shape of gradients and absolute contents for selected sites, indicating different exposures and sediment reworking. Site M1 showed values constant at depth. While three sites in the more protected outer Puck Bay displayed Hg maxima in the top 10 to 20 cmbsf, other sites showed intense mixing down to the observation depth. Different from the offshore sites, the shoreline sandy sites displayed maximum Hg concentrations of 15 µg kg^{-1} reflecting the low contents of substrate for Hg fixation (organic matter and sulfides) and the dilution by quartz.

3.4 Porewater geochemistry

Site M1, located in the Gulf of Gdańsk, showed a decrease in salinity from 10 to 8. The region where Site M1 is located is already known for gas, and freshwater upflow (Idczak et al., 2020). The porewater salinity of the majority of the sites in the outer Puck Bay displayed values between 6 and 9 and an increase with depth (Figure 4 - A). In contrast, the salinity at Site 371330 decreased from 7.3 to 6.4.

At the sandy shoreline sites, all sampled porewater profiles showed some freshening at depth, indicating a substantial influence of fresh groundwater at the shoreline of Puck Bay (Figure 5-A). Therefore, porewater profiles with at least a 70% decrease in salinity at depth are considered, in this study, as SGD-impacted sites, whereas all others are reference sites. The salinity values on the reference profiles ranged from 7.3 to 5.1, and at the SGD-impacted sites, the values reached 0 at depth. Conservative ions such as Na, K, and Mg followed the salinity trends in all profiles.

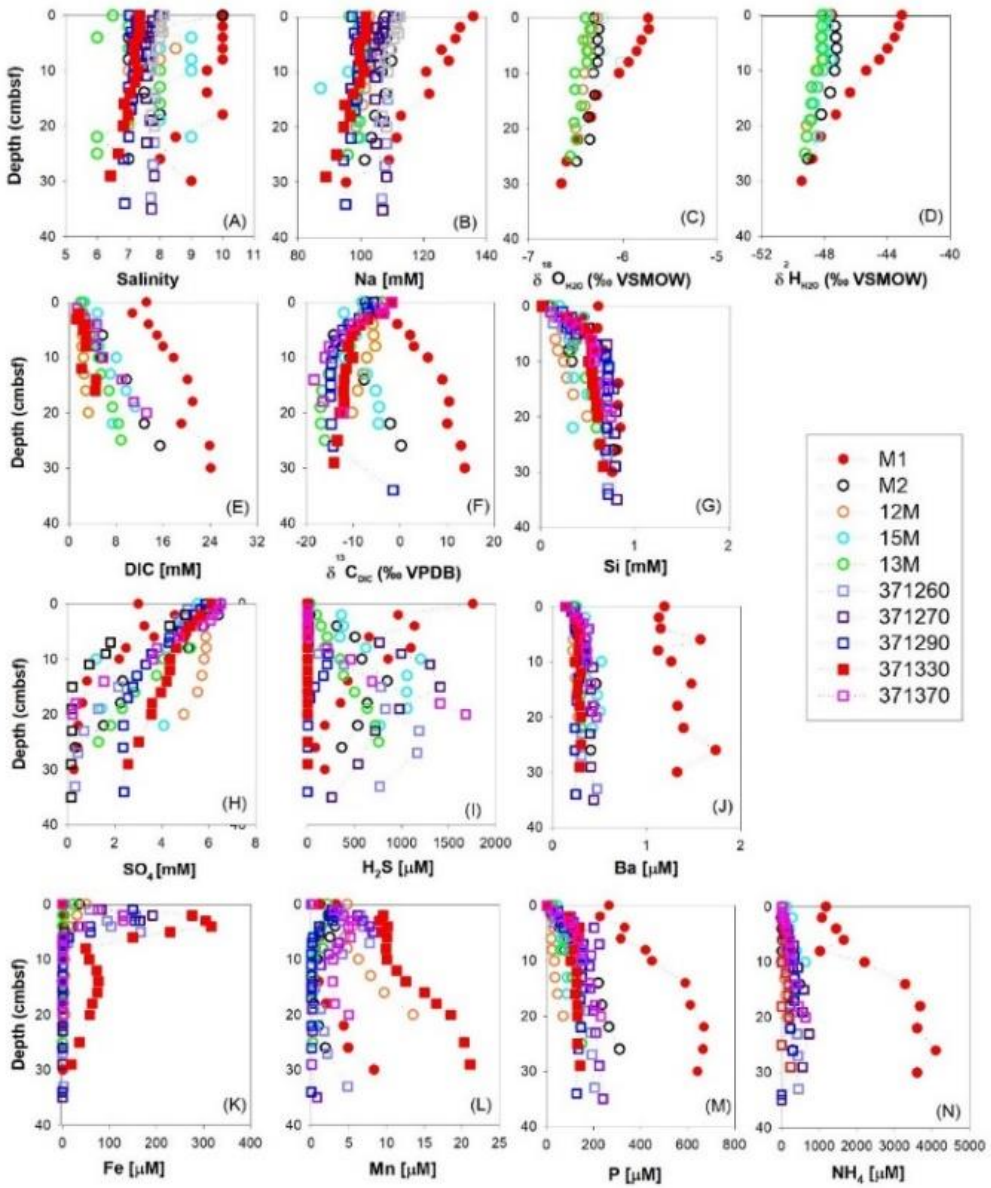

460

461 Figure 4 - Porewater gradients of geochemical parameters in sediment cores from the muddy sites in Puck Bay and one in the Gdańsk Bay
462 (Gdańsk SGD). Samples from 2009 are represented by circles and from 2019 by squares. Filled symbols refer to SGD-impacted sites.

463

464 The $\delta^{18}O_{H2O}$ and $\delta^{2}H_{H2O}$ isotope compositions at the outer Puck Bay sites were between -6.6
465 to -6.0 ‰ and -49.2 to -47.6‰. Site M1 had values decreased from -5.7‰ at the sediment-
466 water interface to -6.6‰ at depth and from -43.1 to -49.5‰, respectively. At the reference sites
467 at the shoreline, the $\delta^{18}O_{H2O}$ and $\delta^{2}H_{H2O}$ signatures varied between -7.0 to -5.4 and -51.7 to -
468 44.0‰ respectively, while at the SGD impacted sites, the values showed a substantial
469 difference throughout the profile. There, the signatures ranged between -10.4 and -6.1‰ and -

76.2 and -47.5‰ for $\delta^{18}O_{H2O}$ and $\delta^{2}H_{H2O,}$ respectively. In addition, analyses of ^{3}H showed higher values in the porewaters of the SGD impacted sites compared to the bottom waters of Puck Bay (Supplementary Table 2).

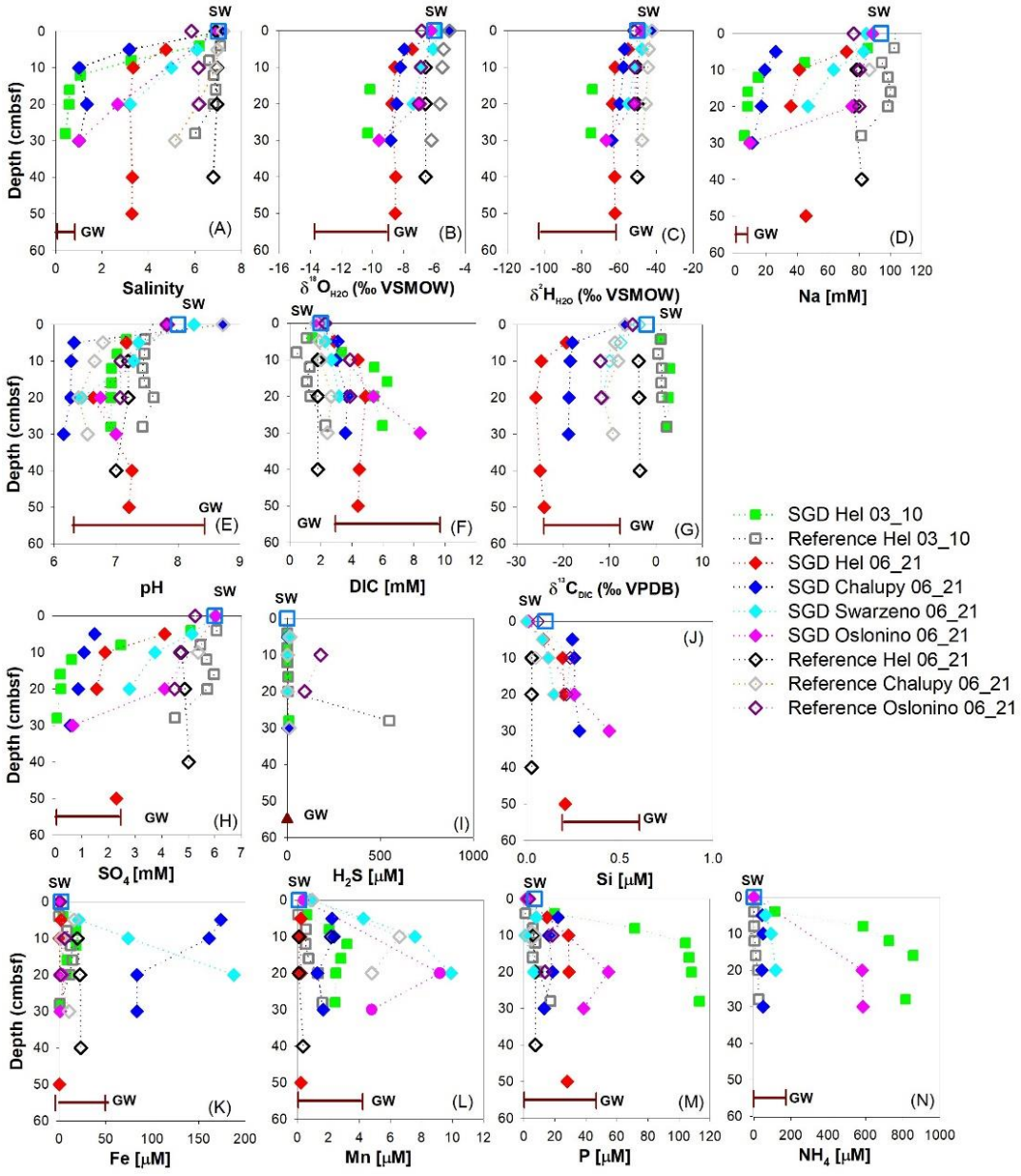

Figure 5 - Porewater profiles from the selected sandy site from Hel, Chałupy, Swarzewo, and Osłonino in Puck Bay. Filled symbols represent SGD-impacted sites. All porewater profiles collected from 2009 to 2021 are presented in Supplementary Figure 3.

Values of pH increased with depth at the offshore sites. Conversely, the pH values at the sandy sites showed a typical decrease with depth from 8.3 to 6.2 (Figure 5- E). Concentrations of DIC

479 at the sites in Puck Bay, including the 371330 Site, ranged between 2.0 and 13, while Site M1
480 showed higher concentrations, reaching 25 mM in the deeper sediments (Figure 4 -E). The
481 $\delta^{13}C_{DIC}$ signatures decreased with depth at most sites. However, there were two sites where the
482 $\delta^{13}C_{DIC}$ signatures became heavier with depth, especially at Site M1 showing values up to +13‰
483 (Figure 4 - F). Concentrations of DIC at the shoreline sites showed values between 0.5 and 8.4
484 mM, and the SGD impacted sites presented higher concentrations (Figure 5 - F). Signatures of
485 $\delta^{13}C_{DIC}$ were between -11.9 and -3.5‰ at the reference sites on the shoreline. The SGD-
486 impacted sites displayed considerable variability, and the signatures varied between -25.9 and
487 +2.9‰.

488 At the sandy site at Hel Peninsula, SGD was associated with CH_4 contributed from the fresh
489 water component (Donis et al., 2017). The stable C and H isotope composition of CH_4 was
490 measured in 2010 and was found to be isotopically light with stable isotope values varying
491 between -63 to -60‰ and -248 and 240‰ for $\delta^{13}C_{CH4}$ and $\delta^{2}H_{CH4}$ respectively (Table 1).
492 However, one sample close to the sediment-water interface showed a heavier isotope
493 composition of -48‰ for $\delta^{13}C_{CH4}$ and -132‰ for $\delta^{2}H_{CH4}$ than those taken from deeper sediment
494 sections (Supplementary Figure 4). Typically, methyl-type fermentation is a dominant
495 formation pathway in freshwater systems, and carbonate reduction dominates in brackish-
496 marine environments (e.g., Whiticar, 1999; Egger et al., 2017).

497 Concentrations of SO_4 at the offshore sites ranged between 0.1 and 6.4 mM, with a decrease at
498 depth. Some of the sites already had values close to 0 at 20 cmbsf.

499 At Site 371330, a less pronounced decrease in the sulfate concentrations was found, dropping
500 from 6.1 to 2.6 at depth. Site M1 showed lower SO_4 values already at the sediment-water
501 interface compared to the bottom waters, and SO_4 was consumed at a depth of about 15 cmbsf.
502 Most sites showed the typical decrease of SO_4 and an increase of H_2S with depth, with

concentrations of the latter ranging between 0 and 1683 μM. In contrast, Site 371330 showed no accumulation of H_2S across the entire profile. Site M1 showed a decrease in H_2S concentrations with depth, with values higher than 2000 μM in the top sediments. At all sandy sites, rapid depletion of SO_4 from bottom water concentrations of around six mM down to values below the detection limit was observed. The mixing with fresh groundwater seems to be the dominant factor for very low concentrations already at 10 cmbsf at the SGD impacted sites. In contrast, the SO_4 ranged between 6.1 and 2.6 mM at the reference sites. The sandy shoreline sites did not show accumulation of H_2S, except the Site Chałupy SGD, which had values up to 1.5 mM at depth.

Without showing clear vertical gradients, concentrations of dissolved Ba ranged between 0.1 and 0.5 μM at all sites in Puck Bay. Site M1 reached values up to 1.7 μM (Figure 4-J). The sandy sites displayed spatial variation with higher concentrations found in Osłonino and Swarzewo, where values reached up to 1.4 μM. In contrast, all values were below 0.5 μM at the Hel site.

With maximum values in the top sediment, dissolved Fe concentrations varied between near zero levels and 192 μM at most offshore sites. Site 371330 showed the same trend; however, the top sediments' values reached 317 μM (Figure 4-J). Site M1 showed concentrations close to 1 μM over the entire core depth. Similar to Fe, concentrations of Mn were higher in the top sediments reaching 14 μM, and Site 371330 showed the highest values (Figure 4-L). The dissolved Fe revealed very heterogeneous profiles at the shoreline sites ranging between near zero and 1032 μM. There was no difference between SGD-impacted and reference sites; however, the concentrations showed a high temporal dynamic at the Hel site. For example, samples collected in 2009 showed maximum concentrations of only 27 μM, whereas the values exceeded 1000 μM in 2010. At the sandy sites, the concentrations of Mn showed a pronounced variability, as observed for Fe. There, the Mn concentrations ranged between near zero and 10

528 μM. The highest Mn concentrations were observed at Swarzewo and Osłonino, and the Hel site
529 again showed higher concentrations in 2010.

530 Regarding the nutrients, Si concentrations were between near zero and 0.8 mM, with only
531 minor differences between the offshore muddy sites. In contrast, the shoreline sites revealed a
532 difference between the reference and SGD impacted sites (Figure 5-J). At the reference sites,
533 the values varied up to 0.3 mM, whereas values reached 0.6 mM at the SGD sites. The
534 concentrations of P ranged between 0.1 and 240 μM and increased with depth at all offshore
535 sites. Site M1 showed the highest concentration reaching 668 μM at depth. Concentrations of
536 P also increased with depth at the sandy sites. The SGD impacted sites showed the highest
537 values of up to 113 μM, whereas the concentrations at the reference site were lower than 60
538 μM. Concentrations of NH_4 ranged between 1.4 and 724 μM at the offshore sites in Puck Bay,
539 and again the Site M1 site showed the highest value of 4103 μM at depth. At the shoreline sites,
540 concentrations of NH_4 were higher in the SGD impacted sites showing values increasing from
541 near zero at the sediment-water interface to 1068 μM at depth. The reference sites reached a
542 maximum value of 146 μM at a depth of 30 cmbsf.

543 Activities of $^{224}Ra_{ex}$ were measured in the porewaters at the shoreline sites at a depth of around
544 50 cmbsf, and the values were 37, 54, 79, and 10 Bq m^{-3} for Hel, Chałupy, Swarzewo, and
545 Osłonino, respectively.

546 **3.5 Direct measurement of seepage rate**

547 Seepage meters were applied in Hel, Chałupy, and Swarzewo (Figure 1) in June 2021 to
548 measure the volumetric seepage rates during the campaign in 2021. These measurements
549 determined the total water flux, but not necessarily the freshwater discharge; however, a
550 lowered salinity and water isotopic values demonstrate its presence.

551 At the Hel site, the water volume change within the seepage meter bags over time intervals of
552 85 and 120 minutes equaled a seepage rate of 45 and 30 L d^{-1} $m^{-2,}$ respectively. The amount of
553 water collected at the Chałupy Site over 143 minutes revealed a seepage rate of 3 L d^{-1} m^{-2}. At
554 the Swarzewo Site, a flux of 1.6 L d^{-1} m^{-2} was obtained over 170 minutes.

555 The salinities of the collected samples at Hel were 5.7 and 6.6, and the corresponding surface
556 water salinity was 6.9. The isotopic composition of the water was lighter than the surface waters
557 of Puck Bay (Table 1, Figure 7), reaching values for $\delta^{18}O_{H2O}$ of -7.1 and -6.6 ‰ and $\delta^{2}H_{H2O}$ of
558 -53.4 and 50.8‰. At the Chałupy site, the salinity of the seepage water was slightly lower than
559 the surface water showing values of 6.9 and 7.2, respectively. The water isotopic signature
560 revealed $\delta^{18}O_{H2O}$ values of -7.3‰ and $\delta^{2}H_{H2O}$ of -54.7 ‰. At the Swarzewo site, the salinity
561 was 6.6 in seepage water and 6.9 in surface water. The water isotopic signature was relatively
562 light in the seepage compared to the surface water (Table 1), with values of -5.8 and -46.1 ‰
563 for $\delta^{18}O_{H2O}$ and $\delta^{2}H_{H2O,}$ respectively.

564 The fresh groundwater fraction for each site was calculated assuming that the sample collected
565 in the seepage bag is a mixing between groundwater and recirculated seawater and by applying
566 an end-member model as:

567 $$V_s \times S_S = V_{gw} \times S_{gw} + V_{sw} \times S_{sw} \quad (4)$$

568 Where S and V are salinity and volume, subscripts S, G, and SW represent the sample,
569 groundwater, and seawater fractions, respectively.

570 The fresh groundwater fraction from the Hel site was 4 and 17%, giving a fresh groundwater
571 flux of 0.05 and 0.5 L m^{-2} d^{-1}. The Chałupy Site had a fraction of 4% freshwater, corresponding
572 to a flux of 0.01 L m^{-2} d^{-1}. At the Swarzeno Site, the fresh fraction was 3%, and a fresh
573 groundwater flux of 0.004 L m^{-2} d^{-1} was obtained.

574 **3.6 Coastal groundwater and surface water entering the Puck Bay**

575 Groundwaters

576 The groundwater composition represents the water sampled from wells (deep groundwater)
577 and piezometers (shallow groundwater) around the coastal zone of Puck Bay. A summary of
578 the results is presented in Table 1.

579 The groundwater isotopic composition of deep groundwaters varied from -13.7 to -9.8‰ and -
580 102.2 to -66.9 ‰, while the groundwater at the piezometers varied between -11.0 and -9.1‰
581 and -80.0 to -62.0‰ for $\delta^{18}O_{H2O}$ and $\delta^{2}H_{H2O,}$ respectively (Table 1, Figure 6). The measured
582 isotopic signatures from the groundwater wells represent groundwater coming from the
583 Cretaceous, Tertiary, and Quaternary based on Piekarek–Jankowska (1996). The heavier
584 signatures on shallow groundwaters were influenced by meteoric water.

585 ^{3}H contents were highest in the shallow wells filtered in the Quarternary strata. Very low
586 activity was found in the groundwaters from the Tertiary of Cretaceous aquifers
587 (Supplementary Table 2). A combined evaluation of ^{3}H and He isotopes analyses indicate ages
588 of around 30, 50-100, 28, > 60, and >>>60 years for wells Wladyslawowo 2, Reda IV (low ^{3}H,
589 but no ^{4}He), Reda 12c, Rumia (low ^{3}H, but low ^{4}He), and the deep production well on Hel
590 Island (low ^{3}H, but high ^{4}He), respectively (Supplementary Table 2). ^{3}H free older water seems
591 to be further admixed into the Wladyslawowo 2 groundwater.

592

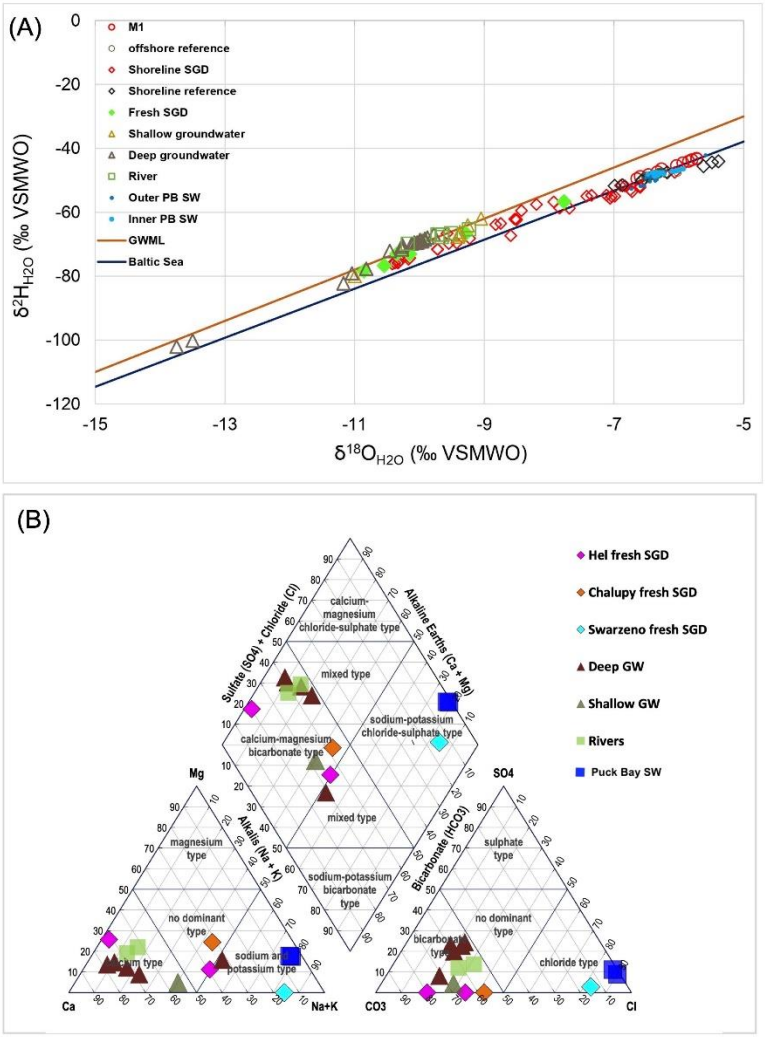

593

594 Figure 6 – (A) The covariation of $\delta^{18}O_{H2O}$ and $\delta^{2}H_{H2O}$ of sandy sites impacted and non-impacted by SGD, muddy sites impacted and non-
595 impacted by SGD, groundwaters, rivers, and Puck Bay surface water. The global meteoric water line (GMWL), the local meteoric water line
596 at Warnemünde (around 500 km west from Puck Bay) (Jenner et al., unpublished data), and the Baltic Sea line (Böttcher et al., unpublished
597 data.) are given for comparison. (B) Piper diagram of the major ions of the rivers (green square), deep groundwater (brown triangle),
598 shallow groundwater (dark green triangle), extrapolated porewater from the SGD impacted sites (pink and orange diamond), and porewater.
599 (Graph created from Stosch, 2022).

600

601 The hydrogeochemical groundwater composition for most deep and shallow groundwaters is
602 classified as Ca-Mg-HCO_3 type (Figure 6, B). Some groundwaters contain higher Na contents,
603 indicative of a mixed type. According to Löffer et al. (2010), this water can be further classified
604 as "old groundwater". Groundwater coming from Cretaceous aquifers was classified as HCO_3-
605 Na according to Piekarek–Jankowska (1996).

Most of the groundwater presented pH values between 7.1 and 7.9 except for one deep groundwater sample on the land site with a value of 8.4 and one piezometer located in Chałupy, which showed a pH value of 6.3. Concentrations of DIC were between 3.1 and 6.2 mM, except in Chałupy, where the DIC concentration in the piezometer was 2.9 mM, and in the groundwater well, 9.0 mM. The $\delta^{13}C_{DIC}$ signatures were spatially heterogeneous. The shallow groundwater showed $\delta^{13}C_{DIC}$ values ranging between -12.1 and 23.8‰, with lighter signatures in the location of Hel. The signatures in the deeper groundwaters ranged between -12.5 and -8.1‰. Heavier values in deeper groundwaters might be associated with the interaction with carbonates, and less contact with organic matter is expected in confined aquifers. Calcium concentrations were higher in the shallow groundwater, with an average concentration of 2.3 mM, while the deep groundwater had an average concentration of 1.8 mM.

Concentrations of Fe and Mn were higher in the deeper groundwaters reaching values of 52 μM and 4.1 μM, respectively, compared to maxima of 2.5 μM and 1.1 μM respectively, in the shallower groundwaters (Table 1). Dissolved Ba had low concentrations of up to 0.7 μM.

Activities of $^{224}Ra_{ex}$ in the deep groundwaters ranged between 0.3 and 13 Bq m^{-3}, and the ^{223}Ra activities ranged between 0 and 0.4 Bq m^{-3}. The $^{224}Ra_{ex}$ activities on the groundwater from the piezometers at the Hel site were 7 and 4 Bq m^{-3} for the campaigns in 2019 and 2021, respectively. The piezometer in Chałupy in 2019 showed higher $^{224}Ra_{ex}$ activities of 48 Bq m^{-3}. Activities of ^{223}Ra were 0.2 and 1 Bq m^{-3} for Hel and Chałupy during the campaign in 2019.

Rivers

The sampled rivers draining into Puck Bay were Reda, Płutnica, Zagórska Struga, and Gizdepka. A summary of the results is presented in Table 1.

The rivers showed water isotope signatures ranging from -10.2 to -9.7‰ and -69.8 to -67.0‰ for $\delta^{18}O_{H2O}$ and $\delta^{2}H_{H2O,}$ respectively. The hydrogeochemical composition of the rivers is classified as Ca-Mg-HCO_3, similar to most groundwaters (Figure 6, B).

The pH ranged between 7.4 and 8.4 (Table 1). Average DIC and $\delta^{13}C_{DIC}$ values were 4.0 mM and -12.3‰, respectively. Concentrations of Ca ranged between 1.8 and 2.4 mM.

Concentrations of Fe and Mn in the rivers ranged from 1.0 to 3.9 µM and 1.4 and 3.2 µM, respectively (Table 1). Dissolved Ba had maximum concentrations in the rivers of about 1.3 µM.

The Ra activities measured in river samples exhibited a small variability among them. The average $^{224}Ra_{ex}$ and ^{223}Ra activities were 1.1 Bq m^{-3} and 0.1 Bq m^{-3}, respectively.

4. Discussion

4.1 Submarine groundwater discharge in the Gulf of Gdańsk and Puck Bay

The bottom waters of Site M1 located in the Gulf of Gdańsk were characterized by high $^{224}Ra_{ex}$ activities compared to the surface waters, indicating SGD occurrence since Ra is derived mainly from SGD (Moore, 2000; Beck et al., 2007b; Rodellas et al., 2012). Furthermore, at this site, the sediment porewater showed a decrease in salinity and water isotope signatures at depth (Figure 4-A), which is caused by an upward flux of fresh groundwater. This finding is in-line with previous investigations conducted in the region of Site M1, where upward flows of freshwater and gas coming from a pockmark structure were reported (Idczak et al., 2020; Brodecka-Goluch et al., 2022).

The outer part of Puck Bay revealed higher $^{224}Ra_{ex}$ activities in the bottom water when compared to the surface waters. Additionally, acoustic images showed sediment layers with a

much more diffuse appearance (Figure 1, C, D) than what would be expected only from CH_4 bubble formations, indicating an additional groundwater flow. In these images, pockmarks structures are visible, which could also be associated with groundwater flow. It is worth mentioning that pockmarks associated with SGD were found in many places around the Baltic Sea, for example, in Eckernförde Bay (Germany), Hanko Bay (Finland), and the Gulf of Gdańsk (Whiticar et al., 1981; Hoffman et al., 2020; Virtasalo et al., 2019; Idczak et al., 2020; Purkamo et al., 2022). Therefore, it can be inferred that SGD is not just limited to specific spots but can also occur in extensive areas throughout the bay.

At the outer Puck Bay, the Site (371330) showed a decrease in the porewater salinity with depth, thus being considered an SGD spot in the central outer Puck Bay.

Once comparing both parts of Puck Bay, submarine groundwater discharge was more evident in the surface water of the inner part of the bay than in the outer part, particularly when pointing out the Ra activities, which showed a > 4-fold enrichment compared to the Baltic Sea activities. This is partly due to the lower water depths that allow a stronger signal of mixing with freshwaters and less volume for dilution. Besides Ra activities, the stable isotope tracers revealed a contribution of different water masses to this area. For example, δ^2H_{H2O} and $\delta^{13}C_{DIC}$ showed high spatial variability, with some areas presenting lighter isotopes (Figure 2) which porewater and/or groundwaters may provide. Concentrations of DIC were slightly higher at the inner bay (Figure 2), indicating porewater fluxes upward.

Besides the observed offshore SGD sites (sites M1 and 371330), the shoreline of Puck Bay is also known for different spots of SGD spots (e.g., Szymczycha et al., 2012, 2020; Kotwicki et al., 2014; Donis et al., 2017; Kłostowska et al., 2019). At the location of the four shoreline sites encompassed in this study (Figure 1), higher Ra activities were found combined with lighter δ^2H_{H2O} and $\delta^{13}C_{DIC}$ signatures. At these locations, the sediment porewater salinity of several

674 sites generally showed a concave shape indicating an upward advective groundwater flow of
675 fresh groundwater.

676 **4.2 Early diagenesis and the impact of submarine groundwater discharge on the surface**
677 **sediments of the Gulf of Gdańsk and Puck Bay**

678 4.2.1 Offshore sites

679 The site located in the Gulf of Gdańsk (Site M1) displayed a decrease in sediment porewater
680 salinity and the $\delta^{2}H_{H2O}$ and $\delta^{18}O_{H2O}$ signatures at depth (Figure 4 -A), proving an upward flow
681 of fresh groundwater.

682 Site M1 is located in an area dominated by clayish silt (Figure 1). The sediments are
683 characterized by high TOC content and the low C: N ratios (Figures 3-A, E); however, it is
684 more likely due to the influence of the Vistula River (± 20 km south) as described by Szymczak-
685 Żyła and Lubecki (2022), and the exchange with the open Baltic Sea than to SGD. The Hg
686 values in the sediments were constant with depth, possibly due to the high sediment mixing
687 caused by gas flow, as observed in a nearby site by Brodecka-Goluch et al. (2022) and Idczak
688 et al. (2020) and the groundwater outflow.

689 Also, at this site, intensive organic matter mineralization was observed. The sediment
690 porewater DIC and NH_4 reached concentrations four times higher than the porewaters at the
691 outer Puck Bay sites. Concentrations of SO_4 were already lower in the top sediments due to
692 intense organic matter mineralization combined with the impact of poor SO_4 groundwater.
693 Following or overlapping the zone of sulfate reduction, methanogenesis became a pathway for
694 organic matter mineralization already in the surface sediments, confirmed by the heavier values
695 of $\delta^{13}C_{DIC}$ (14‰). This is commonly observed in coastal sites with high rates of organic matter
696 deposition (Manh Thang et al., 2012). As a result of the low availability of SO_4 and the absence

of Fe at the sediment-water interface for possible methane oxidation, CH_4 may easily migrate and impact the bottom waters, as observed by Idczak et al. (2020) in a nearby pockmark.

Most of the outer Puck Bay sites, except for Site 371330, revealed porewater gradients of constant salinity and conservative elements concentrations with depth. The surface sediments at these sites are composed of silty clay, clayey silt, and sand silt (Figure 1). The sediment composition was distinct between the sites; however, the TOC/TS contents remained below the predicted Holocene saturation line (Figure 3-F), indicating sulphate mineralization processes (Berner, 1982; Jørgensen and Kasten, 2006). Most sites showed Hg profiles with enhanced contents at 10 and 20 cmbsf, and continuous sedimentations with low disturbance. In contrast, Site M2 showed Hg values constant with depth, indicating some disturbance probably related to gas outflow. Site M2 is located over an extensive regular shallow gas accumulation (Brodecka-Goluch et al., 2022 and reference therein).

The porewaters from the outer Puck Bay sites are shaped by organic matter mineralization using, in particular, SO_4 and a continuous increase in metabolite concentrations (Figure 4 –H, I). The $\delta^{13}C_{DIC}$ composition was typical for marine sediments where high rates of mineralization of organic matter are found (Meister et al., 2019). Lighter isotopic signatures in the uppermost sediments of most sites may indicate methane oxidation. In addition, no disturbance from bubbles was observed in the acoustic images on the top sediment layer. The porewater displayed a high concentration of the main metabolites originating from organic matter mineralization. Site M2 was impacted by methanogenesis already in the top sediments, there SO_4 rapidly decreased to 0, and the $\delta^{13}C_{DIC}$ values turned heavier. Similar to Site M1, this site could also act as a source of CH_4 to the bottom waters.

719 The low Fe concentrations are probably due to the precipitation of Fe sulfides in the anoxic
720 zone (Balzer, 1982; de Beer et al., 2005). However, dissolved Fe and Mn were mobilized in
721 the top sediment in some sites due to the dynamic development of a suboxic zone.

722 The porewater salinity at Site 371330 displayed a slight decrease in porewater salinity together
723 with the other conservative elements (Figure 4-A), suggesting fresh groundwater's impact in
724 the deeper sediments. This site is located in an area composed mainly of silty clay (Figure 1).
725 The contents of TS were lower compared to the other sites within the bay, especially in the top
726 sediments, due to some re-oxidation of sedimentary sulphur species. Dissolved SO_4 remained
727 in the sediment, and H_2S did not accumulate. The lack of H_2S in the porewater profile may
728 cause higher concentrations of dissolved Fe since no precipitation could be formed. Dissolved
729 Fe and Mn were mobilized in the top sediments (Figure 4-K, L).

730 Even though Site 371330 showed some freshening with depth, the chemical gradients were
731 similar to the other sites in the outer Puck Bay; moreover, the gradients are not a result of the
732 mixing process as expected but from strong diagenetic processes.

733 4.2.2 Shoreline sites

734 The sites along the shoreline comprise sediments that are basically composed of medium sandy
735 sediments (Figure 1) and are characterized by low TOC and TS contents (Figure 3-G, H) due
736 to their continuous physical reworking, low clay contents (Morse & Berner, 1995) and intense
737 mineralization of standing stock organic matter (de Beer et al., 2005). In agreement with these
738 sedimentological features, the porewater gradients (Figure 5) suggest that diffusion is strongly
739 superimposed by porewater advection. Driving forces for this process taking place in the top
740 sediments are bottom currents (de Beer et al., 2005; Cook et al., 2007), and, at SGD impacted
741 sites, the upward movements of fluids (Billerbeck et al., 2006). These physical processes are

superimposed to a different degree on a seasonal scale by in situ biogeochemical transformation processes of spatial and temporal intensity (Cook et al., 2007).

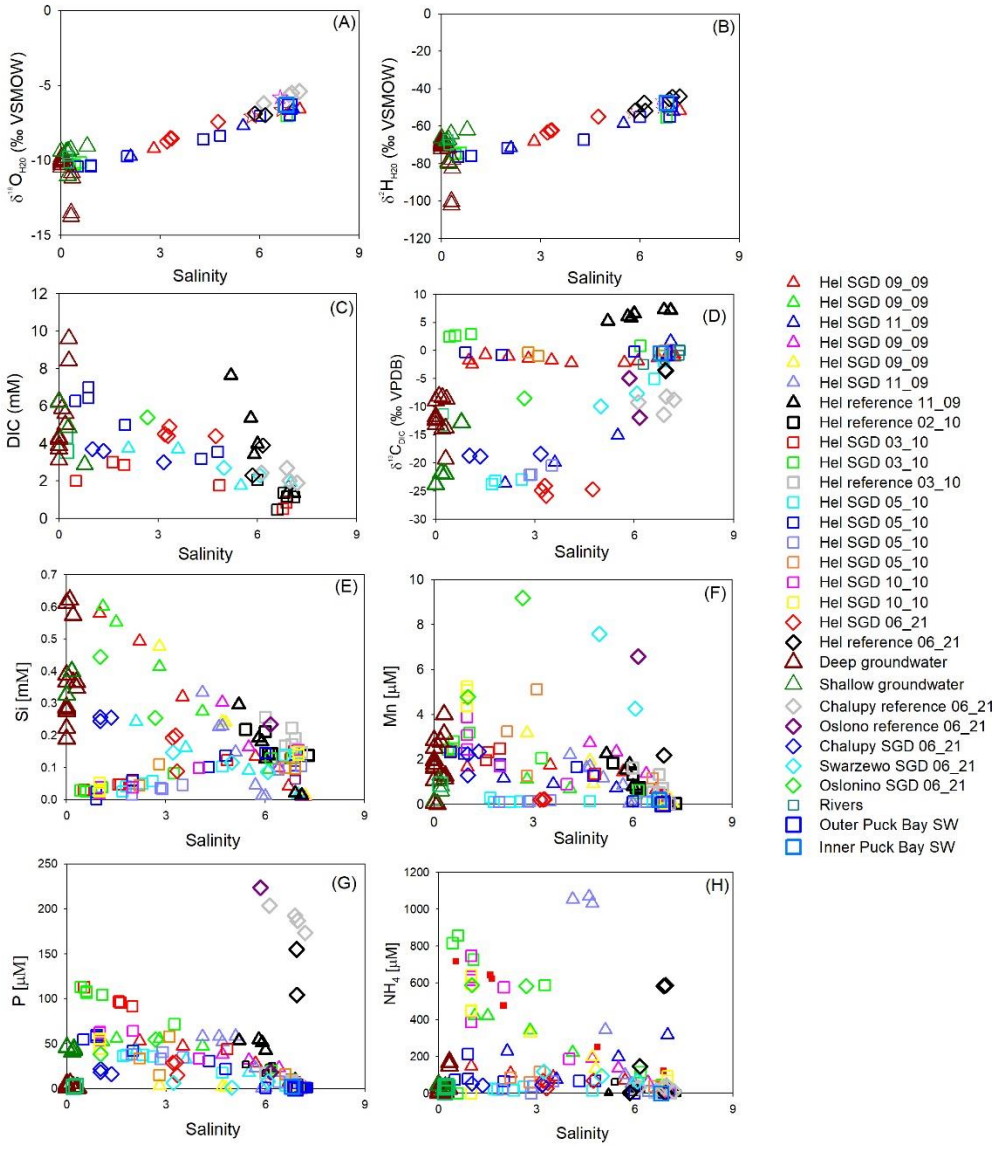

Figure 7 – Distribution relative to the salinity of selected elements from the shoreline sites. All profiles from the Hel site are shown on this plot (data from 2009 to 2021). The stars on panel (A) represent the sample from the seepage meters applied in 06_2021.

The porewater salinity displayed a huge variability between the study sites. There were sites without or only a slight vertical decrease in salinity (Figure 5, Supplementary Figure 3). Most of the sites, however, were chosen to reflect SGD impact, showing a downward decrease and reaching freshwater conditions with depth.

752 The sites with a slight decrease in salinity showed porewater isotopic composition (δ^2H and
753 $\delta^{18}O$) close to the Baltic Sea signatures and were, therefore, not significantly impacted by fresh
754 groundwater. A decrease in pH between 5 and 30 cmbsf simultaneous with a slight increase of
755 DIC indicates active organic matter mineralization with the contribution of SO_4 reduction.
756 Additionally, some sites were impacted by methanogenesis as the $\delta^{13}C_{DIC}$ reached positive
757 values. Dissolved P, NH4, and Mn Concentrations increased with depth, most likely resulting
758 from organic matter mineralization. However, the concentration of the metabolites was very
759 low on these sites since the upward advective flow limited the accumulations of these elements.

760 Steep down salinity gradients that existed at most of the sites, indicating fresh groundwater's
761 impact. The porewater isotopic composition (δ^2H and $\delta^{18}O$) and the ^3H activities at these sites
762 showed a clear mixing between the Baltic Sea and groundwater (Figure 7-A, B).

763 The concentrations of SO_4 dropped in the top 10 cmbsf due to the influence of fresh
764 groundwater depleted in SO_4. The application of a binary mixing shows a slight SO_4 deficit
765 found in most SGD-impacted porewaters (Supplementary Figure 5), indicating that minor net
766 microbial sulfate reduction takes place (c.f. Donis et al., 2017). Previous investigations have
767 furthermore demonstrated the importance of aerobic processes in surface sediments (Cook et
768 al., 2017; Donis et al., 2017).

769 The concentrations of DIC and the $\delta^{13}C_{DIC}$ signatures indicated different biogeochemical
770 processes (Figure 7-C, D). Mixing between fresh groundwater characterized by higher DIC
771 concentrations and dynamic $\delta^{13}C_{DIC}$ and brackish bottom water characterized by lower DIC
772 concentration and $\delta^{13}C_{DIC}$ composition typical for the Baltic Sea. This physical process is
773 superimposed by the remineralization of organic matter resulting in lighter $\delta^{13}C_{DIC}$ values.
774 Methanogenesis takes place at depth, as shown for the coast of Hel (Kotwicki et al., 2014;
775 Donis et al., 2017), and possible re-oxidation effects lead to shifts towards both isotopically

776 lighter and heavier stable isotope signatures. In the top sediments, signatures were lighter than
777 the values found in the non-SGD impacted sites indicating probably oxidation of CH_4.

778 The stable H and C isotope composition of dissolved CH_4 in porewater at the SGD-impacted
779 profiles showed a biogenic origin. They fall into the intermediate region predicted for
780 methanogenesis following the methyl-type fermentation and carbonate reduction pathways
781 (Table 1; Supplementary Figure 4) (e.g., Whiticar, 1999; Egger et al., 2017). Following the
782 classification of Whiticar (1999), the isotope signatures of porewater methane are dominated
783 by the impact of hydrogenotrophic carbonate reduction. A sample close to the sediment-water
784 interface was heavier in both δ13CCH4 and δ2HCH4 than other samples. This difference is
785 most likely due to the aerobic oxidation of methane in the surface sediment, which has been
786 shown to yield similar relative isotope enrichment (Drake et al., 2015).

787 Concentrations of dissolved nutrients (PO_4, NH_4, and Si) were higher in the SGD-impacted
788 sites compared to the non-impacted sites (Figure 7-G, H), demonstrating that the fresh SGD
789 component acts as a nutrient source that is further enhanced by organic matter mineralization.
790 In addition, it should be considered that most elements are expected to flow toward the bottom
791 waters because of the strong upward flow of groundwater, which suppresses the reaction of the
792 elements within the sediments. The higher concentrations of nutrients at SGD sites agree with
793 previous observations (Szymczycha et al., 2012, Donis et al., 2014).

794 The vertical profile of dissolved Fe and Mn in SGD impacted sites is shaped by mixing
795 processes. Higher dissolved Fe concentrations were found at two sites impacted by SGD in the
796 inner Puck Bay (Chałupy and Swarzewo, Figure 1), indicating different processes or
797 sedimentary Fe sources for the different sites. Fe and Mn exceed the concentrations expected
798 based on binary mixing between the bottom and groundwater (Supplementary Figure 5) due to
799 reductive liberation within the mixing zone of the surface sediments (Balzer, 1982; de Beer et

al., 2005). Dissolved Ba in the porewaters reflected the variability of the fresh groundwater sources (Figure 7 –E) and the effect of dilution with brackish waters.

4.2.3 Element fluxes

The dissolved constituents in porewater from the 15 selected sites under and without impact by SGD were modeled to estimate the water and element fluxes across the sediment-water interface and learn about the relative importance of diagenesis versus SGD-induced advection (Figure 8, Supplementary Table 3).

The Na concentrations of the porewaters were used to estimate the groundwater discharge across the sediment-water interface. Using the model approach (section 2.2.3), it was found that the fluxes at the offshore sites (M1, 371330, 371370, M2) are mainly driven by molecular diffusion. The calculated flux of fresh groundwater flux at Site M1 was 0.005 cm d^{-1} and 0.003 cm d^{-1} for Site 371330. The groundwater flow of the sites where SGD had not been noticed was smaller, around 0.001 cm d^{-1}.

At the sandy shoreline sites, where advective processes shaped the profiles, high groundwater flow was obtained compared to the offshore sites (Figure 8). The modeled groundwater flow at the SGD impacted sites varied between 0.01 and 0.03 cm d^{-1}. Advection at the non-SGD impacted sites was found to be much less and to vary in a range of 0 and 0.002 cm d^{-1}.

The associated element fluxes were found to vary between the sites, and they are presented in Supplementary Table 3. The offshore sites were characterized by higher fluxes of DIC, TA, NH_4, and P (Figure 8) out of the sediment, especially at Site M1 resulting from the organic matter mineralization. These results further highlight the importance of microbial catalyzed biogeochemical processes for developing the chemical gradients in the surface sediments.

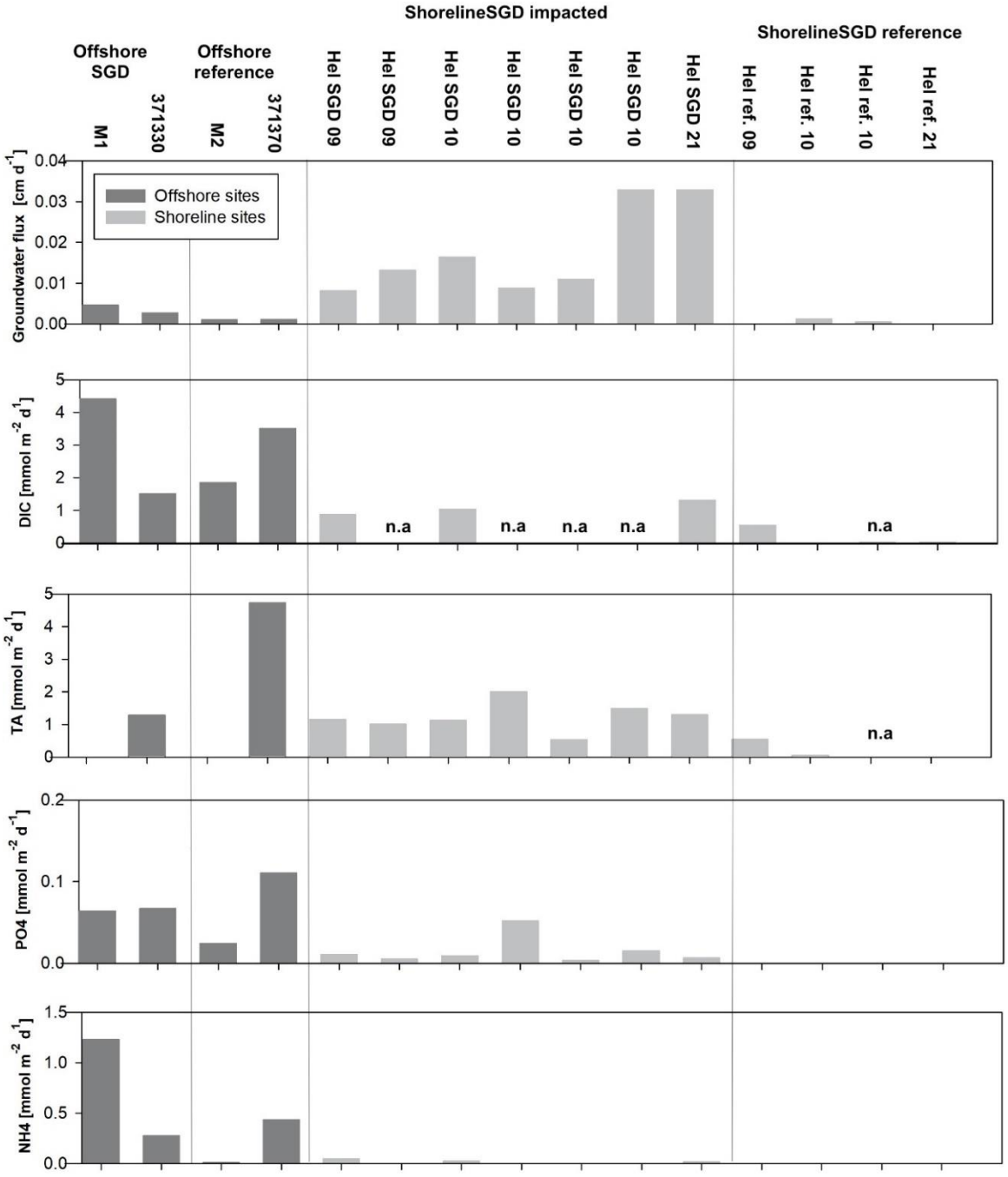

822

823 Figure 8 – Total fluxes (diffuse + mixing + advective) of water and chemical elements for the offshore muddy SGD and reference sites and
824 selected shoreline sandy SGD and reference sites. The fluxes are presented in Supplementary Table 3

825 The chemical fluxes at the sandy shoreline sites were comparatively low despite high advection
826 rates. The calculated fluxes are based on net fluxes, and the advective fluxes might inhibit the
827 elements' accumulation and result in lower element fluxes. However, enhanced fluxes of
828 elements were observed in the profiles impacted by SGD (theoretically, the sites with higher

advective flux), which suggests that the groundwater can be a source of these elements and therefore contributes to bringing additional elements to surface waters. Moreover, the physical pressure of the upward groundwater flow may facilitate the benthic fluxes at the sediment-water interface.

Despite the lower fluxes obtained, the sandy permeable sediments must be considered when addressing the global cycles of matter as they also represent a source of new or recycled elements to the surface waters (Santos et al., 2012).

4.3 The composition of the SGD freshwater component: Shoreline sites

The porewater isotopic signatures at the shoreline sites impacted by SGD (Figure 1) were lying on a mixing line between the surface waters of Puck Bay and the groundwaters (Figure 6). The lighter signatures were found at the bottom profile, plotting close to the groundwater signatures (Figure 6).

The SGD-impacted porewater profiles indicate high spatial and temporal variability (Supplementary Figure 3). The groundwater-seawater mixing zone moves according to external factors like wind direction, precipitation, and sea level (Kłostowska et al., 2019). However, from the salinity gradients, it is possible to roughly estimate that the freshwater composition can be found between 20 and 100 cmbsf at the sandy shoreline sites.

The fresh component of SGD was characterized based on the extrapolation of the profiles to freshwater conditions (the calculation was based on Mg concentrations in groundwater which was ± 0.4 mM). Porewater profiles from Hel, Chałupy, Swarzewo, and Osłonino (Figure 1) were evaluated and compared with values from the ground and river waters around Puck Bay.

The hydrogeochemical composition of the fresh SGD component at Hel and Chałupy was Ca-Mg-HCO_3 type, similar to the groundwater and the rivers in this region, and the site in

852 Swarzewo showed some impact by saline water. The fresh component of SGD on Hel showed
853 a mixing composition (Figure 6, B).

854 The Hel site showed the lightest water isotopic signatures reaching -10.9 and -78.4‰ for
855 $\delta^{18}O_{H2O}$ and $\delta^{2}H_{H2O,}$ respectively, which is probably influenced by groundwater from deep
856 aquifers related to the Cretaceous formation (Piekarek–Jankowska 1996). The ^{3}H activities
857 found on the porewaters of Hel (Supplementary Table 2) indicate the presence of low/free ^{3}H
858 groundwater. Besides Hel, a site on the landside (Osłonino) seems to be influenced by
859 groundwaters from Cretaceous aquifers due to the lighter water isotopic values (Figure 6).

860 Although the $\delta^{13}C_{DIC}$ signatures vary over a wide range (Figure 7-D), the freshwater
861 composition could be calculated to be -19, -16, and -16‰ for Chałupy Swarzewo and Osłonino
862 respectively. These values were similar to the signatures found on deep groundwaters (Table
863 1), and they probably are a result of mixing between soil CO_2 and C3 Plants contributing to the
864 lighter isotopes and Ca dissolution with the heavier isotopes (e.g., Deines et al., 1974).

865 **4.4 Local and regional estimates of SGD contribution for the Puck Bay**

866 4.4.1 Local scale of fresh SGD

867 The modeled groundwater discharge, estimated by the Na gradient, of the 371330 in the central
868 part of the outer Puck Bay was 0.03 L m^{-2} d^{-1}. Higher groundwater flow estimates were obtained
869 for the shoreline site in Hel, varying between 0.01 and 0.03 L m^{-2} d^{-1}. These estimations refer
870 to the fresh upward groundwater flow.

871 The fluxes obtained by the seepage meter also include the recirculated SGD. The fluxes at the
872 Hel shoreline site were between 30-45 L m^{-2} d^{-1}. The fluxes obtained for the sites located in the
873 inner part of the Puck Bay, Chałupy, and Swarzewo, were 1.6 and 3.0 L d^{-1} m^{-2}, respectively.

In this study, the seepage fluxes measured with seepage meters are characteristic of the active SGD sites at the shoreline. Estimates from the present study agree with those already estimated previously by applying seepage meters ranging from 3 to 187 L m^{-2} d^{-1} (e.g., Szymczycha et al. 2012, Kotwicki et al. 2014, Donis et al. 2017). The fluxes are very heterogeneous, as the outflow from the seepage meters are controlled by the geological features on the selected seabed (Burnett et al., 2006).

4.4.2 Regional scale SGD

SGD is, in general, a potential source of Ra (Beck et al., 2007b; Rodellas et al., 2012). The present study uses a Ra isotope mass balance to estimate the total SGD in Puck Bay, following Rodellas et al. (2017). Two separate balances for the outer and the inner part of Puck Bay were constructed.

As sources, SGD, rivers, and diffusion from sediments are considered. The sinks are radioactive decay and net export from the study area. Assuming a steady state, the mass balance can be expressed as:

$$\boldsymbol{Q_{SGD}}^{*} Ra_{SGD} + R + F_D - D - O = 0 \quad (5)$$

Where Q is the volumetric SGD (m^3 d^{-1}), C is the $^{224}Ra_{ex}$ activity of the study area (Bq m^{-3}), R is the input from rivers (Bq d^{-1}), F_D is the contribution from diffuse fluxes from the sediment (Bq d^{-1}), D is the radioactive decay (Bq d^{-1}), and O is the outflow from the inner and outer Puck Bay (Bq d^{-1}).

The river input is estimated as the product of the discharge and the corresponding $^{224}Ra_{ex}$ activities. The Reda river contributes around 76% of the volume of all rivers discharging into the inner bay (Szymczak & Jankowska, 2007). Therefore, it is considered that the discharge of Zagórska Struga, Gizdepka, and Płutnica together represent 24% of the Reda River discharge.

The diffusive flux determined by the Ra diffusion experiment was multiplied by the area of the bay to obtain F_D.

The radioactive decay is the product of the $^{224}Ra_{ex}$, the volume of the bay in study, and the decay constant. The outflow was calculated as:

$$O: \frac{(224Raex\ inner\ or\ outer\ bay - 224Raex\ outer\ bay\ or\ \ Baltic\ Sea) * V\ inner\ or\ outer\ bay}{WA} \quad (6)$$

Where the WA is the apparent water age, which was estimated by using the short-lived radium isotopes as described by Moore (2010):

$$WA: \frac{ln(\frac{224Ra}{223Ra})inner\ or\ outer\ PB - ln(\frac{224Ra}{223Ra})RaSGD}{\lambda 223 - \lambda 224} \quad (7)$$

The Ra-derived estimate of the water ages is 4 ± 2 and 15 ± 8 days for the outer and inner parts of Puck Bay, respectively. It should be noted that water age represents the time elapsed since the water sample became enriched in Ra and was isolated from the source (Moore 2010). With this application, water ages with twice as the half-life of the applied isotope ($t_{½}$ ^{223}Ra: 11.4 days) can be estimated.

Table 2 - Summary of the terms and values used in the Ra mass balance.

Term	Definition	Outer Puck Bay	Inner Puck Bay	Units	Source
A	Area of the bay	255200000	104000000	m^2	Kramarska et al. (1995)
V	Volume of the bay	5231600000	322400000	m^3	Szymczak & Szmytkiewicz 2014
h	average depht of the bay	20.5	3	m	Matciak et al., 2011
Q_{rivers}	Total discharge of Gizdepka, Plutnica and Zagorska Struga rivers		73667.37	$m^3 d^{-1}$	24% of Reda discharge (Szymczak and Piekarek-Jankowska 2007 / IMGW, 2022)
Q_{reda}	Discharge of Reda river		233280	$m^3 d^{-1}$	IMGW,2022
λ224	$^{224}Ra_{ex}$ decay constant	0.19	0.19	d^{-1}	
λ223	$^{223}Ra_{ex}$ decay constant	0.06	0.06	d^{-1}	

WA	Water age	4	15.0	d	Eq. 3
Ra_{reda}	$^{224}Ra_{ex}$ concentration in Reda River		2.2	Bq m^{-3}	this study
Ra_{rivers}	$^{224}Ra_{ex}$ activties in the Gizdepka River		0.5	Bq m^{-3}	this study
Ra_{rivers}	$^{224}Ra_{ex}$ concentration in the Plutnica River		0.9	Bq m^{-3}	this study
Ra_{rivers}	$^{224}Ra_{ex}$ concentration in the Zagórska Struga River		1	Bq m^{-3}	this study
$Ra_{Baltic\ Sea}$	$^{224}Ra_{ex}$ concentration in the Baltic Sea site	0.3		Bq m^{-3}	this study
$Ra_{outer\ PB}$	Average $^{224}Ra_{ex}$ concentration in the Outer Puck Bay	0.5	0.5	Bq m^{-3}	this study
$Ra_{inner\ PB}$	Average of $^{224}Ra_{ex}$ in the inner Puck Bay	1.6	1.6	Bq m^{-3}	this study
F_{dif}	Ra flux out from bottom sediments	0.1	0	Bq m^{-2} d^{-1}	this study
Ra_{SGD}	$^{224}Ra_{ex}$ of porewater Sopot (SGD)	13.6		Bq m^{-3}	this study
Ra_{SGD}	$^{224}Ra_{ex}$ of porewater Hel (SGD)	7		Bq m^{-3}	this study
Ra_{SGD}	$^{224}Ra_{ex}$ of porewater Chalupy (SGD)		31	Bq m^{-3}	this study
Ra_{SGD}	$^{224}Ra_{ex}$ of porewater Swarzeno (SGD)		9	Bq m^{-3}	this study
Ra_{SGD}	$^{224}Ra_{ex}$ of porewater Oslonino (SGD)		79	Bq m^{-3}	this study
	CALCULATIONS				
O	Ra output fluxes	261580000	23642667	Bq d^{-1}	Eq 2
D	Radioactive decay	497002000	98009600	Bq d^{-1}	$^{224}Ra_{ex}PB*V*\lambda 224$ (Valenti et al., 2017)
R	contribution from the inner Puck Bay	23642667		Bq d^{-1}	Eq 2
R	contribution from rivers		572150	Bq d^{-1}	(Q_{rivers} * average of Ra_{rivers}) + ($Q_{reda*}Ra_{reda}$)
F_D	contribution from diffuse fluxes out of bottom sediments	25520000	10400000	Bq d^{-1}	F_{dif} * A
$Q_{SGD}*Ra_{SGD}$	contribution from SGD	640362213	106424437	Bq d^{-1}	(D+O)-(R+Fd+Fs)
Q_{SGD}	Flux of SGD	77	6	10^6 m^3 d^{-1}	Balance/Ra_{SGD}
Q_{SGD}	Flux of SGD per area	301	55	L m^{-2} d^{-1}	QSGD/A

915

916 Considering all the inputs and outputs of the Ra mass balance in the outer Puck Bay, the **Q_{SGD}**
917 was estimated as 77 ± 35 10^6 m^3 d^{-1} (301 L m^{-2} d^{-1}) (Table 2). In order to come up with a
918 discharge in the range of the values already estimated for Puck Bay, we estimated that SGD is
919 taking place in the whole bay (255.2 km^2). This assumption could be realistic to a certain extent
920 as acoustic images showed anomalies on the surface sediments, and salinity in the water
921 column decreased with depth in some sites (Matciak et al., 2015). However, the SGD fluxes
922 estimated here are the sum of the fresh and saline component of SGD, and a balance using
923 long-lived Ra isotopes is required to really differentiate porewater exchange and SGD.

924 Considering all the $^{224}Ra_{ex}$ sources, SGD represents 94 %, the outflow from the inner Puck Bay
925 is 3%, and the diffusion represent 3%. In this balance, the Vistula River was not considered a
926 source of Ra to Puck Bay, which could have an impact depending on the wind direction.
927 Moreover, the contribution from the sediments could also be higher if the diffusion experiment
928 would be done for the different sediments found across the bay.
929 Regarding the inner Puck Bay, $\mathbf{Q_{SGD}}$ was estimated as 6 ±6 10^6 m^3 d^{-1} (55 L m^{-2} d^{-1}) (Table 2).
930 As assumed in the outer Puck Bay, we consider that SGD is taking place on the entire inner
931 bay (104 km^2). At the inner part of the bay, SGD represents 91%, rivers 0.5%, and the diffusion
932 represents 9 %, respectively.
933 The wide range between the discharges is due to the high heterogeneity of the activities found
934 in the end members. The same dynamic was observed in the $^{224}Ra_{ex}$ activities of the
935 groundwaters around Puck Bay, which ranged between 0 and 14 Bq m-3 (Table 1), suggesting
936 that the groundwater discharged into Puck Bay is formed and flows through different lithology.
937 The SGD is around 24 times higher in the inner part of Puck Bay than the discharge of Reda
938 River on the day of sampling (3 m^3 s^{-1}, IMGW, 2022).
939 The estimates from the Ra mass balance are overall in agreement with the ones measured by
940 seepage meters or porewater profiles (this study, Kłostowska et al., 2019, Szymczycha et al.,
941 2012, Kotwicki et al., 2014; Donis et al., 2017) shown in the Supplementary Table 2. This
942 regional approach based on Ra isotopes provides, however, allows for the first time an
943 integrated estimate of the SGD over the whole Puck Bay area.
944
945 *Table 3 - Information of SGD fluxes estimated in different studies for Puck Bay, and, for some sites along the Baltic Sea*

Location	Year sampling	Approach	Discharge	Unit	Reference
Puck Bay	1994	only Fresh SGD	0.4	L m^{-2} d^{-1}	Piekarek–Jankowska 1994, 1996
Hel - Outer Puck Bay	2009-2010	Seepage meter	3-22	L m^{-2} d^{-1}	Szymczycha et al 2012
Hel - Outer Puck Bay	2009/2010	Benthic seepage meters	10 -150	L m^{-2} d^{-1}	Kotwicki et al 2014
Hel - Outer Puck Bay	2009	Benthic chamber	86 ±16	L m^{-2} d^{-1}	Donis et al 2017

Outer Puck Bay (Hel, Jurata, Swarzewo, and Puck)	2017/2018	Chloride tracer	156-242	L m^{-2} d^{-1}	Kłostowska et al., 2019
inner Puck Bay (Chalupy and Oslonino)	2017/2018	Chloride tracer	156 - 242	L m^{-2} d^{-1}	Kłostowska et al., 2019
Hel - outer Puck Bay	2021	Seepage meter	30 - 45	L m^{-2} d^{-1}	This study
Chalupy - inner Puck Bay	2021	Seepage meter	2	L m^{-2} d^{-1}	This study
Swarzewo - inner Puck Bay	2021	Seepage meter	3	L m^{-2} d^{-1}	This study
Site 371330 - Outer Puck Bay	2009	Na profile - only fresh SGD	0.003	L m^{-2} d^{-1}	This study
Hel - outer Puck Bay	2009-2021	Na profile	0.01-0.03	L m^{-2} d^{-1}	This study
outer Puck Bay	2019	Ra isotopes	301	L m^{-2} d^{-1}	This study
inner Puck Bay	2021	Ra isotopes	55	L m^{-2} d^{-1}	This study
Gulf of Finland		geological and hydrogeological methods	0.1	L m^{-2} d^{-1}	Viventsova and Voronov 2003
Eckernforde Bay, Germany	1998/2001	Chloride tracer	<9	L m^{-2} d^{-1}	Schulter et al., 2004
Forsmark, Gulf of Bothnia	2013	Ra isotopes	0.3 -59	L m^{-2} d^{-1}	Krall et al., 2017

The different methods applied in the present study proved that SGD is taking place with high spatial heterogeneity and a larger range in the volumetric fluxes, however, with high variability on the fluxes. The different results are because SGD is a local phenomenon, and assumptions and uncertainties are assumed in the calculations depending on the number of active SGD sites, which is unknown so far. In addition, our values exceed those reported for other regions of the Baltic Sea (Table 3).

5. Conclusions

Puck Bay can be considered a hotspot for submarine groundwater discharge compared to other coastal areas of the Baltic Sea. The current multi-method investigation of the water column, pore waters, and sediments has shown that SGD occurs primarily along the sandy shoreline but can also be detected in the deeper central part of Puck Bay.

Local and regional SGD fluxes were measured directly using seepage meters and further constrained from the Ra isotope mass balance coming up with values between 3 and 300 L m^{-}

960 ^{2} d^{-1}. Element fluxes across the sediment-water interface of organic-rich muds (impacted and
961 non-impacted sites) were found to be driven by early diagenesis. The SGD-impacted sandy
962 sites showed intensive mixing with upward moving freshwater and seawater, and early
963 digenetic processes were less pronounced in shaping the porewater gradients. SGD leads to a
964 release of DIC and TA into bottom waters. The carbon isotopic composition of DIC shows
965 temporal changes, likely driven by dynamics in the availability and reoxidation of biogenic
966 methane. This indicates that CH4 is probably not derived from the original aquifer, but
967 originates from a zone between the deeper aquifer and the overlying sands. Our approach
968 enabled the detection of different freshwater endmembers originating from different aquifers.
969 It also indicates that SGD-derived chemical fluxes strongly depend on the composition and
970 process occurring in the surface sediments. Further research on controlling the spatial and
971 temporal dynamics of SGD is needed to resolve the potentially important quantitative role of
972 SGD in coastal areas.

973 ## Acknowledgements

974 The authors wish to thank the staff at the Hel Marine Station (Institute of Oceanography,
975 University of Gdańsk) for their continuous support during the field campaigns and the
976 stimulating working atmosphere. The crew and the captain of R.V.s Professor Albrecht Penck
977 and Oceania. Karol Kuliński, Jacek Bełdowski, Maciej Chełchowski, Marta Borecka, Monika
978 Lengier, Piotr Balazy, and Seyed Reza Saghravani for the support during the fieldwork. Anne
979 Koehler, Ines Scherff, Dagmar Benesch, Patricia Roeser (IOW), and Marta Borecka (IOPAN|)
980 are thanked for their expert support in the laboratory. Jan Scholten and Patricia Roeser are
981 thankful for the scientific discussions, which helped to improve this manuscript. The water
982 utility companies: "Saur Neptun Gdańsk", "Pucka Gospodarka Komunalna", MPWiK
983 "EKOWIK", "PEWIK GDYNIA", “EKO-HEL BIS”, especially to Radosław Walczak, Konrad

Krampichowski, Julia Nowak, Jarosław Myślisz, Michał Twardowski, Zbigniew Rydz, and all staff members for help during the groundwater sampling.

Funding

Financial support for this work was provided by a DAAD stipend to CMEvA (Doctoral program in Germany 2018/2019, project no. 57381412), to MEB by the BONUS+ project AMBER (BMBF project No.03F0485A), the European Union's Horizon 2020 research and innovation programme under grant agreement no. 730984 (Assemble Plus project), and the Leibniz Institute for Baltic Sea Research, and to BS by Institute of Oceanology Polish academy of sciences (IOPAN) and project nr.2019/34/E/ST10/00217 funded by the Polish National Science Centre. This work is also associated to the DFG-Research Training Group 'Baltic TRANSCOAST' GRK 2000.

Data availability

The raw data supporting the conclusions of this article will be made available by the authors, and the graphically presented data will be stored in the PANGEA database.

Reference

Atlas of Polish marine area bottom habitats. Environmental valorization of marine habitats. 2009 Institute of Oceanology PAS. Available: https://www.iopan.gda.pl/hm/atlas/Atlas_all.pdf

Balzer W. (1982) On the distribution of iron and manganese at the sediment/water interface: thermodynamic versus kinetic control. Geochimica et Cosmochimica Acta, 46: 1153-1161.

Beck A. J.; Tsukamoto, Y.; Tovar-Sanchez, T.; Huerta-Diaz, M.; Bokuniewicz, H. J.; Sanudo-Wlhelmy, S. A. (2007a). Importance of geochemical transformations in determining submarine

groundwater discharge-derived trace metal and nutrient fluxes. Applied Geochemistry, 22:477-490.

Beck A.J., Rapaglia J.P., Cochran K., Bokuniewicz, H.J. (2007b) Radium mass-balance in Jamaica Bay, NY: Evidence for a substantial flux of submarine groundwater. Marine Chemistry, 106:419-441.

Berner R.A. (1982) Burial of organic carbon and Pyrite sulfur in the modern ocean: its geochemical and environmental significance. American journal of science, 282(4): 451-473.

Berner R.A., and Raiswell R. (1983). Burial of organic carbon and pyrite sulfur in sediments over Phanerozoic Time: a new theory. Geochimica et Cosmochimica Acta 47 (5): 855–862.

Billerbeck M., Werner U., Bosselmann K., Walpersdorf E., Huettel M. (2006). Nutrient release from an exposed intertidal sand flat. Marine Ecology Progress Series, 316: 35-51.

Blöschl, G., Bierkens, M. F. P., Chambel, A., Cudennec, C., Destouni, G., Fiori, A., et al. (2019). Twenty-three Unsolved Problems in Hydrology (UPH) – a Community Perspective. Hydrological Science, 64: 1141-1158.

Böttcher M.E., Lipka M., Winde V., Dellwig O., Böttcher E.O., Böttcher T.M.C., Schmiedinger I. (2014) Multi-isotope composition of freshwater sources for the southern North and Baltic Sea. Proc. 23rd SWIM conference, Husum, 46-49, ISBN 978-3-00-046061-6.

Böttcher M. E., and Schmiedinger I. (2021) The Impact of Temperature on the Water Isotope ($^{2}H/^{1}H$, $^{17}O/^{16}O$, $^{18}O/^{16}O$) Fractionation upon Transport through a Low-Density Polyethylene Membrane. Isotopes in Environmental and Health Studies, 57: 183-192.

Böttcher M. E., Mallast U., Massmann G., Moosdorf N., Mueller-Pethke M., and Waska H. (2023). “Coastal-Groundwater Interfaces (Submarine Groundwater Discharge),” in Ecohydrological Interfaces. Editors S. Krause, D. M. Hannah, and N. Grimm (New York, NY: Wiley & Sons).

1029 Brodecka-Goluch A., Lukawska-Matuszewska L., Kotarba M.J., Borkowski A., Idczak J.,
1030 Bolalek J. (2022) Biogeochemistry of three different shallow gas systems in continental shelf
1031 sediments of the South-Eastern Baltic Sea (Gulf of Gdańsk): Carbon cycling, origin of methane
1032 and microbial community composition. Chemical Geology, 597:120799.

1033 Burnett W. C., Aggarwal P. K., Aureli A., Bokuniewicz H., Cable J. E., Charette M. A., Kontar
1034 E., Krupa S., Kulkarni K.M., Loveless A., Moore W.S., Oberdorfer J.A., Oliveira J., Ozyurt
1035 N., Povinec P., Privitera A.M.G., Rajar R., Ramessur, R.T., Turner J.V. (2006). Quantifying
1036 Submarine Groundwater Discharge in the Coastal Zone via Multiple Methods. Science of the
1037 Total Environment, 367: 498–543.

1038 Cerdà-Domènech M., Rodellas V., Folch A., Garcia-Orellana J. (2017). Constraining the
1039 temporal variations of Ra isotopes and Rn in the groundwater end-member: Implications for
1040 derived SGD estimates. Science of the Total Environment, 595:849-857.

1041 Charette M. A, Buesseler K., Andrews J. (2001) Utility of radium isotopes for evaluating the
1042 input and transport of groundwater-derived nitrogen to a Cape Cod estuary. Limnology and
1043 Oceanography, 46(2), 465-470.

1044 Charette M.A., Sholkovitz E.R., Hansel C.M. (2005) Trace element cycling in a subterranean
1045 estuary Part 1. Geochemistry of the permeable sediments. Geochmica et Cosmochimiva Act,
1046 69(8): 2095-2109.

1047 Church T. (1996) An underground route for the water cycle. Nature, 380: 579.

1048 Cline J. D. (1969). Spectrophotometric Determination of Hydrogen Sulfide in Natural Waters.
1049 Limnology and Oceanography, 14:454-458.

1050 Cook P. L. M, Wenzhöfer F., Glud R. N., Janssen F., Huettel M. (2007) Benthic solute
1051 exchange and carbon mineralization in two shallow subtidal sandy sediments: Effect of
1052 advective pore-water exchange. Limnology and oceanography, 52:1943-1963.

de Beer D., Wenzhöfer F., Ferdelman T.G., Boehme S.E., Huettel M., van Beusekom J.E.E., Böttcher M.E., Musat N., Dubilier N. (2005) Transport and mineralization rates in North Sea sandy intertidal sediments, Sylt-rømø basin, waddensea. Limnology and Oceanography, 50: 113:127.

Deines P., Langmuir D., Harmon R.S (1974) Stable carbon isotope ratios and the existence of a gas phase in the evolution of carbonate ground waters. Geochmica et Cosmochimica Acta, 38:1147-1164.

Dippner J.W., Bartl I., Chrysagi E., Holtermann P,, Kremp A,, Thoms F, and Voss M, (2019) Lagrangian Residence Time in the Bay of Gdańsk, Baltic Sea. Frontiers Marine Science, 6:725.

Drake H., Åström M., Heim C. Broman C., Åström J., Whitehouse M., Ivarsson M., Siljeström S., Sjövall. (2015) Extreme 13C depletion of carbonates formed during oxidation of biogenic methane in fractured granite. Nature Communications 6: 7020

Donis D., Janssen F., Liu B., Wenzhöfer F., Dellwig O., Escher P., Spitzy A., Böttcher M.E. (2017). Biogeochemical impact of submarine groundwater discharge on coastal surface sands of the southern Baltic Sea. Estuarine, Coastal and Shelf Science, 189: 131-142.

EEA. European Environment Agency. Data and Maps. EEA coastline. Available: http://www.eea.europa.eu/data-and-maps/data/eea-coastline-for-analysis-2/gis-data/eea-coastline-polygon/@@rdf. Accessed 22.10.2022

Egger M., Hagens M., Sapart C.J., Dijkstra N., van Helmond N.A.G.M., Mogollón J., Risgaard-Petersen N., van der Veen C., Kasten S., Riedinger N., Böttcher M.E., Röckmann T., Jørgensen B.B. & Slomp C.P. (2017) Iron oxide reduction in methane-rich deep Baltic Sea sediments. Geochimica et Cosmochimica Acta, 207: 256-276.

1075 Falkowska L., Piekarek-Jankowska H. (1999) Submarine seepage of fresh groundwater:
1076 disturbance in hydrological and chemical structure of the water column in the Gdansk Basin.
1077 ICES Journal of Marine Science, 56: 153-160.

1078 Froelich P. N., Klinkhammer G. P., Bender M. L., Luedtke N. A., Heath G. R., Cullen D.,
1079 Dauphin P., Hammond D., Hartman B. and Maynard V. (1979) Early oxidation of organic
1080 matter in pelagic sediments of the eastern equatorial Atlantic: suboxic diagenesis. Geochimica
1081 et Cosmochimica Acta, 43: 1075e1090.

1082 Garcia-Solsona E., Garcia-Orellana J., Masqué P., and Dulaiova H. (2008) Uncertainties
1083 Associated with ^{223}Ra and ^{224}Ra Measurements in Water via a Delayed Coincidence Counter
1084 (RaDeCC). Marine Chemistry, 109: 198-219.

1085 Goyetche T., Luquot L., Carrera J., Martínez-Pérez, L., Folch A. (2022) Indentification and
1086 quantification of chemical reactions in a coastal aquifer to assess submarine groundwater
1087 discharge composition. Science of the Total Environment, 838 (1):155978

1088 Grasshoff K., Kremling K., and Ehrhardt M. (2009) Methods of Seawater Analysis. Weinheim:
1089 John Wiley & Sons.

1090 Gupta P., Noone D., Galewsky J., Sweeney C., and Vaughn B. H. (2009): Demonstration of
1091 high-precision continuous measurements of water vapor isotopologues in laboratory and
1092 remote field deployments using wavelength-scanned cavity ring-down spectroscopy (WS-
1093 CRDS) technology. Rapid Commun. Mass Spectrom. 23: 2534–2542.

1094 HELCOM. River and lake outlines around the Baltic Sea based on 1:1,000,000 scale source
1095 maps. Available:
1096 https://metadata.helcom.fi/geonetwork/srv/eng/catalog.search#/metadata/f0edff62-d9fa-4fda-
1097 9b42-da3947ee248a. Accessed at 22.05.2022.

1098 Hoffmann J.J.L., von Deimling J.S., Schröder J.F., Schmidt M., Held P., Crutchley G.J.,
1099 Scholten J., Gorman A.R. (2020) Complex Eyed pockmarks and submarine groundwater
1100 discharge revealed by acoustic data and sediment cores in Eckernförde Bay, SW Baltic Sea.
1101 Geochemistry, Geophysics, Geosystem, 21:e2019GC008825.

1102 Huettel M., Ziebis W., Forster S., Luther W. (1998) Advective transport affecting metal and
1103 nutrient distributions and interfacial fluxes in permeable sediments. Geochmica et
1104 Cosmochimica Acta, 62 (4): 613-631.

1105 IMGW 2022. The data have been processed at the Institute of Meteorology and water
1106 management - National Research Institute Poland.

1107 Idczak J., Brodeck-Goluch A., Lukawska-Matuszewska K., Graca B., Gorska N., Klusek Z.,
1108 Pezacki P. D., Bolalek J. (2020). A geophysical, geochemical,l and microbiological study of a
1109 newly discovered pockmark with active gas seepage and submarine groundwater discharge
1110 (MET1-BH, central Gulf of Gdańsk, southern Baltic Sea). Science of the Total Environment,
1111 742: 140306.

1112 Iversen N. and Jørgensen B. B. (1985) Anaerobic methane oxidation rates at the sulfate-
1113 methane transition in marine sediments from Kattegat and Skagerrak (Denmark). Limnology
1114 Oceanography, 30(5): 944-955.

1115 Jørgensen B. B., Böttcher M. E., Luschen H., Neretin L.N., Volkov I. I. (2004) Anaerobic
1116 methane oxidation and a deep H_2S sink generate isotopically heavy sulfides in Black Sea
1117 sediments. Geochimica et Cosmochimica Acta, 68(9): 2095-2118.

1118 Jørgensen, B. B. and Kasten, S. (2006) Sulfur cycling and methane oxidation. In *Marine*
1119 *Geochemistry* (eds. H. D. Schulz and M. Zabel). Springer-Verlag, Berlin Heidelberg. pp. 271-
1120 309.

1121 Jurasinski G., Janssen M., Voss M., Böttcher M.E., Brede M., Burchard H., Forster S., Gosch
1122 L., Gräwe U., Gründling-Pfaff S., Haider F., Ibenthal M., Karow N., Karsten U., Kreuzburg
1123 M., Lange X., Langer S., Leinweber P., Rezanezhad F., Rehder G., Romoth K., Schade H.,
1124 Schubert H., Schulz-Vogt H., Sokolova I., Strehse R., Unger V., Westphal J., Lennartz B.
1125 (2018) Understanding the Coastal ecocline: Assessing sea-land-interactions at non-tidal, low-
1126 lying coasts through interdisciplinary research. Frontiers Marine Sciences, 5, 342: 1-22.

1127 Kłostowska Z., Szymczycha, B., Kuliński, K., Lengier, M., Łęczyński, L. (2018)
1128 Hydrochemical characterization of various groundwater and seepage water resources located
1129 in the Bay of Puck, Southern Baltic Sea. E3S Web of Conferences 54, 00013.

1130 Kłostowska Z., Szymczycha B., Lengier M., Zarzeczanska D., Dzierzbicka-Glowacka L.
1131 (2019) Hydrogeochemistry and magnitude of SGD in the Bay of Puck, southern Baltic.
1132 Oceanologia, 62: 1-11.

1133 Krall L., Garcia-Orellana J., Trezzi G., and Rodellas V. (2017). Submarine Groundwater
1134 Discharge at Forsmark, Gulf of Bothnia, provided by Ra Isotopes. Marine Chemistry 162: 162–
1135 172.

1136 Kramarska, Regina, et al. (1995) Origin and Evolution of the Puck Lagoon. Journal of Coastal
1137 Research.

1138 Kotwicki L., Grzelak K., Czub M., Dellwig O., Gentz T., Szymczycha B., Böttcher M.E.
1139 (2014). Submarine Groundwater discharge to the Baltic coastal zone: Impacts on the
1140 meiofaunal community. Journal of Marine Systems, 129: 118-126.

1141 Leipe T., Moros M., Kotilainen A., Vallius H., Kabel K., Endler M., Kowalski N. (2013).
1142 Mercury in Baltic Sea Sediments - Natural Background and Anthropogenic Impact.
1143 Geochemistry, 73: 249-259.

1144 Löffer H., Adam C., G. B., Brinschwitz D., Gieseler W., Ginzel G., Grunske K.-A., Heeger D.,
1145 Meinert N., Nillert P., Richter C., and Victor N. (2010). Hydrochemische Typisierung für
1146 Grundwasser im Lockergestein Bereich des norddeutschen Flachlandes. Schriftenreihe für
1147 Geowissenschaften Heft, 18:369-399.

1148 Majewski A. (1990). The Gulf of Gdańsk. Wydawnictwo Geologiczne, Warsaw, Poland (in
1149 Polish).

1150 Matciak M, Nowacki J, Krzyminski W. (2011). Upwelling intrusion into shallow Puck Lagoon,
1151 a part of Puck Bay (the Baltic Sea). International Journal of Oceanography and Hydrobiology:
1152 40, 2.

1153 Matciak M., Bieleninik S., Botur A., Podgórski M., Trzcinska K., Draganska K., Jasniewicz
1154 D., Kurszewska A., Wenta M. (2015). Observations of presumable groundwater seepage
1155 occurrence in Puck Bay (the Baltic Sea). Oceanological and Hydrobiological Studies, 44 (2),
1156 267- 272.

1157 Mayfield, K. K.; Eisenhauer, A.; Ramos, D. P. S.; Higgins, J. A.; Horner, T. J.; Auro, M.;
1158 Magna, T.; Moosdorf, N.; Charette, M. A.; Gonneea, M. E.; Brady, C. E.; Komar, N.; Peucker-
1159 Ehrenbrink, B.; Paytan, A. (2021) Groundwater discharge impacts marine isotopes budgets of
1160 Li, Mg, Ca, Sr, and Ba. Nature communications, 12:148.

1161 Meister P., Liu B., Khalili A., Böttcher M.E., Jørgensen B.B. (2019) Factors controlling the
1162 carbon isotope composition of dissolved inorganic carbon and methane in marine porewater:
1163 An evaluation by reaction transport modelling. Journal of Marine System, 200:103227.

1164 Moore, W.S. (1996). Large groundwater inputs to coastal waters revealed by ^{226}Ra
1165 enrichments. Nature, 380: 612-614.

1166 Moore W. S., and Arnold, R. (1996). Measurement of ^{223}Ra and ^{224}Ra in Coastal Waters Using
1167 a Delayed Coincidence Counter. Journal of Geophysical Research, 101: 1321-1329.

1168 Moore, W. S. (1999). The subterranean estuary: a reaction zone of ground water and sea water.
1169 Marine Chemistry, 65: 111-125.

1170 Moore W.S. (2000) Determining coastal mixing rates using radium isotopes. Continental Shelf
1171 Research, 20: 1993-2007.

1172 Moore W. S. (2006) Radium isotopes as tracers of submarine groundwater discharge in Sicily.
1173 Continental Shelf Research, 26: 852-861.

1174 Moore, W. S. (2010) The effect of submarine groundwater discharge on the Ocean. Annual
1175 Review of Marine Science, 2: 59-88.

1176 Moore W.S., Beck M., Riedel T., Rutgers van der Loeff M., Dellwig O., Shaw T.J.,
1177 Schnetger B., Brumsack H.-J. (2011) Radium-based pore water fluxes of silica, alkalinity,
1178 manganese, DOC, and uranium: A decade of studies in the German Wadden Sea. Geochimica
1179 et Cosmochimica Acta, 75: 6535-6555.

1180 Moosdorf N., Böttcher M.E., Adyasari D., Erkul E., Gilfedder B.S., Greskowiak J., Jenner A-
1181 K., Kotwicki L., Massmann G., Müller-Petke M., Oehler T., Post V., Prien R., Scholten J.,
1182 Siemon B., Ehlert von Ahn C.M., Walther M., Waska H., Wunderlich T. and Mallast U. (2021)
1183 A State-Of-The-Art Perspective on the Characterization of Subterranean Estuaries at the
1184 Regional Scale. Frontiers. Earth Science, 9:601293: 1-26.

1185 Morse J. W., Berner R. A. (1995) What determines sedimentary C/S ratios? Geochimica et
1186 Cosmochimica, 59 (6): 1073-1077.

1187 Oberdorfer J. A., Charette M., Allen M., Martin J. B., Cable J. E. (2008) Hydrogeology and
1188 geochemistry of near-shore submarine groundwater discharge at Flamendo Bay, Ubatuba,
1189 Brazil. Estuarine Coastal and Shelf Science, 76:457-465.

1190 Oehler T., Tamborski J., Rahman S., Moosdorf N., Ahrens J., Mori C., Neuholz R., Schnetger
1191 B., and Beck M. DSi as a tracer for Submarine Grundwater Discharge. Frontiers in Marine
1192 Science, 6:563.

1193 Paytan A., Shellenbarger G.G., Street J.J., Davis K., Young M.B., Moore, W.S. (2006)
1194 Submarine groundwater discharge: An important source of new inorganic nitrogen to coral reef
1195 ecosystems. Limnology and Oceanography, 51(1): 343-348.

1196 Peltonen, K. (2002). Direct Groundwater Inflow to the Baltic Sea. TemaNord, Nordic Councils
1197 of Ministers, Copenhagen, Nether- lands, 79 pp.

1198 Piekarek-Jankowska, H. (1996). Hydrochemical effects of submarine groundwater discharge
1199 to the Puck Bay (Southern Baltic Sea, Poland). Geograhia Polonica 67.

1200 Povinec P. P., Bokuniewicz H., Burnett W. C., Cable J., Charette M., Comanducci J-F., Kontar
1201 E. A., Moore W. S., Oberdorfer J. A., de Oliveira J., Peterson R., Stieglitz T., Taniguchi M.
1202 (2008) Isotope tracing of submarine groundwater discharge offshore Ubatuba, Brazil: results
1203 of the IAEA-Unesco SGD project. Journal of Environmental Radioactivity, 99: 1596-1610.

1204 Purkamo L., von Ahn C.M.E., Jilbert T., Muniruzzaman M., Bange H. W., Jenner A-K.,
1205 Böttcher M.E., Virtasalo J. J. (2022) Impact of submarine groundwater discharge on
1206 biogeochemistry and microbial communities in pockmarks. Geochimica et Cosmochimica
1207 Acta, 334: 14-44.

1208 Purkl S., Eisenhauer A. (2004) Determination of radium isotopes and ^{222}Rn in a groundwater
1209 affected coastal area of the Baltic Sea and the underlying sub-sea floor aquifer. Marine
1210 Chemistry, 87: 137-149.

1211 Qian Q., Clark J. J., Voller V. R., and Stefan, H. G. (2009). Depth-dependent dispersion
1212 coefficient for modeling of vertical solute exchange in a lake bed under surface waves. Journal
1213 of Hydraulic Engineering, 135(3): 187-197.

1214 Racasa ED, Lennartz B, Toro M and Janssen M (2021) Submarine Groundwater Discharge
1215 From Non- Tidal Coastal Peatlands Along the Baltic Sea. Frontiers Earth Science. 9:665802.

1216 Rodellas V., Garcia-Orellana J., Garcia-Solsona E., Masque P., Dominguez J. A., Ballesteros
1217 B.J., Mejias M., Zarroca M. (2012) Quantifying groundwater discharge from different sources
1218 into a Mediterranean wetland by using ^{222}Rn and Ra isotopes. Journal of Hydrology, 466-
1219 467:11-22.

1220 Rodellas V., Garcia-Orellana J., Trezzi G., Masque P., Stieglitz T. C., Bokuniewicz H.,
1221 Cochran J. K., Berdalet E. (2017) Using the radium quartet to quantify submarine groundwater
1222 discharge and porewater exchange. Geochimica et Cosmochimica Acta, 196: 58-73.

1223 Sadat-Noori M., Maher D. T., Santos I. R. (2016) Groundwater Discharge as a Source of
1224 Dissolved Carbon and Greenhouse Gases in a Subtropical Estuary. Estuaries and Coasts,
1225 36:639-656.

1226 Santos I. R., Eyre B. D., Huettel M. (2012) The driving forces of porewater and groundwater
1227 flow in permeable coastal sediments: A review. Estuarine, Coastal and Shelf Science, 98:1-15.

1228 Santos I.R., Chen X., Lecher A.L., Sawyer A.H., Moosdorf N., Rodellas V., Tamborski J., Cho
1229 H-M., Dimova N., Sugimoto R., Bonaglia S., Li H., Hajati M-C., Li L. (2021) Submarine
1230 groundwater discharge impacts on coastal nutrient biogeochemistry. Nature Reviews Earth &
1231 Environment, 2: 307-323.

1232 Schlitzer, R. (2001) Ocean Data View. Available at: http://www.awi-bremerhaven.
1233 de/GEO/ODV.

1234 Seeberg-Elverfeldt J., Schlüter M., Feseker T., and Kölling M. (2005). Rhizon sampling of
1235 porewaters near the sediment-water interface of aquatic systems. Limnology Oceanography
1236 Methods, 3:361–371

1237 Slomp & Van Cappellen (2004) Nutrients inputs to the coastal ocean through submarine
1238 groundwater discharge: controls and potential impact. Journal of Hydrology, 295: 64-86.

1239 Soetaert K., & Meysman F. (2012). Reactive transport in aquatic ecosystems: Rapid model
1240 prototyping in the open source software R. Environmental Modelling & Software, 32: 49-60.

1241 Strady E., Pohl C., Yakushev E. V., Krüger S., and Hennings U. (2008). Pump-CTD-System
1242 for trace metal sampling with a high vertical resolution. A test in the Gotland Basin, Baltic Sea.
1243 Chemosphere 70, 1309–1319.

1244 Schlüter M., Sauter E., Andersen C. E., Dahlgaard H., and Dando P. R. (2004). Spatial
1245 Distribution and Budget for Submarine Groundwater Discharge in Eckernförde Bay (Western
1246 Baltic Sea). Limnology Oceanography, 49: 157–167.

1247 Sültenfuß J., Rhein M., Roether W. (2009) The Bremen mass spectrometric facility for the
1248 measurement of helium isotopes, neon and tritium in water. Isotopes in Environmental and
1249 Health Studies, 45 (2): 1-13.

1250 Szymczak E, Szmytkiewicz A. (2014) Sediment deposition in the Puck Lagoon (Southern
1251 Baltic Sea, Poland). BALTICA: 27:105-118.

1252 Szymczak-Zyla, M.; Lubecki, L. (2022). Biogenic and anthropogenic sources of sedimentary
1253 organic matter in marine coastal areas. A multi-proxy approach based on bulk and molecular
1254 markers. Marine Chemistry, 239:104069.

1255 Szymczycha B., Vogler S., Pempkowiak J. (2012). Nutrient fluxes via submarine groundwater
1256 discharge to the Bay of Puck, southern Baltic Sea. Science of the Total Environment, 438: 86-
1257 93.

1258 Szymczycha, B., Kroeger, K.D., Pempkowiak, J. (2016). Significance of groundwater
1259 discharge along the coast of Poland as a source of dissolved metals to the southern Baltic Sea.
1260 Marine Pollution Bulletin, 109: 151-162.

1261 Szymczycha B., Klostowska Z., Lengier M. Dzierzbicka-Glowacka L. (2020) Significance of
1262 nutrients fluxes via submarine groundwater discharge in the Bay of Puck, southern Baltic Sea.
1263 Oceanologia, 62: 117-125.

1264 Stosch, Heinz-G. (2022). Excel template to plot hydrochemical data into a Piper diagram (1.0).
1265 Zenodo. https://doi.org/10.5281/zenodo.5994293

1266 Tamborski J., Bejannin S., Garcia-Orellana J., Souhaut M., Charbonnier C., Anschutz P., Pujo-
1267 Pay M., Conan P., Crispi O., Monnin C., Stieglitz T., Rodellas V., Andriosa A., Claude C., van
1268 Beek P. (2018) A comparison between water circulation and terrestrially-driven dissolved
1269 silica fluxes to the Mediterranean Sea traced using radium isotopes. Geochmica et
1270 Cosmochimica Acta 238: 496-515.

1271 Tamisier M., Schmidt M., Vogt C., Kümmel S., Stryhanyuk H., Musat N., Richnow H-H. and
1272 Musat F. (2022) Iron corrosion by methanogenic archaea characterized by stable isotope effects
1273 and crust mineralogy. Environmental Microbiology, 24(2): 583-595.

1274 Taniguchi M., Burnett W. C., Cable J. E., Turner J. V. (2002) Investigation of submarine
1275 groundwater discharge. Hydrology Processes, 16: 2115-2129.

1276 Taniguchi, M., Dulaim, H., Burnett, K. M., Santos, I. R., Sugimoto, R., Stieglitz, T., Kim G.,
1277 Moosdorf N., Burnett W. (2019). Submarine Groundwater Discharge Updates on its
1278 Measurement Techniques, Geophysical Drivers, Magnitudes, and Effects. Frontiers
1279 Environmental Science, 7:141.

1280 Top Z., Brand L.E., Corbett R.D., Burnett W., Chanton J. (2001) Helium and radon as tracers
1281 of groundwater input into Florida Bay. Journal of coastal research, 17(4): 859-868.

1282 Van den Berg C. M. G. and Rogers H. (1987) Determination of alkalinities of estuarine waters
1283 by a two-point potentiometric titration. Marine chemistry, 20: 219-226.

1284 Virtasalo J.J., Schroeder J.F., Luoma S., Majaniemi J., Mursu J., and Scholten J. (2019).
1285 Submarine Groundwater Discharge Site in the First Salpausselkä Ice-Marginal Formation,
1286 South Finland. Solid Earth-EGU, 10: 405-432.

1287 Viventsowa E.E., Voronov A.N. (2003) Groundwater discharge to the Gulf of Finland (Baltic
1288 Sea): ecological aspects. Environmental Geology, 45: 221-225.

1289 von Ahn C.M.E., Scholten J.C., Malik C., Feldens P., Liu B., Dellwig O., Jenner A-K.
1290 Papenmeier S., Schmiedinger I., Zeller M.A. and Böttcher M.E. (2021) A multi-tracer study of
1291 freshwater sources for a temperate urbanized coastal bay (Southern Baltic Sea). Frontiers
1292 Environment Science, 9:642346.

1293 Winde V., Böttcher M.E., Escher P., Böning P., Beck M., Liebezeit G., Schneider B. (2014)
1294 Tidal and spatial variations of $DI^{13}C$ and aquatic chemistry in a temperate tidal basin during
1295 winter time. Journal of Marine Systems, 129: 394-402.

1296 Whiticar M.J., and Werner F. (1981). Pockmarks: Submarine Vents of Natural Gas or
1297 Freshwater Seeps? Geo-Marine Letters, 1:193-199.

1298 Whiticar M.J and Faber E. (1986) Methane oxidation in sediment and water column
1299 environments – Isotope evidence. Advance in Organic Geochemistry, 10: 759-768.

1300 Whiticar, M.J. (1999). Carbon and hydrogen isotope systematics of bacterial formation and
1301 oxidation of methane. Chemical Geology, 161: 291-314.

1302 Zektzer I. S., Ivanov V. A., Meskheteli A. V. (1973) The problem of direct groundwater
1303 discharge to the seas. Journal of Hydrology, 20: 1-36.

1304

1305

Chapter 4. Impact of submarine groundwater discharge on biogeochemistry and microbial communities in pockmarks

Available online at www.sciencedirect.com

ScienceDirect

Geochimica et Cosmochimica Acta 334 (2022) 14–44

Geochimica et Cosmochimica Acta

www.elsevier.com/locate/gca

Impact of submarine groundwater discharge on biogeochemistry and microbial communities in pockmarks

Lotta Purkamo [a,*], Cátia Milene Ehlert von Ahn [b], Tom Jilbert [c], Muhammad Muniruzzaman [a], Hermann W. Bange [d], Anna-Kathrina Jenner [b], Michael Ernst Böttcher [b,e,f], Joonas J. Virtasalo [g]

[a] *Water Management Solutions, Geological Survey of Finland (GTK), Vuorimiehentie 5, FI-02150 Espoo, Finland*
[b] *Geochemistry and Isotope Biogeochemistry Group, Leibniz Institute for Baltic Sea Research (IOW), Seestraße 15, D-18119 Warnemünde, Germany*
[c] *Environmental Geochemistry Group, Department of Geosciences and Geography, Gustaf Hällströmin katu 2, University of Helsinki, Finland*
[d] *Marine Biogeochemistry, GEOMAR Helmholtz Centre for Ocean Research Kiel, Düsternbrooker Weg 20, D-24105 Kiel, Germany*
[e] *Marine Geochemistry, University of Greifswald, D-17489 Greifswald, Friedrich-Ludwig-Jahn-Straße 17a, Germany*
[f] *Department of Maritime Systems, Interdisciplinary Faculty, University of Rostock, D-18059 Rostock, Albert-Einstein-Straße 21, Germany*
[g] *Marine Geology, Geological Survey of Finland (GTK), Vuorimiehentie 5, FI-02150 Espoo, Finland*

Received 7 December 2021; accepted in revised form 29 June 2022; available online 21 July 2022

Abstract

The impact of submarine groundwater discharge (SGD) on coastal sea biogeochemistry has been demonstrated in many recent studies. However, only a few studies have integrated biogeochemical and microbiological analyses, especially at sites with pockmarks of different degrees of groundwater influence. This study investigated biogeochemical processes and microbial community structure in sediment cores from three pockmarks in Hanko, Finland, in the northern Baltic Sea. Pockmark data were supplemented by groundwater and seawater measurements. Two active pockmarks showed SGD rates of 0.02 cm d^{-1} and 0.31 cm d^{-1}, respectively, based on porewater Cl^- profiles, while a third pockmark had no SGD influence. Reactive transport modelling (RTM) established that the porewater systems of these active pockmarks are dominated by advection, resulting in the focusing of biogeochemical reactions and the microbial community into a thin zone at the sediment surface. The advection further reduces the accumulation of organic matter in the surface sediments, resulting in the absence of a sulfate-methane transition zone (SMTZ) at these pockmarks. Furthermore, the RTM estimated low rates of consumption of SO_4^{2-}, and low rates of production of CH_4, NH_4^+, DIC at the active pockmarks. Archaeal communities in the active pockmarks were dominated by ammonia-oxidizing archaea of predominantly groundwater origin. In contrast, at the inactive pockmark, the lack of SGD has permitted rapid deposition of organic-rich mud. The porewater system in the inactive pockmark is dominated by diffusion, leading to orders of magnitude higher metabolite concentrations at depth compared to the active pockmarks. The biogeochemical environment in the inactive pockmark resembles typical organic-rich mud seafloor in the area, with sulphate reduction and methanogenesis dominating organic matter remineralization. Accordingly, methanogens dominate the archaeal community, whereas sulfate reducers dominate the bacterial community. RTM results suggest that sulfate-mediated anaerobic oxidation of methane (S-AOM) also occurs at this site. Although depth-integrated fluxes of SO_4^{2-}, CH_4, NH_4, DIC at the inactive pockmark are orders of magnitude higher compared to the active pockmarks, processes at the inactive pockmark represent internal recycling in the coastal sea. Fluxes observed at the active pockmarks, although comparatively small in magnitude, are partly influenced by external inputs to the sea through SGD. Hence, effluxes across the sediment–water interface at these sites partly represent direct external fluxes to the marine environment, in addition to

* Corresponding author.
E-mail address: lotta.purkamo@gtk.fi (L. Purkamo).

https://doi.org/10.1016/j.gca.2022.06.040

diagenetic recycling at the benthic interface. The study highlights that SGD can result in significant spatial heterogeneity of biogeochemical processes and microbial community structure in the coastal zone, and that the overall effects of SGD and associated solute fluxes at an SGD site are a function of the number of pockmarks, the rate of SGD, and the ratio of active to inactive pockmarks.

Keywords: Submarine groundwater discharge; Microbial community; Reactive transport modelling; Coastal sediment; Baltic Sea

1. INTRODUCTION

Coastal aquifers are groundwater systems connecting the exchange of water and substances between land and sea, and represent specific hydrogeological characteristics that lead to submarine groundwater discharge (SGD) into marine ecosystems. SGD is commonly defined as the flow of groundwater from coastal aquifers to the sea often with a fraction of admixed recirculated seawater, and it is increasingly recognized by the scientific community as an important pathway for material transport across the land-sea interface (e.g., Church, 1996; Moore, 2010; Knee and Paytan, 2011; Moosdorf et al., 2021). The global flux of fresh SGD to the Ocean has been estimated to an equivalent of about 1% of riverine discharge (Luijendijk et al., 2020; Zhou et al., 2019) and the fluxes of N and P through fresh SGD alone to the global ocean are estimated to reach up to 10% of those derived from river discharge (Cho et al., 2018). The N and P fluxes through total SGD (fresh + recir culated seawater), however, may exceed riverine inputs on the global scale (Cho et al., 2018), and can substantially impact coastal ecosystems and water quality on regional and local scales (Johannes, 1980; Bernard et al., 2014; Oehler et al., 2021; Santos et al., 2021; Böttcher et al., 2020). SGD may have implications on the production of dissolved and gaseous metabolites, such as NH_4^+, DIC, CH_4, and H_2S (e.g., Schlüter et al., 2004; Idczak et al., 2020; O'Reilly et al., 2021). One of the challenging ongoing questions is the representativity of groundwater observation wells for the freshwater component reaching the mixing zone with sea water (e.g., Beck et al., 2007; von Ahn et al., 2021), and another one, the role of diagenetic processes in marine sediments covering the aquifers for the modulation of the fluid composition finally being released to the coastal waters (e.g., Donis et al., 2017).

SGD can occur at sites close to the shoreline or further offshore, and the internal structure and uneven permeability distribution in aquifers can result in focusing of the groundwater discharge, leading to the development of local depressions (pockmarks) on the seafloor as observed by Jensen et al. (2002), Virtasalo et al. (2019) and Hoffmann et al. (2020). Physical and chemical gradients in pockmarks induced by SGD add to the heterogeneity of the seafloor because they provide distinct biogeochemical environments with specific active biological communities and microbial metabolisms compared with the surrounding seafloor (Kotwicki et al., 2014; Lecher and Mackey, 2018 and references within). For example, changes in salinity have been shown to affect the composition of seafloor microbial community structure and biogeochemical activity (Santoro et al., 2008; Lee et al., 2017; Klier et al., 2018; Donis et al., 2017; Adyasari et al. 2019). SGD can also affect the benthic community through a significant reduction in the meiofaunal density (Kotwicki et al. 2014).

In the Baltic Sea, the presence of pockmarks associated with SGD has been described in a several areas mostly restricted in the southern part: Eckernförde Bay in Germany (e.g., Whiticar and Werner, 1981; Schlüter et al., 2004; Hoffmann et al., 2020), the Laholm Bay in Sweden (Vanek and Lee, 1991), and Gulf of Gdansk in Poland (Idczak et al., 2020). A recent study in the northern Baltic Sea, in Hanko (Finland), documented a distinct SGD release for up to 20 pockmarks on the sandy shore platform slope at water depth between 4 and 17 m (Virtasalo et al., 2019). The geological structure of the silicate rock aquifer, and groundwater flow pathways to the pockmark area, were successfully modelled by Luoma et al. (2021). However, studies relating SGD and the microbial community composition remain scarce in the Baltic Sea (Idczak et al. 2020), as well as in coastal sea areas in general (Haverkamp et al. 2014; Adyasari et al. 2019, 2020).

The present study investigates the biogeochemical processes and microbial community structure in seafloor pockmarks at the Hanko SGD site in the northern Baltic Sea (Virtasalo et al., 2019; Fig. 1). The major aims were to quantify SGD and associated material fluxes from individual pockmarks to gain understanding about the impacts of salinity, SGD rate and organic matter availability on the microbial ecology and production of organic metabolites of ecosystem importance.

2. STUDY AREA

The Hanko SGD site is located in Lappohja, on the southeastern side of the Hanko cape on the south coast of Finland. The location is characterized by an arc-shaped sandy beach, a sandy shore platform that extends 100–250 m seaward sloping gently to ca. 4 m water depth, and a steep slope to ca. 17 m water depth within ca. 50 m distance (Fig. 1). The SGD takes place predominantly through pockmarks, which are up to 25 m wide and 2 m deep depressions on the edge and slope of the shore platform. Approximately twenty pockmarks have been identified at the site, but only three larger ones have been studied in detail: B, D and E (Fig. 1). Elevated ^{222}Rn activities 1 m above pockmarks B and D in May 2018 indicate fresh groundwater discharge rates of 0.40 – 1.22 cm d^{-1} (Virtasalo et al., 2019). Pockmark E was found to be covered by a soft mud layer, and did not show ^{222}Rn activity above background values, which indicates that it is cur-

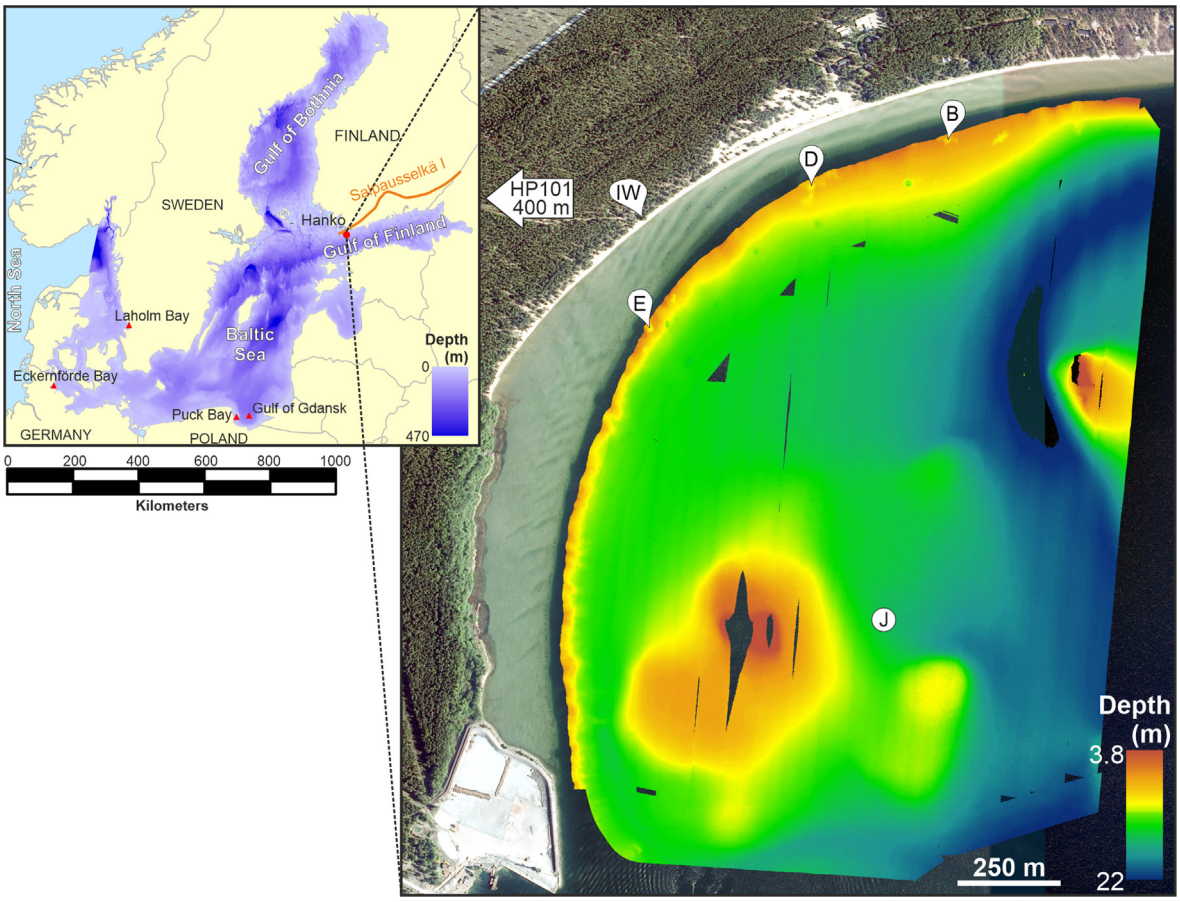

Fig. 1. Multibeam bathymetric image over the study area. The locations of pockmarks B, D and E, offshore seawater reference station J, and the obsolete water intake well (IW) are indicated. Groundwater observation well HP101 is located ca. 400 m west from the upper left side of the image. Red dot in the inset indicates the Hanko SGD site studied here. Red triangles indicate other documented SGD sites in the Baltic Sea region (Vanek and Lee, 1991; Schlüter et al., 2004; Szymczycha et al., 2012; Idczak et al., 2020). Aerial photograph: National Land Survey of Finland Topographic Database 04/2017. Baltic Sea bathymetric map: EMODnet Bathymetry DTM 2020. Modified from Virtasalo et al. (2019). (For interpretation of the references to colour in this figure legend, the reader is referred to the web version of this article.)

rently inactive. Comparable fresh groundwater discharge rates between 1.2 and 1.6 cm d^{-1} were estimated by a transient groundwater flow model for the same date (Luoma et al., 2021).

The shore platform and pockmarks are located in the distal part of ice-contact fan deposits that belong to the First Salpausselkä ice-marginal formation (Virtasalo et al., 2019), which is an extensive and narrow ridge that is composed of sand and gravel, with till beds particularly on its northwestern (ice-proximal) side (Fyfe, 1990; Kujansuu et al., 1993). The ridge was deposited in front of the Fennoscandian continental ice-sheet, in an ice-contact lake that was >100 m deep in Hanko (Fyfe, 1990), by 12,100 varve years before the year 2000, when the retreat of the ice margin came to a halt for ca. 217 years during the Younger Dryas climatic cooling (Sauramo, 1923; Saarnisto and Saarinen, 2001). The sediments rest on the Paleoproterozoic crystalline bedrock that mainly consists of quartz diorite and granodiorite (Kielosto et al., 1996). As a result of initially rapid glacio-isostatic land uplift (today 4 mm yr^{-1}; Kakkuri, 2012), the First Salpausselkä ridge has emerged above sea level. The top of the ice-marginal formation was exposed to waves and eventually to wind as it gradually rose from the sea, and the original ridge morphology became truncated and flattened from the top (Fyfe, 1990).

The Hanko area belongs to the humid continental climate type with cold, wet winters, and to the mixed-coniferous forest zone. The mean annual air temperature is 6.0 °C, with the mean minimum air temperature of 3.3 °C and the mean maximum air temperature of 8.8 °C. The mean annual precipitation is 634 mm during the period 1981–2010 (Pirinen et al., 2012). The annual mean sea surface salinity ranges between 4.5 and 6.5 and the annual mean sea surface temperature ranged between 4 and 9 °C during the period 1927–2011 (Merkouriadi and Leppäranta, 2014). The low salinity results from the high riverine runoff from the large Baltic Sea catchment area, and from the long distance to the narrow connection to the North Sea through the Danish straits. The sea is annually covered by ice on average 69 days (1891–2012), and the ice season usually ends in April (Merkouriadi and Leppäranta, 2014). The sea is essentially non-tidal, but irregular water level fluctuations of as much as 2.1 m take

place as a result of variations in wind and atmospheric pressure (Wolski et al., 2014).

3. MATERIALS & METHODS

3.1. Sample collection

Seawater, sediment and porewater samples were collected on 26–27th of September 2019 (Table 1) at pockmarks B, D and E onboard the R.V. Geomari of the Geological Survey of Finland (GTK).

Seawater samples were collected using a Limnos water sampler at three depths: surface water 2 m below sea surface, mid-water 6 m below sea surface, and bottom water 1 m above the pockmark bottom. In addition, a surface water sample was collected from the offshore reference station J. Samples for methane analyses were poured into triplicate 20 mL glass vials that were sealed with rubber caps avoiding air bubbles and preserved by adding 50 μL of $HgCl_2$(aq) (0.7 g $HgCl_2$ dissolved in 10 mL water) through the caps using a needle. Samples for dissolved ammonium (NH_4^+) were filtered through 0.45 μm cellulose acetate disposable membrane filters (Carl Roth, Karlsruhe, Germany) in pre-rinsed 20 mL PE vials and kept frozen until analysis. For microbiological analyses, bottom water samples above pockmarks and a control seawater sample from offshore station (two replicate samples from each, marked a and b) were poured into 500 mL acid-cleaned and autoclaved glass bottles (Schott), closed and stored in cool and dark until analysis.

Sediment cores from the pockmarks B and D with the penetration of 5 and 11 cm, respectively, were collected using a box corer (18 × 18 × 25 cm), because the stiff fine sand composition of the pockmark bottom prevented sufficient penetration by a Gemax corer. The box corer had an internal removable plastic liner, which captured the near-bottom water and sediment with an undisturbed surface. The water was carefully removed prior to the removal of the plastic liner in order to preserve the sediment core intact. Porewater salinity was measured using a hand refractometer (ATAGO) with a precision of 1 ‰. Samples for methane, multielement, Cl^-, NH_4^+, DIC and $\delta^{13}C_{DIC}$ analyses were extracted by pushing separate sets of rhizons (Rhizosphere Research Products, Wageningen, The Netherlands) to the side of the core at 1 cm intervals in a zig-zag pattern for the entire core length. For multielement and Cl^- analyses, 10 mL of porewater was transferred from the Rhizon syringes to 15 mL polyethylene tubes at each depth. No preservatives were added to the samples because the multielement and Cl^- analyses commenced within a few days. For methane analysis, 2 mL of porewater was collected in the rhizon syringe under vacuum. 8 mL of nitrogen gas (N_2, purity 5.0) was injected into the syringe via a 3-way tap, and the water–gas mixture was allowed to reach ambient temperature (25 °C), before being equilibrated by shaking for 5 mins. 5 mL of headspace gas was then extracted via a 3-way tap into a dry syringe and subsequently into a pre-evacuated 3 mL Exetainer® vial with double-wadded septum for storage (Labco ltd., Lampeter, Ceredigion, United Kingdom). Samples for DIC and $\delta^{13}C_{DIC}$ were filled without headspace into 3 mL Exetainer® tubes (Labco ltd., Lampeter, Ceredigion, United Kingdom), previously cleaned with 2% HNO_3 and pre-filled with 25 μL $HgCl_2$. All porewater samples were sealed and stored in cool and dark until analysis. For NH_4^+, 2 mL of porewater were transferred into pre-rinsed Eppendorf plastic vials and kept frozen until analysis. A sediment core from the pockmark E was collected using a Gemax twin-barrel short gravity corer (internal diameter 9 cm), which penetrated 54 cm into the soft mud, preserving the sediment surface intact. Porewater samples were collected by separate sets of Rhizons, pushed into the sediment and overlying water at 2 cm intervals through pre-drilled holes on the side of the core liner. Further processing of these samples was identical to those from the box cores described above.

After porewater extraction, the box-cores were sliced using a knife at 1 cm vertical intervals for multielement composition analysis and at 1.5–2.5 cm and 3.5–4.5 cm depths for microbial community analyses. Sedimentologic structure of the cores was inspected during the slicing. The Gemax core of pockmark E was cut in 1 cm sample slices using a rotary device. The twin of the pockmark E Gemax-core was split lengthwise for sedimentological inspection. Sediment samples were sealed and stored in cool and dark prior to analysis. Sediment subsamples (two replicates from each, marked a and b) for molecular microbiology community analysis were frozen in dry ice in the field and kept at −20 °C until further analysis.

Groundwater samples of the observation well HP101 and an obsolete water intake well near the shoreline were collected on 28th of September 2019 (Table 1). Prior to sampling, the waters were measured for temperature, electrical conductivity, pH, dissolved oxygen and redox potential using a WTW Multiline *P*4 meter (WTW GmbH, Weilheim, Germany). Observation well HP101 was sampled using a suction pump and allowing the pumped water to

Table 1
Sampling sites, and the types and dates of samples collected.

	Latitude N (WGS84)	Longitude E (WGS84)	Water samples	Porewater samples	Sediment samples
Pockmark B, active	59°53.771′	23°14.478′	26 September 2019	26 September 2019	26 September 2019
Pockmark D, active	59°53.700′	23°14.129′	26 September 2019	26 September 2019	26 September 2019
Pockmark E, inactive	59°53.501′	23°13.732′	27 September 2019	27 September 2019	27 September 2019
Offshore station J, seawater reference	59°53.164′	23°14.367′	27 September 2019		
Groundwater, observation well HP101	59°53.616′	23°12.674′	28 September 2019		
Groundwater, obsolete water intake well	59°53.660′	23°13.688′	28 September 2019		

run for several minutes until the measured parameters reached stable values in order to obtain fresh samples. Groundwater level was measured at 4.36 m, and the base of the pump filter was lowered to ca. 8.5 m below the top of the well steel surface casing. The obsolete water intake well was sampled by collecting water that was gently leaking from its wall. Samples for multielement and Cl^- analyses were collected in 100 mL polyethylene bottles with no preservatives added. Groundwater and water column samples for methane analyses were collected into triplicate 20 mL glass vials that were sealed with rubber caps avoiding air bubbles and preserved by adding 50 µL of $HgCl_2$(aq) solution through the caps using a needle. Samples for DIC and $\delta^{13}C_{DIC}$ were filled without headspace into 3 mL Exetainer® tubes (LABCO ltd., Lampeter, Ceredigion, United Kingdom), previously cleaned with HNO_3, washed, dried and filled with 25 µL saturated $HgCl_2$ solution. Samples for microbiological analyses were collected into duplicate 1000 mL acid-washed and autoclaved Schott bottles. All water samples were sealed and stored in cool and dark until analysis. For NH_4^+ analysis, 15 mL of porewater were transferred into pre-rinsed 20 mL polyethylene bottles and kept frozen until analysis.

3.2. Analytical methods

3.2.1. Analysis of water samples

Groundwater, seawater and porewater samples were analyzed at the accredited laboratory Eurofins Labtium Ltd in Espoo, Finland. Alkalinity (as HCO_3^-), electrical conductivity, pH and $KMnO_4$ consumption of the unfiltered and unpreserved groundwater samples were measured immediately upon arrival at the laboratory. Multielement composition of seawater, groundwater and porewater samples were analyzed using inductively coupled plasma optical emission and mass spectrometry (ICP-OES and ICP-MS). Ca, Fe, K, Li, Mg, Mn, Na, and S were analyzed by ICP-OES (method SFS-EN ISO 11885) using a Thermo Scientific iCAP 7600 Duo Spectrometer, whereas Ag, Al, As, B, Ba, Be, Bi, Cd, Co, Cr, Cu, I, Li, Mn, Mo, Ni, P, Pb, Rb, Sb, Se, Sr, Th, Tl, U, V, and Zn were analyzed by ICP-MS (SFS-EN ISO 17294-2) using a ThermoScientific iCAP Q spectrometer (Thermo Fisher Scientific Inc., Waltham, Massachusetts, USA). In all water samples, the measured S is considered to consist essentially of SO_4^{2-}. Chloride was analyzed with ion chromatography (SFS-EN ISO10304-1) using a Dionex ICS-2000 system (Dionex Co., Sunnyvale, California, USA). To check the quality of the analysis, blind duplicate samples were included in the analysis batch.

For methane analysis of porewaters, helium (He) was injected into the Exetainer® vials to achieve a pressure of 2.0 bar prior to autoinjection into the gas chromatograph (Agilent technologies 7890B custom, equipped with flame ionization detector (FID), electron capture detector (ECD) and thermal conductivity detector (TCD), and He used as carrier gas). Methane (CH_4) mole fractions were determined by FID. Simultaneous measurement of N_2 and O_2 + Ar (TCD) allowed a 100% sum to be calculated for estimation of normalized CH_4 mole fractions in the unpressurized headspace sample. Temporal drifts of CH_4 signals due to detector sensitivity were accounted for by analyzing standard gas samples at 12-sample intervals (Penttilä et al., 2013). Headspace CH_4 mole fractions were converted to total dissolved CH_4 concentrations in the original porewater sample (C_{tot} in equation (1)) using Henry's Law (Myllykangas et al., 2017). The first term on the right side represents the contribution to C_{tot} of dissolved gas released into the headspace during equilibration, while the second term represents the contribution from gas remaining in the dissolved phase:

$$C_{tot} = (X_{HS} \cdot P_{atm} \cdot V_{HS})/(R \cdot T \cdot V_{aq}) + F \cdot X_{HS} \cdot P_{atm} \quad (1)$$

where X_{HS} is the mole fraction of the CH_4 in the headspace in ppm, P_{atm} is the pressure in the headspace in atm (set to 1 atm), V_{HS} and V_{aq} are the headspace and water volume in mL respectively, R is the gas constant (0.08206 L atm/K mol^{-1}), T the temperature in Kelvin during equilibration (293 K), and F is the temperature/salinity-dependent equilibrium solubility coefficient of CH_4 in mol/L atm^{-1}, as detailed in Wiesenburg and Guinasso (1979).

Groundwater and seawater column samples were analyzed for methane at GEOMAR Helmholtz Centre for Ocean Research Kiel, Germany, within a few weeks after sampling. For the determination of CH_4 concentrations, the static-headspace equilibration method was applied, followed by gas chromatographic separation and detection with a FID as described in Bange et al. (2010). Calibration of the FID was performed with standard gas mixtures of 1806.10 – 3003.79 ppb CH_4 in synthetic air, which have been calibrated against NOAA-certified primary gas standards in the laboratory of the Max Planck Institute for Biogeochemistry in Jena, Germany. Final dissolved CH_4 concentrations (C_{tot}) were calculated according to equation (1).

$\delta^{13}C_{DIC}$ values were determined as described by Winde et al. (2014) by means of isotope-ratio-monitoring mass spectrometry (irmMS) using a Thermo Finnigan MAT253 gas mass spectrometer attached to a Thermo Electron Gas Bench II via a Thermo Electron Conflo IV split interface. Solutions were allowed to react for at least 18 h at room temperature before introduction into the mass spectrometer. International and in-house standards were used for calibration of measured isotope ratios towards the V-PDB scale. Throughout the paper, isotope ratios are expressed in mUr that equals the traditional ‰ in the ∂-notation (Brand and Coplen, 2012).

The concentrations of NH_4^+ were analyzed spectrophotometrically based on Berthelot reaction following Grasshoff et al. (2009) on a QuAAtro autoanalyzer system (Seal Analytical, Southampton, UK).

3.2.2. Analysis of sediment samples

Sediment samples were analyzed for ^{137}Cs activity content to constrain sedimentation rate in each core. The ^{137}Cs activity of untreated samples was measured for 60 min, using a BrightSpec bMCA-USB pulse height analyser coupled to a well-type NaI(Tl) detector at the GTK (Ojala et al., 2017). No corrections were applied for the results because the aim was only to detect relative ^{137}Cs

activity peaks. Due to the possible post-depositional downward transport of ^{137}Cs through bioturbation and diffusion (Holby and Evans, 1996; Klaminder et al., 2012), the depth of peak ^{137}Cs activity (rather than the initial increase) was assumed to represent the fallout from the 1986 Chernobyl nuclear disaster.

After the non-destructive ^{137}Cs analysis, sediment samples were freeze-dried, homogenized and halved, with one half analyzed for multielement composition and the other for grain size distribution at the laboratory (Eurofins Labtium ltd, Kuopio, Finland). The material for multielement analysis was sieved through a 63 μm mesh, and 0.2 g of the passed-through fraction was digested in a four-acid mixture of hydrofluoric acid, perchloric acid, hydrochloric acid and nitric acid (USGS Methods T01 and T20). After evaporation of the acids at 160 °C, the resulting gel was dissolved in 1 M HNO_3, and analyzed for element concentrations. Al, Ba, Be, Ca, Cr, Cu, Fe, K, Li, Mg, Mn, Mo, Na, Ni, P, Pb, S, Sc, Sr, Ti, V, Y, Zn, and Zr were analyzed by ICP-OES using Ta Thermo Scientific iCAP 6500 Duo spectrometer, whereas Ag, As, Bi, Cd, Ce, Co, Dy, Er, Eu, Gd, Hf, Ho, La, Lu, Nb, Nd, Pr, Rb, Sb, Sm, Sn, Ta, Tb, Th, Tl, Tm, U, and Yb were analyzed by ICP-MS using a Thermo Scientific iCAP Qc spectrometer (Thermo Fisher Scientific, Inc., Waltham, Massachusetts, USA). Because HF dissolves silicate minerals, the digestion is considered as "near-total digestion" (Hall et al., 1996). The commercial sediment reference materials QCGBMS304-6, QCMESS-4, QCNIST8704, CO153B and in-house standards were used for assessing measurement accuracy. Element concentrations for all reference materials measured with each sample batch fell well within ± 10% of the certified values. Mercury was measured separately for 0.2 g samples through thermal decomposition, amalgamation and atomic absorption spectrometry (US EPA Method 7473) using an Altec AMA254 Hg-analyzer (Altec, Prague, Czech Republic). Solid-phase contents of carbon and nitrogen in the samples were analyzed by thermal combustion elemental analysis (TCEA) using an Elementar vario MAX Cube elemental analyzer (Elementar Analysensysteme GmbH, Langensebold, Germany). Total inorganic carbon (TIC) was analyzed using a Thermo Finnigan MAT 253 gas mass spectrometer coupled with a Thermo Electron Gas Bench II via a Thermo Electron Conflo IV split interface (Schaller et al., 2022). Solid $CaCo_3$, Li_2CO_3, and liquid $NaHCO_3$ standards were used to scale the mass 44 measurements to TIC contents (Supplementary Material, Table S1).

The sediment grain size distribution was measured on freeze-dried samples by wet-sieving through 20 mm, 6.3 mm, 2 mm, 0.63 mm, 0.2 mm and 0.063 mm ISO 3110/1 test sieves. The samples were pretreated with excess H_2O_2 to remove organic matter prior to the analysis. The < 63 μm size fraction was further analyzed down to 0.6 μm using a Micromeritics Sedigraph III 5120 X-ray absorption sedimentation analyzer (Micromeritics Co., Norcross, Georgia, USA). The granulometric results were merged with sedimentation data in Sedigraph software. Median grain size was calculated according to the geometric Folk and Ward (1957) graphical measures, as implemented in the Rysgran 2.1.0 package in the R 4.0.2 software environment. The clay fraction is defined here as grain sizes smaller than 2 μm, whereas mud is composed of the clay and silt (<63 μm) fractions, and sand is defined by grain sizes between 63 μm to 2 mm (Blott and Pye, 2012).

3.2.3. Biomass collection and DNA extraction

Biomass was collected from water samples by filtering in a laminar flow hood. Filters were frozen to −20 °C prior to DNA extraction. Groundwater samples (1500 mL) were filtered through 0.1 μm PES filters (Corning Inc., Corning, NY, USA), and seawater samples (500 mL) were filtered first through 0.2 μm CA filters (Corning Inc., Corning, NY, USA) and flow through from parallel samples was pooled and further filtered through 0.1 μm PES filter. Filter paper was cut out of the funnel and placed into a sterile 50 mL plastic tube and frozen prior to further processing. DNA was extracted with DNeasy PowerWater kit (Qiagen, Hilden, Germany) according to the manufacturer's protocol, starting from step 5. DNA was eluted with 100 μL of EB buffer provided by the kit.

DNA extraction for sediment samples was done directly using DNEasy Powersoil Pro Kit (Qiagen, Hilden, Germany). Sediment samples were thawed, and 250 mg of each sample was weighed to bead tubes provided by the extraction kit. DNA was extracted according to the kit manufacturer's instructions and elution was done with 100 μL of the kit's C6 solution.

DNA concentrations of the samples were measured with Qubit 2.0 Fluorometer (Invitrogen by Life Technologies, Carlsbad, CA, USA) using Qubit dsDNA HS reagent and Buffer solutions according to the manufacturer's protocol.

3.2.4. Sequencing and data analysis

Sequencing of the 16S rRNA gene region V3-V4 of bacteria was done using f357F- 5′-TACGGGAGGCAGCAG-3′ and 800R- 5′-CCAGGGTATCTAATCC-3′ primers (Turner et al., 1999; Kisand et al., 2002, respectively) and archaeal 16S rRNA gene region V3-V6 was sequenced with 340F- 5′-CCCTAYGGGGYGCASCAG-3′ and 1000R5′-GAGARGWRGTGCATGGCC-3′ primers (Gantner et al., 2011) in Eurofins Genomics (Konstanz, Germany). Sequencing was performed with Illumina MiSeq 300x300 paired-end read protocol. Sequences were processed according to MOTHUR's (v. 1.43.0) MiSeq SOP with a phylotype-based approach, omitting the mock community analysis and using default settings if not otherwise stated (Kozich et al., 2013). Bacterial sequences were quality checked and screened with make.contigs command following screen.seqs using the following parameters: maxambig = 0, maxlength = 475, and archaeal sequences maxambig = 4, maxlength = 468. *Escherichia coli* J01859.1 (for bacteria) or *Methanobacterium paludis* NC_015574.1 (for archaea) 16S rRNA gene sequence was used to reveal the exact start and end position of the sequences in the alignment. Using those as parameters for the region of interest, pcr.seqs command was used to shrink the reference alignment. One difference per 100 bases was allowed in preclustering, thus diffs = 4 for both bacteria and archaea (with average sequence length of 415 and

432, respectively) were chosen. Chimeric sequences were identified and removed, and sequences classified using Silva_nr v.138 taxonomy. Sequences classified as Chloroplasts, Mitochondria, unknown and Archaea or Bacteria (from bacterial or archaeal sequencing data, respectively) were removed from the dataset using remove.lineage command. Sequences were assigned to OTUs using phylotype method as described in MOTHUR's MiSeq SOP. Data was standardized according to the lowest number of sequences in the samples (bacteria: 44310, archaea: 2631). Rarefaction, and different diversity, coverage and richness estimates were calculated using parameters calc = nseqs-coverage-sobs-shannon-npshannon-invsimpson-chao-ace in MOTHUR. A biom.file for both archaeal and bacterial communities was constructed and used in RStudio v. 3.6.3 for visualization of the data using e.g., biomformat, ggplot2, ggpubr and ggsci packages. Statistical analyses for microbial communities and selected environmental variables were done in PAST 3.04 (Hammer et al., 2001). Principal coordinates analysis from Hellinger-transformed relative abundance data of archaeal and bacterial communities was done using Bray-Curtis and Jaccard similarity indices.

3.2.5. Quantification of ribosomal RNA gene copy numbers of bacteria and archaea and microbes potentially involved in N and C cycling and sulfate reduction

The enumeration of the 16S rRNA gene copies was done with quantitative PCR and results were used as a proxy for the total number of bacteria or archaea in samples. Quantification of nitrate reduction potential of the microbes was made using *narG* and ammonia oxidation with *amo*A marker genes. The methanotrophic community was quantified using qPCR assay based on *pmo*A gene and the potentially methanogenic community was quantified using *mcr*A gene. Putative sulfate reducers were quantified using *dsrB* marker gene. BioLine SensiFAST SYBR® No-ROX 5X mastermix (Meridian Life Science, Inc., Memphis, TN, USA) was used for mastermix preparation with 1 ul of template DNA in a single reaction. All samples were analyzed in triplicate reactions. Analyses were performed in LightCycler® 480 Instrument (Roche Diagnostics Corp., Indianapolis, IN, USA). A melting curve analysis was done after the amplification protocol to reveal any unspecific amplification. Melting curve analysis consisted of 95 °C for 10 s, 65 °C for 1 min, ramping to 95 °C with 0,11 °C/s and 5 acquisitions per °C. The program ended with cooling the reactions to 40 °C. Details for each qPCR assay are shown in Supplementary Material (Table S2).

3.3. Reactive transport modeling

The measurements performed at different pockmarks are quantitatively interpreted by means of multicomponent reactive transport modeling and by adopting a transient diagenetic model described in earlier studies (e.g., Reed et al., 2011a,b; Rooze et al., 2016; Egger et al., 2016a). This allows obtaining a better understanding of the diagenetic and burial processes from a mechanistic perspective as well as investigating the impact of individual mechanisms on the overall behavior within a coupled system. The model includes the cycling of a wide range of dissolved solutes and particulate sediment species by explicitly taking into account the advective transport both in the aqueous and solid phases, molecular diffusion in the pore water, bioturbation in the solid phase, and a suite of inter- and intra-phase biogeochemical reactions (e.g., Wang and Van Cappellen, 1996; Boudreau 1997). In all pockmarks, the modeling is performed along a 1-D sediment column, which is representative of the upper sediment layer below the seafloor.

3.3.1. Equations for multicomponent transport in sediment and porewater

The governing mass balance equations describing multicomponent reactive transport of solutes and solids in sediments can be described as,

$$\phi \frac{\partial C_{w,i}}{\partial t} = -\phi u \frac{\partial C_{w,i}}{\partial x} + \phi (D_i + D_b) \frac{\partial^2 C_{w,i}}{\partial x^2} + \sum_{r=1}^{N_r} \upsilon_{ir} R_r \quad (2)$$

$$(1-\phi) \frac{\partial C_{s,j}}{\partial t} = -(1-\phi) v \frac{\partial C_{s,j}}{\partial x} + (1-\phi) D_b \frac{\partial^2 C_{s,j}}{\partial x^2} + \sum_{r=1}^{N_r} \upsilon_{jr} R_r \quad (3)$$

where $C_{w,i}$ [ML^{-3}] and $C_{s,j}$ [ML^{-3}] represent the concentrations of i-th aqueous and j-th solid species, respectively, ϕ [-] is the porosity, D_i [L^2T^{-1}] denotes the diffusion/dispersion coefficient of the dissolved species, i in porewater, D_b [L^2T^{-1}] is the bioturbation coefficient (also known as biodiffusion coefficient) representing random small-scale displacements of solute and solid species by benthic fauna (e.g., Boudreau, 1987), x [L] is the distance from the sediment–water interface, and t [T] is the time. u [LT^{-1}] and v [LT^{-1}] represent the advective velocities of the aqueous and solid phase constituents, respectively, whereas the last quantities in the above equations denote the net reactive source/sink term with υ_{ir}[-],υ_{jr}[-] being the stoichiometric coefficient for species i and j, respectively, for the r-th reaction and R_r [$ML^{-3}T^{-1}$] being the reaction rate for r-th reaction.

In the simulations presented in this study, the porosity was considered to be depth-dependent to take into account the effects of sediment compaction (e.g., Meysman et al., 2005). In fact, the spatially-variable pattern of porosity was clearly evident in the observed profiles for all three pockmarks. We adopt the following function, which also has been utilized in numerous earlier studies focusing on submarine systems (e.g., Reed et al., 2011a,b; Egger et al., 2016a; Rooze et al., 2016):

$$\phi(x) = \phi_\infty + (\phi_0 - \phi_\infty) \exp\left(-\frac{x}{\zeta}\right) \quad (4)$$

where ϕ_0[-] is the porosity at the sediment–water interface (SWI), ϕ_∞[-] is the asymptotic porosity value at deeper depths in the sediment, and ζ [L] denotes the porosity attenuation factor or the so-called e-folding distance. The value of ζ was obtained by fitting Eq. (4) against the porosity profiles measured at different pockmarks as illustrated in the Supplementary Material (Fig. S5).

Due to a spatially variable description of porosity, both the advective velocity and the effective diffusion coefficient

also become depth-dependent quantities in the reactive transport model. In the simulations presented in the following sections, the diffusion coefficients for the dissolved and particulate chemical species were parameterized according the following relationships:

$$D_i = \frac{D_{aq,i}}{\tau} = \frac{D_{aq,i}}{1 - 2\ln(\phi)} \quad (5)$$

$$D_b(x) = D_{b0} \exp\left(-\frac{x}{\xi}\right) \quad (6)$$

where Eq. (5) represents a correction of the aqueous diffusion coefficient $D_{aq,i}$ [L^2T^{-1}] for the tortuosity (τ [-]) in porous media (Boudreau, 1996), and Eq. (6) describes the variation of the bioturbation coefficient (also termed as biodiffusion coefficient), D_b along the sediment depth with D_{b0} [L^2T^{-1}] and ξ [L] being the biodiffusion coefficient at the sediment–water interface and the mixed layer depth, respectively. The latter implies that the intensity of biogenic mixing follows an exponential decrease with depth due to the decline in faunal density with increasing depth into the sediment (e.g., Rooze et al., 2016). For simplicity, the diffusive fluxes of the dissolved/solid species are modeled with a simple Fickian formulation although the charge-induced Coulombic interactions can also exert additional controls on the transport of dissolved charged solutes (e.g., Boudreau et al., 2004; Giambalvo et al., 2002; Rolle et al., 2013; Muniruzzaman et al., 2014; Muniruzzaman and Rolle, 2015, 2017).

Furthermore, the advective velocity in the aqueous phase was estimated by optimizing the chloride concentration profiles against the analytical solution of the advection–dispersion equation under the steady-state condition. The optimization was performed as a non-linear least square method and the detailed implementation scheme is reported in the Supplementary Material. The advective velocity obtained for the different pockmarks was directly fed into the reactive transport simulations as parameter u [LT^{-1}] in Eq. (3). In contrast, the advection of the solid phase components were determined by constraining the reactive transport numerical model against the measured sediment profiles. The ^{137}Cs activity measurements provide an initial basis for the sedimentation rate for pockmark E, but further adjustment was needed in the reactive transport model to explain the observed profiles. The detailed list of the input parameters describing the flow and transport processes are reported in the Supplementary Material (Table S4, S5, S6).

3.3.2. Chemical reaction network

The transported species in the water and solid phases are tightly coupled via a wide range of biogeochemical reactions. The reaction network considered in the reactive transport simulations includes a total of 32 chemical reactions, which can be categorized into two main groups: a) primary redox reactions, and b) other biogeochemical reactions. Table 2 lists the complete set of chemical reactions incorporated in the model, and their stoichiometry as well as rate expressions were compiled from Reed et al. (2011a,b), Rooze et al. (2016) and Egger et al. (2016a). The primary redox reactions mainly include the degradation of organic matter (OM) through a variety of respiratory reactions involving O_2, NO_3^-, MnO_2, $Fe(OH)_3$ and SO_4^{2-} as terminal electron acceptors. The successive consumption of these oxidants during organic matter decomposition is typically described by Monod kinetics, which ensures the preferential use of the oxidant with the highest free energy yield followed by a sequential use of the oxidant with the next highest energy yield (Froelich et al., 1979; Berg et al., 2003; Wang and van Cappellen, 1996; Boudreau, 1996). Once these electron acceptors are exhausted, organic matter decomposition occurs via methanogenesis, where OM acts as both the electron acceptor and donor. For sulfate reduction and methanogenesis reactions, an attenuation factor, (Table S7, Supplementary Material), is considered to reproduce the slower progress of organic matter degradation during these mechanisms compared to the reactions driven by other oxidants (e.g. Moodley et al., 2005; Reed et al., 2011a, b).

The effects of distinct crystallinity and reactivity of organic matter, Mn oxides and Fe oxides were considered by assuming three different pools, representing highly reactive (α), less reactive (β) and nonreactive (γ) phases (e.g., Jørgensen, 1978; Westrich and Berner, 1984; Middelburg, 1989). In all simulations, a C:N:P ratio of 106:16:1 was used for all three organic matter pools for simplicity and it was sufficient to consistently explain the measured profiles. For Fe and Mn oxides, only the α phase was assumed to participate in OM degradation, whereas the β phase is mainly involved in the oxidation of Fe^{2+}, sulfides and methane (Table 2). In fact, this conceptualization of different reactivity for these solid species was particularly needed in order to allow the persistence of iron oxy(hydroxi)des and MnO_2 phases at deeper sediment depths (i.e., coexistence of these electron acceptors with OM) as observed in the pockmark sediment profiles.

The secondary biogeochemical reactions as listed in Table 2 describe various mineral precipitation/dissolution reactions, reoxidation of reduced metabolites, and a suite of homogeneous and heterogeneous chemical reactions. In particular, the oxidation of CH_4 is an important mechanism in this system and will be discussed in the following sections. All these secondary chemical reactions (R8 - *R*32) were simulated by considering a bimolecular rate law with the exception of a few cases where the reaction was assumed to follow a first order law (R21, R25-R28). The rate expressions for all these reactions along with the kinetic parameters used in the model are summarized in the Supplementary Material (Table S7, S8).

3.3.3. Numerical Implementation

The resulting system of equations describing the coupling between multicomponent transport of aqueous/solid species and chemical reactions was numerically solved with a finite element method (FEM) utilizing the finite element solver COMSOL Multiphysics (e.g., Rolle et al. 2018). Based on the chemical reaction network described in Table 2, we considered a total of 27 chemical species (Table S5, Supplementary Material) that are sufficient to illustrate the complete biogeochemistry of our system. In

Table 2
Chemical reaction pathways and stoichiometries implemented in the diagenetic model.

Primary redox reactions	
$OM^{\alpha,\beta} + a\ O_2 \rightarrow NH_4^+ + c\ H_3PO_4 + a\ H_2O$	R1
$OM^{\alpha,\beta} + \frac{4a}{5}\ NO_3^- + \frac{4a}{5}\ H^+ \rightarrow a\ CO_2 + b\ NH_4^+ + c\ H_3PO_4 + \frac{2a}{5}\ N_2 + \frac{7a}{5}\ H_2O$	R2
$OM^{\alpha,\beta} + 2\ a\ MnO_2^{\alpha} + 4\ a\ H^+ \rightarrow a\ CO_2 + b\ NH_4^+ + c\ H_3PO_4 + 2\ a\ Mn^{2+} + 3\ a\ H_2O$	R3
$OM^{\alpha,\beta} + 4\ a\ Fe(OH)_3^{\alpha} + 4\ a\chi^{\alpha}\ Fe_{ox}P + 12\ a\ H^+ \rightarrow a\ CO_2 + b\ NH_4^+\ (c + 4\ a\ \chi^{\alpha})\ H_3PO_4 + 4\ a\ Fe^{2+} + 13\ a\ H_2O$	R4
$OM^{\alpha,\beta} + \frac{a}{2}\ SO_4^{2-} + a\ H^+ \rightarrow a\ CO_2 + b\ NH_4^+ + c\ H_3PO_4 + \frac{a}{2}\ H_2S + a\ H_2O$	R5
$OM^{\alpha,\beta} \rightarrow \frac{a}{2}\ CO_2 + b\ NH_4^+ + c\ H_3PO_4 + \frac{a}{2}\ CH_4$	R6
$CO_2 + 4\ H_2 \rightarrow CH_4 + 2\ H_2O$	R7
Secondary redox and other reactions	
$2\ O_2 + NH_4^+ + 2\ HCO_3^- \rightarrow NO_3^- + 2\ CO_2 + 3\ H_2O$	R8
$O_2 + 2\ Mn^{2+} + 4\ HCO_3^- \rightarrow 2\ MnO_2^{\alpha} + 4\ CO_2 + 2\ H_2O$	R9
$O_2 + 4\ Fe^{2+} + 8\ HCO_3^- + 2\ H_2O + 4\ \chi^{\alpha}H_2PO_4^- \rightarrow 4\ Fe(OH)_3^{\alpha} + 4\ \chi^{\alpha}Fe_{ox}P + 8\ CO_2$	R10
$2\ O_2 + FeS \rightarrow SO_4^{2-} + Fe^{2+}$	R11
$7\ O_2 + 2\ Fe_S2 + 2\ H_2O \rightarrow 4\ SO_4^{2-} + 2\ Fe^{2+} + H^+$	R12
$2\ O_2 + H_2S + 2\ HCO_3^- \rightarrow SO_4^{2-} + 2\ CO_2 + 2\ H_2O$	R13
$2\ O_2 + CH_4 \rightarrow CO_2 + 2\ H_2O$	R14
$MnO_2^{\alpha,\beta} + 2\ Fe^{2+} + 2\ \chi^{\alpha}\ H_2PO_4^- + 2\ H_2O + 2\ HCO_3^- \rightarrow 2\ Fe(OH)_3^{\alpha} + 2\ \chi^{\alpha}\ Fe_{ox}P + Mn^{2+} + 2\ CO_2$	R15
$MnO_2^{\alpha,\beta} + H_2S + 2CO_2 \rightarrow Mn^{2+} + S_0 + 2\ HCO_3^-$	R16
$2\ Fe(OH)3^{\alpha} + 2\ \chi^{\alpha}Fe_{ox}P + H_2S + 4\ CO_2 \rightarrow 2\ Fe^{2+} + 2\ \chi^{\alpha}H_2PO_4^- + S_0 + 4\ HCO_3^- + 2\ H_2O$	R17
$2\ Fe(OH)3^{\beta} + 2\ \chi^{\beta}\ Fe_{ox}P + H_2S + 4\ CO_2 \rightarrow 2\ Fe^{2+} + 2\ \chi^{\beta}\ H_2PO_4^- + S_0 + 4\ HCO_3^- + 2\ H_2O$	R18
$Fe^{2+} + 2\ H_2S \rightarrow FeS + 2H^+$	R19
$FeS + H_2S \rightarrow FeS_2 + H_2$	R20
$4\ S_0 + 4\ H_2O \rightarrow 3\ H_2S + SO_4^{2-} + 2H^+$	R21
$FeS + S_0 \rightarrow FeS_2$	R22
$SO_4^{2-} + CH_4 + CO_2 \rightarrow 2\ HCO_3^- + H_2S$	R23
$CH_4 + 8\ Fe(OH)_3^{\alpha,\beta} + 8\ \chi^{\alpha,\beta}\ Fe_{ox}P + 15H^+ \rightarrow HCO_3^- + 8\ Fe^{2+} + 8\ \chi^{\alpha,\beta}\ H_2PO_4^- + 21\ H_2O$	R24
$Fe(OH)_3^{\alpha} + (\chi^{\alpha} - \chi^{\beta})Fe_{ox}P \rightarrow Fe(OH)_3^{\beta} + (\chi^{\alpha} - \chi^{\beta})H_2PO_4^-$	R25
$Fe(OH)3^{\beta} + (\chi^{\beta} - \chi^{\gamma})Fe_{ox}P \rightarrow Fe(OH)_3^{\gamma} + (\chi^{\beta} - \chi^{\gamma})H_2PO_4^-$	R26
$MnO_2^{\alpha} \rightarrow MnO_2^{\beta}$	R27
$MnO_2^{\beta} \rightarrow MnO_2^{\gamma}$	R28
$3\ Fe^{2+} + 2\ HPO_4^{2-} \rightarrow Fe_3(PO_4)_2 + 2\ H^+$	R29
$Fe^{2+} + CO_3^{2-} \rightarrow FeCO_3$	R30
$FeCO_3 + H_2S \rightarrow FeS + HCO_3^- + H^+$	R31
$Fe_3(PO_4)_2 + 3\ H_2S \rightarrow 3\ FeS + 2\ HPO_4^{2-} + 4\ H^+$	R32

all pockmarks, the simulation was performed for a period of 50 years. The pockmarks were modeled as 1-D reactive transport systems and any possible multidimensional effect was ignored for the sake of brevity. For the dissolved species, a fixed concentration boundary with the bottom water composition was applied at the sediment–water interface, whereas a flux boundary was employed for the solid components. In contrast, a zero gradient and a free flux boundary conditions were applied for the dissolved and particulate chemical species, respectively, at the bottom of the domain. In this step, the model depth was set long enough to avoid any potential interference of the lower boundary condition with the model results in the upper sediments. The simulations were performed as a forward modeling fashion without attempting any inverse modeling scheme. Pockmark B and D were simulated by considering a sediment groundwater discharge rate in the upward direction, whereas pockmark E was considered to be fully diffusion controlled. Such an assumption is justified because pockmark E shows rather constant Cl^- concentration profiles, resembling a negligible impact of groundwater discharge. A summary of the input parameters used in the simulation of different pockmarks are provided in the Supplementary Material (Table S4, S6, S8).

3.4. Research data

Geochemical and grain-size data of the sediment samples, and geochemical data of all the water samples are available in the PANGAEA repository (Virtasalo, 2022; Virtasalo et al., 2022). DNA sequences and related metadata are available at European Nucleotide Archive under study PRJEB44075, where archaeal sequence IDs are ERS6176640-ERS6176659 and bacterial sequence IDs ERS6177874-ERS6177845.

4. RESULTS

4.1. Pockmark sediment composition

The box core sediment samples collected from pockmarks B and D are composed of structureless, poorly sorted fine sand with very low carbon content (range 0.17–0.69 mmol g^{-1} TOC; Fig. 2). The sediment surface in both cores is covered by a thin layer of brownish organic-rich fluffy material (Supplementary Material, Fig. S1). In contrast, the gravity core from pockmark E is composed of very poorly sorted dark-grey clay that is rich in carbon (range 2.0–5.5 mmol g^{-1} TOC; Fig. 2). The clay

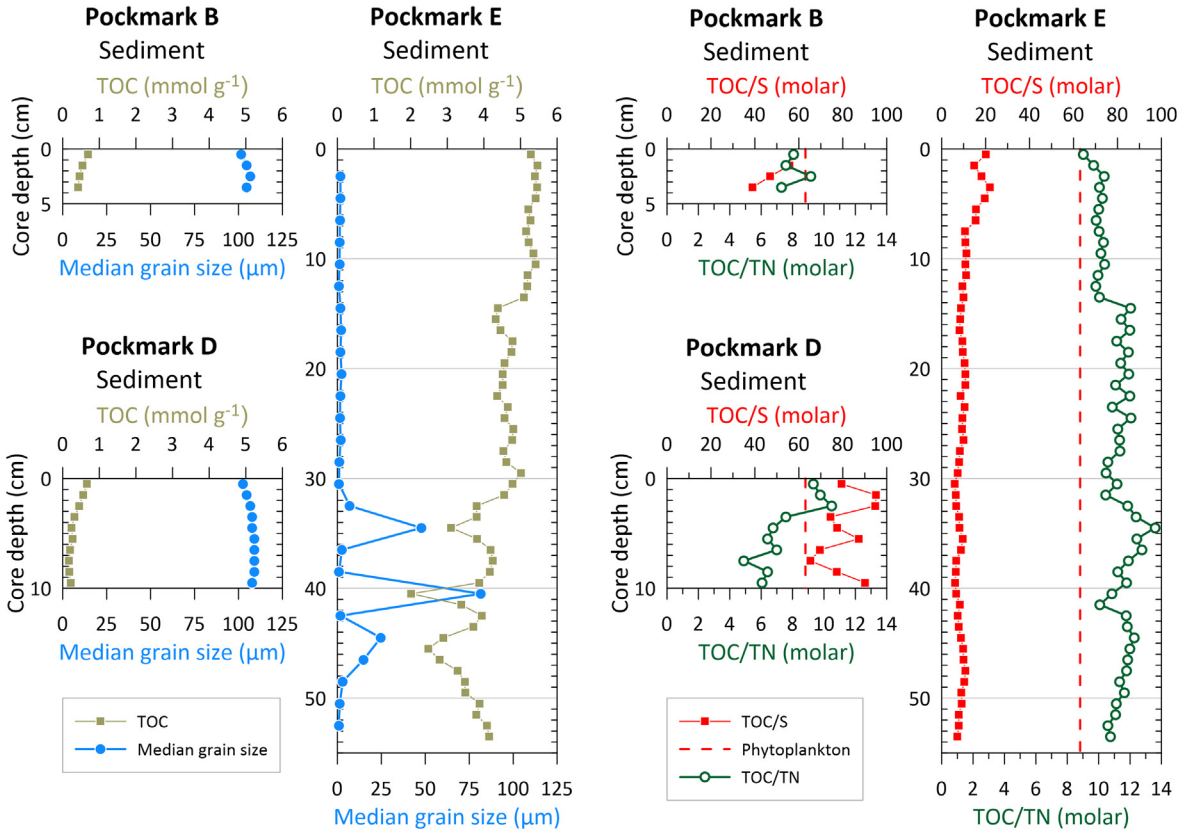

Fig. 2. Vertical distributions of TOC, median grain size, the TOC/S, and the TOC/TN ratio in sediment cores from pockmarks B, D and E. Red vertical dashed line indicates the mean TOC/S ratio of 63 of the Baltic Sea phytoplankton (Kumblad and Bradshaw, 2008). (For interpretation of the references to colour in this figure legend, the reader is referred to the web version of this article.)

is structureless with abundant plant fragments and a few thin interbeds of silt (Supplementary Material, Fig. S1). The sediment surface was dark grey at the time of coring, indicative of reducing conditions at the sediment–water interface.

The ^{137}Cs activity peak of 69.2 Bq kg^{-1} at the depth of 47–48 cm in the core from pockmark E is assigned the year 1986 (Supplementary Material, Fig. S2). Linear sedimentation rate in that core above this age-depth control point is calculated at 1.44 cm yr^{-1}. The interpreted depth of the year 1986 is supported by sediment Hg content, which shows a strong downward increase in the lower part of the core (Supplementary Material, Fig. S2). According to previous studies, Hg contents in the western Gulf of Finland are highest in sediment layers deposited in the early 1970 s and decline upwards (Vallius, 2014). Therefore, the pockmark E core must be younger than 1970 because the downward Hg increase likely continues below the core base. The ^{137}Cs contents in the cores from pockmarks B and D are at the background levels (<10 Bq kg^{-1}) except for the topmost 2–3 cm layers. The ^{137}Cs activity peak of 1986 seems not to be recorded in these cores.

The molar TOC/TN ratios are low in the cores from pockmarks B and D and range between 4.9 and 10.5, whereas the TOC/TN ratios are higher in the pockmark E core (range 9.0–13.6; Fig. 2). The TOC/S ratios are high in the pockmark B and D cores and range between 39 and 95, which is close to and above the mean ratio of 63 of the Baltic Sea phytoplankton (Kumblad and Bradshaw, 2008). The TOC/S ratios are lower in the pockmark E core (range 5.9–22) and show a downward decreasing trend.

4.2. Pockmark porewater, seawater and groundwater composition

Porewater Cl^- concentrations in the core from pockmark E are close to 100 mmol/L (Fig. 3), which is a typical value for the Baltic Sea water (Table 3). In contrast, porewater Cl^- concentrations are very low in pockmark D (range 0.21–7.62 mmol/L; measured salinity 0), indicating a strong fresh groundwater influence up to the sediment surface (groundwater Cl^- concentration 0.07–1.34 mmol/L). Pockmark B has intermediate porewater Cl^- concentrations that approach seawater values at the sediment surface (range 45.1–84.6 mmol/L; salinity range 2–6). Porewater SO_4^{2-} concentrations are low in pockmark D (range 0.08–0.41 mmol/L) and in the lower part of the core from pockmark E (Fig. 3). Porewater SO_4^{2-} concentrations increase strongly toward the core top in pockmark E, and in pockmark B, exceeding 3.5 mmol/L. Overall, SO_4^{2-} concentration profiles are similar to Cl^- concentration profiles in

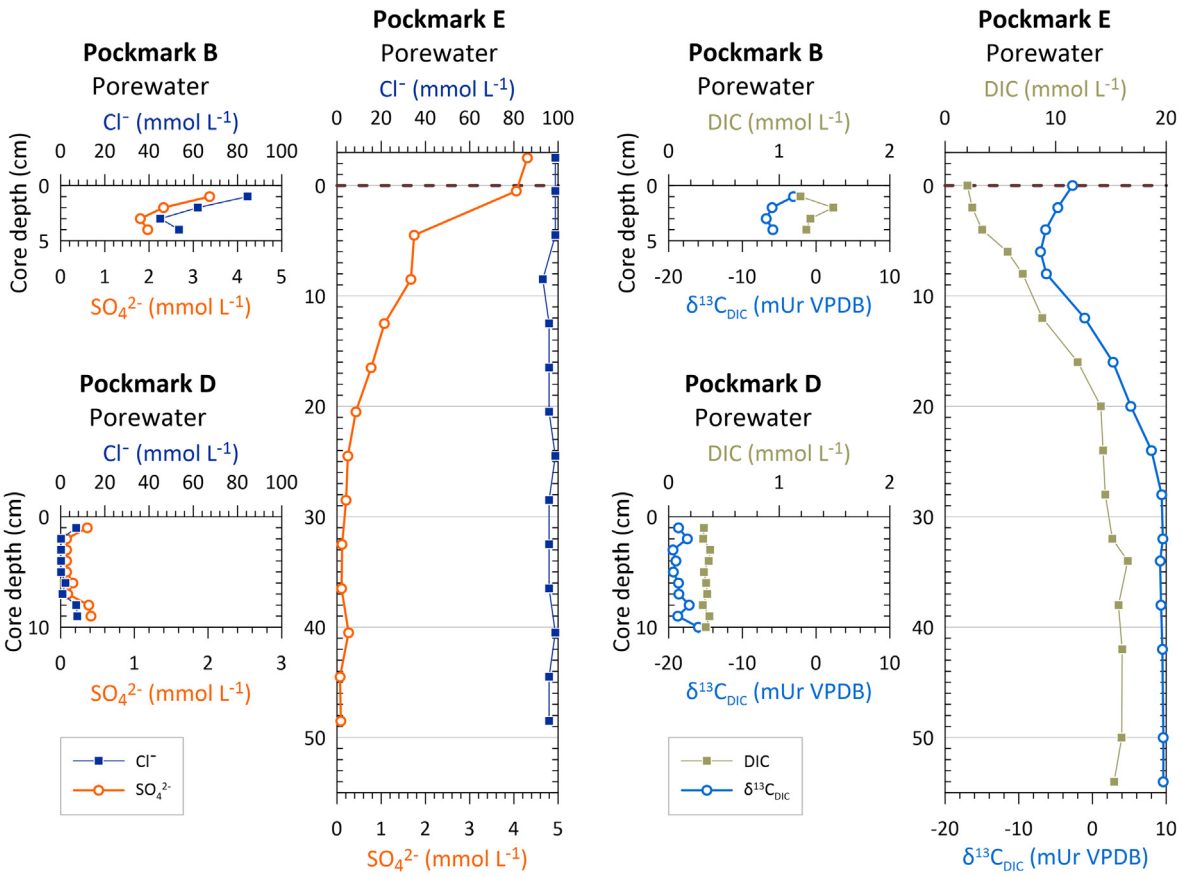

Fig. 3. Vertical distributions of Cl^-, SO_4^{2-}, DIC and $\delta^{13}C_{DIC}$ in sediment core porewater from pockmarks B, D and E. Dashed horizontal line indicates the sediment–water interface in the pockmark E core.

Table 3
Concentrations in the water column at the pockmark locations, the offshore station and in the groundwater.

Sampling sites	Sampling depth (m)	Cl^- (mmol/L)	S (mmol/L)	CH_4* (μmol/L)	NH_4^+ (μmol/L)
Pockmark B, active	2	83.2	3.80	0.047 +/− 0.006	0.7
	6			0.021 +/− 0.001	0.6
	10	101.5	4.61	0.021 +/− 0.0002	0.6
Pockmark D, active	2	97.3	4.24	0.035 +/− 0.003	0.0
	6			0.020 +/− 0.002	0.6
	10	100.1	4.58	0.006 +/− 0.0009	0.2
Pockmark E, inactive	2	88.9	3.98	0.027 +/− 0.002	0.4
	6			0.020 +/− 0.002	0.4
	10	100.1	4.60	0.021 +/− 0.0006	0.0
Offshore station J	2			0.035 +/− 0.004	0.5
Groundwater, observation well HP101		0.07	0.10	0.044 +/− 0.0008	0.7
Groundwater, obsolete water intake well		1.34	0.18	0.006 +/− 0.002	0.4

* Given as a mean +/− estimated standard deviation (see Bange et al., 2010) based on the CH_4 measurements of the triplicate water column and groundwater samples (see Section 3.1 Sample collection).

pockmarks B and D, whereas this is not the case for pockmark E.

Porewater DIC concentrations are low in pockmark D (range 0.31–0.38 mmol/L), whereas they are somewhat higher in pockmark B (range 1.2–1.5 mmol/L) and significantly higher in pockmark E (range 2.0–16.5 mmol/L; Fig. 3). Porewater DIC concentrations decrease strongly toward the core top in pockmark E. Porewater $\delta^{13}C_{DIC}$ values are strongly negative in pockmark D (from −19.4 to −16.0 mUr), and slightly negative in pockmark B (from −6.8 to −3.0 mUr; Fig. 3). Porewater $\delta^{13}C_{DIC}$ values are ca. + 9.5 mUr below the 25 cm depth in pockmark E and

decrease upward towards a pronounced minimum of −7.1 mUr at 6 cm depth, before increasing to −2.7 mUr at the sediment surface.

Porewater CH_4 concentrations are low in pockmark D (range 0.038–0.066 μmol/L), whereas they are higher in pockmark B (range 0.127–0.372 μmol/L) and orders of magnitude higher in pockmark E (949–1841 μmol/L below 5 cm depth; Fig. 4). We note that the values below 5 cm depth may be subject to outgassing of CH_4 from the sediment core on deck prior to porewater sampling (e.g., Egger et al., 2016a,b; Egger et al., 2017) and thus underestimate the true value. Porewater CH_4 concentrations decrease strongly toward the core top in pockmark E and reach 24.2 μmol/L above the sediment–water interface (Fig. 4). However, this value is still significantly elevated with respect to porewaters in pockmarks B and D. Similarly, porewater NH_4^+ concentrations are low in pockmark D (range 3.2–12.4 μmol/L) and higher in pockmark B (range 24.0–42.5 μmol/L; Fig. 4). Porewater NH_4^+ concentrations are much higher in pockmark E and show a strong upward-decreasing trend (range 166–1974 μmol/L).

CH_4 concentrations in the seawater column above the pockmarks, at the offshore station J and in the groundwater wells were in the range from 0.006 μmol/L to 0.047 μmol/L (Fig. 4; Table 3). Surface seawater samples from the depth of 2 m at the pockmark locations and at the offshore station J showed CH_4 concentrations between 0.03 and 0.05 μmol/L. Lower CH_4 concentrations of ca. 0.02 μmol/L were measured in the bottom (10 m) and intermediate-depth (6 m) samples from the pockmark locations, with a very low CH_4 concentration of 0.006 μmol/L in the bottom water at pockmark D. The groundwater observation well HP101 showed a CH_4 concentration of 0.04 μmol/L that is within the range of the sea surface water samples. The water intake well had a very low CH_4 concentration of 0.006 μmol/L.

4.3. Groundwater discharge rate estimates

The pore water Cl^- concentration profiles in pockmarks B and D exhibit typical concave shapes (Fig. 5) with a clear indication of steep concentration gradients from the top of the sediment layer located at the interface between the seawater and freshwater. In contrast, pockmark E shows minimal concentration gradient as suggested by the uniform profile along the depth. This transition in Cl^- concentra-

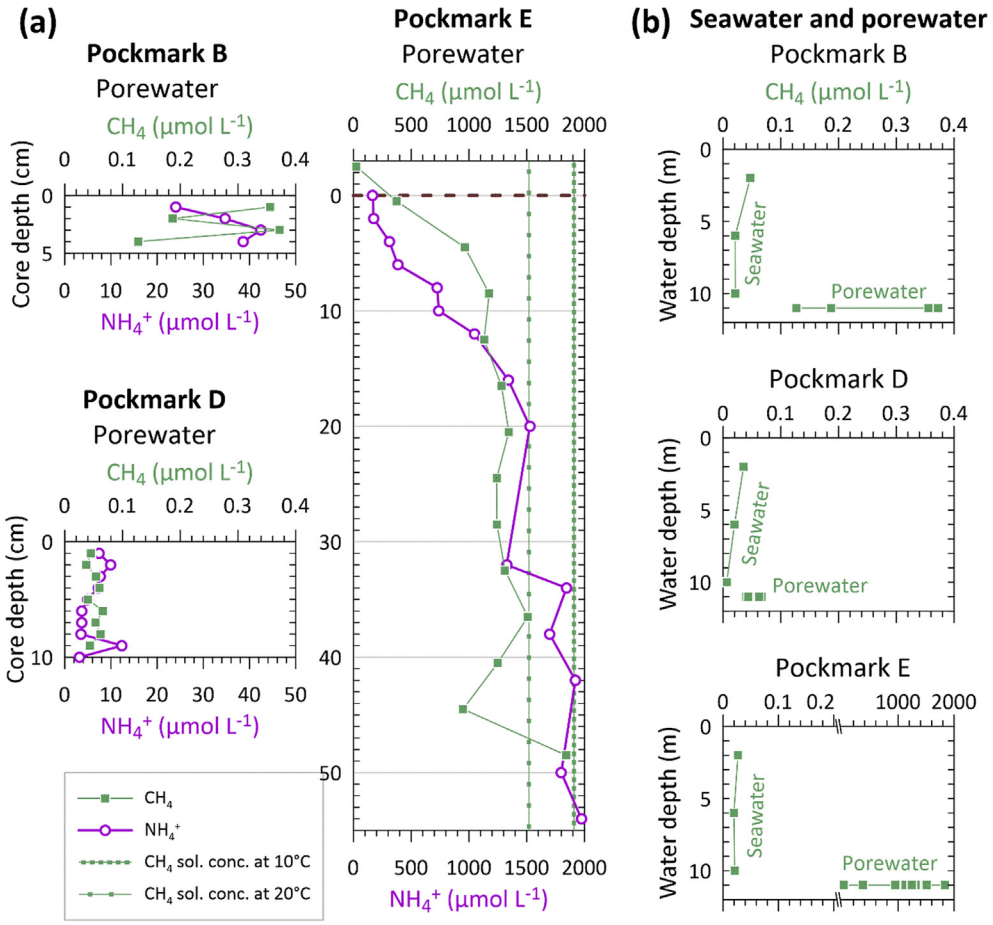

Fig. 4. Vertical distributions of CH_4, and NH_4^+ in sediment core porewater from pockmarks B, D and E (a) and CH_4 concentrations in the seawater column and porewater for pockmarks B, D and E(b). Dashed horizontal line indicates the sediment–water interface in the pockmark E core. Vertical lines indicate solubility concentration for CH_4 at the in-situ temperature of 10 °C and at 20 °C, calculated following Mogollón et al., (2013). Note the x-axis break in the pockmark E water column panel.

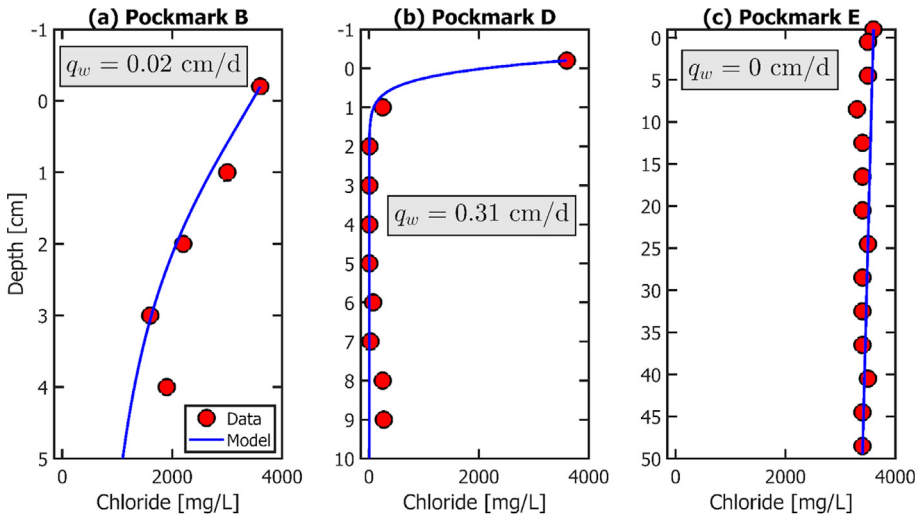

Fig. 5. Measured (markers) and simulated (lines) porewater chloride profiles along the depth in pockmarks B (a), D (b) and E (c).

tions along the sediment depth and the specific shape of the concentration profiles are ultimately controlled by the dynamic balance between the advective and diffusive/dispersive transport. Since chloride is chemically inert for most of the geochemical reactions occurring in these pockmarks, the observed Cl^- profiles were used to estimate the groundwater discharge rates across the seafloor. This was performed by fitting the chloride spatial profiles in different pockmarks against the analytical solution of the advection–dispersion equation as outlined in Section S2.

The results of the optimization performed with the least-squares curve fitting are summarized in Fig. 5 and Table S4 (Supplementary Material). The modelled porewater profiles indicate a clear trend of upward flow of freshwater in both pockmark B and D locations, while in pockmark E, no similar trend in the whole profile of 50 cm could be seen. It is also apparent that a relatively higher porewater specific discharge was obtained in pockmark D ($qw = 0.31$ cm d^{-1}) compared to that of pockmark B ($qw = 0.02$ cm d^{-1}, Table S4, Supplementary Material). Such behavior is consistent with the observed trends in their concentration profiles because freshwater front clearly migrates at a higher rate in pockmark D leading to the steepest concentration profile. In contrast, pockmark E shows a flat profile indicating the signature of inactive pockmarks, where transport processes are mainly driven by the diffusion mechanism from the sediment–water interface. Furthermore, pockmark B represents an intermediate system, where the behavior is collectively dominated by both the advective and diffusive fluxes. The groundwater discharge rates obtained from these fitting procedures were directly used in the reactive transport simulations presented in the next sections.

4.4. Total number of all microbes and functional groups

The total number of bacteria (using the 16S rRNA gene copy number as a proxy) varied between the sample types. Pockmark sediments contained the most microbes of any sample type. Bacterial 16S rRNA gene copy numbers ranged from 9.9×10^9-9.8×10^{10} (Table 4), of which pockmark E had the highest copy numbers. Total copy numbers of archaea ranged from 7.7×10^7 to 1.3×10^9, and as with bacteria, pockmark E contained the highest copy numbers. Compared between the different sampling depths, archaeal copy numbers were higher in the deeper sample in pockmark E, on a similar level in both depths in pockmark D, and higher in the shallower sample in pockmark B. Total copy numbers of bacteria in seawater samples above pockmarks was around 10^6 and archaea 10^4. In the offshore control site, archaeal copy numbers were 1.3×10^3, i.e., one order of magnitude lower than those above pockmarks. Groundwater samples contained the lowest number of microbes. Observation well 101 had 4.2×10^5 bacterial gene copies, while the obsolete water intake well had one order of magnitude less, 4.8×10^4 copies. Similarly, archaeal copy numbers were low, ranging from 614 in the observation well and 157 in the water intake well.

Potential metabolic functionality of microbes in sediments, groundwater and seawater were determined with quantitative PCR. Denitrifying consortium was measured using *nar*G gene as a proxy. The highest number of *nar*G genes was observed in the shallower sample of pockmark B (5.46×10^8) (Fig. 6, Supplementary Material, Table S3). The deeper sample from the same pockmark had 9.77×10^6 copies of *nar*G. A similar depth-related decreasing trend was observed in pockmark D, which had the overall lowest number of *nar*G copies in sediment samples. Second highest numbers were observed in pockmark E sediments, 3.24×10^7 in shallower and 8.94×10^7 in the deeper section. A decreasing trend in relation to sampling depth was also observed in *amo*A gene copies, proxy for ammonia oxidation, in pockmarks B and D. The copy numbers ranged from 10^8 to 10^6. In contrast, in pockmark E sediment *amo*A copy number was higher in deeper sediment, reaching 1.20×10^8, while the shallower sample had around one tenth of the copy number of *amo*A gene, 3.67×10^7 copies. *Nar*G and *amo*A gene copy numbers in all seawater samples were around 10^3, except *amo*A copies

Table 4
Number of 16S rRNA gene copies, sequencing statistics and ecological diversity, richness, evenness, dominance and abundance-based coverage estimates.

Sampling site	Total number of 16S rRNA gene copies		Total number of sequences		Observed OTUs		Coverage		Diversity						Richness			
									Shannon H'		Nonparametric Shannon		Inverse Simpson		Chao1		ACE	
	Bac	Arc	Bac	Arc	Bac	Arc	Bac	Arc	Bac	Arc	Bac	Arc	Bac	Arc	Bac	Arc	Bac	Arc
Seawater B, 1 m above pockmark	1.70E+06	1.82E+04	104,705	60,959	423	6	0.998	0.999	4.24	0.03	4.25	0.04	25.39	1.01	516.6	8.2	512.1	11.0
Seawater D, 1 m above pockmark	1.47E+06	2.54E+04	90,371	103,678	408	5	0.998	0.999	4.22	0.03	4.23	0.03	29.11	1.01	506.9	6.9	515.8	12.9
Seawater E, 1 m above pockmark	2.98E+06	3.20E+04	104,201	67,584	410	7	0.998	0.999	4.14	0.05	4.15	0.05	24.91	1.01	507.2	1.0	490.1	10.9
Seawater, offshore station J	2.51E+06	1.32E+03	108,308	2631	390	7	0.998	1.000	4.18	0.33	4.19	0.33	25.74	1.14	480.9	7.0	476.2	8.9
Pockmark B, active sediment, 1.5–2.5 cm depth	7.29E+10	1.37E+08	62,726	21,823	771	26	0.996	0.997	4.98	2.08	5.00	2.09	75.48	6.02	939.3	36.2	926.9	48.8
Pockmark B, active sediment, 3.5–4.5 cm depth	1.72E+10	7.73E+07	73,730	23,791	704	28	0.996	0.997	4.88	2.00	4.90	2.02	69.84	4.99	895.6	36.5	871.2	46.2
Pockmark D, active sediment, 1.5–2.5 cm depth	1.37E+10	4.80E+08	85,009	64,909	542	14	0.997	0.999	4.56	1.65	4.57	1.66	48.49	4.43	701.5	16.6	699.5	20.5
Pockmark D, active sediment , 3.5–4.5 cm depth	9.88E+09	4.43E+08	85,902	63,482	448	14	0.997	0.999	4.25	1.64	4.26	1.65	34.55	4.52	599.2	16.4	610.6	20.4
Pockmark E, inactive sediment, 1.5–2.5 cm depth	6.32E+10	5.35E+08	68,256	40,512	798	34	0.996	0.997	5.12	2.39	5.14	2.40	83.62	8.06	976.0	41.4	946.3	45.5
Pockmark E, inactive sediment, 3.5–4.5 cm depth	9.84E+10	1.34E+09	82,152	39,728	779	35	0.996	0.997	4.97	2.40	4.99	45.93	71.72	8.32	965.5	42.2	943.9	45.9
Groundwater, observation well HP101	4.21E+05	6.14E+02	88,174	8018	311	20	0.998	0.999	2.69	1.84	2.70	1.84	4.76	4.03	415.3	20.3	445.3	21.8
Groundwater, obsolete water station	4.84E+04	1.57E+02	98,431	n/a	323	n/a	0.998	n/a	3.01	n/a	3.02	n/a	8.82	n/a	392.0	n/a	389.0	n/a

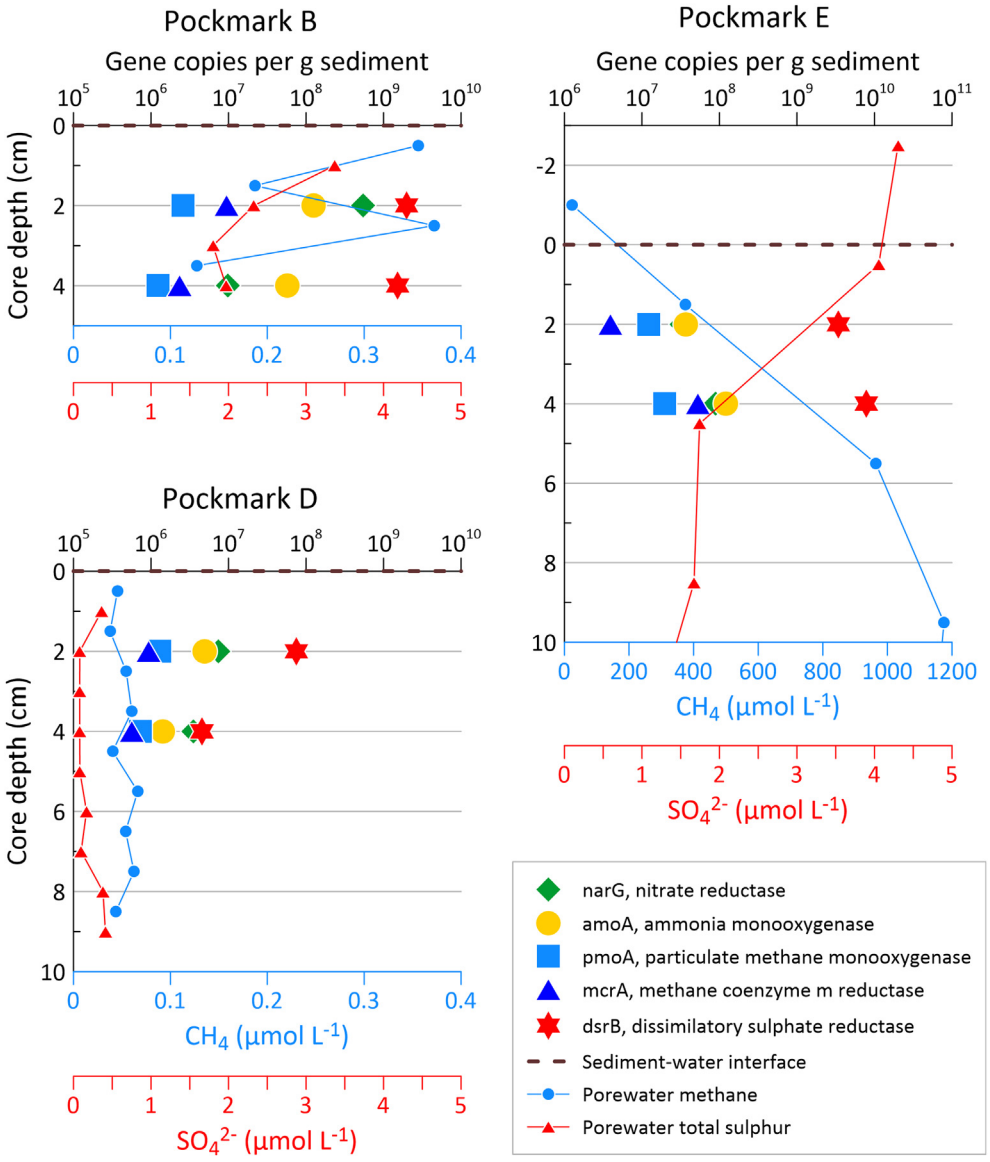

Fig. 6. Functional gene copy numbers of microbial populations in pockmark sediments, and concentrations of CH_4 and SO_4^{2-} in sediment porewaters. TS is interpreted to be mostly SO_4^{2-}.

were slightly lower in control seawater, 6.24×10^2 (Supplementary Material, Table S3). Groundwater samples had even lower copy numbers of *nar*G, 613 in HP101 and 55 copies in the water intake well near shoreline. Also, *amo*A copies in both groundwater samples were <100.

Methane cycling microbial consortia were identified with *pmo*A and *mcr*A. *Pmo*A is characteristic for the aerobic methane oxidation process, while the *mcr*A gene is functioning in both methanogens and anaerobic methane oxidizers. Pockmark E sediments had the highest numbers of *pmo*A genes (1.23×10^7 and 1.97×10^7 for the shallow and deep samples, respectively). Lowest numbers were detected from the deeper samples from pockmark B and D, 1.24×10^6 and 7.29×10^5, respectively. The highest number of *mcr*A copies were detected both in the deeper sample of pockmark E (5.25×10^7 gene copies) and from shallower sample from pockmark B (9.4×10^6 gene copies), although pockmark E had >1000 × higher methane concentrations. Pockmark D had lowest methane concentrations and lowest number of *mcr*A copies (on average 7.48×10^5). In seawater samples, *pmo*A copy number was 130 or less, and *pmo*A copies in groundwater samples were below detection limit (16 copies). *Mcr*A marker gene copies were on average 5.53×10^2 in seawater, and near the detection limit (49 copies or less) in groundwater.

The number of sulfate reducers, measured with *dsr*B marker gene, was overall highest of all functional groups determined in this study, and the highest number of sulfate reducers was detected in the deeper sample of pockmark E (7.88×10^9). However, the shallower sample from pockmark E and both samples from pockmark B were also at the 10^9 level. Pockmark D had clearly lower numbers of

*dsr*B copies, 7.48×10^7 (1.5–2.5 cm) and 4.53×10^6 (3.5–4.5 cm). Seawater from offshore station J had the highest amount of *dsr*B copies of all seawater samples, 4.26×10^4, and seawater samples above pockmarks ranged from 9.48×10^3 in pockmark E to 3.20×10^3 in pockmark D. Groundwater samples contained < 101 *dsr*B copies.

4.5. Microbial community diversity and composition

The dataset after quality control was composed of 2 299 000 (70 %) bacterial and 986 085 (30 %) archaeal sequences. Seawater samples had the highest number of bacterial sequences, ranging from 90 371 (above pockmark D) to 108 308 (seawater control sample from offshore station J) (Table 4). Conversely, the highest number of archaeal sequences (sample average of 103 678) was detected from seawater above pockmark D, while control seawater had the overall lowest number of archaeal sequences (2631). In sediments, the number of bacterial sequences ranged from 62 736 (pockmark B) to 85 902 (pockmark D) and archaeal numbers were 21 823 (pockmark B) to 64 909 (pockmark D). The number of bacterial sequences in groundwater samples were higher than in pockmark sediments but lower than in seawater, while archaeal sequence number in groundwater sample from observation well HP101 was lower than in sediments and seawater samples above pockmarks. Archaeal sequences were not retrieved from the obsolete water intake well.

Sediments had higher numbers of observed bacterial OTUs compared to groundwater and seawater samples (Table 4). Between the different sediment depths, the number of sequences retrieved from deeper sediment in pockmarks B and E was higher than in shallow samples. In pockmark D, there was no significant difference between the two sampling depths. Observed archaeal OTUs were much less than bacterial OTUs, and most OTUs were observed from sediments.

Rarefaction analysis showed that the archaeal community was extensively sequenced in most of the samples as rarefaction curves reached a plateau (Supplementary Material, Fig. S3). However, pockmark E and B rarefaction curves remained exponential, so these were not exhaustive sequenced. Similarly, rarefaction curves of bacterial communities (Supplementary Material, Fig. S4) in pockmark E and B, as well as the upper section of sediment in pockmark D remained exponential.. Rarefaction curves for sequences of bacterial communities from other samples showed that most of the diversity of the bacterial community in these had been captured by sequencing. Sequencing coverage for both archaeal and bacterial communities was high, ranging from 0.996 in bacteria in pockmark B and E to 1.000 in offshore station J seawater archaea (Table 4).

The most diverse environment studied was the pockmark sediment, according to all diversity indices (Shannon's H' diversity index, nonparametric Shannon and inverse Simpson index) (Table 4). Both archaeal and bacterial diversity was highest in pockmark E sediments, second highest in pockmark B and third highest in pockmark D. Seawater bacterial communities were nearly as diverse as those in pockmark D, but archaeal diversity was significantly lower in seawater samples than in other samples. Groundwater communities exhibited the lowest bacterial diversity. Species richness according to Chao1 richness index was highest in pockmark E, then pockmark B and D sediments. Seawater samples had equivalent bacterial species richness, lower than in sediments but higher than in groundwater. Archaeal species richness was, on the contrary, higher in groundwater than in seawater, and also in pockmark D sediment. Abundance-based coverage estimates (ACE) followed similar trends as Chao1 richness estimates.

Archaeal community structure varied between the different locations and samples. In class level comparison, the most abundant archaeal class was *Nitrososphaeria* that was detected in all samples but was most dominant in seawater samples taken above pockmarks, and least abundant in pockmark E sediment (Fig. 7). The most common OTU belonging to *Nitrososphaeria* class in seawater, pockmark B and E sediments was affiliating with *Candidatus* Nitrosopumilus, while in pockmark D sediment, another OTU affiliated with *Nitrosopumilaceae* was the most common OTU in this class (Supplementary Material, Krona charts "Arch_sed", "Arch_SW", "Arch_GW"). In addition, *Candidatus* Nitrosotalea -affiliating OTU was also abundant in pockmark D sediment and in groundwater from the observation well. The most abundant OTU in groundwater, belonging to *Nitrososphaeria* class, affiliated with *Nitrosoarchaeum*. *Nanoarchaeia* was the second-most dominant class, especially abundant in pockmark sediments, and of all samples, most abundant in pockmark E. Abundant OTUs in this class affiliated with *Woesearcheales*. Bathyarchaea were the most abundant in the lower section of pockmark B sediment, but also detected from pockmark E and groundwater samples. Methanogenic archaeal classes, *Methanomicrobia* and *Methanosarcinia* were mainly detected in pockmark E. Methanomicrobial OTUs were related to *Methanogenium*, *Methanospirillum*, *Methanocorpusculum*, *Methanolinea*, *Methanoregula* and *Methanoculleus*. OTUs affiliating with *Methanosarcina*, *Methanolobus*, *Methanosaeta* and ANME-2a-2b represented the *Methanosarcinia* class. *Thermoplasmata* -affiliating OTUs were abundant in pockmark E and in the lower sample of pockmark B. The groundwater sample community was composed of OTUs belonging to unclassified Crenarchaota and many low abundance OTUs in addition to the abovementioned *Candidatus* Nitrosotalea and *Nitrosoarchaeum*.

Gammaproteobacterial OTUs were the most abundant group in all pockmark sediments (Fig. 8). A detailed taxonomic inspection showed that many of these were affiliated with *Comamonadaceae* and *Nitrosomonadaceae* (Supplementary Material, Krona chart "Bac_sed"). In comparison to other sediments, abundant bacteria in sediment D communities were affiliating with *Nitrospira*, the actinobacterial MB-A2-108 group and unclassified bacterial OTUs. In addition, *Gemmatimonadales* -affiliating OTUs were more common in pockmark D than in other pockmark sediments. Alphaproteobacteria represented higher relative abundance in pockmark D, with *Rhizobiales* a major group. In pockmarks B and E, alphaproteobacterial *Rhodobacteraceae* were abundant in addition to *Rhizobiales*. Similarly to

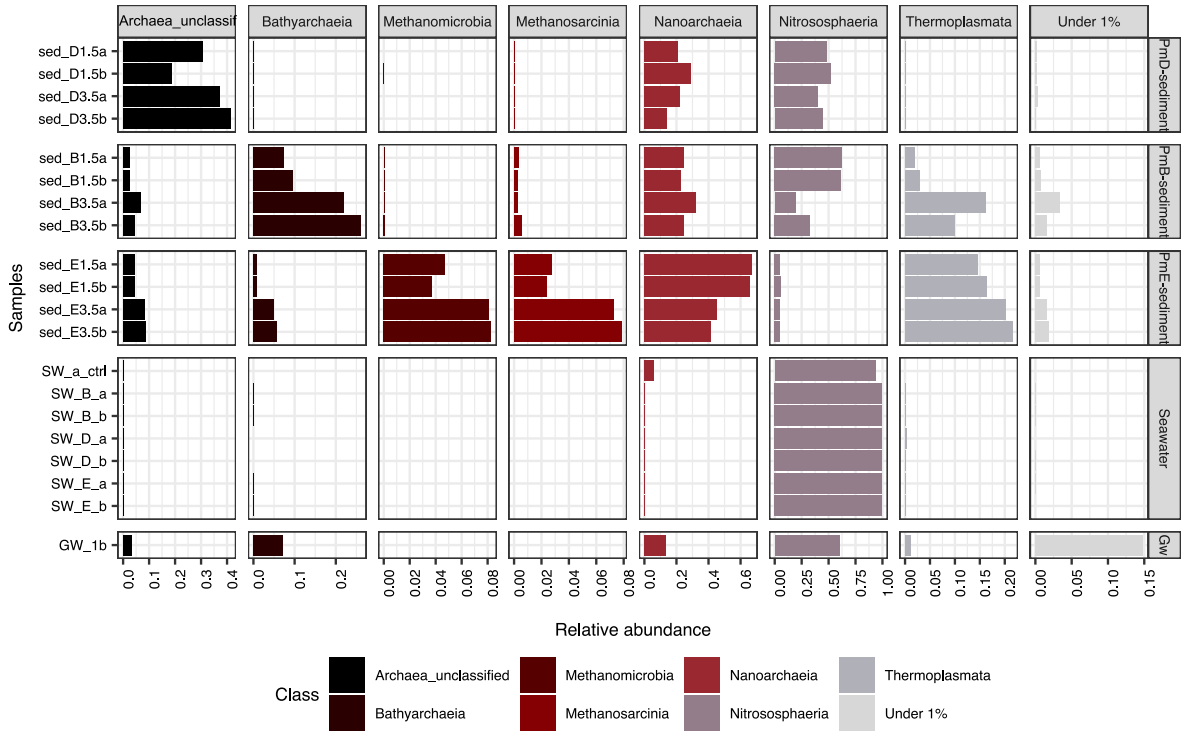

Fig. 7. Class level archaeal diversity in sediments (sed), seawater (SW) and groundwater (GW). Pockmarks (*Pm*) are labeled D, B and E, and 1.5 or 3.5 correspond to the depth in cm from which they were retrieved. Lowercase a and b mark the duplicate samples. Note that the relative abundance scale in × axis is different between panels, compare samples inside class, not between classes.

Alphaproteobacteria, pockmark D sediment hosted a relatively higher abundance of Burkholderiales compared to pockmarks B and E. *Polyangia* and *Thermoleophilia* had similar abundances in pockmark D and B, while typical sulfate reducer classes *Desulfobacteria* (*Desulfosarcina* and *Desulfosarcinaceae* OTUs) and *Desulfobulbia* (*Desulfocapsaceae*, *Desulfobulbaceae* and *Desulforhopalus* OTUs) were abundant in pockmarks B and E. Bacteroidia were equally abundant in seawater samples and in the upper layer of sediment E, however these were not represented by the same OTUs. Rare OTUs (representing <1% of the total community) were common in all sediment samples, but less abundant in seawater and groundwater samples. Seawater communities were composed mainly of Gammaproteobacteria (*Pseudohongiella*, *Methylophilaceae*), Bacteroidia (*Fluviicola*, *Sphingobacterales* and *Flavobacterales* -affiliating OTUs), Alphaproteobacteria (*Pseudorhodobacter*), Actinobacteria (*Sporichthyaceae* -affiliating OTU) and Acidimicrobia (*Ilumatobacteraceae* OTU) (Supplementary Material, Krona chart "Bac_SW"). Gammaproteobacteria (*Pseudomonas*, *Rhodoferax*, *Undibacterium* OTUs) were the main component of groundwater from HP101, while Alphaproteobacteria (*Brevundimonas* and *Caulobacter* -affiliating OTUs) and gammaproteobacterial *Hydrogenophaga* dominated the obsolete water intake well groundwater community (Supplementary Material, Krona chart "Bac_GW).

Diversity between the samples was visualized with PCoA plots. Using Bray-Curtis dissimilarity index based on abundance estimates and Jaccard index based on presence/absence of species, different sample types divide clearly into separate groups (Fig. 9). Looking into archaeal (Fig. 9a,c) and bacterial (Fig. 9b,d) communities in different samples, pockmarks E and B group together, but are separate from pockmark D, seawater sample, and groundwater samples. The main observations are reproduced in both the Bray-Curtis and Jaccard index approaches to the PCoA.

5. DISCUSSION

This study investigates biogeochemistry and microbial community structure in three pockmarks formed by SGD. Pockmarks B and D were formed in fine sand on the slope of a shore platform at the water depth of 11 m and ca. 200 m from shoreline. Pockmark E was also formed in fine sand but has later been passively covered by organic-rich mud. Previous ^{222}Rn measurements of near-bottom water showed that pockmarks B and D are sites of active groundwater discharge, whereas pockmark E is currently inactive (Virtasalo et al., 2019). Below we discuss the contrasting biogeochemical settings and microbial communities of the different sites, before considering the broader implications of our findings.

5.1. Biogeochemical setting

The sediment and porewater geochemical characteristics indicate a contrasting set of early diagenetic processes between the active pockmarks (B, D) and the inactive

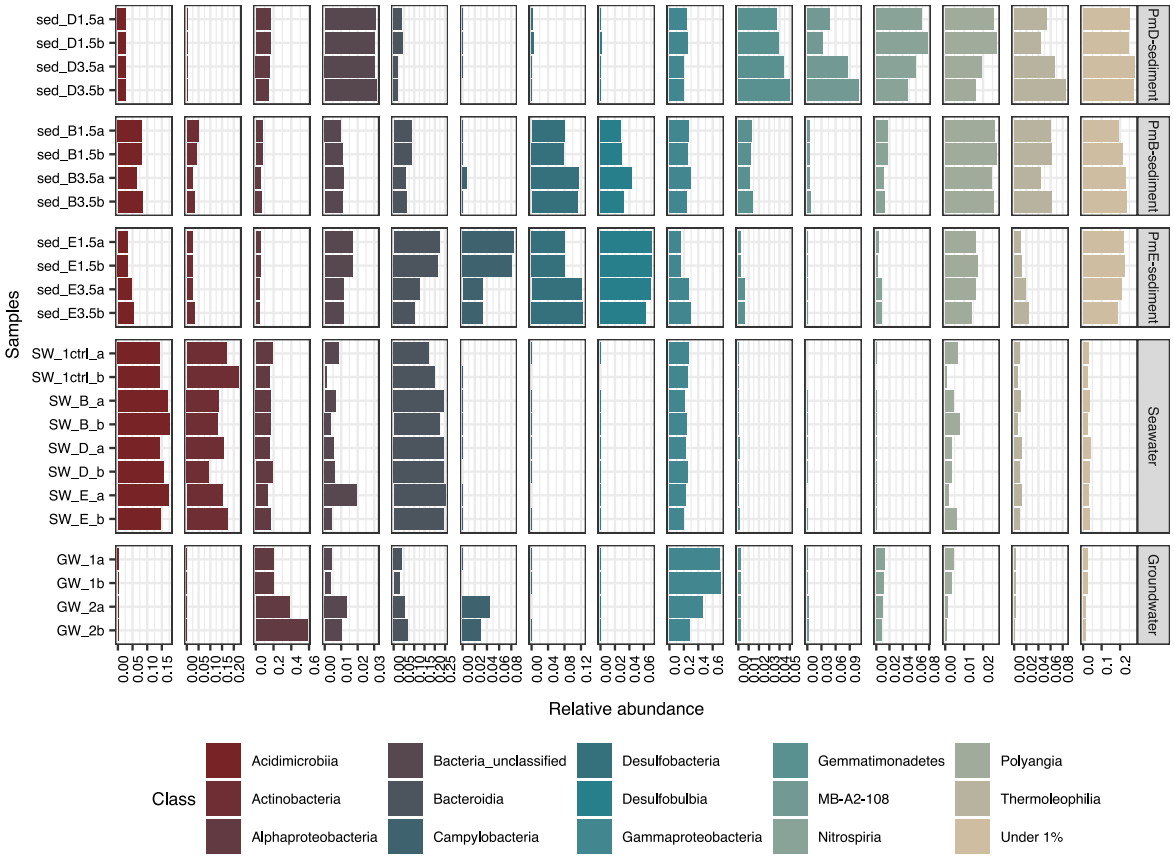

Fig. 8. Class level bacterial diversity in sediments (sed), seawater (SW) and groundwater (GW). Pockmarks (*Pm*) are labeled D, B and E, and 1.5 or 3.5 correspond to the depth in cm from which they were retrieved. Lowercase a and b mark the duplicate samples. Note that the relative abundance scale in × axis is different between panels, compare samples inside class, not between classes. In the legend, each panel of 3 classes corresponds to the above three facets.

pockmark (E). At pockmark E, insignificant groundwater contribution was calculated from the Cl^- profile (Fig. 5). The porewater diagenetic zonation at this site is strongly reminiscent of typical organic matter-rich muddy seafloor in this area, as described in several recent studies (Jilbert et al., 2018; Myllykangas et al., 2020a; Jokinen et al., 2020) and consistent with early diagenesis in a brackish setting with a limited amount of dissolved sulfate in the bottom waters (Froelich et al., 1979; Jørgensen and Kasten, 2006). The setting is characterized by compressed zones of oxic and suboxic remineralization close to the sediment–water interface, and a shallow sulfate-methane transition zone (SMTZ), reflecting the high demand for electron acceptors for anaerobic remineralization of organic matter. Accordingly, pockmark E sediments were enriched in TOC, at >4% throughout most of the profile (Fig. 2), and porewaters displayed high concentrations of NH_4^+ and DIC (up to >1500 μM and >15000 μM, respectively), the principal metabolites from organic matter remineralization. Sediment TOC/S ratio was also low at pockmark E (Fig. 2) indicating pyrite formation (Berner, 1970) as well as sulfurization of organic matter (Brüchert, 1998; Passier et al., 1999, Werne et al., 2008) during early diagenesis. In contrast, significant groundwater contribution was calculated from the Cl^- profiles of pockmarks B and D (Fig. 5). Lower TOC contents and negligible accumulation of metabolites (DIC, NH_4^+) in the porewaters suggest that early diagenetic processes exert a less important control on porewater chemistry at pockmarks B and D (Figs. 3, 4), supporting the interpretation of an advection-dominated system. There is thus no indication of the development of a SMTZ as observed at pockmark E, and much less indication of enrichment of sediments with sulfur (TOC/S weight ratios 40–60 and 60–90 at B and D, respectively; Fig. 2). In general, the contrast between low rates of diagenetic processes in active pockmarks and high rates in the surrounding sediment environments resembles the result of Whiticar (2002) for similar investigation in Eckernförde Bay.

The reactive transport simulations capture the essential features of the porewater (Fig. 10) and solid-phase profiles (Fig. 11) and confirm the overall contrast between the active and passive pockmarks. The model was able to simultaneously reproduce the spatial concentration profiles of most chemical species observed in each pockmark. We note that the poor fit of the CH_4 data from pockmark E below 10 cm depth (Fig. 10n) may reflect the impact of degassing from the sediment core during sampling, leading to underestimated concentrations in the deeper part of the core (e.g., Egger et al., 2016a,b; Egger et al., 2017). The effects of the diagenetic processes and biogeochemical

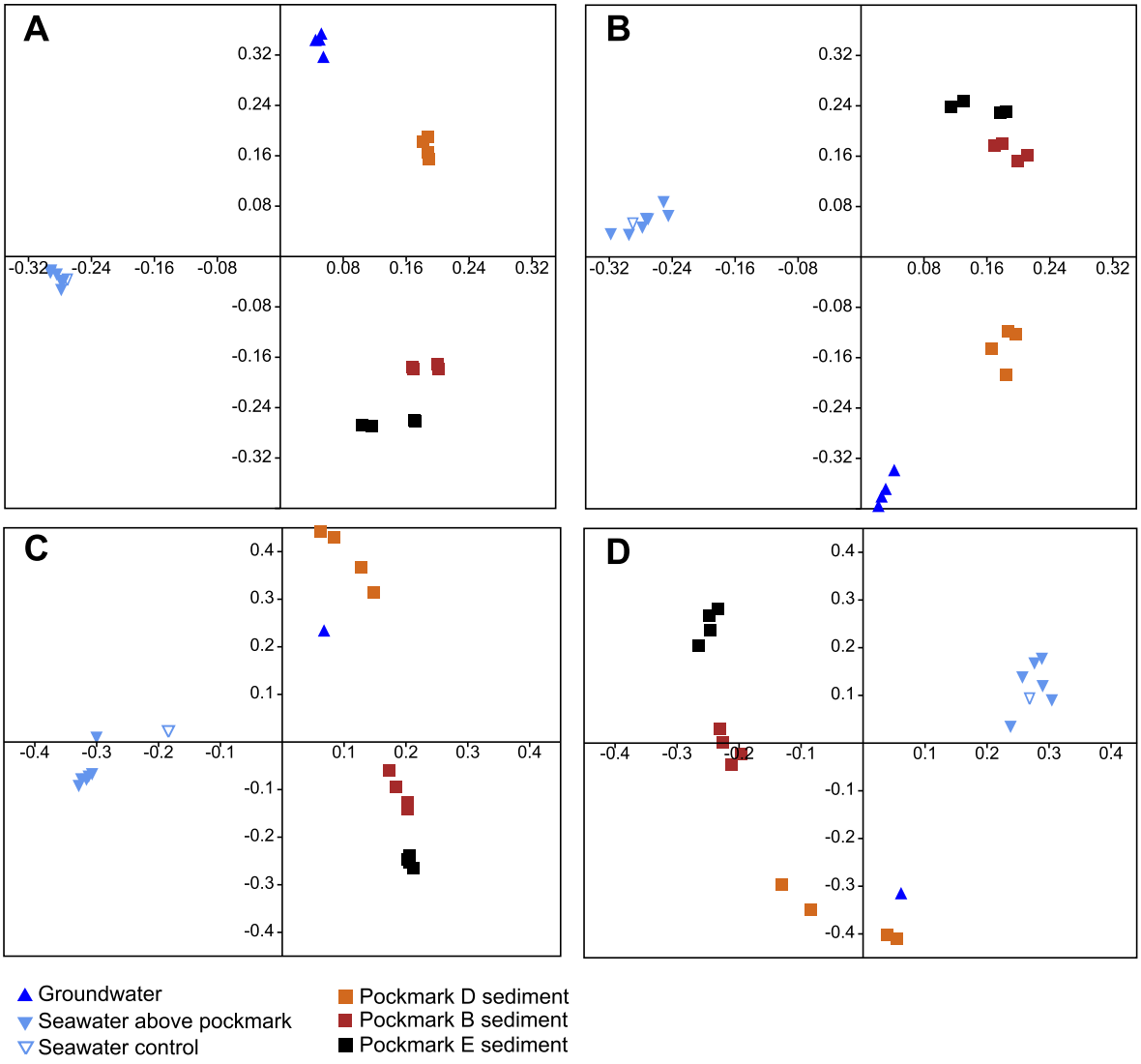

Fig. 9. Bray-Curtis -based PCoA of archaeal (A) and bacterial (B) OTUs. Jaccard -based PCoA of archaeal (C) and bacterial (D) OTUs.

reactions are clearly evident in the solute concentration profiles because SO_4^{2-} (which is a reactant in primary redox reactions) concentrations show a clear trend for consumption (second column panels, Fig. 10) with sediment depth, compared to the conservative chloride species. This effect is most pronounced in pockmark E (first column panels, Fig. 10). A similar trend is also observed in the modeled profiles of other electron acceptor species (results not shown). In contrast, NH_4^+, CH_4, and DIC profiles indicate a signature for gradual production of these species with depth due to OM degradation reactions, leading to an outgoing solute flux across the sediment–water interface (third to fifth column panels, Fig. 10).

The model output shows that the contrasting profiles of metabolites such as NH_4^+, CH_4 and DIC between the pockmarks can be explained by the variable influence of SGD. Discharge rates can affect the accumulation of organic matter and other sediment phases (being much higher at pockmark E), but also the availability of porewater oxidants such as O_2 and SO_4^{2-} for primary redox reactions due to upwards advective flow. Furthermore, the upward advective flow in pockmarks B and D drives the transport of the reaction products to the upper active oxidation zone (top ca. 2 cm), where these species are further consumed by the secondary reactions and the available oxidants in the shallow depths (Fig. 10c-e, h-j). In contrast, this vertical recirculation does not occur in pockmark E, leading to orders of magnitude higher concentration levels for these species in deeper layers (Fig. 10m-o). The model also confirms that a direct correlation exists between these species' concentrations and the magnitude of the upward water flux, with the lowest concentration magnitude observed in pockmark D, which represents the highest SGD rate. The situation is opposite in pockmark E, where groundwater discharge was nonexistent, and the behavior of pockmark B lies in between these two cases.

Fig. 11 shows a comparison between the observed and simulated TOC and TN profiles in the solid phase for differ-

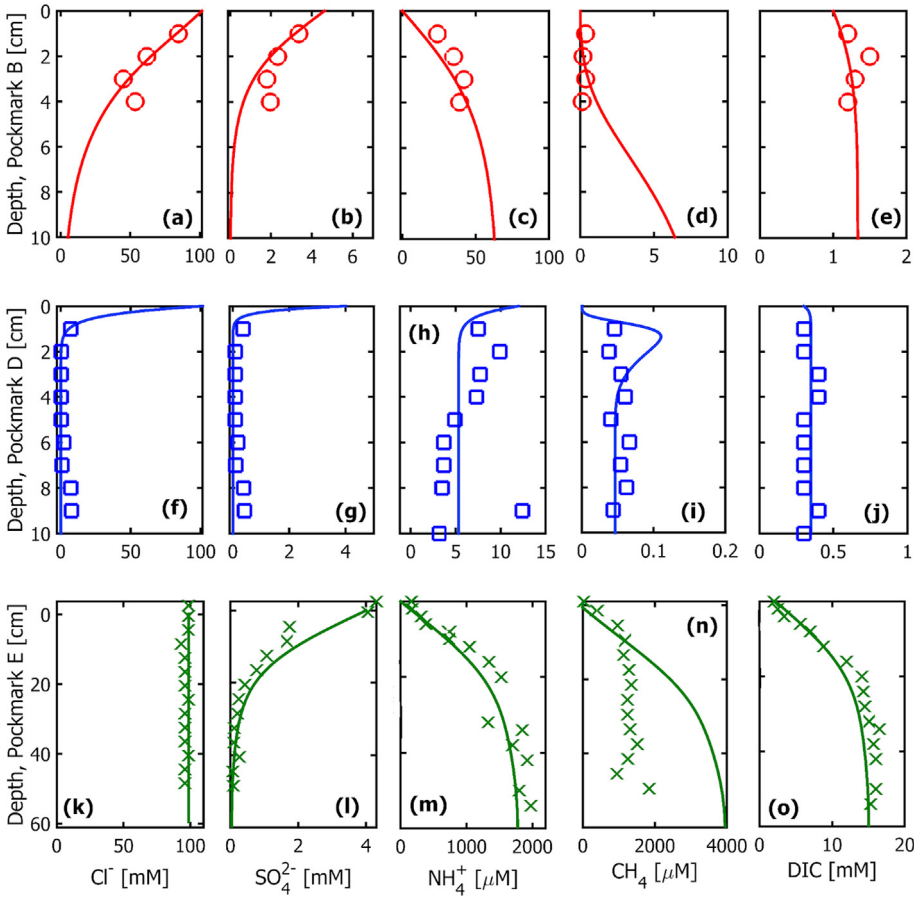

Fig. 10. Observed (symbols) and modeled (lines) porewater profiles for Cl^- (a,f,k), SO_4^{2-} (b,g,l), NH_4^+ (c,h,m), CH_4 (d,I,n), and DIC (e,j,o) from pockmarks B (top row panels, a-e), D (middle row panels, f-j) and E (bottom row panels, k-o). The measured porewater CH_4 concentrations are expected to be lower than the in-situ values due to degassing from the sediment core during sampling (e.g., Egger et al., 2016a,b; Egger et al., 2017).

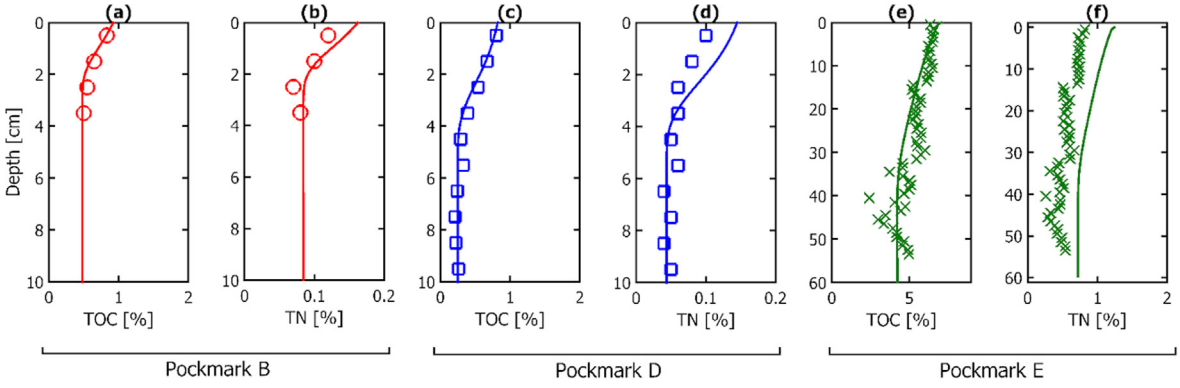

Fig. 11. Observed (symbols) and modeled (lines) solid-phase carbon (a,c,e) and nitrogen (b,d,f) profiles from pockmarks B (a-b), D (c-d) and E (e-f).

ent pockmarks. The model could reproduce the sediment concentration profiles for all the cases except for a minor disagreement for TN in pockmark E (Fig. 11f). This can be explained by the uncertainty related to the conceptualization of the initial definition of C:N:P ratio of the organic matter in the model. The effects of sedimentation rate are apparent in these profiles as an incoming front is clearly observed from the top boundary of the domain for both elements, implying constant sedimentation. Deposition of organic matter and other sediment components is expected at the inactive pockmark due to lower energy setting, but the addition of organic matter in the surface layer at the

active pockmarks is noteworthy. Mixing of organic-rich fluffy material by wave action to the sediment surface layer of pockmarks B and D may provide a mechanism for constant incorporation of low amounts of organic matter in the top 1–2 cm at these sites (Huettel et al., 1996). Indeed, images of the sediment surface in box cores at these pockmarks document the presence of fluffy organic material on the sediment surface (Supplementary Material, Fig. S1). It was necessary to consider sedimentation to occur at all pockmarks in order to model the observed profiles, with a temporally constant sedimentation rate sufficient to match the measured solid phase profiles. The model also confirms a much higher sedimentation rate in pockmark E (0.43 cm yr^{-1}) compared to that of pockmark B and D (3×10^{-7}, Supplementary Material, Table S4), as also validated with the ^{137}Cs activity measurements (Section 4.1). Such contrasting sedimentation rates are also evident in the solid phase concentration profiles, because both the TOC and TN fronts propagated up to a depth of ~40 to 50 cm in pockmark E (Fig. 11e-f), whereas these fronts moved only until ~2–3 cm depth in the two active pockmarks (Fig. 11a-d).

The model also allows a deeper inspection of the reactive transport mechanisms by facilitating the quantification of solute fluxes and biogeochemical process rates in the depth domain at each pockmark (Fig. 12). For brevity, we visualize the flux and reaction rate profiles only for SO_4^{2-} and CH_4, which are key reactants and products, respectively, with respect to the geochemical system studied. The model output confirms that diffusive fluxes dominate solute transport at the inactive pockmark E, while advective fluxes contribute to upwards transport of both SO_4^{2-} and CH_4 at the active pockmarks B and D (Fig. 12, left two column panels). The highest advective fluxes (green dash-dotted lines) of SO_4^{2-} are observed close to the sediment–water interface at pockmark D ($>1 \times 10^{-7}$ mol $m^{-2}s^{-1}$), where the strong upwards flow of groundwater (Fig. 5) is much stronger than the downwards diffusion (red dashed lines) of SO_4^{2-} from the bottom water. However, the situation is different for the reaction products (e.g., CH_4) as the produced solute quantities generally imply an upward diffusive flux from the active reaction zone to the upper boundary. Consequently, the advective and diffusive flux components act in an additive fashion leading to a higher total flux (blue solid lines) in most locations of the simulation domain (second column panels, Fig. 12).

With respect to biogeochemical process rates, strong contrasts are also observed between the pockmarks. The observation of a shallow SMTZ at pockmark E suggests important roles for both sulfate reduction and methanogenesis in organic matter remineralization at this site. The modeling results confirm that rates of both processes are orders of magnitude higher at pockmark E than pockmarks B and D (maximum rates up to 5×10^{-8} mol/m^{-3} s^{-1}). Furthermore, the zones of sulfate reduction and methanogenesis overlap in the depth domain (Fig. 12, right column panels), as commonly observed in diffusion-dominated coastal sites with high rates of organic matter deposition (e.g., Thang et al., 2013; Sawicka and Brüchert, 2017). In contrast, high groundwater discharge rates at the active pockmarks shift the reaction fronts upwards into rather compressed zones close to the sediment–water interface and enhance the sediment–water fluxes. This is most pronounced at pockmark D, where sulfate reduction and methanogenesis are limited to the uppermost 4 cm of the sediment column (Fig. 12).

In sedimentary settings where upwards diffusing methane meets downwards-diffusing sulfate at the SMTZ, sulfate-mediated anaerobic oxidation of methane (S-AOM) is expected to occur, thus dividing the consumption of sulfate between OM remineralization and methane oxidation (e.g., Jørgensen et al., 2019). The model output shows that S-AOM occurs at pockmark E in a similar depth range to organoclastic sulfate reduction (Fig. 12, right). Estimated rates of S-AOM in the model account for approximately 10% of total sulfate consumption at this depth. Furthermore, the effects of iron-mediated anaerobic oxidation of methane (Fe-AOM) are also visible in the active pockmarks (Fig. 12d, h). According to the model, Fe-AOM rates become increasingly important at greater depths in pockmark B and D, whereas the consumption of CH_4 due to Fe-AOM is almost negligible compared to the other mechanisms in pockmark E. Table 5 summarizes the simulated fluxes and reaction rates for selected species.

Further evidence for the presence of S-AOM at pockmark E is given by a combined analysis of porewater SO_4^{2-}, DIC and δ^{13}C-DIC data, following the modified Rayleigh-evaluation approach of Miller et al. (2017). The first part of the analysis employs the principle that the balance between dissimilatory sulfate reduction and S-AOM is reflected in the ratio of change in sulfate (ΔSO_4^{2-}) to change in dissolved inorganic carbon (ΔDIC), where *change* refers to the offset from the bottom water value at a given depth in the porewaters (Kastner et al., 2008; Hu et al., 2015; Wu et al., 2018). SMTZ environments dominated by S-AOM yield theoretical ratios close to 1, while those dominated by dissimilatory sulfate reduction yield theoretical ratios close to 2, due to the differing stoichiometries of sulfate consumption and DIC production between the two reactions. Miller et al. (2017) added the parameter DIC*δ^{13}C-DIC, a concentration-normalized expression of the stable carbon isotopic ratio of DIC, to a second part of the analysis, with the logic that deviations to negative δ^{13}C-DIC coincident with low $\Delta DIC/\Delta SO_4^{2-}$ provide supporting evidence for S-AOM due to the transfer of isotopically light C from CH_4 to DIC.

The results of the analysis show evidence for a contribution of S-AOM to total sulfate reduction in the depth interval corresponding to the SMTZ (0–10 cm) at pockmark E. This interval shows $\Delta DIC/\Delta SO_4^{2-}$ values of consistently < 2 (Fig. 13a). The same samples are characterized by negative DIC*δ^{13}C-DIC (Fig. 13b, seen also as a negative δ^{13}C-DIC excursion in Fig. 3). This evidence supports the interpretation of S-AOM in this interval. We note, however, that the absolute value of the negative δ^{13}C-DIC excursion is less extreme than often observed in fully marine SMTZ settings (e.g., Whiticar, 1999), due to dilution of the signal by concurrent methanogenesis (Jilbert et al., 2021). In contrast to pockmark E, the active pockmarks B and D show negative

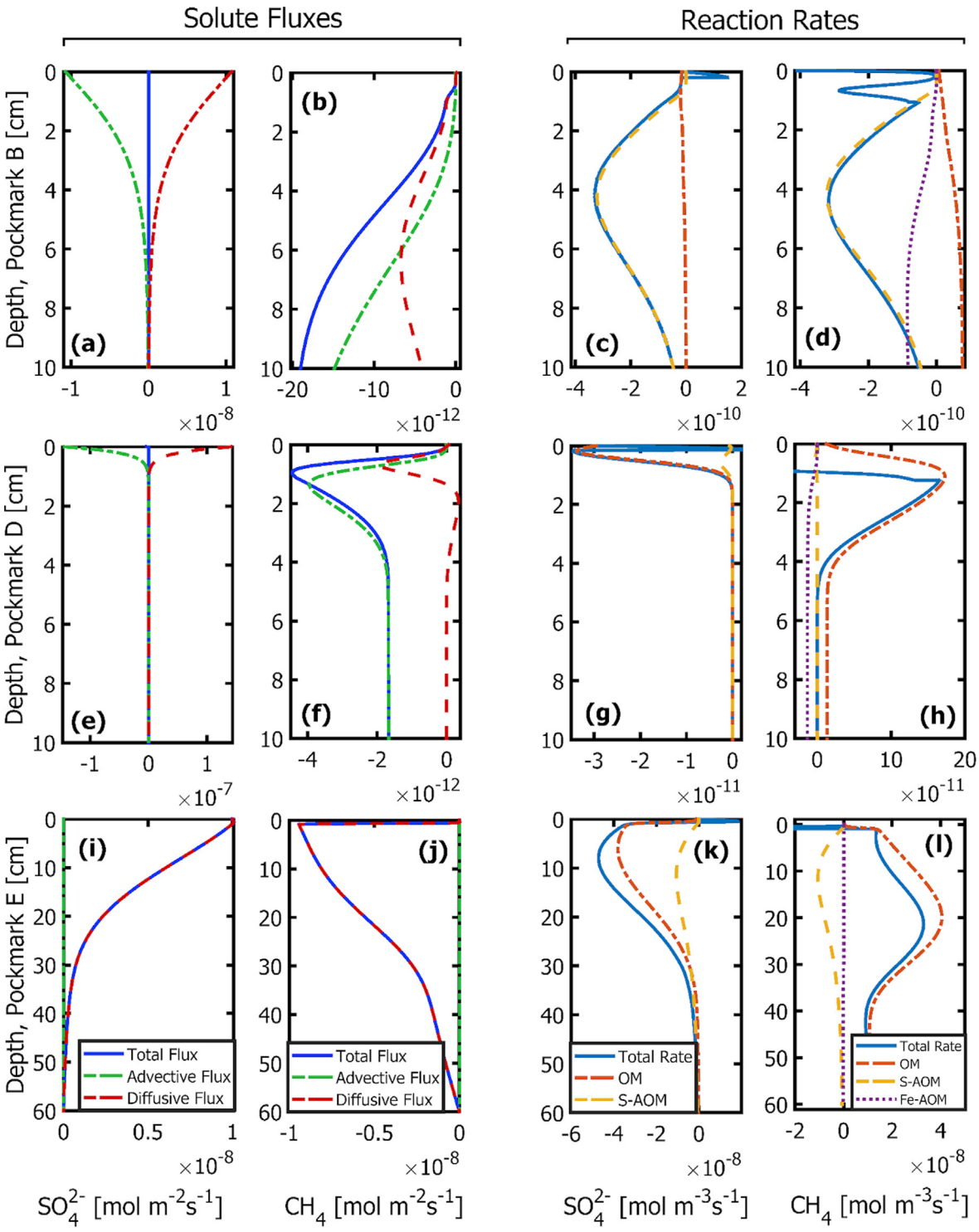

Fig. 12. Modeled flux components (left two column panels) and reaction rates (right two column panels) of SO_4^{2-} (first and third column panels) and CH_4 (second and fourth column panels) at sites B (a-d), D (e-h) and E (i-l): modeled rates of SO_4^{2-} consumption, CH_4 production and CH_4 consumption by different processes in the reaction network. OM = coupled to remineralization of organic matter; S-AOM = sulfate-mediated anaerobic oxidation of methane; Fe-AOM = Fe-oxide mediated anaerobic oxidation of methane.

values for ΔDIC, reflecting the lower values of DIC in porewaters compared to bottom waters and confirming the lack of evidence for significant rates of diagenetic processes.

Porewater CH_4 concentrations in all three pockmarks were significantly higher than the dissolved CH_4 concentrations measured in the seawater column above pockmarks

Table 5
Summary of fluxes and reaction rates for different pockmarks.

Quantity	Species	Integrated over depth[#] [mol m^{-1} s^{-1}] / [mol m^{-2} s^{-1}]*			Value at sediment–water interface [mol m^{-2} s^{-1}] / [mol m^{-3} s^{-1}]*		
		Pockmark			Pockmark		
		B	D	E	B	D	E
Flux	SO_4^{2-}	9.71×10^{-13}	2.10×10^{-13}	1.44×10^{-9}	2.37×10^{-11}	1.92×10^{-11}	1.01×10^{-8}
	CH_4	9.96×10^{-13}	2.03×10^{-13}	2.34×10^{-9}	1.14×10^{-13}	4.80×10^{-14}	8.00×10^{-13}
	NH_4^+	1.55×10^{-11}	1.92×10^{-11}	1.15×10^{-9}	-1.85×10^{-10}	-2.03×10^{-10}	-6.06×10^{-9}
	DIC	3.13×10^{-10}	1.25×10^{-9}	5.11×10^{-9}	-3.36×10^{-9}	-1.26×10^{-8}	-1.30×10^{-7}
	NO_3^-	1.12×10^{-12}	3.57×10^{-13}	7.99×10^{-12}	1.80×10^{-10}	9.41×10^{-11}	2.80×10^{-10}
Reaction rate	SO_4^{2-}	1.87×10^{-11}	1.75×10^{-13}	1.02×10^{-8}	-1.16×10^{-11}	-3.02×10^{-11}	-9.38×10^{-10}
	CH_4	1.91×10^{-11}	7.21×10^{-12}	1.96×10^{-8}	-4.09×10^{-10}	-1.96×10^{-10}	3.76×10^{-10}
	NH_4^+	3.30×10^{-11}	1.21×10^{-11}	7.37×10^{-9}	5.00×10^{-9}	-1.84×10^{-9}	2.92×10^{-7}
	DIC	2.56×10^{-10}	1.60×10^{-10}	5.35×10^{-8}	3.35×10^{-8}	3.34×10^{-8}	1.94×10^{-6}
	NO_3^-	1.81×10^{-10}	1.02×10^{-10}	2.15×10^{-9}	-2.36×10^{-8}	-1.68×10^{-8}	-1.14×10^{-7}

[#] The depth-integrated quantities were calculated using the absolute values of fluxes and reaction rates without explicitly considering their sign/direction: i.e., using $\int_0^L |J_i|dx$ for fluxes and $\int_0^L |R_i|dx$ for reaction rates.
* The first one refers to the unit of fluxes, whereas the second one indicates the unit of reaction rates.

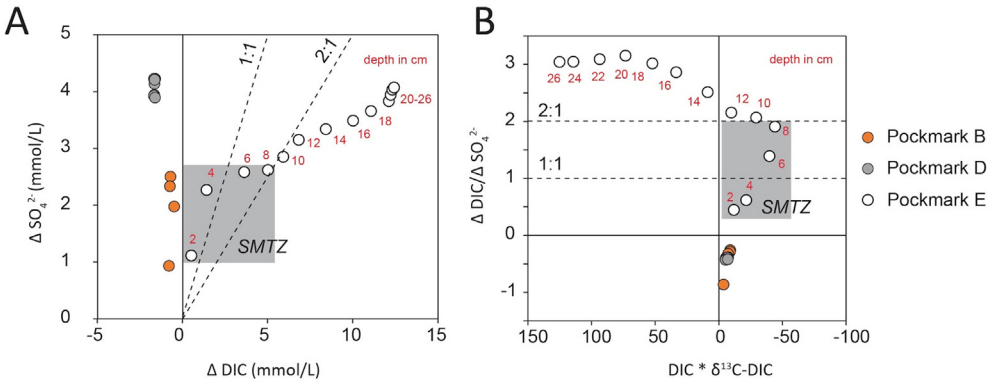

Fig. 13. A. Relationship between change in sulfate (ΔSO_4^{2-}) and change in dissolved inorganic carbon (ΔDIC), estimated for each porewater sample (for pockmark E, only the uppermost 26 cm are reported) relative to non-groundwater influenced near-bottom water data. Positive values of ΔDIC indicate an enrichment relative to near-bottom water, while positive values of ΔSO_4^{2-} indicate a depletion. B. Relationship between the ratio $\Delta DIC/\Delta SO_4^{2-}$ and the parameter DIC*δ^{13}C-DIC, a concentration-normalized expression of the stable isotopic ratio of DIC, for the same samples. In both A and B, depth (cm) of each sample at pockmark E is indicated in red, while 1:1 and 2:1 ratios of $\Delta DIC/\Delta SO_4^{2-}$ are indicated with dashed lines. Samples falling within the sulfate-methane transition zone (SMTZ) are indicated by the gray fields. (For interpretation of the references to colour in this figure legend, the reader is referred to the web version of this article.)

(Fig. 4 and Table 3). This implies that the active pockmarks B and D as well as the inactive pockmark E acted as sources of CH_4 to the seawater column. This is in agreement with the results of previous studies of CH_4 fluxes from pockmarks in the Baltic Sea (e.g., Bussmann and Suess, 1998; Idczak et al., 2020; Pimenov et al., 2010). However, in contrast to the studies by Bussmann and Suess (1998) in the Eckernförde Bay, and Pimenov et al. (2010) in the Gdansk Basin, (Fig. 1), CH_4 concentrations in the sea surface water (2 m) were elevated compared to the deeper water samples at all the pockmark site studied here (Fig. 4). This may result from the fact that the water columns above the pockmarks were stratified as indicated by the lower Cl^- concentrations measured at 2 m water depth compared to the Cl^- concentrations in 10 m water depth (Table 3). Obviously, a CH_4-enriched surface water layer, probably originating from river discharge, was encountered during the study in September 2019. The fact that CH_4 concentrations in the surface layer above the pockmarks were comparable to the CH_4 concentration at 2 m water depth at the offshore station J (Table 3) is line with the idea of a surface layer mainly affected by river discharge. The CH_4 bottom water concentrations measured during the seasonal study at the active pockmark site in Eckernförde Bay (Bussmann and Suess,1998) ranged from 0.011 (February 1999) to 0.441 µmol/L (December 1994) and were, thus, higher than the CH_4 concentrations at 10 m water depth (0.006 – 0.021 µmol/L) at the active pockmarks B and D but much lower than the CH_4 concentration in the bottom water (24.2 µmol/L) at the inactive pockmark E measured in September 2019. This indicates that CH_4 concentration gradients across the sediment–water interface at pockmark sites are highly variable in space and time. Therefore, any estimate of the overall input of CH_4 to the overlying water

column is associated with high uncertainty when neglecting the spatial–temporal variability of the CH_4 fluxes from pockmarks.

5.2. Microbial communities

Sediment in pockmark E can be considered "typical" for muddy sediments in the coastal Baltic Sea according to its microbial community structure, and the microbiological data largely concur with the sediment and porewater geochemistry. The high numbers of functional genes for sulfate reduction and methanogenesis agree with the high modelled reaction rates at pockmark E, compared to lower numbers of functional marker gene copies and reaction rates in pockmarks B and D. Furthermore, the archaeal and bacterial community in pockmark E resembles that of sediments from the nearby Pojo bay described in Myllykangas et al. (2020b). Archaeal taxa belonging to *Methanomicrobia* and *Thermoplasmata* as well as to *Woesearchaeota* were the most dominant groups in sediments of pockmark E as well as in Pojo Bay (Myllykangas et al., 2020b). Detection of the methanogenic community and higher numbers of methanogenesis marker gene *mcr*A correspond to high CH_4 concentrations in porewaters of the pockmark E, compared to the active pockmarks. The methanogenic community contains both hydrogenotrophs and aceticlastic methanogens. Woesearchaeota, a recently proposed archaeal phylum (Castelle et al., 2015) are defined as heterotrophs with metabolic deficiencies. Therefore, these organisms likely demand a partnering organism(s) or complementary existence of other microbes. A potential syntrophic relationship between methanogens and Woesearchaota has been suggested, as these organisms co-occur most often with *Methanobacteria* and *Methanomicrobia*, which were also found from pockmark E sediment (Liu et al., 2018). In addition to Woesearchaeota, Thermoplasmata complement the archaeal heterotrophic community in pockmark E.

Dominant bacteria in pockmark E were gammaproteobacteria, deltaproteobacterial sulfate reducers and *Bacteroidia* that in addition to corresponding to Baltic sea coastal sediments, also resemble surficial sediments of inactive pockmarks from Oslofjord, Norway (Haverkamp et al., 2014). Sulfate reducers (for example *Desulfubulbaceaea*) that were abundant in the sampled shallow sediments of pockmark E, have been detected elsewhere in Hanko cape sediment, where these have been shown to be resistant to hypoxic conditions (Sinkko et al., 2019). Sulfate reduction marker genes were present in order(s) of magnitude higher numbers in pockmark E compared to the other two pockmarks, again agreeing with the modelled high flux and sulfate reduction rates in the first $\sim$ 20 cm of pockmark E sediment. The detection of high numbers of both *mcr*A gene copies could indicate the presence of anaerobic methane oxidizing organisms (Hallam et al., 2003) in addition to methanogenesis, although only a small fraction of the archaeal community was representing those typical ANMEs (anaerobic methane-oxidizing archaea).

While the microbial community in pockmark E resembles other typical sediment communities in the pelagic Baltic Sea, the effect of SGD is clear in the pockmark B and especially in pockmark D sediment communities. Likely the groundwater advection obstructs the formation of SMTZ and thus limits the number of microbes involved in these processes. This could be due to a combination of low OM accumulation rates, low nutrient content of the groundwater or more oxygenated fluid seepage through the seafloor (Idczak et al., 2020). However, numerous nitrogen cycling organisms were detected in the active pockmarks. For example, OTUs affiliating with *Candidatus* Nitrosotalea were abundant in both pockmark D sediment and in groundwater from the observation well. The members of this candidate taxon have been described to be chemolithotrophic ammonia oxidizers (Lehtovirta-Morley et al., 2011, 2016; Prosser and Nicol, 2016). Interestingly, the two cultivated organisms of this lineage are obligate acidophiles (Prosser and Nicol, 2016). OTUs affiliating with another archaeal ammonia oxidizer *Nitrosoarchaeum* were detected in groundwater and both active pockmarks. *Nitrosoarchaeum* organisms are typical in aquatic environments with low salinity (Tolar et al., 2019), thus their abundance in groundwater and active pockmarks in our study is not surprising. Similarly, thaumarchaeal ammonia oxidizing archaea, which were dominating the seawater archaeal communities but also found in relatively high abundance in active pockmark sediments here, are major ammonia oxidizers in the oceans. *Nitrosopumilaceae* is especially dominant in oxygen minimum zones and the bathypelagic realm (Stahl and De La Torre, 2012; Muck et al., 2019).

Bacterial communities in pockmark D sediment differed from B and E with relatively high abundance of Nitrospira. These nitrifying bacteria are highly abundant, diverse and ubiquitous in natural ecosystems (Lücker et al., 2010). *Nitrospira* perform a critical second step of oxidation of nitrite to nitrate in nitrification, and some members of *Nitrospira* can perform complete nitrification from ammonia to nitrate (comammox)(Lücker et al., 2010; Koch et al., 2015; Koch et al., 2019). In the active pockmarks B and D therefore, a rather developed nitrogen cycle may exist that includes AOA converting ammonia to nitrite and secondly *Nitrospira*-like organisms oxidizing nitrite to nitrate. Efficient nitrogen cycling is especially important to ecosystems with limited amounts of substrates such as the active pockmarks in our case. The copy numbers of nitrogen cycling genes did not clearly reflect the concentrations of ammonium, with similar copy numbers for *amo*A at sites D and E (Fig. 6), but this might be due to the primer mismatches and unspecificity of the assay (Könneke et al., 2005). In addition, gene abundances are not to be used solely as a proxy for biogeochemical processes (Rocca et al., 2015).

The active pockmarks D and B appear to have the higher overall microbial density as well as higher functional gene copy numbers in the near-surface sediment, while in the inactive pockmark E has much higher copy numbers of all measured genes deeper in the sediment. As microbial activity and diversity hotspots are usually formed in the interfaces or mixing zones (McClain et al., 2003; Stegen et al., 2016), this can explain the higher copy numbers in the near-surface in active pockmarks. Namely, the physical forces, such as wave action, perturb the surface of the active

pockmarks mixing the fluffy organic substances on the sediment surface (see Supplementary Material, Fig. S1) into the first few centimeters of the sediment column (Huettel et al., 1996), thus providing more substrate for the microbial community compared to the deeper layers. These observations are confirmed by the reactive transport modeling results, which show that most of the reactions occur in the first few centimeters in the active pockmark sediments (Fig. 12).

Previous studies have shown that the freshwater and saline water mixing zone can be a diversity hotspot and induce the growth of rare taxa (Rocca et al., 2020; Ruiz-González et al., 2021 and references therein). However, the most diverse communities in our study were detected from the inactive pockmark E, where higher and more varied organic matter content likely plays a role in diversifying microbial communities (Delgado-Baquerizo et al., 2016). Specifically, the microbial community requires diverse abilities to degrade the versatile and likely more recalcitrant organic material ending up into the inactive pockmark sediment.

Based on our results on the microbial community composition in active and inactive pockmarks and the literature of the prevalent microbial communities hosted by the seafloor in the coastal Baltic sea, we can conclude that focused SGD at pockmark localities change the local seafloor microbial community composition. This can mean activation of rare biosphere but also inactivation of other members of the community, thus impacting the ecosystem processes (Allison and Martiny 2008, Ruiz-González et al., 2021 and references therein). However, a part of the community appears to be resistant to the environmental change, and when groundwater flow seizes and the pockmark turns into an inactive one, the microbial community will alter again towards the typical seafloor community. Therefore, although the microbial community structure changes, it appears to be able to perform as the original one, thus staying functionally redundant (Allison and Martiny, 2008).

5.3. Impact of SGD on biogeochemical processes and microbial community in the coastal zone

Discharge rates calculated for pockmarks B and D based on porewater Cl^- profiles are 0.02 cm d^{-1} and 0.31 cm d^{-1}, respectively (Fig. 5). These values are in general agreement with the simulated average discharge rates from the groundwater flow model of 0.22 cm d^{-1} (range 0.0–1.21 cm d^{-1}) and 0.28 cm d^{-1} (range 0.0–1.60 cm d^{-1}) for fine sand in the pockmark area for autumn 2017 and spring 2020, respectively (Luoma et al., 2021). The discharge rates (range 0.4–1.2 cm d^{-1}) estimated by ^{222}Rn measurements in May 2018 are higher but those rates were measured 1 m above pockmark bottom and integrate SGD over a larger area in each pockmark, with potential influence from the neighbouring pockmarks (Virtasalo et al., 2019). Unpublished underwater videos show patchy water discharge from the pockmark sediment surface. SGD rates similar to those estimated for pockmarks B and D have been calculated for pockmarks in Eckernförde Bay applying the same methodology (mean 0.05 cm d^{-1}, maximum 0.9 cm d^{-1}, Schlüter et al., 2004).

Our results demonstrate a strong impact of SGD on both biogeochemical reaction rates and the microbial community composition responsible for the reactions. Pockmark D shows the impacts most clearly, with high rates of vertical advection compressing the reactants available for biogeochemical reactions into a narrow zone at the sediment surface, leading to a focusing of the microbial community into the uppermost centimeters of the sediment column. Coupled with the physical effect of SGD reducing the accumulation of OM, this also results in the absence of a SMTZ at this site. This differs from other pockmark sites in the Baltic Sea (Schlüter et al., 2004; Idczak et al., 2020), suggesting that the groundwater impact on biogeochemistry is more pronounced at our study location.

With only a few published studies on microbiology at the groundwater–seawater mixing zones in coastal aquifers and especially in pockmarks associated with SGD, commonalities in microbial community structure in these systems are still the topic of active research (Ruiz-González et al., 2021). However, the microbial community structure in the active pockmarks B and D appears comparable to other SGD sites (Idczak et al., 2020; Adyasari et al., 2019, 2020). Gamma- and Alphaproteobacteria have been reported as the typical phyla in bacterial communities, similarly to our study. Salinity is identified as the most important factor in shaping the microbial community in oxic Baltic Sea sediments (Klier et al., 2018), hence the influence of groundwater on the communities at sites B, D, and E is partly expressed through contrasting salinity in the porewaters. Adyasari et al. (2019) reported *Burkholderia*-affiliating OTUs specifically representing fresh groundwater species. Similarly, in groundwater and the groundwater-dominated pockmark D, the proportions of *Burkholderiales* were relatively high. Salinity also has an effect on ammonia oxidizing microbial communities. According to Santoro et al. (2008), the bacterial dominance of the ammonia-oxidizing community declines with decreasing salinity. Similarly, in our study the abundance of ammonia oxidizing bacteria was lower in pockmark D with 0 salinity compared to pockmarks E and B where salinity was up to 6.

The inactive pockmark E displays a sedimentation rate several times higher than those documented for nearby organic-rich mud seafloor areas (0.3–0.5 cm yr^{-1}; Jokinen et al., 2020). In contrast, active pockmarks B and D have not had substantial deposition in the recent past due to strong SGD. This pronounced change in sedimentation rate upon deactivation of the pockmark E is important for understanding solute fluxes at the sediment–water interface at different stages of the life cycle of these systems. Since sediment deposition is the key control of OM delivery to the seafloor, and locally elevated deposition rates are expected to impact biogeochemical processes and microbial community composition in pockmark sediments (Idczak et al., 2020; O'Reilly et al., 2021) pockmark E expectedly displays far higher concentrations and fluxes of metabolites and CH_4 at the sediment–water interface than the active pockmarks. Moreover, the exceptionally high sedimentation rates in pockmark E suggest that inactive pockmarks

may act as a localized sediment trap due to their bathymetric configuration. This raises the possibility that inactive pockmarks in this system act as a hotspot for diffusive nutrient and gas fluxes to bottom waters, in contrast to the active pockmarks where solute fluxes are comparatively low despite high rates of advection (Table 5). These results highlight the importance of redox-dependent processes taking place in subterranean estuaries on the development of the chemical gradients at the fresh-salt water interface (Beck et al., 2007; Moosdorf et al., 2021). However, two further pertinent observations follow from this. Firstly, the diffusive fluxes of nutrients and CH_4 observed at inactive pockmarks result from OM cycling that may be considered "internal" to the marine system, because the primary source of the decaying OM in the sediment column is settling plankton detritus, while nutrient fluxes from SGD, even if small, must be considered as external inputs. Second, persistently inactive pockmarks are expected to fill in over time (Pau and Hammer, 2013), especially in coastal areas where sediment deposition predominantly takes place from lateral near-bottom sediment transport (Virtasalo et al., 2014; Jokinen et al., 2015). Thus, it is likely that the eventual fate of an inactive pockmark is a setting with a similar sedimentation regime to the surrounding seafloor areas. The overall effect of the SGD-related pockmarks on solute fluxes at any point in time is expected to be a function of the number of individual pockmarks, the rate of SGD, and the ratio of active to inactive pockmarks in the system as a whole.

6. CONCLUSIONS

This present study investigates how SGD impacts on biogeochemical processes and microbial community structure in a coastal sea area. The impacted active sites were compared to the diagenesis-dominated reference site.

SGD rates calculated from porewater Cl^- profiles show strong groundwater influence for pockmarks B and D. Their porewater systems are dominated by groundwater advection, which pushes the reactants available for biogeochemical reactions into a narrow zone at the sediment surface and leads to a focusing of the microbial activity into the top part of the sediment column. The advection further reduces the accumulation of OM in the surface sediments, resulting in the absence of SMTZ in these pockmarks. Reactive transport modelling consequently estimates low depth-integrated fluxes of SO_4^{2-}, CH_4, NH_4^+, DIC at pockmarks B and D, and further suggests Fe-AOM to contribute to methane oxidation in these pockmarks. Groundwater influence is visible in the microbial community structure of the active pockmarks, in which notable populations of ammonia-oxidizing archaea and nitrifying bacteria are of predominantly groundwater origin.

The lack of SGD permits rapid deposition of organic-rich mud in the currently inactive pockmark E. The porewater system at this site is dominated by diffusion, leading to orders of magnitude higher concentrations of CH_4, NH_4^+, DIC at depth compared to pockmarks B and D. The biogeochemical environment in pockmark E resembles typical organic-rich mud seafloor in the area, with sulfate reduction and methanogenesis as the dominant organic matter remineralization pathways. Reactive transport modelling shows that S-AOM occurs in the pockmark at a similar depth range to organoclastic sulfate reduction, and accounts for approximately 10% of total sulfate consumption at this depth. The presence of S-AOM is supported by porewater DIC, SO_4^{2-} and $\delta^{13}C$-DIC signatures. Methanogens are relatively more abundant in the archaeal community in pockmark E compared to active pockmarks, whereas sulfate reducers dominate the bacterial community. Although the depth-integrated fluxes of SO_4^{2-}, CH_4, NH_4, DIC at pockmark E are orders of magnitude higher compared to pockmarks B and D, processes at this site are driven by recent OM accumulation and thus represent internal recycling in the coastal sea. In contrast, processes at the active pockmarks B and D are partially mediated by SGD inputs and therefore effluxes of dissolved substances across the sediment–water interface must be considered to be influenced by external inputs to the sea.

DECLARATION OF COMPETING INTEREST

The authors declare that they have no known competing financial interests or personal relationships that could have appeared to influence the work reported in this paper.

ACKNOWLEDGEMENTS

This work resulted from the BONUS SEAMOUNT project supported by BONUS (Art 185), funded jointly by the EU and the Academy of Finland (grant no. 311983). CV was supported by DAAD via a PhD stipend (project no. 57381412). This study was conducted within the framework of the Research Training Group 'Baltic TRANSCOAST' funded by the DFG (Deutsche Forschungsgemeinschaft) under grant number GRK 2000 (www.baltic-transcoast.uni-rostock.de). This is Baltic TRANSCOAST publication no. GRK2000/0055. TJ acknowledges support from Academy Research Fellowship 317684. This study has utilized research infrastructure facilities provided by FINMARI (Finnish Marine Research Infrastructure network). Annette Kock (GEOMAR Helmholtz Centre for Ocean Research Kiel) is acknowledged for her support on the CH_4 water column measurements. Malin Bomberg and Päivi Kinnunen (VTT Technical Research Centre) are thanked for the opportunity to perform qPCR in their facilities. CV and MB wish to thank Iris Schmiedinger for expert laboratory and mass spectrometric support. Expert support from the captain and the crew of R/V Geomari and the people who further assisted in the fieldwork is gratefully acknowledged.

APPENDIX A. SUPPLEMENTARY MATERIAL

Supplementary material to this article can be found online at https://doi.org/10.1016/j.gca.2022.06.040.

REFERENCES

Adyasari D., Hassenrück C., Oehler T., Sabdaningsih A. and Moosdorf N. (2019) Microbial community structure associated with submarine groundwater discharge in northern Java (Indonesia). *Sci. Total Environ.* **689**, 590–601.

Adyasari D., Hassenrück C., Montiel D. and Dimova N. (2020) Microbial community composition across a coastal hydrological system affected by submarine groundwater discharge (SGD). *PLoS ONE* **15**, e0235235.

Allison S. D. and Martiny J. B. H. (2008) Resistance, resilience, and redundancy in microbial communities. *Proc. Natl. Acad. Sci. U. S. A.* **105**, 11512–11519.

Bange H. W., Bergmann K., Hansen H. P., Kock A., Koppe R., Malien F. and Ostrau C. (2010) Dissolved methane during hypoxic events at the Boknis Eck Time Series Station (Eckernförde Bay, SW Baltic Sea). *Biogeosciences* **7**, 1279–1284.

Beck A. J., Tsukamoto Y., Tovar-Sanchez A., Huerta-Diaz M., Bokuniewicz H. J. and Sañudo-Wilhelmy S. A. (2007) Importance of Geochemical Transformations in Determining Submarine Groundwater Discharge-Derived Trace Metal and Nutrient Fluxes. *Appl. Geochem.* **22**, 477–490.

Berg P., Rysgaard S. and Thamdrup B. (2003) Dynamic modeling of early diagenesis and nutrient cycling. A case study in an Arctic marine sediment. *Am. J. Sci.* **303**, 905–955.

Bernard R. J., Mortazavi B., Wang L., Ortmann A. C., MacIntyre H. and Burnett W. C. (2014) Benthic nutrient fluxes and limited denitrification in a sub-tropical groundwater-influenced coastal lagoon. *Mar. Ecol. Prog. Ser.* **504**, 13–26.

Berner R. A. (1970) Sedimentary pyrite formation. *Am. J. Sci.* **268**, 1–23.

Blott S. J. and Pye K. (2012) Particle size scales and classification of sediment types based on particle size distributions: review and recommended procedures. *Sedimentology* **59**, 2071–2096.

Böttcher M. E., Mallast U., Massmann G., Moosdorf N., Müller-Petke M. and Waska H. (2020) Coastal-Groundwater interfaces (submarine groundwater discharge). In *Ecohydrological Interfaces* (ed. S. Krause). Wiley, USA.

Boudreau B. P. (1987) A steady-state diagenetic model for dissolved carbonate species and pH in the porewaters of oxic and suboxic sediments. *Geochim. Cosmochim. Acta* **51**, 1985–1996.

Boudreau B. P. (1996) The diffusive tortuosity of fine-grained unlithified sediments. *Geochim. Cosmochim. Acta* **60**, 3139–3142.

Boudreau B. P. (1997) *Diagenetic Models and their Implementation: Modelling Transport and Reactions in Aquatic Sediments*. Springer-Verlag, Heidelberg.

Boudreau B. P., Meysman F. J. R. and Middelburg J. J. (2004) Multicomponent ionic diffusion in porewaters: coulombic effects revisited. *Earth Planet. Sci. Lett.* **222**, 653–666.

Brand W. A. and Coplen T. B. (2012) Stable Isotope Delts: Tiny, yet Robust Signatures in Nature. *Isotopes Environ. Health Stud.* **48**, 393–409.

Brüchert V. (1998) Early diagenesis of sulfur in estuarine sediments: the role of sedimentary humic and fulvic acids. *Geochim. Cosmochim. Acta* **62**, 1567–1586.

Bussmann I. and Suess E. (1998) Groundwater seepage in Eckernförde Bay (Western Baltic Sea): Effect on methane and salinity distribution of the water column. *Continen. Shelf Res.* **18**, 1795–1806.

Castelle C. J., Wrighton K. C., Thomas B. C., Hug L. A., Brown C. T., Wilkins M. J., Frischkorn K. R., Tringe S. G., Singh A., Markillie L. M., Taylor R. C., Williams K. H. and Banfield J. F. (2015) Genomic expansion of domain archaea highlights roles for organisms from new phyla in anaerobic carbon cycling. *Curr. Biol.* **25**, 690–701.

Cho H.-M., Kim G., Kwon E. Y., Moosdorf N., Garcia-Orellana J. and Santos I. R. (2018) Radium tracing nutrient inputs through submarine groundwater discharge in the global ocean. *Sci. Rep.* **8**, 2439.

Church T. M. (1996) An underground for the water cycle. *Nature* **380**, 579–580.

Delgado-Baquerizo M., Maestre F. T., Reich P. B., Jeffries T. C., Gaitan J. J., Encinar D., Berdugo M., Campbell C. D. and Singh B. K. (2016) Microbial diversity drives multifunctionality in terrestrial ecosystems. *Nat. Commun.* **7**, 1–8.

Donis D., Janssen F., Liu B., Wenzhöferö F., Dellwig O., Escher P., Spitzy A. and Böttcher M. E. (2017) Biogeochemical Impact of Submarine Groundwater Discharge on Coastal Surface Sands of the Southern Baltic Sea. *Est., Coast. Shelf Sci.* **189**, 131–142.

Egger M., Lenstra W., Jong D., Meysman F. J., Saoart C. J., Van der Veen C., Rockmann T., Gonzales S. and Slomp C. P. (2016b) Rapid sediment accumulation results in high methane effluxes from coastal sediments. *PLos One* **11**.

Egger M., Kraal P., Jilbert T., Sulu-Gambari F., Sapart C. J., Rockmann T. and Slomp C. P. (2016a) Anaerobic oxidation of methane alters sediment records of sulfur, iron and phosphorus in the Black Sea. *Biogeosciences* **13**, 5333–5355.

Egger M., Hagens M., Sapart C. J., Dijkstra N., van Helmond N. A. G. M., Mogollón J. M., Risgaard-Petersen N., van der Veen C., Kasten S., Riedinger N., Böttcher M. E., Röckmann T., Jørgensen B. B. and Slomp C. P. (2017) Iron oxide reduction in methane-rich deep Baltic Sea sediments. *Geochim. Cosmochim. Acta* **207**, 256–276.

Folk R. L. and Ward W. C. (1957) Brazos river bar: a study in the significance of grain size parameters. *J. Sediment. Petrol.* **27**, 3–26.

Froelich P. N., Klinkhammer G. P., Bender M. L., Luedtke N. A., Heath G. R., Cullen D., Dauphin P., Hammond D., Hartman B. and Maynard V. (1979) Early oxidation of organic matter in pelagic sediments of the eastern equatorial Atlantic: suboxic diagenesis. *Geochim. Cosmochim. Acta* **43**, 1075e1090.

Fyfe G. J. (1990) The effect of water depth on ice-proximal glaciolacustrine sedimentation: Salpausselkä I, southern Finland. *Boreas* **19**, 147–164.

Gantner S., Andersson A. F., Alonso-Sáez L. and Bertilsson S. (2011) Novel primers for 16S rRNA-based archaeal community analyses in environmental samples. *J. Microbiol. Methods* **84**, 12–18.

Giambalvo E. R., Steefel C. I., Fisher A. T., Rosenberg N. D. and Wheat C. G. (2002) Effect of fluid-sediment reaction on hydrothermal fluxes of major elements, eastern flank of the Juan de Fuca Ridge. *Geochim. Cosmochim. Acta* **66**, 1739–1757.

Grasshoff K., Kremling K. and Ehrhardt M. (2009) *Methods of Seawater Analysis*. John Wiley & Sons, Weinheim.

Hall G. E. M., Vaive J. E., Beer R. and Hoashi M. (1996) Selective leaches revisited, with emphasis on the amorphous Fe oxyhydroxide phase extraction. *J. Geochem. Explor.* **56**, 59–78.

Hallam S. J., Girguis P. R., Preston C. M., Richardson P. M. and DeLong E. F. (2003) Identification of methyl coenzyme M reductase A (mcrA) genes associated with methane-oxidizing archaea. *Appl. Environ. Microbiol.* **69**, 5483–5491.

Hammer Ø., Harper D. A. T. and Ryan P. D. (2001) Past: Paleontological Statistics Software Package for education and data analysis. *Paleontología Electrónica* **4**, 1–9 http://palaeo-electronica.org/2001_1/past/issue1_01.html.

Haverkamp T. H. A., Hammer Ø. and Jakobsen K. S. (2014) Linking Geology and Microbiology: Inactive Pockmarks Affect Sediment Microbial Community Structure. *PLoS ONE* **9**, e85990.

Hoffmann J. J. L., Schneider von Deimling J., Schröder J. F., Schmidt M., Held P., Crutchley G. J., Scholten J. and Gorman A. R. (2020) Complex eyed pockmarks and submarine groundwater discharge revealed by acoustic data and sediment cores in

Eckernförde Bay, SW Baltic Sea. *Geochem. Geophys. Geosyst.* **21**, e2019GC008825.

Holby O. and Evans S. (1996) The vertical distribution of Chernobyl-derived radionuclides in a Baltic Sea sediment. *J. Environ. Radioactiv.* **33**, 129–145.

Hu Y., Feng D., Liang Q., Xia Z., Linying C. and Chen D. (2015) Impact of anaerobic oxidation of methane on the geochemical cycle of redox-sensitive elements at cold-seep sites of the northern South China Sea. *Deep-Sea Res. Part II-Top. Stud. Oceanogr.* **122**, 84–94.

Huettel M., Ziebis W. and Forster S. (1996) Flow-induced uptake of particulate matter in permeable sediments. *Limnol. Oceanogr.* **4l**, 309–322.

Idczak J., Brodecka-Goluch A., Łukawska-Matuszewska K., Graca B., Gorska N., Klusek Z., Pezacki P. D. and Bolałek J. (2020) A geophysical, geochemical and microbiological study of a newly discovered pockmark with active gas seepage and submarine groundwater discharge (MET1-BH, central Gulf of Gdańsk, southern Baltic Sea). *Sci. Total Environ.* **742**, 140306.

Jensen J. B., Kuijpers A., Bennike O., Laier T. and Werner F. (2002) New geological aspects for freshwater seepage and formation in Eckernförde Bay, western Baltic. *Cont. Shelf Res.* **22**, 2159–2173.

Jilbert T., Asmala E., Schroder C., Tiihonen R., Myllykangas J., Virtasalo J. J., Kotilainen A., Peltola P., Ekholm P. and Hietanen S. (2018) Impacts of flocculation on the distribution and diagenesis of iron in boreal estuarine sediments. *Biogeosciences* **15**, 1243–1271.

Jilbert T., Cowie G., Lintumäki L., Jokinen S., Asmala E., Sun X., Mörth C.-M., Norkko A. and Humborg C. (2021) Anthropogenic inputs of terrestrial organic matter influence carbon loading and methanogenesis in coastal Baltic Sea sediments. *Front. Earth Sci.* **9**.

Johannes R. E. (1980) The ecological significance of the submarine groundwater discharge. *Mar. Ecol. Prog. Ser.* **3**, 365–373.

Jokinen S. A., Virtasalo J. J., Kotilainen A. T. and Saarinen T. (2015) Varve microfabric record of seasonal sedimentation and bottom flow-modulated mud deposition in the coastal northern Baltic Sea. *Mar. Geol.* **366**, 79–96.

Jokinen S. A., Jilbert T., Tiihonen-Filppula R. and Koho K. (2020) Terrestrial organic matter input drives sedimentary trace metal sequestration in a human-impacted boreal estuary. *Sci. Total Environ.* **717**, 137047.

Jørgensen B. B. (1978) A comparison of methods for the quantification of bacterial sulfate reduction in coastal marine sediments, II. Calculations from mathematical models. *Geomicrobiol. J.* **1**, 29–51.

Jørgensen B. B., Beulig F., Egger M., Petro C., Scholtze C. and Røy H. (2019) Organoclastic sulfate reduction in the sulfate-methane transition of marine sediments. *Geochim. Cosmochim. Acta* **254**, 231–325.

Jørgensen B. B. and Kasten S. (2006) Sulfur cycling and methane oxidation. In *Marine Geochemistry* (eds. H. D. Schulz and M. Zabel). Springer-Verlag, Berlin Heidelberg, pp. 271–309.

Kakkuri J. (2012) Fennoscandian land uplift: past, present and future. In *From the Earth's Core to Outer Space* (ed. I. Haapala). Springer-Verlag, Berlin Heidelberg, pp. 127–136.

Kastner M., Claypool G. and Robertson G. (2008) Geochemical constraints on the origin of the pore fluids and gas hydrate distribution at Atwater Valley and Keathley Canyon, northern Gulf of Mexico. *Mar. Pet. Geol.* **25**, 860–872.

Kielosto S., Kukkonen M., Stén C.-G. and Backman B. (1996) *Hangon ja Perniön kartta-alueiden maaperä. Summary: Quaternary deposits in the Hanko and Perniö map-sheet areas, Geological map of Finland 1 : 100 000. Explanation to the maps of Quaternary deposits, sheets 2011 and 2012*. Geological Survey of Finland, Espoo.

Kisand V., Cuadros R. and Wikner J. (2002) Phylogeny of culturable estuarine bacteria catabolizing riverine organic matter in the northern Baltic Sea. *Appl. Environ. Microbiol.* **68**, 379–388.

Klaminder J., Appleby P., Crook P. and Renberg I. (2012) Postdeposition diffusion of ^{137}Cs in lake sediment: implications for radiocaesium dating. *Sedimentology* **59**, 2259–2267.

Klier J., Dellwig O., Leipe T., Jürgens K. and Herlemann D. P. R. (2018) Benthic Bacterial Community Composition in the Oligohaline-Marine Transition of Surface Sediments in the Baltic Sea Based on rRNA Analysis Available at:. *Front. Microbiol.* **9**, 236 http://journal.frontiersin.org/article/10.3389/fmicb.2018.00236/full.

Knee K. and Paytan A. (2011) 4.08 submarine groundwater discharge: a source of nutrients, metals, and pollutants to the coastal ocean. *Treatise Estuar. Coast. Sci.* **4**, 205–233.

Koch H., Lücker S., Albertsen M., Kitzinger K., Herbold C., Spieck E., Nielsen P. H., Wagner M. and Daims H. (2015) Expanded metabolic versatility of ubiquitous nitrite-oxidizing bacteria from the genus Nitrospira. *Proc. Natl. Acad. Sci. U. S. A* **112**, 11371–11376.

Koch H., van Kessel M. A. H. J. and Lücker S. (2019) Complete nitrification: insights into the ecophysiology of comammox Nitrospira. *Appl. Microbiol. Biotechnol.* **103**, 177–189.

Könneke M., Bernhard A. E., de la Torre J. R., Walker C. B., Waterbury J. B. and Stahl D. (2005) Isolation of an autotrophic ammonia-oxidizing marine archaeon. *Nature* **437**, 543–546.

Kotwicki L., Grzelak K., Czub M., Dellwig O., Gentz T., Szymczycha B. and Böttcher M. E. (2014) Submarine groundwater discharge to the Baltic coastal zone: Impacts on the meiofaunal community. *J. Mar. Syst.* **129**, 118–126.

Kozich J. J., Westcott S. L., Baxter N. T., Highlander S. K. and Schloss P. D. (2013) Development of a dual-index sequencing strategy and curation pipeline for analyzing amplicon sequence data on the Miseq Illumina sequencing platform. *Appl. Environ. Microbiol.* **79**, 5112–5120.

Kujansuu R., Uusinoka R., Herola E. and Sten C.-G. (1993) *Tammisaaren kartta-alueen maaperä. Summary Quaternary deposits in the Tammisaari map-sheet area, Geological map of Finland 1 : 100 000. Explanation to the maps of Quaternary deposits, sheet 2014*. Geological Survey of Finland, Espoo.

Kumblad L. and Bradshaw C. (2008) *Element composition of biota, water and sediment in the Forsmark area, Baltic Sea: concentrations, bioconcentration factors and partitioning coefficients (Kd) of 48 elements*. Swedish Nuclear Fuel and Waste Management Co, Stockholm.

Lecher A. L. and Mackey K. R. M. (2018) Synthesizing the Effects of Submarine Groundwater Discharge on Marine Biota. *Hydrology* **5**, 60.

Lee E., Shin D., Hyun S. P., Ko K. S., Moon H. S., Koh D. C., Ha K. and Kim B. Y. (2017) Periodic change in coastal microbial community structure associated with submarine groundwater discharge and tidal fluctuation. *Limnol. Oceanogr.* **62**, 437–451.

Lehtovirta-Morley L. E., Stoecker K., Vilcinskas A., Prosser J. I. and Nicol G. W. (2011) Cultivation of an obligate acidophilic ammonia oxidizer from a nitrifying acid soil. *Proc. Natl. Acad. Sci. U. S. A.* **108**, 15892–15897.

Lehtovirta-Morley L. E., Sayavedra-Soto L. A., Gallois N., Schouten S., Stein L. Y., Prosser J. I. and Nicol G. W. (2016) Identifying Potential Mechanisms Enabling Acidophily in the Ammonia-Oxidizing Archaeon *Candidatus Nitrosotalea devanaterra*. *Appl. Environ. Microbiol.* **82**, 2608–2619.

Liu X., Li M., Castelle C. J., Probst A. J., Zhou Z., Pan J., Liu Y., Banfield J. F. and Gu J.-D. (2018) Insights into the ecology,

evolution, and metabolism of the widespread Woesearchaeotal lineages Available at:. *Microbiome* **6**, 102 https://microbiomejournal.biomedcentral.com/articles/10.1186/s40168-018-0488-2.

Lücker S., Wagner M., Maixner F., Pelletier E., Koch H., Vacherie B., Rattei T., Damsté J. S. S., Spieck E., Le Paslier D. and Daims H. (2010) A Nitrospira metagenome illuminates the physiology and evolution of globally important nitrite-oxidizing bacteria. *Proc. Natl. Acad. Sci. U. S. A.* **107**, 13479–13484.

Luijendijk E., Gleeson T. and Moosdorf N. (2020) Fresh groundwater discharge insignificant for the world's oceans but important for coastal ecosystems. *Nat. Commun.* **11**, 1260.

Luoma S., Majaniemi J., Pullinen A., Mursu J. and Virtasalo J. J. (2021) Geological and groundwater flow model of a submarine groundwater discharge site at Hanko (Finland), northern Baltic Sea. *Hydrogeol. J.* **29**, 1279–1297.

McClain M. E., Boyer E. W., Dent C. L., Gergel S. E., Grimm N. B., Groffman P. M., Hart S. C., Harvey J. W., Johnston C. A., Mayorga E., McDowell W. H. and Pinay G. (2003) Biogeochemical Hot Spots and Hot Moments at the Interface of Terrestrial and Aquatic Ecosystems. *Ecosystems* **6**, 301–312.

Merkouriadi I. and Leppäranta M. (2014) Long-term analysis of hydrography and sea-ice data in Tvärminne, Gulf of Finland, Baltic Sea. *Clim. Change* **124**, 849–859.

Meysman F. J. R., Boudreau B. P. and Middelburg J. J. (2005) Modeling reactive transport in sediments subject to bioturbation and compaction. *Geochim. Cosmochim. Acta* **69**, 3601–3617.

Middelburg J. J. (1989) A simple rate model for organic matter decomposition in marine sediments. *Geochim. Cosmochim. Acta* **53**, 1577–1581.

Miller C. M., Dickens G. R., Jakobsson M., Johansson C., Koshurnikov A., O'Regan M., Muschitiello F., Stranne C. and Morth C. (2017) Pore water geochemistry along continental slopes north of the East Siberian Sea: inference of low methane concentrations. *Biogeosciences* **14**, 2929–2953.

Mogollón J. M., Dale A. W., Jensen J. B., Schlüter M. and Regnier P. (2013) A method for the calculation of anaerobic oxidation of methane rates across regional scales: an example from the Belt Seas and The Sound (North Sea-Baltic Sea transition). *Geo-Mar. Lett.* **33**, 299–310.

Moodley L., Middelburg J. J., Herman P. M. J., Soetaert K. and de Lange G. J. (2005) Oxygenation and organic-matter preservation in marine sediments: Direct experimental evidence from ancient organic carbon–rich deposits. *Geology* **33**, 889–892.

Moore W. S. (2010) The effect of submarine groundwater discharge on the ocean. *Annu. Rev. Mar. Sci.* **2**, 59–88.

Moosdorf N., Böttcher M. E., Adyasari D., Erkul E., Gilfedder B., Greskowiak J., Jenner A.-K., Kotwicki L., Massmann G., Petke M. M., Oehler T., Post V., Prien R., Scholten J., Siemon B., von Ahn C. M. E., Walther M., Waska H., Wunderlich T. and Mallast U. (2021) A State-Of-The-Art Perspective on the Characterization of Subterranean Estuaries at the Regional Scale. *Front. Earth Sci.* **9**, 601293.

Muck S., De Corte D., Clifford E. L., Bayer B., Herndl G. J. and Sintes E. (2019) Niche Differentiation of Aerobic and Anaerobic Ammonia Oxidizers in a High Latitude Deep Oxygen Minimum Zone Available at:. *Front. Microbiol.* **10**, 2141 https://www.frontiersin.org/article/10.3389/fmicb.2019.02141/full.

Muniruzzaman M. and Rolle M. (2015) Impact of multicomponent ionic transport on pH fronts propagation in saturated porous media. *Water Resour. Res.* **51**, 6739–6755.

Muniruzzaman M. and Rolle M. (2017) Experimental investigation of the impact of compound-specific dispersion and electrostatic interactions on transient transport and solute breakthrough. *Water Resour. Res.* **53**, 1189–1209.

Muniruzzaman M., Haberer C. M., Grathwohl P. and Rolle M. (2014) Multicomponent ionic dispersion during transport of electrolytes in heterogeneous porous media: Experiments and model-based interpretation. *Geochim. Cosmochim. Acta* **141**, 656–669.

Myllykangas J., Jilbert T., Jakobs G., Rehder G., Werner J. and Hietanen S. (2017) Effects of the 2014 major Baltic inflow on methane and nitrous oxide dynamics in the water column of the central Baltic Sea. *Earth Syst. Dyn.* **8**, 817–826.

Myllykangas J., Hietanen S. and Jilbert T. (2020a) Legacy effects of eutrophication on modern methane dynamics in a boreal estuary. *Estuaries Coasts* **43**, 189–206.

Myllykangas J. P., Rissanen A. J., Hietanen S. and Jilbert T. (2020b) Influence of electron acceptor availability and microbial community structure on sedimentary methane oxidation in a boreal estuary. *Biogeochemistry* **148**, 291–309.

O'Reilly S. S., Jordan S. F., Monteys X., Simpson A. J., Allen C. C. R., Szpak M. T., Murphy B. T., McCarron S. G., Soong R., Wu B., Jenne A., Grey A. and Kelleher B. P. (2021) Production of methane and gaseous compounds by surface microbial activity in a small pockmark field, Dunmanus Bay, Ireland. *Estuar. Coast. Shelf Sci.* **255**, 107340.

Oehler T., Ramasamy M., George M. E., Babu S. D. S., Dähnke K., Ankele M., Böttcher M. E., Santos I. R. and Moosdorf N. (2021) Tropical beaches attenuate groundwater nitrogen pollution flowing to the ocean. *Environ. Sci. Technol.* **55**, 8432–8438.

Ojala A. E. K., Luoto T. P. and Virtasalo J. J. (2017) Establishing a high-resolution surface sediment chronology with multiple dating methods – testing ^{137}Cs determination with Nurmijärvi clastic-biogenic varves. *Quat. Geochronol.* **37**, 32–41.

Passier H. F., Böttcher M. E. and Lange G. J. D. (1999) Sulphur Enrichment in Organic Matter of Eastern Mediterranean Sapropels: A Study of Sulphur Isotope Partitioning. *Aquat. Geochem.* **5**, 99–118.

Pau M. and Hammer Ø. (2013) Sediment mapping and long-term monitoring of currents and sediment fluxes in pockmarks in the Oslofjord, Norway. *Mar. Geol.* **346**, 262–273.

Penttilä A., Slade E. M., Simojoki A., Riutta T., Minkkinen K. and Roslin T. (2013) Quantifying beetle-mediated effects on gas fluxes from dung pats. *PLoS One* **8**.

Pimenov N. V., Ulyanova M. O., Kanapatsky T. A., Veslopolova E. F., Sigalevich P. A. and Sivkov V. V. (2010) Microbially mediated methane and sulfur cycling in pockmark sediments of the Gdansk Basin, Baltic Sea. *Geo-Marine Letters* **30**, 439–448.

Pirinen P., Simola H., Aalto J., Kaukoranta J.-P., Karlsson P. and Ruuhela R. (2012) *Climatological Statistics of Finland 1981–2010*. Finnish Meteorological Institute, Helsinki.

Prosser J. I. and Nicol G. W. (2016) *Candidatus* Nitrosotalea. In *Bergey's Manual of Systematics of Archaea and Bacteria* (ed. W. B. Whitman). Wiley, Hoboken, New Jersey, pp. 1–7.

Reed D. C., Slomp C. P. and Gustafsson B. G. (2011a) Sedimentary phosphorus dynamics and the evolution of bottom-water hypoxia: A coupled benthic-pelagic model of a coastal system. *Limnol. Oceanogr.* **56**, 1075–1092.

Reed D. C., Slomp C. P. and de Lange G. J. (2011b) A quantitative reconstruction of organic matter and nutrient diagenesis in Mediterranean Sea sediments over the Holocene. *Geochim. Cosmochim. Acta.* **75**, 5540–5558.

Rocca J. D., Simonin M., Bernhardt E. S., Washburne A. D. and Wright J. P. (2020) Rare microbial taxa emerge when communities collide: freshwater and marine microbiome responses to experimental mixing. *Ecology* **101**, [Accessed November 4, 2021].

Rocca J. D., Hall E. K., Lennon J. T., Evans S. E., Waldrop M. P., Cotner J. B., Nemergut D. R., Graham E. B. and Wallenstein M. D. (2015) Relationships between protein-encoding gene abundance and corresponding process are commonly assumed yet rarely observed. *ISME J.* **9**, 1693–1699.

Rolle M., Muniruzzaman M., Haberer C. M. and Grathwohl P. (2013) Coulombic effects in advection-dominated transport of electrolytes in porous media: Multicomponent ionic dispersion. *Geochim. Cosmochim. Acta* **120**, 195–205.

Rolle M., Sprocati R., Masi M., Jin B. and Muniruzzaman M. (2018) Nernst-Planck-based description of transport, Coulombic interactions, and geochemical reactions in porous media: Modeling approach and benchmark experiments. *Water Resour Res.* **54**, 3176–3195.

Rooze J., Egger M., Tsandev I. and Slomp C. P. (2016) Iron-dependent anaerobic oxidation of methane in coastal surface sediments: Potential controls and impact. *Limnol. Oceanogr.* **61**, S267–S282.

Ruiz-González C., Rodellas V. and Garcia-Orellana J. (2021) The microbial dimension of submarine groundwater discharge: current challenges and future directions. *FEMS Microbiol. Rev.* **45**, 1–25.

Saarnisto M. and Saarinen T. (2001) Deglaciation chronology of the Scandinavian Ice Sheet from the Lake Onega Basin to the Salpausselkä end moraines. *Global Planet. Change* **31**, 387–405.

Santoro A. E., Francis C. A., de Sieyes N. R. and Boehm A. B. (2008) Shifts in the relative abundance of ammonia-oxidizing bacteria and archaea across physicochemical gradients in a subterranean estuary. *Environ. Microbiol.* **10**, 1068–1079.

Santos I. R., Chen X., Lecher A. L., Sawyer A. H., Moosdorf N., Rodellas V., Tamborski J., Cho H.-M., Dimova N., Sugimoto R., Bonaglia S., Li H., Hajati M.-C. and Li L. (2021) Submarine groundwater discharge impacts on coastal nutrient biogeochemistry. *Nat. Rev. Earth Environ.* **2**, 307–323.

Sauramo M. (1923) Studies on the Quaternary varve sediments in southern Finland. *Bulletin de la Commission géologique de Finlande* **60**, 1–164.

Sawicka J. E. and Brüchert V. (2017) Annual variability and regulation of methane and sulfate fluxes in Baltic Sea estuarine sediments. *Biogeosciences* **14**, 325–339.

Schaller S., Böttcher M. E., Buechi M. W., Epp L. S., Fabbri S. C., Gribenski N., Harms U., Krastel S., Liebezeit A., Lindhorst K., Marxen H., Raschke U., Schleheck D., Schmiedinger I., Schwalb A., Vogel H., Wessels M. and Anselmetti F. S. (2022) Postglacial evolution of Lake Constance: sedimentological and geochemical evidence from a deep-basin sediment core. *Swiss J. Geosci.* **115**. doi.10.1186/s00015-022-00412-1.

Schlüter M., Sauter E. J., Andersen C. E., Dahlgaard H. and Dando P. R. (2004) Spatial distribution and budget for submarine groundwater discharge in Eckernförde Bay (western Baltic Sea). *Limnol. Oceanogr.* **49**, 157–167.

Sinkko H., Hepolehto I., Lyra C., Rinta-Kanto J. M., Villnäs A., Norkko J., Norkko A. and Timonen S. (2019) Increasing oxygen deficiency changes rare and moderately abundant bacterial communities in coastal soft sediments. *Sci. Rep.*, 9.

Stahl D. A. and de la Torre J. R. (2012) Physiology and Diversity of Ammonia-Oxidizing Archaea. *Annu. Rev. Microbiol.* **66**, 83–101.

Stegen J. C., Fredrickson J. K., Wilkins M. J., Konopka A. E., Nelson W. C., Arntzen E. V., Chrisler W. B., Chu R. K., Danczak R. E., Fansler S. J., Kennedy D. W., Resch C. T. and Tfaily M. (2016) Groundwater–surface water mixing shifts ecological assembly processes and stimulates organic carbon turnover. *Nat. Commun.* **7**, 11237.

Szymczycha B., Vogler S. and Pempkowiak J. (2012) Nutrient fluxes via submarine groundwater discharge to the Bay of Puck, southern Baltic Sea. *Sci. Total Environ.* **438**, 86–93.

Thang N. M., Bruechert V., Formolo M., Wegener G., Ginters L., Jørgensen B. B. and Ferdelman T. G. (2013) The impact of sediment and carbon fluxes on the biogeochemistry of methane and sulfur in littoral Baltic Sea sediments (Himmerfjarden, Sweden). *Estuaries Coasts* **36**, 98–115.

Tolar B. B., Mosier A. C., Lund M. B. and Francis C. A. (2019). In *Nitrosarchaeum. Bergey's Manual of Systematics of Archaea and Bacteria*. Wiley, Hoboken, New Jersey, pp. 1–9.

Turner S., Pryer K. M., Miao V. P. W. and Palmer J. D. (1999) Investigating deep phylogenetic relationships among cyanobacteria and plastids by small subunit rRNA sequence analysis. In *Journal of Eukaryotic Microbiology Society of Protozoologists*, pp. 327–338.

Vallius H. (2014) Heavy metal concentrations in sediment cores from the northern Baltic Sea: declines over the last two decades. *Mar. Pollut. Bull.* **79**, 359–364.

Vanek V. and Lee D. R. (1991) Mapping submarine groundwater discharge areas - an example from Laholm Bay, southwest Sweden. *Limnol. Oceanogr.* **36**, 1250–1262.

Virtasalo, J.J., 2022. Multielement and grain-size data of short sediment cores from the Hanko submarine groundwater discharge site, northern Baltic Sea, Finland. *PANGAEA*, doi:10.1594/PANGAEA.942288.

Virtasalo, J.J., von Ahn, C., Jilbert, T., Bange, H.W., Jenner, A., Böttcher, M.E., Luoma, S., Lahaye, Y., 2022. Multielement, Cl^-, CH_4, NH_4, DIC concentrations and δ^2H, $\delta^{18}O$, δ^7Li, $\delta^{34}S$, $^{87}S/^{86}Sr$, $\delta^{13}C$-DIC composition of groundwater, seawater, and pockmark porewater from Hanko SGD site, Finland. *PANGAEA*, doi:10.1594/PANGAEA.942547.

Virtasalo J. J., Schröder J. F., Luoma S., Majaniemi J., Mursu J. and Scholten J. (2019) Submarine groundwater discharge site in the First Salpausselkä ice-marginal formation, south Finland. *Solid Earth* **10**, 405–423.

Virtasalo J. J., Ryabchuk D., Kotilainen A. T., Zhamoida V., Grigoriev A., Sivkov V. and Dorokhova E. (2014) Middle Holocene to present sedimentary environment in the easternmost Gulf of Finland (Baltic Sea) and the birth of the Neva River. *Mar. Geol.* **350**, 84–96.

von Ahn C. M. E., Scholten J. C., Malik C., Feldens P., Liu B., Dellwig O., Jenner A.-K., Papenmeier S., Schmiedinger I., Zeller M. A. and Böttcher M. E. (2021) A Multi-Tracer Study of Fresh Water Sources for a Temperate Urbanized Coastal Bay (Southern Baltic Sea). *Front. Environ. Sci.* **9**, 642346.

Wang Y. and Van Cappellen P. (1996) A multicomponent reactive transport model of early diagenesis?: Application to redox cycling in coastal marine sediments. *Geochim. Cosmochim. Acta* **60**, 2993–3014.

Werne J. P., Lyons T. W., Hollander D. J., Schouten S., Hopmans E. C. and Sinninge Damsté J. S. (2008) Investigating pathways of diagenetic organic matter sulfurization using compound-specific sulfur isotope analysis. *Geochim. Cosmochim. Acta* **72**, 3489–3502.

Westrich J. T. and Berner R. A. (1984) The role of sedimentary organic matter in bacterial sulfate reduction: The *G* model tested. *Limnol. Oceanogr.* **29**, 236–249.

Whiticar M. (1999) Carbon and hydrogen isotope systematics of bacterial formation and oxidation of methane. *Chem. Geol.* **161**, 291–314.

Whiticar M. J. (2002) Diagenetic relationship of methanogenesis, nutrients, acoustic turbidity, pockmarks and freshwater seepages in Eckernförde Bay. *Mar. Geol.* **182**, 29–53.

Whiticar M. J. and Werner F. (1981) Pockmarks: submarine vents of natural gas or freshwater seeps. *Geo-Mar. Lett.* **1**, 193–199.

Wiesenburg D. and Guinasso N. (1979) Equilibrium solubilities of methane, carbon-monoxide, and hydrogen in water and sea-water. *J. Chem. Eng. Data* **24**, 356–360.

Winde V., Böttcher M. E., Escher P., Böning P., Beck M., Liebezeit G. and Schneider B. (2014) Tidal and spatial variations of DI13C and aquatic chemistry in a temperate tidal basin during winter time. *J. Mar. Syst.* **129**, 394–402.

Wolski T., Wiśniewski B., Giza A., Kowalewska-Kalkowska H., Boman H., Grabbi-Kaiv S., Hammarklint T., Holfort J. and Lydeikaite Z. (2014) Extreme sea levels at selected stations on the Baltic Sea coast. *Oceanologia* **56**, 259–290.

Wu Z., Liu B., Escher P., Kowalski N. and Böttcher M. E. (2018) Carbon diagenesis in different sedimentary environments of the subtropical Beibu Gulf, South China Sea. *J. Mar. Sys.* **186**, 68–84.

Zhou Y. Q., Sawyer A. H., David C. H. and Famiglietti J. S. (2019) Fresh submarine groundwater discharge to the near-global coast. *Geophys. Res. Lett.* **46**, 5855–5863.

Associate editor: Filip Meysman

Chapter 5. Spatial and temporal variations in the isotope hydrobiogeochemistry of a managed river draining towards the southern Baltic Sea

Spatial and temporal variations in the isotope hydrobiogeochemistry of a managed river draining towards the southern Baltic Sea

Cátia Milene Ehlert von Ahn[1], Michael Ernst Böttcher*[1,2,3], Christoph Malik[1,4], Julia Westphal[1,5], Benjamin Rach[1,6], Carla Nantke[1], Anna-Kathrina Jenner[1], Rhodelyn Saban[1], Vera Winde[1,7], Iris Schmiedinger[1]

[1]Geochemistry & Isotope Biogeochemistry, Leibniz Institute for Baltic Sea Research (IOW), D-18119 Warnemünde, Germany
[2]Marine Geochemistry, University of Greifswald, D- 17489 Germany
[3]Interdisciplinary Faculty, University of Rostock, D- 18055, Germany
[4]present address: Umweltplan, D-17489 Greifswald, Germany
[5]present address: National Agency of Agriculture and the Environment of Mecklenburg-Western Pomerania (Stalu-MM), D-18069 Rostock, Germany
[6]present address: Bioplan, Institute of Applied Biology and Landscape Management, D-18211 Nienhagen, Germany
[7]present address: Hydroisotop, D-85301 Schweitenkirchen, Germany
* michael.boettcher@io-warnemuende.de

Abstract

The flow path of a river draining a lowland in the southern Baltic Sea, the Warnow River, was investigated to evaluate its freshwater composition as a source of dissolved substances to regional coastal waters. A spatial study was carried out on April 2019 to follow the variations from the source to the estuary. A temporal study in the composition as a function of the season, during 5 years (2017-2021), was carried out at a site just before the river reaches the estuary. Surface water was sampled to analyze major and tracer elements, stable (H, C, O, S), and unstable (Ra) isotopes. The results show that the composition of the Warnow River along the flow path is controlled by a complex interplay between in-situ processes, exchange with the atmosphere, diffuse groundwater, and surface water inlets. On a temporal scale, pH, nutrient, and redox-sensitive trace element concentrations are strongly impacted by pelagic primary production in spring. During summer and autumn, influences occurred by benthic microbial activity, associated diffusive release from soils/sediments, and surface water inlets. Throughout the investigation period, the Warnow River was a source of isotopically light CO_2 to the atmosphere and DIC to the estuarine waters. The delivered DIC concentrations seem to vary with the season due to changes in biological pelagic and benthic activity. DOC was derived from a mixture of C3 organic sources and fertilizers. From concentration-discharge relationships, examples of dilution, mobilization, and chemostasis trends were found. Discharge-controlled seasonal

trends are superimposed by system-internal processes and the hydrological consequences of river and drainage management. Our analysis thus provides new insights into the controls on the variations of water and solutes in a managed river at the land-sea interface as part of the regional hydrological cycle of a lowland catchment-coastal water system.

Key words: Multiisotopes (H, C, O, S, Ra), carbon system, nutrients, trace elements, sulfur cycle, lowland catchment, Baltic Sea

Introduction

The transfer of freshwater, particulate, and dissolved substances from the continents to the oceans takes place mainly via surface runoff (Degens et al., 1991; Walsh, 1991; Wollast, 1991; Dürr et al., 2011; Hartmann et al., 2014) and submarine groundwater discharge (SGD; Knee and Paytan, 2011; Luijendijk et al., 2020; Moosdorf et al., 2021). the fresh-salt water mixing zone creates a 'hot zone' in the ecohydrological land-sea interface and provides reactants for biogeochemical element transformations. These reactions control the release of elements that finally discharge to the coastal waters (Lerman et al., 2004; 2007; Hartmann et al., 2014; Moosdorf et al., 2021).

The processes impacting the river hydrochemistry along the flow path are dominated mainly by the mixing between ground and surface waters, exchange with the atmosphere, and river-bed sediments (House & Denison, 1997, 2002; Kronvang et al., 2007; Nutzmann & Lewandowski, 2009; Huotarie et al., 2013; Cantera et al., 2018) They are further superimposed by biological processes like photosynthesis, microbially catalyzed degradation of organic matter and associated chemical reactions. These processes are, in addition, closely coupled to the climate zone, the soils, the land use in the catchment area, the annual flow regime, and the residence time of water (Pawellek et al., 2005).

Direct and indirect anthropogenic activities have physically reshaped the river pathways, modified the flow regime, and changed the biogeochemistry at the land-ocean boundary in many regions of the world (Lerman et al., 2004). Climate change induced sea-level rise, coastal hydrography, and groundwater recharge modifications. Changes in near-coastal waters impact the overall processes in the surface and

subsurface estuaries (Humborg et al., 2002, 2006; Knee and Paytan, 2011; Han et al., 2018). However, the quantitative controls for the hydrology at the land-ocean interface belong to the still unsolved problems in hydrology (Blöschl et al., 2019).

The Warnow River (WR) is a managed river draining a coastal lowland catchment towards the southern Baltic Sea, Germany. Due to its partial regulation and the shallow physical gradient of its pathway, parts resemble a lake system (e.g., Bischoftsky & Nausch, 2019). The overall hydrological balance of the WR is controlled by an artificial drainage system in the lowland catchment (Hennig & Hilgert, 2007; Deutsch et al., 2006; Kahle et al., 2018). The surface water of WR was previously the subject of primarily spatial hydrochemical research focusing mainly on the dynamics of nitrogen and phosphorous (Nausch et al., 2017; Kahle et al., 2018; Bitschofsky & Nausch, 2019). It is worth noting that, within the past 15 years, anthropogenic influence regarding nutrients has improved.

The present study presents a spatial and temporal (2017-2022) investigation of the fresh water part of the WR before entering the estuarine mixing zone. The results of hydrogeochemical and multi-isotope (H, C, O, S, Ra) measurements are combined for the first time. Our results demonstrate the importance of system internal processes for nutrient, trace metals, and sulfur-carbon cycling in response to the slow flow regime of the WR. And the importance of seasonality on the biogeochemical transformations and their impact on riverine element fluxes toward the estuary. It additionally allows for an endmember characterization of fresh surface water for a compositional differentiation from other freshwater sources, like SGD.

2. Materials and Methods

2.1. Study area

The Warnow River is located in Mecklenburg-Western Pomerania (northeastern Germany). It drains a coastal lowland catchment into the Southern Baltic Sea at the city of Rostock (Figure 1). The WR has a length of 155 km and a drainage area of about 3280 km^2, which is mainly dominated by agricultural and forested areas (Pagenkopf, 2001; Bitschofsky & Nausch, 2019).

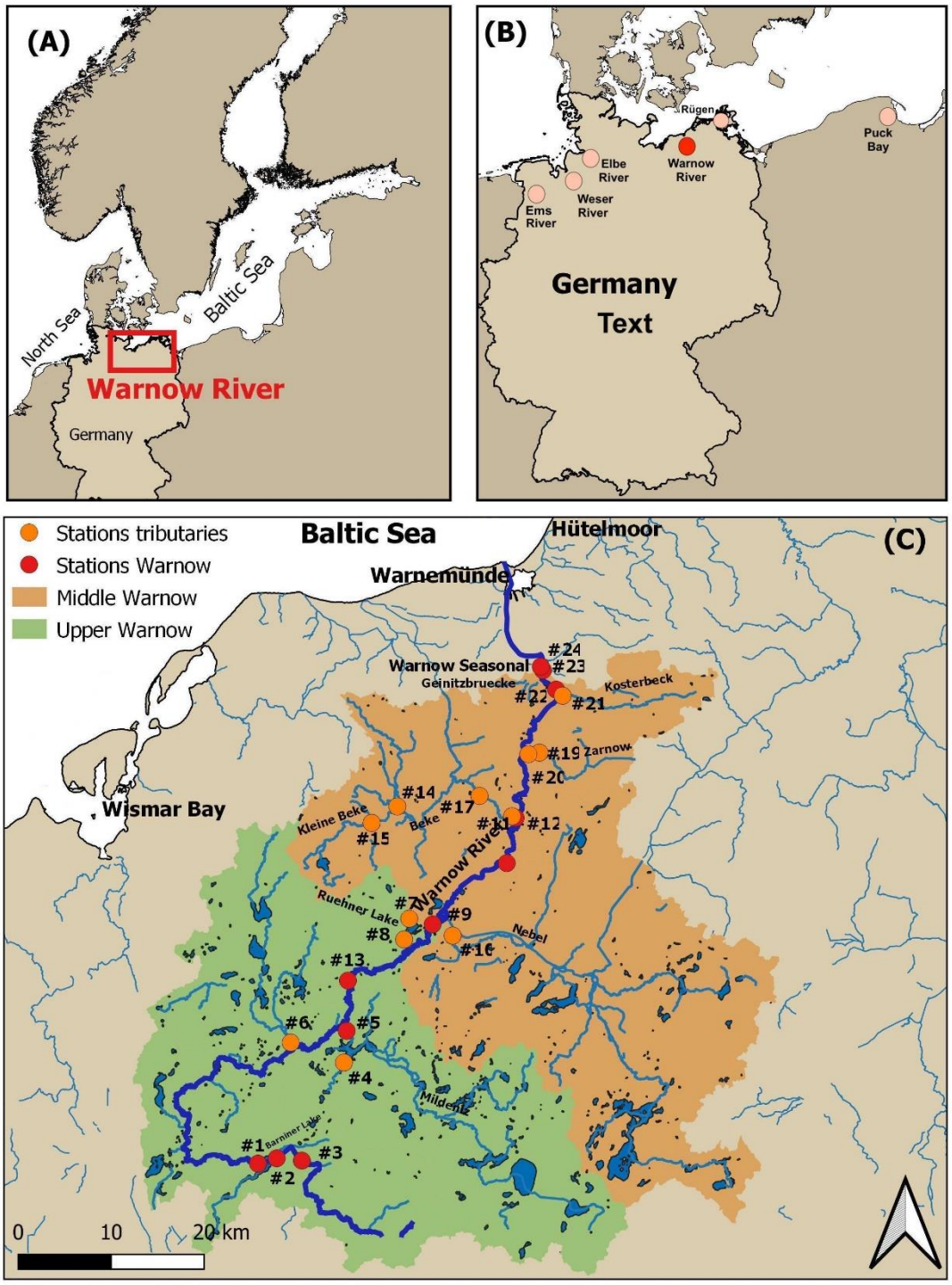

Figure 1 – (A) Baltic Sea Map showing the location of Warnow river. (B) Map of Germany showing the location of the rivers presented in Table 2, and the location of Puck Bay in Poland. (C) Map of the sampling locations along the Warnow River (red), its tributaries (orange), and the catchments of the upper (green) and middle (brown) courses. Source shapefiles: EAE, LUNG.

The WR is the second largest river system of Mecklenburg-Western Pomerania (Jurasinski et al., 2018), with a long-term average discharge of 12.3 m^{-3} s^{-1} (Bitschofsky & Nausch, 2019). The catchment area is divided into three sub-basins: upper, middle,

and lower Warnow (e.g., Bitschofsky & Nausch, 2019). The present study focuses on the freshwater part of the upper and middle Warnow catchment area (Figure 1). About 75% of the agricultural land in the sub-basin middle Warnow is water-logged soils, with up to an estimated 50% of the agricultural area being artificially drained (Bockholt & Kappes, 1994; Hennig & Hilgert, 2007; Bitschofsky & Nausch, 2019). Most parts of the river flow path through the upper and middle Warnow are lined with wetland- and bog-type areas.

The WR is characterized by a high load of nutrients (total nitrogen (N): 4140 t yr^{-1}, phosphorous (P): 200 t yr^{-1}), and an internal production rate of about 650 g C m^{-2} yr^{-1} (Deutsch et al., 2006; Bitschofsky & Nausch, 2019).

The WR is managed by a weir at the lower end of the middle Warnow in Rostock (Figure 1), which essentially hinders brackish Baltic Sea water from entering the area upstream during storms and allows the use of the WR for drinking water production. The weir furthermore modifies the flow velocity in the middle Warnow and the widening of the river bed in the freshwater part, thereby enhancing bank storage and supporting the development of wet ecosystems at the river margins.

2.2 Sampling Methods

A field campaign focusing on spatial trends along the flow path of the WR and including different tributaries took place on 29-30th April 2019. A total of 23 stations along the upper and middle WR were sampled. At the lower end of the middle Warnow (Figure 1; Table 2), campaigns were carried out weekly in 2017 and monthly between 2018 and 2021 (Figure 1). The discharge of the WR measured at the end of the middle Warnow at Geinitzbrück (Figure 1) was very dynamic. The values ranged between near 0 and 70 m^3 s^{-1} in summer and winter, respectively (Figure 2, SM Table 1). The discharge data for the WR were provided by the National Agency of Agriculture and the Environment of Mecklenburg-Western Pomerania (Stalu-MM), Rostock, Germany.

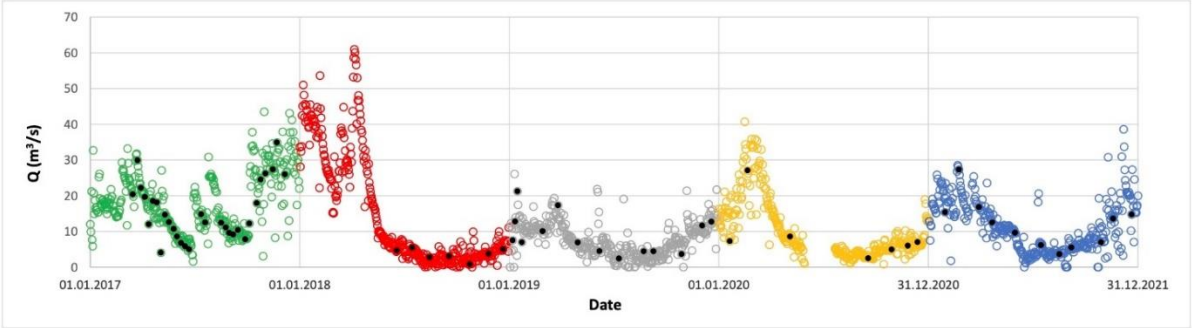

Figure 2 -Variations in the discharge of Warnow River (Rostock, Geinitzbrücke; see Figure 1) from 2017 to 2021, with marked sampling dates (black dots).

The water was sampled using a plastic beaker attached to a telescopic rod. The pH, salinity, conductivity, and dissolved oxygen were measured on-site using handylab pH 11, handylab LF 11 (Schott), or a Hach HQ40d multimeter (Hach, EUA) analytical device. Subsequently, the samples were taken via plastic syringes and filtered through 0.45 µm cellulose acetate disposable filters (Carl Roth, Germany).

Samples for major ions (Na, Mg, Ca, K, S), nutrients (P, Si), and trace elements (Ba, Fe, Li, Mn, Sr) were filled into acid-cleaned PE bottles and acidified with concentrated HNO_3. Chloride (Cl), NH_4, and sulfate (stable S and O isotopes) samples were taken into pre-rinsed polyethylene bottles. Samples for dissolved inorganic carbon (DIC) and $\delta^{13}C_{DIC}$ were filled without headspace into acid pre-cleaned 12 cm glass Exetainer® and conserved with saturated $HgCl_2$ solution. Samples for $\delta^{18}O$ and $\delta^{2}H$ of water were collected in 1.5 cm glass vials sealed with a PTFE-coated septum cap. Samples for dissolved organic carbon (DOC) concentration and $\delta^{13}C_{DOC}$ measurements were filtered through Nylon membrane filters (Carl Roth, Germany) into pre-cleaned brown glass bottles and acidified with concentrated HCl. All samples were stored under dark and cool conditions until further processing, except for nutrient sampling aliquots, which were kept frozen until analysis.

For radium isotopes ($^{224}Ra_{ex}$), a large volume of water (30 L) was collected using a submersible pump and filtered through a 1 µm filter into a gallon. The water was then pumped at a flow rate of about 1 L min^{-1} through MnO_2-coated acrylic fibers that were washed and partly dried for further measurements (Garcia-Solsona et al., 2008).

Sampling and isotope hydrogeochemical analyses of hard water creeks discharging from Rügen Island are described in Winde (2009). A sampling of the Elbe River was

done on board RV Ludwig Prandtl, and the analytical methods are described by Kowalski et al. (2013).

Sampling at EMS and Weser followed the same procedure as described above.The rivers Zagórska Struga and Gizdepka discharging into Puck Bay (Figure 1), Poland, were sampled in June 2021 and followed the same procedures as described above.

2.3 Analytical Methods

Major ions, nutrients, and trace elements were analyzed by inductively coupled plasma optical emission spectrometry, ICP-OES (Thermo, iCAP 7400 Duo, Thermo Fischer Scientific), using Sc as an internal standard. The measurements revealed precision and accuracy of better than ±5 and ±8%, respectively (Kowalski et al., 2013; von Ahn et al., 2021). As the surface waters were generally oxidized, the measured total S represents dissolved sulfate (SO_4). Concentrations of Cl during the spatial campaign were determined by an electric potentiometric precipitation titration (Schott instruments), which is based on the changing electrical potential difference of the solution by quantitative precipitation of Cl^- ions due to titration with a 0.05 N $AgNO_3$ solution. Analytical accuracy was constantly checked with an international reference standard (OSIL Atlantic Seawater 35). Dissolved NH_4 was analyzed spectrophotometrically following Grasshoff et al. (2009) on a QuAAtro autoanalyzer system (Seal Analytical, Southampton, UK).

Concentrations of DIC were measured by comparing the mass 44 signal from isotope analyses with calibrated $NaHCO_3$ solutions (Wu et al., 2018), and $\delta^{13}C_{DIC}$ values were determined as described by Winde et al. (2014, 2017) by means of continuous-flow isotope-ratio-monitoring mass spectrometry (CF-irmMS) using a Thermo Finnigan MAT253 gas mass spectrometer attached to a Thermo Electron Gas Bench II via a Thermo Electron Conflo IV split interface. Solutions were allowed to react for at least 18 hours before introduction into the mass spectrometer. The international calibration materials NBS-19, IAEA Li carbonate standard, and Solnhofener Plattenkalk were used to calibrate measured isotope signals towards the V-PDB scale. Values of $\delta^{18}O$ and $\delta^{2}H$ of water were analyzed with a LCRDS (laser cavity-ring-down-spectroscopy) system (Picarro L2140-I; Böttcher & Schmiedinger, 2021). The reference materials SLAP and VSMOW were used to calibrate measured isotope ratios towards the

VSMOW scale. The ratios of $^{34}S/^{32}S$ and $^{18}O/^{16}O$ of dissolved SO_4 were analyzed on $BaSO_4$ that was precipitated by adding $BaCl_2$ solution to pre-heated acidified samples, further washed with deionized water, dried and tempered at 500°C (Siebert et al., 2021). DOC concentrations and $\delta^{13}C_{DOC}$ values were measured using an Elementar isot TOC cube (Kirkels et al., 2014) connected to a Thermo Electron MAT 253 mass spectrometer. Carbon isotope ratios of DOC were calibrated to the VPDB scale using IAEA caffeine ($\delta^{13}C$ = -27.77 mUr vs. VPDB) and sucrose (IAEA-CH-6, $\delta^{13}C$ = -10.45 mUr vs. VPDB) intercalibration materials and the DOC concentrations were calibrated using the mass-44 response to dissolved caffeine and sucrose solutions, and the integration function of the isotTOC, respectively. All stable isotope results are presented in the δ-notation. The given 'mUr' (milliUrey) values are equivalent to the traditional '‰' (Brand & Coplen, 2012).

Activities of ^{224}Ra were measured with radium-delayed coincidence counters (RaDeCC) (Moore and Arnold, 1996; Garcia-Orellana et al., 2021) within 3 days after the sampling. After about a month, another measurement was conducted for the determination of ^{224}Ra supported by ^{228}Th; this measurement was then subtracted from the initial ^{224}Ra to obtain the $^{224}Ra_{ex.}$ Activities of $^{224}Ra_{ex}$ were calculated following and the expected error of the measurement is 7% Garcia-Solsona et al. (2008). The calibration of the detectors was done once a month using ^{232}Th with certificated activities.

A physico-chemical interpretation of the hydrochemical measurements was carried out using PHREEQC (Parkhurst & Appelo, 2013). Where no Cl data was measured during the temporal investigation, the value from the spatial campaign was used to balance the alkali ions. Saturation indices wrt. calcite, amorphous silica, and barite, the CO_2 partial pressure, as well as total alkalinity (TA) were calculated. Physicochemical constants from Plummer & Busenberg (1982) were used for the dissociation constants in the dissolved carbonate system and the solubility product of pure calcite.
Specific concentration pairs of anions and cations ((Na+K) versus Cl and (Ca+Mg) versus (SO_4+0.5 DIC)) were found to be stoichiometrically well balanced.

3. Results and Discussion

3.1. Spatial variations

The Warnow River discharge on the day of the sampling campaign in late April 2019 increased from 4.6 $m^3 s^{-1}$ at the beginning of the middle Warnow at Bützow (109 km distance from the source) to 6.89 $m^3 s^{-1}$ at the end of the middle Warnow (Figure1). At the beginning of the middle Warnow, the river changes to an impounded narrow lake-like characteristic (Bitschofsky & Nausch, 2019). The slight difference in morphological height and the reduced flow velocity in this area lead to a water residence time of about a week (Schlungbaum and Selig, 1996, Selig and Schlungbaum, 2002). The tributaries Nebel, Beke, Zarnow, and Kösterbek (Figure 1) enter the WR along the flow path before the end of the middle Warnow with a discharge during the sampling campaign of 1.9, 0.6, 0.06, and 0.2 $m^3 s^{-1}$, respectively, contributing to the overall WR discharge. However, the discharge at the end of the middle Warnow was lower than the mentioned sum of the WR discharge at Bützow and the tributaries (7.4 $m^3 s^{-1}$). This confirms the relatively long residence time in contact with the atmosphere, which may lead to higher evaporative water loss both of the Warnow and the interactions with the surrounding peat and wetlands close to the WR lowlands.

The water isotopic composition of the WR and the tributaries ranged from -8.0 to -5.0 mUr and -55.1 and -38.3 mUr for the stable $\delta^{18}O_{H2O}$ and $\delta^{2}H_{H2O}$, respectively. These values are positioned close to the LMWL at Warnemünde and to the composition of Mecklenburg-Western Pomerania (MWP) groundwaters (Jenner, 2018; Malik et al., 2022) (Figure 3), and a shift towards heavier isotope data is observed downstream from the upper to the middle Warnow (Figure 4). This is due to evaporative loss of water from the slowly running surface waters (Gat, 1996; Horita et al., 2008; Luz et al., 2009), and possible mixing with tributaries that already underwent enhanced evaporation (e.g., Zarnow and Kösterbeck catchments; Figure 1) due the high presence of lakes in the region. The water isotope composition is within the range of other German rivers entering the Baltic and North Sea (Table 2; Böttcher et al., 2014; Reckerth et al., 2017)

Table 1 Isotope hydrogeochemical results for spatial variations at the Warnow River (W), selected tributaries (T) and drain (D) in April 2019 (see Figure 1 and text). N.d.: not determined. Nox: NO2+NO3

Coordinates		Station	Type	Name	Q	T	EC25	pH	Na	K	Ca	Mg	Cl	SO4	□34S-SO4	□18O-SO4	DIC	□13C-DIC	Ta	DOC	□13C-DOC	Si	PO4	Nox	NO2	NO3	NH4	Li	Fe	Mn	Ba	□18O-H2O	□2H-H2O
R	H				(m³/s)	(°C)	(µS/cm)		(mM)	(mM)	(mM)	(mM)	(mM)	(mM)	(mUr)	(mUr)	(mM)	(mUr)	(mM)	(mM)	(mUr)	(µM)	(µM)	(µM)	(µM)	(µM)	(µM)	(µM)	(µM)	(µM)	(µM)	(mUr)	(mUr)
32678143	5943339	1	W	Warnow (Barniner Lake - Escape)		14.4	577	8.3	0.8	0.1	2.5	0.4	1.0	1.0	-1.3	7.1	3.4	-8.4	3.5	0.9	-30.4	12	0.2	6.1	0.6	5.6	6.9	0.8	0.6	2.8	0.3	-6.97	-49.8
32680137	5943981	2	W	Warnow (Barniner Lake - Intake)		11.4	681	8.0	0.7	0.1	3.3	0.5	0.8	1.1	-2.1	7.1	5.0	-12.4	4.9	0.8	-30.4	193	5.9	82.3	1.7	80.7	5.7	1.1	1.6	3.8	0.5	-7.91	-55.0
32682843	5943831	3	W	Warnow (Demen - Forest)		11.5	708	7.9	0.7	0.1	3.3	0.5	0.8	1.2	-1.7	6.1	5.0	-12.7	4.9	0.9	-32.1	206	0.0	108.6	2.5	106.1	7.3	1.2	1.7	5.7	0.5	-7.99	-55.1
32687094	5957882	4	T	Mildenitz (Sternberger Burg)		16.3	537	8.4	0.9	0.1	2.3	0.4	0.9	0.8	-0.1	8.5	3.6	-6.8	3.7	1.0	-30.3	20	0.1	1.6	0.1	1.4	3.2	1.2	0.3	1.1	0.4	-5.61	-42.4
32686758	5958862	5	W	Warnow (Gross Goernow)		15.6	626	8.4	1.9	0.1	2.4	0.5	1.5	0.8	-0.8	8.1	3.9	-9.3	4.0	0.8	-28.6	91	0.5	13.7	1.1	12.6	5.5	1.6	1.0	1.0	0.5	-6.59	-47.7
32681160	5956395	6	T	Brueeler Bach (Weitendorf)		15.3	636	8.2	2.1	0.1	2.0	0.5	1.9	0.6	0.4	9.9	3.8	-8.2	3.8	1.0	-30.8	54	0.7	7.8	0.7	7.1	7.5	1.8	1.7	2.2	0.5	-5.56	-42.2
32693285	5970100	7	T	Ruehner Lake - Intake (Steinhagen)		15.2	656	8.4	0.9	0.2	3.0	0.5	0.9	0.5	0.9	n.d.	6.0	-11.5	6.1	1.1	-29.0	259	6.3	206.1	10.1	196	20.0	1.5	3.2	1.9	0.5	-7.36	-51.1
32692832	5967866	8	T	Seebach - Ruehner Lake (Steinhagen)		19.2	469	8.7	0.8	0.1	1.9	0.5	0.8	0.6	4.3	n.d.	3.3	-6.5	3.5	1.0	-30.7	128	0.4	2.8	0.4	2.4	1.2	0.9	0.7	0.6	0.3	-4.96	-38.3
32695811	5969602	9	W	Warnow (Steinhagen by Buetzow)	4.63	16.1	591	8.3	1.2	0.1	2.3	0.4	1.2	0.8	-0.4	8.0	3.7	-8.5	3.7	0.8	-29.4	60	0.2	9.8	0.7	9.2	3.0	1.4	1.0	3.1	0.4	-6.28	-46.1
32698000	5968491	10	T	Nebel (by Wollken)	1.93	16.1	728	7.9	1.9	0.1	2.4	0.5	1.9	0.7	3.9	8.9	4.5	-10.5	4.4	1.1	-30.3	151	0.3	17.1	1.0	16.2	5.6	1.9	2.9	3.3	0.5	-6.40	-46.6
32703776	5981447	11	T	Beke (Schwaan)	0.614	15.8	837	8.0	2.0	0.1	3.0	0.6	2.2	0.8	3.1	8.5	5.6	-12.7	5.6	1.2	-31.5	171	11.2	49.9	2.1	47.9	13.4	2.0	2.7	5.7	0.5	-7.80	-53.5
32704158	5981294	12	W	Warnow (Schwaan)		16.1	632	8.3	1.5	0.1	2.3	0.5	1.5	0.7	1.1	7.5	3.8	-8.3	3.9	0.9	-32.2	30	0.3	0.4	0.2	0.1	4.6	1.5	0.7	0.9	0.5	-6.10	-45.0
32687015	5963244	13	W	Warnow (Eickhof)		13.3	594	7.8	1.2	0.1	2.2	0.4	1.3	0.7	-0.5	8.8	3.4	-8.7	3.3	0.8	-30.6	60	0.3	10.8	0.6	10.1	3.9	1.4	1.2	1.8	0.4	-6.22	-45.3
32691527	5981964	14	T	Tessenitz (Juergenshagen)		12	749	7.9	1.5	0.1	3.0	0.5	1.5	0.6	2.1	8.2	5.4	-12.2	5.3	1.0	-31.0	216	1.8	69.1	3.2	65.9	8.8	1.4	2.8	1.1	0.4	-7.72	-52.8
32688870	5980116	15	T	Kleine Beke (Juergenshagen)		10.5	797	7.9	1.3	0.1	3.4	0.6	1.4	1.1	-1.4	n.d.	5.0	-12.6	4.9	1.2	-30.6	94	7.7	88.9	1.4	87.5	4.4	1.1	1.4	1.7	0.4	-6.70	-46.9
32688925	5980150	16	D	Drain (Kleine Beke - Juergenshagen)		11.7	692	7.2	0.9	0.1	3.0	0.5	0.8	0.5	n.d.	n.d.	5.3	-14.4	4.6	0.8	-31.4	227	0.0	684.3	0.3	684.0	6.3	1.0	0.1	0.1	0.4	-8.05	-54.0
32700217	5983453	17	T	Beke (Boebberow)		14.5	859	8.0	2.3	0.1	3.0	0.6	2.5	0.8	2.3	8.1	5.2	-12.4	5.1	0.9	-29.0	178	0.1	12.0	0.4	11.6	1.8	2.2	2.1	3.2	0.5	-7.73	-53.4
32703429	5976442	18	W	Warnow (Werle)		17.5	630	8.1	1.5	0.1	2.3	0.5	1.6	0.7	1.2	8.1	3.6	-8.6	3.6	1.0	-29.7	49	0.2	1.8	0.3	1.5	1.8	1.5	1.1	1.4	0.5	-6.05	-45.2
32706386	5988288	19	T	Zarnow (Reez)	0.06	14	766	8.0	1.2	0.1	3.3	0.6	1.6	1.1	1.7	7.4	4.7	-12.5	4.7	1.5	-29.4	204	0.7	16.3	0.9	15.5	4.1	1.2	4.6	4.8	0.5	-7.60	-53.2
32705214	5988109	20	T	Zarnow (Forest)		13.1	774	8.1	1.3	0.1	3.3	0.6	1.6	1.1	1.7	8.8	4.8	-12.7	4.8	0.9	-27.5	223	0.8	21.1	1.0	20.0	4.5	1.3	4.7	3.9	0.5	-7.67	-53.4
32708591	5994428	21	T	Koesterbeck (Kessin)	0.18	14.3	690	8.1	1.1	0.1	2.9	0.5	1.2	0.8	2.6	8.5	4.4	-12.3	4.4	1.1	-28.1	144	0.7	23.6	1.4	22.2	2.8	1.0	14.3	3.2	0.4	-7.58	-52.7
32707852	5995077	22	W	Warnow (Kessin)		17.5	649	8.4	1.5	0.1	2.3	0.5	1.6	0.8	1.1	7.3	3.6	-8.2	3.7	1.0	-29.7	14	0.1	-0.4	0.2	-0.6	0.5	1.5	0.5	0.3	0.5	-6.24	-45.8
32706352	5996845	24	W	Warnow (Garden Area)	6.89	16.3	651	8.5	1.6	0.1	2.4	0.5	1.7	0.8	1.5	n.d.	3.7	-8.3	3.8	1.0	-28.2	12	3.1	0.1	0.0	0.0	0.6	1.5	0.2	0.3	0.5	-6.23	-45.9

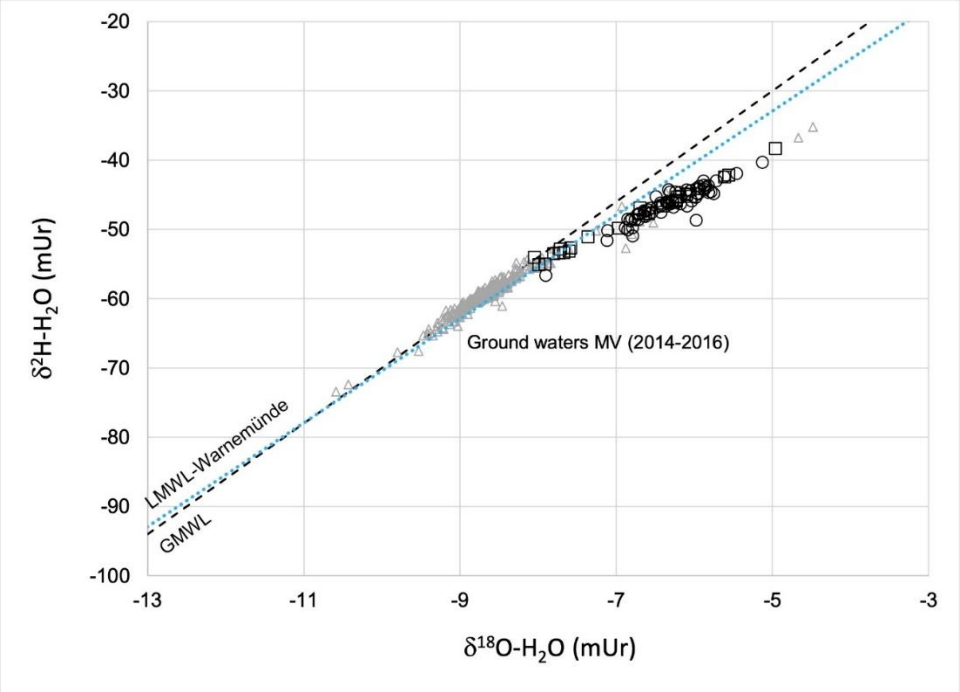

Figure 3 - Stable water isotope composition of the Warnow river and its tributaries during spatial (black circles) and temporal (black squares) campaigns, compared to the GMWL (black dashed line), the LMWL at Warnemünde (blue pointed lines), and ground waters of MWP (grey triangles; 2014-2016; Jenner, 2018; Malik et al., 2022).

The composition of the WR can be classified as typical Ca-HCO_3 water under the anthropogenic impact like observed for other systems draining the coastal areas of the Baltic and North Sea (e.g., Winde et al., 2014; Campeau et al., 2017, Table 2).

The changes in the isotope hydrochemical composition along the WR flow path, in particular for redox-sensitive elements, are not substantially impacted by mixing with the tributaries (Figure 4), probably due to their low discharge at the time of the sampling, but reflect exchange with the interstitial waters, groundwater, and/or pelagic system internal processes (e.g., Trettin et al., 1999; Nutzmann & Lewandowski, 2009).

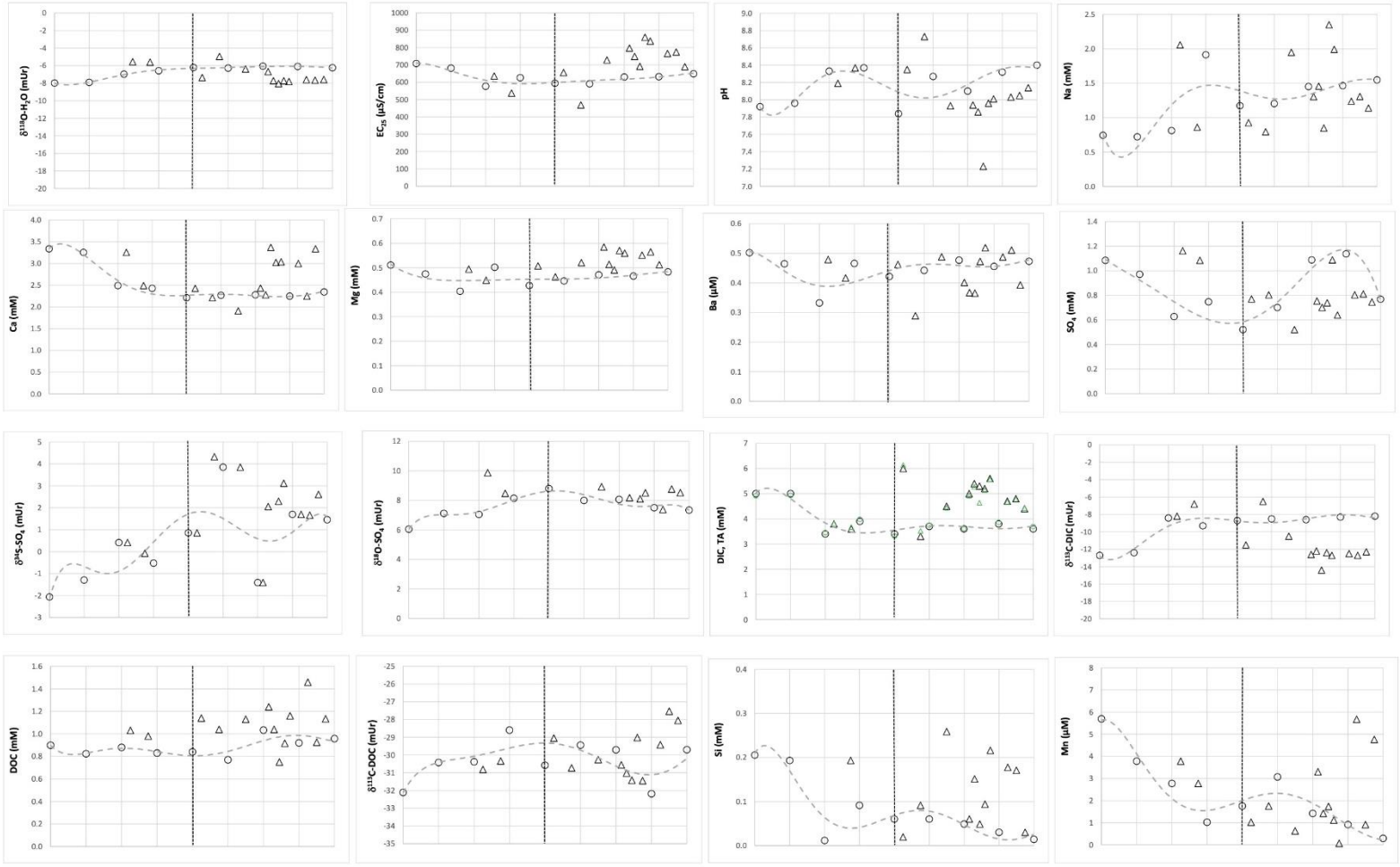

Figure 4 - Spatial variations of isotope hydrogeochemical variables along the WR (circles) and selected tributaries (triangles) on April 29th and 30th, 2019. Note: The station numbering does not consider river lengths but follows the order given Figure 1. DIC: black, TA: green. Dashed line: Polynomal fit of WR compositional variation; vertical pointed line: Transition between the upper and middle parts of the WR catchment. The full data set is summarized in Table 1.

The relatively long residence time of the water and the slow flow rates at the middle Warnow (Schlungbaum and Selig, 1996; Selig and Schlungbaum, 2002) may have enhanced benthic-pelagic fluxes of elements like Mn, P, and DIC during times of high biological activity in the surface sediments and the marginal areas (see Section 3.2).

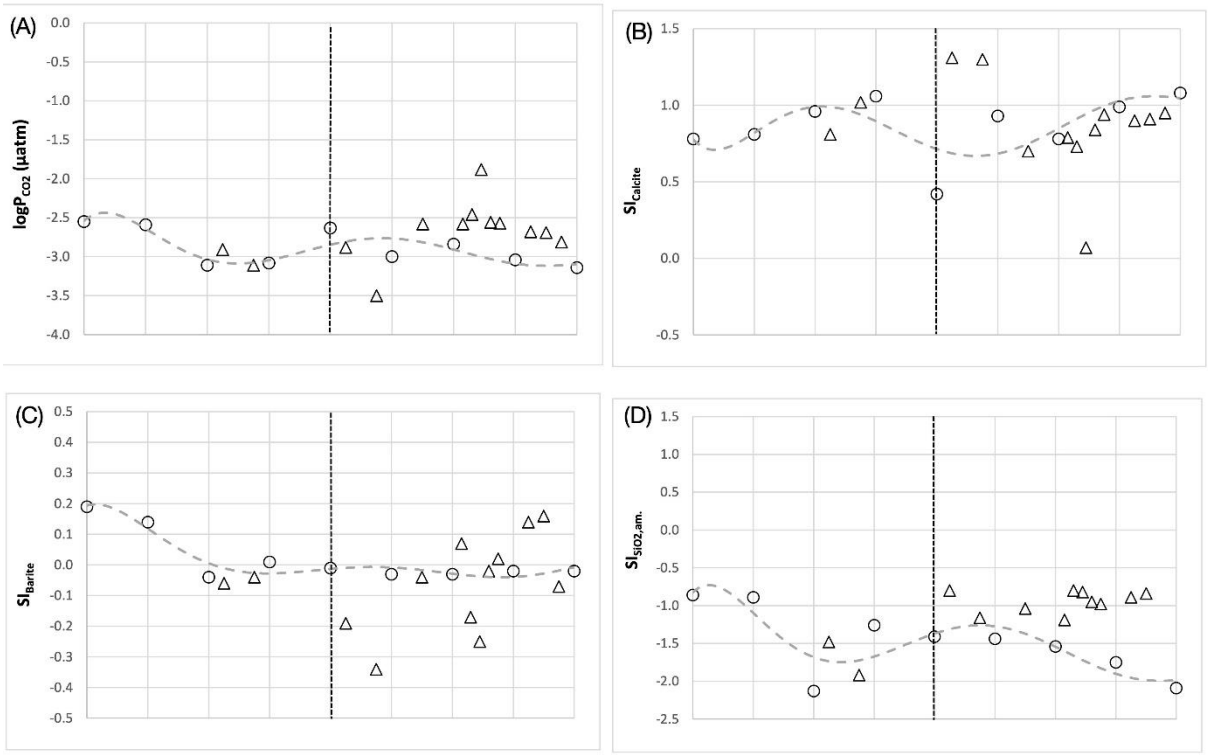

Figure 5 - Spatial variations of selected meta analyses for the WR (circles) and selected tributaries (triangles) on April 29th and 30th, 2019. (A) pCo2, (B) SI calcite, (C) SI Barite, (D) SI amorphous silica Note: The station numbering does not consider river lengths but follows the order given Figure 1. DIC: black, TA: green. Dashed line: Polynomal fit of WR compositional variation; vertical pointed line: Transition between the upper and middle parts of the WR catchment. The full data set is summarized in Table 1.

The average concentration of DIC found in the upper Warnow was 3.9 mM, which is in the range of concentrations found in the groundwaters of MWP (Malik et al., 2022; Jenner, 2018; Böttcher et al., unpublished data). The average $\delta^{13}C_{DIC}$ (about -9 mUr) indicates the uptake of biogenic soil CO_2 that drives corrosion of carbonate mineral loads derived from agricultural management in the soil zone, followed by the dissolution of natural carbonates occurring in the aquifer (Campeau et al., 2017; Kape et al., 2010; Deines et al., 1974). These subterrestrial processes are, further, upon contact with the atmosphere superimposed by the evasion of CO_2 (Michaelis et al., 1985), the exchange between the river bed and the water body (Trettin et al., 1999),

photosynthesis (Liu & Dreybrodt, 2015) and the local mixing with inlets of different composition (-13 to -7 mUr, Figure 4).

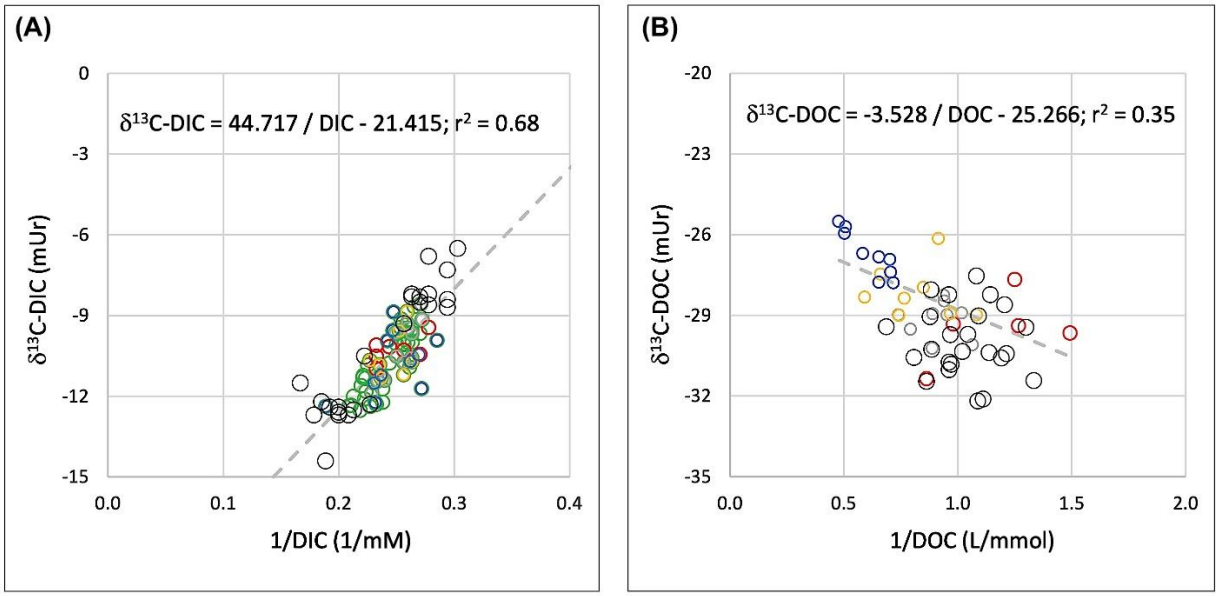

Figure 6 - Keeling plot analysis for source/sink determination of (A) DIC and (B) DOC. Colored symbols: temporal campaigns (see Figures 2 and 8 for details); black and white circles: spatial campaign (April, 2019).

Overall, the $\delta^{13}C_{DIC}$ changes along the pathway towards an enrichment (Figure 4), indicating that CO_2 degassing and biological assimilation are the dominant processes controlling the spatial changes during sampling. Most tributaries are enriched in DIC and depleted in $\delta^{13}C_{DIC}$ when compared to the WR, with values reaching 6 mM and -12.7 mUr, respectively (Figure 3), which are also in the range of compositions found in groundwaters of MWP (Jenner, 2018; Malik et al., 2022;) and may be the consequence of fen contributions.

The calculated CO_2 partial pressures in the WR were always found to exceed the modern atmospheric value in NW Europe (Figure 5; Kitidis et al., 2019), therefore, allowing CO_2 to physically degas from the river surface to the atmosphere (e.g., Michaelis et al., 1985; Borges et al., 2006). Furthermore, due to the pressure difference controlled by the liberation of CO_2, and further photosynthetic activity, the WR was supersaturated wrt. calcite ($CaCO_3$; Figure 5) to the degree that, in some parts, the surface water may allow in-situ calcium carbonate formation (Michaelis et al., 1985). Whereas photosynthesis would lower the CO_2 partial pressure, carbonate formation would counteract and enhance the potential evasion (Michaelis et al., 1985). As found for the stoichiometric balance between alkali elements and Cl (Figure 5), the sum of

the earth's alkaline element concentrations was well correlated by SO_4 and DIC, assuming essentially closed system dissolution of aquifer carbonates (Figure 6; Langmuir, 1971; Deines et al., 1974).

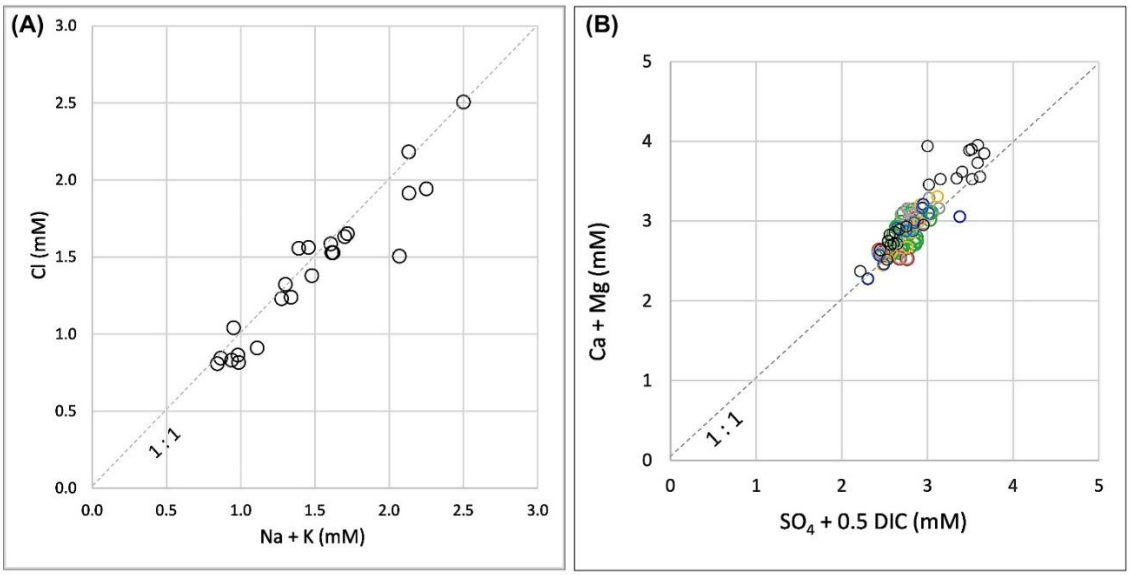

Figure 7 - Covariation of dissolved Cl versus the sum of Na and K (A); spatial campaign), and Ca + Mg versus SO4 + 0.5 DIC (B); all campaigns). Concentrations during the spatial sampling (black circles) campaign between lake Barnin and Kessin (Figure 1).

The DOC concentrations do not vary substantially along the flow path of the WR, ranging between 0.8 and 1.9 mM (Figure 4). The $\delta^{13}C_{DIC}$, with an average value of -30 mUr, indicates a terrestrial origin with values close to the ones of C3 organic matter (Figure 5; Hoefs, 1973; Han et al., 2018; Sun et al., 2022). A Keeling-plot evaluation of the data (Figure 6) yields a shift towards more heavy stable isotope values with increasing concentration, likely due to a mixture of natural background DOC with fertilizer compounds (Han et al., 2018; Sun et al., 2022) that can be of modern or groundwater derived origin.

It is interesting to note that the coupled $\delta^{34}S$ and $\delta^{18}O$ isotope signature of dissolved sulfate of the WR developed from values that are likely dominated by subterrestrial microbial oxidation of pyrite (Figure 8; Schwientek et al., 2008; Zhang et al., 2012; Malik et al., 2022) towards heavier isotope data. This may indicate the impact of microbial sulfate reduction (Fritz et al., 1989; Böttcher et al., 1998; Malik et al., 2022) or the contribution from atmospheric deposition or fertilizers (Vitòria et al., 2004; Schwientek et al., 2018). The impact of sulfur transformations in the wet organic-rich

areas lining the middle Warnow banks could also be deduced, but require a further detailed study.

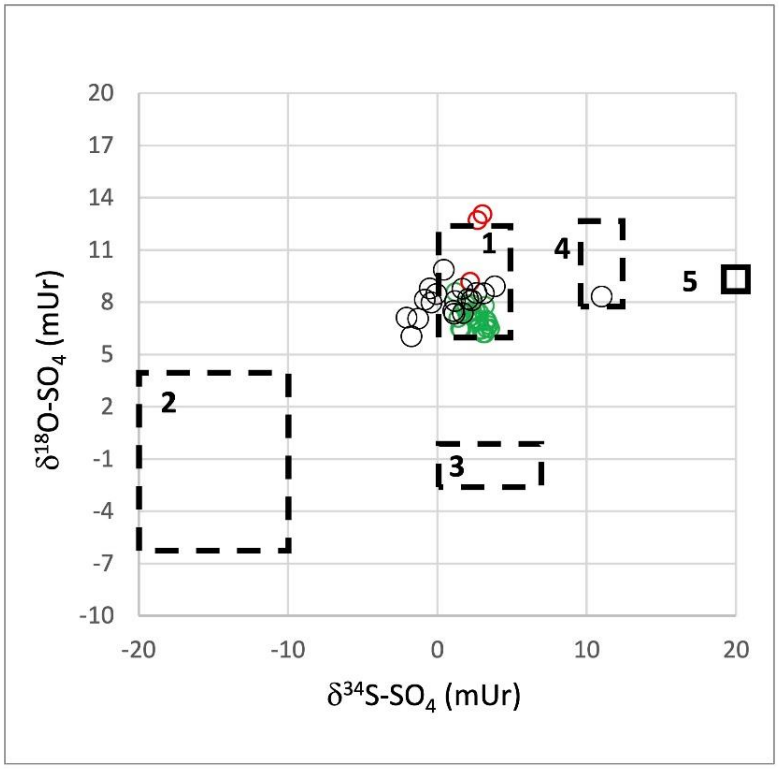

Figure 8 - Covariation of the S and O isotope composition of dissolved sulfate of the Warnow and its tributaries. Fields of potential sulfate sources are added, too (Schwientek et al., 2008, Böttcher 1999; Böttcher et al., 2007): 1: Atmospheric deposition, 2: pyrite oxidation; 3: fertilizers, 4: Permian Zechstein sulfate, 5: Baltic seawater sulfate and seaspray.

*Table 2 - Compilation of the isotope hydrochemical compostion at the Warnow river during seasonal campaigns, in comparison with results for small rivers and hard water creeks entering the southern Baltic Sea in the Puck Bay and at Jasmund (Rügen), respectively, and rivers draining into the southern North Sea. 3 creeks: Östlicher Höllgrund, westlicher Höllgrund, Limmer Bach. *:1.2021. ‘: calculated with PhreeqC. “: samples from September 28th, 2022. **: from Neumann et al. (2015). Rhine data taken from van der Weijden & Middelburg (1989) and Buhl et al. (1991; Site 27 in fall 1988(‘)). n.d.: not determined; n.a.: not applicable; n.g.: not given.*

	Upper Warnow (2017-2021)	Upper Warnow (18.08.2022)	Zagórska Struga (28.06.2021)	Gizdepka (30.06.2021)	Rügen, 3 creeks (3.+4.12.2008)	Rügen, Limmer Bach 15.09.2021	Baltic Sea, WMD (23.01.2019)	Elbe, Station Z1 (8.9.2009)	Weser, Farge (04.08.2021)	Ems, Herbrun (03.08.2021)	Rhine, Lobith (1975-1984)
Q (m^3/s)	0.79 / 34.9	1.19	n.m.	n.m.	n.m.	n.m.	n.a.				832/7150
T (°C)	1.2 / 23.0	24.6	18.1	18.9	3.9/6.1	14.4	2.5	18.7	21.7	21.6	2.3 / 26.0
EC_{25} (µS/cm)	602 / 789	721	351	497	725/783	673	27000	976	1031	585	440 / 1310
pH	7.21 / 8.45	7.45	7.53	7.36	8.21/8.38	8.20	7.82	8.59	7.76	7.69	6.9 / 8.1
Ca (mM)	1.84 / 2.80	2.02	2.0	2.4	2.99/3.38	2.8	5.1	2.12	1.7	1.5	1.35 / 2.52
Mg (mM)	0.41 / 0.56	0.49	0.3	0.4	0.46/0.61	0.5	24.1	0.56	1.7	0.3	0.35 / 0.60
Na (mM)	1.05 / 2.43	1.8	0.7	1.2	0.7/0.8	0.6	195	3.55	4.5	1.9	0.73 / 5.30
K (mM)	0.11 / 0.16	0.1	0.1	0.1	0.1/0.2	0.1	4.8	0.26	0.6	0.3	0.1 / 0.3
SO_4 (mM)	0.53 / 1.01	0.55	0.4	0.6	0.9/1.1	0.6	13.3	0.4	1.2	0.6	0.45 / 1.24
DIC (mM)	3.5 /5.3	n.d.	3.6	4.4	4.9/5.5'	4.90	1.8	n.d.	2.7	2.6	n.d.
TA (mM)	3.2 / 4.7 (2018-2022)	n.d.	3.4'	4.0'	4.95/5.57	4.94'	2.0	n.d.	2.6'	2.5'	2.02 / 3.28
DOC (mM)	0.7 / 2.1 (2018-2021)	0.9	n.d.	n.d.	n.d.	n.d.	n.d.	n.d.	n.d.	n.d.	n.d.
O_2 (mg/L)	3.3 / 12.9 (2018-2019)	n.d.	9.3	7.5	12	10	13.1	8.7	7.7	8.7	n.g.
Si (µM)	15 /418	225	283	383	310	351	17	18	150	160	3.6 / 150
P (µM)	0.3 / 6.4	3.2	1.8	3.5	n.d.	0.9	1.7	0.7	1.1	0.1	6.6 / 25
NO_3 (µM)	0 / 430	n.d.	46	94	n.d.	n.d.	0	55**	n.d.	n.d.	150 / 415
NH_4 (µM)	0 / 25	n.d.	2	3	n.d.	n.d.	2	n.d.	n.d.	n.d.	7.1 / 243
Mn (µM)	<0.1 /3.8	0.1	0.3	0.9	0.1/0.2	0.3	0.1	0.1	0.2	2.9	0.1 / 8349
Fe (µM)	0.1 / 3.7	0.3	1.1	1.0	0.2/0.4	0.1	0.4	0.3	0.2	1.4	0.2 / 36
Sr (µM)	4.4 / 5.3	5.0	1.7	2.5	3.6	3.5	42.4	5.1	6.8	4.7	n.d.
Ba (µM)	0.27 / 0.48	0.39	0.1	0.2	0.4	0.4	0.1	0.3	0.6	4.1	n.d.
Li (µM)	0.7 / 1.7	1.7	0.7	0.6	1.0	1.1	11	2.7	1.2	1.3	n.d.
$d^{18}O$-H_2O (mUr)	-5.13 / -7.90	-5.38	-10.18	-9.72	-9.37/-9.93"		-4.16	n.d.	-7.54	n.d.	-9.6'
$d^{2}H$-H_2O (mUr)	-43.4 / -56.7	-42.2	-69.8	-67.0	-61.8/-64.5"		-31.7	n.d.	-53.6	n.d.	n.d.
$d^{13}C$-DIC (mUr)	-8.6 / -12.5	n.d.	-11.2	-13.4	-12.0/-13.8	-11.6	-0.6	-9.4	-13.0	-13.3	-8.2'
$d^{13}C$-DOC (mUr)	-25.5 / -31.4	-28.9	n.d.	n.d.	n.d.	n.d.	n.d.	n.d.	n.d.	n.d.	n.d.
$d^{34}S$-SO_4 (mUr)	0.4 /5.0 (2017-2019)	n.d.	n.d.	n.d.	n.d.	n.d.	22.2	n.d.	n.d.	n.d.	n.d.
$d^{18}O$-SO_4 (mUr)	6.2 / 8.6 (2018)	n.d.	n.d.	n.d.	n.d.	n.d.	9.5	n.d.	13.2	16.2	n.d.
$^{224}Ra_{ex}$ (mBq L^{-1})	0.48/1.53 (2021)	n.d.	n.d.	n.d.	n.d.	n.d.	2.78*	n.d.	n.d.	n.d.	n.d.

The WR is found to be saturated or even slightly supersaturated wrt. barite ($BaSO_4$; Figure 5), dissolved Ba, initially derived from rock weathering (Charbonnier et al., 2022). If the physicochemical saturation status reflects control of dissolved Ba concentrations by in-situ barite precipitation is currently not clear, and it requires further investigations, including the phase analytical composition of the WR suspended loads.

The (under)saturation state of the WR and its tributaries (Figure 5) wrt. Amorphous silica is consistent with the temporal investigations (Figure 10; see next chapter) and indicates silica-consuming primary production during spring.

Overall, the development of the isotope hydrochemical composition of the WR before entering the estuary is a consequence of the mixing between different, mostly diffusive, water sources superimposed by biogeochemical interactions and potential evaporation.

3.2 Temporal variations

At the transition of the freshwater zone towards the temporarily brackish water-impacted estuary, compositional dynamics were followed over 5 years (2017-2021; Figure 9, SM Table 2). Different seasonal adaptions of the investigated variables were found consistently during this period.

The temperature trends during sampling were similar and typical for the humid temperate climate zone, with a pronounced maximum during summer and a minimum during winter (Figure 9). The water isotopes were consistent throughout all years, with a slight maximum observed during summer (Figure 9). This matches the overall trend in regional precipitation (Böttcher et al., 2014; Stumpp et al., 2014; Malik et al., 2022;), but may reflect the surface water evaporation in the middle Warnow due to the low flow regime (Figure 3).

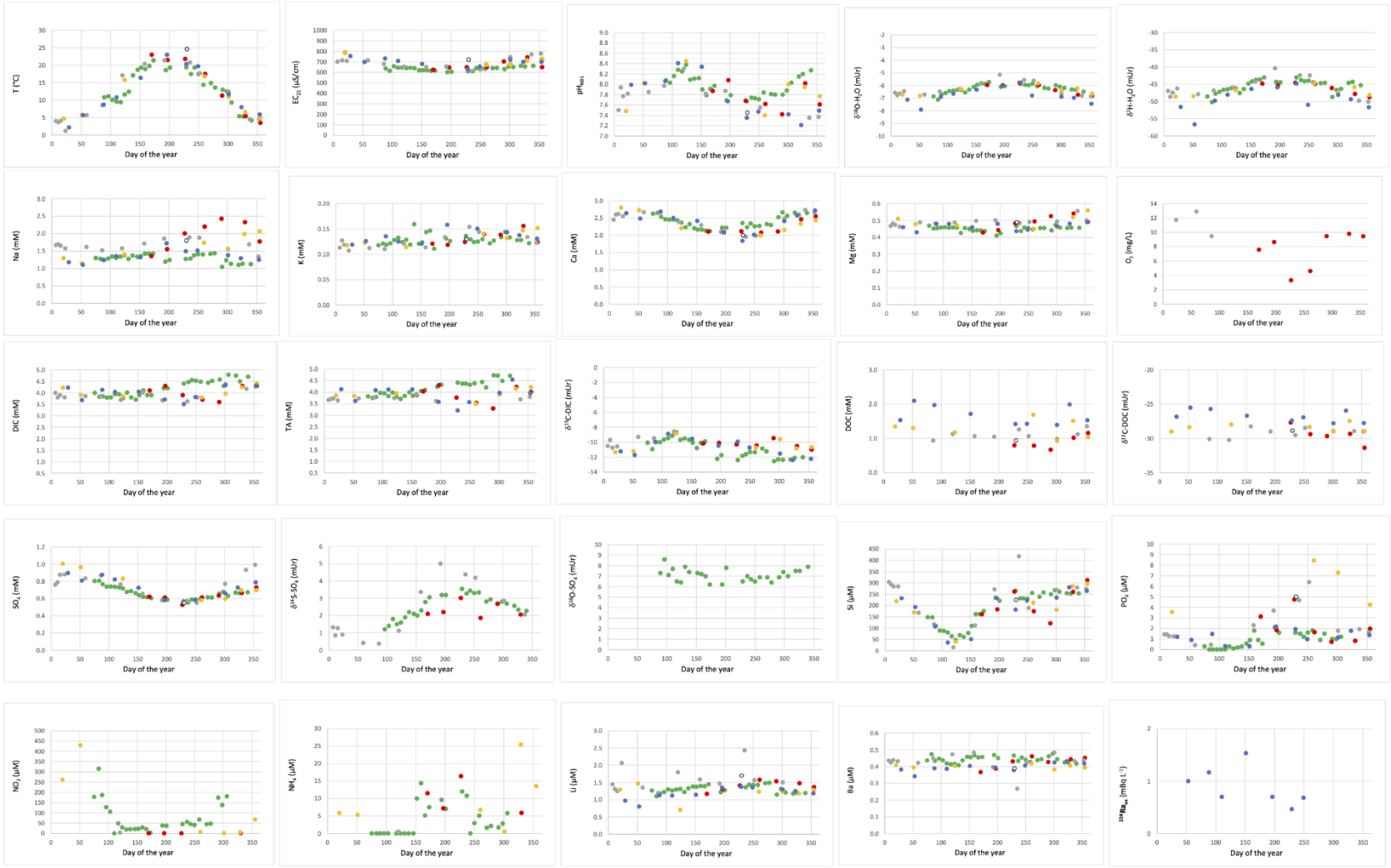

401

402 *Figure 9 Temporal variations of physical and isotope hydrogeochemical variables at the Rostock weir, at the end of middle Warnow (Figure 1). Colors indicate different years*
403 *(compare to Figure 2).* 2017: Green; 2018: red; 2019: dark grey; 2020: yellow; 2021: blue; 2022: light grey

The electrical conductivity showed a slight minimum during summer time which seems to be mainly related to the trend in dissolved Ca and SO_4 (Figure 9). In contrast, the concentrations of Na showed a slight increase during the winter period especially in 2019 (Figure 9), which can be caused by the low discharge conditions (Figure 2). No substantial seasonal changes were observed for K and the trace elements Li, Ba, and Sr.

The most pronounced seasonal variations were observed for pH, nutrients, and redox-sensitive trace metals. The pH values showed a distinct maximum during the spring season, indicating the establishment of a phytoplankton bloom. This is further confirmed by the pronounced decrease in the dissolved concentrations of Si, NO_3, PO_4, and DIC during spring (Figure 9), which is in agreement with N and P in previous investigations (Deutsch et al., 2006; Kahle et al., 2018; Bitschovsky & Nausch, 2019).

Due to the assimilation of isotopic light DIC, the $\delta^{13}C_{DIC}$ values showed a slight maximum during the spring blooms. A Keeling-type analysis of all measured DIC and $\delta^{13}C_{DIC}$ data shows a consistent trend with an overall carbon isotope enrichment factor of about -20 mUr (Figure 6). In autumn and winter, the DIC and TA concentrations displayed high dynamics, likely associated with the differences in the discharge. The calculated CO_2 partial pressure in the surface WR indicates the potential source function of the river for liberating CO_2 into the atmosphere, except for the spring bloom period, when near-equilibrium conditions were established (Figure 10).

As observed for the spatial trend, all samples were substantially supersaturated with respect to pure calcite with maximum values during summer time (Figure 10). Therefore, in-situ calcite precipitation probably took place and may have been responsible for the slight decrease in dissolved Ca during this season.

The DOC concentrations showed only minor seasonal variations (Figure 9), but higher differences were observed between the years. The $\delta^{13}C_{DOC}$ were close to C3 organic matter as observed for the spatial trend.

Dissolved NH_4 concentrations were low in spring until the summer, when enhanced benthic biological activity led to an element release from soils and sediments, which

was associated with an increase in Si, P, and Mn, as well as a decrease in dissolved O_2 (Figure 9). The post-summer data display differences within and between the years, likely due to a complex interplay between release rates and redox-dependent in-situ pelagic processes.

Undersaturation with respect to amorphous silica indicates the continuous potential of the WR to dissolve further diatom shells throughout the year (Figure 10). A pronounced minimum in SI values during the spring bloom indicates that dissolved silica was consumed by diatoms for shell production. Barite saturation was established during spring and winter, but the WR was undersaturated during summer due to sulfate depletion (Figure 9).

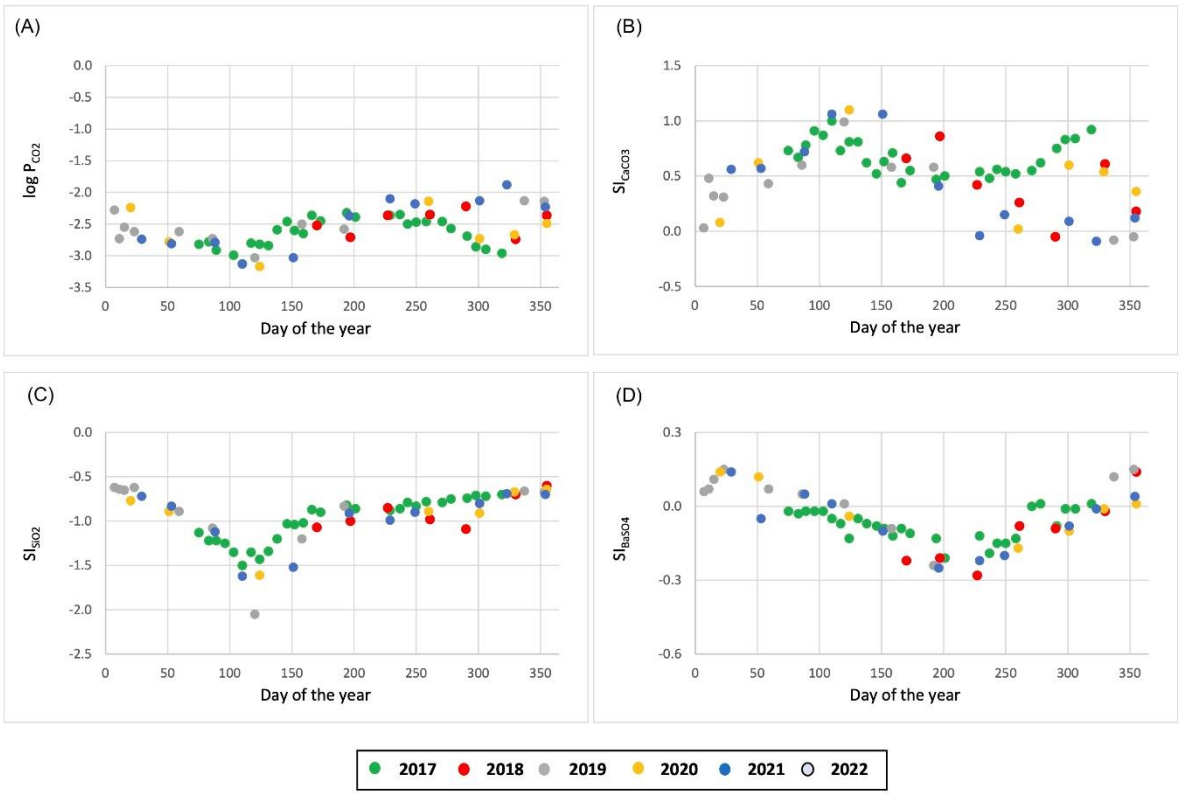

Figure 10 - Temporal variations in meta data derived by the physico-chemical interpretation of the hydrochemical composition of surface waters at the Rostock weir (end of the middle Warnow). Colors indicate different years (compare Figure 2).

The decrease in sulfate concentrations during summer is accompanied by an increase in the $\delta^{34}S$ but not the $\delta^{18}O$ isotope values (Figure 9). The impact of anoxic solutions that underwent unidirectional microbial sulfate reduction would lead to a common increase in both heavy isotopes of the residual sulfate (Fritz et al., 1989; Böttcher et

al., 1998; Malik et al., 2022), whereas the oxidation of sulfide(s) would cause a common decrease (van Stempvoort & Krouse, 1994). Therefore, the observed covariation trend (Figure 8) may be caused by changes in mixing proportions between solutions with different sulfur-cycling process histories, probably involving transformations of sulfur intermediates (Böttcher et al., 2001, 2005) or organic sulfur compounds (Zak et al., 2021).

The $^{224}Ra_{ex}$ activities varied between 0.5 and 1.5 Bq m-3, and there was no substantial variation with time. The results found in this study are similar to values reported for the river Rhine (Eikenberg et al., 2001) and streams draining into the Wismar Bay south from the WR (Figure 1; von Ahn et al., 2021) and freshwaters entering the Baltic Sea coastline close to Eckernförde via an underground passage (Purlik and Eisenhauer, 2004). These results will be used as an endmember value for a future fresh water balance of the coastal area of the WR catchment.

3.3 Element fluxes to coastal waters

A quantitative estimate of the controls of isotope hydrochemistry by hydrological boundary conditions was carried out here using concentration (c) and discharge (Q) relationships. These were obtained by fitting powerlaw relationships between concentrations (c) and discharges (Q) to the data (Clow and Drever, 1996; Musolff et al., 2015; Knapp et al., 2020), and transforming the result to a linear relationship in a double-logarithmic space:

$$Log_{10}(c) = log_{10}(a) + b\ log_{10}(Q)$$

where $log_{10}(a)$ and b are the intercept and slope of the c-Q relationship, respectively. For the present study, the discharge data were normalized to the average discharge of the time series, $log_{10}(Q/Q_{mean})$, which directly reflects the expected concentration at the mean discharge.

The evaluation of the measured temporal data trends for 5 years (2017-2021) gave examples for three different types of system responses: Dilution (Na, Si), mobilization (Ca, DIC, TA, NO_3), and even chemostasis (e.g., Ba, Li, Sr, Mg, K) trends (Figure 11,

SM Figure 1). The observed relationships for the dissolved compounds in the WR are strongly caused by the superimposition of seasonality and associated system-internal processes, and the hydrological consequences from river and drainage management. The results differ from un-managed rivers with small to medium-sized catchment areas, where often strong dilution effects are associated with increasing discharge due to the mixing with a recent surface water flow component (e.g., Böttcher & Usdowski, 1993; Knapp et al., 2020).

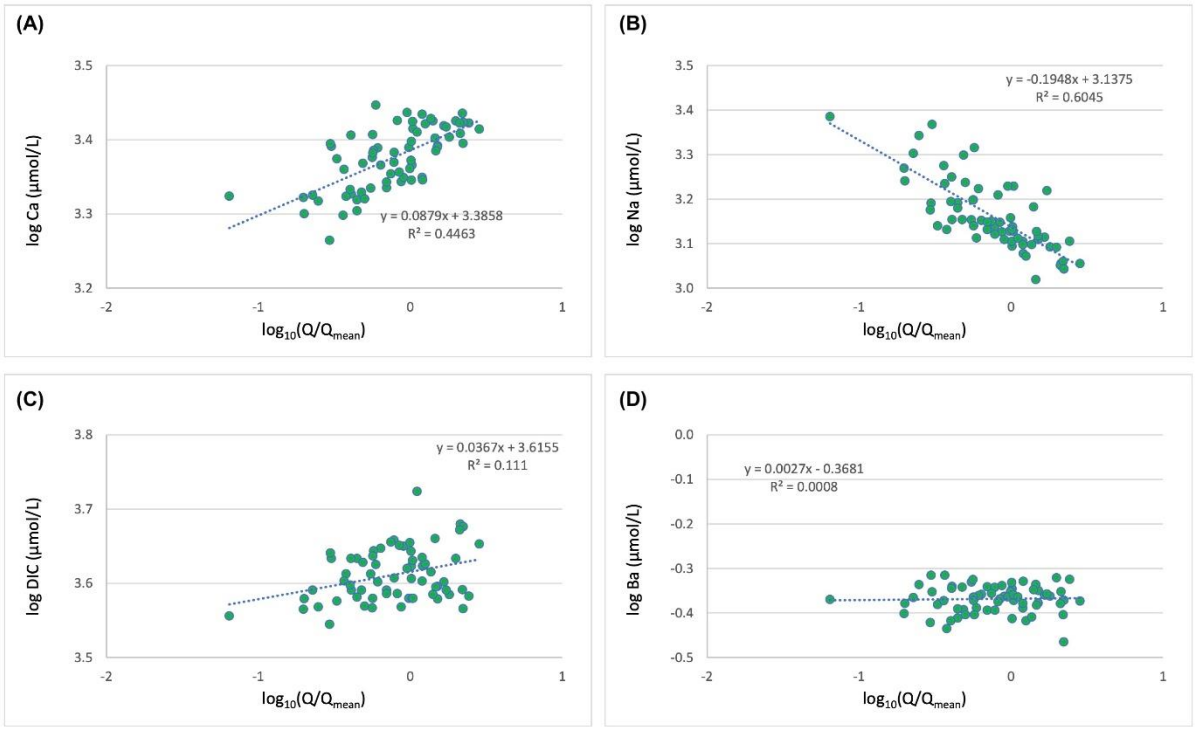

Figure 11 - Variations of selected hydrogeochemical variables at the Rostock weir as a function of normalized discharge (log-log plot). Mean discharge at the end of the Middle Warnow is 12.3 m3/s (Bitschovsky & Nausch, 2019). Examples describing the covariations in years 2017 to 2021 are given for chemostasis (Ba), mobilization (Ca, DIC), and dilution (Na). Note: Correlations are generally similar but statistically more significant when only autumn/winter values are considered. This indicates that system internal processes include biological activity, solid-solute interactions, and or specific local hydrological phenomena.

From the concentration-discharge relationships, mean riverine dissolved loads for the WR entering the estuary were calculated considering a mean discharge of 12.3 m^3/s (Bischofsky & Nausch, 2019). The results, summarized in Table 3, demonstrate that the WR has a substantial regional impact on the coastal waters for the different considered elements. When focusing on nutrient loads, the estimates are still relevant compared to larger river systems of the Baltic Sea (Hänninen et al., 2021).

Since the c-Q relationships may be baased by the Warnow-water management and the exceptionally low discharge rates during the observation period, the calculated

loads should be taken with caution. Additionally, longer time series provide more reliable information on loads and most likely improve the c-Q relation.

Table 3 - Calculated element loads for the upper Warnow River at the end of the middle catchment at a mean discharge of 12.3 $m^3 s^{-1}$ (see text for explanation), based on the C-Q approach. Note: Due to high redox-dependent pelagic variability, values for Mn, NH4, are only estimates

Element	Load, Upper Warnow (mol/d)
Ca	2583562
Mg	493650
Na	1458542
K	135618
SO_4	758611
DIC	4384487
TA	4281726
DOC	1510837
P	1361
Si	177059
$N\text{-}NO_3$	63288
$N\text{-}NH_4$	5243
Ba	455
Sr	5233
Li	1338
Mn	6467

The comparison with other smaller and larger rivers draining into the North and Baltic Seas (Table 2) demonstrates the potential importance of catchment lithology for the composition of surface waters.

This exemplifies compositional differences, particularly with the dissolved carbonate system, between the rivers draining mostly glacial deposits in their catchment area, and the hard water creeks draining Rügen Island that developed in a carbonate rock catchment (Table 2; Winde, 2009).

The management leads to higher evaporation effects that are reflected in the water isotope composition (Table 2). Our new results also indicate that the WR promotes the release of CO_2 from the coastal surface waters by enhancing the DIC and TA concentrations of fresh water entering the brackish coastal Baltic Sea.

4. Conclusions and outlook

Spatial and temporal investigations of the multi-isotope hydrochemistry of a managed river draining a coastal lowland demonstrate that most changes are caused by system internal processes like biomass production during the spring bloom and the benthic release of elements to the surface waters later during the year. These processes impact the capacity for releasing substances into the coastal waters of the southern Baltic Sea.

A spatial investigation during spring along the flow path of the Warnow River considering surface water inlets shows that diffusive water and element exchanges and system-internal transformations must be considered in interpreting the processes controlling the compositional trends.

It further shows the homogenization capacity of such a slow-flowing system to release substances in the coastal waters of the Baltic Sea. In addition, a more detailed picture of the actual impact of the WR on coastal biogeochemistry requires a detailed discussion on processes taking place in the estuarine part under temporal influence by mixing with brackish Baltic Sea water. The results of the present study further highlight the need for a more detailed investigation of the coupled carbon-sulfur cycling in the wetlands and bog areas in the Warnow River catchment area.

Acknowledgments and dedication

The authors wish to thank A. Köhler and O. Dellwig for expert ICP-OES support. To P.Roeser for the scientific discussions. We gratefully acknowledge the provision of hydrological data for the Warnow River by R. Boerner and O. Leschner (National Agency of Agriculture and the Environment of Mecklenburg-Western Pomerania (Stalu-MM)). The publication is dedicated to the memory of Jörn Anders, Dirk P. und Gisela Rodehorst, Henning C. Scholz, and Ruth E.B. Oeß, who recently passed away.

Funding

This study was supported by the DFG Research Training Group Baltic TRANSCOAST, the DAAD (via stipend to the first author within the doctoral program in Germany 2018/2019), and the carbon cycle part is a contribution to the BMBF project

COOLSTYLE as part of CARBOSTORE. This is Baltic TRANSCOAST publication #, and CARBOSTORE publication No.002.

Data availability

All raw data are provided either in the Tables or in the Supplementary material. Further information can be obtained from the authors upon request.

References

Berner, E.K., Berner, R.A. (2012) Global environment: Water, air, and geochemical cycles. Princeton University Press, 1-444.

Bitschofsky, F., Nausch, M. (2019) Spatial and seasonal variations in phosphorus speciation along a river in a lowland catchment (Warnow, Germany). Science of the Total Environment 657, 671–685.

Blöschl, G., Bierkens, M.F.P., Chambel, A., Cudennec, C., Destouni, G., Fiori, A., Kirchner, J.W., McDonnell, J.J., Savenije, H.G.G. et al. & Zhang, Y. (2019) Twenty-three unsolved problems in hydrology (UHP): A community perspective. *Hydrological Sciences Journal* 64, 1141-1158.

Bockholt, R., Kappes, K. (1994) Stoffaustrag über Entwässerungssysteme - ein aktueller Niedermoorgrünland - Ackerland - Vergleich, ökologische Untersuchungen im Warnow-Einzugsgebiet II, 2/1994, LAUN M-V, 136–146.

Böttcher, M.E., Brumsack, H.J., de Lange, G.J. (1998) Sulfate reduction and related stable isotope (34S, 18O) variations in interstitial waters from the eastern Mediterranean. Proceedings of the Ocean Drilling Program: Scientific Results. 160, 365–376. ttps://doi.org/10.2973/odp.proc.sr.160.002.1998

Böttcher M.E., Lipka M., Winde V., Dellwig O., Böttcher E.O., Böttcher T.M.C., Schmiedinger I. (2014) Multi-isotope composition of freshwater sources for the southern North and Baltic Sea. Proc. 23rd SWIM conference, Husum, 46-49, ISBN 978-3-00-046061-6.

Böttcher, M.E., Schmiedinger I. (2021) The impact of temperature on the water isotope ($^{2}H/^{1}H$, $^{17}O/^{16}O$, $^{18}O/^{16}O$) fractionation upon transport through a low-density polyethylene membrane. Isot. Env. Health Stud., 57: 183-192.

Böttcher, M.E., Thamdrup, B., Gehre, M., Theune, A. (2005) $^{34}S/^{32}S$ and $^{18}O/^{16}O$ fractionation during sulfur disproportionation by *Desulfobulbus propionicus*. Geomicrobiol. J. 22, 219-226.

Böttcher, M.E., Thamdrup, B., Vennemann, T.W. (2001) Oxygen and sulfur isotope fractionation during anaerobic bacterial disproportionation of elemental sulfur. Geochim. Cosmochim. Acta 65, 1601-1609.

Böttcher, M.E., Usdowski E. (1993) $^{34}S/^{32}S$ ratios of the dissolved sulphate of river, well and spring waters in a gypsum-carbonate karst area at the southwest edge of the Harz Mountains. *Z. dt. geol. Ges*. 144, 471-477.

Borges, A. L.-S. Schiettecatte, Abril G., B. Delille, Gazeau, F. (2006) Carbon dioxide in European coastal waters. Estuar. Coast. Shelf Sci. 70: 375–387.

Brand, W. A. and Coplen, T. B. (2012) Stable isotope deltas: Tiny, yet robust signatures in nature. Isot. Environ. Health Stud., 48: 393–409.

Buhl, D., Neuser, R.D., Richter, D.K., Riedel, D., Roberts, B., Strauss, H., Veizer, J. (1991) Nature and nurture: Environmental isotope story of the river Rhine. Naturwissenschaften 78: 337-346.

Campeau, A., Wallin, M.B., Giseler, R., Löfgren, S., Mörth, C.-M., Schiff, S., Venkiteswaran, J.J., Bishop, K. (2017) Multiple sources and sinks of dissolved inorganic carbon across Swedish streams, refocusing the lens of stable C isotopes. *Scientific Reports,* 7, 9158

Cantera, C.G., Scassol, R.A., Tufo, A., Villalba, L.B., dos Santos Afonso, M. (2018) Mobility of trace elements between the river water, the sediments, and the pore water of Las Catonas Stream, Buenos Aires Province, Argentina. *Environm. Earth Sci.* 77, 535

Charbonnier Q., Bouchez J., Gaillardet J., Gayer E., Porder S. (2022) A global imbalance in potassium and barium river export: The result of biological uptake? *Geochemical Perspectives Letters* 21, https://doi.org/10.7185/geochemlet.2214

Clow, D. and Drever, J. (1996) Weathering rates as a function of flow through an alpine soil, Chem. Geol., 132, 131–141, https://doi.org/10.1016/S0009-2541(96)00048-4.

Degens E.T., Kempe S., Richey J.E. (1991) Biogeochemistry of major world rivers. SCOPE 42, 1-356.

Deines, P., Langmuir, D., Harmon, R.S. (1974) Stable carbon isotope ratios and the existence of a gas phase in the evolution of carbonate ground waters. Geochim. Cosmochim. Acta. 38, 1147–1164. https://doi.org/10.1016/0016-7037(74)90010-6

Deutsch, B., Mewes, M., Liskow, I., Voss, M. (2006) Quantification of diffuse nitrate inputs into a small river system using stable isotopes of oxygen and nitrogen in nitrate. Organic Geochemistry 37, 1333-1342.

Dürr H.H., Meybeck M., Hartmann J., Laruelle G.G., Roubeix V. (2011) Global spatial distribution of natural riverine silica inputs to the coastal zone. Biogeosciences 8, 597-620.

Ehlert von Ahn, C.M., Dellwig O., Szymczycha B., Kotwicki L., Rooze J., Endler R., Escher P., Schmiedinger I., Sültenfuß J., Diak M., Gehre M., Struck U., Vogler S., Böttcher, M.E. (2022) Submarine groundwater discharge into a semi-enclosed coastal bay of the southern Baltic Sea: A multi-method approach. Science of the Total Environment, submitted

Eikenberg, J., Tricca, A., Vezzu, G., Stille, P., Bajo, S., Ruethi, M. (2001) $^{228}Ra/^{226}Ra/^{224}Ra$ and $^{87}Sr/^{86}Sr$ isotope relationships for determining interactions between ground and river water in the upper Rhine valley. J. Env. Radioact. 54, 133-162.

Fritz, P., Basharmal, G.M., Drimmie, R.J., Ibsen, J., Qureshi, R.M. (1989) Oxygen isotope exchange between sulphate and water during bacterial reduction of sulphate. Chemical Geology: Isotope Geoscience section. 79, 99-105.

Garcia-Orellana, J., Rodellas V., Tamborski, J. Diego-Feliu, M., van Beek, P. Weinstein, Y., Charette, M. Alorda-Kleinglass, A., Michael, H.A. Stieglitz, T., Scholten, J. (2021) Radium isotopes as submarine groundwater discharge (SGD) tracers: Review and recommendations. Earth-Science Reviews, 220: 103681.

Garcia-Solsona, E., Garcia-Orellana, J., Masque, P., and Dulaiova, H. (2008). Uncertainties Associated with ^{223}Ra and ^{224}Ra Measurements in Water via a Delayed Coincidence Counter (RaDeCC). Mar. Chem. 109, 198–219. doi:10.1016/j.marchem.2007.11.006

Gat, J. (1996). Oxygen and Hydrogen Isotopes in the Hydrological Cycle. Annu.Rev. Earth Planet. Sci. 24, 225–262. doi:10.1146/annurev.earth.24.1.225

Grasshoff K., Kremling K., and Ehrhardt M. (2009) Methods of Seawater Analysis. Weinheim: John Wiley & Sons

Hänninen, J., Mäkinen, K., Rajasilta, M., Vuorinen, I. (2021) The Baltic Sea and the adjacent North Sea silicate concentrations. Est. Coast. Shelf Sci., 249, 107110

Han Q., Wang B., Liu C-Q., Wang F., Peng X., Liu X.-L. (2018) Carbon biogeochemical cycle is enhanced by damming in a karst river. Science of the Total Environment 616–617, 1181–1189

Hartmann J., Lauerwald R., Moosdorf, N. (2014) A brief overview of the GLObal RIver CHemistry Database, GLORICH. Procedia Earth and Planetary Science 10: 23 – 27.

Hennig, H., Hilgert, T. (2007) Dränabflüsse – Der Schlüssel zur Wasserbilanzierung im nordostdeutschen Tiefland. – Hydrologie und Wasserbewirtschaftung 51, 248–257.

Hoefs, J. (1973) Stable isotope geochemistry. Springer.

Horita J, Rozanski K, Cohen S. (2008) Isotope effects in the evaporation of water: a status report of the Craig–gordon model. Isot Env Health Stud. 44:23–49.

House WA, Denison FH. (1997) Nutrient dynamics in a lowland stream impacted by sewage effluent: Great Ouse, England. Sci Total Environ. 205, 25-49. doi: 10.1016/s0048-9697(97)00086-7.

House WA, Denison FH. (2002) Exchange of inorganic phosphate between river waters and bed-sediments. Environ Sci Technol 36, 4295-4301. doi: 10.1021/es020039z.

Humborg, C., Pastuszak, M., Aigars, J., Siegmund, H., Mörth, C. M., Ittekkot, V.: Decreased silica land-sea fluxes through damming in the Baltic Sea catchment – significance of particle trapping and hydrological alterations (2006) Biogeochemistry, 77, 265–281

Humborg, C., Blomqvist, S., Avsan, E., Bergensund, Y., Smedberg, E., Brink, J., Mörth, C. M. (2002) Hydrological alterations with river damming in northern Sweden: Implications for weath- ering and river biogeochemistry, Global Biogeochem. Cycles, 16

Jenner, A.-K. (2018) Ground water development in North-Eastern Germany as deduced from the hydrogeochemical and stable isotope composition of selected drinking waters. MSc thesis, Leibniz IOW & University of Greifswald, 1-70.

Jurasinski, G., Janssen, M., Voss, M., Böttcher, M.E., Brede, M., Burchard, H., Forster, S., Gosch, L., Gräwe, U., Gründling-Pfaff, S., Haider, F., Ibenthal, M., Karow, N., Karsten, U., Kreuzburg, M., Lange, X., Langer, S., Leinweber, P., Rezanezhad, F., Rehder, G., Romoth, K., Schade, H., Schubert, H., Schulz-Vogt, H., Sokolova, I., Strehse, R., Unger, V., Westphal, J., Lennartz, B. (2018) Understanding the coastal ecocline: Assessing sea-land-interactions at non-tidal, low-lying coasts through interdisciplinary research. *Front. Mar. Sciences* 5, 342, 1-22.

Kahle, P., Bauwe, A., Lennartz, B. (2018) Übersichtsbeitrag zu Untersuchungen zum Nährstoffaustrag im künstlich entwässerten Tieflandeinzugsgebiet der Zarnow, Mecklenburg-Vorpommern. Hydrol. Wasserbewirtsch. 62, 159–172.

Kape, H.-E,, Pöplau, R., Nawotke, C. (2010) Richtige Kalkung - Grundlage für einen erfolgreichen Pflanzenbau. Ministerium für Landwirtschaft, Umwelt und Verbraucherschutz MV. DüV-10-13: 1-6.

Kirkels, F. M. S. A., Cerli, C. , Federherr, E., Gao, J. , Kalbitz, K. (2014) A novel high-temperature combustion based system for stable isotope analysis of dissolved organic carbon in aqueous samples. II: optimization and assessment of analytical performance. Rap. Com. Mass Spec., 28: 2574-2586, 10.1002/rcm.7053.

Kitidis, V., Shutler J.D., Ashton I., Warren M., Brown I., Findlay H., Hartman S.E., Sanders R., Humphreys M., Kivimäe C., Greenwood N., Hull T., Pearce D., et al. (2019) Winter weather controls net influx of atmospheric CO_2 on the north-west European shelf. Scientific Reports (2019) 9:20153

Knapp, J.L.A., von Freyberg J., Studer, B., Kiewiet, L., Kirchner, J.W.1,2,4 (2020) Concentration–discharge relationships vary among hydrological events, reflecting differences in event characteristics. Hydrol. Earth Syst. Sci., 24, 2561–2576. https://doi.org/10.5194/hess-24-2561-2020

Knee, K.L. & Paytan, A. (2011) Submarine groundwater discharge: A source of nutrients, metals, and pollutants to the coastal ocean. In: Wolanski, E. & McLusky, D.S. (eds.) *Treatise on Estuarine and Coastal Science* 4, 205-233.

Kowalski N., Dellwig O., Beck M., Gräwe U., Neubert N., Nägler T., Badewien T.H., Brumsack H.-J., van Beusekom J.E.E., Böttcher M.E. (2013) Pelagic molybdenum concentration anomalies and the impact of sediment re-oxidation in two tidal systems of the North Sea. Geochim. Cosmochim. Acta 119, 198-211.

Kronwang B., Andersen, I.KI., Hoffmann, C.C., Pedersen, M.L., Ovesen, N.B., Andersen, H.E. (2007) Water exchange and deposition of sediment and phosphorus during inundation of natural and restored lowland floodplains. *Water, Air, and Soil Pollution* 181: 115–121

Langmuir, D. (1971) The geochemistry of some carbonate ground waters in central Pennsylvania. Geochim. Cosmochim. Acta. 35, 1023–1045: https://doi.org/https://doi.org/10.1016/0016-7037(71)90019-6

Lerman, A., Mackenzie, F. T., Ver, L. M. (2004) Coupling of the perturbed C-N-P cycles in industrial time. Aquatic Geochemistry 10: 3-32.

Lerman, A., Wu, L., Mackenzie, F. T. (2007) CO_2 and H_2SO_4 consumption in weathering and material transport to the ocean, and their role in the global carbon balance, 106: 326-350.

Liu, Z., Dreybrodt, W., 2015. Significance of the carbon sink produced by H_2O-carbonate-CO_2-aquatic phototroph interaction on land. Sci. Bull. 60:182–191.

Luijendijk, E., Gleeson, T., Moosdorf, N. (2020) Fresh groundwater discharge insignificant for the world's oceans but important for coastal ecosystems. Nat. Commun., 11, Article e1260

LUNG, 2001. Landesamt für Umwelt, Naturschutz u. Geologie. Gewässernetz M-V. DOP / DTK10 / DTK25

Malik C., Böttcher M.E., Jenner, A.-K., Schmiedinger I., Löffler, S. (2022) Akkumulation von Sulfat und Karbonat in Grundwasser an der Ostseeküste: Eine Multi-Isotopen hydrogeochemische Ursachenanalyse. Grundwasser, submitted.

Michaelis, J., Usdowski, E., Menschel, G. (1985) Partitioning of ^{13}C and ^{12}C on the degassing of CO_2 and the precipitation of calcite - Rayleigh-type fractionation and a kinetic model. Am. J. Sci., 285, 318–327.

Moore, W. S., and Arnold, R. (1996). Measurement of 223Ra and 224Ra in Coastal Waters Using a Delayed Coincidence Counter. J. Geophys. Res. 101, 1321–1329.

Moosdorf N., Böttcher M.E., Adyasari D., Erkul E., Gilfedder B., Greskowiak J., Jenner A.-K., Kotwicki L., Massmann G., Mueller-Pethke M., Oehler T., Post V., Prien R., Scholten J., Siemon B., von Ahn C.M.E., Walther M., Waska H., Wunderlich, Mallast U. (2021) A state-of-the-art perspective on the characterization of subterranean estuaries at the regional scale. Frontiers in Earth Sciences, 9: 601293: 1-26.

Musolff, A., Schmidt, C., Selle, B., Fleckenstein, J. H. (2015) Catchment controls on solute export, Adv. Water Resour., 86, 133–146, https://doi.org/10.1016/j.advwatres.2015.09.026.

Nausch, M., Woelk, J., Kahle, P., Nausch, G., Laipe, T., Lennartz B. (2017) Phorphorosu fractions in discxharges from artificially draines lowland catchments (Warnow River, Baltic Sea). Agricult. Man. 187, 77-87.

Nutzmann G., Lewandowski J. (2009) Exchange between ground water and surface water at the lowland River Spree. Grundwasser 14:195-205

Pagenkopf, W., 2001. Aktuelle Nährstoffbilanzierung für Teilgebiete des Einzugsgebiets der Warnow. Geodaten Integration & Analyse, Berlin.

Parkhurst, D.L., and Appelo, C.A.J., 2013, Description of input and examples for PHREEQC version 3—A computer program for speciation, batch-reaction, one-dimensional transport, and inverse geochemical calculations: U.S. Geological Survey Techniques and Methods, book 6, chap. A43, 497 p.

Pawellek, F., Frauenstein, F., Veizer, J. (2002) Hydrochemistry and isotope geochemistry of the upper Danube River. Geochim. Cpsmochim. Acta 66: 3839-3854.

Plummer N.L., Busenberg, E. (1982) The solubilities of calcite, aragonite and vaterite in CO_2-H_2O solutions between 0 and 90°C, and an evaluation of the aqueous model for the system $CaCO_3$-CO_2-H_2O. Geochim. Cosmochim. Acta 46, 1011-1046

Purlik, S., Eisenhauer, A. (2004) Determination of radium isotopes and ^{222}Rn in a groundwater affected coastal area of the Baltic Sea and the underlying sub-sea floor aquifer. Mar. Chem. 87, 137-149.

Reckerth, A., Stichler, W., Schmidt, A., Stumpp, C. (2017) Long-term data set analysis of stable isotopic composition in German rivers. J. Hydrol. 552: 718-731.

Schlungbaum, G., Selig, U. (1996) Die Warnow - ein typischer norddeutscher Flachlandfluß und seine Bedeutung für den Nährstoffeintrag in die Ostsee. Rostocker Meeresbiologische Beiträge. 4, 67–84.

Schwientek; M., Einsiedl, F., Stichler, W., Stögbauer, A. (2008) Evidence for denitrification regulated by pyrite oxidation in a heterogeneous porous groundwater system. Chem. Geol. 255: 60-67.

Seibert, S.L., Böttcher, M.E., Waska, H., Holt, T., Pollmann, T., Massmann, G. (2021) Hydrogeochemistry of near-surface groundwater on a developing barrier island (Spiekeroog, Germany): The role of inundation, season and vegetation. J. Hydrol., 597: 126139

Selig, U., Schlungbaum, G. (2002) Longitudinal patterns of phosphorus and phosphorus binding in sediment of a lowland lake–river system. Hydrobiologia 472, 67–76.

Stumpp, C., Klaus, J., Stichler, W. (2014) Analysis of long-term stable isotopic composition in German precipitation. J. Hydrol. 517351-361.

Sun C., Liu J., Li M., Zang J., Wang L., Wu W., Zhang A., Wang J., Ran X. (2022) Inventory of riverine dissolved organic carbon in the Bohai Rim. Environmental Pollution 293, 118601

Trettin, R., Grischek, T., Strauch, G., Malleean, G., Nestler, W. (1999) The suitability and usage of ^{18}O and chloride as natural tracers for bank filtrate at the middle river Elbe. *Isot. Environm. Health Stud.* 35, 331–350.

van der Weijden, C.H., Middelburg. J.J. (1989) Hydrogeochemistry of the river Rhine: Long term and seasonal variability, elemental budgets, base level, and pollution. Water Res., 23, 1247-1266.

Vitòria L., Ptero, N., Soler, A., Scanals, A. (2004) Fertilizer characterization: Isotopic data (N, S, O, C, and Sr). Environ. Sci. Technol. 2004, 38, 3254-3262

von Ahn C. M. E., Scholten J., Malik C., Feldens P., Liu B., Dellwig O., Jenner A.-K., Papenmeier S., Schmiedinger I., Zeller M.A., Böttcher M.E. (2021) A multi-tracer study of fresh submarine and surface water sources for a temperate urbanize coastal bay. Front. Environm. Sci., 9: 642346.

Walsh J.J. (1991) Importance of continental margins in the marine biogeochemical cycling of carbon and nitrogen. Nature 350:53–55. doi:10.1038/350053a0

Winde, V. (2009) Flächenhafte Änderung physikochemischer Parameter im Verlauf von kalkabscheidenden Bächen auf Rügen. Diplomkartierung, Leibniz IOW & Universität Greifswald, 1-22.

Winde, V., Böttcher, M. E., Escher, P., Böning, P., Beck, M., Liebezeit, G., Schneider, B. (2014) Tidal and spatial variations of DI^{13}C and aquatic chemistry in a temperate tidal basin during winter time. J. Mar. Syst. 129, 394–402.

Winde V., Böttcher M.E., Voss M., Mahler A. (2017) Bladder wrack (*Fucus vesiculosus*) as an environmental bio-monitor in an urbanized fjord of the western Baltic Sea. Isot. Environ. Health Stud. 53, 563-579.

Winde V., Escher P., Schneider B., Böning P., Al-Raei A.M., Liebezeit G., Böttcher M.E. (2014) Carbon isotopes in DIC trace submarine groundwater discharge and advective pore water efflux in tidal areas of the southern North Sea. Proc. 23rd SWIM conference, Husum, 42-45

Wollast, R. (1991) The coastal organic carbon cycle: fluxes, sources, and sinks. In: Mantoura M.R.F.C., Martin J.M., Wollast R. (eds.) Ocean margin processes in global change. Wiley, London, 365–382

Wu Z., Liu B., Escher P., Kowalski N., Böttcher M.E. (2018) Carbon diagenesis in different sedimentary environments of the subtropical Beibu Gulf, South China Sea, J. Mar. Sys., 186: 68-84.

Zak, D., Hupfer, M., Cabezas, A., Jurasinski, G., Audet J., Kleeberg A., McInnes R., Kristiansen S.M., Petersen, R.J., Liu, H., Goldhammer T. (2021) Sulphate in freshwater ecosystems: A review of sources, biogeochemical cycles, ecotoxicological effects and bioremediation. Earth- Science Reviews 212, 103446

Zhang Y.-C., Slomp, C.P., Broers H.P., Passier H.F., Böttcher, M.E., Omoregie E.O., Lloyd J.R., Polya D.A., van Cappellen P. (2012) Isotopic and microbiological signatures of pyrite-driven denitrification linked to pyrite oxidation in a sandy aquifer. Chem. Geol., 300-301, 123-132.

Chapter 6. A State-Of-The-Art Perspective on the Characterization of Subterranean Estuaries at the Regional Scale

frontiers in Earth Science

REVIEW
published: 14 May 2021
doi: 10.3389/feart.2021.601293

A State-Of-The-Art Perspective on the Characterization of Subterranean Estuaries at the Regional Scale

Nils Moosdorf[1,2,3], Michael Ernst Böttcher[4,5,6], Dini Adyasari[1], Ercan Erkul[2], Benjamin S. Gilfedder[7], Janek Greskowiak[8], Anna-Kathrina Jenner[4], Lech Kotwicki[9], Gudrun Massmann[8], Mike Müller-Petke[10], Till Oehler[1], Vincent Post[11], Ralf Prien[12], Jan Scholten[2], Bernhard Siemon[11], Cátia Milene Ehlert von Ahn[4], Marc Walther[13], Hannelore Waska[14], Tina Wunderlich[2] and Ulf Mallast[15]*

[1]Department for Biogeochemistry / Geology, Leibniz Centre for Tropical Marine Research (ZMT), Bremen, Germany, [2]Institute of Geosciences, University of Kiel, Kiel, Germany, [3]Southern Cross Geoscience, Southern Cross University, Lismore, NSW, Australia, [4]Geochemistry and Isotope Biogeochemistry, Leibniz Institute for Baltic Sea Research (IOW), Warnemünde, Germany, [5]Marine Geochemistry, University of Greifswald, Greifswald, Germany, [6]Department of Maritime Systems, Interdisciplinary Faculty, University of Rostock, Rostock, Germany, [7]Department of Hydrology, Bayreuth Center of Ecology and Environmental Research (Bayceer), University of Bayreuth, Bayreuth, Germany, [8]Institut für Biologie und Umweltwissenschaften, University of Oldenburg, Oldenburg, Germany, [9]Institute of Oceanology, Polish Academy of Sciences, Sopot, Poland, [10]Leibniz Institute for Applied Geophysics (LIAG), Hannover, Germany, [11]Federal Institute for Geosciences and Natural Resources, Hanover, Germany, [12]Marine Chemistry, Leibniz Institute for Baltic Sea Research (IOW), Warnemünde, Germany, [13]Technische Universität Dresden, Faculty of Environmental Sciences, Department of Forest Sciences, Chair of Forest Biometrics and Forest Systems Analysis, 01062 Dresden, Germany, [14]Institute for Chemistry and Biology of the Marine Environment (ICBM), University of Oldenburg, Oldenburg, Germany, [15]Helmholtz Centre for Environmental Research (UFZ), Leipzig, Germany

Subterranean estuaries the, subsurface mixing zones of terrestrial groundwater and seawater, substantially influence solute fluxes to the oceans. Solutes brought by groundwater from land and solutes brought from the sea can undergo biogeochemical reactions. These are often mediated by microbes and controlled by reactions with coastal sediments, and determine the composition of fluids discharging from STEs (i.e., submarine groundwater discharge), which may have consequences showing in coastal ecosystems. While at the local scale (meters), processes have been intensively studied, the impact of subterranean estuary processes on solute fluxes to the coastal ocean remains poorly constrained at the regional scale (kilometers). In the present communication, we review the processes that occur in STEs, focusing mainly on fluid flow and biogeochemical transformations of nitrogen, phosphorus, carbon, sulfur and trace metals. We highlight the spatio-temporal dynamics and measurable manifestations of those processes. The objective of this contribution is to provide a perspective on how tracer studies, geophysical methods, remote sensing and hydrogeological modeling could exploit such manifestations to estimate the regional-scale impact of processes in STEs on solute fluxes to the coastal ocean.

Keywords: subterranean estuary, submarine groundwater discharge, coastal aquifer, upscaling, biogeochemistry, geophysics, numerical modeling, ecology

OPEN ACCESS

Edited by:
Frédéric Frappart, UMR5566 Laboratoire d'études en géophysique et océanographie spatiales (LEGOS), France

Reviewed by:
Andrea Pain, University of Maryland Center for Environmental Science (UMCES), United States
David Brankovits, Texas A&M University at Galveston, United States
Gwénaëlle Chaillou, Université du Québec à Rimouski, Canada

****Correspondence:***
Nils Moosdorf
nils.moosdorf@leibniz-zmt.de

Specialty section:
This article was submitted to Hydrosphere, a section of the journal Frontiers in Earth Science

Received: *31 August 2020*
Accepted: *04 February 2021*
Published: *14 May 2021*

Citation:
Moosdorf N, Böttcher ME, Adyasari D, Erkul E, Gilfedder BS, Greskowiak J, Jenner A-K, Kotwicki L, Massmann G, Müller-Petke M, Oehler T, Post V, Prien R, Scholten J, Siemon B, Ehlert von Ahn CM, Walther M, Waska H, Wunderlich T and Mallast U (2021) A State-Of-The-Art Perspective on the Characterization of Subterranean Estuaries at the Regional Scale. Front. Earth Sci. 9:601293. doi: 10.3389/feart.2021.601293

INTRODUCTION

Along global coastlines, meteoric groundwater discharges into the ocean (Church, 1996; Taniguchi et al., 2002; Zhou et al., 2019; Luijendijk et al., 2020). The subsurface zone where meteoric groundwater mixes with saltwater was termed the subterranean estuary (STE) by Moore (1999). This term was defined as "a coastal aquifer where groundwater derived from land drainage measurably dilutes saltwater that has invaded the aquifer through a free connection to the sea" (Moore, 1999). The relevance of STEs for matter cycling and coastal ecology is increasingly recognized by the scientific community (Rocha et al., 2021).

The term estuary originates from hydrology and is defined as the area where fresh river water and saline seawater mix (Prandle, 2009). Riverine estuaries are biogeochemical reactors that, amongst other processes, filter out about 20% of the dissolved silicon through reverse weathering (Tréguer and De La Rocha, 2013) or degas substantial amounts of riverine transported organic carbon as CO_2 (Laruelle et al., 2010). By now, it is accepted that riverine solute fluxes to the coastal realm cannot be meaningfully quantified without considering transformations in the mixing zone of river estuaries (e.g., Kipp et al., 2020). For submarine groundwater discharge (SGD), the same should hold for subterranean estuaries (Robinson et al., 2018).

STEs are characterized by waters with geochemical signatures controlled by steep (physico-)chemical gradients of mixing terrestrial groundwater and seawater (Moore, 1999). The groundwater-seawater mixing zone embraces thematically different scientific fields, sometimes leading to confusion in terminologies. The term STE, for instance, is partly overlapping with the term 'coastal aquifers', which describes a groundwater system at the interface of land and sea in hydrogeology (Duque et al., 2020; Jiao and Post, 2019). Mixing of fresh and saline groundwater occurs differently in porous sedimentary aquifers than in karst or volcanic aquifers since the former have longer residence times and a higher reaction area between solid and fluid phase. STEs of the latter type are termed 'anchialine' (Bishop et al., 2015). Other studies use the term STE for karstic environments (e.g., Gonneea et al., 2014). In these situations, hydrology plays a major role in biogeochemical reactions (Brankovits et al., 2018), which is amplified by the karst's hydrogeological conditions. However, if karstic aquifers discharge in submarine springs with sufficient discharge rates, this can lead to freshwater mixing with seawater in the ocean itself in the form of plume-like structures (e.g., Fleury et al., 2007), whose nutrient fluxes can trigger algal blooms (Chen et al., 2020). Karst areas cover large parts of the global coastline (Goldscheider et al., 2020) and are essential groundwater-ocean interaction areas. Nevertheless, since processes in these conduit-systems differ sharply from those in porous sediments, we focus our assessment on STEs composed of porous sediments (**Figure 1**). Thus, we here use the term STE to describe the zone where fresh and saline groundwater mix in porous coastal aquifers in the subsurface, which is in line with the marine scientific literature (Robinson et al., 2018; Duque et al., 2020).

While STEs share the name estuary and the freshwater-saltwater mixing zone, they differ sharply from their riverine counterparts. The term "estuary" itself is questionable for STEs, since some definitions of estuaries also encompass the shape of the water body, e.g., as "semi-enclosed", basically referring to rivers (Wolanski, 2007). One crucial difference is residence time, which is in the order of days in riverine estuaries (Rasmussen and Josefson, 2002) and can be decades in STEs (e.g., Grünenbaum et al., 2020). The different residence time leads to different mixing processes: while in rivers, mixing can be in turbulent flow driven by wind, flow in STEs is generally linear and advection-dispersion driven. While in river estuaries, water-solid interaction is mostly limited to suspended or surface sediment as solid phase, STEs provide a wide range of minerals and solids to interact due to a lower water/rock ratio. In some STEs, anoxic conditions develop along subsurface flow-paths or be promoted by the inflow of O_2-free groundwater, which changes the biogeochemical reactions compared to STEs where oxic conditions prevail (Slomp and Van Cappellen, 2004) or to oxic surface waters flowing through riverine estuaries. Thus, despite river estuaries and STEs sharing parts of their name, the processes involved can be very different. Also, while rivers can be treated as point sources of solutes and particulates to the coastal ocean, STEs can occur along long stretches of coast, and their geochemistry can vary substantially at the meter scale (e.g., Beck et al., 2016; Ehlert et al., 2016; Beck et al., 2017; Waska et al., 2019b) and even more at the regional scale.

In general, biogeochemical reactions alter the composition of terrestrial groundwater and saltwater that flow through STEs. Thus, the biogeochemical composition of the resulting SGD will not represent a conservative mixing between the fresh and saline waters entering the STE. In many STEs, the contribution of marine water circulating through the sediment ("marine SGD") to the total water fluxes exceeds that of terrestrial groundwater (e.g., Lopez et al., 2020). Groundwater of marine origin in the seafloor sediment and STEs will here be called "saline groundwater." Flow and transport in STEs are highly dynamic and locally variable. While discharge from unconfined shallow aquifers occurs near the shoreline, discharge from confined aquifers has been observed several kilometers offshore, depending on the hydrogeological conditions (Burnett et al., 2003; Gustafson et al., 2019). Mixing of fluids triggers biogeochemical reactions that can change the discharge composition compared to the original end-members (i.e., fresh groundwater and saltwater). Understanding the coupling between the physical and biogeochemical processes is the prerequisite to understand the role of STEs in controlling the geochemical composition of SGD (Robinson et al., 2018). Processes in STEs can substantially influence the water quality of the receiving water bodies and the biological processes in coastal waters (e.g., productivity, food web structure) and the full spectrum of the species inhabiting them, from bacteria (Adyasari et al., 2019a), algae, through grazers, detritivores, to invertebrates (Miller and Ullman, 2004), predatory fish (Pisternick et al., 2020), and birds (Kotwicki et al., 2014; Lecher and Mackey, 2018). The processes controlling the solute fluxes through STEs have been

FIGURE 1 | Examples of beach settings in which active STEs developed. Left panel: Varkala Beach, India, where SGD seeps through the pore space below the waterline (Oehler et al., 2019b) (Photograph: T. Oehler). Middle panel: Trou aux Biches, Mauritius, where SGD is seeping out of the beach face during low tide (Photograph: J. Scholten). Right panel: SGD seeping along preferential flow-paths into the Wadden Sea near Cuxhaven, Germany (Photograph: Nils Moosdorf). Note that an STE often is not directly visible from the surface.

named among the main currently unsolved problems in hydrology (Blöschl et al., 2019).

Groundwater salinity distribution in STEs is typically characterized by a wedge of dense, saline groundwater that thins from the ocean inland underneath a fresh water body at the bottom of an aquifer (**Figure 2**). Along these water bodies' interface, the fresh and saline groundwater mix and a zone of intermediate salinities forms. Another saline recirculation cell, where saltwater infiltrates into the sediment, the so-called 'upper saline plume' (USP), can occur in settings with a sloping land surface where tides and waves run up along the beach (e.g., Lebbe, 1981; Robinson et al., 2007). Between the USP and the saltwater wedge, a 'freshwater discharge tube' evolves, focusing fresh SGD along the low water line under an active SGD seepage zone. These distinct water bodies have been described to shift, expand and contract as a consequence of seasonal groundwater recharge variations (Michael et al., 2005), spring-neap tidal cycles (Abarca et al., 2013; Heiss and Michael, 2014) or intensified wave conditions (Robinson et al., 2014). The shape of the STE is controlled by a large number of factors, such as geological heterogeneity (Geng et al., 2020), terrestrial groundwater discharge (Heiss and Michael, 2014), tidal amplitude (Abarca et al., 2013), sediment topography (Robinson et al., 2006; Waska et al., 2019b; Grünenbaum et al., 2020), or even seawater temperature (Kim et al., 2020).

STEs have been investigated from local, regional (Beck and Brumsack, 2012; Jurasinski et al., 2018) to global perspective (Beck et al., 2013; Rahman et al., 2019), and groundwater dynamics and driving forces have been reviewed (Santos et al., 2012; Robinson et al., 2018). For example, in Waquoit Bay, a comprehensive suite of STE studies related to biogeochemistry (Charette et al., 2005; Charette and Sholkovitz, 2006; Saenz et al., 2012; Gonneea et al., 2014), hydrology (Michael et al., 2005; Spiteri et al., 2008b), and tracer application (Dulaiova et al., 2008) has been conducted. The coastline of the Gulf of Mexico has provided a diverse geological background for local STE studies: from sandy beaches and lagoon systems in Florida (Santos et al., 2008; Roy et al., 2011; Pain et al., 2019), via an organic-rich STE in the eastern part of Mobile Bay, Alabama (Montiel et al., 2019), to developed karst system in Yucatan, Mexico (Gonneea et al., 2014; Brankovits et al., 2017; Brankovits et al., 2018). Biogeochemical STE studies in North America have also been conducted in the eastern (Hays and Ullman, 2007; O'Connor et al., 2018; Tamborski et al., 2017) and western (Santoro et al., 2008; Boehm et al., 2014; Brown and Boehm, 2016) coastal areas of the contiguous United States, as well as boreal parts of Alaska (Lecher et al., 2016a) and Canada (Couturier et al., 2016; Sirois et al., 2018).

Many relevant field studies have been conducted outside North America. The development of an upper saline plume and the freshwater tube underneath was first demonstrated in Belgium by Lebbe (1981). He developed the conceptual model for the salinity distribution in unconfined aquifers influenced by tides based on field measurements and mathematical modeling. The Wadden Sea, located in the southern North Sea, is a well-studied system where various geochemical (Beck et al., 2017; Linkhorst et al., 2017; Reckhardt et al., 2017; Rullkötter, 2009; Seidel et al., 2015; Waska et al., 2019b), hydrological (Moore et al., 2011; Seibert et al., 2019), as well as microbiological and biogeochemical (Musat et al., 2006; Al-Raei et al., 2009) studies have been conducted. Here, STEs have been shown to function as a coastal filter for material exchange and transformation. They are characterized by a high input of organic matter, intensive nutrient recycling, and organic matter remineralization rates (Billerbeck et al., 2006; Al-Raei et al., 2009). Other studied STEs in Europe are the Baltic Sea coast (Szymczycha et al., 2012; Donis et al., 2017; Jurasinski et al., 2018; Virtasalo et al., 2019) and the coast of France (Anschutz et al., 2009; Charbonnier et al., 2013; Oehler et al., 2017). In Asia-Pacific, STE studies were conducted in South Korea (Kim et al., 2012; Lee et al., 2017) with particular attention paid to the volcanic Jeju Island (Kim et al., 2011; Kim et al., 2013), China (Liu et al., 2012; Wang et al., 2015; Yang et al., 2015; Jiang et al., 2020), Japan (Uchiyama et al., 2000; Nakada et al., 2011), Indonesia (Adyasari et al., 2019b), Cook Island (Erler et al., 2014), and Australia (Robinson et al., 2006; Robinson et al., 2007; Sanders et al., 2012).

The delivery of nutrients by terrestrial groundwater has been plentifully addressed also at continental to global scales (e.g., Beusen et al., 2013; Sawyer et al., 2016; Luijendijk et al., 2020), typically by multiplying the estimated water flux by the nutrient concentration of the fresh groundwater to obtain the nutrient mass flux. Such estimates do not consider the biogeochemical reactions in the STE that modulate the actual inputs to the coastal ocean. Local-scale studies have revealed the critical influence of biogeochemical reactions in the STE on land-ocean solute fluxes

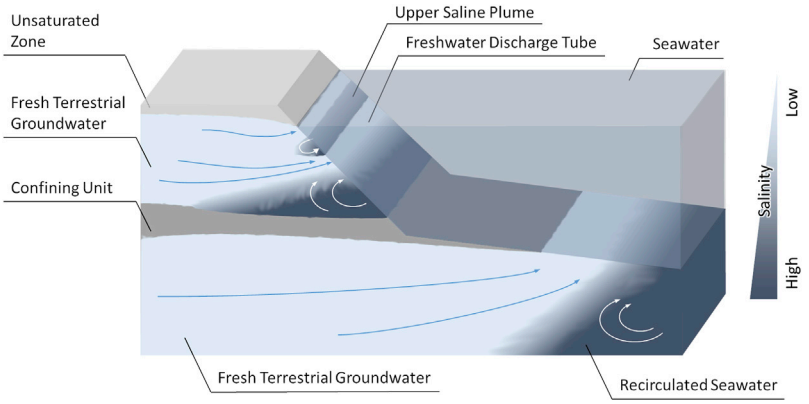

FIGURE 2 | Cross-section of a coastline highlighting the different parts of a subterranean estuary (STE).

and coastal ecology, even though STEs only cover a narrow stretch of the coast. This influence happens most certainly on a local and regional scale and is likely to have a significant effect on global scales. However, what remains unclear is how the knowledge and process descriptions at the local scale can be translated to the regional scale so that the impact of terrestrial SGD on the marine environment can be better quantified. We define the local scale as coastline lengths between 10^0–10^2 m and the regional scale at 10^3–10^5 m. Here, we summarize local scale knowledge about processes in STEs and outline perspectives toward the representation and extrapolation of these processes at the regional scale.

BIOGEOCHEMICAL CYCLING IN SUBTERRANEAN ESTUARIES

Subterranean estuaries are biogeochemically active, characterized by microbially mediated element release, fixation and transformation reactions (Charette et al., 2005; Spiteri et al., 2008a; McGrath et al., 2012; Beck et al., 2017; Duque et al., 2020). Biogeochemical reactions within the STE and the export of reaction products into coastal waters can have wide-reaching consequences for ecologically detrimental coastal processes such as eutrophication and associated oxygen depletion of bottom waters (Slomp and Van Cappellen, 2004; Dybas, 2005), modification of ocean derived substances (e.g., detrital matter including POC and S species: Shum and Sundby, 1996), buffering or enhancing ocean acidification (Wang et al., 2014; Santos et al., 2015; Liu et al., 2017), and transport of contaminants from the land to the sea (Brovelli et al., 2007; Wang et al., 2012). Depending on redox conditions and water flux rates, this can be crucial in determining element speciation and balances in coastal waters with effects for phytoplankton productivity and potentially eutrophication (Taniguchi et al., 2019). Increased primary productivity can further intensify the transfer of nutrients and possible contaminants from lower to higher trophic levels.

Organic carbon forms a primary electron donor in the coastal subsurface, which interacts with various electron acceptors (e.g., O, N, S, Fe and Mn species) derived from the sea or transported within the aquifer. Organic carbon stimulates a cascade of biogeochemical reactions relevant for local to global element turnover rates and budgets at the land-sea interface (Goodridge and Melack, 2014; Couturier et al., 2017; Cho et al., 2018; Seibert et al., 2019). Organic carbon quality, i.e., the fitness of organic molecules for microbial use as an electron donor (and sometimes acceptor), is dependent on its molecular composition, which is usually a complex mixture of terrestrial and marine-derived chemical moieties (Seidel et al., 2015).

The steep physicochemical gradients and enhanced microbial activity in STEs can also lead to mineralization processes of organic matter and hydrocarbons (Akam et al., 2020) as well as reoxidation reactions (Roy et al., 2013). These processes alter the redox conditions and the proton activity and may lead to the formation of authigenic solid phases, like carbonate, sulfide, sulfate or phosphate minerals (O'Connor et al., 2018; Riechelmann et al., 2020; Roy et al., 2013). Mineral formation may limit the concentrations of dissolved trace elements like metals being co-precipitated during iron sulfide formation (e.g., Huerta-Diaz and Morse, 1992). However, mineral formation also adds to the STE function as a filtering barrier between the terrestrial groundwater system and the sea for harmful chemical compounds. A well-known example of this is the so-called 'iron curtain,' an iron oxide rich zone that forms when oxic seawater is cycled through the beach sediments and mixes with anoxic or sub-oxic terrestrial groundwater (Chambers and Odum, 1990; Charette and Sholkovitz, 2002; Spiteri et al., 2006; Linkhorst et al., 2017; Sirois et al., 2018). The large sorption capacity of these iron oxides can be responsible for fixating aqueous pollutants, such as P and As species, before they become entwined in coastal food webs (Chambers and Odum, 1990; Bone et al., 2006; Beck et al., 2010).

Biogeochemically active areas can be unevenly distributed within the STE. This effect is amplified by the geological heterogeneity of flow regimes (Geng et al., 2020). Typically, certain conditions lead to the formation of biogeochemical 'hot-spots', areas of enhanced microbiological and chemical

activity that drive the modification and transformation of ions and molecules in the subsurface (Santos et al., 2008). Microbial activity and community changes with salinity (Adyasari et al., 2019a). While the processes causing the observed spatial distribution of hot-spots are still poorly understood, an appropriate substrate (chemical and physical) is needed, as is an active flux of reactive electron acceptors and donors to maintain an energy flux for the microbial metabolism.

Thus, knowing the hydrogeology of a site (water origin, flow paths, residence times, mixing processes, and aquifer properties) is crucial for understanding the distribution of hot spots in STEs (Goodridge and Melack, 2014). Modeling suggested that density-driven flow can enhance mixing in an STE when dense saline water from the upper saline plume or periodic flooding sinks into the underlying freshwater lens due to 'salt fingering' (Greskowiak, 2014). Other studies show the importance of heterogeneity of hydrogeological parameters in controlling an STE's shape (Weinstein et al., 2007) and the associated biogeochemical reactions (Heiss et al., 2020).

The temporal equivalent of 'hot-spot' is often termed 'hot moment'. The recognition that high element turnover (reactivity) areas are temporally dynamic is important (Liu et al., 2017; Waska et al., 2019b). Hot moments imply that enhanced biogeochemical activity areas are stationary neither in time nor location and will fluctuate depending on hydrological and chemical boundary conditions (Seidel et al., 2015). The incorporation of hot moments into the framework of biogeochemical activity in the subsurface has helped understand the previously ambiguous distributions of elements and molecules, e.g., in the framework of groundwater-river interaction (Vidon et al., 2010). At the coast, storms may, for instance, physically impact the freshwater input, the availability of substrates, or the seafloor morphology, which would change STE behavior. Due to storms, SGD rates can strongly change in a matter of days (Cho et al., 2021). More generally, hot moments in STE can be created through movements of the salinity gradient, when, e.g., phosphorus can desorb from aquifer sediment with increasing salinity and cause a spike of P fluxes to the ocean that is not directly connected to terrestrial or marine inputs (Flower et al., 2017). Hot moments can also result from shifts in groundwater flow paths due to changed wave activity, which have been hypothesized to trigger pulses of arsenic transport into coastal waters due to instability of iron oxyhydroxides under changing redox conditions (Rakhimbekova et al., 2018). Water residence time is an essential factor influencing chemical reaction kinetics in the STE. For instance, in Waquoit Bay, longer residence times during winter caused attenuation of the groundwater nutrient load within the STE, whereas during periods of shorter residence time, SGD was nutrient-enriched (Gonneea and Charette, 2014).

The characterization of mineral authigenesis and its proxy potential in the STE requires sediment core material from the coastal and hinterland zone, best vertically resolved along transects through the STE to gain regional information. Whereas the physicochemical characterization of the aqueous solutions may allow for the identification of the current situation, the solid phases, when combined with appropriate age control, provide information about past SGD (Böttcher and Dietzel, 2010) as well as the movement of the geochemical mixing zone within the STE in response to sea-level change (Roy et al., 2010; Hong et al., 2018). The sea-level rise since the last glacial maximum caused a landward movement of STEs. Isotopic composition of authigenic minerals documents past changes in the land-sea hydrological conductivity and the evolution of the paleoenvironment.

In the following, the biogeochemical cycling of individual compounds in STEs will be discussed.

Carbon

Subterranean estuaries receive carbon (C) from both terrestrial and marine sources. Terrestrial dissolved inorganic carbon (DIC) is principally derived from biological processes taking place in the soil, and further influenced by biogeochemical processes in the groundwater (Bögli, 1980; Clark and Fritz, 1997; Deines et al., 1974). Terrestrial dissolved organic carbon (DOC) in STEs is either transported from the soil zone of the surrounding watersheds to the coast via groundwater or leached from vascular-plant material buried in coastal aquifers, such as paleosols (Sirois et al., 2018) or peat layers. Marine DOC is supplied to STEs by infiltrating seawater and produced locally in the STEs through remineralization of particulate organic matter (POM), for example, from coastal phytoplankton and macrobenthic beach wrack (Kim et al., 2019). DOC from both sources is transformed in STEs by microbial activity into CO_2 and CH_4.

Generally, terrestrial groundwater contributions will enhance the regional potential of coastal seawater to degas CO_2 to the atmosphere and contribute to primary productivity. However, DIC from terrestrial groundwater may also induce intense carbonate mineral dissolution (if terrestrial groundwater is oversaturated in CO_2) or lead to the precipitation of secondary carbonates (Deines et al., 1974; Wigley et al., 1978). The dissolution of carbonates in beach sands could be a substantial pH-buffer preventing acidic groundwater from changing coastal marine environments. Mixing between different water masses may impact the saturation states of carbonate minerals in an aqueous solution (Bögli, 1980; Hanshaw and Back, 1979), which amplifies the STE effect on the carbon cycle. Carbonate dissolution in the groundwater-seawater mixing zone can form caves and caverneous structures (Mylroie and Carew, 1990). At the regional scale, the total amount of carbonate dissolution through saturation effects of mixing groundwater and seawater was estimated on the Yucatan Peninsula (Hanshaw and Back, 1980). Therefore, carbonate dissolution structures may potentially be used to derive information about STE activity at regional scales or trace back STEs over geological time scales. Precipitation or dissolution of authigenic carbonate minerals could develop characteristic C and O isotope as well as trace metal signatures that can be used to deduce the composition of past solute gradients in an STE (Böttcher and Dietzel, 2010).

SGD can also be a source of methane (CH_4) to coastal waters (Lecher et al., 2016b; O'Reilly et al., 2015), and CH_4 gradients have been used to identify sites of SGD (e.g., Cable et al., 1996; Böttcher et al., 2021). In the Baltic Sea, seepage of terrestrial

groundwater associated with CH_4 releases was observed (Whiticar and Werner, 1981; Whiticar, 2002). STEs, both in karstic and porous settings, can be hotspots for CH_4 oxidation that removes CH_4 from groundwater before discharging into surface waters (Schutte et al., 2016; Brankovits and Pohlman, 2020). High variability in temporal (seasonal) and spatial (among geographically similar STEs) CO_2 and CH_4 concentrations and fluxes have been observed (Pain et al., 2019; Pain et al., 2020), complicating extrapolations to the regional scale.

Mineralization of DOM and CH_4 in STEs changes ratios of total alkalinity (TA) over DIC depending on the involved electron acceptors and superimposing biogeochemical processes (Akam et al., 2020). The mineralization can result in characteristic carbon isotope signatures (Deines et al., 1974; Meister et al., 2019). Sheltered, organic-rich STEs with sulfate reduction as a dominant remineralization pathway may become enriched with DOC and TA (e.g., Sippo et al., 2016). The mineralization of organic carbon in STEs is often linked to several overlapping mechanisms, which can vary over seasonal cycles, such as the advective flow of terrestrial groundwater and saltwater and the availability of organic carbon (Kim and Kim, 2017; Liu et al., 2017; Kim et al., 2019). Marine-derived organic matter is assumed to be more abundant and more labile than terrestrially derived organic matter (Seidel et al., 2015) and is accompanied by an injection of oxygen, which accelerates mineralization rates. This "priming" by labile organic carbon and supply of oxygen may impact remineralization of groundwater-imported terrestrial DOC, but how and to which extent is weakly known. Since seawater circulation volumes exceed terrestrial groundwater throughputs in many STEs, marine DOC inputs could primarily determine the activity of the STE microbial reactor. Hence, most DOC released back into the coastal water column could be recycled/transformed. However, the relative contributions of terrestrial and marine organic carbon, as well as the function of the STE as a net source or net sink of organic carbon, are highly variable in space and time (Webb et al., 2019).

Carbon cycling in the STE on a local scale is best understood based on parallel profiling on land and at the seaside of the groundwater-seawater mixing zone since both terrestrial- and marine processes can control DIC and DOC fluxes. Besides direct tracking and benthic measurements of SGD leaving an STE (Donis et al., 2017), stable C isotope compositions of DIC, DOC and CH_4 are useful variables in the characterization and even quantification of internal processes and modulations in STEs (e.g., Winde et al., 2014; Donis et al., 2017; Meister et al., 2019; Pain et al., 2019; Pain et al., 2020). Also, DOM molecular traits can elucidate organic carbon cycling in STEs (Seidel et al., 2015). At the regional scale, the C cycle is particularly complex to represent because of the considerable heterogeneity of unconfined aquifers and the formation of metabolically diverse 'hot spots'. Therefore, an abundance of information is necessary both from the land- and marine sides of the STE.

Nitrogen

Subterranean estuaries may act as either a source or sink of nitrogen (N). Microorganisms catalyze different reactions of reactive N, which include nitrate (NO_3^-), nitrite (NO_2^-), and ammonium (NH_4^+). The core nitrogen cycle involves four reductions [N fixation ($N_2 \rightarrow NH_4^+$), denitrification ($NO_3^- \rightarrow N_2$)], assimilatory nitrate reduction ($NO_3^- \rightarrow NH_4^+$), and dissimilatory nitrate reduction to ammonium (DNRA, $NO_3^- \rightarrow NH_4^+$) as well as two oxidation pathways [nitrification ($NH_4^+ \rightarrow NO_3^-$)] and anaerobic ammonium oxidation (anammox, $NH_4^+ \rightarrow N_2$) (Kanehisa and Goto, 2000). The nitrogen cycle further includes organic nitrogen mineralization, or ammonification, which is the breakdown of organic N (N_{org}), leading to the release of NH_4^+.

Nitrogen usually enters the system via N fixation (Fulweiler et al., 2007; Rao and Charette, 2012), organic input from terrestrial and marine sources, or terrestrial groundwater in the form of nitrate (Weinstein et al., 2011). STEs were classified as nutrient-contaminated STEs when they receive elevated amounts of nitrate from terrestrial groundwater and uncontaminated STEs when they produce nitrate internally from the mineralization of organic matter (Santos et al., 2009b; Loveless and Oldham, 2010; Robinson et al., 2018). In the latter case, tidal pumping provides N_{org} to the STE, which later is remineralized into NH_4^+ or nitrified to create NO_2^- and NO_3^- (Ullman et al., 2003; Santos et al., 2008; Charbonnier et al., 2013). The nitrifying microorganisms are aerobic chemoautotrophs; thus, nitrification generally occurs at the oxic surface layer of STEs where the ammonification rate is high, and N_{org} input and oxygen concentration are abundant (Santoro et al., 2008).

It has been shown that nitrate may be removed in permeable intertidal sediments from circulating seawater (Marchant et al., 2016), in some locations by up to 70% (Wong et al., 2020). Permanent biological removal of reactive N (NO_3^- and NH_4^+) from the STE may be achieved through biological assimilation, denitrification and anammox, provided that contact time between the aqueous and solid phase of an STE is sufficient. Denitrification is reportedly the primary biogeochemical process responsible for N loss in coastal and marine systems (Canfield et al., 2010) and performed by a wide range of bacteria and archaea, mostly heterotrophic microorganisms. Particulate organic carbon (POC) in the coastal aquifer was reported as a major control on denitrification in STE (Kim et al., 2020). Under conditions where NO_3^- inputs exceed the availability of carbon substrate for denitrification, DNRA may occur (Tiedje, 1988; Gardner et al., 2006), which, however, preserves N in the system as NH_4^+. Anammox, another process of biological N removal (Jetten et al., 1998), may occur in an anaerobic, NH_4^+-abundant, low organic matter environment (Sáenz et al., 2012). The co-occurrences of N transformation processes, such as simultaneous nitrification-denitrification, has been found in the STE due to the oxygen and organic matter stratification (Hays and Ullman, 2007; Erler et al., 2014) or rapid mixing of different water masses, creating both oxic and anoxic microzones (Uchiyama et al., 2000; Kroeger and Charette, 2008).

The N transformation processes are controlled mainly by groundwater residence time (Santos et al., 2008; Gonneea and Charette, 2014), redox condition (Slomp and Van Cappellen, 2004), availability of electron donors (Santoro, 2010), and mixing

rate of freshwater and saltwater (Kroeger and Charette, 2008). They have been detected and measured by geochemistry or molecular biology approaches. Stable isotopes ($\delta^{15}N$) and concentrations of reactive N help understand N behavior in STEs (Kroeger and Charette, 2008) and can also be manipulated as a tracer (Erler et al., 2014). Denitrification rates can also be calculated from STE sediment cores (DeSimone and Howes, 1996; Nowicki et al., 1999). Microbial N transformation can be determined by molecular detection, which involves extracting the microbial DNA from water or sediment samples (Santoro et al., 2006; Rogers and Casciotti, 2010; Hong et al., 2018; Adyasari et al., 2020).

Reactions in the nitrogen cycle in STEs are controlled primarily by microbiology. While at the local scale geochemistry or molecular biology assessment methods exist, regional scale tracers for these processes have yet to be identified. They could be indirectly inferred from STE physical properties (e.g., organic matter content and quality in host sediment, residence time, redox conditions) that control reaction rates and types. One example is the use of hyperspectral imaging to identify phytoplankton and CDOM concentration or total suspended solids (e.g., Brando and Dekker, 2003) and benthic information (e.g., Vahtmäe et al., 2020) in coastal waters if the signal is strong and clear enough given possible depth and turbidity. Lastly, if substantial quantities of gaseous N_2 are produced by denitrification, it could be detected by geophysical methods under favorable conditions.

Phosphorus

Phosphorous (P) inputs into terrestrial groundwater are mainly derived from fertilizers, waste and sewage (Slomp and Van Cappellen, 2004), to a minor extent from the mineralization of organic matter (Froelich et al., 1979) or released from minerals as geogenic sources (Kazmierczak et al., 2020; Tao et al., 2020). Geogenic P sources are mostly of local importance and depend on the aquifer mineralogy. In saline groundwater, P is usually derived from the mineralization of organic matter (Froelich et al., 1979). In karstic STEs, where groundwater can reach surface waters via rapid conduit flow pulse, inputs of P are associated with high-intensity rainfall events. In such a system in southern Java (Indonesia), elevated P concentrations were linked to events with high groundwater discharge rates, leading to exceptionally high P inputs into coastal waters (Oehler et al., 2018).

Dissolved P has a high affinity to adsorb at mineral surfaces of carbonates (Gaudette and Lyons, 1980; Burton and Walter, 1990) and iron oxyhydroxides (Einsele, 1936; van der Grift et al., 2014). These minerals can precipitate in STEs, which thereby would reduce the amount of P that is transported via SGD (Pain et al., 2020). In Waquoit Bay, P concentrations are 5–7 times higher in iron oxide rich sands than in the overlying surface sands, indicating how effectively processes in STEs can bind P (Charette and Sholkovitz, 2002).

Phosphorus concentrations along the salinity gradient of STEs usually behave non-conservatively. Elevated P concentrations are often associated with elevated groundwater salinity (Gaudette and Lyons, 1980), e.g., due to desorption from particles (Suzumura et al., 2000), Fe reduction associated with organic matter mineralization, direct P liberation (Froelich et al., 1979), or the release of colloid-bound nutrients (Prouty et al., 2017a). Sporadic P release can also follow occasional saltwater intrusions. Thus, to understand the temporal P transport behavior in an STE, the mobility of the groundwater-seawater mixing zone needs to be known. Depending on the distance to the sediment surface and the SGD flow regime, particulate and dissolved P may be transported to coastal waters (e.g., Lipka et al., 2018). Therefore, the mobility and final release of P to surface waters indirectly depend on redox conditions and the specific composition of the aquifer (Gaudette and Lyons, 1980; Lewandowski et al., 2015).

Phosphorous cycling in the STE is on a local scale best investigated based on the analysis of pore waters and sediments along transects across the terrestrial groundwater end-member through the mixing zone. Porewater analyses should be combined with continuous monitoring of the composition in the pelagic system and complemented by element budgeting. Care has to be taken in separating P in porewater derived from the groundwater against that derived from processes within an STE (Suzumura et al., 2000; Price et al., 2010; Prouty et al., 2017b). Redox conditions in the terrestrial groundwater, as well as the abundance of iron oxyhydroxides and carbonate minerals in the STE sediment need to be known or approximated to estimate the regional scale effect of STEs on P transport and release to the coastal ecosystem.

Sulfur

Subterranean estuaries gain most sulfur (S) from seawater, of which sulfate (SO_4^{2-}) is a major constituent. In brackish-marine sediments, microbial dissimilatory SO_4^{2-} reduction is the primary anaerobic process responsible for the mineralization of organic matter (Jørgensen, 1982), leading to the formation of dissolved sulfide. Sulfate reduction is also responsible for the oxidative conversion of methane into dissolved carbon dioxide (Boetius et al., 2000). Nevertheless, STEs also receive S from terrestrial groundwater, where dissolved SO_4^{2-} may originate from the dissolution of aquifer minerals like gypsum or oxidation of iron sulfides, like pyrite (Zhang et al., 2012). In young water bodies, anthropogenic sources, like acid rain, acid mine drainage and fertilizers, may further enhance SO_4^{2-} loads (Clark and Fritz, 1997; Alorda-Kleinglass et al., 2019).

In STEs containing sufficient electron donors, SO_4^{2-} reduction might be enhanced and can outcompete methanogenesis (Slomp and Van Cappellen, 2004). These systems can differ substantially in their biogeochemical processes and thereby in their release of climate-relevant gas emissions (Böttcher et al., 2021). Hydrogen sulfide may furthermore be re-oxidized by solid and aqueous species or be precipitated as iron sulfides (Luther et al., 1991; Rickard, 1997), thus acting as a sink for other dissolved metals (Huerta-Diaz and Morse, 1992). Overall, the dissolved SO_4^{2-} availability controls the biogeochemical element cycling in the groundwater-seawater mixing zone and specifically the coupled sulfur-carbon-metal cycle. In particular, the coupled stable sulfur and oxygen isotope composition of dissolved SO_4^{2-} in the STE pore waters provides information about sources, sinks and

cycling of sulfur (Fritz et al., 1989; Zhang et al., 2012) that may even be traced in an impacted shallow water column. Using sulfur isotopes as a tracer will be difficult at the regional scale due to the many involved controls and high sampling effort necessary.

Metals

Dissolved metal concentrations in pore waters of STEs (e.g., Ba, Cd, Cu, Fe, Mn, Mo, Pb, Zn) depend strongly on the mineralogy of the aquifer and may be enriched by anthropogenic contamination (Bone et al., 2007; Knee and Paytan, 2011). Many of the trace metals have particular ecological relevance as (micro)nutrients or toxins (Salt et al., 1995; Beck et al., 2010), and their signatures may be recognizable in near-shore STE sediments (Knee and Paytan, 2011). Submarine groundwater discharge is relevant for marine alkaline earth metal composition (Mayfield et al., 2021), a significant source of rare earth elements to the ocean and could be the missing link in the global distribution of Neodynium (Nd), a key proxy for oceanic water-mass mixing (Johannesson and Burdige, 2007; Chevis et al., 2015; Paffrath et al., 2020). Formation of complexes and colloids, sorption on the surface of particles, ion exchange, and changes in speciation are some of the relevant processes that control metal mobility, reactivity and toxicity (Charette and Sholkovitz, 2006; Waska et al., 2019a). The interactions between solutes and aquifer particles exert a firm control on trace metal transport in STEs and are strongly influenced by redox and pH conditions, salinity, and ligand availability (Knee and Paytan, 2011).

One of the quantitatively most abundant metals in STEs is iron (Fe). Its mobility is highly sensitive to changes in redox milieu and pH (Spiteri et al., 2006). Upon precipitation, iron-oxyhydroxides (FeOOH) and iron sulfides (FeS) provide a substrate for sorption and incorporation of metals, Si, As, DOM, and especially P (Huerta-Diaz and Morse, 1992; van der Grift et al., 2014). Furthermore, a substantial impact of FeOOH precipitation on the fractionation of different DOM fractions was described (Linkhorst et al., 2017). Iron mineral formation in the STE may remove selected trace metals from the aqueous solution (Charette and Sholkovitz, 2002; Charette and Sholkovitz, 2006; Böttcher and Dietzel, 2010) and release them later, when the reactive front may have shifted. Karst systems, in particular, can be efficient pathways for the exfiltration of metal-enriched waters through an STE into the coastal zone due to short aquifer residence times, enhanced flow rates, and a low mineral surfaces to groundwater volume ratio (Knee and Paytan, 2011; Pain et al., 2020).

The use of trace metals to identify SGD in the coastal waters depends on their reactivity in redox and pH gradients. Mn, for instance, remains mobile for some time even under oxic conditions (Kowalski et al., 2012; Winde et al., 2014), whereas Fe is efficiently fixed in the STE. This stability difference leads to fractionation of these metals (Balzer, 1982) and the trace metals that sorb on them. On a regional scale, selected trace metals like Mn or Ba in the water column may help to detect and even quantify SGD in tidal areas (Kowalski et al., 2012; Winde et al., 2014).

APPROACHES TO ASSESSING STE PROCESSES AT THE REGIONAL SCALE

Geochemical Tracers

Geochemical tracers can help to identify locations of STEs as well as processes within them. In general, tracers are characterized by distinct differences in concentrations or isotopic compositions between groundwater and seawater. Salinity or conductivity is a ubiquitous tracer since freshening of coastal ocean waters without a nearby surficial terrestrial source is an indicator of STE influence. However, traces of freshening diminish quickly due to mixing with seawater, and interpretations can be ambiguous due to other potential freshwater sources, such as rain.

Thus, other geochemical tracers with higher sensitivity, i.e., large concentration differences between groundwater and seawater, are applied. These are e.g. the natural radionuclides of radon (^{222}Rn; $t_{½}$ = 3.8 days; Rn in following) and radium (^{224}Ra; $t_{1/2}$ = 3.7 days; ^{223}Ra; $t_{1/2}$ = 11.4 days; ^{228}Ra; $t_{1/2}$ = 5.75 years; ^{226}Ra; $t_{1/2}$ = 1,600 years, Ra in the following), which are generally enriched in STE groundwater compared to surface waters. They can provide qualitative and quantitative information on sources and types of water sources to the STE, estimates of seawater residence times in the STE, as well as an overall quantification of the water flux out of the STE (i.e., SGD) into the coastal sea and open ocean (Taniguchi et al., 2019), while the results often include large uncertainties (Rodellas et al., 2021).

In addition to imports by sea- and groundwater, a fraction of the Ra and Rn in STEs pore waters is produced locally in sediment mineral grains by the decay of the radioactive parents Thorium (Th) and ^{226}Ra, respectively. In pore waters with low chloride content Ra is typically immobilized by sorption to clay and Fe and Mn oxide surfaces whereas, at salinities > ~3 practical salinity units (PSU), it behaves conservatively and can be used to trace water flow paths and fluxes (Webster et al., 1994). As an inert noble gas, Rn is not affected by the chemical composition of pore waters and geochemical reactions within the STE. The Ra and Rn pore water concentration will depend on the thorium/radium content of aquifer sediments, the recoiled efficiency, the residence time (i.e., the time elapsed since the water entered the STE) as well as Mn and Fe redox cycling. As seawater Ra and Rn concentrations usually are low, enrichment of these isotopes in coastal waters can be used to locate water fluxes out of the STE and quantify them in a mass balance approach assuming a known groundwater endmember (e.g., Garcia-Solsona et al., 2008).

A sampling of radionuclides can be done by boat at regional scales (Moore, 2000; Schubert et al., 2019; Stieglitz et al., 2010) (**Figure 3**). Time series measurements provide information on the temporal component of Ra and Rn fluxes and thus can be used to understand the dynamics of SGD in response to changing boundary conditions such as tides or storm events (Burnett and Dulaiova, 2003; Santos et al., 2009a). However, identifying STEs and associated terrestrial groundwater flux remains very challenging due to overlapping groundwater circulation processes and pathways, which are difficult to differentiate based on Rn and Ra only.

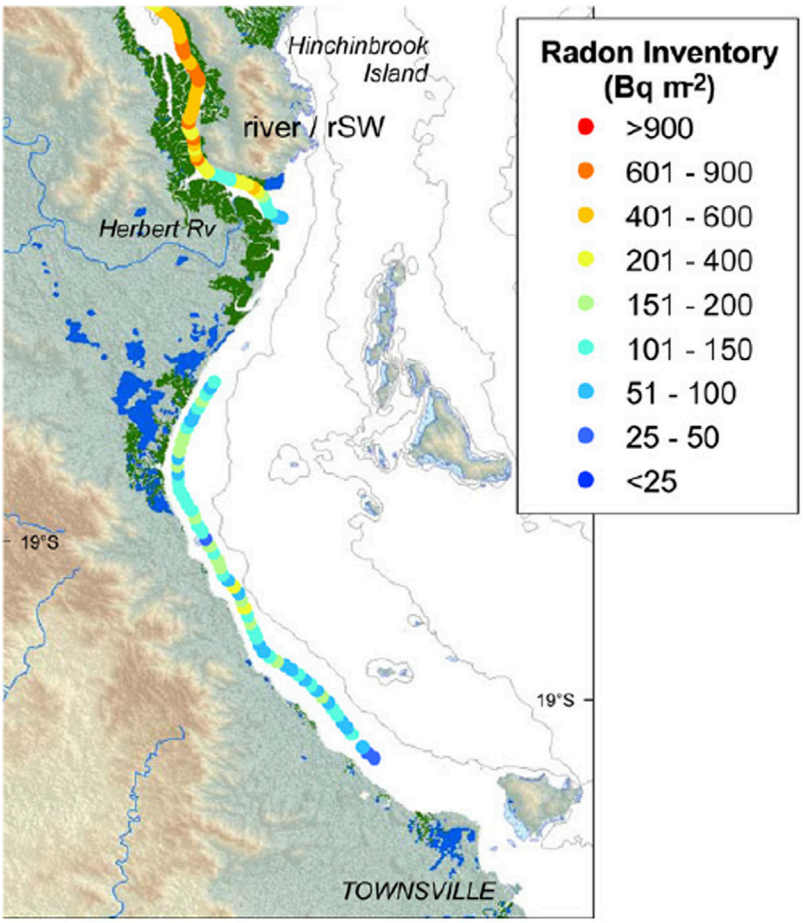

FIGURE 3 | Example of a regional scale Rn survey in Queensland, Australia (Stieglitz et al., 2010). Permission for reprint was provided by the copyright-holder.

The quantification of SGD using Rn and Ra is based on solving a mass balance of these radionuclides, considering all their major sources and sinks. It is usually done on sub-regional scales of up to 100s of meters, with notable exceptions for the Atlantic Ocean (Moore et al., 2008), the Mediterranean Sea (Rodellas et al., 2015) and the global oceans (Kwon et al., 2014). The quantification can be done either assuming a steady-state or using a non-steady-state approach when influxes from the STE are transient (Burnett et al., 2003; Moore, 2003; Hwang et al., 2005; Burnett et al., 2006). The steady-state assumption needs to be critically appraised when analyzing field data used in the mass-balance calculation, especially when using Rn. Turbulent conditions caused by wind and wave action can lead to excessive degassing before and during field campaigns so that the assumption of steady state between source and loss terms is not met. Indeed, it can be difficult to measure any Rn in surface waters following rough conditions. The 'memory' effect of variable degassing for the Rn balance tends to be around 5 days, but depends on factors such as water depth. In general, a non-steady state mass-balance together with continuous Rn measurements is better suited to dynamic conditions in the coastal zone (e.g., Santos et al., 2009c; Gilfedder et al., 2015).

The concentrations of tracers in SGD, i.e., the end-member concentrations of Ra and Rn, must be known to translate a mass flux into a water flux. Constraining these end-member concentrations is one of the most critical and uncertain steps of mass balance approaches. Groundwater concentrations may have substantial temporal and spatial variations caused by the heterogeneity of parent isotopes, different groundwater circulation pathways, hydrological and marine forcing, changes of geochemical processes within the STE as well as variability in terrestrial sources (Gonneea et al., 2013; Cho and Kim, 2016; Rocha et al., 2016; Cerda-Domenech et al., 2017). To overcome this problem, averaging a large number of end-member concentration measurements or taking the maximum and minimum end-member concentration to provide an envelope of possible SGD flux rates are common approaches (Moore, 1996; Beck et al., 2007). Nevertheless, the variability in the end-member concentrations remains the primary challenge for reliable quantification of SGD since shortcomings in accounting for the heterogeneity of end-members at local- and regional scales remain unsolved.

On a local scale, seepage meter measurements, as well as water balances, allow independent verifications of radionuclide-based

SGD rates (Povinec et al., 2012). However, on regional scales, verifications are still lacking or show systematic differences between tracer and model approaches (Prieto and Destouni, 2011). Nevertheless, Ra and Rn isotopes can be applied to map spatial and temporal changes in SGD, which under certain conditions would be a first indicator for the potential presence of an STE. Ra and Rn isotopes were used in regional scale SGD estimates.

Another isotopic tracer that can be applied for STE studies is the stable isotope composition of water ($^{2}H/^{1}H$, $^{18}O/^{16}O$, here shortly called "water isotopes"), which is a well-established tracer in hydro (geo)logical studies for the quantification of mixing processes and the deduction of water mass sources. Terrestrial groundwater is substantially more depleted in the heavier isotopes than seawater (Gat, 1996; Hoefs, 2018) and contains further information about the integrated meteorological conditions in the recharge area. Therefore, water isotopes are widely used in studies of SGD or STE (e.g., Burnett et al., 2006; Povinec et al., 2011; Rocha et al., 2016; Oehler et al., 2017; Duque et al., 2019). Time series can reveal the variability of terrestrial groundwater inputs on different time scales, particularly in dynamic karst STEs. Although still in its infancy, the extension of stable isotope characterization toward a triple isotope approach considering ^{17}O (resp. ^{17}O excess Sharp et al., 2018) may allow freshwater sourcing on the scale of regional STEs. Minerals formed in the mixing zone may record the parent solution's isotopic signature, providing opportunities for studies of past STE conditions.

Besides the stable isotopes of water, groundwater formed after the early 1960s may contain tritium (^{3}H), which has been used for dating purposes (Begemann and Libby, 1957; Bethke and Johnson, 2008). Meanwhile, the anthropogenic component, the atmospheric contamination of the water cycle by surface nuclear tests, has reached a natural background level. However, combined with its daughter isotope ^{3}He and Ne (Tolstikhin and Kamenskii, 1969; Sültenfuss et al., 2009), tritium still can be used for regional age estimation of the freshwater component in STEs (Röper et al., 2012; Post et al., 2019; Grünenbaum et al., 2020). The accumulation of ^{4}He is furthermore used in older groundwater dating (Bethke and Johnson, 2008). Other noble gas isotopes useful in the hydrogeology of STEs are ^{39}Ar and ^{85}Kr (e.g., Sánchez-Úbeda et al., 2018).

Local-scale geochemical investigation of STEs ideally includes vertical transects through the STE, a detailed physicochemical analysis, and solid-phase profiles from core material for a further microanalysis to identify precipitated authigenic solid phases. Measuring transects along the beach face enables mapping the spatial distribution of the biogeochemical environment, reactions and residence times over distances from tens to hundreds of meters. Larger scale mapping is challenging due to labor-intensive field sampling and increasing heterogeneity of the subsurface at larger scales meaning that extrapolation between transects is difficult.

Different circulation pathways in the STE can also be examined by exploiting the different half-lives of Ra isotopes, ranging from tidal to seasonal time scales. Assuming a steady-state hydrological situation, residence times can be estimated applying a general advective transport model in which the concentration of Ra and Rn in pore waters is a function of the supply of the radionuclides and their loss by decay and advection (Bokuniewicz et al., 2015; Tamborski et al., 2017). One of the main uncertainties in this approach is the lithological composition (mineral content, grain size, porosity) of the STE, which is assumed to be homogenous in space and in time throughout the STE. In reality, however, the heterogeneity in the STE causes a wide range of radionuclide supply rates (Beck and Cochran, 2013). Furthermore, temporally and spatially variable geochemical cycling of Fe and Mn and associated oxides profoundly influence the Ra pore water release (Gonneea et al., 2008). Since Ra is conservative in saline waters only, Ra-based residence times are only meaningful when seawater dominates the circulation through the STE. In contrast, Rn can be applied in both the fresh and brackish parts of the STE but is sensitive to ^{226}Ra distributions in the sediments as the parent isotope. Short term hydrological forcing like tides, wave set-up and induced circulation may also cause non-steady-state situations resulting in biases in residence times estimates. Finally, mixing of waters with different ages can lead to errors in the residence time estimates (which is similar to the real mean age of a water parcel) (Post et al., 2013; Gilfedder et al., 2019). As mixing is a linear process while radioactive decay and radioactive ingrowth are exponential (Bethke and Johnson, 2002), a systematic underestimation of the real mean age can occur if waters of different ages mix. One approach to circumvent this problem is the use of isotope ratios like, e.g., $^{224}Ra/^{223}Ra$. This method is very accurate if one water mixes with another one having zero activity (e.g., negligible Ra in freshwater) but does not work if the age difference between the water masses is large.

Residence time measurements tend to be point measurements at specific times. Verification of residence times based on radioisotopes is complicated to obtain. Comparing Ra- and Rn-based residence times may be one approach (Tamborski et al., 2017). Alternatively, pore water residence times may be compared to those derived by the ratio of water volume in the STE and the water flux out of the STE (Colbert et al., 2008).

Ra and Rn isotopes can be combined with other tracers, such as temperature (Cranswick et al., 2014), salinity (Example in **Figure 3**), or dissolved silicon (DSi) (Waska and Kim, 2011; Oehler et al., 2019b). Since DSi behaves rather conservatively during transport through the STE, it can be used to trace processes that change other solutes in groundwater in STE, such as N or P (Oehler et al., 2019b). Another example is the combination of CO_2 measurements and Rn measurements (e.g., Cyronak et al., 2014; Santos et al., 2015; Macklin et al., 2019). While this ties CO_2 concentrations to SGD intensity, it does not yet differentiate if the CO_2 is a product of STE processes or if the coastal groundwater just has elevated CO_2 concentrations that originated from the terrestrial groundwater. Similarly, CH_4 was combined with Rn as a tracer of SGD (Cable et al., 1996; Dulaiova et al., 2010) but could also be used for tracing processes in STE that generate CH_4. Using C stable isotopes as a tracer (Winde et al., 2014; Donis et al., 2017) and considering elemental mass balances (Deines et al., 1974) may be a successful approach.

The measurement of chemical tracers of STE processes at larger scales is associated with the problem to observe and measure the parameters with sufficient temporal and spatial resolution to resolve the underlying processes. Because tracer concentrations are modified upon emerging from the subsurface, sensors near the sea bottom are best suited to detect STE processes. The metabolites of typical benthic biogeochemical anaerobic OM degradation processes, like Mn^{2+} and NH_4^+, may, after benthic-pelagic coupling, survive the oxidation within the oxic water column for some time (Kowalski et al., 2012; Winde et al., 2014). Since some liberated trace elements will be reoxidized and sorbed to suspended particles, regional investigations will have to consider both the dissolved and the solid phases (Kowalski et al., 2012). Whereas the dissolved substances may be detected using discrete or continuous sampling techniques (Petersen et al., 2011; Kowalski et al., 2012), solid-phase sampling for geochemical analysis is limited to discrete sampling. Measurements can also be performed by autonomous underwater vehicles, which could automatically trace signals, like temperature, conductivity or Rn-isotopes, of groundwater discharge and scout for STEs (Tholen et al., 2019).

New combinations of sensors would help to detect STEs. Optical spectrometers in the UV-visible range of the light spectrum can be used to determine the concentration of nitrate, nitrite, HS^-, humic acids or DOC rapidly and without the use of reagents. It is to be expected that the optical absorption spectra will allow identifying water influenced by STEs. Sensors for the oxidation-reduction-potential (or, when referenced to the potential of a Standard Hydrogen Electrode, E_h) have been used for the estimation of concentrations of redox-sensitive elements in the redoxcline of the Baltic Sea (Meyer et al., 2014) or detecting hydrothermal plumes in the deep ocean (e.g., Baker et al., 2005). Combining several sensor types should allow the detection of STE signals in waters close to the bottom.

Geochemical tracers can help to regionally assess the amounts of SGD and point to the presence of STEs. They can also be applied at the local scale to draw quantitative conclusions about residence times in STEs and thus infer information about their reaction kinetics. At the regional scale, discrete and continuous measurements can be done. Still, these measurements will consist of discrete sampling points, and the feasibility of sampling will limit their resolution and coverage, which needs to be scaled according to the variability of the processes and tracers considered.

Ecological Tracers

Biodiversity in terrestrial groundwater recently received increased scientific attention (e.g., Hancock et al., 2005; Humphreys, 2008). Environmental gradients affect marine organisms in coastal waters. N and P are growth-limiting nutrients for most phytoplankton and macrophytes species that form the primary producers of the marine food web. Externally added nutrients alter the cycles of energy-flow between the pelagic and benthic zones, changing the community structure and population dynamics of both pelagic and benthic systems (Johannes, 1980; Sugimoto et al., 2017; Grzelak et al., 2018). A similar adaption to an increase in the concentration of nutrients can also be observed in the case of changes in other physical or chemical parameters of the environment: salinity, amount of light in the water column, amount of C species, heavy metals, O_2 concentration, the presence of hydrogen sulfide, or changes in pH. For example, observed changes in the chemical composition of bioavailable C in the Yucatan coastal waters result in lower coral cover, smaller size and reduced species richness (Crook et al., 2012). Benthic meio- and macrofaunal organisms may react to changes in the environment. Differences in benthic microbiology were observed in STE compared to purely saline beach waters, but little is known about microbial communities in STE (Santoro et al., 2006; Santoro et al., 2008; Santoro, 2010; Adyasari et al., 2019a; Adyasari et al., 2020). Thus, depending on location or environmental factors, STE may change species richness and diversity of meiofauna (Kotwicki et al., 2014; Encarnação et al., 2015; Welti et al., 2015; Grzelak et al., 2018). Similarly, macrofaunal communities can respond; their biodiversity can increase due to food supply (Waska and Kim, 2010; Pisternick et al., 2020) or may be reduced due to salinity stress or changes in pH (Zipperle and Reise, 2005; Migné et al., 2011; Utsunomiya et al., 2017). However, while the named ecological responses can highlight an STE presence, they will be hard to interpret as tracers of processes within that STE.

Since the impact of microbially mediated biogeochemical processes in the physicochemical gradients of STEs can be diverse (e.g., Beck et al., 2011), it is useful to apply the established methods to study the communities of organisms and associated biogeochemical processes occurring in the entire ecosystem. Methods of assessing abundance, activity, biomass and diversity include taxonomic phytoplankton analyses in water samples, fauna and microbial activity analyses in sediment cores, or fish assessment in the water. For ecological studies on the impacts of processes in STEs, these methods are combined with thermal infrared cameras or Ra/Rn tracing (Sugimoto et al., 2017; Grzelak et al., 2018). Simultaneous measurements of ^{222}Rn with other biological parameters allow assessing the reaction of biota activity on products of STEs (Taniguchi et al., 2019). Stable isotopes of N and C can also be used to trace STE products in the food web. Several studies have traced the behavior and fate of groundwater DIN using the isotope $\delta^{15}N$ of seagrass and macroalgae (Winde et al., 2017; Andrisoa et al., 2019) and gradients in the stable carbon isotope ratio between fresh and marine end-members (Gramling et al., 2003; Winde et al., 2017).

Consistent integration of hydrographic and biogeochemical research with bio-monitoring, elementary approaches and stable isotope analyses while considering higher trophic levels like fish and trophic flows in coastal ecosystems would enable the estimation of the direct impact of processes in STEs on ecosystems. While not yet done, specific species may have the potential to indicate STE processes in specific environments. Research in this direction is emerging (Lecher and Mackey, 2018), but additional knowledge is required before ecology can be used as a tracer for STE processes.

Geophysical Methods

From a geophysical perspective, the changes of physical and geochemical conditions under the seafloor associated with the presence of STEs are detectable by measuring properties such as electrical conductivity (EC), acoustic impedance (AI), or temperature. STEs can affect 1) the seafloor itself, e.g., its morphology, 2) the sediment or rock below it and 3) the properties of the water column, e.g., turbidity or sea-surface temperature.

At the local scale, geophysical methods can delineate the shape of an STE in detail. The EC difference between the terrestrial groundwater and saltwater is the most prominent parameter for local scale geophysical STE observation. The EC of freshwater varies depending on the total amount of dissolved ions, and literature puts it below 300 µS/cm (Kirsch, 2006), 1,000 µS/cm (Jiao and Post, 2019), or 2000 µS/cm (Langguth and Voigt, 2004). The EC of surficial seawater is orders of magnitude higher, > 40,000 µS/cm, depending on the temperature and thus latitude (Tyler et al., 2017). However, mineral grains, clay aggregates and organic matter in the STE also affect EC and need to be considered. Particularly sediment porosity and clay content strongly influence the overall EC of the bulk (rocks plus groundwater) volume (Archie, 1942). The high EC of clay leads to the general challenge of distinguishing freshwater saturated clays from brackish water saturated sands that may have very similar EC values. Gamma radiation of potassium, thorium and uranium at the surface helps to distinguish between clayey and sandy sediments (Siemon et al., 2020), as does an acoustic impedance contrast that seismic methods can show.

Many approaches that use electromagnetic fields (EM) emitted and detected by coils are available to represent subsurface properties (frequency-domain EM, time-domain-EM and slingram/ground-conductivity meter: Kirsch, 2006). Frequency-domain (sinusoidal transmitter currents) and time-domain EM (on/off transmitter currents) are typically used to obtain depth resolution at a single measurement point or along transects (Auken et al., 2003). Moving ground-conductivity meters are used for fast lateral mapping of EC but with limited depth resolution (e.g., De Smedt et al., 2013). Locating freshwater and thus STEs, at the regional scale can be realized using airborne or ship-based EC measuring methods.

Airborne methods use helicopters or fixed-wing aircraft to carry the geophysical systems at about 20–100 m above ground, covering 100–200 km of profiles or typically 10–50 km^2 per hour (**Figure 4**). In airborne EM, frequency-domain systems focus on near-surface (1–100 m) investigation of the spatial bulk EC (Siemon et al., 2015; Siemon et al., 2019; Siemon et al., 2020), whereas time-domain systems enable some deeper (5–500 m) investigation (Siemon et al., 2009; Steuer et al., 2009), depending on the conductivity distribution of the subsurface. Apart from electrical conductivity or resistivity, airborne radiometry maps the gamma radiation of the upper few decimeters of the surface (Wilford et al., 1997; IAEA, 2003). This technique has not yet been applied toward Ra/Rn concentrations in seawater but might be a pathway forward to map those isotopes with broader spatial coverage. Besides, semi-airborne methods using a ground-based transmitter and a helicopter-borne receiver have been developed recently to increase the penetration. While deep penetration is less important for STE investigation, UAV-based concepts can supplement the helicopter by a drone carrying the EM sensor in the future and hopefully enable cheaper investigations at the several kilometer scale. Finally, ship-based EM measurements have been applied to detect SGD (Müller, 2010; Müller et al., 2011).

Another EC method is electrical resistivity tomography (ERT), which, on land, uses steel electrodes pinned to the ground measuring the resistivity (the reciprocal of electrical conductivity) of the sediment by injecting a direct current (Stieglitz, 2005; Swarzenski et al., 2006). ERT has been used to observe the saltwater recirculation zone (Morrow et al., 2010) and its temporal changes (e.g., Johnson et al., 2015; Sutter and Ingham, 2017). ERT also can detect induced polarization effects caused by iron oxides (Mansoor and Slater, 2007). While this has not yet been applied to STEs, it could analyze Fe-cycling in the mixing zone. Measurements of magnetic-resonance also provide information on iron oxides and their concentrations (Keating and Knight, 2007; Costabel et al., 2018) and provide subsurface porosity and hydraulic conductivity (e.g., Müller-Petke and Yaramanci, 2015).

Marine ship-based measurements of ERT tow floating or submerged streamers behind a boat (Manheim et al., 2004; Day-Lewis et al., 2006; Hermans and Paepen, 2020). A profile of 5 km length can be measured in 1 h, but the conductive seawater limits penetration depth and therefore, streamer lengths of several hundred meters are needed to achieve sufficient penetration depth.

Seafloor morphological SGD proxies, such as pockmarks (e.g., Hoffmann et al., 2020), submarine terraces (Jakobsson et al., 2020), and depressions in carbonate rocks (Oehler et al., 2019a), are visible in the bathymetry. There are several techniques available to map the seafloor. Sidescan sonar data can reveal the location of pockmarks (e.g., Schlüter et al., 2004; Virtasalo et al., 2019), and echo sounders generally can also be applied for this task (Feldens et al., 2018; Papenmeier et al., 2020). Multibeam echo sounders provide high lateral coverage across-track on the seafloor, which is several times the water depth, enabling a fast mapping of larger scales.

Obtaining information on the geological structures by using high-resolution seismic profiling can be relevant for delineating the geometry of STEs (Mosher and Simpkin, 1999). The resulting image shows the reflection amplitudes and times (or depths) resulting from material interfaces with an impedance contrast, where the acoustic impedance is the product of bulk density and compressional velocity. Seismic profiles can be measured simultaneously with geoelectric streamers providing the same estimated profile length of 5 km per hour.

Geophysical methods also allow analyzing biogeochemical processes that occur within STEs, since some products can be identified. Shallow free gas accumulations (e.g., CH_4, N_2) can be mapped on larger scales using multibeam echo sounders. Gas is visible as acoustic blanking, bright spots, acoustic turbidity, or gas chimneys in seismic data (Hovland and Judd, 1988; Judd and Hovland, 1992). Free gas can have multiple origins in the ocean, so SGD does not necessarily cause its occurrence. However, gas-related features along the Belgian coast (Missiaen et al., 2002), in

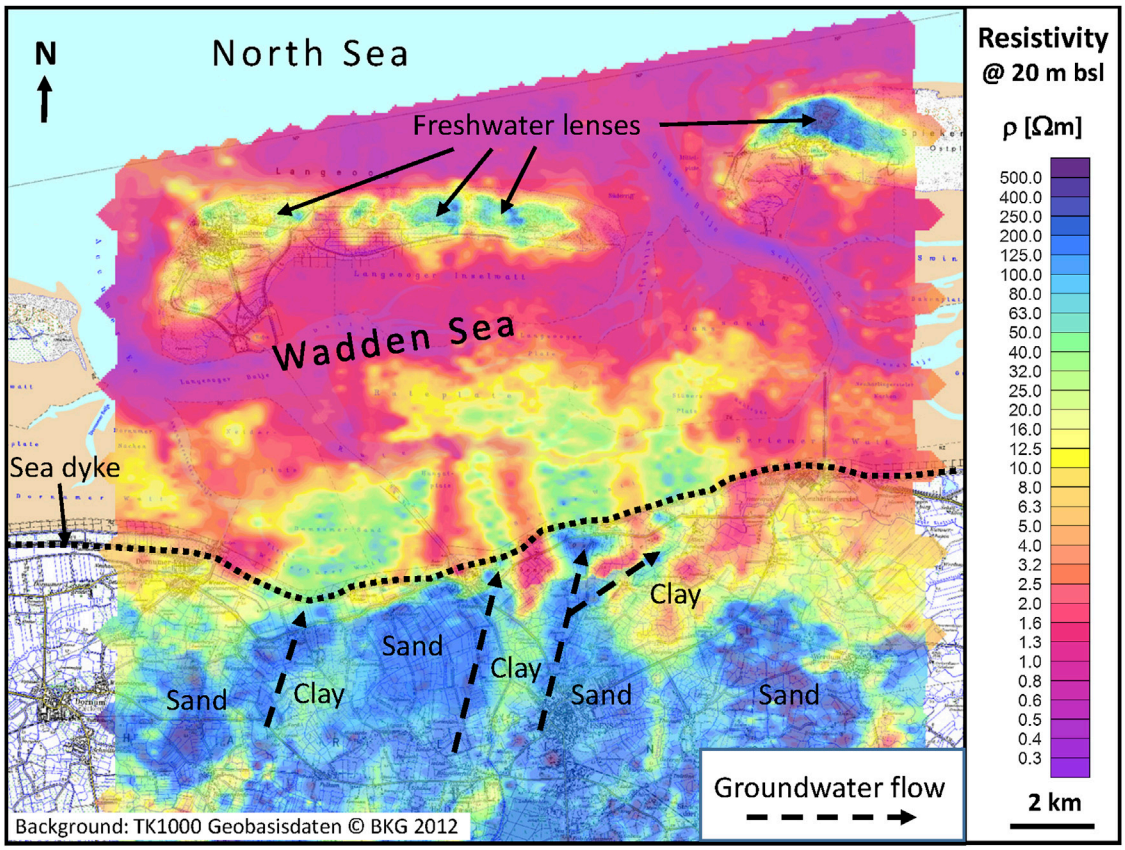

FIGURE 4 | Resistivities at 20 m below sea level derived from HEM inversion models indicating sandy and clayey areas, freshwater lenses on the islands of Langeoog and Spiekeroog and groundwater flow (dashed arrows) towards the Wadden Sea. The sea dyke is indicated by a dotted black line (data from BGR, 2017, background topographic map: BKG, 2012).

Brazil, *Argentina* and South Africa (Weschenfelder et al., 2016) and the North Yellow Sea (Wang et al., 2018) were linked to localized groundwater discharge.

Finding transfer functions linking discrete biogeochemical data and continuous geophysical methods is a promising methodology to extrapolate STE processes to the regional scale. In particular, methods going beyond the "classical" mapping of resistivity (**Figure 4**), which would allow to spot offshore freshening of pore water and thus STEs, have only rarely been applied to characterizing biogeochemical processes in STEs but show a substantial potential. A critical challenge is integrating local information into regional mapping by connecting different scales (point-like measurements, ground-based spatial information, airborne and satellite). Recent developments allow to include point-like or drilling information into ground-based geophysics using different concepts (e.g., Wunderlich et al., 2018) and coupling ground-based geophysics with airborne data (Dickson et al., 2014), providing perspectives for regional-scale assessments that are unviable based on ground-based measurements alone.

Remote Sensing

Remote sensing provides spatially continuous information on a scale from 10^1 to 10^9 m^2 (Böttcher et al., 2021), depending on the platform (ground-based application, remotely operated vehicle, uncrewed erial vehicle (UAV), kite gyrocopter, airplane, satellite). The chosen scale constrains the ground resolution (ground sampling distance), which may vary between 10^0 to 10^2 m. Scale and ground resolution intrinsically determine which STE indicator may be observed (Böttcher et al., 2021). Diffuse discharging groundwater is unlikely to be observed using satellite-based remote sensing, but can be observed with close-range applications or UAVs. However, the effort to cover regional scales is unequally larger for UAVs than for airplane- or satellite-based applications. Given the negligible depth penetration of remote sensing earth observation techniques in most situations, remote sensing can only investigate STE processes indirectly through its surface expressions. Remote sensing can detect terrestrial SGD, map seafloor and coastline morphology to find potential STEs, indicate hydrogeological STE characteristics, and identify STE processes by, e.g., classifying submerged aquatic vegetation that may be influenced by STEs.

Available sensors cover a wide range of the electromagnetic spectrum and can detect/differentiate surface properties that may act as indicators for STE processes or characteristics. The most commonly applied sensor in STE investigations is the thermal infrared (TIR) sensor, which can exploit temperature differences between seawater and terrestrial groundwater at the sea-surface (**Figure 5**). TIR detects groundwater inflow locations by

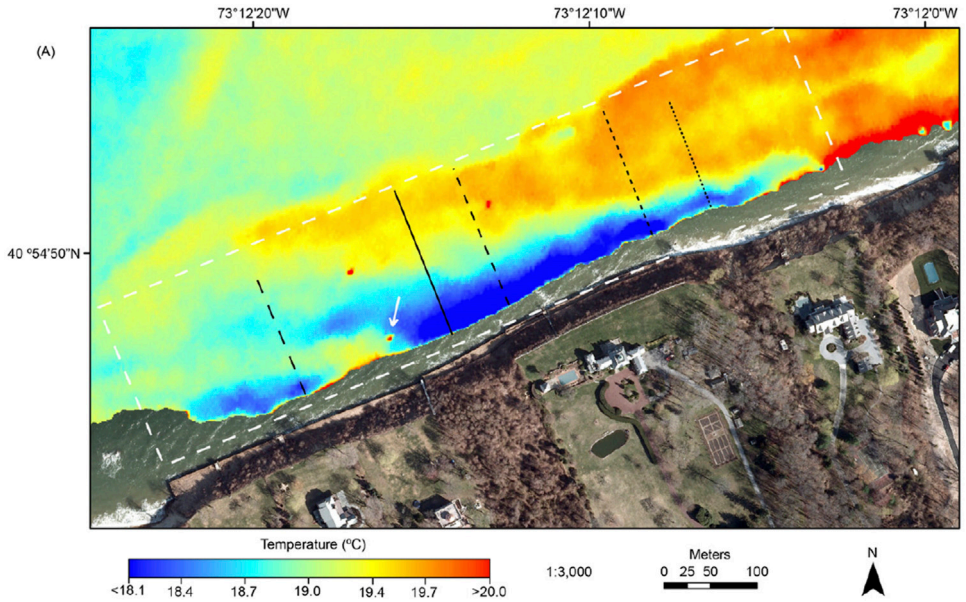

FIGURE 5 | TIR map displaying an area of cool diffuse seepage of terrestrial SGD that indicates an STE (Tamborski et al., 2015). Permission for reprint was provided by the copyright-holder.

identifying a thermal anomaly based on mono-temporal investigations (Fischer et al., 1964; Mejias et al., 2012; Wilson and Rocha, 2012; Kelly et al., 2013; Mallast et al., 2014; Xing et al., 2016), or multi-temporal investigations (Schubert et al., 2014; Oehler et al., 2018), and can be used to quantify freshwater fluxes given *in-situ* reference data of currents and bathymetry (Roseen, 2002; Johnson et al., 2008; Danielescu et al., 2009; Tamborski et al., 2015). The extent and shape of sea-surface temperature anomalies can indicate specific STE processes and characteristics (Chen, 1991; Jirka, 2004). Elongated anomalies oriented perpendicular to the coastline (Shaban et al., 2005) or extensive areas of thermal anomalies (Kelly et al., 2013) point to focused groundwater discharge at a high rate, suggesting a low residence time in STEs. Areas with smaller anomalies close to the coastline distributed over tens of meters alongshore (Tamborski et al., 2015) suggest diffuse discharge. The former is typical for karst or volcanic aquifers from which groundwater discharges along conduits, whereas the latter is commonly associated with sedimentary aquifers. Since higher temperature differences and distinct anomalies are easier to measure by TIR sensors, focused, high-volume discharge is more easily detected than slow, diffuse discharge.

Besides thermally identifying terrestrial groundwater discharge, remote sensing can classify benthic microbiology (e.g., Kazemipour et al., 2012) and submerged aquatic vegetation, which has been found to allow inferences about STEs (e.g., Leitão et al., 2015; Welti et al., 2015). While these observations are connected to local scale *in-situ* investigations, optical remote sensing using multi- and hyperspectral sensors (Klemas, 2016) has successfully been applied in shallow waters but not yet linked to potential terrestrial groundwater influence.

The relationship between STE characteristics indicated by seabed morphology and even operationally provided seafloor maps over regional scales using air- and satellite-borne platforms is similarly unexploited (Siermann et al., 2014; Eugenio et al., 2015). Remotely sensed bathymetry would allow a first-order approximation of potential pockmark sites. Since one of the forces that can produce pockmarks is fluid flow (Hovland et al., 2002), which can be an STE defining process, pockmarks can be seen as hinting toward the potential existence of STEs. Coastline morphology can be shaped by the same processes and may represent a similar indicator (Johannes, 1980).

A drawback of remote sensing methods is that it is challenging to link discrete, *in-situ* measurements to remote sensing data that integrate a multitude of effects other than those caused by an STE presence (e.g., ocean currents, chlorophyll presences). This weakness calls for a multi-scale approach (Lausch et al., 2013) in which an identified STE location is observed synchronously and over long periods with an appropriate *in-situ* sensor array and various airborne to satellite platforms covering different spatial scales. Such long-term sites could be associated with coastal observatories (Schofield et al., 2003) equipped with sensors to measure, e.g., turbidity, EC, pH, oxygen level, and thus be investigated through interdisciplinary approaches (Mollenhauer et al., 2018).

Second, since the temporal variability of the STE-associated processes is high, an interesting approach would be to have a TIR remote sensing approach that enables a multi-temporal observation possibility. The recent advance of UAVs do provide such a possibility, as shown in Mallast and Siebert (2019), but cannot cover a regional scale simultaneously. The revisiting times will be reduced for Landsat with the launch of Landsat-9 in spring 2021 and the Indian-French THRISHNA mission, whose launch is planned for 2024 (Lagouarde et al., 2018). Nano-to mini-satellites can even revisit individual

locations several times per day (Van Ryswyk, 2020). If these vehicles would also carry a TIR sensor and resemble a similarly very high ground resolution of <3 m, a regional to global scale localization of SGD sites and thus STE locations could become possible.

Hydrogeological Modeling

Another way to investigate STEs is through reactive transport models (RTMs), which remains underutilized in STE research (Robinson et al., 2017). Published modeling studies analyzed STEs as a high reactivity zones for, e.g., organic contaminants, nitrate and sulfate (Robinson et al., 2009; Anwar et al., 2014; Kim et al., 2017). The extent to which reactions proceeded was dependent on the degree of dispersive mixing and residence time in the STE, which was controlled by hydrological boundary conditions, such as terrestrial groundwater flux, beach slope and tidal amplitude. Another modeling study also showed the importance of dispersive mixing in STE on organic contaminant removal from groundwater (Nick et al., 2013).

The RTMs mentioned above provided process understanding but lacked confirmation by field data. There are only two field sites where RTMs and observations were integrated. The studies at Waquoit Bay by Spiteri et al. (2008a), Spiteri et al. (2008b), and Spiteri et al. (2008c), formed the earliest applications of RTMs of the STE and showed that the pH change at the interface between terrestrial groundwater and the lower saltwater wedge is an essential factor that controls the oxidation of Fe^{2+} and subsequent adsorption of land derived phosphorus (Spiteri et al., 2008a). Further, model results suggested that enhanced nutrient turnover occurs close to the SGD exit point due to high transverse dispersive mixing of oxic and anaerobic groundwater, resulting from converging groundwater flow toward the sea (Spiteri et al., 2008b; Spiteri et al., 2008c). The other site where model simulations were used to support field data interpretation is at Cape Henlopen, Delaware, USA (Kim et al., 2017). At this site, the field data showed that aerobic respiration led to a depletion of oxygen within the upper saline plume and that nitrate concentrations were lowest where ammonium and particulate organic carbon were highest. Even though their numerical model was able to simulate the general spatial O_2 and N_2 concentration trends, discrepancies remained evident, which the authors attributed to uncaptured heterogeneity and transient processes, as well as the omission of iron and sulfate reduction processes in the model. Thus, this is an example of the difficulties to model STEs due to their high spatial complexity. Modeling can also be applied in combination with isotopic data to elucidate reliable dating information on the STE water age (Bethke and Johnson, 2008; Post et al., 2019), which could provide information for reaction rates.

It is unlikely that numerical, reactive transport models of biogeochemical reactions in STEs can be applied with any reasonable expectation of success at the regional scale. The first reason is that the computational resources required will remain prohibitive in the foreseeable future. The second and perhaps foremost reason is that the input data requirements are unattainable at the regional scale due to the high spatial and temporal variability of STEs. Therefore, regional-scale models of STE nutrient transformations will have to rely on simplified process representations that can be parametrized with input data obtainable at a reasonable effort and cost. There are several essential questions to consider, including: What is an appropriate spatial level of heterogeneity for capturing regional scale processes that could be similar to the representative elementary volume (REV) concept for groundwater flow (cf. Freeze, 1975)? How can processes be integrated along the vertical dimension? How to account for local-scale variability? What is the temporal variability at the intra- and inter-annual scale? Can coastal landscape units be classified according to their geochemical reactivity?

Concerning the last question, one feasible approach to upscale modeling of STE processes might be to identify distinctive zones where controlling factors on the reactions are relatively uniform and then use small-scale model information to extrapolate to a regional-scale area. Working with distinctive uniform zones would imply a classification (e.g., Bokuniewicz et al., 2003). However, levels of homogeneity representative for larger areas are not yet adequately defined, as is the answer to whether and how small-scale temporal variations extrapolate into a larger scale. The terrestrial component of SGD was already modeled at the regional scale (Jarsjö et al., 2008; Befus et al., 2017; Hajati et al., 2019) and global scale (Zhou et al., 2019; Luijendijk et al., 2020) using similar approaches. These models produce spatially explicit estimates of terrestrial SGD that is a necessary prerequisite for STEs. Local scale RTMs highlight the importance of understanding mixing (hydrodynamic dispersion) and sediment organic carbon content, so it would seem reasonable to expect that these at least will have to be accounted for at the regional scale as well. Both are linked to sediment heterogeneity (regarding hydraulic properties and geochemistry) and the variability of hydraulic gradients so that the starting point would be a deterministic understanding of the longshore geological variability and a mechanistic description of the driving forces.

Data products of sufficient quality that represent controls of STE processes are required to model STE processes on the regional scale. The amount of data available at a global scale and high resolution is quickly increasing, but many aspects are not yet adequately covered. Foremost, since STEs occur along the coast, a high-resolution coastline is necessary and available (Sayre et al., 2018). STE sediment properties can be represented by recent datasets focusing on coastal sediment heterogeneity (de Graaf et al., 2017; Zamrsky et al., 2020). Other datasets focusing on the terrestrial aquifer (Gleeson et al., 2014) or marine sediment thickness (Straume et al., 2019) and its properties (Dutkiewicz et al., 2016) are hardly useable at the coast due to their global focus and low spatial resolution. Additional hydrogeological background knowledge would be, e.g., tectonic activity or stress maps, where areas of high tectonic activity would contain more faults and thus more potential pathways for groundwater.

Mixing intensity and processes in STEs will also be controlled by the amount of freshwater discharging (Luijendijk et al., 2020) or the amount of seawater recirculating (Mayfield et al., 2021). Water quality of the incoming freshwater is not known at a global

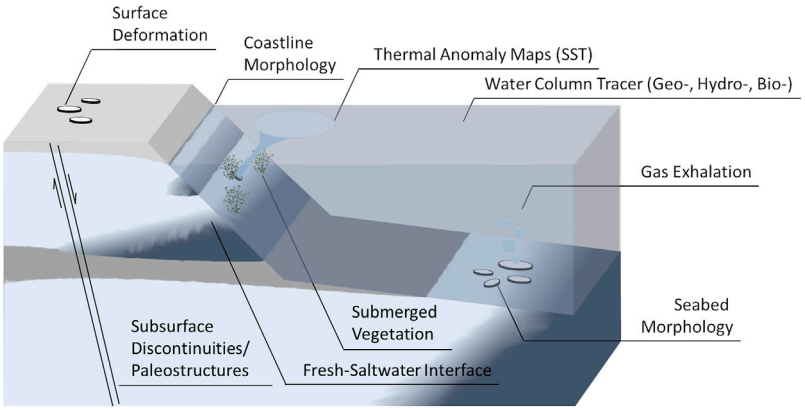

FIGURE 6 | Consequences of hydro (geo)logical and biogeochemical processes in STEs that can be used for extrapolation to the regional scale.

scale, but, as a first crude guess, could be inferred by proxy, e.g., from land-cover (e.g., Arino et al., 2007) or soil (FAOIIASA, ISRIC et al., 2009) datasets. Another option would be to extrapolate from datasets of multiple local groundwater quality measurements (e.g., NAWQA from USGS). In any case, groundwater quality is far less constrained than aquifer properties at large scales. Synthesized data sets of geological and geochemical properties of the subsurface below the seafloor on a regional scale are virtually absent.

Any of the large-scale datasets available have problems resolving the spatial heterogeneity of coasts, so the resulting estimates will not be applicable at the local scale (Geng et al., 2020) but provide first-order estimates for larger scales. This problem is not unique to the coast (e.g., Moosdorf et al., 2010) but amplified by the steep gradients in that setting. Given that the uncertainty of any model-based estimate is going to be very large, rather than focusing on the accuracy of the absolute numbers, it would be preferable to develop approaches that reveal the lateral differences. Such an approach would allow the ranking of different areas in terms of their effect on the coastal systems, highlighting hotspots to be targeted by more detailed investigations or specific measures.

CONCLUSIONS AND PERSPECTIVE

This review of biogeochemical processes in subterranean estuaries highlighted the spatial and temporal variability of these systems. Their reactions and corresponding rates depend on the hydrology of the STEs and the chemical composition of sediments and source waters (terrestrial groundwater and seawater). These controls have to be constrained to budget the processes within STEs and estimate the regional scale effects of STEs.

Characterizing STEs at the regional scale can be achieved through their products (**Figure 6**). The first step of estimating STE activity at a regional scale is to identify locations, amount, and the general extent of STEs. Locations can be identified through continuous measurements of geochemical tracers, e.g., electrical conductivity or Ra/Rn isotopes in the ocean. Biological indicators can point to the existence of STEs. Geophysical methods can provide information about freshened pore water and gas occurrences below the seafloor. Hydrogeological modeling can also estimate the flow behavior, but the necessary data are usually not available to represent larger areas in numerical 3D models realistically. Remote sensing information, for example, TIR images, can additionally show thermal signatures of freshwater influx. Combining observational methods from different disciplinary backgrounds, paired with modeling and hydrogeological data, is most promising for a regional scale effort to locate STEs.

Products of biogeochemical processes can be used to trace processes occurring in STEs (**Figure 6**). These products can be specific chemicals, like, e.g., CO_2, N_2 gas or Mn^{2+}, but also isotopic tracers like δ13C in DIC, δ18O and δ15 N in nitrate, as well as δ2D and δ18O in water. With geophysical methods, gaseous products of STEs can be identified, as well as iron oxides in the sediment, which are an essential control on the biogeochemistry of STEs. Remote sensing allows tracing changes in sea bottom that could indicate properties of the STEs in some cases. Nevertheless, since processes in STEs are spatially and temporally highly variable, discrete *in-situ* observations of specific STE products (e.g., CO_2, N_2, or Mn^{2+}) need to be combined with temporally and spatially continuous and temporally higher resolved data (e.g., remote sensing) using transfer functions.

Reactive transport models (RTM) can act as temporal and spatial link between discrete local scale *in-situ* measurements and spatially continuous regional scale data to extrapolate STE processes onto larger scales. To account for the high variability, quantitative local scale measurements will have to be combined with the concept of representative elementary volume (REV) based on regional-scale data sets such as from geophysical measurements or maps containing hydrogeological information. An RTM would represent each REV to quantify fluxes at scales relevant to the coastal zone and coastal zone management. On that basis, it would be even possible to sort STEs in classes when discussing their regional impact. Particularly, STEs with diffuse porous flow need to be distinguished from STEs in conduits, e.g., in karstic or volcanic settings.

A combination of methods from the presented disciplines promises a pathway toward regional scale estimates of processes in STEs and their impact on land-ocean matter fluxes. That impact may be substantial since local scale studies strongly hint toward their relevance. The processes are known; the products are known; the methods are available. Now is the time to combine methods across disciplines and understand these critical processes.

AUTHOR CONTRIBUTIONS

NM conceived the paper and wrote about upscaling; NM and UM coordinated the paper; UM, HW, and NM got funding for the project; MEB, BG, DA, A-KJ, TO, RP, JS, CE, and HW, contributed the biogeochemical part; LK contributed the biological part; EE, MM-P, BS, and TW, contributed the geophysical part; JG, GM, VP, and MW, contributed the hydrogeological modeling part; UM contributed the remote sensing part. All authors contributed to writing the manuscript and discussing the concept and formulating the overarching themes.

ACKNOWLEDGMENTS

This publication is a result of the DFG supported KiSNet project (MA7041/6-1). MEB and AKJ wish to thank DFG for financial support during research training group BALTIC TRANSCOAST (GRK 2000) and MEB and CvA the DAAD for a Ph.D. stipend for a stay of CvA at IOW. This is BALTIC TRANSCOAST publication No. GRK 2000/0045. HW was funded by the Niedersächsisches Ministerium für Wissenschaft und Kultur (MWK) in the scope of project "BIME" (ZN3184). JS acknowledges the support through the SEAMOUNT BONUS project (art. 185), which is funded jointly by the EU and the Federal Ministry of Education and Research of Germany (BMBF, Grant Nos. 03F0771B). The authors acknowledge the helpful review comments by D. Brankovits, G. Chaillou and A. Pain, and the editorial handling by F. Frappart. Finally, the authors would like to express their gratitude to Bill Burnett, who turns 75 this year. Bill inspired many of us to pursue research in the field of SGD and supported wherever he could. Thank you, Bill.

REFERENCES

Abarca, E., Karam, H., Hemond, H. F., and Harvey, C. F. (2013). Transient groundwater dynamics in a coastal aquifer: the effects of tides, the lunar cycle, and the beach profile. *Water Resour. Res.* 49 (5), 2473–2488. doi:10.1002/wrcr.20075

Adyasari, D., Hassenrück, C., Montiel, D., and Dimova, N. (2020). Microbial community composition across a coastal hydrological system affected by submarine groundwater discharge (SGD). *PLOS ONE* 15 (6), e0235235. doi:10.1371/journal.pone.0235235

Adyasari, D., Hassenrück, C., Oehler, T., Sabdaningsih, A., and Moosdorf, N. (2019). Microbial community structure associated with submarine groundwater discharge in northern Java (Indonesia). *Sci. Total Environ.* 689, 590–601. doi:10.1016/j.scitotenv.2019.06.193

Adyasari, D., Oehler, T., Afiati, N., and Moosdorf, N. (2019). Environmental impact of nutrient fluxes associated with submarine groundwater discharge at an urbanized tropical coast. *Estuarine, Coastal Shelf Sci.* 221, 30–38. doi:10.1016/j.ecss.2019.03.009

Akam, S. A., Coffin, R. B., Abdulla, H. A. N., and Lyons, T. W. (2020). Dissolved inorganic carbon pump in methane-charged shallow marine sediments: state of the art and new model perspectives. *Front. Mar. Sci.* 7. doi:10.3389/fmars.2020.00206

Al-Raei, A. M., Bosselmann, K., Böttcher, M. E., Hespenheide, B., and Tauber, F. (2009). Seasonal dynamics of microbial sulfate reduction in temperate intertidal surface sediments: controls by temperature and organic matter. *Ocean Dyn.* 59 (2), 351–370. doi:10.1007/s10236-009-0186-5

Alorda-Kleinglass, A., Garcia-Orellana, J., Rodellas, V., Cerdà-Domènech, M., Tovar-Sánchez, A., Diego-Feliu, M., et al. (2019). Remobilization of dissolved metals from a coastal mine tailing deposit driven by groundwater discharge and porewater exchange. *Sci. Total Environ.* 688, 1359–1372. doi:10.1016/j.scitotenv.2019.06.224

Andrisoa, A., Stieglitz, T. C., Rodellas, V., and Raimbault, P. (2019). Primary production in coastal lagoons supported by groundwater discharge and porewater fluxes inferred from nitrogen and carbon isotope signatures. *Mar. Chem.* 210, 48–60. doi:10.1016/j.marchem.2019.03.003

Anschutz, P., Smith, T., Mouret, A., Deborde, J., Bujan, S., Poirier, D., et al. (2009). Tidal sands as biogeochemical reactors. *Estuarine Coastal Shelf Sci.* 84 (1), 84–90. doi:10.1016/j.ecss.2009.06.015

Anwar, N., Robinson, C., and Barry, D. A. (2014). Influence of tides and waves on the fate of nutrients in a nearshore aquifer: numerical simulations. *Adv. Water Resour.* 73, 203–213. doi:10.1016/j.advwatres.2014.08.015

Archie, G. E. (1942). The electrical resistivity log as an aid in determining some reservoir characteristics. *Trans. Am. Inst. Mining Metallurgical Eng.* 146, 54–62. doi:10.2118/942054-g

Arino, O., Gross, D., Ranera, F., Bourg, L., Leroy, M., Bicheron, P., et al. (2007). GlobCover: ESA service for global land cover from MERIS. Proceedings of the international geoscience and remote sensing symposium (IGARSS) 2007. Barcelona: IEEE International, 2412–2415.

Auken, E., Jørgensen, F., and Sørensen, K. I. (2003). Large-scale TEM investigation for groundwater. *Exploration Geophys.* 34 (3), 188–194. doi:10.1071/eg0318

Baker, E. T., Massoth, G. J., Nakamura, K.-i., Embley, R. W., de Ronde, C. E. J., and Arculus, R. J. (2005). Hydrothermal activity on near-arc sections of back-arc ridges: results from the mariana trough and lau basin. *Geochem. Geophys. Geosystems* 6 (9). doi:10.1029/2005gc000948

Balzer, W. (1982). On the distribution of iron and manganese at the sediment/water interface: thermodynamic versus kinetic control. *Geochim. Cosmochim. Acta* 46 (7), 1153–1161. doi:10.1016/0016-7037(82)90001-1

Beck, A. J., Charette, M. A., Cochran, J. K., Gonneea, M. E., and Peucker-Ehrenbrink, B. (2013). Dissolved strontium in the subterranean estuary - implications for the marine strontium isotope budget. *Geochim. Cosmochim. Acta* 117, 33–52. doi:10.1016/j.gca.2013.03.021

Beck, A. J., Cochran, J. K., and Sanudo-Wilhelmy, S. A. (2010). The distribution and speciation of dissolved trace metals in a shallow subterranean estuary. *Mar. Chem.* 121 (1-4), 145–156. doi:10.1016/j.marchem.2010.04.003

Beck, A. J., and Cochran, M. A. (2013). Controls on solid-solution partitioning of radium in saturated marine sands. *Mar. Chem.* 156, 38–48. doi:10.1016/j.marchem.2013.01.008

Beck, A. J., Kellum, A. A., Luek, J. L., and Cochran, M. A. (2016). Chemical flux associated with spatially and temporally variable submarine groundwater discharge, and chemical modification in the subterranean estuary at gloucester point, VA (USA). *Estuaries Coasts* 39 (1), 1–12. doi:10.1007/s12237-015-9972-0

Beck, A. J., Tsukamoto, Y., Tovar-Sanchez, A., Huerta-Diaz, M., Bokuniewicz, H. J., and Sañudo-Wilhelmy, S. A. (2007). Importance of geochemical transformations in determining submarine groundwater discharge-derived trace metal and nutrient fluxes. *Appl. Geochem.* 22 (2), 477–490. doi:10.1016/j.apgeochem.2006.10.005

Beck, M., and Brumsack, H.-J. (2012). Biogeochemical cycles in sediment and water column of the Wadden Sea: the example Spiekeroog Island in a regional context. *Ocean Coastal Manag.* 68, 102–113. doi:10.1016/j.ocecoaman.2012.05.026

Beck, M., Reckhardt, A., Amelsberg, J., Bartholomä, A., Brumsack, H.-J., Cypionka, H., et al. (2017). The drivers of biogeochemistry in beach ecosystems: a cross-

shore transect from the dunes to the low-water line. *Mar. Chem.* 190, 35–50. doi:10.1016/j.marchem.2017.01.001

Beck, M., Riedel, T., Graue, J., Köster, J., Kowalski, N., Wu, C. S., et al. (2011). Imprint of past and present environmental conditions on microbiology and biogeochemistry of coastal Quaternary sediments. *Biogeosciences* 8 (1), 55. doi:10.5194/bg-8-55-2011

Befus, K. M., Kroeger, K. D., Smith, C. G., and Swarzenski, P. W. (2017). The magnitude and origin of groundwater discharge to eastern U.S. And Gulf of Mexico coastal waters. *Geophys. Res. Lett.* 44 (20), 396–410. doi:10.1002/2017gl075238

Begemann, F., and Libby, W. F. (1957). Continental water balance, ground water inventory and storage times, surface ocean mixing rates and world-wide water circulation patterns from cosmic-ray and bomb tritium. *Geochim. Cosmochim. Acta* 12 (4), 277–296. doi:10.1016/0016-7037(57)90040-6

Bethke, C. M., and Johnson, T. M. (2008). Groundwater age and groundwater age dating. *Annu. Rev. Earth Planet. Sci.* 36 (1), 121–152. doi:10.1146/annurev.earth.36.031207.124210

Bethke, C. M., and Johnson, T. M. (2002). Paradox of groundwater age. *Geology* 30 (2), 107–110. doi:10.1130/0091-7613(2002)030<0107:poga>2.0.co;2

Beusen, A. H. W., Slomp, C. P., and Bouwman, A. F. (2013). Global land-ocean linkage: direct inputs of nitrogen to coastal waters via submarine groundwater discharge. *Environ. Res. Lett.* 8 (3), 034035. doi:10.1088/1748-9326/8/3/034035

BGR (2017). *Helicopter-borne Electromagnetics (HEM) German North Sea coast – Models*. Bundesanstalt für Geowissenschaften und Rohstoffe (BGR), Hannover, Germany: doi:10.25928/bgr2017heminv_22v5-bg06

Billerbeck, M., Werner, U., Polerecky, L., Walpersdorf, E., deBeer, D., and Huettel, M. (2006). Surficial and deep pore water circulation governs spatial and temporal scales of nutrient recycling in intertidal sand flat sediment. *Mar. Ecol. Prog. Ser.* 326, 61–76. doi:10.3354/meps326061

Bishop, R. E., Humphreys, W. F., Kršinić, F., Sket, B., Iliffe, T. M., Žic, V., et al. (2015). 'Anchialine' redefined as a subterranean estuary in a crevicular or cavernous geological setting. *J. Crustacean Biol.* 35 (4), 511–514. doi:10.1163/1937240x-00002335

BKG (2012). *Rasterdaten Topographische Karte 1:100000 (DTK1000)*. Bundesamt für Kartographie und Geodäsie (BKG), Frankfurt, Germany: Available at https://www.geodatenzentrum.de [Last accessed on July 3, 2012].

Blöschl, G., Bierkens, M. F. P., Chambel, A., Cudennec, C., Destouni, G., Fiori, A., et al. (2019). Twenty-three unsolved problems in hydrology (UPH)—a community perspective. *Hydrol. Sci. J.-J. Des Sci. Hydrologiques* 64 (10), 1141–1158.

Boehm, A. B., Yamahara, K. M., and Sassoubre, L. M. (2014). Diversity and transport of microorganisms in intertidal sands of the California coast. *Appl. Environ. Microbiol.* 80 (13), 3943–3951. doi:10.1128/AEM.00513-14

Boetius, A., Ravenschlag, K., Schubert, C. J., Rickert, D., Widdel, F., Gieseke, A., et al. (2000). A marine microbial consortium apparently mediating anaerobic oxidation of methane. *Nature* 407 (6804), 623–626. doi:10.1038/35036572

Bokuniewicz, H., Buddemeier, R., Maxwell, B., and Smith, C. (2003). The typological approach to submarine groundwater discharge (SGD). *Biogeochemistry* 66 (1, 2), 145–158. doi:10.1023/b:biog.0000006125.10467.75

Bokuniewicz, H., Cochran, J. K., Garcia-Orellana, J., Rodellas, V., Daniel, J. W., and Heilbrun, C. (2015). Intertidal percolation through beach sands as a source of 224,223Ra to Long Island Sound, New York, and Connecticut, United States. *J. Mar. Res.* 73, 123–140. doi:10.1357/002224015816665570

Bone, S. E., Charette, M. A., Lamborg, C. H., and Gonneea, M. E. (2007). Has submarine groundwater discharge been overlooked as a source of mercury to coastal waters?. *Environ. Sci. Technol.* 41 (9), 3090–3095. doi:10.1021/es0622453

Bone, S. E., Gonneea, M. E., and Charette, M. A. (2006). Geochemical cycling of arsenic in a coastal aquifer. *Environ. Sci. Technol.* 40 (10), 3273–3278. doi:10.1021/es052352h

Böttcher, M. E., and Dietzel, M. (2010). Metal-ion partitioning during low-temperature precipitation and dissolution of anhydrous carbonates and sulphates. *EMU Notes in Mineral.* 10, 139–187. doi:10.1180/EMU-notes.10.4

Böttcher, M.E., Mallast, U., Massmann, G., Moosdorf, N., Mueller-Pethke, M., and Waska, H. (2021). "Coastal-Groundwater interfaces (submarine groundwater discharge)," in *Ecohydrological interfaces*. Editors S. Krause, D. M. Hannah, and N. Grimm (New York, NY: Wiley & Sons).

Bögli, A., (1980). *Karst hydrology and physical speleology*. Berlin, UK: Springer, xiii, 284

Brando, V. E., and Dekker, A. G. (2003). Satellite hyperspectral remote sensing for estimating estuarine and coastal water quality. *IEEE Trans. Geosci. Remote Sensing* 41 (6), 1378–1387. doi:10.1109/tgrs.2003.812907

Brankovits, D., Pohlman, J. W., Niemann, H., Leigh, M. B., Leewis, M. C., Becker, K. W., et al. (2017). Methane- and dissolved organic carbon-fueled microbial loop supports a tropical subterranean estuary ecosystem. *Nat. Commun.* 8, 1835. doi:10.1038/s41467-017-01776-x

Brankovits, D., Pohlman, J. W., Ganju, N. K., Iliffe, T. M., Lowell, N., Roth, E., et al. (2018). Hydrologic controls of methane dynamics in karst subterranean estuaries. *Glob. Biogeochem. Cycles* 32 (12), 1759–1775. doi:10.1029/2018gb006026

Brankovits, D., and Pohlman, J. W. (2020). Methane oxidation dynamics in a karst subterranean estuary. *Geochim. Cosmochim. Acta* 277, 320–333. doi:10.1016/j.gca.2020.03.007

Brovelli, A., Mao, X., and Barry, D. A. (2007). Numerical modeling of tidal influence on density-dependent contaminant transport. *Water Resour. Res.* 43 (10). doi:10.1029/2006wr005173

Brown, K. I., and Boehm, A. B. (2016). Transport of fecal indicators from beach sand to the surf zone by recirculating seawater: laboratory experiments and numerical modeling. *Environ. Sci. Technol.* 50 (23), 12840–12847. doi:10.1021/acs.est.6b02534

Burnett, W. C., Aggarwal, P. K., Aureli, A., Bokuniewicz, H., Cable, J. E., Charette, M. A., et al. (2006). Quantifying submarine groundwater discharge in the coastal zone via multiple methods. *Sci. Total Environ.* 367 (2, 3), 498–543. doi:10.1016/j.scitotenv.2006.05.009

Burnett, W. C., and Dulaiova, H. (2003). Estimating the dynamics of groundwater input into the coastal zone via continuous radon-222 measurements. *J. Environ. Radioact.* 69 (1, 2), 21–35. doi:10.1016/S0265-931X(03)00084-5

Burnett, W. C., Bokuniewicz, H., Huettel, M., Moore, W. S., and Taniguchi, M. (2003). Groundwater and pore water inputs to the coastal zone. *Biogeochemistry* 66 (1-2), 3–33. doi:10.1023/b:biog.0000006066.21240.53

Burton, E. A., and Walter, L. M. (1990). The role of pH in phosphate inhibition of calcite and aragonite precipitation rates in seawater. *Geochim. Cosmochim. Acta* 54 (3), 797–808. doi:10.1016/0016-7037(90)90374-t

Cable, J. E., Bugna, G. C., Burnett, W. C., and Chanton, J. P. (1996). Application of 222 Rn and CH4 for assessment of groundwater discharge to the coastal ocean. *Limnol. Oceanogr.* 41 (6), 1347–1353. doi:10.4319/lo.1996.41.6.1347

Canfield, D. E., Glazer, A. N., and Falkowski, P. G. (2010). The evolution and future of Earth's nitrogen cycle. *Science* 330 (6001), 192–196. doi:10.1126/science.1186120

Cerdà-Domènech, M., Rodellas, V., Folch, A., and Garcia-Orellana, J. (2017). Constraining the temporal variations of Ra isotopes and Rn in the groundwater end-member: implications for derived SGD estimates. *Sci. Total Environ.* 595, 849–857. doi:10.1016/j.scitotenv.2017.03.005

Chambers, R. M., and Odum, W. E. (1990). Porewater oxidation, dissolved phosphate and the iron curtain - iron-phosphorus relations in tidal fresh-water marshes. *Biogeochemistry* 10 (1), 37–52. doi:10.1007/bf00000891

Charbonnier, C., Anschutz, P., Poirier, D., Bujan, S., and Lecroart, P. (2013). Aerobic respiration in a high-energy sandy beach. *Mar. Chem.* 155, 10–21. doi:10.1016/j.marchem.2013.05.003

Charette, M. A., Sholkovitz, E. R., and Hansel, C. M. (2005). Trace element cycling in a subterranean estuary: Part 1. Geochemistry of the permeable sediments. *Geochim. Cosmochim. Acta* 69 (8), 2095–2109. doi:10.1016/j.gca.2004.10.024

Charette, M. A., and Sholkovitz, E. R. (2002). Oxidative precipitation of groundwater-derived ferrous iron in the subterranean estuary of a coastal bay. *Geophys. Res. Lett.* 29 (10). doi:10.1029/2001gl014512

Charette, M. A., and Sholkovitz, E. R. (2006). Trace element cycling in a subterranean estuary: Part 2. Geochemistry of the pore water. *Geochim. Cosmochim. Acta* 70 (4), 811–826. doi:10.1016/j.gca.2005.10.019

Chen, H.-B. (1991). *Turbulent buoyant jets and plumes in flowing ambient environments*. Aalborg, Denmark: Department of Civil Engineering, University of Aalborg.

Chen, X., Cukrov, N., Santos, I. R., Rodellas, V., Cukrov, N., and Du, J. (2020). Karstic submarine groundwater discharge into the Mediterranean: radon-based nutrient fluxes in an anchialine cave and a basin-wide upscaling. *Geochim. Cosmochim. Acta* 268, 467–484. doi:10.1016/j.gca.2019.08.019

Chevis, D. A., Johannesson, K. H., Burdige, D. J., Tang, J., Bradley Moran, S., and Kelly, R. P. (2015). Submarine groundwater discharge of rare earth elements to a tidally-mixed estuary in Southern Rhode Island. *Chem. Geol.* 397 (0), 128–142. doi:10.1016/j.chemgeo.2015.01.013

Cho, H.-M., and Kim, G. (2016). Determining groundwater Ra end-member values for the estimation of the magnitude of submarine groundwater discharge using Ra isotope tracers. *Geophys. Res. Lett.* 43 (8), 3865–3871. doi:10.1002/2016gl068805

Cho, H. M., Kim, G., Kwon, E. Y., Moosdorf, N., Garcia-Orellana, J., and Santos, I. R. (2018). Radium tracing nutrient inputs through submarine groundwater discharge in the global ocean. *Sci. Rep.* 8 (1), 2439–2446. doi:10.1038/s41598-018-20806-2

Cho, H. M., Kim, T. H., Moon, J. H., Song, B. C., Hwang, D. W., Kim, T., et al. (2021). Estimating submarine groundwater discharge in Jeju volcanic island (Korea) during a typhoon (Kong-rey) using humic-fluorescent dissolved organic matter-Si mass balance. *Sci. Rep.* 11 (1), 941. doi:10.1038/s41598-020-79381-0

Church, T. M. (1996). An underground route for the water cycle. *Nature* 380 (6575), 579–580. doi:10.1038/380579a0

Clark, I. D., and Fritz, P. (1997). *Environmental isotopes in hydrogeology*. London, NewYork, CRC Press.

Colbert, S. L., Berelson, W. M., and Hammond, D. E. (2008). Radon-222 budget in Catalina Harbor, California: 2. Flow dynamics and residence time in a tidal beach. *Limnol. Oceanogr.* 53 (2), 659–665. doi:10.4319/lo.2008.53.2.0659

Costabel, S., Weidner, C., Müller-Petke, M., and Houben, G. (2018). Hydraulic characterisation of iron-oxide-coated sand and gravel based on nuclear magnetic resonance relaxation mode analyses. *Hydrol. Earth Syst. Sci.* 22 (3), 1713–1729. doi:10.5194/hess-22-1713-2018

Couturier, M., Nozais, C., and Chaillou, G. (2016). Microtidal subterranean estuaries as a source of fresh terrestrial dissolved organic matter to the coastal ocean. *Mar. Chem.* 186, 46–57. doi:10.1016/j.marchem.2016.08.001

Couturier, M., Tommi-Morin, G., Sirois, M., Rao, A., Nozais, C., and Chaillou, G. (2017). Nitrogen transformations along a shallow subterranean estuary. *Biogeosciences* 14 (13), 3321–3336. doi:10.5194/bg-14-3321-2017

Cranswick, R. H., Cook, P. G., and Lamontagne, S. (2014). Hyporheic zone exchange fluxes and residence times inferred from riverbed temperature and radon data. *J. Hydrol.* 519, 1870–1881. doi:10.1016/j.jhydrol.2014.09.059

Crook, E. D., Potts, D., Rebolledo-Vieyra, M., Hernandez, L., and Paytan, A. (2012). Calcifying coral abundance near low-pH springs: implications for future ocean acidification. *Coral Reefs* 31 (1), 239–245. doi:10.1007/s00338-011-0839-y

Cyronak, T., Santos, I. R., Erler, D. V., Maher, D. T., and Eyre, B. D. (2014). Drivers ofpCO2variability in two contrasting coral reef lagoons: the influence of submarine groundwater discharge. *Glob. Biogeochem. Cycles* 28 (4), 398–414. doi:10.1002/2013gb004598

Danielescu, S., MacQuarrie, K. T. B., and Faux, R. N. (2009). The integration of thermal infrared imaging, discharge measurements and numerical simulation to quantify the relative contributions of freshwater inflows to small estuaries in Atlantic Canada. *Hydrol. Process* 23 (20), 2847–2859. doi:10.1002/hyp.7383

Day-Lewis, F. D., White, E. A., Johnson, C. D., Lane, J. W., and Belaval, M. (2006). Continuous resistivity profiling to delineate submarine groundwater discharge-examples and limitations. *The Leading Edge* 25 (6), 724–728. doi:10.1190/1.2210056

de Graaf, I. E. M., van Beek, R. L. P. H., Gleeson, T., Moosdorf, N., Schmitz, O., Sutanudjaja, E. H., et al. (2017). A global-scale two-layer transient groundwater model: development and application to groundwater depletion. *Adv. Water Resour.* 102, 53–67. doi:10.1016/j.advwatres.2017.01.011

De Smedt, P., Saey, T., Lehouck, A., Stichelbaut, B., Meerschman, E., Islam, M. M., et al. (2013). Exploring the potential of multi-receiver EMI survey for geoarchaeological prospection: a 90ha dataset. *Geoderma* 199, 30–36. doi:10.1016/j.geoderma.2012.07.019

Deines, P., Langmuir, D., and Harmon, R. S. (1974). Stable carbon isotope ratios and the existence of a gas phase in the evolution of carbonate ground waters. *Geochim. Cosmochim. Acta* 38 (7), 1147–1164. doi:10.1016/0016-7037(74)90010-6

DeSimone, L. A., and Howes, B. L. (1996). Denitrification and nitrogen transport in a coastal aquifer receiving wastewater discharge. *Environ. Sci. Technol.* 30 (4), 1152–1162. doi:10.1021/es950366p

Dickson, N. E. M., Comte, J.-C., McKinley, J., and Ofterdinger, U. (2014). Coupling ground and airborne geophysical data with upscaling techniques for regional groundwater modeling of heterogeneous aquifers: case study of a sedimentary aquifer intruded by volcanic dykes in Northern Ireland. *Water Resour. Res.* 50 (10), 7984–8001. doi:10.1002/2014wr015320

Donis, D., Janssen, F., Liu, B., Wenzhöfer, F., Dellwig, O., Escher, P., et al. (2017). Biogeochemical impact of submarine ground water discharge on coastal surface sands of the southern Baltic Sea. *Estuarine Coastal Shelf Sci.* 189, 131–142. doi:10.1016/j.ecss.2017.03.003

Dulaiova, H., Camilli, R., Henderson, P. B., and Charette, M. A. (2010). Coupled radon, methane and nitrate sensors for large-scale assessment of groundwater discharge and non-point source pollution to coastal waters. *J. Environ. Radioact* 101 (7), 553–563. doi:10.1016/j.jenvrad.2009.12.004

Dulaiova, H., Gonneea, M. E., Henderson, P. B., and Charette, M. A. (2008). Geochemical and physical sources of radon variation in a subterranean estuary - implications for groundwater radon activities in submarine groundwater discharge studies. *Mar. Chem.* 110 (1, 2), 120–127. doi:10.1016/j.marchem.2008.02.011

Duque, C., Jessen, S., Tirado-Conde, J., Karan, S., and Engesgaard, P. (2019). Application of stable isotopes of water to study coupled submarine groundwater discharge and nutrient delivery. *Water* 11 (9), 842. doi:10.3390/w11091842

Duque, C., Michael, H. A., and Wilson, A. M. (2020). The subterranean estuary: technical term, simple analogy, or source of confusion? *Water Resour. Res.* 56 (2), e2019WR026554. doi:10.1029/2019wr026554

Dutkiewicz, A., O'Callaghan, S., and Müller, R. D. (2016). Controls on the distribution of deep-sea sediments. *Geochem. Geophys. Geosyst.* 17 (8), 3075–3098. doi:10.1002/2016gc006428

Dybas, C. L. (2005). Dead zones spreading in world oceans. *Bioscience* 55 (7), 552–557. doi:10.1641/0006-3568(2005)055[0552:dzsiwo]2.0.co;2

Ehlert, C., Reckhardt, A., Greskowiak, J., Liguori, B. T. P., Böning, P., Paffrath, R., et al. (2016). Transformation of silicon in a sandy beach ecosystem: insights from stable silicon isotopes from fresh and saline groundwaters. *Chem. Geology* 440, 207–218. doi:10.1016/j.chemgeo.2016.07.015

Einsele, W. (1936). Über die Beziehungen des Eisenkreislaufs zum Phosphatkreislauf im eutrophen See. *Archiv für Hydrobiologie* 29, 664–686.

Encarnação, J., Leitão, F., Range, P., Piló, D., Chícharo, M. A., and Chícharo, L. (2015). Local and temporal variations in near-shore macrobenthic communities associated with submarine groundwater discharges. *Mar. Ecol.* 36 (4), 926–941. 10.1111/maec.12186

Erler, D. V., Santos, I. R., Zhang, Y., Tait, D. R., Befus, K. M., Hidden, A., et al. (2014). Nitrogen transformations within a tropical subterranean estuary. *Mar. Chem.* 164, 38–47. doi:10.1016/j.marchem.2014.05.008

Eugenio, F., Marcello, J., and Martin, J. (2015). High-resolution maps of bathymetry and benthic habitats in shallow-water environments using multispectral remote sensing imagery. *IEEE Trans. Geosci. Remote Sensing* 53 (7), 3539–3549. doi:10.1109/tgrs.2014.2377300

Feldens, P., Schulze, I., Papenmeier, S., Schönke, M., and Schneider von Deimling, J. (2018). Improved interpretation of marine sedimentary environments using multi-frequency multibeam backscatter data. *Geosciences* 8 (6), 214. doi:10.3390/geosciences8060214

Fisher, W. A., Moxham, R. M., Polcyn, F., and Landis, G. H. (1964). Infrared Surveys of Hawaiian Volcanoes: aerial surveys with infrared imaging radiometer depict volcanic thermal patterns and structural features. *Science* 146 (364), 733–742. doi:10.1126/science.146.3645.733

Fleury, P., Bakalowicz, M., and de Marsily, G. (2007). Submarine springs and coastal karst aquifers: a review. *J. Hydrol.* 339 (1–2), 79–92. doi:10.1016/j.jhydrol.2007.03.009

Flower, H., Rains, M., Lewis, D., Zhang, J.-Z., and Price, R. (2017). Saltwater intrusion as potential driver of phosphorus release from limestone bedrock in a coastal aquifer. *Estuarine Coastal Shelf Sci.* 184, 166–176. doi:10.1016/j.ecss.2016.11.013

Freeze, R. A. (1975). A stochastic-conceptual analysis of one-dimensional groundwater flow in nonuniform homogeneous media. *Water Resour. Res.* 11 (5), 725–741. doi:10.1029/wr011i005p00725

Fritz, P., Basharmal, G. M., Drimmie, R. J., Ibsen, J., and Qureshi, R. M. (1989). Oxygen isotope exchange between sulphate and water during bacterial reduction of sulphate. *Chem. Geol. Isotope Geosci. Sect.* 79 (2), 99–105. doi:10.1016/0168-9622(89)90012-2

Froelich, P. N., Klinkhammer, G. P., Bender, M. L., Luedtke, N. A., Heath, G. R., Cullen, D., et al. (1979). Early oxidation of organic matter in pelagic sediments

of the eastern equatorial Atlantic: suboxic diagenesis. *Geochim. Cosmochim. Acta* 43 (7), 1075–1090. doi:10.1016/0016-7037(79)90095-4

Fulweiler, R. W., Nixon, S. W., Buckley, B. A., and Granger, S. L. (2007). Reversal of the net dinitrogen gas flux in coastal marine sediments. *Nature* 448 (7150), 180–182. doi:10.1038/nature05963

Garcia-Solsona, E., Masque, P., Garcia-Orellana, J., Rapaglia, J., Beck, A. J., Cochran, J. K., et al. (2008). Estimating submarine groundwater discharge around Isola La Cura, northern Venice Lagoon (Italy), by using the radium quartet. *Mar. Chem.* 109 (3-4), 292–306. doi:10.1016/j.marchem.2008.02.007

Gardner, W. S., McCarthy, M. J., An, S., Sobolev, D., Sell, K. S., and Brock, D. (2006). Nitrogen fixation and dissimilatory nitrate reduction to ammonium (DNRA) support nitrogen dynamics in Texas estuaries. *Limnol. Oceanogr.* 51 (1part2), 558–568. doi:10.4319/lo.2006.51.1_part_2.0558

Gat, J. R. (1996). Oxygen and hydrogen isotopes in the hydrologic cycle. *Annu. Rev. Earth Planet. Sci.* 24 (1), 225–262. doi:10.1146/annurev.earth.24.1.225

Gaudette, H. E., and Lyons, W. B. (1980). *Phosphate geochemisty in nearshore carbonate sediments a suggestion of apatite formation*, Durham.

Geng, X., Michael, H. A., Boufadel, M. C., Molz, F. J., Gerges, F., and Lee, K. (2020). Heterogeneity affects intertidal flow topology in coastal beach aquifers. *Geophys. Res. Lett.* 47 (17), e2020GL089612. doi:10.1029/2020gl089612

Gilfedder, B. S., Cartwright, I., Hofmann, H., and Frei, S. (2019). Explicit modeling of radon-222 in HydroGeoSphere during steady state and dynamic transient storage. *Ground Water* 57 (1), 36–47. doi:10.1111/gwat.12847

Gilfedder, B. S., Frei, S., Hofmann, H., and Cartwright, I. (2015). Groundwater discharge to wetlands driven by storm and flood events: quantification using continuous Radon-222 and electrical conductivity measurements and dynamic mass-balance modelling. *Geochim. Cosmochim. Acta* 165, 161–177. doi:10.1016/j.gca.2015.05.037

Gleeson, T., Moosdorf, N., Hartmann, J., and van Beek, L. P. H. (2014). A glimpse beneath earth's surface: GLobal HYdrogeology MaPS (GLHYMPS) of permeability and porosity. *Geophys. Res. Lett.* 41 (11), 3891–3898. doi:10.1002/2014gl059856

Goldscheider, N., Chen, Z., Auler, A. S., Bakalowicz, M., Broda, S., Drew, D., et al. (2020). Global distribution of carbonate rocks and karst water resources. *Hydrogeol J.* 28 (5), 1661–1677. doi:10.1007/s10040-020-02139-5

Gonneea, M. E., and Charette, M. A. (2014). Hydrologic controls on nutrient cycling in an unconfined coastal aquifer. *Environ. Sci. Technol.* 48 (24), 14178–14185. doi:10.1021/es503313t

Gonneea, M. E., Charette, M. A., Liu, Q., Herrera-Silveira, J. A., and Morales-Ojeda, S. M. (2014). Trace element geochemistry of groundwater in a karst subterranean estuary (Yucatan Peninsula, Mexico). *Geochimica Et Cosmochimica Acta* 132, 31–49. doi:10.1016/j.gca.2014.01.037

Gonneea, M. E., Morris, P. J., Dulaiova, H., and Charette, M. A. (2008). New perspectives on radium behavior within a subterranean estuary. *Mar. Chem.* 109 (3-4), 250–267. doi:10.1016/j.marchem.2007.12.002

Gonneea, M. E., Mulligan, A. E., and Charette, M. A. (2013). Seasonal cycles in radium and barium within a subterranean estuary: implications for groundwater derived chemical fluxes to surface waters. *Geochim. Cosmochim. Acta* 119, 164–177. doi:10.1016/j.gca.2013.05.034

Goodridge, B. M., and Melack, J. M. (2014). Temporal evolution and variability of dissolved inorganic nitrogen in beach pore water revealed using radon residence times. *Environ. Sci. Technol.* 48 (24), 14211–14218. doi:10.1021/es504017j

Gramling, C. M., McCorkle, D. C., Mulligan, A. E., and Woods, T. L. (2003). A carbon isotope method to quantify groundwater discharge at the land-sea interface. *Limnol. Oceanogr.* 48 (3), 957–970. doi:10.4319/lo.2003.48.3.0957

Greskowiak, J. (2014). Tide-induced salt-fingering flow during submarine groundwater discharge. *Geophys. Res. Lett.* 41 (18), 6413–6419. doi:10.1002/2014gl061184

Grünenbaum, N., Greskowiak, J., Sültenfuß, J., and Massmann, G. (2020). Groundwater flow and residence times below a meso-tidal high-energy beach: a model-based analyses of salinity patterns and 3H-3He groundwater ages. *J. Hydrol.* 587, 124948. doi:10.1016/j.jhydrol.2020.124948

Grzelak, K., Tamborski, J., Kotwicki, L., and Bokuniewicz, H. (2018). Ecostructuring of marine nematode communities by submarine groundwater discharge. *Mar. Environ. Res.* 136, 106–119. doi:10.1016/j.marenvres.2018.01.013

Gustafson, C., Key, K., and Evans, R. L. (2019). Aquifer systems extending far offshore on the U.S. Atlantic margin. *Sci. Rep.* 9 (1), 8709. doi:10.1038/s41598-019-44611-7

Hajati, M. C., Sutanudjaja, E., and Moosdorf, N. (2019). Quantifying regional fresh submarine groundwater discharge with the lumped modeling approach CoCa-rfsgd. *Water Resour. Res.* 55 (7), 5321–5341. doi:10.1029/2018wr024248

Hancock, P. J., Boulton, A. J., and Humphreys, W. F. (2005). Aquifers and hyporheic zones: towards an ecological understanding of groundwater. *Hydrogeol J.* 13 (1), 98–111. doi:10.1007/s10040-004-0421-6

Hanshaw, B. B., and Back, W. (1980). Chemical mass-wasting of the northern yucatan Peninsula by groundwater dissolution. *Geology* 8 (5), 222–224. doi:10.1130/0091-7613(1980)8<222:cmotny>2.0.co;2

Hanshaw, B. B., and Back, W. (1979). "Major geochemical processes in the evolution of carbonate-aquifer systems," in *Developments in water science*. Editors W. Back and D. A. Stephenson (New York, NY: Elsevier), 287–312.

Hays, R. L., and Ullman, W. J. (2007). Dissolved nutrient fluxes through a sandy estuarine beachface (Cape Henlopen, Delaware, USA): Contributions from fresh groundwater discharge, seawater recycling, and diagenesis. *Estuaries Coasts* 30 (4), 710–724. doi:10.1007/bf02841967

Heiss, J. W., Michael, H. A., and Koneshloo, M. (2020). Denitrification hotspots in intertidal mixing zones linked to geologic heterogeneity. *Environ. Res. Lett.* 15 (8), 084015. doi:10.1088/1748-9326/ab90a6

Heiss, J. W., and Michael, H. A. (2014). Saltwater-freshwater mixing dynamics in a sandy beach aquifer over tidal, spring-neap, and seasonal cycles. *Water Resour. Res.* 50 (8), 6747–6766. doi:10.1002/2014wr015574

Hermans, T., and Paepen, M. (2020). Combined inversion of land and marine electrical resistivity tomography for submarine groundwater discharge and saltwater intrusion characterization. *Geophys. Res. Lett.* 47 (3). doi:10.1029/2019gl085877

Hoefs, J. (2018). *Stable isotope geochemistry*. Göttingen, German: Springer-Nature. doi:10.1007/1978-3-319-78527-1

Hoffmann, J. J. L., von Deimling, J. S., Schroder, J. F., Schmidt, M., Held, P., Crutchley, G. J., et al. (2020). Complex eyed pockmarks and submarine groundwater discharge revealed by acoustic data and sediment cores in Eckernforde Bay, SW Baltic Sea. *Geochem. Geophys. Geosystems* 21 (4). doi:10.1029/2019gc008825

Hong, Y., Wu, J., Wilson, S., and Song, B. 2018). Vertical stratification of sediment microbial communities along geochemical gradients of a subterranean estuary located at the Gloucester Beach of Virginia, United States. *Front. Microbiol.* 9, 3343. doi:10.3389/fmicb.2018.03343

Hovland, M., Gardner, J. V., and Judd, A. G. (2002). The significance of pockmarks to understanding fluid flow processes and geohazards. *Geofluids* 2 (2), 127–136. doi:10.1046/j.1468-8123.2002.00028.x

Hovland, M., and Judd, A. (1988). *Seabed pockmarks and seepages: impact on geology, biology and the marine environment*. Sterling House London: Graham & Trodman. doi:10.13140/RG.2.1.1414.1286

Huerta-Diaz, M. A., and Morse, J. W. (1992). Pyritization of trace metals in anoxic marine sediments. *Geochimica Et Cosmochimica Acta* 56 (7), 2681–2702. doi:10.1016/0016-7037(92)90353-k

Humphreys, W. F. (2008). Rising from Down Under: developments in subterranean biodiversity in Australia from a groundwater fauna perspective. *Invert. Syst.* 22 (2), 85–101. doi:10.1071/is07016

Hwang, D. W., Kim, G. B., Lee, Y. W., and Yang, H. S. (2005). Estimating submarine inputs of groundwater and nutrients to a coastal bay using radium isotopes. *Mar. Chem.* 96 (1-2), 61–71. doi:10.1016/j.marchem.2004.11.002

IAEA (2003). *Guidelines for radioelement mapping using gamma ray spectrometry data*. Vienna: International Atomic Energy Agency (IAEA).

FAOIIASA, ISRIC; ISSCAS; JRC (2009). "Harmonized World Soil Database (version 1.1)," in *Rome and laxenburg*. Editor I. FAO.

Jakobsson, M., O'Regan, M., Mörth, C.-M., Stranne, C., Weidner, E., Hansson, J., et al. (2020). Potential links between Baltic Sea submarine terraces and groundwater seeping. *Earth Surf. Dynam.* 8 (1), 1–15. doi:10.5194/esurf-8-1-2020

Jarsjö, J., Shibuo, Y., and Destouni, G. (2008). Spatial distribution of unmonitored inland water discharges to the sea. *J. Hydrol.* 348 (1, 2), 59–72. doi:10.1016/j.jhydrol.2007.09.052

Jetten, M. S., Strous, M., Van de Pas-Schoonen, K. T., Schalk, J., van Dongen, U. G., van de Graaf, A. A., et al. (1998). The anaerobic oxidation of ammonium. *FEMS Microbiol. Rev.* 22 (5), 421–437. doi:10.1111/j.1574-6976.1998.tb00379.x

Jiang, S., Zhang, Y. X., Jin, J., Wu, Y., Wei, Y. J., Wang, X. L., et al. (2020). Organic carbon in a seepage face of a subterranean estuary: Turnover and microbial interrelations. *Sci. Total Environ.*, 725, 138220. doi:10.1016/j.scitotenv.2020.138220

Jiao, J., and Post, V. (2019). *Coastal hydrogeology*. Cambridge: Cambridge University Press.

Jirka, G. H. (2004). Integral model for turbulent buoyant jets in unbounded stratified flows. Part I: Single round jet. *Environ. Fluid Mech.* 4 (1), 1–56. doi:10.1023/a:1025583110842

Johannes, R. (1980). The ecological significance of the submarine discharge of groundwater. *Mar. Ecol. Prog. Ser.* 3 (4), 365–373. doi:10.3354/meps003365

Johannesson, K. H., and Burdige, D. J. (2007). Balancing the global oceanic neodymium budget: evaluating the role of groundwater. *Earth Planet. Sci. Lett.* 253 (1, 2), 129–142. doi:10.1016/j.epsl.2006.10.021

Johnson, A. G., Glenn, C. R., Burnett, W. C., Peterson, R. N., and Lucey, P. G. (2008). Aerial infrared imaging reveals large nutrient-rich groundwater inputs to the ocean. *Geophys. Res. Lett.* 35 (15), 6. doi:10.1029/2008gl034574

Johnson, T. C., Versteeg, R. J., Day-Lewis, F. D., Major, W., and Lane, J. W. (2015). Time-lapse electrical geophysical monitoring of amendment-based biostimulation. *Ground Water* 53 (6), 920–932. doi:10.1111/gwat.12291

Jørgensen, B. B. (1982). Mineralization of organic-matter in the Sea Bed - the role of Sulfate reduction. *Nature* 296 (5858), 643–645.

Judd, A. G., and Hovland, M. (1992). The evidence of shallow gas in marine sediments. *Continental Shelf Res.* 12 (10), 1081–1095. doi:10.1016/0278-4343(92)90070-z

Jurasinski, G., Janssen, M., Voss, M., Böttcher, M. E., Brede, M., Burchard, H., et al. (2018). Understanding the coastal ecocline: assessing sea-land interactions at non-tidal, low-ling Coasts through interdisciplinary research. *Front. Mar. Sci.* 5. doi:10.3389/fmars.2018.00342

Kanehisa, M., and Goto, S. (2000). KEGG: kyoto encyclopedia of genes and genomes. *Nucl. Acids Res.* 28 (1), 27–30. doi:10.1093/nar/28.1.27

Kazemipour, F., Launeau, P., and Méléder, V. (2012). Microphytobenthos biomass mapping using the optical model of diatom biofilms: Application to hyperspectral images of Bourgneuf Bay. *Remote Sensing Environ.* 127, 1–13. doi:10.1016/j.rse.2012.08.016

Kazmierczak, J., Postma, D., Müller, S., Jessen, S., Nilsson, B., Czekaj, J., et al. (2020). Groundwater-controlled phosphorus release and transport from sandy aquifer into lake. *Limnol. Oceanogr.* 65 (9), 2188–2204. doi:10.1002/lno.11447

Keating, K., and Knight, R. (2007). A laboratory study to determine the effect of iron oxides on proton NMR measurements. *Geophysics* 72 (1), E27–E32. doi:10.1190/1.2399445

Kelly, J. L., Glenn, C. R., and Lucey, P. G. (2013). High-resolution aerial infrared mapping of groundwater discharge to the coastal ocean. *Limnol. Oceanogr. Methods* 11, 262–277. doi:10.4319/lom.2013.11.262

Kim, G., Kim, J.-S., and Hwang, D.-W. (2011). Submarine groundwater discharge from oceanic islands standing in oligotrophic oceans: Implications for global biological production and organic carbon fluxes. *Limnol. Oceanogr.* 56 (2), 673–682. doi:10.4319/lo.2011.56.2.0673

Kim, J., and Kim, G. (2017). Inputs of humic fluorescent dissolved organic matter via submarine groundwater discharge to coastal waters off a volcanic island (Jeju, Korea). *Sci. Rep.* 7, 7921. doi:10.1038/s41598-017-08518-5

Kim, K. H., Heiss, J. W., Geng, X., and Michael, H. A. (2020). Modeling hydrologic controls on particulate organic carbon contributions to beach aquifer biogeochemical reactivity. *Water Resour. Res.* 56 (10), e2020WR027306. doi:10.1029/2020wr027306

Kim, K. H., Heiss, J. W., Michael, H. A., Cai, W.-J., Laattoe, T., Post, V. E. A., et al. (2017). Spatial patterns of groundwater biogeochemical reactivity in an intertidal beach aquifer. *J. Geophys. Res. Biogeosci.* 122 (10), 2548–2562. doi:10.1002/2017jg003943

Kim, K. H., Michael, H. A., Field, E. K., and Ullman, W. J. (2019). Hydrologic shifts create complex transient distributions of particulate organic carbon and biogeochemical responses in beach aquifers. *J. Geophys. Res. Biogeosci.* 124 (10), 3024–3038. doi:10.1029/2019jg005114

Kim, T.-H., Kwon, E., Kim, I., Lee, S.-A., and Kim, G. (2013). Dissolved organic matter in the subterranean estuary of a volcanic island, Jeju: Importance of dissolved organic nitrogen fluxes to the ocean. *J. Sea Res.* 78, 18–24. doi:10.1016/j.seares.2012.12.009

Kim, T.-H., Waska, H., Kwon, E., Suryaputra, I. G. N., and Kim, G. (2012). Production, degradation, and flux of dissolved organic matter in the subterranean estuary of a large tidal flat. *Mar. Chem.* 142–144, 1–10. doi:10.1016/j.marchem.2012.08.002

Kipp, L. E., Henderson, P. B., Wang, Z. A., and Charette, M. A. (2020). Deltaic and estuarine controls on mackenzie river solute fluxes to the arctic Ocean. *Estuaries and coasts*. 42, 1992-2014. doi:10.1007/s12237-020-00739-8

Kirsch, R. (2006). *Groundwater Geophysics—a tool for hydrogeology*. Flintbek, Germany, Springer.

Klemas, V. V. (2016). Remote Sensing of Submerged Aquatic VegetationSeafloor mapping along continental shelves, *Res. Tech. Visualizing Benthic Environments*. 13, 125–140. doi:10.1007/978-3-319

Knee, K. L., and Paytan, A. (2011). "4.08 - Submarine groundwater discharge: a source of nutrients, metals, and pollutants to the coastal ocean", in *Treatise on estuarine and coastal science*. Waltham: Academic Press, 205–233.

Kotwicki, L., Grzelak, K., Czub, M., Dellwig, O., Gentz, T., Szymczycha, B., et al. (2014). Submarine groundwater discharge to the Baltic coastal zone: Impacts on the meiofaunal community. *J. Mar. Syst.* 129, 118–126. doi:10.1016/j.jmarsys.2013.06.009

Kowalski, N., Dellwig, O., Beck, M., Grunwald, M., Dürselen, C.-D., Badewien, T. H., et al. (2012). A comparative study of manganese dynamics in the water column and sediments of intertidal systems of the North Sea. *Estuarine Coast. Shelf Sci.* 100, 3–17. doi:10.1016/j.ecss.2011.03.011

Kroeger, K. D., and Charette, M. A. (2008). Nitrogen biogeochemistry of submarine groundwater discharge. *Limnol. Oceanogr.* 53 (3), 1025. doi:10.4319/lo.2008.53.3.1025

Kwon, E. Y., Kim, G., Primeau, F., Moore, W. S., Cho, H.-M., DeVries, T., et al. (2014). Global estimate of submarine groundwater discharge based on an observationally constrained radium isotope model. *Geophys. Res. Lett.* 41 (23), 2014GL061574. doi:10.1002/2014gl061574

Lagouarde, J.-P., Bhattacharya, B. K., Crebassol, P., Gamet, P., Babu, S. S., Boulet, G., et al. (2018). The Indian-French Trishna mission: Earth observation in the thermal infrared with high spatio-temporal resolution. IGARSS 2018-2018 IEEE international geoscience and remote sensing symposium. IEEE, 4078–4081.

Langguth, H. R., and Voigt, R. (2004). *Hydrogeologische methoden*. Berlin, Heidelberg: Springer, 1014.

Laruelle, G. G., Dürr, H. H., Slomp, C. P., and Borges, A. V. (2010). Evaluation of sinks and sources of CO2in the global coastal ocean using a spatially-explicit typology of estuaries and continental shelves. *Geophys. Res. Lett.* 37 (15), doi:10.1029/2010gl043691

Lausch, A., Pause, M., Merbach, I., Zacharias, S., Doktor, D., Volk, M., et al. (2013). A new multiscale approach for monitoring vegetation using remote sensing-based indicators in laboratory, field, and landscape. *Environ. Monit. Assess.* 185 (2), 1215–1235. doi:10.1007/s10661-012-2627-8

Lebbe, L. (1981). *The subterranean flow of fresh and salt water underneath the western Belgian beach*. Uppsala, Sweden: Proceedings of the 7th Salt Water Intrusion Meeting, 193–219.

Lecher, A. L., Chien, C.-T., and Paytan, A. (2016a). Submarine groundwater discharge as a source of nutrients to the North Pacific and Arctic coastal ocean. *Mar. Chem.* 186, 167–177. doi:10.1016/j.marchem.2016.09.008

Lecher, A. L., Kessler, J., Sparrow, K., Garcia-Tigreros Kodovska, F., Dimova, N., Murray, J., et al. (2016b). Methane transport through submarine groundwater discharge to the North Pacific and Arctic Ocean at two Alaskan sites. *Limnol. Oceanogr.* 61 (S1), S344–S355. doi:10.1002/lno.10118

Lecher, A., and Mackey, K. (2018). Synthesizing the effects of submarine groundwater discharge on Marine Biota. *Hydrology* 5 (4), 60. doi:10.3390/hydrology5040060

Lee, E., Shin, D., Hyun, S. P., Ko, K.-S., Moon, H. S., Koh, D.-C., et al. (2017). Periodic change in coastal microbial community structure associated with submarine groundwater discharge and tidal fluctuation. *Limnol. Oceanogr.* 62 (2), 437–451. doi:10.1002/lno.10433

Leitão, F., Encarnação, J., Range, P., Schmelz, R. M., Teodósio, M. A., and Chícharo, L. (2015). Submarine groundwater discharges create unique benthic

communities in a coastal sandy marine environment. *Estuarine Coastal Shelf Sci.* 163, 93–98. doi:10.1016/j.ecss.2015.06.007

Lewandowski, J., Meinikmann, K., Nützmann, G., and Rosenberry, D. O. (2015). Groundwater - the disregarded component in lake water and nutrient budgets. Part 2: effects of groundwater on nutrients. *Hydrol. Process.* 29 (13), 2922–2955. doi:10.1002/hyp.10384

Linkhorst, A., Dittmar, T., and Waska, H. (2017). Molecular fractionation of dissolved organic matter in a shallow subterranean estuary: the role of the iron curtain. *Environ. Sci. Technol.* 51 (3), 1312–1320. doi:10.1021/acs.est.6b03608

Lipka, M., Böttcher, M. E., Wu, Z., Sültenfuß, J., Jenner, A.-K., Westphal, J., et al. (2018). Ferruginous groundwaters as a source of P, Fe, and DIC for coastal waters of the southern Baltic Sea: (Isotope) hydrobiogeochemistry and the role of an iron curtain. *E3s Web Conf.* 54, 00019. doi:10.1051/e3sconf/20185400019

Liu, Q., Charette, M. A., Breier, C. F., Henderson, P. B., McCorkle, D. C., Martin, W., et al. (2017). Carbonate system biogeochemistry in a subterranean estuary - Waquoit Bay, USA. *Geochim. Cosmochim. Acta* 203, 422–439. doi:10.1016/j.gca.2017.01.041

Liu, Q., Dai, M., Chen, W., Huh, C.-A., Wang, G., Li, Q., et al. (2012). How significant is submarine groundwater discharge and its associated dissolved inorganic carbon in a river-dominated shelf system? *Biogeosciences* 9 (5), 1777–1795. doi:10.5194/bg-9-1777-2012

Lopez, C. V., Murgulet, D., and Santos, I. R. (2020). Radioactive and stable isotope measurements reveal saline submarine groundwater discharge in a semiarid estuary. *J. Hydrol.* 590, 125395. doi:10.1016/j.jhydrol.2020.125395

Loveless, A. M., and Oldham, C. E. (2010). Natural attenuation of nitrogen in groundwater discharging through a sandy beach. *Biogeochemistry* 98 (1–3), 75–87. doi:10.1007/s10533-009-9377-x

Luijendijk, E., Gleeson, T., and Moosdorf, N. (2020). Fresh groundwater discharge insignificant for the world's oceans but important for coastal ecosystems. *Nat. Commun.* 11 (1), 1260. doi:10.1038/s41467-020-15064-8

Luther, G. W., Church, T. M., and Powell, D. (1991). Sulfur speciation and sulfide oxidation in the water column of the Black Sea. *Deep Sea Res. A. Oceanographic Res. Pap.* 38, S1121–S1137. doi:10.1016/s0198-0149(10)80027-5

Macklin, P. A., Suryaputra, I. G. N. A., Maher, D. T., Murdiyarso, D., and Santos, I. R. (2019). Drivers of CO2 along a mangrove-seagrass transect in a tropical bay: Delayed groundwater seepage and seagrass uptake. *Continental Shelf Res.* 172, 57–67. doi:10.1016/j.csr.2018.10.008

Mallast, U., Gloaguen, R., Friesen, J., Rödiger, T., Geyer, S., Merz, R., et al. (2014). How to identify groundwater-caused thermal anomalies in lakes based on multi-temporal satellite data in semi-arid regions. *Hydrol. Earth Syst. Sci.* 18 (7), 2773–2787. doi:10.5194/hess-18-2773-2014

Mallast, U., and Siebert, C. (2019). Combining continuous spatial and temporal scales for SGD investigations using UAV-based thermal infrared measurements. *Hydrol. Earth Syst. Sci.* 23 (3), 1375–1392. doi:10.5194/hess-23-1375-2019

Manheim, F. T., Krantz, D. E., and Bratton, J. F. (2004). Studying ground water under delmarva coastal bays using electrical resistivity. *Ground Water* 42 (7), 1052–1068. doi:10.1111/j.1745-6584.2004.tb02643.x

Mansoor, N., and Slater, L. (2007). On the relationship between iron concentration and induced polarization in marsh soils. *Geophysics* 72 (1), A1–A5. doi:10.1190/1.2374853

Marchant, H. K., Holtappels, M., Lavik, G., Ahmerkamp, S., Winter, C., and Kuypers, M. M. M. (2016). Coupled nitrification-denitrification leads to extensive N loss in subtidal permeable sediments. *Limnol. Oceanogr.* 61 (3), 1033–1048. doi:10.1002/lno.10271

Mayfield, K. K., Eisenhauer, A., Santiago Ramos, D. P., Higgins, J. A., Horner, T. J., Auro, M., et al. (2021). Groundwater discharge impacts marine isotope budgets of Li, Mg, Ca, Sr, and Ba. *Nat. Commun.* 12 (1), 148. doi:10.1038/s41467-020-20248-3

McGrath, G. S., Paik, K., and Hinz, C. (2012). Microtopography alters self-organized vegetation patterns in water-limited ecosystems. *J. Geophys. Research-Biogeosciences* 117. doi:10.1029/2011jg001870

Meister, P., Liu, B., Khalili, A., Böttcher, M. E., and Jørgensen, B. B. (2019). Factors controlling the carbon isotope composition of dissolved inorganic carbon and methane in marine porewater: An evaluation by reaction-transport modelling. *J. Mar. Syst.* 200, 103227. doi:10.1016/j.jmarsys.2019.103227

Mejías, M., Ballesteros, B. J., Antón-Pacheco, C., Domínguez, J. A., Garcia-Orellana, J., Garcia-Solsona, E., et al. (2012). Methodological study of submarine groundwater discharge from a karstic aquifer in the Western Mediterranean Sea. *J. Hydrol.* 464-465, 27–40. doi:10.1016/j.jhydrol.2012.06.020

Meyer, D., Prien, R. D., Dellwig, O., Waniek, J. J., and Schulz–Bull, D. E. (2014). Electrode measurements of the oxidation reduction potential in the Gotland Deep using a moored profiling instrumentation. *Estuarine Coastal Shelf Sci.* 141, 26–36. doi:10.1016/j.ecss.2014.02.001

Michael, H. A., Mulligan, A. E., and Harvey, C. F. (2005). Seasonal oscillations in water exchange between aquifers and the coastal ocean. *Nature* 436 (7054), 1145–1148. doi:10.1038/nature03935

Migné, A., Ouisse, V., Hubas, C., and Davoult, D. (2011). Freshwater seepages and ephemeral macroalgae proliferation in an intertidal bay: II. Effect on benthic biomass and metabolism. *Estuarine, Coastal Shelf Sci.* 92 (1), 161–168. doi:10.1016/j.ecss.2010.12.023

Miller, D. C., and Ullman, W. J. (2004). Ecological consequences of ground water discharge to Delaware Bay, United States. *Ground Water* 42 (7), 959–970. doi:10.1111/j.1745-6584.2004.tb02635.x

Missiaen, T., Murphy, S., Loncke, L., and Henriet, J.-P. (2002). Very high-resolution seismic mapping of shallow gas in the Belgian coastal zone. *Continental Shelf Res.* 22 (16), 2291–2301. doi:10.1016/s0278-4343(02)00056-0

Mollenhauer, H., Kasner, M., Haase, P., Peterseil, J., Wohner, C., Frenzel, M., et al. (2018). Long-term environmental monitoring infrastructures in Europe: observations, measurements, scales, and socio-ecological representativeness. *Sci. Total Environ.* 624, 968–978. doi:10.1016/j.scitotenv.2017.12.095

Montiel, D., Lamore, A. F., Stewart, J., Lambert, W. J., Honeck, J., Lu, Y., et al. (2019). Natural groundwater nutrient fluxes exceed anthropogenic inputs in an ecologically impacted estuary: lessons learned from Mobile Bay, Alabama. *Biogeochemistry* 145 (1), 1–33. doi:10.1007/s10533-019-00587-0

Moore, W. S., Beck, M., Riedel, T., Rutgers van der Loeff, M., Dellwig, O., Shaw, T. J., et al. (2011). Radium-based pore water fluxes of silica, alkalinity, manganese, DOC, and uranium: A decade of studies in the German Wadden Sea. *Geochim. Cosmochim. Acta* 75 (21), 6535–6555. doi:10.1016/j.gca.2011.08.037

Moore, W. S. (2000). Determining coastal mixing rates using radium isotopes. *Continental Shelf Res.* 20 (15), 1993–2007. doi:10.1016/s0278-4343(00)00054-6

Moore, W. S. (1996). Large groundwater inputs to coastal waters revealed by 226Ra enrichments. *Nature* 380 (6575), 612–614. doi:10.1038/380612a0

Moore, W. S., Sarmiento, J. L., and Key, R. M. (2008). Submarine groundwater discharge revealed by 228Ra distribution in the upper Atlantic Ocean. *Nat. Geosci.* 1 (5), 309–311. doi:10.1038/ngeo183

Moore, W. S. (2003). Sources and fluxes of submarine groundwater discharge delineated by radium isotopes. *Biogeochemistry* 66 (1, 2), 75–93. doi:10.1023/b:biog.0000006065.77764.a0

Moore, W. S. (1999). The subterranean estuary: a reaction zone of ground water and sea water. *Mar. Chem.* 65 (1, 2), 111–125. doi:10.1016/s0304-4203(99)00014-6

Moosdorf, N., Hartmann, J., and Dürr, H. H. (2010). Lithological composition of the North American continent and implications of lithological map resolution for dissolved silica flux modeling. *Geochem. Geophys. Geosyst.* 11, . doi:10.1029/2010gc003259

Morrow, F. J., Ingham, M. R., and McConchie, J. A. (2010). Monitoring of tidal influences on the saline interface using resistivity traversing and cross-borehole resistivity tomography. *J. Hydrol.* 389 (1-2), 69–77. doi:10.1016/j.jhydrol.2010.05.022

Mosher, D. C., and Simpkin, P. G. (1999). Environmental marine Geoscience 1. Status and trends of marine high-resolution seismic reflection profiling: Data acquistion. *Geosci. Can.* 26, 174–188.

Müller, H. (2010). *Characterization of marine near-surface sediments by electromagnetic profiling.* Bremen: University of Bremen.

Müller, H., von Dobeneck, T., Nehmiz, W., and Hamer, K. (2011). Near-surface electromagnetic, rock magnetic, and geochemical fingerprinting of submarine freshwater seepage at Eckernförde Bay (SW Baltic Sea). *Geo-mar Lett.* 31 (2), 123–140. doi:10.1007/s00367-010-0220-0

Müller-Petke, M., and Yaramanci, U. (2015). "11.13 - Tools and Techniques: Nuclear Magnetic Resonance," in *Treatise on geophysics*. Editor G. Schubert. Second Edition (Oxford: Elsevier), 419–445.

Musat, N., Werner, U., Knittel, K., Kolb, S., Dodenhof, T., van Beusekom, J. E., et al. (2006). Microbial community structure of sandy intertidal sediments in the North Sea, Sylt-Rømø Basin, Wadden Sea. *Syst. Appl. Microbiol.* 29 (4), 333–348. doi:10.1016/j.syapm.2005.12.006

Mylroie, J. E., and Carew, J. L. (1990). The Flank Margin model for dissolution cave development in carbonate platforms. *Earth Surf. Process. Landforms* 15 (5), 413–424. doi:10.1002/esp.3290150505

Nakada, S., Yasumoto, J., Taniguchi, M., and Ishitobi, T. (2011). Submarine groundwater discharge and seawater circulation in a subterranean estuary beneath a tidal flat. *Hydrol. Process* 25 (17), 2755–2763. doi:10.1002/hyp.8016

Nick, H., Raoof, A., Centler, F., Thullner, M., and Regnier, P. (2013). Reactive dispersive contaminant transport in coastal aquifers: numerical simulation of a reactive Henry problem. *J. Contam. Hydrol.* 145, 90–104. doi:10.1016/j.jconhyd.2012.12.005

Nowicki, B. L., Requintina, E., Van Keuren, D., and Portnoy, J. (1999). The role of sediment denitrification in reducing groundwater-derived nitrate inputs to Nauset Marsh Estuary, Cape Cod, Massachusetts. *Estuaries* 22 (2), 245–259. doi:10.2307/1352981

O'Connor, A. E., Krask, J. L., Canuel, E. A., and Beck, A. J. (2018). Seasonality of major redox constituents in a shallow subterranean estuary. *Geochim. Cosmochim. Acta* 224, 344–361. doi:10.1016/j.gca.2017.10.013

O'Reilly, C., Santos, I. R., Cyronak, T., McMahon, A., and Maher, D. T. (2015). Nitrous oxide and methane dynamics in a coral reef lagoon driven by pore water exchange: Insights from automated high-frequency observations. *Geophys. Res. Lett.* 42 (8), 2885–2892. doi:10.1002/2015gl063126

Oehler, T., Bakti, H., Lubis, R. F., Purwoarminta, A., Delinom, R., and Moosdorf, N. (2019a). Nutrient dynamics in submarine groundwater discharge through a coral reef (western Lombok, Indonesia). *Limnol. Oceanogr.* 64 (6), 2646–2661. doi:10.1002/lno.11240

Oehler, T., Eiche, E., Putra, D., Adyasari, D., Hennig, H., Mallast, U., et al. (2018). Seasonal variability of land-ocean groundwater nutrient fluxes from a tropical karstic region (southern Java, Indonesia). *J. Hydrol.* 565, 662–671. doi:10.1016/j.jhydrol.2018.08.077

Oehler, T., Mogollón, J. M., Moosdorf, N., Winkler, A., Kopf, A., and Pichler, T. (2017). Submarine groundwater discharge within a landslide scar at the French Mediterranean coast. *Estuarine Coastal Shelf Sci.* 198, 128–137. doi:10.1016/j.ecss.2017.09.006

Oehler, T., Tamborski, J., Rahman, S., Moosdorf, N., Ahrens, J., Mori, C., et al. (2019b). DSi as a Tracer for Submarine Groundwater Discharge. *Front. Mar. Sci.* 6 (563). doi:10.3389/fmars.2019.00563

Paffrath, R., Pahnke, K., Behrens, M. K., Reckhardt, A., Ehlert, C., Schnetger, B., et al. (2020). Rare earth element behavior in a sandy subterranean estuary of the southern North Sea. *Front. Mar. Sci.* doi:10.3389/fmars.2020.00424

Pain, A. J., Martin, J. B., and Young, C. R. (2019). Sources and sinks of CO_2 and CH_4 in siliciclastic subterranean estuaries. *Limnol. Oceanogr.* 64 (4), 1500–1514. doi:10.1002/lno.11131

Pain, A. J., Martin, J. B., Young, C. R., Valle-Levinson, A., and Mariño-Tapia, I. (2020). Carbon and phosphorus processing in a carbonate karst aquifer and delivery to the coastal ocean. *Geochim. et Cosmochim. Acta* 269, 484–495. doi:10.1016/j.gca.2019.10.040

Papenmeier, S., Darr, A., Feldens, P., and Michaelis, R. (2020). Hydroacoustic mapping of geogenic hard substrates: challenges and review of German approaches. *Geosciences* 10 (3), 100. doi:10.3390/geosciences10030100

Petersen, W., Schroeder, F., and Bockelmann, F.-D. (2011). FerryBox - Application of continuous water quality observations along transects in the North Sea. *Ocean Dyn.* 61 (10), 1541–1554. doi:10.1007/s10236-011-0445-0

Pisternick, T., Lilkendey, J., Audit-Manna, A., Dumur Neelayya, D., Neehaul, Y., and Moosdorf, N. (2020). Submarine groundwater springs are characterized by distinct fish communities. *Mar. Ecol.*, 41 (5), e12610. doi:10.1111/maec.12610

Post, V. E. A., Houben, G. J., Stoeckl, L., and Sültenfuß, J. (2019). *Behaviour of tritium and tritiogenic helium in freshwater lens groundwater systems: insights from Langeoog island*. Germany: Geofluids, 1494326

Post, V. E. A., Vandenbohede, A., Werner, A. D., and Maimun, M. D. (2013). Groundwater ages in coastal aquifers. *Adv. Water Resour.* 57, 1–11. doi:10.1016/j.advwatres.2013.03.011

Povinec, P. P., Burnett, W. C., Beck, A., Bokuniewicz, H., Charette, M., Gonneea, M. E., et al. (2012). Isotopic, geophysical and biogeochemical investigation of submarine groundwater discharge: IAEA-UNESCO intercomparison exercise at Mauritius Island. *J. Environ. Radioact* 104, 24–45. doi:10.1016/j.jenvrad.2011.09.009

Prandle, D., (2009). *Estuaries: dynamics, mixing, sedimentation, and morphology*. Cambridge: Cambridge University Press, ix, 236

Price, R. M., Savabi, M. R., Jolicoeur, J. L., and Roy, S. (2010). Adsorption and desorption of phosphate on limestone in experiments simulating seawater intrusion. *Appl. Geochem.* 25 (7), 1085–1091. doi:10.1016/j.apgeochem.2010.04.013

Prieto, C., and Destouni, G. (2011). Is submarine groundwater discharge predictable?. *Geophys. Res. Lett.* 38. doi:10.1029/2010gl045621

Prouty, N. G., Cohen, A., Yates, K. K., Storlazzi, C. D., Swarzenski, P. W., and White, D. (2017a). Vulnerability of Coral Reefs to Bioerosion From Land-Based Sources of Pollution. *J. Geophys. Res.*122 (12), 9319–9331. doi:10.1002/2017JC013264

Prouty, N. G., Swarzenski, P. W., Fackrell, J. K., Johannesson, K., and Palmore, C. D. (2017b). Groundwater-derived nutrient and trace element transport to a nearshore Kona coral ecosystem: Experimental mixing model results. *J. Hydrol. Reg. Stud.* 11, 166–177. doi:10.1016/j.ejrh.2015.12.058

Rahman, S., Tamborski, J. J., Charette, M. A., and Cochran, J. K. (2019). Dissolved silica in the subterranean estuary and the impact of submarine groundwater discharge on the global marine silica budget. *Mar. Chem.* 208, 29–42. doi:10.1016/j.marchem.2018.11.006

Rakhimbekova, S., O'Carroll, D. M., Andersen, M. S., Wu, M. Z., and Robinson, C. E. (2018). Effect of Transient Wave Forcing on the Behavior of Arsenic in a Nearshore Aquifer. *Environ. Sci. Technol.* 52 (21), 12338–12348. doi:10.1021/acs.est.8b03659

Rao, A. M. F., and Charette, M. A. (2012). Benthic nitrogen fixation in an eutrophic estuary affected by groundwater discharge. *J. Coast. Res.* 280 (2), 477–485. doi:10.2112/jcoastres-d-11-00057.1

Rasmussen, B., and Josefson, A. B. (2002). Consistent estimates for the residence time of micro-tidal estuaries. *Estuarine Coastal Shelf Sci.* 54 (1), 65–73. doi:10.1006/ecss.2001.0836

Reckhardt, A., Beck, M., Greskowiak, J., Schnetger, B., Böttcher, M. E., Gehre, M., et al. (2017). Cycling of redox-sensitive elements in a sandy subterranean estuary of the southern North Sea. *Mar. Chem.* 188, 6–17. doi:10.1016/j.marchem.2016.11.003

Rickard, D. (1997). Kinetics of pyrite formation by the H2S oxidation of iron (II) monosulfide in aqueous solutions between 25 and 125°C: The rate equation. *Geochim. Cosmochim. Acta* 61 (1), 115–134. doi:10.1016/s0016-7037(96)00321-3

Riechelmann, S., Mavromatis, V., Buhl, D., Dietzel, M., and Immenhauser, A. (2020). Controls on formation and alteration of early diagenetic dolomite: A multi-proxy δ44/40Ca, δ26Mg, δ18O and δ13C approach. *Geochim. Cosmochim. Acta* 283, 167–183. doi:10.1016/j.gca.2020.06.010

Robinson, C., Brovelli, A., Barry, D. A., and Li, L. (2009). Tidal influence on BTEX biodegradation in sandy coastal aquifers. *Adv. Water Resour.* 32 (1), 16–28. doi:10.1016/j.advwatres.2008.09.008

Robinson, C. E., Xin, P., Santos, I. R., Charette, M. A., Li, L., and Barry, D. A. (2017). Groundwater dynamics in subterranean estuaries of coastal unconfined aquifers: Controls on submarine groundwater discharge and chemical inputs to the ocean. *Adv. Water Resour.*

Robinson, C. E., Xin, P., Santos, I. R., Charette, M. A., Li, L., and Barry, D. A. (2018). Groundwater dynamics in subterranean estuaries of coastal unconfined aquifers: Controls on submarine groundwater discharge and chemical inputs to the ocean. *Adv. Water Resour.* 115, 315–331. doi:10.1016/j.advwatres.2017.10.041

Robinson, C., Gibbes, B., and Li, L. (2006). Driving mechanisms for groundwater flow and salt transport in a subterranean estuary. *Geophys. Res. Lett.* 33 (3). doi:10.1029/2005gl025247

Robinson, C., Li, L., and Barry, D. A. (2007). Effect of tidal forcing on a subterranean estuary. *Adv. Water Resour.* 30 (4), 851–865. doi:10.1016/j.advwatres.2006.07.006

Robinson, C., Xin, P., Li, L., and Barry, D. A. (2014). Groundwater flow and salt transport in a subterranean estuary driven by intensified wave conditions. *Water Resour. Res.* 50 (1), 165–181. doi:10.1002/2013wr013813

Rocha, C., Robinson, C. E., Santos, I. R., Waska, H., Michael, H. A., and Bokuniewicz, H. J. (2021). A place for subterranean estuaries in the coastal zone. Estuarine. *Coastal Shelf Sci.* 250, 107167. doi:10.1016/j.ecss.2021.107167

Rocha, C., Veiga-Pires, C., Scholten, J., Knoeller, K., Gröcke, D. R., Carvalho, L., et al. (2016). Assessing land-ocean connectivity via submarine groundwater discharge (SGD) in the Ria Formosa Lagoon (Portugal): combining radon measurements and stable isotope hydrology. *Hydrol. Earth Syst. Sci.* 20 (8), 3077–3098. doi:10.5194/hess-20-3077-2016

Rodellas, V., Garcia-Orellana, J., Masqué, P., Feldman, M., and Weinstein, Y. (2015). Submarine groundwater discharge as a major source of nutrients to the Mediterranean Sea. *Proc. Natl. Acad. Sci. USA* 112 (13), 3926–3930. doi:10.1073/pnas.1419049112

Rodellas, V., Stieglitz, T. C., Tamborski, J. J., van Beek, P., Andrisoa, A., and Cook, P. G. (2021). Conceptual uncertainties in groundwater and porewater fluxes estimated by radon and radium mass balances. *Limnol. Oceanogr.* 11, 676. doi:10.1002/lno.11678

Rogers, D. R., and Casciotti, K. L. (2010). Abundance and diversity of archaeal ammonia oxidizers in a coastal groundwater system. *Appl. Environ. Microbiol.* 76 (24), 7938–7948. doi:10.1128/AEM.02056-09

Röper, T., Kröger, K. F., Meyer, H., Sültenfuss, J., Greskowiak, J., and Massmann, G. (2012). Groundwater ages, recharge conditions and hydrochemical evolution of a barrier island freshwater lens (Spiekeroog, Northern Germany). *J. Hydrol.* 454-455, 173–186. doi:10.1016/j.jhydrol.2012.06.011

Roseen, R. M. (2002). *Quantifying groundwater discharge using thermal imagery and conventional groundwater exploration techniques for estimating the nitrogen loading to a meso-scale inland estuary. Durham.*

Roy, M., Martin, J. B., Cable, J. E., and Smith, C. G. (2013). Variations of iron flux and organic carbon remineralization in a subterranean estuary caused by inter-annual variations in recharge. *Geochim. Cosmochim. Acta* 103, 301–315. doi:10.1016/j.gca.2012.10.055

Roy, M., Martin, J. B., Cherrier, J., Cable, J. E., and Smith, C. G. (2010). Influence of sea level rise on iron diagenesis in an east Florida subterranean estuary. *Geochim. Cosmochim. Acta* 74 (19), 5560–5573. doi:10.1016/j.gca.2010.07.007

Roy, M., Martin, J. B., Smith, C. G., and Cable, J. E. (2011). Reactive-transport modeling of iron diagenesis and associated organic carbon remineralization in a Florida (USA) subterranean estuary. *Earth Planet. Sci. Lett.* 304 (1, 2), 191–201. doi:10.1016/j.epsl.2011.02.002

Rullkötter, J. (2009). The back-barrier tidal flats in the southern North Sea-a multidisciplinary approach to reveal the main driving forces shaping the system. *Ocean Dyn.* 59 (2), 157–165. doi:10.1007/s10236-009-0197-2

Sáenz, J. P., Hopmans, E. C., Rogers, D., Henderson, P. B., Charette, M. A., Schouten, S., et al. (2012). Distribution of anaerobic ammonia-oxidizing bacteria in a subterranean estuary. *Mar. Chem.* 136, 137, 7–13. doi:10.1016/j.marchem.2012.04.004

Salt, D. E., Blaylock, M., Kumar, N. P., Dushenkov, V., Ensley, B. D., Chet, I., et al. (1995). Phytoremediation: a novel strategy for the removal of toxic metals from the environment using plants. *Biotechnology (NY)* 13 (5), 468–474. doi:10.1038/nbt0595-468

Sánchez-Úbeda, J. P., Manuel, L.-C., Calvache, M., Purtschert, R., Engesgaard, P., Martín-Montañés, C., et al. (2018). *Groundwater age dating in motril-salobreña coastal aquifer with environmental tracers 3H/3He, 4He, 85Kr, and 39Ar)*, Spain. Granada. δ18O/δ2H, 287–295.

Sanders, C. J., Santos, I. R., Barcellos, R., and Silva Filho, E. V. (2012). Elevated concentrations of dissolved Ba, Fe and Mn in a mangrove subterranean estuary: Consequence of sea level rise?. *Continental Shelf Res.* 43, 86–94. doi:10.1016/j.csr.2012.04.015

Santoro, A. E., Boehm, A. B., and Francis, C. A. (2006). Denitrifier community composition along a nitrate and salinity gradient in a coastal aquifer. *Appl. Environ. Microbiol.* 72 (3), 2102–2109. doi:10.1128/AEM.72.3.2102-2109.2006

Santoro, A. E., Francis, C. A., de Sieyes, N. R., and Boehm, A. B. (2008). Shifts in the relative abundance of ammonia-oxidizing bacteria and archaea across physicochemical gradients in a subterranean estuary. *Environ. Microbiol.* 10 (4), 1068–1079. doi:10.1111/j.1462-2920.2007.01547.x

Santoro, A. E. (2010). Microbial nitrogen cycling at the saltwater-freshwater interface. *Hydrogeol J.* 18 (1), 187–202. doi:10.1007/s10040-009-0526-z

Santos, I. R., Beck, M., Brumsack, H.-J., Maher, D. T., Dittmar, T., Waska, H., et al. (2015). Porewater exchange as a driver of carbon dynamics across a terrestrial-marine transect: Insights from coupled 222Rn and pCO2 observations in the German Wadden Sea. *Mar. Chem.* 171, 10–20. doi:10.1016/j.marchem.2015.02.005

Santos, I. R., Burnett, W. C., Chanton, J., Dimova, N., and Peterson, R. N. (2009a). Land or ocean?: Assessing the driving forces of submarine groundwater discharge at a coastal site in the Gulf of Mexico. *J. Geophys. Res.-Oceans* 114, 11. doi:10.1029/2008jc005038

Santos, I. R., Burnett, W. C., Dittmar, T., Suryaputra, I. G. N. A., and Chanton, J. (2009b). Tidal pumping drives nutrient and dissolved organic matter dynamics in a Gulf of Mexico subterranean estuary. *Geochim. Cosmochim. Acta* 73 (5), 1325–1339. doi:10.1016/j.gca.2008.11.029

Santos, I. R., Dimova, N., Peterson, R. N., Mwashote, B., Chanton, J., and Burnett, W. C. (2009c). Extended time series measurements of submarine groundwater discharge tracers (222Rn and CH4) at a coastal site in Florida. *Mar. Chem.* 113 (1, 2), 137–147. doi:10.1016/j.marchem.2009.01.009

Santos, I. R., Eyre, B. D., and Huettel, M. (2012). The driving forces of porewater and groundwater flow in permeable coastal sediments: a review. *Estuarine Coastal Shelf Sci.* 98, 1–15. doi:10.1016/j.ecss.2011.10.024

Santos, I. R. S., Burnett, W. C., Chanton, J., Mwashote, B., Suryaputra, I. G. N. A., and Dittmar, T. (2008). Nutrient biogeochemistry in a Gulf of Mexico subterranean estuary and groundwater-derived fluxes to the coastal ocean. *Limnol. Oceanogr.* 53 (2), 705. doi:10.4319/lo.2008.53.2.0705

Sawyer, A. H., David, C. H., and Famiglietti, J. S. (2016). Continental patterns of submarine groundwater discharge reveal coastal vulnerabilities. *Science* 353 (6300), 705–707. doi:10.1126/science.aag1058

Sayre, R., Noble, S., Hamann, S., Smith, R., Wright, D., Breyer, S., et al. (2018). A new 30 meter resolution global shoreline vector and associated global islands database for the development of standardized ecological coastal units. *J. Oper. Oceanogr.*, 12, 1–10. doi:10.1080/1755876X.2018.1529714

Schlüter, M., Sauter, E. J., Andersen, C. E., Dahlgaard, H., and Dando, P. R. (2004). Spatial distribution and budget for submarine groundwater discharge in Eckernförde Bay (Western Baltic Sea). *Limnol. Oceanogr.* 49 (1), 157–167. doi:10.4319/lo.2004.49.1.0157

Schofield, O., Glenn, S., Bissett, P. W., Frazer, T. K., Iglesias-Rodriguez, D., and Moline, M. A. (2003). Development of regional coastal ocean observatories and the potential benefits to marine sanctuaries. *Mar. Technol. Soc. J* 37 (1), 54–67. doi:10.4031/002533203787537456

Schubert, M., Petermann, E., Stollberg, R., Gebel, M., Scholten, J., Knöller, K., et al. (2019). Improved approach for the investigation of submarine groundwater discharge by means of radon mapping and radon mass balancing. *Water* 11 (4), 749. doi:10.3390/w11040749

Schubert, M., Scholten, J., Schmidt, A., Comanducci, J., Pham, M., Mallast, U., et al. (2014). Submarine groundwater discharge at a single spot location: evaluation of different detection approaches. *Water* 6 (3), 584–601. doi:10.3390/w6030584

Schutte, C. A., Wilson, A. M., Evans, T., Moore, W. S., and Joye, S. B. (2016). Methanotrophy controls groundwater methane export from a barrier island. *Geochim. Cosmochim. Acta* 179, 242–256. doi:10.1016/j.gca.2016.01.022

Seibert, S. L., Greskowiak, J., Prommer, H., Böttcher, M. E., and Massmann, G. (2019). Modeling of biogeochemical processes in a barrier island freshwater lens (Spiekeroog, Germany). *J. Hydrol.* 575, 1133–1144. doi:10.1016/j.jhydrol.2019.05.094

Seidel, M., Beck, M., Greskowiak, J., Riedel, T., Waska, H., Suryaputra, I. N. A., et al. (2015). Benthic-pelagic coupling of nutrients and dissolved organic matter composition in an intertidal sandy beach. *Mar. Chem.* 176, 150–163. doi:10.1016/j.marchem.2015.08.011

Shaban, A., Khawlie, M., Abdallah, C., and Faour, G. (2005). Geologic controls of submarine groundwater discharge: application of remote sensing to north Lebanon. *Environ. Geol.* 47 (4), 512–522. doi:10.1007/s00254-004-1172-3

Sharp, Z. D., Wostbrock, J. A. G., and Pack, A. (2018). Mass-dependent triple oxygen isotope variations in terrestrial materials. *Geochem. Persp. Let.* 7, 27–31. doi:10.7185/geochemlet.1815

Shum, K. T., and Sundby, B. (1996). Organic matter processing in continental shelf sediments - The subtidal pump revisited. *Mar. Chem.* 53 (1, 2), 81–87. doi:10.1016/0304-4203(96)00014-x

Siemon, B., Auken, E., and Christiansen, A. V. (2009). Laterally constrained inversion of helicopter-borne frequency-domain electromagnetic data. *J. Appl. Geophys.* 67 (3), 259–268. doi:10.1016/j.jappgeo.2007.11.003

Siemon, B., Costabel, S., Voss, W., Meyer, U., Deus, N., Elbracht, J., et al. (2015). Airborne and ground geophysical mapping of coastal clays in Eastern Friesland, Germany. *Geophysics* 80 (3), Wb21–Wb34. doi:10.1190/geo2014-0102.1

Siemon, B., Ibs-von Seht, M., Steuer, A., Deus, N., and Wiederhold, H. (2020). Airborne Electromagnetic, Magnetic, and Radiometric Surveys at the German North Sea Coast Applied to Groundwater and Soil Investigations. *Remote Sensing* 12 (10). doi:10.3390/rs12101629

Siemon, B., van Baaren, E., Dabekaussen, W., Delsman, J., Dubelaar, W., Karaoulis, M., et al. (2019). Automatic identification of fresh-saline groundwater interfaces from airborne electromagnetic data in Zeeland, the The Netherlands. *Near Surf. Geophys.* 17 (1), 3–25.

Siermann, J., Harvey, C., Morgan, G., and Heege, T. (2014). *Satellite derived bathymetry and digital elevation models (DEM), international petroleum technology conference*. Qatar: International Petroleum Technology ConferenceDoha, 10.

Sippo, J. Z., Maher, D. T., Tait, D. R., Holloway, C., and Santos, I. R. (2016). Are mangroves drivers or buffers of coastal acidification? Insights from alkalinity and dissolved inorganic carbon export estimates across a latitudinal transect. *Glob. Biogeochem. Cycles* 30 (5), 753–766. doi:10.1002/2015gb005324

Sirois, M., Couturier, M., Barber, A., Gélinas, Y., and Chaillou, G. (2018). Interactions between iron and organic carbon in a sandy beach subterranean estuary. *Mar. Chem.* 202, 86–96. doi:10.1016/j.marchem.2018.02.004

Slomp, C. P., and Van Cappellen, P. (2004). Nutrient inputs to the coastal ocean through submarine groundwater discharge: controls and potential impact. *J. Hydrol.* 295 (1–4), 64–86. doi:10.1016/j.jhydrol.2004.02.018

Spiteri, C., Cappellen, P. V., and Regnier, P. (2008a). Surface complexation effects on phosphate adsorption to ferric iron oxyhydroxides along pH and salinity gradients in estuaries and coastal aquifers. *Geochim. Cosmochim. Acta* 72 (14), 3431–3445. doi:10.1016/j.gca.2008.05.003

Spiteri, C., Regnier, P., Slomp, C. P., and Charette, M. A. (2006). pH-Dependent iron oxide precipitation in a subterranean estuary. *J. Geochem. Explorat.* 88 (1–3), 399–403. doi:10.1016/j.gexplo.2005.08.084

Spiteri, C., Slomp, C. P., Charette, M. A., Tuncay, K., and Meile, C. (2008b). Flow and nutrient dynamics in a subterranean estuary (Waquoit Bay, MA, USA): Field data and reactive transport modeling. *Geochim. Cosmochim. Acta* 72 (14), 3398–3412. doi:10.1016/j.gca.2008.04.027

Spiteri, C., Slomp, C. P., Tuncay, K., and Meile, C. (2008c). Modeling biogeochemical processes in subterranean estuaries: Effect of flow dynamics and redox conditions on submarine groundwater discharge of nutrients. *Water Resour. Res.* 44 (2), 18. doi:10.1029/2007wr006071

Steuer, A., Siemon, B., and Auken, E. (2009). A comparison of helicopter-borne electromagnetics in frequency- and time-domain at the Cuxhaven valley in Northern Germany. *J. Appl. Geophys.* 67 (3), 194–205. doi:10.1016/j.jappgeo.2007.07.001

Stieglitz, T. C., Cook, P. G., and Burnett, W. C. (2010). Inferring coastal processes from regional-scale mapping of 222Radon and salinity: examples from the Great Barrier Reef, Australia. *J. Environ. Radioact* 101 (7), 544–552. doi:10.1016/j.jenvrad.2009.11.012

Stieglitz, T. (2005). Submarine groundwater discharge into the near-shore zone of the Great Barrier Reef, Australia. *Mar. Pollut. Bull.* 51 (1–4), 51–59. doi:10.1016/j.marpolbul.2004.10.055

Straume, E. O., Gaina, C., Medvedev, S., Hochmuth, K., Gohl, K., Whittaker, J. M., et al. (2019). GlobSed: Updated Total Sediment Thickness in the World's Oceans. *Geochem. Geophys. Geosyst.* 20 (4), 1756–1772. doi:10.1029/2018gc008115

Sugimoto, R., Kitagawa, K., Nishi, S., Honda, H., Yamada, M., Kobayashi, S., et al. (2017). Phytoplankton primary productivity around submarine groundwater discharge in nearshore coasts. *Mar. Ecol. Prog. Ser.* 563, 25–33. doi:10.3354/meps11980

Sültenfuss, J., Roether, W., and Rhein, M. (2009). The Bremen mass spectrometric facility for the measurement of helium isotopes, neon, and tritium in water. *Isotopes Environ. Health Stud.* 45 (2), 83–95.

Sutter, E., and Ingham, M. (2017). Seasonal saline intrusion monitoring of a shallow coastal aquifer using time-lapse DC resistivity traversing. *Near Surf. Geophys.* 15 (1), 59–73. doi:10.3997/1873-0604.2016039

Suzumura, M., Ueda, S., and Sumi, E. (2000). Control of phosphate concentration through adsorption and desorption processes in groundwater and seawater mixing at sandy beaches in Tokyo Bay, Japan. *J. Oceanogr.* 56 (6), 667–673. doi:10.1023/a:1011125700301

Swarzenski, P. W., Burnett, W. C., Greenwood, W. J., Herut, B., Peterson, R., Dimova, N., et al. (2006). Combined time-series resistivity and geochemical tracer techniques to examine submarine groundwater discharge at Dor Beach, Israel. *Geophys. Res. Lett.* 33 (24), 6. doi:10.1029/2006gl028282

Szymczycha, B., Vogler, S., and Pempkowiak, J. (2012). Nutrient fluxes via submarine groundwater discharge to the Bay of Puck, southern Baltic Sea. *Sci. Total Environ.* 438, 86–93. doi:10.1016/j.scitotenv.2012.08.058

Tamborski, J. J., Cochran, J. K., and Bokuniewicz, H. J. (2017). Application of 224Ra and 222Rn for evaluating seawater residence times in a tidal subterranean estuary. *Mar. Chem.* 189, 32–45. doi:10.1016/j.marchem.2016.12.006

Tamborski, J. J., Rogers, A. D., Bokuniewicz, H. J., Cochran, J. K., and Young, C. R. (2015). Identification and quantification of diffuse fresh submarine groundwater discharge via airborne thermal infrared remote sensing. *Remote Sensing Environ.* 171, 202–217. doi:10.1016/j.rse.2015.10.010

Taniguchi, M., Burnett, W. C., Cable, J. E., and Turner, J. V. (2002). Investigation of submarine groundwater discharge. *Hydrol. Process* 16 (11), 2115–2129. doi:10.1002/hyp.1145

Taniguchi, M., Dulai, H., Burnett, K. M., Santos, I. R., Sugimoto, R., Stieglitz, T., et al. (2019). Submarine Groundwater Discharge: Updates on Its Measurement Techniques, Geophysical Drivers, Magnitudes, and Effects. *Front. Environ. Sci.* 7 (14), 141. doi:10.3389/fenvs.2019.00141

Tao, Y., Deng, Y., Du, Y., Xu, Y., Leng, Z., Ma, T., et al. (2020). Sources and enrichment of phosphorus in groundwater of the Central Yangtze River Basin. *Sci. Total Environ.* 737, 139837. doi:10.1016/j.scitotenv.2020.139837

Teubner, P. P., Breier, R., Coppola, L., Groening, M., Jeandel, C., Jull, A. J. T., et al. (2011). Tracing of water masses using a multi isotope approach in the southern Indian Ocean. *Earth Planet. Sci. Lett.* 302 (1-2), 14–26. doi:10.1016/j.epsl.2010.11.026

Tholen, C., Nolle, L., and Werner, J. (2019). "On the Influence of Localisation and Communication Error on the Behaviour of a Swarm of Autonomous Underwater Vehicles", in *Recent advances in soft computing*. Cham: Springer International Publishing, 68–79.

Tiedje, J. M. (1988). Ecology of denitrification and dissimilatory nitrate reduction to ammonium. *Biol. anaerobic Microorg.* 717, 179–244.

Tolstikhin, I. N., and Kamenskii, I. L. (1969). Determination of groundwater age by the T- 3He method. *Geochem. Int.* 6, 810–811.

Tréguer, P. J., and De La Rocha, C. L. (2013). The World Ocean Silica Cycle. *Annu. Rev. Mar. Sci.* 5 (1), 477–501. doi:10.1146/annurev-marine-121211-172346

Tyler, R. H., Boyer, T. P., Minami, T., Zweng, M. M., and Reagan, J. R. (2017). Electrical conductivity of the global ocean. *Earth Planets Space* 69 (1), 156. doi:10.1186/s40623-017-0739-7

Uchiyama, Y., Nadaoka, K., Rölke, P., Adachi, K., and Yagi, H. (2000). Submarine groundwater discharge into the sea and associated nutrient transport in a sandy beach. *Water Resour. Res.* 36 (6), 1467–1479. doi:10.1029/2000wr900029

Ullman, W. J., Chang, B., Miller, D. C., and Madsen, J. A. (2003). Groundwater mixing, nutrient diagenesis, and discharges across a sandy beachface, Cape Henlopen, Delaware (USA). *Estuarine, Coastal Shelf Sci.* 57 (3), 539–552. doi:10.1016/s0272-7714(02)00398-0

Utsunomiya, T., Hata, M., Sugimoto, R., Honda, H., Kobayashi, S., Miyata, Y., et al. (2017). Higher species richness and abundance of fish and benthic invertebrates around submarine groundwater discharge in Obama Bay, Japan. *J. Hydrol. Reg. Stud.* 11, 139–146. doi:10.1016/j.ejrh.2015.11.012

Vahtmäe, E., Paavel, B., and Kutser, T. (2020). How much benthic information can be retrieved with hyperspectral sensor from the optically complex coastal waters?. *J. Appl. Remote Sensing* 14 (1), 016504. doi:10.1117/1.jrs.14.016504

van der Grift, B., Rozemeijer, J. C., Griffioen, J., and van der Velde, Y. (2014). Iron oxidation kinetics and phosphate immobilization along the flow-path from groundwater into surface water. *Hydrol. Earth Syst. Sci.* 18, 4687–4702. doi:10.5194/hess-18-4687-2014

Van Ryswyk, M. (2020). *Planet announces 50 cm SkySat imagery, tasking dashboard and up to 12x* Available:https://www.planet.com/pulse/tasking-dashboard-50cm-12x-revisit-announcement/.Revisit Planet News.

Vidon, P., Allan, C., Burns, D., Duval, T. P., Gurwick, N., Inamdar, S., et al. (2010). Hot Spots and Hot Moments in Riparian Zones: Potential for Improved Water Quality Management1. *JAWRA J. Am. Water Resour. Assoc.* 46 (2), 278–298. doi:10.1111/j.1752-1688.2010.00420.x

Virtasalo, J. J., Schröder, J. F., Luoma, S., Majaniemi, J., Mursu, J., and Scholten, J. (2019). Submarine groundwater discharge site in the First Salpausselkä ice-marginal formation, south Finland. *Solid Earth* 10 (2), 405–423. doi:10.5194/se-10-405-2019

Wang, B., Zhang, X., Luan, Z., Chen, C. A., and Yan, J. (2018). Seabed domes with circular depressions in the North Yellow Sea. *J. Ocean. Limnol.* 36 (6), 2154–2165. doi:10.1007/s00343-019-7173-6

Wang, D., Lin, W., Yang, X., Zhai, W., Dai, M., and Arthur Chen, C.-T. (2012). Occurrences of dissolved trace metals (Cu, Cd, and Mn) in the Pearl River Estuary (China), a large river-groundwater-estuary system. *Continental Shelf Res.* 50–51, 54–63. doi:10.1016/j.csr.2012.10.009

Wang, G., Jing, W., Wang, S., Xu, Y., Wang, Z., Zhang, Z., et al. (2014). Coastal Acidification Induced by Tidal-Driven Submarine Groundwater Discharge in a Coastal Coral Reef System. *Environ. Sci. Technol.* 48 (22), 13069–13075. doi:10.1021/es5026867

Wang, G., Wang, Z., Zhai, W., Moore, W. S., Li, Q., Yan, X., et al. (2015). Net subterranean estuarine export fluxes of dissolved inorganic C, N, P, Si, and total alkalinity into the Jiulong River estuary, China. *Geochimica Et Cosmochimica Acta* 149, 103–114. doi:10.1016/j.gca.2014.11.001

Waska, H., Brumsack, H.-J., Massmann, G., Koschinsky, A., Schnetger, B., Simon, H., et al. (2019a). Inorganic and organic iron and copper species of the subterranean estuary: Origins and fate. *Geochim. Cosmochim. Acta* 259, 211–232. doi:10.1016/j.gca.2019.06.004

Waska, H., Greskowiak, J., Ahrens, J., Beck, M., Ahmerkamp, S., Böning, P., et al. (2019b). Spatial and temporal patterns of pore water chemistry in the inter-tidal zone of a high energy beach. *Front. Mar. Sci.* 6 (154), 12. doi:10.3389/fmars.2019.00154

Waska, H., and Kim, G. (2010). Differences in microphytobenthos and macrofaunal abundances associated with groundwater discharge in the intertidal zone. *Mar. Ecol. Prog. Ser.* 407, 159–172. doi:10.3354/meps08568

Waska, H., and Kim, G. (2011). Submarine groundwater discharge (SGD) as a main nutrient source for benthic and water-column primary production in a large intertidal environment of the Yellow Sea. *J. Sea Res.* 65 (1), 103–113. doi:10.1016/j.seares.2010.08.001

Webb, J. R., Santos, I. R., Maher, D. T., Tait, D. R., Cyronak, T., Sadat-Noori, M., et al. (2019). Groundwater as a source of dissolved organic matter to coastal waters: Insights from radon and CDOM observations in 12 shallow coastal systems. *Limnol. Oceanogr.* 64 (1), 182–196. doi:10.1002/lno.11028

Webster, I. T., Hancock, G. J., and Murray, A. S. (1994). Use of Radium Isotopes to Examine Pore-Water Exchange in an Estuary. *Limnol. Oceanogr.* 39 (8), 1917–1927. doi:10.4319/lo.1994.39.8.1917

Weinstein, Y., Yechieli, Y., Shalem, Y., Burnett, W. C., Swarzenski, P. W., and Herut, B. (2011). What is the role of fresh groundwater and recirculated seawater in conveying nutrients to the Coastal Ocean? *Environ. Sci. Technol.* 45 (12), 5195–5200. doi:10.1021/es104394r

Weinstein, Y., Burnett, W. C., Swarzenski, P. W., Shalem, Y., Yechieli, Y., and Herut, B. (2007). Role of aquifer heterogeneity in fresh groundwater discharge and seawater recycling: An example from the Carmel coast, Israel. *J. Geophys. Res.-Oceans* 112 (C12), 12. doi:10.1029/2007jc004112

Welti, N., Gale, D., Hayes, M., Kumar, A., Gasparon, M., Gibbes, B., et al. (2015). Intertidal diatom communities reflect patchiness in groundwater discharge. *Estuarine, Coastal Shelf Sci.* 163, 116–124.doi:10.1016/j.ecss.2015.06.006

Weschenfelder, J., Klein, A. H. F., Green, A. N., Aliotta, S., de Mahiques, M. M., Ayres Neto, A., et al. (2016). The control of palaeo-topography in the preservation of shallow gas accumulation: Examples from Brazil, Argentina and South Africa. *Estuarine Coastal Shelf Sci.* 172, 93–107. doi:10.1016/j.ecss.2016.02.005

Whiticar, M. J. (2002). Diagenetic relationships of methanogenesis, nutrients, acoustic turbidity, pockmarks and freshwater seepages in Eckernforde Bay. *Mar. Geol.* 182 (1, 2), 29–53. doi:10.1016/s0025-3227(01)00227-4

Whiticar, M. J., and Werner, F. (1981). Pockmarks: Submarine vents of natural gas or freshwater seeps?. *Geo-Marine Lett.* 1 (3), 193–199. doi:10.1007/bf02462433

Wigley, T. M. L., Plummer, L. N., and Pearson, F. J. (1978). Mass transfer and carbon isotope evolution in natural water systems. *Geochim. Cosmochim. Acta* 42 (8), 1117–1139. doi:10.1016/0016-7037(78)90108-4

Wilford, J., Bierworth, P. N., and Pearson, M. A., C. (1997). Application of airborne gamma ray spectrometry in soil/regolith mapping. *J. Aust. Geol. Geophys.* 17, 201–216.

Wilson, J., and Rocha, C. (2012). Regional scale assessment of Submarine groundwater discharge in Ireland combining medium resolution satellite imagery and geochemical tracing techniques. *Remote Sensing Environ.* 119 (0), 21–34. doi:10.1016/j.rse.2011.11.018

Winde, V., Böttcher, M. E., Voss, M., and Mahler, A. (2017). Bladder wrack (Fucus vesiculosus) as a multi-isotope bio-monitor in an urbanized fjord of the western Baltic Sea. *Isotopes Environ. Health Stud.* 53 (6), 563–579. doi:10.1080/10256016.2017.1316980

Winde, V., Böttcher, M. E., Escher, P., Böning, P., Beck, M., Liebezeit, G., et al. (2014). Tidal and spatial variations of DI^{13}C and aquatic chemistry in a temperate tidal basin during winter time. *J. Mar. Syst.* 129, 396–404. doi:10.1016/j.jmarsys.2013.08.005

Wolanski, E., (2007). *Estuarine ecohydrology*. Amsterdam; Oxford, Elsevier, xi, 157.

Wong, W. W., Applegate, A., Poh, S. C., and Cook, P. L. M. (2020). Biogeochemical attenuation of nitrate in a sandy subterranean estuary: insights from two stable isotope approaches. *Limnol Oceanogr* 65 (12), 3098–3113. doi:10.1002/lno.11576

Wunderlich, T., Fischer, P., Wilken, D., Hadler, H., Erkul, E., Mecking, R., et al. (2018). Constraining electric resistivity tomography by direct push electric conductivity logs and vibracores: an exemplary study of the Fiume Morto silted riverbed (Ostia Antica, western Italy). *Geophysics* 83 (3), B87–B103. doi:10.1190/geo2016-0660.1

Xing, Q., Braga, F., Tosi, L., Lou, M., Zaggia, L., Teatini, P., et al. (2016). Detection of low salinity groundwater seeping into the Eastern Laizhou Bay (China) with the aid of landsat thermal data. *J. Coastal Res.* 74, 149–156. doi:10.2112/si74-014.1

Yang, L., Chen, C.-T. A., Hong, H., Chang, Y.-C., and Lui, H.-K. (2015). Mixing behavior and bioavailability of dissolved organic matter in two contrasting subterranean estuaries as revealed by fluorescence spectroscopy and parallel factor analysis. *Estuarine Coastal Shelf Sci.* 166, 161–169. doi:10.1016/j.ecss.2014.10.018

Zamrsky, D., Karssenberg, M. E., Cohen, K. M., Bierkens, M. F. P., and Oude Essink, G. H. P. (2020). Geological heterogeneity of coastal unconsolidated groundwater systems worldwide and its influence on offshore fresh groundwater occurrence. *Front. Earth Sci.* 7 (339). doi:10.3389/feart.2019.00339

Zhang, Y.-C., Slomp, C. P., Broers, H. P., Bostick, B., Passier, H. F., Böttcher, M. E., et al. (2012). Isotopic and microbiological signatures of pyrite-driven denitrification in a sandy aquifer. *Chem. Geol.* 300–301, 123–132. doi:10.1016/j.chemgeo.2012.01.024

Zhou, Y., Sawyer, A. H., David, C. H., and Famiglietti, J. S. (2019). Fresh submarine groundwater discharge to the near-global coast. *Geophys. Res. Lett.* 46, 5855–5863. doi:10.1029/2019gl082749

Zipperle, A., and Reise, K. (2005). Freshwater springs on intertidal sand flats cause a switch in dominance among polychaete worms. *J. Sea Res.* 54 (2), 143–150. doi:10.1016/j.seares.2005.01.003

Conflict of Interest: The authors declare that the research was conducted in the absence of any commercial or financial relationships that could be construed as a potential conflict of interest.

Chapter 7. Conclusion

7.1 Summary of this study

The aim of this study was to investigate the role of submarine groundwater discharge on the biogeochemistry of the coastal Baltic Sea. Benthic diagenesis of surface sediments and surface waters were also evaluated. Multiple (isotopic) geochemical tracers were used to characterize different freshwater sources and combined with other interdisciplinary techniques. Hydrochemical gradients in coastal surface waters and sedimentary porewaters were used to get mechanistic insight into the composition and processes driving SGD and the transformations of dissolved substances into coastal waters. The investigations were carried out exemplarily in selected coastal areas of Germany, Poland, and Finland.

A multidisciplinary approach was used to identify SGD. Surface water gradients towards the open Baltic Sea of stable and Ra isotopes suggested the discharge of terrestrial groundwater. Geophysical acoustic profiles identified potential areas impacted by seepage and their potential extrapolations. At one site, it was possible to identify that port infrastructure-related activities reduced the sediment thickness above a shallow coastal aquifer and promoted the enhancement of SGD.

SGD was estimated based on local and regional geochemical approaches, and the derived fluxes showed high variability, up to values comparable to surface water runoff. These results are in agreement with the existing literature, demonstrating that quantitative results can be obtained for local and sometimes regional scales, but global quantitative estimates are still very difficult to infer.

The isotopic hydrogeochemical composition of the freshwater component of SGD was characterized, and it was comparable to nearby-coastal groundwater but less to the river water composition. Stable isotopes in SGD revealed the contribution of meteoric water and groundwaters of probably different ages, derived from aquifers built of layers of different geological ages.

In the porewaters of SGD-impacted sites, steep gradients for salinity and conservative elements were formed, but a more complex depth trend is often observed for elements impacted by early diagenesis in the overlying surface sediments. Dissolved sulfate was depleted in the sediments at the majority of sites. Due to dilution effects, the gradient in

SGD-impacted sites was more pronounced than expected for sediments under sole diagenetic control. The $\delta^{13}C_{DIC}$ signature in porewater clearly allows for the identification of the different processes, including fresh-brackish water mixing, organic matter degradation, and sometimes methane oxidation. In the northern part of the Baltic Sea, the upward flow of groundwater prevented the deposition of reactive organic matter in pockmarks with high SGD fluxes. It resulted in less intense diagenetic processes, and low dissolved mineralized elements were accumulated.

Summarizing, the SGD-derived elemental fluxes to coastal waters were controlled both by water-rock-microbe interactions in the aquifers and further modulation by diagenesis in the overlying surface sediments. The intensity of the latter depends on the availability of organic matter to drive microbial activity and the possible supply of methane from deeper strata. Muddy sites were associated with higher organic matter and were more active in terms of mineralization rates and metabolite concentrations, even without impact by SGD. At these sites, high element fluxes across the sediment-water interface were observed, reflecting the dominance of organic matter mineralization in generating fluxes towards the bottom waters. In permeable sandy sediments, on the other hand, the elemental fluxes across the sediment-water interface without SGD were lower, but enhanced under SGD impact. Conversely, the saline SGD leads to nutrient cycling within sediments with enhanced permeability and being positioned deeper from the low water line.

Seasonal investigations of a river entering the coastal Baltic Sea have allowed for the identification of processes controlling the composition of surface water endmembers entering an estuary under anthropogenic management. Hydrogeochemical changes are caused mainly by system internal processes such as biomass production and benthic release of elements to the surface water on seasonal scales that render discharge-concentration relationships specific.

Overall, this study contributes to our understanding of the importance of local and regional SGD to waters and substances in coastal areas in the humid climate zone. In particular, it becomes clear that combined interdisciplinary, and multi-proxy approaches

are essential to better assess SGD in coastal environments with complex coastal hydrogeology.

7.2 Future work

Relevant studies have been carried out in recent decades to improve our understanding of the occurrence of SGD and its impact on the biogeochemical cycles. However, there are still many open questions that can be the subject of further research projects.

- The precise discharge known for river inlets is still not quantifiable for SGD in many regions. More advanced work should be done in this direction, and a combination of appropriate methods, as shown in the present study, is still often not applied.
- The results of this study show that SGD impacts porewater compositions and biogeochemical cycles in coastal areas. However, a more detailed mid- and long-term investigations are needed to evaluate the importance of SGD elemental budgets for coastal waters.
- Further studies of coastal bays impacted by anthropogenic activities should consider the link between anthropogenic disturbances by managing activities that may alter pressure gradients and connections between groundwater and seawater. For example, channeling may create a passage for groundwater inputs via SGD to coastal waters.
- On a global scale, it is essential to assess the impact of SGD-associated elemental fluxes on the carbon cycle in order to get insight into possible effects on ocean acidification and the buffering capacity that controls the release of CO_2 to the atmosphere. It seems that aquifer lithology has a significant impact on the TA/DIC ratio of surface and ground waters entering the coast and that processes in the catchment are important drivers of this control.
- The Baltic Sea presents diverse regions where SGD can potentially occur. Most aquifers appear to be shallow and close to the sea bottom, facilitating the connection between groundwater and surface waters. Moreover, many of the found pockmarks structures have been associated with SGD and methane fluxes impacting the water

column. Therefore, it would be essential to identify and investigate new SGD areas to better estimate the effects on the coastal waters of the Baltic Sea and to close the water and elemental budgets for this important coastal sea as an example for other areas along the continents.

References

Note: The reference refers only to Chapter 1

Bauer J.E., Cai W-J., Raymond P.A., Bianchi T.S., Hopkinson C.S., Regnier P.A.G. (2013) The changing carbon cycle of the coastal ocean. Nature, 504:61-70. doi:10.1038/nature12857

Beck A.J., Tsukamoto Y., Tovar-Sanchez A., Huerta-Diaz M., Bokuniewicz H. J., and Sañudo-Wilhelmy S. A. (2007). Importance of Geochemical Transformations in Determining Submarine Groundwater Discharge- Derived Trace Metal and Nutrient Fluxes. Applied Geochemistry, 22: 477–490. doi:10.1016/j.apgeochem.2006.10.005

Bejannin S., Tamborski J. J., van Beek P., Souhaut M., Stieglitz T., Radakovitch O., Claude C., Conan P., Pujo-Pay M., Crispi O., Le Roy E. and Estournel C. (2020). Nutrient Fluxes Associated with Submarine Groundwater Discharge from Karstic Coastal Aquifers (Côte Bleue, French Mediterranean Coastline). Frontiers Environmental Science, 7: 205. doi:10.3389/fenvs.2019.00205

Berner E. K., Berner R. A. (1996) Global Environment: Water, Air, and Geochemical Cycles. New Jersey, USA: Prentice Hall, Inc.

BGR & UNESCO (eds.) (2019): International Hydrogeological Map of Europe 1:1,500,000 (IHME1500). Digital map data v1.2. Hannover/Paris.

Bitschofsky F. & Nausch M. (2019) Spatial and seasonal variations in phosphorus speciation along a river in a lowland catchment (Warnow, Germany). Science of the Total Environment, 657: 671-685. dx.doi.org/10.1016/j.agwat.2017.03.006 0378-3774

Boudreau B.P. and Jorgensen B.B. (2001) The Benthic Boundary Layer, Transport Processes and Biogeochemistry. Oxford University Press, New York

Böttcher M.E., Oelschläger B., Höpner T., Brumsack H.-J., Rullkötter J. (1998) Sulfate reduction related to the early diagenetic degradation of organic matter and "black spot" formation in tidal sandflats of the German Wadden Sea: stable isotope (^{13}C, ^{34}S, ^{18}O) and other geochemical results. Organic Geochemistry, 29 (5-7): 1517-1530. doi.org/10.1016/S0146-6380(98)00124-7

Böttcher M E., Hespenheide B., Llobet-Brossa E., Beardsley C., Larsen O., Schramm A., Wieland A., Böttcher G., Berninger U., and Amann R. (2000). The biogeochemistry, stable isotope geochemistry, and microbial community structure of a temperate intertidal mudflat: an integrated study. Continental Shelf Research, 20(12-13): 1749-1769. doi.org/10.1016/S0278-4343(00)00046-7

Böttcher M. E., Mallast U., Massmann G., Moosdorf N., Mueller-Pethke M., and Waska H. 1025 (2023). "Coastal-Groundwater Interfaces (Submarine Groundwater Discharge)," in 1026 Ecohydrological Interfaces. Editors S. Krause, D. M. Hannah, and N. Grimm (New York, NY: 1027 Wiley & Sons).

Brookflied A.E., Hansen A.T., Sullivan P.L., Czuba J.A., Kirk M.E. Li L., Newcomer M.E., Wilkinson G. (2021) Predicting algal blooms: Are we overlooking groundwater?

Science of The Total Environment, 769: 144442. doi.org/10.1016/j.scitotenv.2020.144442

Burnett W.C., Bokuniewicz H., Huettel M. Moore W.S., Taniguchi M. Groundwater and pore water inputs to the coastal zone. Biogeochemistry 66, 3–33 (2003). https://doi.org/10.1023/B:BIOG.0000006066.21240.53

Burnett W., Aggarwal P., Aureli A., Bokuniewicz H., Cable J., Charette M., Kontar E., Krupa, S., Kulkarni K., Loveless A., Moore W., Oberdorfer J., Oliveira J., Ozyurt N., Povinec, P., Privitera A., Rajar R., Ramessur R., Scholten J., . . . Turner J. (2006). Quantifying submarine groundwater discharge in the coastal zone via multiple methods. Science of The Total Environment, 367(2-3): 498-543. https://doi.org/10.1016/j.scitotenv.2006.05.009

Bussmann I., & Suess E. (1998). Groundwater seepage in Eckernförde Bay (western Baltic Sea): Effect on methane and salinity distribution of the water column. Continental Shelf Research, 18(14–15): 1795–1806. doi.org/10.1016/S0278-4343(98)00058-2

Bussmann I., Dando P., Niven S., and Suess, E. (1999). Groundwater seepage in the marine environment: Role for mass flux and bacterial activity. Marine Ecology Progress Series, 178(1): 169–177. doi.org/10.3354/meps178169

Cable J.E., Burnett J.P, Chanton P., Corbett, D.R., Cable P.H. (1997) Field evaluation of Seepage meters in the coastal marine environment. Estuarine, coastal and shelf science, 45: 367-375. doi.org/10.1006/ecss.1996.0191

Carstensen J., Conley D.J., Almroth-Rosell E., Asmala E., Bonsdorff E., Fleming-Lehtinen V., Gustafsson B.G., Gustafsson C., Heiskanen A-S., Janas U., Norkko A., Slomp C., Villnäs A., Voss M., Zilius M. (2020) Factors regulating the coastal nutrient filter in the Baltic Sea. Ambio, 49: 1194–1210. doi.org/10.1007/s13280-019-01282-y

Chakrabarti R., Mondal S., Schankar Acharya S.S., Lekha J.S., Sengupta D. (2018) Submarine groundwater discharge derived strontium from the Bengal Basin traced in Bay of Bengal water samples. Scientific Reports, 8:4383. DOI:10.1038/s41598-018-22299-5

Chen X., Zhang F., Lao Y., Wanf X., Jinzhou D., and Santos, R.I. (2018) Submarine groundwater discharge-derived carbon fluxes in Mangroves: An important component of Blue Carbon Budgets. Journal of Geophysical Research: Oceans, 123: 6962-6979. doi.org/10.1029/2018JC014448

Chester R. (2000) Marine Geochemistry. 2nd ed. John Wiley & Sons.

Cho H-M.H., Kim G., Kwon E.Y., Moosdorf N., Garcia-Orellana J., Santos I.R. (2018) Radium tracing nutrients inputs through submarine groundwater discharge in the global ocean. Scientific Reports, 8:2439. doi: 10.1038/s41598-018-20806-2

Church T. M. (1996). An underground route for the water cycle. Nature, 380(18):579?580. doi.org/10.1038/380579a0

Degens E.T., Kempe S., Richey J.E. (1991) Biogeochemistry of major world rivers. SCOPE, 42: 1-356.

Don Racasa E., Lennartz B., Toro M., Jansse M. (2021) Submarine groundwater discharge from Non-Tidal Coastal Peatlands along the Baltic Sea. Frontiers Earth Science, 9: 6655802. doi: 10.3389/feart.2021.665802

Donis D., Janssen F., Liu B., Wenzhöfer F., Dellwig O., Escher P., Spitzy A., Böttcher M.E. (2017). Biogeochemical impact of submarine groundwater discharge on coastal surface sands of the southern Baltic Sea. Estuarine, Coastal and Shelf Science, 189: 131-142. http://dx.doi.org/10.1016/j.ecss.2017.03.003

Donnelly C., Yang W. & Dahné J. River discharge to the Baltic Sea in a future climate. Climatic Change, 122: 157–170 (2014). doi.org/10.1007/s10584-013-0941-y

Duarte T. K., Pongkijvorasin S., Roumasset J., Amato D., and Burnett K. (2010). Optimal management of a Hawaiian Coastal Aquifer with nearshore marine Ecological Interactions. Water Resources Research, 46:W11545. doi: 10.1029/2010WR009094

Eurogeographics (2020). Administrative units. Acessed on 12 December 2022. https://ec.europa.eu/eurostat/web/gisco/geodata/reference-data/administrative-units-statistical-units

Idczak J., Brodeck-Goluch A., Lukawska-Matuszewska K., Graca B., Gorska N., Klusek Z., Pezacki P. D., Bolalek J. (2020). A geophysical, geochemical,l and microbiological study of a newly discovered pockmark with active gas seepage and submarine groundwater discharge (MET1-BH, central Gulf of Gdansk, southern Baltic Sea). Science of the Total Environment, 742: 140306. doi.org/10.1016/j.scitotenv.2020.140306.

Ikonen J., Hendriksson N., Luoma S., Lahaye Y., Virtasalo J. (2022) Behaviour of Li, S and Sr isotopes in the subterranean estuary and seafloor pockmarks of the Hanko submarine groundwater discharge site in Finland, northern Baltic Sea, 147: 105471. doi.org/10.1016/j.apgeochem.2022.105471

Falkowska L., Piekarek-Jankowska H. (1999) Submarine seepage of fresh groundwater: disturbance in hydrological and chemical structure of the water column in the Gdansk Basin. ICES Journal of Marine Science, 56: 153-160.

Froelich P.N., Klinkhammer G.P., Bender M.L., Luedtke N.A., Heath G.R., Cullen D., Dauphin P., Hammond D., Hartman B., Maynard V. (1979) Early oxidation of organic matter in pelagic sediments of the eastern equatorial Atlantic: suboxic diagenesis. Geochimica et Cosmochimica Acta, 43:1075–1090. doi:10.1016/0016-7037(79)90095-4

Glover R. E. (1959) The pattern of fresh-water flow in a coastal aquifer. Journal of Geophysical Research, 64(4): 457-459, doi:10.1029/JZ064i004p00457.

Harff J., Björck S., Hoth P. (2011) The Baltic Sea Basin: Introduction. In: In: Harff, J., Björck, S., Hoth, P. (eds) The Baltic Sea Basin. Central and Eastern European Development Studies (CEEDES). Springer, Berlin, Heidelberg. https://doi.org/10.1007/978-3-642-17220-5_7.

Hartmann J., Lauerwald R., Moosdorf, N. (2014) A brief overview of the GLObal RIver

CHemistry Database, GLORICH. Procedia Earth and Planetary Science 10: 23 – 27.

HELCOM (2018): State of the Baltic Sea - Second HELCOM holistic assessment 2011-2018. Baltic Environment Proceedings 155.

Hoffmann J. J. L., Schneider von Deimling J., Schröder J. F., Schmidt M., Held P., Crutchley G. J., Scholten J., Gorman A.R.(2020). Complex eyed pockmarks and submarine groundwater discharge revealed by acoustic data and sediment cores in Eckernförde Bay, SW Baltic Sea. Geochemistry, Geophysics, Geosystems, 21: e2019GC008825. doi.org/10.1029/2019GC008825

Hyacinthe C., Anschutz P., Carbonel P., Jouanneau J-M., Jorissen (2001) Early diagenetic processes in the muddy sediments of the Bay of Biscay. Marine Geology, 177: 111-128. doi.org/10.1016/S0025-3227(01)00127-X.

Hovland, M., Judd, A.G., 1988. Seabed Pockmarks and Seepages. Impact on Geology, Biology and the Marine Environment. Graham & Trotman, Londom, UK.

Jørgensen, B.B. (2006) Bacteria and Marine Biogeochemistry. In Marine geochemistry (eds H.D. Schulz & M. Zabel), 2nd editions. Springer-Verlag, Berlin, Heidelberg.

Jørgensen, B.B. & Kasten, S. (2006) Sulfur cycling and methane oxidation. In Marine geochemistry (eds H.D. Schulz & M. Zabel), pp. 271–309. Springer, Berlin, Heidelberg.

Jurasinski G., Janssen M., Voss M., et al. (2018). Understanding the Coastal Ecocline: Assessing Sea–Land Interactions at Non-tidal, Low-Lying Coasts Through Interdisciplinary Research. Frontiers in Marine Science. https://doi.org/10.3389/fmars.2018.00342.

Kaleris V., Lagas G., Marczinek S., Piotrowski J.A. (2002) Moddeling submarine groundwater discharge: an example from the western Baltic Sea. Journal of Hydrology, 265: 76-99. doi10.1016/S0022-1694(02)00093-8

Keil R.G., Montluçon D.B., Prahl F., Hedges, J. (1994) Sorptive preservation of labile organic matter in marine sediments. Nature, 370:549-552. doi.org/10.1038/370549a0

Kłostowska Z., Szymczycha B., Lengier M., Zarzeczanska D., Dzierzbicka-Glowacka L. (2019) Hydrogeochemistry and magnitude of SGD in the Bay of Puck, southern Baltic. Oceanologia, 62: 1-11. doi.org/10.1016/j.oceano.2019.09.001

Knee Karen L., Street Joseph H., Grossman Eric E., Boehm Alexandria B., Paytan Adina (2010) Nutrient inputs to the coastal ocean from submarine groundwater discharge in a groundwater-dominated system: Relation to land use (Kona coast, Hawaii, U.S.A.), Limnology and Oceanography, 55: 1105–1122. doi: 10.4319/lo.2010.55.3.1105.

Knee KL & Paytan A (2011) Submarine Groundwater Discharge: A Source of Nutrients, Metals, and Pollutants to the Coastal Ocean. In: Wolanski E and McLusky DS (eds.) Treatise on Estuarine and Coastal Science, Vol 4, pp. 205–233.

Kotwicki L., Grzelak K., Czub M., Dellwig O., Gentz T., Szymczycha B., Böttcher M.E. (2014). Submarine Groundwater discharge to the Baltic coastal zone: Impacts on the

meiofaunal community. Journal of Marine Systems, 129: 118-126. dx.doi.org/10.1016/j.jmarsys.2013.06.009

Krall L., Garcia-Orellana J., Trezzi G., and Rodellas V. (2017). Submarine Groundwater Discharge at Forsmark, Gulf of Bothnia, provided by Ra Isotopes. Marine Chemistry, 162: 162–172. doi:10.1016/j.marchem.2017.09.003

Kwon E.Y., Kim G., Primeau F., Moore W.S., Cho H.M., Devries T., Sarmiento J.L., Charette M.A., Cho Y-K. (2014) Global estimated of submarine groundwater discharge based on an observationally constrained radium isotope model. Geophysical Research Letters, 41(23): 8438-8444. doi.org/10.1002/2014GL061574

Lecher A.L., Mackey K.R.M. (2018) Synthesizing the effects of submarine groundwater discharge on Marine Biota. Hydrology, 5(4):60. doi.org/10.3390/hydrology5040060

Lee D.R. (1977) A device for measuring seepage flux in lakes and estuaries. Limnology & Oceanography 22, 140-147. doi.org/10.4319/lo.1977.22.1.0140

Lipka M., Böttcher M.E., Wu Z., Sültenfuß J., Jenner A-K., Westphal J., Dellwig O., Escher P., Schmiedinger I., Winde V., Struck U. (2018) Ferruginous groundwaters as a source of P , Fe , and DIC for coastal waters of the southern Baltic Sea : (Isotope) hydrobiogeochemistry and the role of an iron curtain. E3S Web of Conferences, 54. doi.org/10.1051/e3sconf/20185400019

Luijendijk E., Gleeson T., Moosdorf N. (2020). Fresh groundwater discharge insignificant for the world's oceans but important for coastal ecosystems. Nature Communication, 11: e1260 doi.org/10.1038/s41467-020-15064-8.

Luoma S., Majaniemi J., Pullinen A., Mursu J., Virtasalo J.J. (2021) Geological and groundwater flow model of a submarine groundwater discharge site at Hanko (Finland), northern Baltic Sea. Hydrogeology Journal, 29: 1279–1297. doi.org/10.1007/s10040-021-02313-3

Marczinek S., & Piotrowski J. A. (2002). Grundwasserströmung und-beschaffenheit im Einzugsgebiet der Eckernförder Bucht, Schleswig-Holstein. Grundwasser, 7(2), 101–110. doi.org/10.1007/s007670200015

Mallast U. & Siebert C. (2019) Combining continuous spatial and temporal scales for SGD investigations using UAV-based thermal infrared measurements. Hydrology and Earth System Sciences, 23: 1375-1392. doi.org/10.5194/hess-23-1375-2019.

Matciak M., Bieleninik S., Botur A., Podgórski M., Trzcinska K., Draganska K., Jasniewicz D., Kurszewska A., Wenta M. (2015). Observations of presumable groundwater seepage occurrence in Puck Bay (the Baltic Sea). Oceanological and Hydrobiological Studies, 44 (2): 267- 272. doi.org/10.1515/ohs-2015-0025

Mayfield K.K., Eisenhauer A., Santiago Ramos D.P. Higgins J.A., Horner, T.J., Auro M., Magna T., Moosdorf N., Charette M., Gonneea M.E., Brady C.E., Komar N., Peucker-Ehrenbrink B., Paytan A. (2021) Groundwater discharge impacts marine isotope budgets of Li, Mg, Ca, Sr, and Ba. Nature Communications, 12: 148. doi.org/10.1038/s41467-

020-20248-3

McKenzie T., Holloway C., Dulai H., Tucker J.P., Sugumoto R., Toshimi N., Harada K., Santos I.R. (2020). Submarine groundwater discharge: A previously undocumented source of contaminants of emerging concern to the coastal ocean (Sydney, Australia). Marine Pollution Bulletin, 160: 111519. doi.org/10.1016/j.marpolbul.2020.111519

Moore W.S. (1996) Large groundwater inputs to coastal waters revealed by 226Ra enrichments. Nature, 380:612-614. doi.org/10.1038/380612a0

Moore W.S. (1999). The subterranean estuary: a reaction zone of ground water and sea water. Marine Chemistry, 65 (1, 2): 111–125. doi:10.1016/s0304-4203(99) 00014-6

Moore W.S (2000) Determining coastal mixing rates using radium isotopes. Continental Shelf Research, 20: 1993-2007. doi.org/10.1016/S0278-4343(00)00054-6

Moore W. S. (2006) Radium isotopes as tracers of submarine groundwater discharge in Sicily. Continental Shelf Research, 26: 852-861. doi:10.1016/j.csr.2005.12.004

Moore W.S., Blanton J.O. and Joye, S. B. (2006) Estimates of flushing times, submarine groundwater discharge, and nutrient fluxes to Okatee Estuary, South Carolina. Journal of Geophysical research, 111: C09006. doi:10.1029/2005JC003041

Moore W.S. (2010) The effects of Submarine Grroundwater Discharge on the Ocean. Annual Reviews of Marine Science, 2:59-88. 10.1146/annurev-marine-120308-081019

Moosdorf, N., and Oehler, T. (2017). Societal use of fresh submarine groundwater discharge: An overlooked water resource. Earth-Science Reviews, 171: 338–348. doi: 10.1016/j.earscirev.2017.06.00

Pagenkopf W., 2001. Aktuelle Nahrstoffbilanzierung fur Teilgebiete des Einzugsgebiets der Warnow. Geodaten Inte-gration & Analyse, Berlin.

Pain A.J., Martin J.B., Young C.R. (2019) Sources and sinks of CO_2 and CH_4 in siliciclastic subterranean estuaries. Limnology and Oceanography, 64(4): 1500-1514. doi.org/10.1002/lno.11131

Peltonen K. (2002) Direct groundwater flow to the Baltic Sea. Nordic Council of Ministers, Copenhagen (145 pp.)

Piekarek-Jankowska, H. (1996). Hydrochemical effects of submarine groundwater discharge 1198 to the Puck Bay (Southern Baltic Sea, Poland). Geograhia Polonica 67.

Povinec P. P., Bokuniewicz H., Burnett W. C., Cable J., Charette M., Comanducci J-F., Kontar E. A., Moore W. S., Oberdorfer J. A., de Oliveira J., Peterson R., Stieglitz T., Taniguchi M. (2008) Isotope tracing of submarine groundwater discharge offshore Ubatuba, Brazil: results of the IAEA-Unesco SGD project. Journal of Environmental Radioactivity, 99: 1596-1610. doi:10.1016/j.jenvrad.2008.06.010

Povinec P.P., Burnett W.C., Beck A., Bokuniewicz H., Charette M., Gonneea M.E., Groening M., Ishitobi T., Kontar E., Kwong L.L.W., Marie D.E.P., Moore W.S., Oberdorfer J.A., Peterson R., Ramessur R., Rapaglia J., Stieglitz T., Top Z. (2012).

Isotopic, geophysical and biogeochemical investigation of submarine groundwater discharge: IAEA-UNESCO intercomparison exercise at Mauritius Island. Journal of Environmental Radioactivity, 104: 24-45. doi.org/10.1016/j.jenvrad.2011.09.009

Prena J. (1995). Temporal Irregularities in the Macrobenthic Community and Deep-Water Advection in Wismar Bay (Western Baltic Sea). Estuarine Coastal Shelf Science, 41:705–717. doi:10.1006/ecss.1995.0085

Qian L., Charette M.A., Henderson P.B., McCorkle D.C., Martin W., Dai M. (2014) Effect of submarine groundwater discharge on the coastal ocean inorganic carbon cycle. Limnology Oceanography, 59(5): 1529-1554.

Rana V., Milke J., Gałczyńska M. (2021). Inorganic and Organic Pollutants in Baltic Sea Region and Feasible Circular Economy Perspectives for Waste Management: A Review. In: Baskar, C., Ramakrishna S., Baskar S., Sharma R., Chinnappan A., Sehrawat R. (eds) Handbook of Solid Waste Management. Springer, Singapore. https://doi.org/10.1007/978-981-15-7525-9_80-1

Reckhardt A., Beck M., Greskkowiak J., Schnetger B., Böttcher M.E., Gehre M., Brumsack H-J. (2017) Cycling of redox-sensitive elements in a sandy subterranean estuary of the southern North Sea. Marine Chemistry, 188:6-17.

Reeburgh W.S. (1983) Rates of Biogeochemical Processes in Anoxic Sediments. Annual Review of Earth and Planetary Sciences, 11, 269–298. 10.1146/annurev.ea.11.050183.001413

Rodellas, V., Garcia-Orellana, J., Masqu?e, P., Feldman, M., Weinstein, Y., 2015. Sub-marine groundwater discharge as a major source of nutrients to the Mediter- ranean Sea. Proc. Natl. Acad. Sci. U. S. A. 112, 3926e3930. http://dx.doi.org/ 10.1073/pnas.1419049112.

Rodellas V., Garcia-Orellana J., Trezzi G., Masque P., Stieglitz T.C., Bokuniewicz H., Cochran J.K., Berdalet E. (2017) Using the radium quartet to quantify submarine groundwater discharge and porewater exchange. Geochmica et Cosmochimica Acta, 196: 58-73. doi.org/10.1016/j.gca.2016.09.016

Rocha C., Veiga-Pires C., Scholten J., Knoeller K., Gröcke D. R., Carvalho, L., Anibal J., and Wilson J. (2016). Assessing land-ocean connectivity via submarine groundwater discharge (SGD) in the Rio Formosa Lagoon (Portugal): combining radon measurements and stable isotope hydrology. Hydrology and Earth Systems Sciences, 20(8): 3077–3098. doi:10.5194/hess-20-3077-2016

Rullkötter, J. (2006) Organic Matter: The Driving Force for Early Diagenesis. In Marine geochemistry (eds H.D. Schulz & M. Zabel), pp. 125–168. Springer, Berlin, Heidelberg.

Santos I.R., Eyre B.D., Huettel M. (2012) The driving forces of porewater and groundwater flow in permeable coastal sediments: A review. Estuarine, coastal and shelf science, 98:1-15. doi:10.1016/j.ecss.2011.10.024

Santos I. R., Chen X., Lecher A. L., Sawyer A. H., Moosdorf N., Rodellas V., Tamborski

J., Cho H-M., Dimova N., Sugymoto R., Bonaglia S., Li H., Hajati M-C., Li, L. (2021). Submarine Groundwater Discharge Impacts on Coastal Nutrient Biogeochemistry. Nature Review Earth & Environment, 2: 307–323. doi:10.1038/s43017- 021-00152-0

Schafmeister M-T., and Darsow A. (2004). Potential Change in Groundwater Discharge as Response to Varying Climatic Conditions – an Experimental Model Study at Catchment Scale, in The Baltic Sea Basin. Editors J. Harff and S. Bjorck (Springer), 449. doi.org/10.1007/978-3-642-17220-5_19.

Schlüter M., Sauter E. J., Andersen C. E., Dahlgaard H., and Dando, P. R. (2004). Spatial distribution and budget for submarine ground- water discharge in Eckernförde Bay (western Baltic Sea). Limnology and Oceanography, 49(1): 157–167. doi.org/10.4319/ lo.2004.49.1.0157.

Schreiber L., Munz M., Salzmann T., Oswald S. (2021) Modellierung der Strömungsdynamik in einem revitalisierten Küstenmoorgebiet an der Ostsee. Grundwasser - Zeitschrift der Fachsektion Hydrogeologie. doi.org/10.1007/s00767-021-00486-y.

Schultz H.D. (2006) Quantification of Early diagenesis: dissolved constituents in porewater and signals in the solid phase. In Marine geochemistry (eds H.D. Schulz & M. Zabel), 2nd editions. Springer-Verlag, Berlin, Heidelberg.

Seibert S. L., Böttcher M. E., Waska H., Holt T., Pollmann T., Greskowiak J., Massmann G. (2021). Hydrogeochemistry of near-surface groundwater on a developing barrier island (Spiekeroog, Germany): the role of inundation, season and vegetation. Journal of Hydrology, 597:126139. doi: 10.1016/j.jhydrol.2021.126139

Struck U., Emeis K., Voss M., Christiansen C., and Kunzendorf, H. (2000) Records of southern and central Baltic Sea eutrophication in $\delta^{13}C$ and $\delta^{15}N$ of sedimentary organic matter. Marine Geology, 164(3-4): 157-171. doi.org/10.1016/S0025-3227(99)00135-8

Szymczycha B., Vogler S., Pempkowiak J. (2012). Nutrient fluxes via submarine groundwater discharge to the Bay of Puck, southern Baltic Sea. Science of the Total Environment, 438: 86-1256 93. dx.doi.org/10.1016/j.scitotenv.2012.08.058

Szymczycha B., Miotk M., Pempkowiak J. (2013) Submarine groundwater discharge as a source of Mercury in the Bay of Puck, the southern Baltic Sea. Water Air Soil Pollut, 224-1542. Doi 10.1007/s11270-013-1542-0

Szymczycha B., Maciejewska A., Pempkowiak J. (2014) Could submarine groundwater discharge be a significant carbon source to the southern Baltic Sea? Oceanologia, 56(2): 327-347. doi:10.5697/oc.56-2.327

Szymczycha B., Kroeger K.D., Pempkowiak J. (2016) Significance of groundwater discharge along the coast of Poland as a source of dissolved metals to the southern Baltic Sea. Marine Pollution Bulletin, 109: 151-162. dx.doi.org/10.1016/j.marpolbul.2016.06.008

Szymczycha B., Boreck M., Białk-Bielińska A., Siedlewicz G., Pazdro K. (2020)

Submarine groundwater discharge as a source of pharmaceutical and caffeine residues in coastal ecosystem: Bay of Puck, southern Baltic Sea case study. Science of The Total Environment, 713:136522.

Szymczycha B., Kłostowska Ż., Lengier M., & Dzierzbicka-Głowacka L. (2020). Significance of nutrient fluxes via submarine groundwater discharge in the Bay of Puck, southern Baltic Sea. Oceanologia, 62(2): 117-125. doi.org/10.1016/j.oceano.2019.12.004.

Taniguchi M., Burnett W.C., Cable J.E. and Turner J.V. (2002) Investigation of submarine groundwater discharge. Hydrologica Processes, 16: 2115-2129. doi.org/10.1002/hyp.1145

Taniguchi M., Burnett W.C., Christopher F., Paulsen R.J., Rourke D.O., Steve, L., Christoff, J.L. (2003). Spatial and temporal distributions of submarine groundwater discharge rates obtained from various types of seepage meters at a site in the Northeastern Gulf of Mexico. Biogeochemistry, 66: 35-53. doi.org/10.1023/B:BIOG.0000006090.25949.8d

Taniguchi M., Dulai H., Burnett K.M., Santos I.R., Sugimoto, R., Stieglitz, T., Kim, G., Moosdorf, N., & Burnett, W.C. (2019). Submarine Groundwater Discharge: Updates on Its Measurement Techniques, Geophysical Drivers, Magnitudes, and Effects. Frontiers in Environmental Science, 7. doi.org/10.3389/fenvs.2019.00141

Thamdrup B., Fossing H. and Jørgensen, B.B. (1994) Manganese, iron and sulfur cycling in a coastal marine sediment, Aarhus bay, Denmark. Geochimica et Cosmochimica Acta, 58, 5115–5129. doi.org/10.1016/0016-7037(94)90298-4

Thompson C., Smith L., Maji R. (2007) Hydrogeological modeling of submarine groundwater discharge on the continental shelf of Louisiana. JGR Oceans, 112: C03014, doi:10.1029/2006JC003557

USGS. United States Geological survey. Water science school (2022). Available on: https://www.usgs.gov/special-topics/water-science-school/science/water-cycle. Accessed: December 8th 2022.

USGS. United States Geological survey. Submarine Groundwater Discharge (2022). Available on: https://www.usgs.gov/centers/pcmsc/science/submarine-groundwater-discharge. Accessed: December 10th 2022.

Valiela I., Costa J., Foreman K., Teal J. M., Howes B., & Aubrey D. (1990). Transport of Groundwater-Borne Nutrients from Watersheds and Their Effects on Coastal Waters. Biogeochemistry, 10(3): 177–197. http://www.jstor.org/stable/1468685

van de Velde S., Van Lancker V., Hidalgo-Martinez S., Berelson W.M., Meysman F.J.R. (2018) Anthropogenic disturbance keeps the coastal seafloor biogeochemistry in a transient state. Scientific Reports, 8: 5582. doi.org/10.1038/s41598-018-23925-y

Virtasalo J. J., Schroeder J. F., Luoma S., Majaniemi J., Mursu J., and Scholten J. (2019). Submarine Groundwater Discharge Site in the First Salpausselkä Ice- Marginal

Formation, South Finland. Solid Earth-EGU, 10: 405–432. doi:10.5194/se-10-405-2019

Viso R., McCoy C., Gayes P., Quafisi D. (2010) Geological controls on submarine groundwater discharge in Long Bay, South Carolina (USA). Continental Shelf Research, 30: 335-341. doi.org/10.1016/j.csr.2009.11.014

Viventsowa E.E., Voronov A.N. (2003) Groundwater discharge to the Gulf of Finland (Baltic Sea): ecological aspects. Environmental Geology, 45: 221-225. doi 10.1007/s00254-003-0869-z

Zetsche, E., Thornton, B., Midwood, A. J. & Witte, U. (2011) Utilisation of different carbon sources in a shallow estuary identified through stable isotope techniques. Continental Shelf Research, 31: 832–840

Walsh J.J. (1991) Importance of continental margins in the marine biogeochemical cycling of carbon and nitrogen. Nature, 350:53–55. doi:10.1038/350053a0

Whiticar M. J., & Werner F. (1981). Pockmarks: Submarine vents of natural gas or freshwater seeps? Geo-Marine Letters, 1(3–4): 193–199. doi.org/10.1007/BF02462433

Whiticar M. J. (2002). Diagenetic relationships of methanogenesis, nutrients, acoustic turbidity, pockmarks and freshwater seepages in Eckernförde Bay. Marine Geology, 182(1–2): 29–53. doi.org/10.1016/S0025-3227(01)00227-4

Wollast R. (1991) The coastal organic carbon cycle: fluxes, sources, and sinks. In: Mantoura M.R.F.C., Martin J.M., Wollast R. (eds.) Ocean margin processes in global change. Wiley, London, 365–382.

Acknowledgments

If this doctoral thesis is now a reality, it is thanks to the effort and contribution of many people.

An exceptional thank you to my supervisor, Michael Böttcher, for believing in me and, for the guidance in taking our research always forward. Thank you for inspiring me and for teaching me everything I have learned. I have always considered myself extremely lucky to have you as my supervisor.

I am grateful for all friends and colleagues I have made at IOW. A special thanks to Anna, who has shared the PhD time by my side with much happiness. To Iris, for the immense help throughout this work. A very special thanks to Juliana and Patricia for being my family here, for all your patience, and for always being there. I would like to thank Inken, Julia, and Miguel for taking me by the hand, showing me the IOW, Rostock, and helping me with life here Germany. I am thankful to all my colleagues in the geology department, who helped me go further with my research and for creating an excellent working environment. A special thanks to Sasha, Svenja, Peter, Olaf, Anne, Ines, Antonia, Ben, Rhodelyn, Carla, and Marie. I had great moments working with you all. I would also like to express my gratitude to all those who have actively participated in the research during these years of my PhD. Many people helped me make this work successful, which are acknowledged in each chapter, and especially my co-authors. It was a pleasure to work with you all; I had so much fun in our field campaigns around the Baltic Sea. A special thanks to Beata and Jan Scholten for the incredible cooperation. Thanks to my Baltic Transcoast colleagues. During the training school, we had great moments together. I am thankful to all those who, outside IOW life, have made it possible for this to go ahead. For the encouragement and support, but, above all, for enjoying all this time with me! Special thanks to the Paty Weg group: Steffi, Jule, David, and Felix. The corações de alcachofra group: Cristina, Alex, Mathilde and Steffi, and to Hagen, Heike, and to my DAAD friend Ana. You all made Rostock the best place in the world. Thanks for making me happy ☺ I would like to thank my friends from across the ocean, in Brazil, who have been greatly missed here, but even from afar they have always supported me. In special

to Paola, and Graci that follow my journey since always. And finally, but not last important, I would like to thank all my family. I would like to thank my family, especially my cousins-brothers: Amanda, Julia Leandro and Laercio, Cristiane, Pedro and Erick, my dinda and dindo, Leani, my grandfather. My grandmother and Tiomir (who are looking after me from heaven). You have been essential in my journey up to here.

The most special thanks of all goes to my mother, to whom I dedicate this work. Thank you for all the teachings, the dedication and the support that made me always fly further. I love you, Mom.

With deep gratitude, I want to acknowledge the support of DAAD for providing the funds that made this doctoral project possible. To the IOW for providing all support needed during this research.

Funding

This thesis was elaborated with funding provided to the PhD candidate by the German Academic Exchange Service (DAAD) within the Doctoral program 2018/19.

The work was also supported by the Deutsche Forschungsgemeinschaft (DFG) within the framework of the Research Training Group' Baltic TRANSCOAST' funded under grant number GRK 2000, where the candidate participated and acquired credits for the training.

The work was also strongly supported by the Leibniz Institute for Baltic Sea Research Warnemuende (IOW), where most scientific activities were carried out. All other funding supporting this work are appropriately mentioned in the corresponding papers/manuscripts.

Appendix

Suplementary Material published together with the article: **"A multi-tracer study of fresh water sources for a temperate urbanized coastal bay (southern Baltic Sea)." – Chapter 2**

Supplementary Material

1 Supplementary Data

The supplementary tables and figures mentioned in the text, but not include in the Figures/Table list of the manuscript are added to this document. Once the manuscript is accepted, a table with all raw data used to plot graphs, create maps and tables in the manuscript will be included here as well.

1.1 Supplementary Figures and Tables

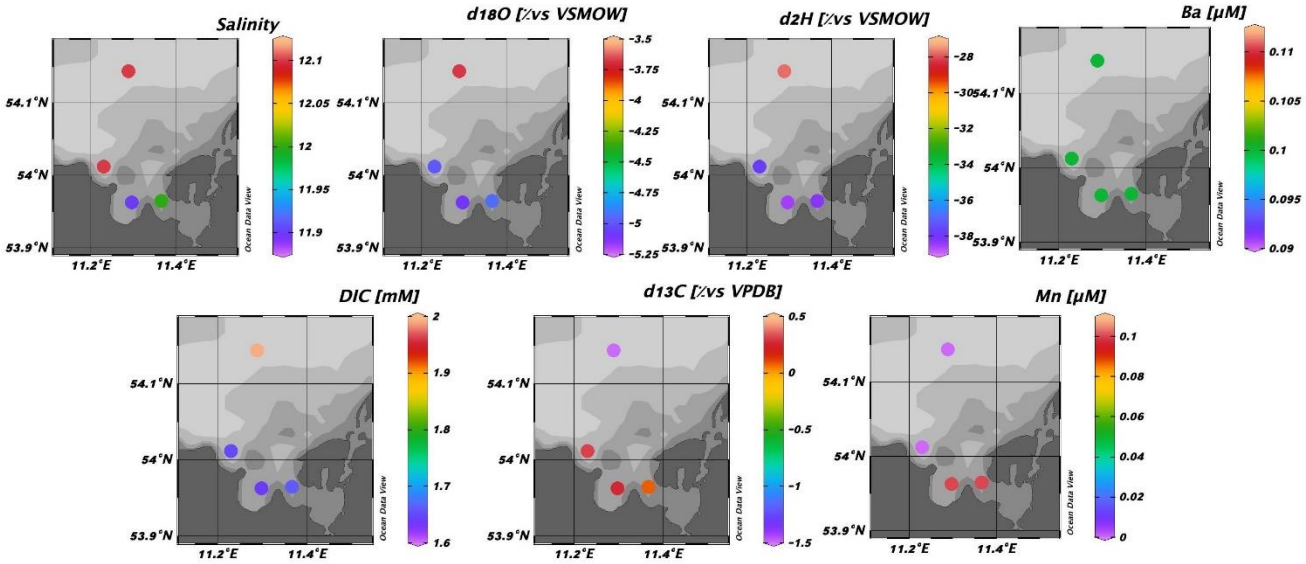

Supplementary Figure 1 - Spatial distribution of the Salinity, $\delta^{18}O_{H2O}$, $\delta^{2}H_{H2O}$, barium, dissolved inorganic carbon, $\delta^{13}C_{DIC}$ and manganese for the bottom water samples of Wismar Bay.

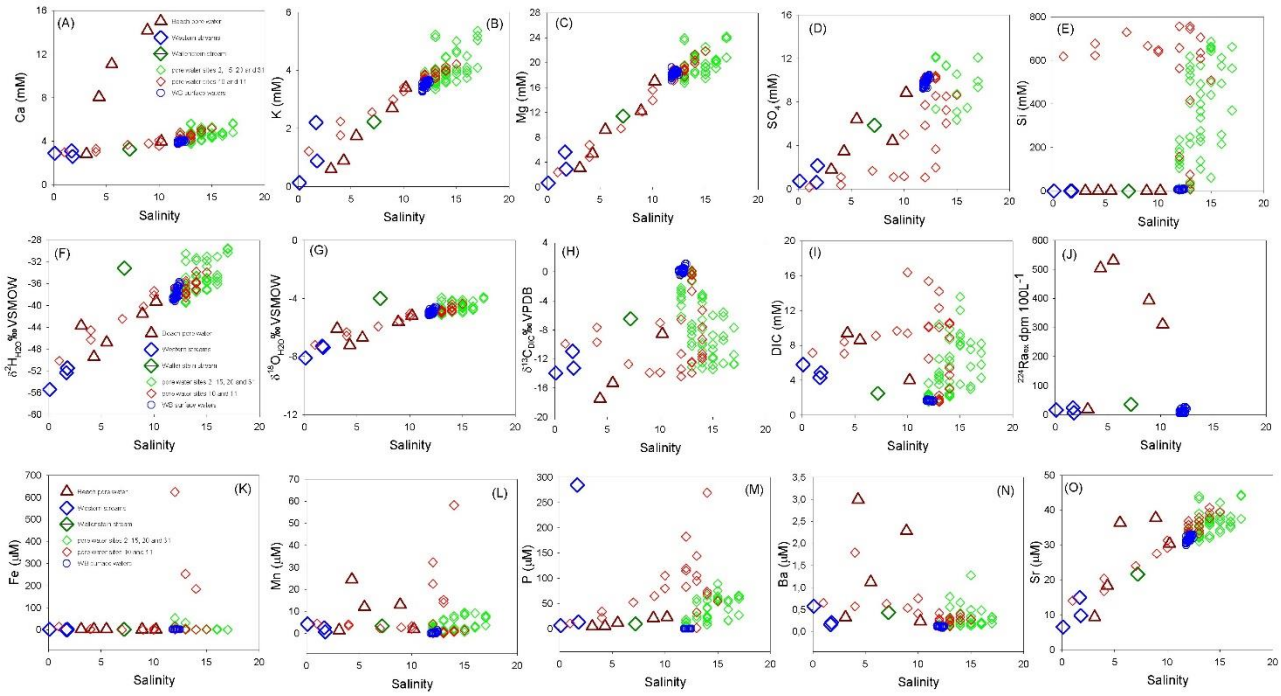

Supplmentary Figure **2** – **Salinity plotted against** Calcium (A), Potassium (B), Magnesium (C), Sulphate (D), Silicate (E), δ^2H_{H2O} (F), $\delta^{18}O_{H2O}$ (G), $\delta^{13}C_{DIC}$ (H), DIC (I), $^{224}Ra_{ex}$ (J), Fe (K), Mn (L), P (M), Ba (N) and Sr (O) **for beach pore water, western streams, Wallensteisn stream, surface and pore waters of Wismar Bay.**

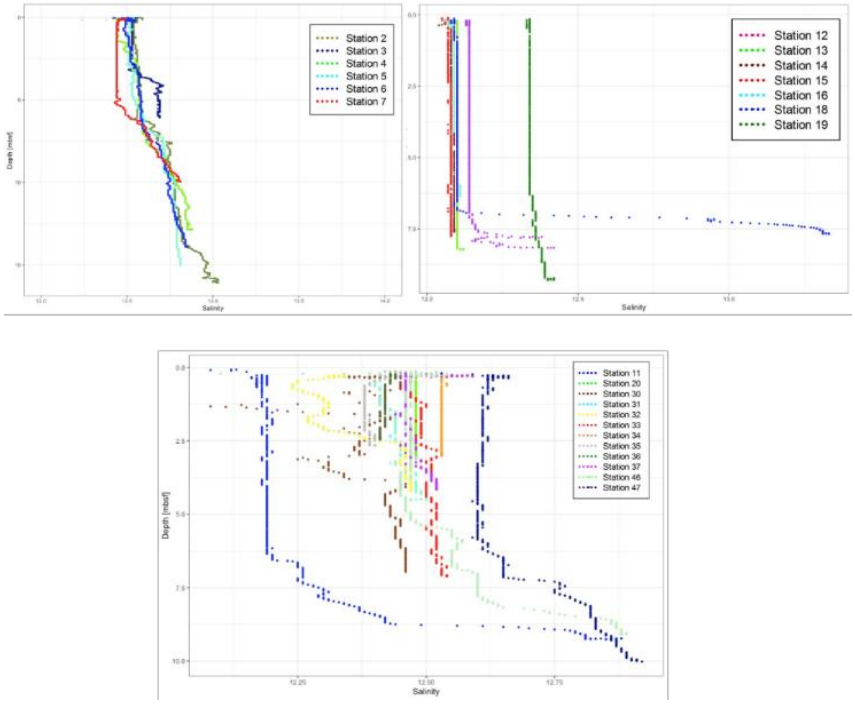

Supplementary Figure 3. (A) Vertical water column profiles of the sites where CTD was applied (Supplementary Table 1)

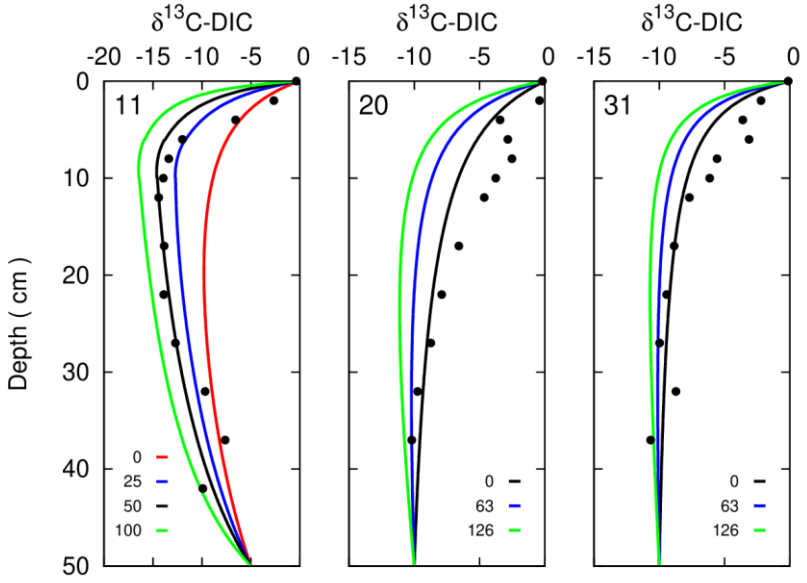

Supplementary Figure 4. Sensitivity test of OM mineralization rate in station 11, 20 and 31. In station 11, the lines with different colors refer to the additional OM mineralization rate due to reactive metal oxide ranging from 0 mM/yr to 100 mM/yr. In stations 20 and 31, the lines with different colors refer to the accumulated OM mineralization rate (0, 63 and 126 nmol cm-2d-1).

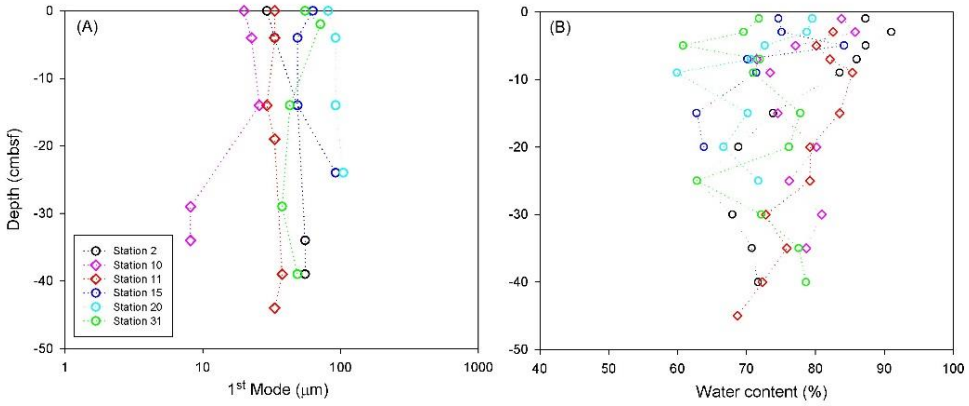

Supplementary Figure 5. (A) Vertical profile of grain size and (B) water content from the sediment samples

1.2 Supplementary Tables

Supplementary Table 1 – Information of coordinates and sampling strategy in all 47 stations sampled in Wismar Bay

Stations	Coordinates		Sampling strategy (depth of sampling)
Station 1	54.1438	11.2886	CTD, water sampling (8 and 24 m)
Station 2	54.0118	11.2301	CTD, water sampling (4,8 and 24 m) and core
Station 3	54.0109	11.2026	CTD, water sampling and radium sampling (2 m)
Station 4	54.0118	11.2459	CTD, water sampling (2 m)
Station 5	54.0121	11.2289	CTD, water sampling (2 m)
Station 6	54.0039	11.2290	CTD, water sampling (2 m)
Station 7	53.9895	11.2284	CTD, water sampling (2 m)
Station 8	53.9872	11.2264	CTD, water sampling (2 m)
Station 9	53.9844	11.2262	CTD, water sampling (2 m)
Station 10	53.9626	11.2972	CTD, water sampling (2m) and core
Station 11	53.9647	11.3661	CTD, water sampling (2 m) and core
Station 13	53.9545	11.3013	CTD, water sampling and radium sampling (2 m)
Station 14	53.9497	11.3033	CTD, water sampling (2 m)
Station 15	53.9472	11.3047	CTD, water sampling (2 m) and core
Station 16	53.9880	11.2704	CTD, water sampling (2 m)
Station 17	53.9532	11.2706	CTD, water sampling (2 m)
Station 18	53.9758	11.2936	CTD, water sampling (2 m)
Station 19	53.9768	11.3213	CTD, water sampling (2 m)
Station 20	53.9366	11.4203	CTD, water sampling (2 m) and core
Station 21	53.9418	11.3071	CTD, water sampling (1 m)
Station 22	53.9427	11.3070	CTD, water sampling (1 m)
Station 23	53.9433	11.3061	CTD, water sampling (1 m)
Station 24	53.9445	11.3051	CTD, water sampling (1 m)
Station 25	53.9324	11.2705	CTD, water sampling (1 m)
Station 26	53.9335	11.2702	CTD, water sampling (1 m)
Station 27	53.9351	11.2699	CTD, water sampling (1 m)
Station 28	53.9362	11.2698	CTD, water sampling (1 m)
Station 29	53.9722	11.3536	CTD, water sampling (2 m)
Station 30	53.9583	11.3855	CTD, water sampling (2 m)
Station 31	53.9551	11.4022	CTD, water sampling (2 m) and core
Station 32	53.9562	11.4276	CTD, water sampling (2 m)
Station 33	53.9094	11.4415	CTD, water sampling (2 m)
Station 34	53.9152	11.4362	CTD, water sampling (2 m)
Station 35	53.9225	11.4289	CTD, water sampling (2 m)
Station 36	53.9290	11.4247	CTD, water sampling (2 m)
Station 37	53.9506	11.4379	CTD, water sampling (2 m)
Station 38	53.9320	11.4748	CTD, water sampling (1 m)
Station 39	53.9336	11.4696	CTD, water sampling (1 m)
Station 40	53.9358	11.4650	CTD, water sampling (1 m)
Station 41	53.9382	11.4566	CTD, water sampling (1 m)

Station 42	53.9912	11.4421	CTD, water sampling (1 m)
Station 43	53.9858	11.4409	CTD, water sampling (1 m)
Station 44	53.9793	11.4401	CTD, water sampling (1 m)
Station 45	53.9687	11.4387	CTD, water sampling (1 m)
Station 46	53.9933	11.3302	CTD, water sampling (2 m)
Station 47	54.0156	11.3258	CTD, water sampling (2 m)

Suplementary Table 2 - ^{223}Ra, ^{224}Ra, $^{224}Ra_{ex}$ activties in Wismar Bay, streams surface waters and beach pore water.

Sites	Depth [m]	Ra 224 [dpm 100L]	Ra 223 [dpm 100L]	Ra 224ex [dpm 100L]
Station 1	8	1.49		1.09
Station 1	24	18.81	0.68	17.46
Station 2	4	4.98		4.25
Station 2	8	3.06		2.58
Station 2	16	2.80		2.33
Station 3		5.86		5.03
Station 4		5.15		4.34
Station 5		5.34		4.38
Station 6		6.83		5.89
Station 7		7.84		7.17
Station 8		9.38		8.45
Station 9		21.54	1.02	20.64
Station 11	2	6.45		5.76
Station 11	8	7.71	0.52	7.01
Station 12	2	8.29		7.39
Station 12	8	6.25		5.39
Station 13		4.79		3.94
Station 14		4.65	0.31	3.64
Station 15		5.85		5.31
Station 16		6.89		6.27
Station 17		7.13		6.48
Station 18		5.35		4.74
Station 19		7.01		6.40
Station 20		20.90	0.00	19.84
Station 21		12.62	0.52	11.76
Station 22		11.63	0.67	10.71
Station 23		9.08	0.43	8.06
Station 24		5.23		4.46
Station 25		11.80	0.60	10.93
Station 26		7.32		6.30

Station 27		7.56		6.55
Station 28		6.40		5.81
Station 29		8.01		7.28
Station 30		11.52	0.68	10.95
Station 31		10.04	0.79	9.37
Station 32		12.59	0.90	11.90
Station 33		18.42	1.24	17.33
Station 34		13.94	0.66	13.26
Station 35		15.06	0.97	14.26
Station 36		14.93	0.95	14.35
Station 37		14.15	1.02	13.40
Station 38		27.45	1.61	26.52
Station 39		14.94	0.91	14.20
Station 40		14.28	0.90	13.43
Station 41		13.63	0.92	12.78
Station 42		20.83	1.42	20.21
Station 43		21.01	1.68	19.92
Station 44		23.28	1.54	22.10
Station 45		20.12	1.50	19.22
Station 46		6.56	0.35	5.92
Station 47		3.62		3.13
Western stream 1	0.2	24.34	0.56	23.69
Western stream 2	0.2	6.84	0.15	6.29
Western stream 3	0.2	15.61	0.40	15.40
Wallenstein stream	0.2	36.24	0.93	34.88
Beach pore water 1	0.4	408.79	10.64	392.89
Beach pore water 2	0.8	25.77	0.46	17.56
Beach pore water 3	1.0	518.74	18.51	503.84
Beach pore water 4	1.0	547.08	13.44	530.02
Beach pore water 5	1.8	310.88	8.82	308.89

Supplementary Table 3 - Methods and DIN-standards used for in-situ measurements and hydrochemical analysis of ground water from the wells.

Analysis/Method		DIN-standard
Conservation of samples and water sample treatment		DIN EN ISO 5667-3(A21) 2004-05
Extraction for analysis of selected elements		DIN EN ISO 15587-2 (A32) 2002-2007
pH		DIN EN ISO 10523 2012-04
T		DIN 38 404-C4 1976-12
O2(aq)	Iodometric	DIN EN 25813 (G 21) 1992-10
O2(aq)	electrochemical	DIN EN ISO 25814 (G22) 1992-11
specific conductivity		DIN EN 27 888 (C8) 1993-11

Supplementary Table 4 – Parameters and boundary conditions for the modeling

	Symbol	Unit	11	10	15	2	20	31
RC-parameter	*a*	yr	100	100	100	100	-	-
RC-parameter	ν	-	0.2	0.2	0.2	0.2	-	-
Initial TOC	G_0	wt %	6	8	4.5	4	-	-
Isotope of TOC	δ^{13}TOC	‰VPDB	-20	-20	-20	-20	-	-
Boundary condition at sediment-water interface								
Sulfate	$[SO_4^{2-}]$	mM	11	10	10	15	13	12
DIC	[DIC]	mM	2	2	2	2	1	1
Isotope of DIC	δ^{13}DIC	‰VPDB	0	0	0	0	0	0
Boundary condition at 50 cm								
Sulfate	$[SO_4^{2-}]$	mM	0	0	4	6	6	2
DIC	[DIC]	mM	17	6	16	9	8	15
Isotope of DIC	δ^{13}DIC	‰VPDB	-10	-5	-13	-12	-10	-10

Suplementary Material published together with the article: **"Submarine groundwater discharge into a semi-protected coastal bay of the southern Baltic Sea: A multi-method approach" – Chapter 3**

Supplementary Material for

Submarine groundwater discharge into a semi-protected coastal bay of the southern Baltic Sea: A multi-method approach

Catia Milene Ehlert von Ahn[1], Olaf Dellwig[1], Beata Szymczycha[2], Lech Kotwicki[2], Jurjen Rooze[1], Rudolf Endler[3], Peter Escher[1,4], Iris Schmiedinger[1], Magdalena Diak[2], Matthias Gehre[5], Jürgen Sültenfuß[6], Ulrich Struck[7], Susan Vogler[1] and Michael Ernst Böttcher[1,8,9*]

[1]Geochemistry & Isotope Biogeochemistry, Leibniz Institute for Baltic Sea Research (IOW), Warnemünde, Germany.
[2] Institute of Oceanology, Polish Academy of Sciences (IOPAN), Sopot, Poland.
[3]Marine Geophysics, Leibniz Institute for Baltic Sea Research (IOW), Warnemünde, Germany.
[4]current address: Ecoandmore Freiburg, Germany.
[5]Department of Isotope Biogeochemistry, Helmholtz Centre for Environmental Research (UFZ), Leipzig-Halle, Germany.
[6]Institute of Environmental Physics, University of Bremen, Bremen, Germany.
[7]Free University Museum for Natural History, Berlin, Germany.
[8]Marine Geochemistry, University of Greifswald, Greifswald, Germany.
[9]Interdisciplinary Faculty, University of Rostock, Rostock, Germany.
*michael.boettcher@io-warnemuende.de

Contents

Introduction

This document presents additional figures and tables obtained from the present study which helps to discuss the results.

Supplementary Figures

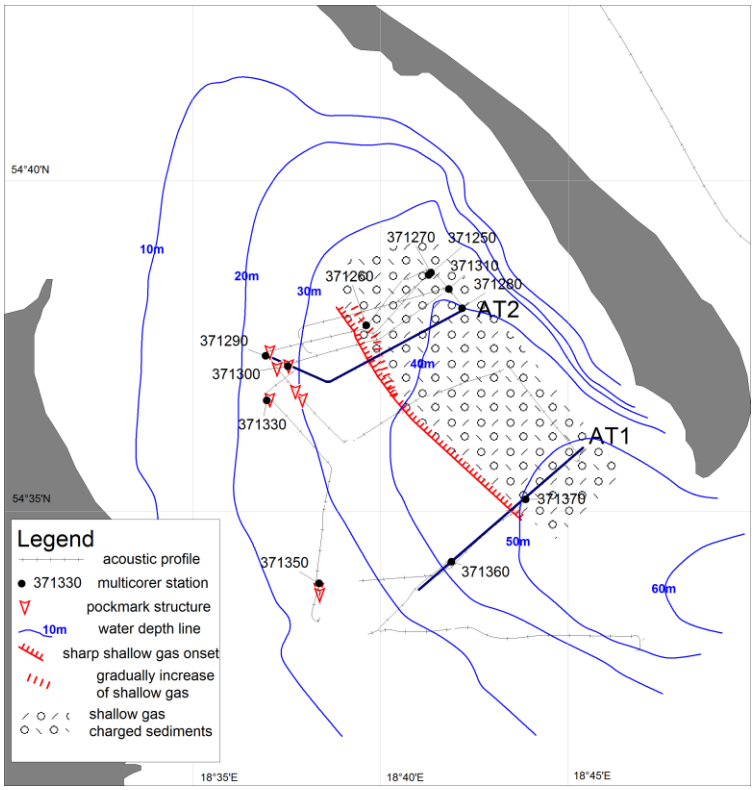

Supplementary Figure 1. Study area where the geophysical surveys were carried out during the campaign in 2009. AT1 and AT2 are presented in the Supplementary Figure 2.

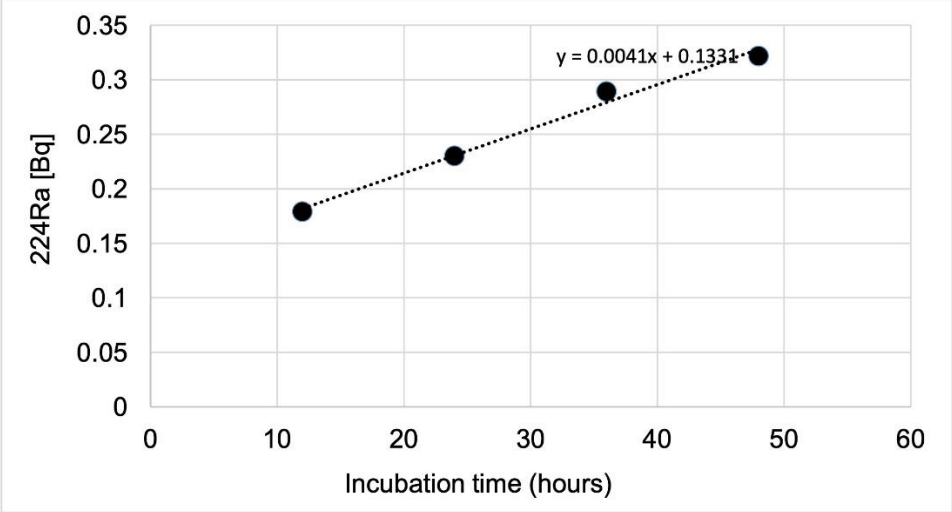

Supplementary Figure 2 Accumulated diffusive ^{224}Ra activities as a function of time corrected for surface area of o the beaker 0.2 m^2.

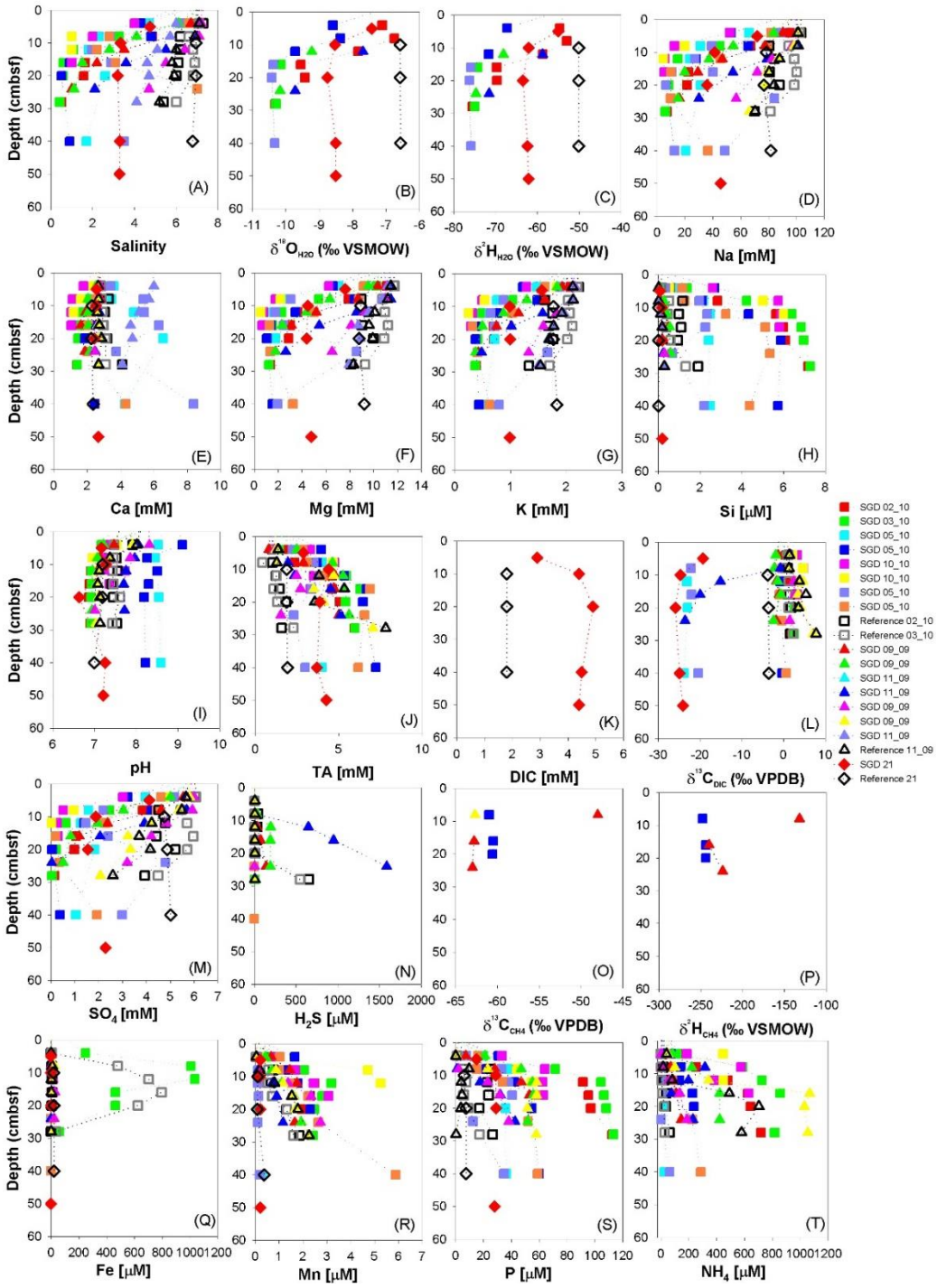

Supplementary Figure 3. Vertical porewater profile from all profiles collected in Hel in 2009, 2010, and 2021.

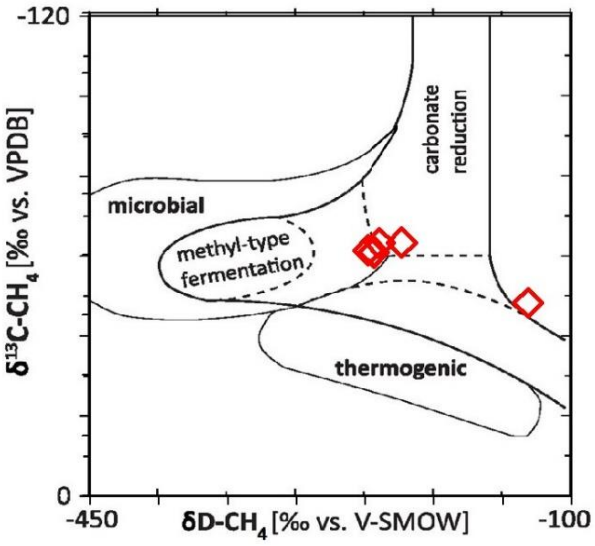

Supplementary Figure 4. Stable isotope composition of dissolved methane in porewater under SGD-impacted sites in 2009 and 2010 (Table 1). Underlying is the methane isotope classification modified from Whiticar (1999) and taken from Egger et al. (2017).

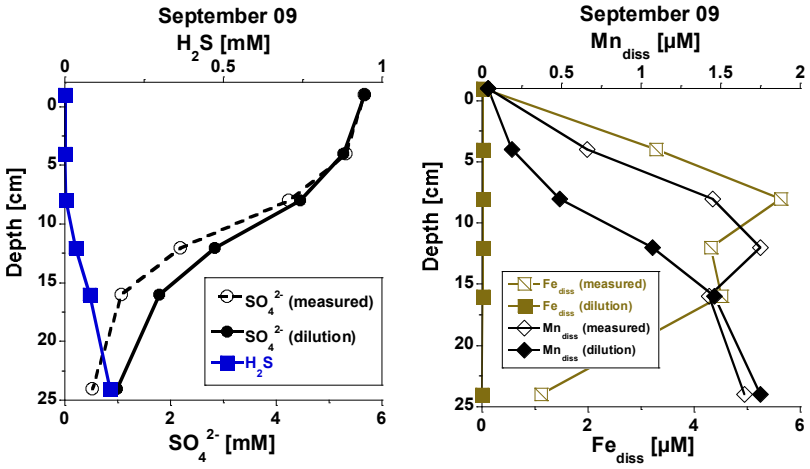

Supplementary Figure 5. Porewater profile of SO4, H_2S, Mn, and Fe from September 2009.

Supplementary Tables

Supplementary Table 1 – Information of coordinates and sampling strategy in all sampled sites

Sampling date	Site	Depth Site (m)	Latitude	Longitute	Sampling
2009-06-25	371150		54.5512	18.7836	CTD, water column
2009-06-25	371160		54.553	18.6631	CTD, water column
2009-06-25	371170		54.5695	18.6999	CTD, water column
2009-06-25	371180		54.5859	18.7301	CTD, water column
2009-06-25	371190		54.5982	18.7556	CTD, water column
2009-06-25	371200				CTD, water column
2009-06-25	371220		54.6013	18.6548	CTD, water column
2009-06-25	371230		54.6232	18.6171	CTD, water column, sediment core (371290)
2009-06-25	371240		54.6296	18.6607	CTD, water column, sediment core (371260)
2009-06-26	371250		54.5512	18.7836	CTD, water column, sediment core (371270)
2009-06-27	371330		54.6113	18.6161	CTD, water column, sediment core
2009-06-27	371370		54.5695	18.6999	CTD, water column, sediment core
2019-10-07	33 M/P1	108	54.8340	19.3282	Surface water
2019-10-07	M1	79	54.5715	19.1647	Water column, sediment core
2019-10-07	ZUZOL 60		54.4499	19.0579	Surface water
2019-10-08	MW1C		54.3795	18.9512	Surface water
2019-10-08	MW3C		54.4144	18.9802	Surface water
2019-10-09	17M	23	54.6000	18.6083	Surface water
2019-10-09	18M	27	54.5803	18.6293	Surface water
2019-10-09	23M	27.5	54.5569	18.6529	Surface water
2019-10-09	2M		54.5556	18.5789	Surface water
2019-10-09	22M	47	54.5813	18.7010	Surface water
2019-10-09	M2	50	54.6003	18.7330	Water column, sediment core
2019-10-09	72M	38	54.6125	18.7616	Surface water
2019-10-09	12M/B14	27	54.6267	18.6159	Surface water, sediment core
2019-10-09	16M	38.5	54.6281	18.6641	Surface water
2019-10-09	19M	43	54.6035	18.6784	Surface water
2019-10-09	20M		54.6261	18.7292	Surface water
2019-10-10	15M	36	54.6447	18.7025	Surface water, sediment core
2019-10-10	14M	28	54.6636	18.6753	Surface water
2019-10-10	MP2		54.6749	18.6051	Surface water
2019-10-10	11M/B12	14	54.6216	18.5783	Surface water
2019-10-10	4M(MECH)		54.6166	18.5602	Surface water
2019-10-10	3M	10	54.6052	18.5567	Surface water
2019-10-10	10M	13	54.6451	18.5699	Surface water

2019-10-10	13M	33	54.6376	18.6386	Surface water, sediment core
2019-10-11	MP1		54.6878	18.5827	Surface water
2019-10-12	2M_a_160m		54.5543	18.5602	Surface water
2019-10-12	2M_b_345m		54.5546	18.5632	Surface water
2019-10-12	2M_c_770m		54.5537	18.5717	Surface water
2019-10-12	3M_a_160m		54.5893	18.5289	Surface water
2019-10-12	3M_b_1070m		54.6021	18.5400	Surface water
2019-10-12	3M_c_1600m		54.6036	18.5477	Surface water
2019-10-12	10M_a_150m		54.6458	18.5201	Surface water
2019-10-12	10M_b_500m		54.6463	18.5256	Surface water
2019-10-12	10M_c_1900m		54.6475	18.5477	Surface water
2019-10-12	72M_a_500m		54.6188	18.6096	Surface water
2019-10-12	72M_b_150m		54.6170	18.7721	Surface water
2019-10-13	7M		54.7001	18.6000	Surface water
2019-10-13	InnerBay1_150m_SWARZEWO		54.7619	18.4094	Surface water
2019-10-13	InnerBay1_500m_SWARZEWO		54.7603	18.4146	Surface water
2019-10-13	InnerBay1_1000m_SWARZEWO		54.7581	18.4215	Surface water
2019-10-13	InnerBay2_150m_Chalupy		54.7789	18.4399	Surface water
2019-10-13	InnerBay2_550m_Chalupy		54.7753	18.4489	Surface water
2019-10-13	InnerBay2_1000m_Chalupy		54.7712	18.4407	Surface water
2019-10-13	Rn_7		54.77	18.458	Surface water
2019-10-13	Rn_6		54.773	18.452	Surface water
2019-10-13	Rn_5		54.768	18.447	Surface water
2019-10-13	Rn_4		54.772	18.44	Surface water
2019-10-13	Rn_3		54.775	18.445	Surface water
2019-10-13	Rn_2		54.778	18.44	Surface water
2019-10-13	Rn_18		54.775	18.438	Surface water
2019-10-13	Rn_1		54.775	18.433	Surface water
2019-10-13	Rn_17		54.772	18.447	Surface water
2019-10-13	Rn_16		54.768	18.453	Surface water
2019-10-13	Rn_15		54.768	18.445	Surface water
2019-10-13	Rn_14		54.768	18.437	Surface water
2019-10-13	Rn_13		54.773	18.435	Surface water
2019-10-13	Rn_12		54.772	18.427	Surface water
2019-10-13	Rn_11		54.768	18.433	Surface water
2019-10-13	Rn_10		54.765	18.44	Surface water
2019-10-13	Rn_9		54.762	18.447	Surface water
2019-10-13	Rn_8		54.767	18.452	Surface water
2019-10-13	Rn_7		54.77	18.452	Surface water
2021-06-24	SW_7		54.729	18.426	Surface water
2021-06-24	SW_15		54.735	18.437	Surface water

2021-06-24	SW_37		54.740	18.458	Surface water
2021-06-24	SW_12		54.746	18.445	Surface water
2021-06-24	SW_11		54.751	18.432	Surface water
2021-06-24	SW_14		54.755	18.416	Surface water
2021-06-24	SW_16		54.764	18.435	Surface water
2021-06-24	SW_43		54.772	18.444	Surface water
2021-06-24	SW_21		54.749	18.505	Surface water
2021-06-24	SW_23		54.739	18.491	Surface water
2021-06-24	SW_18		54.727	18.475	Surface water
2021-06-24	SW_17		54.730	18.495	Surface water
2021-06-24	SW_8		54.712	18.535	Surface water
2021-06-24	SW_25		54.721	18.550	Surface water
2021-06-24	SW_22		54.729	18.565	Surface water
2021-06-24	SW_13		54.678	18.500	Surface water
2021-06-24	SW_9		54.672	18.489	Surface water
2021-06-24	SW_10		54.665	18.478	Surface water
2009/2010/2021	Hel Site		54.605	18.801	Surface water, porewater and sediment
2021-06-17	Chalupy Site		54.668	18.466	Surface water, porewater and sediment
2021-06-18	Swarzewo Site		54.779	18.453	Surface water, porewater and sediment
2021-06-28	Oslonino Site		54.762	18.408	Surface water, porewater and sediment
2019/2021	Piazometer_Hel island		54.607	18.801	Groundwater
2021-06-22	2/6 Jurata	148	54.680	18.719	Groundwater
2021-06-22	1/5 Jurata	154	54.679	18.717	Groundwater
2021-06-22	Wladyslawowo 7a	180	54.785	18.370	Groundwater
2021-06-22	Wladyslawowo 8	180	54.787	18.366	Groundwater
2021-06-22	Wladyslawowo 2a	120			Groundwater
2021-06-22	Puck 8		54.711	18.402	Groundwater
2021-06-22	Puck 6a		54.710	18.402	Groundwater
2021-06-22	Puck 5a		54.713	18.404	Groundwater
2021-06-23	Czarny Dwór 14b		54.399	18.614	Groundwater
2021-06-23	Czarny Dwór K2		54.416	18.600	Groundwater
2021-06-23	Brodwino B5		54.457	18.521	Groundwater
2021-06-23	Gdynia 8b czwarto		54.475	18.548	Groundwater
2021-06-23	Gdynia K4 Kreda		54.474	18.548	Groundwater
2011	Reda I		18.388	54.614	Groundwater
2011	Reda II		18.385	54.618	Groundwater
2011	Rumia		18.427	54.567	Groundwater
2011/2021	Reda River		54.637	18.440	Surface Water
2011/2021	Płutnica River		54.728	18.393	Surface Water
2011/2021	Zagórska Struga River		54.624	18.439	Surface Water
2011/2021	Gizdepka River		54.406	18.245	Surface Water

Supplementary Table 2 – Dating of groundwater of selected groundwater wells around Puck Bay, and porewater extracted from a SGD impacted site in Hel.

Name of the Well	Filter depth	Tritium	err-tritium	3He	4He	Ne	3He/4He	Ne/He	radiogenic 4He
	[m]	[TU]	[TU]	[ccSTP/kg]	[ccSTP/kg]	[ccSTP/kg]			[ccSTP/kg]
Porewater Hel SGD impacted	0	3.6	0.13						
Porewater Hel SGD impacted	0	3.7	0.20						
Wladyslawowo 2		2.6	0.10	1.1E-10	5.6E-05	2.4E-04	1.9E-06	4.20	0
Reda IV	30	0.1	0.03	7.6E-11	5.6E-05	2.3E-04	1.3E-06	4.18	0
Reda 12c	10	4.6	0.15	1.1E-10	5.2E-05	2.2E-04	2.2E-06	4.23	0
Rumia K1, artesian	180	0.0	0.03	8.1E-11	6.5E-05	2.5E-04	1.2E-06	3.89	3.7E-06
Well Hel		0.0	0.03	1.7E-10	3.1E-03	3.4E-04	5.3E-08	0.11	3.0E-03

Supplementary Table 3 - Element fluxes calculated to selected sites from offshore sites (Site M1, Site M2, 371330, 371370), and selected profiles from Hel site including sites impacted and not impacted by SGD. Negative values mean upward fluxes. (On the Figure 8 on the manuscript the fluxes are multiplied by -1 to have a better visualization of the fluxes)

Element Fluxes (mM m-2 d-1)									
SDG IMPACTED SITES						**REFERENCE SITES**				
	Diffuse flux	Mixing Flux	Advection flux	Total flux			Diffuse flux	Mixing Flux	Advection flux	Total flux
Site M1						**Site M2**				
P	-0.1	0.0	0.0	-0.1		P	0.0	0.0	0.0	0.0
DIC	-3.9	0.0	-0.5	-4.4		DIC	-1.8	0.0	0.0	-1.9
TA	0.0	0.0	0.0	0.0						
NH4	-1.2	0.0	-0.1	-1.2		NH4	0.0	0.0	0.0	0.0
Site 371330						**Site 371370**				
P	-0.1	0.0	0.0	-0.1		P	-0.1	0.0	0.0	-0.1
DIC	-1.5	0.0	0.0	-1.5		DIC	-3.5	0.0	0.0	-3.5
TA	-1.3	0.0	0.0	-1.3		TA	-4.7	0.0	0.0	-4.7
NH4	-0.3	0.0	0.0	-0.3		NH4	-0.4	0.0	0.0	-0.4
Hel SGD 11_09						**Hel reference 11_09**				
P	0.0	0.0	0.0	0.0		P	0.0	0.0	0.0	0.0
DIC	-0.2	-0.5	-0.2	-0.9		DIC	-0.5	0.0	0.0	-0.5
TA	-0.3	-0.8	-0.2	-1.3		TA	-0.5	0.0	0.0	-0.5
NH4	0.0	0.0	0.0	0.0		NH4	-0.1	0.0	0.0	-0.1
Hel SGD 11_09						**Hel reference 02_10**				
P	0.0	0.0	0.0	0.0		P	0.0	-0.3	0.0	-0.3
TA	-0.6	-0.3	-0.1	-1.0		TA	0.0	0.0	0.0	-0.1
NH4	0.0	0.0	0.0	0.0		NH4	0.0	0.0	0.0	0.0
Hel SGD 05_10						**Hel reference 03_10**				
P	0.0	0.0	0.0	0.0		P	0.0	0.0	0.0	0.0
DIC	-0.2	-0.3	-0.5	-1.0		DIC	0.0	0.0	0.0	0.0
TA	-0.2	-0.3	-0.6	-1.1		TA	0.0	0.0	0.0	0.0
NH4	0.0	0.0	0.0	0.0		NH4	0.0	0.0	0.0	0.0
Hel SGD 02_10						**Hel reference 06_21**				
P	0.0	0.0	0.0	-0.1		P	0.0	0.0	0.0	0.0
DIC	0.0	0.0	0.0	0.0		DIC	0.0	0.0	0.0	0.0
TA	-0.2	-1.6	-0.2	-2.0		TA	0.0	0.0	0.0	0.0
NH4	0.0	0.0	0.0	0.0		PO4	0.0	0.0	0.0	0.0
Hel SGD 10_10						NH4	0.0	0.0	0.0	0.0
P	0.0	0.0	0.0	0.0						
TA	-0.4	0.0	-1.1	-1.5						
NH4	0.0	0.0	0.0	0.0						

Hel SGD 06_21										
P	0.0	0.0	0.0	0.0						
DIC	-0.4	0.0	-1.0	-1.3						
TA	-0.4	0.0	-0.9	-1.3						
NH4	0.0	0.0	0.0	0.0						

Suplementary Material published together with the article: **"Impact of submarine groundwater discharge on biogeochemistry and microbial communities in pockmarks" – Chapter 4**

Note: Only part of the supplementary material is presented here in this thesis. All the information regarding the microbiological data and their respective analysis are also presented as a Supplementary Material, on the published paper, however it is note presented here because it refers to a interactive visualization. The complete information can be found on: https://doi.org/10.1016/j.gca.2022.06.040.

Supplementary Material for

Impact of submarine groundwater discharge on the benthic biogeochemistry and microbial communities in pockmarks

Lotta Purkamo[1],Cátia M. Ehlert von Ahn[2], Tom Jilbert[3], Muhammad Muniruzzaman[1], Hermann W. Bange[4], Anna Jenner[2], Michael E. Böttcher[2] and Joonas J. Virtasalo[5]

[1]Water Management Solutions, Geological Survey of Finland (GTK), Vuorimiehentie 5, 02151 Espoo, Finland
[2]Geochemistry and Isotope Biogeochemistry Group, Leibniz Institute for Baltic Sea Research Warnemünde (IOW), Seestrasse 15, D-18119 Rostock, Germany
[3]Environmental Geochemistry Group, Department of Geosciences and Geography, Gustaf Hällströmin katu 2, University of Helsinki, Finland
[4]Marine Biogeochemistry, GEOMAR Helmholtz Centre for Ocean Research Kiel, Düsternbrooker Weg 20, D-24105 Kiel, Germany
[5]Marine Geology, Geological Survey of Finland (GTK), Vuorimiehentie 5, 02150 Espoo, Finland

Contents

Introduction

This document presents additional data obtained from the study site as well as the input parameters used in the reactive transport simulations. Particularly, the hydraulic, transport, and reaction parameters used in the reactive transport model are summarized. Furthermore, we also report the numerical optimization scheme used in the estimation of depth-dependent porosity function and submarine groundwater discharge rate for different pockmarks.

S1 Additional data for different pockmarks

S1.1 Sediment core data

Figure S1. Photos of the sediment box-cores from pockmarks B and D, and the lengthwise split Gemax gravity-core from pockmark E.

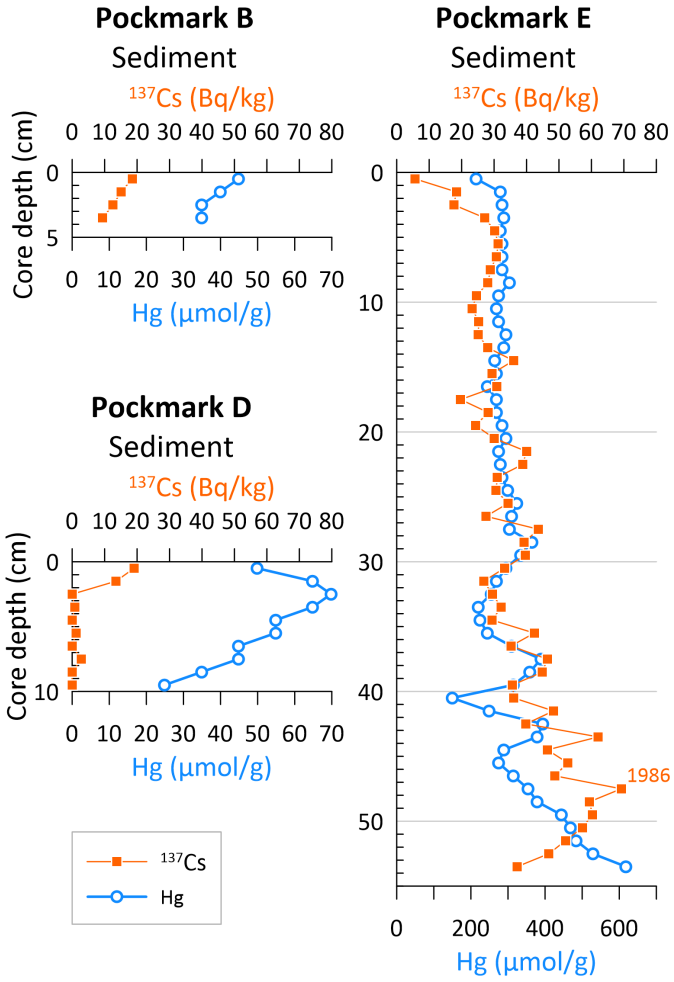

Figure S2. Vertical distribution of ^{137}Cs activity content in sediment cores from pockmarks B, D and E. The interpreted depth of the year 1986 is indicated.

Table S1. Inorganic carbon contents in the sediment

Pockmark	**Depth [cm]**	**TIC [%dwt.]**
B	1	0.03
B	2	0.02
B	3	0.03
B	4	0.02
D	1	0.02
D	2	0.02
D	3	0.02
D	4	0.03
D	5	0.02
D	6	0.02
D	7	0.03
D	8	0.02
D	9	0.02
D	10	0.02
E	2	0.10
E	4	0.15
E	6	0.09
E	8	0.06
E	10	0.08
E	12	0.06
E	16	0.06
E	20	0.06
E	24	0.06
E	28	0.06
E	32	0.06
E	36	0.06
E	40	0.05
E	44	0.06
E	48	0.06
E	52	0.08
E	56	0.06

S1.2 Microbiological data

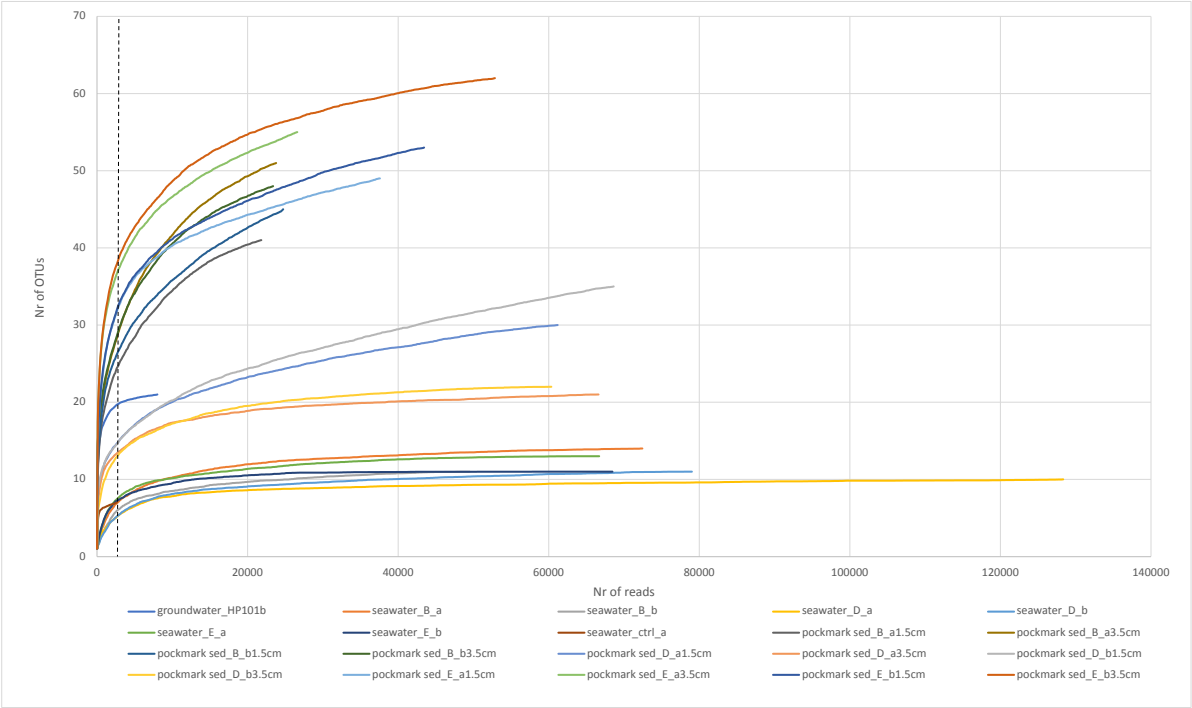

Figure S3. Rarefaction curves for the archaeal 16S rRNA gene sequences. Lowercase a and b correspond to parallel sequencing samples.

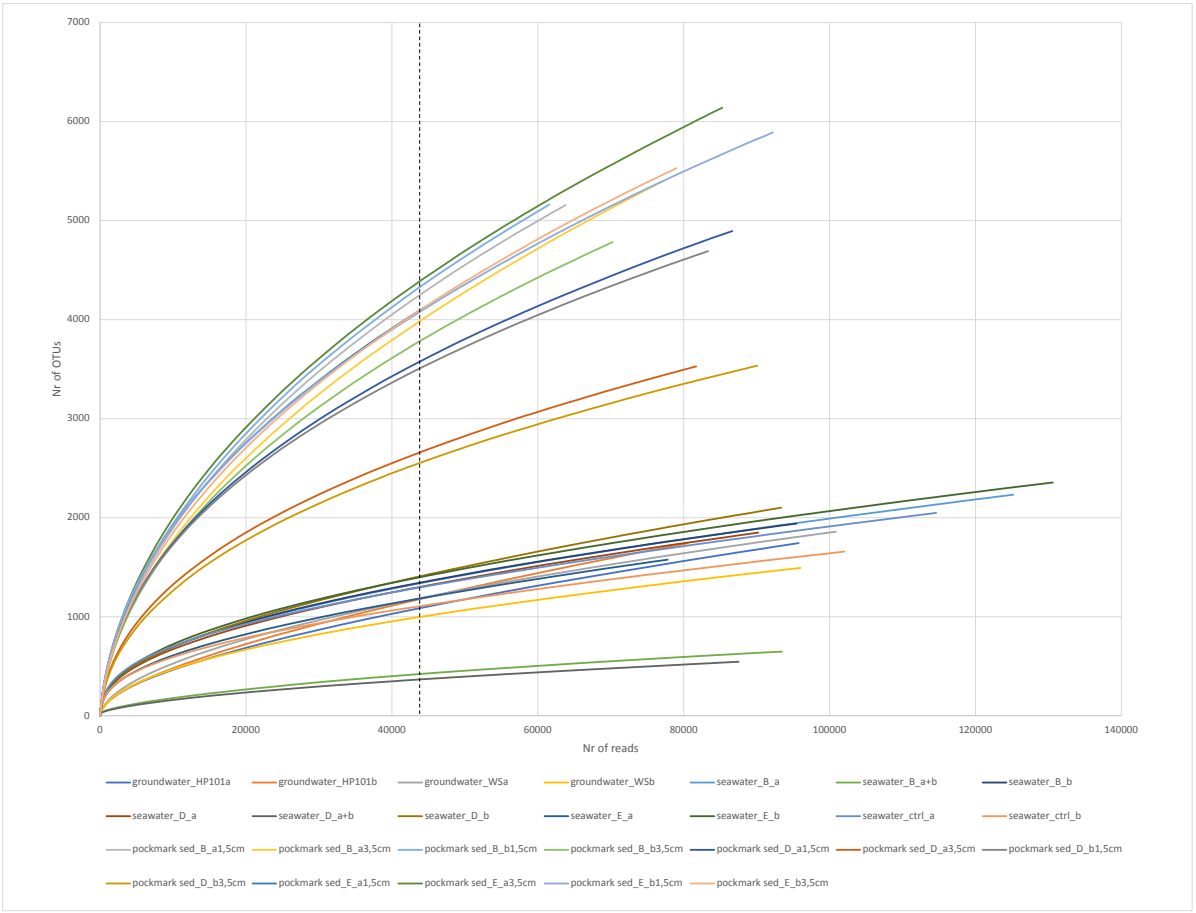

Figure S4. Rarefaction curves for the bacterial 16S rRNA gene sequences. Lowercase a and b correspond to parallel sequencing samples.

Table S2. Quantitative PCR specifications.

Gene/Function	**Abbreviation**	**Primers**	**Fragment Size bp**	**Annealing Temperature**	**Standard Used**	**Dilution Series**	**Primer References**
Bacterial 16S rRNA	16SrRNA A0785r	A0341f	444	57	*Escherichia coli* ATCC 31608	$10^8 - 10^2$	Klindworth et al. (2013)
Archaeal 16S rRNA	16SrRNA A744r	A344f	430	57	*Halobacterium salinarum* DSM 3754	$10^8 - 10^2$	Bomberg et al. (2015)
Ammonia oxidation	amoA amoA2R	amoA1f	419	59	*Nitrosomonas europaea* VTT E-042735	$10^7 - 10^1$	Rotthauwe et al. (1997) Stephen et al. (1999)
Nitrate reduction	narG 2050r	1960f	110	59	*Pseudomonas aeruginosa* PA01 VTT E-113166	$10^7 - 10^1$	López-Gutiérrez et al. (2004)
Methane oxidation	pmoA pmor	pmoF1	330	55	*Methylococcus capsulatus* ATCC 33009	$10^7 - 10^1$	Cheng et al. (1999)
Methanogenesis	mcrA Me3r	Me1f	760	55	*Methanothermobacter thermoautotrophicus* DSM 1053	$10^7 - 10^1$	Hales et al. (1996)
Sulfate reduction	dsrB dsr4r	dsr2060f	370	56	*Desulfobulbus propionicus K6* (E-06220 VTT Culture collection)	$10^7 - 10^1$	Geets et al. (2006) Wagner et al. (1998)

Detailed taxonomic affiliations of the archaea and bacteria detected from pockmarks, groundwater and seawater at Hanko site are available as Krona-charts separately in .html file format in zipped folder "Krona charts".

Table S3. Functional marker gene copy numbers.

Sample	narG	amoA	pmoA	mcrA	dsrB
Pockmark sed_B_1,5cm	5.46×10^{08}	1.25×10^{08}	2.59×10^{06}	9.40×10^{06}	1.98×10^{09}
Pockmark sed_B_3,5cm	9.77×10^{06}	5.76×10^{07}	1.24×10^{06}	2.33×10^{06}	1.53×10^{09}
Pockmark sed_D_1,5cm	7.41×10^{06}	4.92×10^{06}	1.30×10^{06}	9.33×10^{05}	7.48×10^{07}
Pockmark sed_D_3,5cm	3.52×10^{06}	1.43×10^{06}	7.29×10^{05}	5.62×10^{05}	4.53×10^{06}
Pockmark sed_E_1,5cm	3.24×10^{07}	3.67×10^{07}	1.23×10^{07}	3.90×10^{06}	3.40×10^{09}
Pockmark sed_E_3,5cm	8.94×10^{07}	1.20×10^{08}	1.97×10^{07}	5.25×10^{07}	7.88×10^{09}
Pockmark sed DNA extraction ctrl .	7	n/a	192	92	4.30×10^{04}
Seawater above B	983	5.06×10^{03}	174	592	3.68×10^{03}
Seawater above D	1.22×10^{03}	3.37×10^{03}	53	400	3.20×10^{03}
Seawater above E	1.17×10^{03}	5.89×10^{03}	81	531	9.48×10^{03}
Seawater above ctrl.	1.04×10^{03}	624	54	689	4.26×10^{04}
Groundwater HP101	614	89	3	19	4.65×10^{03}
Groundwater WSl	55	17	1	3	350
Seawater+ groundwater DNA extr. ctrl.	0	0	0	47	1.60×10^{04}

S2 Numerical Modeling

S2.1 Estimation of groundwater discharge rates and depth-dependent porosity function

Groundwater discharge rates into seawater were calculated on the basis of porewater profiles of Cl^-, which is typically an inert tracer with respect to sorption mechanisms as well as chemical reactions (e.g., Schlüter et al., 2004). Therefore, the distribution of chloride in sediment porewater is a good indicator of mixing between the seawater and freshwater because Cl^- profiles are exclusively controlled by physical transport processes such as advection, diffusion and dispersion. Consequently, the propagation and distribution of chloride in such systems can be adequately described by the classical advection-dispersion equation, which under the assumption of homogeneous, isothermal and steady-state conditions takes the form:

$$\phi u \frac{\partial C_{Cl^-}}{\partial x} - \phi D_{Cl^-} \frac{\partial^2 C_{Cl^-}}{\partial x^2} = 0 \tag{1}$$

where, u [m/s] is the advective velocity (also termed as seepage velocity) in the vertical direction, C_{Cl} [mg/L] is the concentration of chloride, ϕ [-] represents the porosity, D_{Cl^-} [m^2/s] is the hydrodynamic dispersion coefficient, and x [m] is the sediment depth below the seafloor. The term ϕu is often termed as the specific discharge or Darcy flux in porous media ($q_w = \phi u$). The chloride dispersion coefficient, D_{Cl^-} can be parameterized considering the effects of tortuosity, temperature and porewater salinity (Boudreau et al., 1997; Oehler et al., 2017):

$$D_{Cl^-} = \frac{D_{aq,Cl^-}}{1 - 2\ln(\phi)} + \alpha u \tag{2}$$

where α [cm] is the dispersivity coefficient. The first term represents the contribution of the molecular diffusion and the second term refers to the mechanical dispersion term, which is a function of the flow velocity. In this study, the porosity was observed to be spatially variable

parameter, and hence its dependence is described by an expontial function, as described in the main paper:

$$\phi(x) = \phi_\infty + (\phi_0 - \phi_\infty) \exp\left(-\frac{x}{\zeta}\right) \tag{3}$$

By considering a finite domain and upon considering the following boundary conditions,

$$\begin{aligned} C_{Cl^-}(x = 0) &= C_{Bot} \\ C_{Cl^-}(x = L) &= C_{Top} \end{aligned} \tag{4}$$

the steady-state advection-dispersion equation can be solved analytically as:

$$C_{Cl^-}(x) = C_{Bot} + (C_{Top} - C_{Bot}) \left(\frac{1 - \exp\left(\frac{-\phi u x}{\phi D_{Cl^-}}\right)}{1 - \exp\left(\frac{-\phi u L}{\phi D_{Cl^-}}\right)} \right) \tag{5}$$

where C_{Bot} refers to the initial Cl^- concentration at the bottom of the sediment layer (i.e., initial freshwater concentration), C_{Top} represents the concentration at the top of the sediment layer (i.e., at the interface between the sweater and freshwater), and L is the total depth of the sediment layer.

The above analytical solution can be fitted against the experimentally measured chloride porewater profiles in order to quantify the vertical seepage velocity (u) within the sediment layer. Since the porosity is a depth-dependent parameter, the advective velocity in the aqueous phase also becomes a spatially-variable parameter. Therefore, it is convenient to estimate the specific dischanrge ($q_w = \phi u$), which can be assumed constant along the depth, instaed of the seepage velocity.

$$C_{Cl^-}(x) = C_{Bot} + (C_{Top} - C_{Bot}) \left(\frac{1 - \exp\left(\frac{-q_w x}{\phi D_{Cl^-}}\right)}{1 - \exp\left(\frac{-q_w L}{\phi D_{Cl^-}}\right)} \right) \tag{6}$$

Prior to the estimation of the porewater velocity/specific discharge, the porosity function was optimized against the observed porosity profiles to obtain ζ parameter (Figure S1). Afterwards, the chloride concentration profiles were fit againist the above analytical solution to determine the submarine groundwater discharge rates at different pockcmarks. Note that this fitting was performed only for pockmarks B and D because pockmark E shows clear evidence of negligible advection as reflected in flat concentration profile. The best fit parameters obtained from this optimization scheme were directly fed into the reactive transport simulations.

In this optimization procedure, we adopt the Levenberg-Marquardt algorithm by utilizing the MATLAB function *lsqnonlin* to solve the nonlinear least squares problem. In this step, the e-folding distance, ζ, and the specific discharge (q_w) were considered to be the only fitting

parameter during the optimization of porosity and chloride profiles, respectively. A similar approach was also adopted in numerous earlier studies focussing on submarine groundwater discharge (e.g., Schlüter et al., 2004; Oehler et al., 2017). In the optimization procedure, the following objective function was utilized:

$$\Xi^2 = \Sigma_{i=1}^{N} \left(\frac{O_i - M_i}{O_i} \right)^2$$

where N is the number of data points, and O_i and M_i represent the measured and the model predicted concentrations.

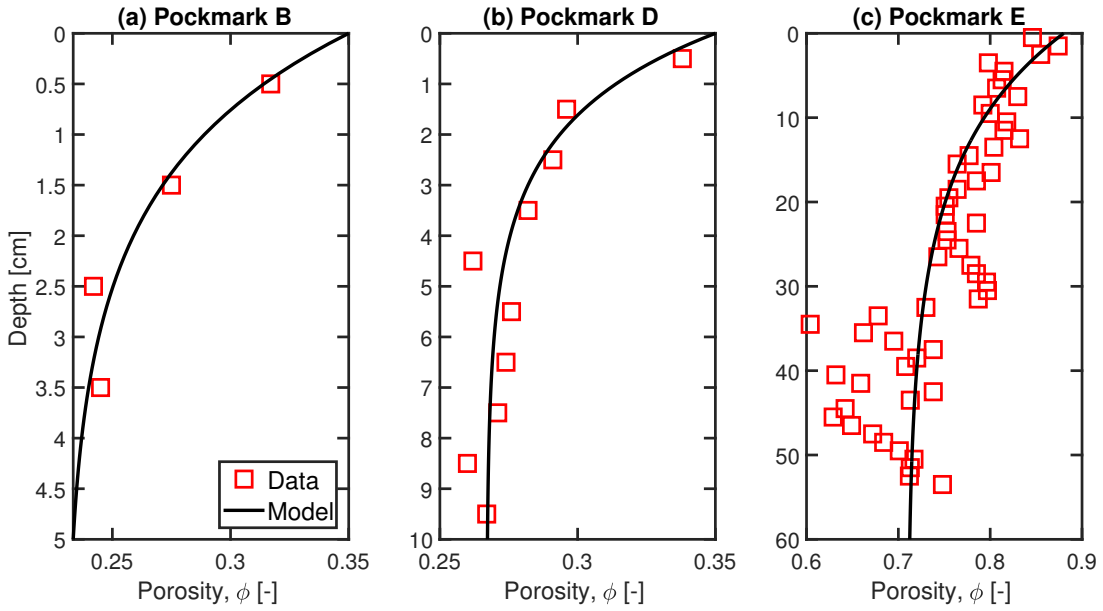

Figure S5. Measured (markers) and modeled (lines) porosity profiles at pockmark B (a), D (b), and E (c).

S2.2 Reactive transport model parameters

Table S4. Hydraulic, transport and other physical parameters used in the model.

Parameter	Symbol	Unit	Pockmark B	Pockmark D	Pockmark E
Porosity at sediment-water interface	ϕ_0	-	0.35	0.35	0.88
Porosity at depth	ϕ_∞	-	0.23	0.26	0.71
Porosity e-folding distance	ζ	cm	1.41	1.75	14.1
Sediment density	ρ_s	g cm^{-3}	2.31	2.31	2.31
Temperature	T	°C	8	8	8
C:N:P ratio of organic matter	-	-	106:16:1	106:16:1	106:16:1
P:Fe ratio for $Fe(OH)_3^\alpha$	χ^α	-	0.1	0.1	0.1
P:Fe ratio for $Fe(OH)_3^\beta$	χ^β	-	0.055	0.055	0.055
P:Fe ratio for $Fe(OH)_3^\gamma$	χ^γ	-	0.03	0.03	0.03
Bioturbation coefficient at surface	D_{b0}	cm^{2}a^{-1}	2.72×10^{-2}	1.35×10^{-1}	2.7
Mixed layer depth	ξ	cm	1.3	1.6	13
Porewater specific discharge	q_w	cm d^{-1}	0.02	0.31	0
Advective velocity of solids at depth	$\frac{F_{sed}}{\rho_s(1-\phi_\infty)}$	cm a^{-1}	3×10^{-7}	3×10^{-7}	0.43

Table S5. Aqueous and solid phase species considered in the reactive transport model.

Species	Notation	Type	Coefficient, D_{aq} [m^{2}s^{-1}]
Organic matter[a]	$OM^{\alpha,\beta,\gamma}$	Solid	-
Manganese oxides[a]	$Fe(OH)_3^{\alpha,\beta,\gamma}$	Solid	-
Iron oxides[a]	$MnO_2^{\alpha,\beta,\gamma}$	Solid	-
Iron monosulfide	FeS	Solid	-
Pyrite	FeS_2	Solid	-
Siderite	$FeCO_3$	Solid	-
Elemental sulfur	S_0	Solid	-
Iron-oxide-bound phosphorous	$Fe_{ox}P$	Solid	-
Vivianite	$Fe_3(PO_4)_2$	Solid	-
Organic phosphorous	P_{org}	Solid	-
Authigenic (Ca) phosphorous	$P_{authi,Ca-P}$	Solid	-
Detrital phosphorous	P_{Detr}	Solid	-
Chloride	Cl^-	Solute	1.23×10^{-9}
Oxygen	O_2	Solute	1.42×10^{-9}
Sulfate	SO_4^{2-}	Solute	6.49×10^{-10}
Manganese	Mn^{2+}	Solute	4.17×10^{-10}
Iron	Fe^{2+}	Solute	4.36×10^{-10}
Hydrogen sulfide[b]	ΣH_2S	Solute	1.33×10^{-9}
Methane	CH_4	Solute	1.12×10^{-9}
Ammonium[b]	ΣNH_4^+	Solute	1.20×10^{-9}
Nitrate	NO_3^-	Solute	1.15×10^{-9}
Phosphate	ΣHPO_4^{2-}	Solute	4.45×10^{-10}
Dissolved inorganic carbon	DIC	Solute	7.15×10^{-10}

[a] α, β and γ denote highly reactive, less reactive and nonreactive pools, respectively.

[b] Σ denotes all the species and aqueous complexes.

[c] Aqueous diffusion coefficient values are taken from Cussler (2009) and Lasaga (1989), and corrected for temperature and viscosity at 8°C.

Table S6. Boundary condition at the sediment-water interface (SWI).

Flux/Concentration[a]	**Unit**	**Pockmark B**	**Pockmark D**	**Pockmark E**
OM^{α}	mol $m^{-2}s^{-1}$	8.22×10^{-16}	8.22×10^{-16}	1.14×10^{-6}
OM^{β}	mol $m^{-2}s^{-1}$	3.29×10^{-15}	3.29×10^{-15}	7.12×10^{-7}
OM^{γ}	mol $m^{-2}s^{-1}$	1.65×10^{-13}	1.46×10^{-13}	1.58×10^{-8}
$Fe(OH)_3^{\alpha}$	mol $m^{-2}s^{-1}$	0	0	0
$Fe(OH)_3^{\beta}$	mol $m^{-2}s^{-1}$	0	0	0
$Fe(OH)_3^{\gamma}$	mol $m^{-2}s^{-1}$	1.01×10^{-13}	1.01×10^{-13}	3.20×10^{-7}
MnO_2^{α}	mol $m^{-2}s^{-1}$	8.62×10^{-19}	8.62×10^{-20}	3.95×10^{-13}
MnO_2^{β}	mol $m^{-2}s^{-1}$	8.62×10^{-19}	8.62×10^{-20}	3.95×10^{-13}
MnO_2^{γ}	mol $m^{-2}s^{-1}$	2.33×10^{-15}	2.33×10^{-15}	2.69×10^{-9}
FeS	mol $m^{-2}s^{-1}$	0	0	0
FeS_2	mol $m^{-2}s^{-1}$	0	0	0
$FeCO_3$	mol $m^{-2}s^{-1}$	0	0	0
S_0	mol $m^{-2}s^{-1}$	0	0	0
$Fe_{ox}P$	mol $m^{-2}s^{-1}$	3.05×10^{-18}	3.05×10^{-18}	4.39×10^{-12}
$Fe_3(PO_4)_2$	mol $m^{-2}s^{-1}$	0	0	0
P_{org}	mol $m^{-2}s^{-1}$	0	0	0
$P_{authi,Ca-P}$	mol $m^{-2}s^{-1}$	0	0	0
P_{Detr}	mol $m^{-2}s^{-1}$	5.42×10^{-18}	5.42×10^{-18}	7.80×10^{-12}
Cl^-	mM	101.55	101.55	98.73
O_2	mM	0.0018	0.0018	0.18
SO_4^{2-}	mM	4.62	4	4
Mn^{2+}	mM	10^{-10}	10^{-10}	10^{-10}
Fe^{2+}	mM	7.16×10^{-4}	7.16×10^{-4}	7.16×10^{-4}
ΣH_2S	mM	10^{-10}	10^{-10}	10^{-10}
CH_4	mM	3.64×10^{-7}	3.64×10^{-7}	0.024
ΣNH_4^+	mM	10^{-10}	10^{-10}	10^{-10}
NO_3^-	mM	0.012	0.012	0.01
ΣHPO_4^{2-}	mM	10^{-10}	10^{-10}	10^{-10}
DIC	mM	1	0.3	2

[a] Fluxes were used for the solid species, whereas the concentrations were used for the dissolved species.

Table S7. Reaction rate expressions used in the reactive transport model.

Primary redox reactions	
$R1$	$R_1 = k_{\alpha,\beta}\mathrm{OM}^{\alpha,\beta}\left(\frac{[\mathrm{O_2}]}{K_{\mathrm{O_2}}+[\mathrm{O_2}]}\right)$
$R2$	$R_2 = k_{\alpha,\beta}\mathrm{OM}^{\alpha,\beta}\left(\frac{[\mathrm{NO_3^-}]}{K_{\mathrm{NO_3^-}}+[\mathrm{NO_3^-}]}\right)\left(\frac{[\mathrm{O_2}]}{K_{\mathrm{O_2}}+[\mathrm{O_2}]}\right)$
$R3$	$R_3 = k_{\alpha,\beta}\mathrm{OM}^{\alpha,\beta}\left(\frac{[\mathrm{MnO_2^\alpha}]}{K_{\mathrm{MnO_2^\alpha}}+[\mathrm{MnO_2^\alpha}]}\right)\left(\frac{[\mathrm{NO_3^-}]}{K_{\mathrm{NO_3^-}}+[\mathrm{NO_3^-}]}\right)\left(\frac{[\mathrm{O_2}]}{K_{\mathrm{O_2}}+[\mathrm{O_2}]}\right)$
$R4$	$R_4 = k_{\alpha,\beta}\mathrm{OM}^{\alpha,\beta}\left(\frac{[\mathrm{Fe(OH)_3^\alpha}]}{K_{\mathrm{Fe(OH)_3^\alpha}}+[\mathrm{Fe(OH)_3^\alpha}]}\right)\left(\frac{[\mathrm{MnO_2^\alpha}]}{K_{\mathrm{MnO_2^\alpha}}+[\mathrm{MnO_2^\alpha}]}\right)\left(\frac{[\mathrm{NO_3^-}]}{K_{\mathrm{NO_3^-}}+[\mathrm{NO_3^-}]}\right)\left(\frac{[\mathrm{O_2}]}{K_{\mathrm{O_2}}+[\mathrm{O_2}]}\right)$
$R5$	$R_5 = \Psi k_{\alpha,\beta}\mathrm{OM}^{\alpha,\beta}\left(\frac{[\mathrm{SO_4^{2-}}]}{K_{\mathrm{SO_4^{2-}}}+[\mathrm{SO_4^{2-}}]}\right)\left(\frac{[\mathrm{Fe(OH)_3^\alpha}]}{K_{\mathrm{Fe(OH)_3^\alpha}}+[\mathrm{Fe(OH)_3^\alpha}]}\right)\left(\frac{[\mathrm{MnO_2^\alpha}]}{K_{\mathrm{MnO_2^\alpha}}+[\mathrm{MnO_2^\alpha}]}\right)\left(\frac{[\mathrm{NO_3^-}]}{K_{\mathrm{NO_3^-}}+[\mathrm{NO_3^-}]}\right)\left(\frac{[\mathrm{O_2}]}{K_{\mathrm{O_2}}+[\mathrm{O_2}]}\right)$
$R6$	$R_6 = \Psi k_{\alpha,\beta}\mathrm{OM}^{\alpha,\beta}\left(\frac{[\mathrm{SO_4^{2-}}]}{K_{\mathrm{SO_4^{2-}}}+[\mathrm{SO_4^{2-}}]}\right)\left(\frac{[\mathrm{Fe(OH)_3^\alpha}]}{K_{\mathrm{Fe(OH)_3^\alpha}}+[\mathrm{Fe(OH)_3^\alpha}]}\right)\left(\frac{[\mathrm{MnO_2^\alpha}]}{K_{\mathrm{MnO_2^\alpha}}+[\mathrm{MnO_2^\alpha}]}\right)\left(\frac{[\mathrm{NO_3^-}]}{K_{\mathrm{NO_3^-}}+[\mathrm{NO_3^-}]}\right)\left(\frac{[\mathrm{O_2}]}{K_{\mathrm{O_2}}+[\mathrm{O_2}]}\right)$
$R7$	$R_7 = k_1\mathrm{DIC}\left(\frac{[\mathrm{SO_4^{2-}}]}{K_{\mathrm{SO_4^{2-}}}+[\mathrm{SO_4^{2-}}]}\right)\left(\frac{[\mathrm{Fe(OH)_3^\alpha}]}{K_{\mathrm{Fe(OH)_3^\alpha}}+[\mathrm{Fe(OH)_3^\alpha}]}\right)\left(\frac{[\mathrm{MnO_2^\alpha}]}{K_{\mathrm{MnO_2^\alpha}}+[\mathrm{MnO_2^\alpha}]}\right)\left(\frac{[\mathrm{NO_3^-}]}{K_{\mathrm{NO_3^-}}+[\mathrm{NO_3^-}]}\right)\left(\frac{[\mathrm{O_2}]}{K_{\mathrm{O_2}}+[\mathrm{O_2}]}\right)$
Secondary redox and other reactions	
$R8$	$R_8 = k_2[\mathrm{O_2}][\mathrm{NH_4^+}]$
$R9$	$R_9 = k_3[\mathrm{O_2}][\mathrm{Mn^{2+}}]$
$R10$	$R_{10} = k_4[\mathrm{O_2}][\mathrm{Fe^{2+}}]$
$R11$	$R_{11} = k_5[\mathrm{O_2}][\mathrm{FeS}]$
$R12$	$R_{12} = k_6[\mathrm{O_2}][\mathrm{FeS_2}]$
$R13$	$R_{13} = k_7[\mathrm{O_2}][\Sigma\mathrm{H_2S}]$
$R14$	$R_{14} = k_8[\mathrm{O_2}][\mathrm{CH_4}]$
$R15$	$R_{15} = k_9[\mathrm{MnO_2^{\alpha,\beta}}][\mathrm{Fe^{2+}}]$
$R16$	$R_{16} = k_{10}[\mathrm{MnO_2^{\alpha,\beta}}][\Sigma\mathrm{H_2S}]$
$R17$	$R_{17} = k_{11}[\mathrm{Fe(OH)_3^\alpha}][\Sigma\mathrm{H_2S}]$
$R18$	$R_{18} = k_{12}[\mathrm{Fe(OH)_3^\beta}][\Sigma\mathrm{H_2S}]$
$R19$	$R_{19} = k_{13}[\mathrm{Fe^{2+}}][\Sigma\mathrm{H_2S}]$
$R20$	$R_{20} = k_{14}[\mathrm{FeS}][\Sigma\mathrm{H_2S}]$
$R21$	$R_{21} = k_{15}[\mathrm{S_0}]$
$R22$	$R_{22} = k_{16}[\mathrm{FeS}][\mathrm{S_0}]$
$R23$	$R_{23} = k_{17}[\mathrm{SO_4^{2-}}][\mathrm{CH_4}]$
$R24$	$R_{24} = k_{18}[\mathrm{Fe(OH)_3^{\alpha,\beta}}][\mathrm{CH_4}]$
$R25$	$R_{25} = k_{19}[\mathrm{Fe(OH)_3^\alpha}]$
$R26$	$R_{26} = k_{20}[\mathrm{Fe(OH)_3^\beta}]$
$R27$	$R_{27} = k_{21}[\mathrm{MnO_2^\alpha}]$
$R28$	$R_{28} = k_{22}[\mathrm{MnO_2^\beta}]$
$R29$	$R_{29} = k_{23}[\mathrm{Fe^{2+}}][\mathrm{HPO_4^{2-}}]$
$R30$	$R_{30} = k_{24}[\mathrm{Fe^{2+}}][DIC]$
$R31$	$R_{31} = k_{25}[\mathrm{FeCO_3}][\Sigma\mathrm{H_2S}]$
$R32$	$R_{32} = k_{26}[\mathrm{Fe_3(PO_4)_2}][\Sigma\mathrm{H_2S}]$

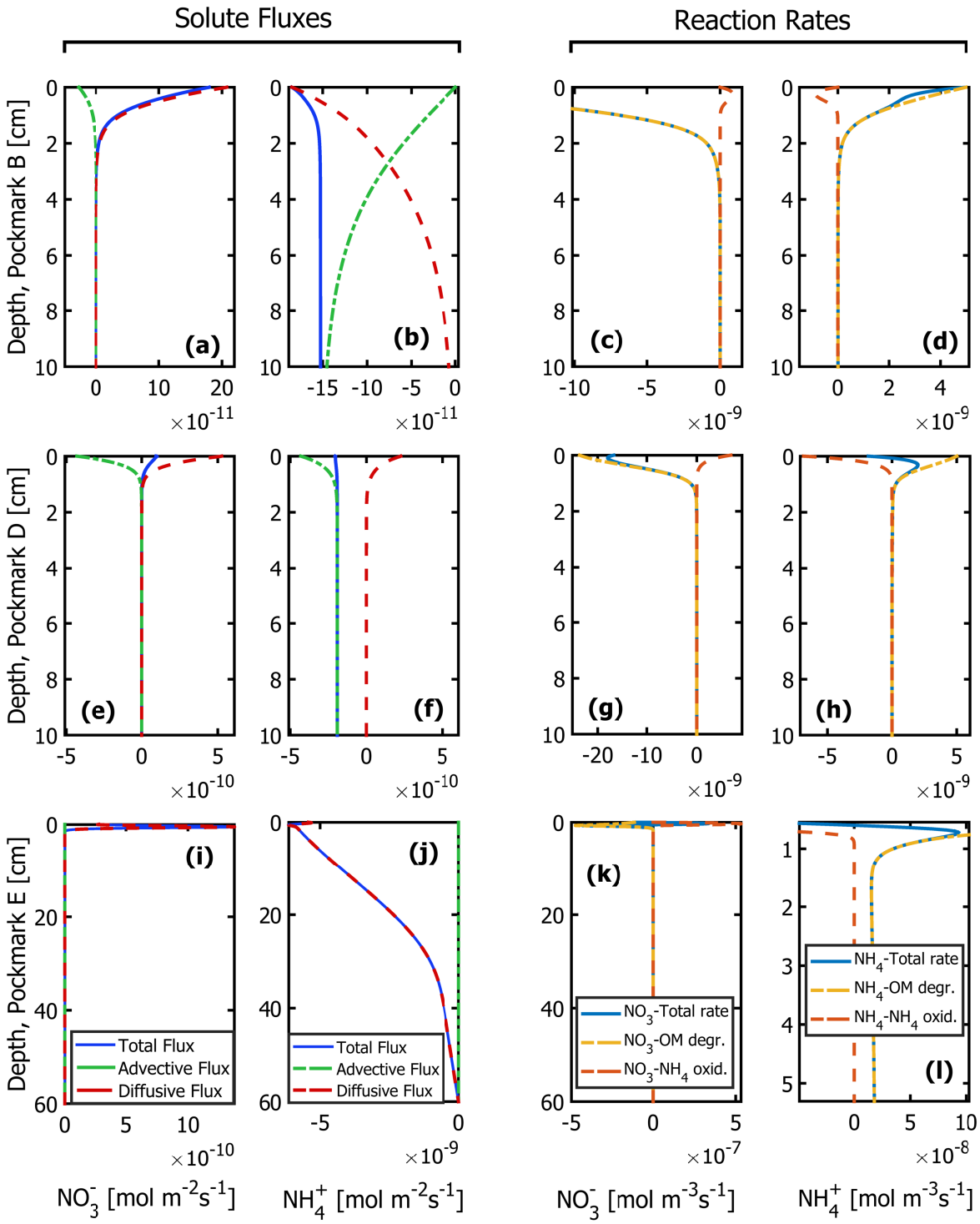

Figure S6. Modeled flux components (left two column panels) and reaction rates (right two column panels) of NO_3^- (first and third column panels) and NH_4^+ (second and fourth column panels) at sites B (a-d), D (e-h) and E (i-l): modeled rates of NO_3^- consumption, NH_4^+ production and NH_4^+ consumption by different processes in the reaction network. OM = coupled to remineralization of organic matter; NH_4^+ = oxidation of NH_4^+.

Table S8. Reaction parameters used in the reactive transport simulations.

Parameter	Unit	Pockmark B	Pockmark D	Pockmark E	Literature value
k_α	a^{-1}	0.05	0.05	0.05	0.05—1.62
k_β	a^{-1}	0.0086	0.0086	0.0086	0.0086
K_{O_2}	mM	0.02	0.02	0.02	0.001—0.03
$K_{NO_3^-}$	mM	0.004	0.004	0.004	0.004—0.08
K_{MnO_2}	μmol g^{-1}	4	4	4	4
$K_{Fe(OH)_3}$	μ mol g^{-1}	65	65	65	65—100
$K_{SO_4^{2-}}$	mM	1.6	1.6	1.6	1.6
Ψ	-	0.0042	0.0084	0.0042	0.00157—0.075
k_1	$mM^{-1}a^{-1}$	0.0011	0.0011	0.0011	0.0011
k_2	$mM^{-1}a^{-1}$	10^4	10^4	10^4	5×10^3—3.9×10^4
k_3	$mM^{-1}a^{-1}$	10^4	10^4	10^4	10^4
k_4	$mM^{-1}a^{-1}$	1.4×10^5	1.4×10^5	1.4×10^5	1.4×10^5
k_5	$mM^{-1}a^{-1}$	300	300	300	300
k_6	$mM^{-1}a^{-1}$	1	1	1	1
k_7	$mM^{-1}a^{-1}$	160	160	160	$\geq$160
k_8	$mM^{-1}a^{-1}$	2×10^7	1×10^7	2×10^7	1×10^7
k_9	$mM^{-1}a^{-1}$	2	2	2	2
k_{10}	$mM^{-1}a^{-1}$	20	20	20	20
k_{11}	$mM^{-1}a^{-1}$	9.5	9.5	9.5	$\leq$100
k_{12}	$mM^{-1}a^{-1}$	0.95	0.95	0.95	0.95
k_{13}	$mM^{-1}a^{-1}$	1.2×10^4	1.2×10^4	2.25×10^3	1×10^2—1.48×10^4
k_{14}	$mM^{-1}a^{-1}$	3×10^{-4}	3×10^{-4}	3×10^{-4}	3.15
k_{15}	a^{-1}	3	3	3	3
k_{16}	$mM^{-1}a^{-1}$	1	1	1	7
k_{17}	$mM^{-1}a^{-1}$	14	14	0.14	10
k_{18}	$mM^{-1}a^{-1}$	0.48	0.024	8.8×10^{-6}	0.0074
k_{19}	a^{-1}	0.6	0.6	0.6	0.6
k_{20}	a^{-1}	1.3×10^{-5}	1.3×10^{-5}	1.3×10^{-5}	Model constrained
k_{21}	a^{-1}	1.8	1.8	1.8	1.8
k_{22}	a^{-1}	1.8×10^{-3}	1.8×10^{-3}	1.8×10^{-3}	1.8×10^{-3}
k_{23}	$mM^{-1}a^{-1}$	1.04	0.052	5.2×10^{-3}	Model constrained
k_{24}	$mM^{-1}a^{-1}$	0.135	0.122	2.7×10^{-4}	Model constrained
k_{25}	$mM^{-1}a^{-1}$	8×10^{-4}	8×10^{-4}	8×10^{-4}	Model constrained
k_{26}	$mM^{-1}a^{-1}$	8×10^{-4}	8×10^{-4}	8×10^{-4}	Model constrained

References

Bomberg M., Nyyssönen M., Pitkänen P., Lehtinen A. and Itävaara M. (2015) Active Microbial Communities Inhabit Sulphate-Methane Interphase in Deep Bedrock Fracture Fluids in Olkiluoto, Finland. *Biomed Res. Int. 2015*

Boudreau B. P. (1997) *Diagenetic Models and their Implementation: Modelling Transport and Reactions in Aquatic Sediments.* Springer-Verlag, Heidelberg.

Cheng Y. S., Halsey J. L., Fode K. A., Remsen C. C. and Collins M. L. (1999) Detection of methanotrophs in groundwater by PCR. *Appl. Environ. Microbiol.* **65**, 648–651.

Cussler E. L. (2009) *Diffusion: Mass Transfer in Fluid Systems*, third ed. Cambridge University Press, New York, USA.

Geets J., Borremans B., Diels L., Springael D., Vangronsveld J., Van Der Lelie D. and Vanbroekhoven K. (2006) DsrB gene-based DGGE for community and diversity surveys of sulfate-reducing bacteria. *J. Microbiol. Methods* **66**, 194–205.

Hales B. A., Edwards C., Ritchie D. A., Hall G., Pickup R. W. and Saunders J. R. (1996) Isolation and identification of methanogen-specific dna from blanket bog feat by pcr amplification and sequence-analysis. *Appl. Environ. Microbiol.* **62**, 668–675.

Klindworth A., Pruesse E., Schweer T., Peplies J., Quast C., Horn M., Glöckner F. O., Klindworth A., Pruesse E., Schweer T., Horn M. and Glo F. O. (2013) Evaluation of general 16S ribosomal RNA gene PCR primers for classical and next-generation sequencing-based diversity studies. *Nucleic Acids Res.* **41**, 1–11.

Lasaga A. C. (1998) *Kinetic Theory in the Earth Sciences*. Princeton University Press, Princeton, New Jersey.

López-Gutiérrez J. C., Henry S., Hallet S., Martin-Laurent F., Catroux G. and Philippot L. (2004) Quantification of a novel group of nitrate-reducing bacteria in the environment by real-time PCR. *J. Microbiol. Methods* **57**, 399–407.

Oehler T., Mogollón J.M., Moosdorf N., Winkler A., Kopf A., Pichler T. (2017) Submarine groundwater discharge within a landslide scar at the French Mediterranean coast. *Estuar. Coast Shelf Sci.* **198**,128–137.

Rotthauwe J.-H. H., Witzel K.-P. P. and Liesack W. (1997) The ammonia monooxygenase structural gene amoA as a functional marker: molecular fine-scale analysis of natural ammonia-oxidizing populations. *Appl. Environ. Microbiol.* **63**, 4704–4712.

Schlüter M., Sauter E. J., Andersen C. E., Dahlgaard H. and Dando P. R. (2004) Spatial distribution and budget for submarine groundwater discharge in Eckernförde Bay (western Baltic Sea). *Limnol. Oceanogr.* **49**, 157–167.

Stephen J. R., Chang Y. J., Macnaughton S. J., Kowalchuk G. A., Leung K. T., Flemming C. A. and White D. C. (1999) Effect of toxic metals on indigenous soil -subgroup proteobacterium ammonia oxidizer community structure and protection against toxicity by inoculated metal-resistant bacteria. *Appl. Environ. Microbiol.*

Wagner M., Roger A. J., Flax J. L., Brusseau G. A. and Stahl D. A. (1998) Phylogeny of dissimilatory sulfite reductases supports an early origin of sulfate respiration. *J. Bacteriol.* **180**, 2975–2982.

Suplementary Material published together with the article: **"Spatial and temporal variations in the isotope hydrobiogeochemistry of a managed river draining towards the southern Baltic Sea" – Chapter 5**

Supplementary Material for

Spatial and temporal variations in the isotope hydrobiogeochemistry of a managed river draining towards the southern Baltic Sea

Cátia Milene Ehlert von Ahn[1], Michael Ernst Böttcher*[1,2,3], Christoph Malik[1,4], Julia Westphal[1,5], Benjamin Rach[1,6], Carla Nantke[1], Anna-Kathrina Jenner[1], Rhodelyn Saban[1], Vera Winde[1,7], Iris Schmiedinger[1]

[1]Geochemistry & Isotope Biogeochemistry, Leibniz Institute for Baltic Sea Research (IOW), D-18119 Warnemünde, Germany

[2]Marine Geochemistry, University of Greifswald, D- 17489, Germany

[3]Interdisciplinary Faculty, University of Rostock, D- 18055, Germany

[4]present address: Umweltplan, D-17489 Greifswald, Germany

[5]present address: National Agency of Agriculture and the Environment of Mecklenburg-Western Pomerania (Stalu-MM), D-18069 Rostock, Germany

[6]present address: Bioplan, Institute of Applied Biology and Landscape Management, D-18211 Nienhagen, Germany

[7]present address: Hydroisotop, D-85301 Schweitenkirchen, Germany

* michael.boettcher@io-warnemuende.de

Contents

Introduction

This document presents additional figures and tables obtained from the present study which helped to discuss the results.

Supplementary Figure

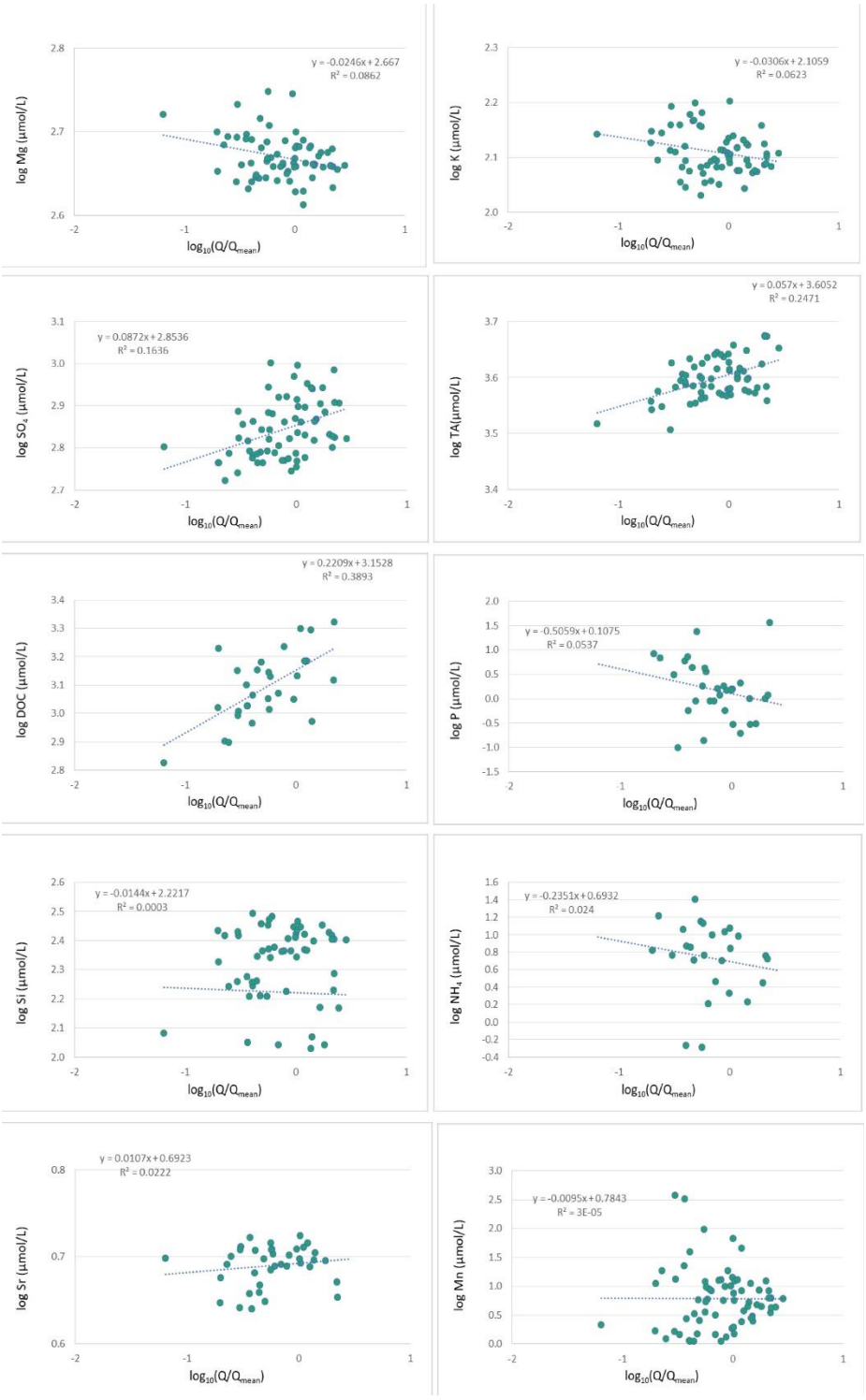

Supplementary Figure 1 - Variations of selected hydrogeochemical variables at the Rostock weir as a function of normalized discharge (log-log plot). Mean discharge at the end of the Middle Warnow is 12.3 m3/s (Bitschovsky & Nausch, 2019).

Supplementary Tables

Supplementary Table 1 - Discharge data from the period of the temporal investigation of this study (2017 to 2021). Data obtained from: by the National Agency of Agriculture and the Environment of Mecklenburg-Western Pomerania (Stalu-MM), Rostock, Germany.

Date	Q (m^3/s)	Date	Q (m^3/s)	Date	Q (m^3/s)	Date	Q (m^3/s)	Date	Q (m^3/s)	Date	Q (m^3/s)	Date	Q (m^3/s)	Date	Q (m^3/s)	Date	Q (m^3/s)	Date	Q (m^3/s)	Date	Q (m^3/s)	Date	Q (m^3/s)	Date	Q (m^3/s)
1/1/17	12.0	05/22/17	10.6	10/10/17	37.8	2/28/18	15.4	7/19/18	4.27	12/7/18	5.53	4/27/19	6.47	9/15/19	3.60	2/3/20	19.0	6/23/20	n.d.	11/11/20	6.51	4/1/21	12.6	8/20/21	4.04
1/2/17	9.87	05/23/17	10.3	10/11/17	34.0	3/1/18	15.1	7/20/18	3.42	12/8/18	4.54	4/28/19	5.51	9/16/19	2.75	2/4/20	10.9	6/24/20	n.d.	11/12/20	6.42	4/2/21	17.3	8/21/21	4.77
1/3/17	21.2	05/24/17	11.5	10/12/17	32.5	3/2/18	30.9	7/21/18	5.18	12/9/18	5.07	4/29/19	6.89	9/17/19	3.05	2/5/20	25.9	6/25/20	n.d.	11/13/20	6.78	4/3/21	16.0	8/22/21	4.05
1/4/17	7.65	05/25/17	10.7	10/13/17	25.5	3/3/18	22.7	7/22/18	1.80	12/10/18	7.41	4/30/19	6.89	9/18/19	1.71	2/6/20	14.7	6/26/20	n.d.	11/14/20	6.69	4/4/21	18.9	8/23/21	4.02
1/5/17	5.83	05/26/17	10.7	10/14/17	32.9	3/4/18	20.0	7/23/18	4.72	12/11/18	0.445	5/1/19	6.45	9/19/19	4.65	2/7/20	24.1	6/27/20	n.d.	11/15/20	6.87	4/5/21	9.53	8/24/21	4.96
1/6/17	32.7	05/27/17	9.93	10/15/17	27.4	3/5/18	19.6	7/24/18	3.46	12/12/18	6.29	5/2/19	5.24	9/20/19	4.29	2/8/20	21.8	6/28/20	n.d.	11/16/20	5.45	4/6/21	15.0	8/25/21	3.82
1/7/17	20.7	05/28/17	8.89	10/16/17	27.1	3/6/18	18.6	7/25/18	3.67	12/13/18	8.73	5/3/19	6.34	9/21/19	2.93	2/9/20	19.0	6/29/20	n.d.	11/17/20	7.36	4/7/21	13.7	8/26/21	0.683
1/8/17	14.9	05/29/17	6.59	10/17/17	25.5	3/7/18	20.2	7/26/18	4.02	12/14/18	9.96	5/4/19	3.83	9/22/19	2.21	2/10/20	19.6	6/30/20	n.d.	11/18/20	6.07	4/8/21	12.8	8/27/21	n.d.
1/9/17	18.7	05/30/17	10.4	10/18/17	17.9	3/8/18	21.4	7/27/18	2.58	12/15/18	5.89	5/5/19	6.57	9/23/19	1.98	2/11/20	24.1	7/1/20	n.d.	11/19/20	6.53	4/9/21	16.9	8/28/21	n.d.
1/10/17	16.6	05/31/17	8.04	10/19/17	24.8	3/9/18	24.8	7/28/18	3.14	12/16/18	4.60	5/6/19	5.50	9/24/19	4.00	2/12/20	29.5	7/2/20	n.d.	11/20/20	2.22	4/10/21	14.5	8/29/21	n.d.
1/11/17	16.0	06/01/17	8.56	10/20/17	20.7	3/10/18	26.9	7/29/18	2.51	12/17/18	5.35	5/7/19	4.27	9/25/19	2.06	2/13/20	27.1	7/3/20	n.d.	11/21/20	10.2	4/11/21	8.13	8/30/21	n.d.
1/12/17	15.9	06/02/17	8.15	10/21/17	23.0	3/11/18	26.9	7/30/18	1.65	12/18/18	4.98	5/8/19	3.54	9/26/19	4.51	2/14/20	30.9	7/4/20	n.d.	11/22/20	5.90	4/12/21	23.6	8/31/21	2.69
1/13/17	16.9	06/03/17	7.19	10/22/17	22.0	3/12/18	29.2	7/31/18	2.16	12/19/18	5.01	5/9/19	5.75	9/27/19	2.87	2/15/20	40.7	7/5/20	n.d.	11/23/20	6.97	4/13/21	n.d.	9/1/21	8.07
1/14/17	15.3	06/04/17	7.84	10/23/17	15.7	3/13/18	37.3	8/1/18	3.30	12/20/18	4.66	5/10/19	5.12	9/28/19	3.56	2/16/20	34.3	7/6/20	n.d.	11/24/20	6.35	4/14/21	15.5	9/2/21	6.77
1/15/17	15.4	06/05/17	7.20	10/24/17	27.1	3/14/18	39.0	8/2/18	2.71	12/21/18	5.00	5/11/19	7.02	9/29/19	4.24	2/17/20	33.1	7/7/20	n.d.	11/25/20	5.98	4/15/21	11.1	9/3/21	4.94
1/16/17	25.2	06/06/17	6.62	10/25/17	24.5	3/15/18	38.2	8/3/18	0.780	12/22/18	7.02	5/12/19	5.64	9/30/19	4.90	2/18/20	30.2	7/8/20	n.d.	11/26/20	4.90	4/16/21	14.6	9/4/21	7.42
1/17/17	26.1	06/07/17	8.59	10/26/17	24.1	3/16/18	26.6	8/4/18	3.75	12/23/18	6.97	5/13/19	7.18	10/1/19	5.39	2/19/20	23.4	7/9/20	n.d.	11/27/20	3.35	4/17/21	15.0	9/5/21	5.23
1/18/17	19.2	06/08/17	6.74	10/27/17	12.7	3/17/18	37.6	8/5/18	1.28	12/24/18	7.50	5/14/19	5.49	10/2/19	7.02	2/20/20	27.1	7/10/20	n.d.	11/28/20	4.84	4/18/21	16.3	9/6/21	5.48
1/19/17	17.7	06/09/17	8.06	10/28/17	32.0	3/18/18	44.8	8/6/18	2.60	12/25/18	6.40	5/15/19	5.14	10/3/19	3.77	2/21/20	26.2	7/11/20	n.d.	11/29/20	8.82	4/19/21	13.5	9/7/21	5.59
1/20/17	17.6	06/10/17	8.83	10/29/17	3.09	3/19/18	36.2	8/7/18	0.033	12/26/18	6.92	5/16/19	1.43	10/4/19	10.5	2/22/20	27.0	7/12/20	n.d.	11/30/20	9.54	4/20/21	13.2	9/8/21	5.12
1/21/17	17.1	06/11/17	8.56	10/30/17	17.6	3/20/18	26.9	8/8/18	1.31	12/27/18	6.53	5/17/19	6.54	10/5/19	2.12	2/23/20	17.3	7/13/20	n.d.	12/1/20	3.71	4/21/21	12.5	9/9/21	4.97
1/22/17	18.7	06/12/17	7.65	10/31/17	43.5	3/21/18	32.6	8/9/18	0.718	12/28/18	7.35	5/18/19	7.25	10/6/19	12.3	2/24/20	22.8	7/14/20	n.d.	12/2/20	8.26	4/22/21	8.41	9/10/21	4.17
1/23/17	18.9	06/13/17	5.77	11/1/17	31.2	3/22/18	29.2	8/10/18	3.49	12/29/18	7.15	5/19/19	9.78	10/7/19	6.58	2/25/20	34.2	7/15/20	n.d.	12/3/20	7.35	4/23/21	14.7	9/11/21	5.40
1/24/17	18.2	06/14/17	7.56	11/2/17	26.2	3/23/18	29.8	8/11/18	0.112	12/30/18	4.37	5/20/19	6.28	10/8/19	5.88	2/26/20	14.6	7/16/20	n.d.	12/4/20	6.12	4/24/21	11.6	9/12/21	6.31

1/25/17	18.2	06/15/17	5.86	11/3/17	29.3	3/24/18	30.1	8/12/18	1.75	12/31/18	11.1	5/21/19	6.64	10/9/19	6.88	2/27/20	35.9	7/17/20	n.d.	12/5/20	6.29	4/25/21	9.24	9/13/21	5.67
1/26/17	17.7	06/16/17	6.29	11/4/17	32.9	3/25/18	29.5	8/13/18	1.04	1/1/19	6.86	5/22/19	5.57	10/10/19	5.36	2/28/20	33.5	7/18/20	n.d.	12/6/20	4.32	4/26/21	11.9	9/14/21	5.66
1/27/17	17.4	06/17/17	6.83	11/5/17	27.4	3/26/18	28.4	8/14/18	1.63	1/2/19	n.d.	5/23/19	5.10	10/11/19	6.74	2/29/20	34.2	7/19/20	n.d.	12/7/20	8.52	4/27/21	9.55	9/15/21	5.55
1/28/17	16.8	06/18/17	7.67	11/6/17	31.3	3/27/18	27.2	8/15/18	2.79	1/3/19	11.4	5/24/19	5.10	10/12/19	5.20	3/1/20	33.6	7/20/20	n.d.	12/8/20	5.88	4/28/21	9.07	9/16/21	6.29
1/29/17	16.2	06/19/17	6.87	11/7/17	30.1	3/28/18	26.0	8/16/18	1.87	1/4/19	12.3	5/25/19	3.28	10/13/19	6.16	3/2/20	24.9	7/21/20	5.20	12/9/20	7.07	4/29/21	5.89	9/17/21	5.37
1/30/17	14.9	06/20/17	4.60	11/8/17	30.9	3/29/18	22.4	8/17/18	1.61	1/5/19	4.45	5/26/19	3.98	10/14/19	6.22	3/3/20	27.6	7/22/20	4.90	12/10/20	6.52	4/30/21	13.5	9/18/21	9.49
1/31/17	16.6	06/21/17	7.86	11/9/17	31.3	3/30/18	33.6	8/18/18	2.19	1/6/19	10.8	5/27/19	4.60	10/15/19	6.31	3/4/20	35.9	7/23/20	5.53	12/11/20	5.48	5/1/21	9.94	9/19/21	7.53
2/1/17	19.3	06/22/17	5.02	11/10/17	27.4	3/31/18	31.7	8/19/18	1.06	1/7/19	7.50	5/28/19	3.14	10/16/19	10.4	3/5/20	27.9	7/24/20	4.73	12/12/20	7.04	5/2/21	10.6	9/20/21	7.69
2/2/17	17.6	06/23/17	7.90	11/11/17	29.3	4/1/18	29.4	8/20/18	1.48	1/8/19	4.74	5/29/19	4.91	10/17/19	8.50	3/6/20	14.7	7/25/20	3.74	12/13/20	6.67	5/3/21	11.1	9/21/21	6.04
2/3/17	17.7	06/24/17	7.03	11/12/17	23.3	4/2/18	38.9	8/21/18	2.51	1/9/19	n.d.	5/30/19	3.16	10/18/19	8.15	3/7/20	35.4	7/26/20	4.64	12/14/20	6.04	5/4/21	11.1	9/22/21	6.68
2/4/17	18.1	06/25/17	6.58	11/13/17	19.6	4/3/18	43.7	8/22/18	1.04	1/10/19	26.1	5/31/19	3.44	10/19/19	7.81	3/8/20	33.2	7/27/20	3.92	12/15/20	6.25	5/5/21	11.3	9/23/21	6.35
2/5/17	18.9	06/26/17	5.94	11/14/17	34.6	4/4/18	53.2	8/23/18	1.22	1/11/19	12.8	6/1/19	7.53	10/20/19	7.57	3/9/20	27.4	7/28/20	4.49	12/16/20	5.98	5/6/21	10.9	9/24/21	6.73
2/6/17	21.8	06/27/17	3.48	11/15/17	27.4	4/5/18	58.6	8/24/18	2.56	1/12/19	13.9	6/2/19	4.78	10/21/19	3.53	3/10/20	28.4	7/29/20	4.23	12/17/20	6.07	5/7/21	11.5	9/25/21	5.64
2/7/17	19.8	06/28/17	3.39	11/16/17	27.9	4/6/18	61.0	8/25/18	0.050	1/13/19	10.6	6/3/19	21.9	10/22/19	6.60	3/11/20	29.1	7/30/20	4.18	12/18/20	7.18	5/8/21	10.4	9/26/21	5.99
2/8/17	19.8	06/29/17	1.56	11/17/17	26.4	4/7/18	60.1	8/26/18	2.06	1/14/19	3.22	6/4/19	21.1	10/23/19	8.20	3/12/20	29.8	7/31/20	3.74	12/19/20	6.08	5/9/21	10.1	9/27/21	5.90
2/9/17	17.3	06/30/17	19.4	11/18/17	26.9	4/8/18	58.2	8/27/18	0.870	1/15/19	21.2	6/5/19	12.1	10/24/19	7.56	3/13/20	23.2	8/1/20	3.57	12/20/20	6.91	5/10/21	9.54	9/28/21	6.02
2/10/17	17.1	07/01/17	20.6	11/19/17	8.20	4/9/18	56.6	8/28/18	1.06	1/16/19	17.5	6/6/19	15.4	10/25/19	6.62	3/14/20	25.3	8/2/20	5.93	12/21/20	6.88	5/11/21	9.15	9/29/21	7.02
2/11/17	15.5	07/02/17	22.4	11/20/17	25.7	4/10/18	40.1	8/29/18	0.300	1/17/19	10.9	6/7/19	4.50	10/26/19	6.84	3/15/20	33.0	8/3/20	4.35	12/22/20	8.49	5/12/21	11.8	9/30/21	5.47
2/12/17	15.8	07/03/17	20.7	11/21/17	29.0	4/11/18	53.0	8/30/18	1.58	1/18/19	14.0	6/8/19	5.43	10/27/19	6.64	3/16/20	24.6	8/4/20	5.38	12/23/20	8.27	5/13/21	10.1	10/1/21	5.75
2/13/17	15.1	07/04/17	16.9	11/22/17	34.9	4/12/18	46.7	8/31/18	5.74	1/19/19	14.4	6/9/19	3.96	10/28/19	3.66	3/17/20	28.8	8/5/20	3.01	12/24/20	8.99	5/14/21	11.6	10/2/21	5.26
2/14/17	15.1	07/05/17	19.5	11/23/17	32.1	4/13/18	48.1	9/1/18	3.21	1/20/19	11.9	6/10/19	4.08	10/29/19	5.51	3/18/20	26.0	8/6/20	1.66	12/25/20	18.9	5/15/21	10.5	10/3/21	5.24
2/15/17	14.0	07/06/17	18.5	11/24/17	22.7	4/14/18	46.6	9/2/18	3.37	1/21/19	13.3	6/11/19	7.59	10/30/19	7.55	3/19/20	22.6	8/7/20	2.82	12/26/20	17.7	5/16/21	10.6	10/4/21	5.25
2/16/17	14.1	07/07/17	14.9	11/25/17	32.9	4/15/18	44.7	9/3/18	1.80	1/22/19	10.8	6/12/19	8.14	10/31/19	k.A.	3/20/20	16.6	8/8/20	4.83	12/27/20	14.3	5/17/21	8.28	10/5/21	7.63
2/17/17	14.2	07/08/17	14.5	11/26/17	33.3	4/16/18	42.8	9/4/18	4.85	1/23/19	6.94	6/13/19	8.46	11/1/19	6.21	3/21/20	22.0	8/9/20	4.26	12/28/20	13.0	5/18/21	10.7	10/6/21	8.02
2/18/17	14.4	07/09/17	12.8	11/27/17	29.5	4/17/18	41.0	9/5/18	3.55	1/24/19	13.7	6/14/19	7.67	11/2/19	6.78	3/22/20	24.7	8/10/20	2.75	12/29/20	13.8	5/19/21	11.4	10/7/21	7.78
2/19/17	14.3	07/10/17	11.3	11/28/17	29.5	4/18/18	38.4	9/6/18	1.55	1/25/19	10.8	6/15/19	6.93	11/3/19	7.13	3/23/20	22.1	8/11/20	2.54	12/30/20	12.7	5/20/21	11.7	10/8/21	8.17
2/20/17	15.3	07/11/17	15.5	11/29/17	24.9	4/19/18	37.7	9/7/18	3.46	1/26/19	9.41	6/16/19	6.19	11/4/19	3.07	3/24/20	19.6	8/12/20	2.34	12/31/20	13.5	5/21/21	11.6	10/9/21	8.72
2/21/17	16.0	07/12/17	10.9	11/30/17	22.6	4/20/18	35.5	9/8/18	0.606	1/27/19	10.3	6/17/19	6.31	11/5/19	7.61	3/25/20	18.6	8/13/20	2.55	1/1/21	12.8	5/22/21	11.1	10/10/21	6.65
2/22/17	17.9	07/13/17	14.8	12/1/17	17.2	4/21/18	33.4	9/9/18	3.23	1/28/19	9.92	6/18/19	5.83	11/6/19	21.4	3/26/20	17.6	8/14/20	3.68	1/2/21	12.8	5/23/21	10.7	10/11/21	11.0
2/23/17	18.3	07/14/17	16.0	12/2/17	37.9	4/22/18	31.1	9/10/18	0.982	1/29/19	12.1	6/19/19	8.18	11/7/19	14.8	3/27/20	17.2	8/15/20	3.02	1/3/21	7.49	5/24/21	9.89	10/12/21	5.11

2/24/17	18.8	07/15/17	14.8	12/3/17	28.7	4/23/18	29.6	9/11/18	2.74	1/30/19	11.1	6/20/19	6.50	11/8/19	13.1	3/28/20	16.2	8/16/20	1.32	1/4/21	11.8	5/25/21	9.54	10/13/21	10.0
2/25/17	29.3	07/16/17	14.4	12/4/17	17.7	4/24/18	16.9	9/12/18	1.27	1/31/19	11.4	6/21/19	5.09	11/9/19	12.5	3/29/20	6.24	8/17/20	1.00	1/5/21	11.5	5/26/21	9.28	10/14/21	8.30
2/26/17	27.0	07/17/17	13.3	12/5/17	29.3	4/25/18	32.7	9/13/18	2.79	2/1/19	10.2	6/22/19	3.84	11/10/19	11.0	3/30/20	19.8	8/18/20	3.12	1/6/21	17.6	5/27/21	10.4	10/15/21	7.38
2/27/17	27.5	07/18/17	12.2	12/6/17	26.0	4/26/18	30.6	9/14/18	2.69	2/2/19	9.65	6/23/19	6.68	11/11/19	10.1	3/31/20	20.7	8/19/20	3.60	1/7/21	19.1	5/28/21	10.7	10/16/21	7.80
2/28/17	26.7	07/19/17	10.3	12/7/17	25.7	4/27/18	28.6	9/15/18	0.968	2/3/19	11.4	6/24/19	2.63	11/12/19	10.4	4/1/20	17.3	8/20/20	1.95	1/8/21	17.7	5/29/21	10.5	10/17/21	6.45
3/1/17	25.5	07/20/17	12.5	12/8/17	26.5	4/28/18	26.9	9/16/18	2.84	2/4/19	11.3	6/25/19	6.07	11/13/19	9.97	4/2/20	16.1	8/21/20	3.39	1/9/21	17.6	5/30/21	10.0	10/18/21	7.70
3/2/17	25.0	07/21/17	13.9	12/9/17	30.1	4/29/18	26.1	9/17/18	1.11	2/5/19	8.95	6/26/19	6.01	11/14/19	9.42	4/3/20	14.2	8/22/20	2.25	1/10/21	16.5	5/31/21	9.63	10/19/21	8.86
3/3/17	24.3	07/22/17	11.6	12/10/17	26.8	4/30/18	18.6	9/18/18	3.04	2/6/19	10.5	6/27/19	3.57	11/15/19	4.65	4/4/20	16.2	8/23/20	2.07	1/11/21	16.0	6/1/21	9.50	10/20/21	7.91
3/4/17	21.2	07/23/17	15.3	12/11/17	8.72	5/1/18	28.9	9/19/18	0.751	2/7/19	9.45	6/28/19	3.44	11/16/19	14.0	4/5/20	14.5	8/24/20	2.82	1/12/21	16.3	6/2/21	7.95	10/21/21	4.92
3/5/17	23.5	07/24/17	12.9	12/12/17	33.8	5/2/18	23.7	9/20/18	2.60	2/8/19	9.66	6/29/19	4.36	11/17/19	8.88	4/6/20	15.2	8/25/20	2.69	1/13/21	15.1	6/3/21	6.47	10/22/21	k.A.
3/6/17	11.7	07/25/17	6.51	12/13/17	13.0	5/3/18	22.2	9/21/18	1.81	2/9/19	10.3	6/30/19	3.05	11/18/19	9.86	4/7/20	13.8	8/26/20	4.22	1/14/21	15.2	6/4/21	5.72	10/23/21	k.A.
3/7/17	33.2	07/26/17	30.8	12/14/17	43.1	5/4/18	21.1	9/22/18	1.06	2/10/19	10.4	7/1/19	1.67	11/19/19	9.21	4/8/20	13.5	8/27/20	3.68	1/15/21	25.8	6/5/21	6.04	10/24/21	19.3
3/8/17	29.1	07/27/17	25.3	12/15/17	37.7	5/5/18	20.0	9/23/18	2.06	2/11/19	9.22	7/2/19	1.69	11/20/19	9.84	4/9/20	13.1	8/28/20	4.57	1/16/21	24.7	6/6/21	6.39	10/25/21	12.4
3/9/17	24.9	07/28/17	25.2	12/16/17	32.8	5/6/18	19.1	9/24/18	0.281	2/12/19	16.9	7/3/19	2.31	11/21/19	9.74	4/10/20	12.6	8/29/20	3.52	1/17/21	19.9	6/7/21	6.14	10/26/21	10.9
3/10/17	24.5	07/29/17	25.4	12/17/17	35.1	5/7/18	18.6	9/25/18	5.01	2/13/19	12.8	7/4/19	0.475	11/22/19	10.6	4/11/20	12.2	8/30/20	4.54	1/18/21	17.8	6/8/21	4.78	10/27/21	10.9
3/11/17	24.2	07/30/17	26.1	12/18/17	41.2	5/8/18	17.6	9/26/18	3.99	2/14/19	12.3	7/5/19	1.24	11/23/19	10.9	4/12/20	11.4	8/31/20	4.06	1/19/21	18.3	6/9/21	4.84	10/28/21	6.97
3/12/17	22.8	07/31/17	25.4	12/19/17	29.6	5/9/18	17.1	9/27/18	1.85	2/15/19	11.5	7/6/19	3.42	11/24/19	11.5	4/13/20	9.60	9/1/20	3.78	1/20/21	21.7	6/10/21	4.26	10/29/21	11.4
3/13/17	22.1	08/01/17	25.1	12/20/17	37.8	5/10/18	17.0	9/28/18	1.17	2/16/19	11.2	7/7/19	0.338	11/25/19	10.8	4/14/20	11.6	9/2/20	4.53	1/21/21	23.6	6/11/21	4.69	10/30/21	8.18
3/14/17	21.9	08/02/17	25.1	12/21/17	26.6	5/11/18	16.3	9/29/18	3.87	2/17/19	10.8	7/8/19	0.936	11/26/19	10.2	4/15/20	12.2	9/3/20	3.47	1/22/21	23.5	6/12/21	3.68	10/31/21	9.23
3/15/17	20.9	08/03/17	23.4	12/22/17	30.9	5/12/18	16.1	9/30/18	2.06	2/18/19	10.8	7/9/19	3.12	11/27/19	10.1	4/16/20	11.2	9/4/20	3.35	1/23/21	24.0	6/13/21	3.50	11/1/21	8.16
3/16/17	20.4	08/04/17	24.4	12/23/17	35.2	5/13/18	15.0	10/1/18	n.d.	2/19/19	10.5	7/10/19	5.36	11/28/19	10.8	4/17/20	13.9	9/5/20	4.01	1/24/21	23.2	6/14/21	2.06	11/2/21	7.07
3/17/17	19.8	08/05/17	22.9	12/24/17	26.0	5/14/18	13.9	10/2/18	4.99	2/20/19	6.84	7/11/19	2.43	11/29/19	7.97	4/18/20	9.78	9/6/20	3.11	1/25/21	22.5	6/15/21	8.42	11/3/21	7.26
3/18/17	16.9	08/06/17	22.0	12/25/17	32.0	5/15/18	12.9	10/3/18	0.97	2/21/19	11.9	7/12/19	2.81	11/30/19	13.4	4/19/20	9.74	9/7/20	3.31	1/26/21	21.2	6/16/21	n.d.	11/4/21	2.48
3/19/17	21.5	08/07/17	21.3	12/26/17	27.9	5/16/18	11.6	10/4/18	4.56	2/22/19	10.3	7/13/19	6.12	12/1/19	10.8	4/20/20	9.04	9/8/20	3.10	1/27/21	21.2	6/17/21	3.12	11/5/21	9.85
3/20/17	25.4	08/08/17	15.3	12/27/17	17.4	5/17/18	8.11	10/5/18	1.97	2/23/19	11.9	7/14/19	2.05	12/2/19	10.1	4/21/20	8.56	9/9/20	2.97	1/28/21	19.5	6/18/21	1.33	11/6/21	19.0
3/21/17	29.8	08/09/17	21.0	12/28/17	29.3	5/18/18	9.87	10/6/18	0.040	2/24/19	10.9	7/15/19	3.84	12/3/19	11.7	4/22/20	8.56	9/10/20	2.59	1/29/21	15.4	6/19/21	1.14	11/7/21	16.3
3/22/17	31.5	08/10/17	15.9	12/29/17	30.1	5/19/18	10.2	10/7/18	0.29	2/25/19	11.0	7/16/19	1.07	12/4/19	9.71	4/23/20	8.17	9/11/20	3.30	1/30/21	23.4	6/20/21	2.20	11/8/21	2.89
3/23/17	31.8	08/11/17	12.7	12/30/17	24.0	5/20/18	9.30	10/8/18	7.11	2/26/19	10.7	7/17/19	3.59	12/5/19	9.77	4/24/20	7.53	9/12/20	2.93	1/31/21	19.9	6/21/21	2.15	11/9/21	30.8
3/24/17	29.9	08/12/17	16.6	12/31/17	22.0	5/21/18	9.97	10/9/18	2.31	2/27/19	10.4	7/18/19	3.02	12/6/19	9.41	4/25/20	8.16	9/13/20	2.57	2/1/21	17.1	6/22/21	2.51	11/10/21	15.9
3/25/17	28.2	08/13/17	13.4	1/1/18	33.6	5/22/18	9.48	10/10/18	1.30	2/28/19	10.1	7/19/19	19.0	12/7/19	9.50	4/26/20	8.11	9/14/20	2.80	2/2/21	18.2	6/23/21	3.58	11/11/21	18.0
3/26/17	26.4	08/14/17	14.2	1/2/18	28.1	5/23/18	9.36	10/11/18	1.08	3/1/19	9.18	7/20/19	1.63	12/8/19	10.3	4/27/20	7.13	9/15/20	2.62	2/3/21	10.9	6/24/21	2.99	11/12/21	14.4

3/27/17	25.0	08/15/17	13.2	1/3/18	32.4	5/24/18	8.56	10/12/18	6.09	3/2/19	10.1	7/21/19	4.55	12/9/19	9.70	4/28/20	7.22	9/16/20	3.36	2/4/21	18.2	6/25/21	2.55	11/13/21	13.4
3/28/17	23.2	08/16/17	13.2	1/4/18	33.8	5/25/18	8.61	10/13/18	2.09	3/3/19	9.08	7/22/19	0.384	12/10/19	9.16	4/29/20	6.56	9/17/20	2.46	2/5/21	21.9	6/26/21	1.94	11/14/21	12.0
3/29/17	23.4	08/17/17	12.4	1/5/18	42.5	5/26/18	7.94	10/14/18	2.48	3/4/19	11.1	7/23/19	5.93	12/11/19	13.5	4/30/20	8.77	9/18/20	4.51	2/6/21	18.6	6/27/21	3.67	11/15/21	21.1
3/30/17	22.2	08/18/17	11.8	1/6/18	45.1	5/27/18	8.70	10/15/18	1.56	3/5/19	6.35	7/24/19	6.01	12/12/19	10.2	5/1/20	8.89	9/19/20	2.72	2/7/21	14.6	6/28/21	2.73	11/16/21	14.5
3/31/17	21.4	08/19/17	13.3	1/7/18	51.0	5/28/18	7.45	10/16/18	1.22	3/6/19	14.4	7/25/19	5.30	12/13/19	13.0	5/2/20	9.32	9/20/20	2.53	2/8/21	1.75	6/29/21	3.67	11/17/21	13.7
4/1/17	20.9	08/20/17	13.2	1/8/18	48.2	5/29/18	6.22	10/17/18	2.74	3/7/19	12.2	7/26/19	9.57	12/14/19	17.6	5/3/20	8.87	9/21/20	2.44	2/9/21	18.2	6/30/21	2.33	11/18/21	13.6
4/2/17	20.4	08/21/17	10.1	1/9/18	41.9	5/30/18	7.27	10/18/18	1.92	3/8/19	10.3	7/27/19	n.d.	12/15/19	14.6	5/4/20	8.57	9/22/20	2.62	2/10/21	22.4	7/1/21	5.43	11/19/21	14.2
4/3/17	21.3	08/22/17	12.7	1/10/18	45.6	5/31/18	7.42	10/19/18	2.36	3/9/19	10.4	7/28/19	n.d.	12/16/19	13.8	5/5/20	7.61	9/23/20	2.55	2/11/21	19.3	7/2/21	3.39	11/20/21	12.6
4/4/17	20.8	08/23/17	14.4	1/11/18	40.6	6/1/18	7.28	10/20/18	2.57	3/10/19	9.37	7/29/19	n.d.	12/17/19	12.2	5/6/20	8.91	9/24/20	2.36	2/12/21	16.4	7/3/21	3.87	11/21/21	8.34
4/5/17	20.5	08/24/17	12.9	1/12/18	45.3	6/2/18	7.06	10/21/18	2.96	3/11/19	12.1	7/30/19	3.60	12/18/19	15.7	5/7/20	8.35	9/25/20	3.15	2/13/21	14.7	7/4/21	4.26	11/22/21	16.0
4/6/17	19.6	08/25/17	11.1	1/13/18	44.0	6/3/18	7.49	10/22/18	0.780	3/12/19	14.3	7/31/19	4.27	12/19/19	12.7	5/8/20	7.62	9/26/20	2.21	2/14/21	14.1	7/5/21	3.80	11/23/21	9.39
4/7/17	19.3	08/26/17	10.9	1/14/18	42.0	6/4/18	5.88	10/23/18	4.02	3/13/19	11.7	8/1/19	6.32	12/20/19	12.1	5/9/20	7.01	9/27/20	6.24	2/15/21	14.1	7/6/21	2.90	11/24/21	17.3
4/8/17	18.9	08/27/17	9.40	1/15/18	40.9	6/5/18	7.92	10/24/18	0.791	3/14/19	11.6	8/2/19	2.62	12/21/19	16.1	5/10/20	5.89	9/28/20	5.89	2/16/21	14.8	7/7/21	3.38	11/25/21	15.7
4/9/17	18.2	08/28/17	11.3	1/16/18	39.1	6/6/18	5.68	10/25/18	5.53	3/15/19	12.7	8/3/19	5.54	12/22/19	12.8	5/11/20	2.84	9/29/20	4.92	2/17/21	15.3	7/8/21	3.57	11/26/21	6.04
4/10/17	17.0	08/29/17	10.1	1/17/18	39.4	6/7/18	5.59	10/26/18	4.38	3/16/19	17.4	8/4/19	4.55	12/23/19	13.1	5/12/20	10.9	9/30/20	4.83	2/18/21	20.9	7/9/21	3.39	11/27/21	9.88
4/11/17	16.3	08/30/17	6.77	1/18/18	34.2	6/8/18	5.30	10/27/18	0.86	3/17/19	18.4	8/5/19	3.09	12/24/19	14.7	5/13/20	6.13	10/1/20	4.87	2/19/21	26.8	7/10/21	18.2	11/28/21	16.1
4/12/17	16.9	08/31/17	9.58	1/19/18	45.5	6/9/18	6.46	10/28/18	n.d.	3/18/19	17.3	8/6/19	3.80	12/25/19	11.4	5/14/20	7.32	10/2/20	4.50	2/20/21	28.5	7/11/21	20.6	11/29/21	4.36
4/13/17	12.0	09/01/17	8.00	1/20/18	42.8	6/10/18	8.38	10/29/18	1.31	3/19/19	14.3	8/7/19	n.d.	12/26/19	13.6	5/15/20	6.21	10/3/20	2.99	2/21/21	28.1	7/12/21	6.61	11/30/21	20.7
4/14/17	20.3	09/02/17	8.24	1/21/18	42.4	6/11/18	7.02	10/30/18	9.91	3/20/19	19.3	8/8/19	0.160	12/27/19	5.12	5/16/20	5.67	10/4/20	6.39	2/22/21	27.3	7/13/21	7.02	12/1/21	18.7
4/15/17	15.9	09/03/17	9.20	1/22/18	42.4	6/12/18	6.29	10/31/18	7.48	3/21/19	17.1	8/9/19	1.71	12/28/19	21.7	5/17/20	6.14	10/5/20	4.32	2/23/21	25.8	7/14/21	6.61	12/2/21	5.25
4/16/17	21.2	09/04/17	8.60	1/23/18	41.6	6/13/18	6.51	11/1/18	2.56	3/22/19	15.0	8/10/19	3.77	12/29/19	14.7	5/18/20	4.89	10/6/20	3.96	2/24/21	24.0	7/15/21	6.15	12/3/21	30.9
4/17/17	17.3	09/05/17	11.7	1/24/18	39.7	6/14/18	5.93	11/2/18	3.77	3/23/19	15.5	8/11/19	2.84	12/30/19	12.9	5/19/20	4.67	10/7/20	4.05	2/25/21	22.8	7/16/21	6.61	12/4/21	15.8
4/18/17	19.2	09/06/17	7.31	1/25/18	41.3	6/15/18	5.82	11/3/18	1.56	3/24/19	14.6	8/12/19	1.87	12/31/19	8.37	5/20/20	6.84	10/8/20	4.39	2/26/21	21.5	7/17/21	6.29	12/5/21	3.26
4/19/17	23.2	09/07/17	9.14	1/26/18	38.7	6/16/18	6.00	11/4/18	2.88	3/25/19	9.62	8/13/19	3.49	1/1/20	16.3	5/21/20	6.49	10/9/20	4.36	2/27/21	20.8	7/18/21	5.27	12/6/21	38.6
4/20/17	18.5	09/08/17	13.5	1/27/18	40.8	6/17/18	5.80	11/5/18	2.73	3/26/19	13.4	8/14/19	1.29	1/2/20	12.9	5/22/20	5.40	10/10/20	4.57	2/28/21	19.8	7/19/21	4.66	12/7/21	33.7
4/21/17	16.8	09/09/17	8.48	1/28/18	39.3	6/18/18	4.35	11/6/18	3.54	3/27/19	17.3	8/15/19	3.31	1/3/20	11.9	5/23/20	5.73	10/11/20	4.71	3/1/21	19.2	7/20/21	3.90	12/8/21	27.3
4/22/17	13.8	09/10/17	12.2	1/29/18	39.4	6/19/18	4.64	11/7/18	2.81	3/28/19	13.4	8/16/19	1.75	1/4/20	11.0	5/24/20	5.40	10/12/20	4.87	3/2/21	18.3	7/21/21	3.88	12/9/21	24.3
4/23/17	16.1	09/11/17	10.2	1/30/18	36.4	6/20/18	4.87	11/8/18	1.72	3/29/19	14.0	8/17/19	1.66	1/5/20	11.5	5/25/20	2.27	10/13/20	6.03	3/3/21	17.6	7/22/21	3.89	12/10/21	22.8
4/24/17	16.9	09/12/17	10.6	1/31/18	44.8	6/21/18	4.99	11/9/18	2.78	3/30/19	13.3	8/18/19	3.03	1/6/20	16.4	5/26/20	8.93	10/14/20	0.828	3/4/21	13.7	7/23/21	3.60	12/11/21	21.0
4/25/17	13.5	09/13/17	10.3	2/1/18	43.6	6/22/18	6.69	11/10/18	3.37	3/31/19	10.0	8/19/19	2.26	1/7/20	15.3	5/27/20	4.70	10/15/20	7.37	3/5/21	20.1	7/24/21	4.30	12/12/21	20.8

4/26/17	16.5	09/14/17	9.42	2/2/18	36.2	6/23/18	6.51	11/11/18	3.10	4/1/19	15.1	8/20/19	5.06	1/8/20	14.1	5/28/20	1.37	10/16/20	7.65	3/6/21	16.5	7/25/21	2.77	12/13/21	20.5
4/27/17	18.1	09/15/17	10.4	2/3/18	37.6	6/24/18	7.05	11/12/18	3.42	4/2/19	12.0	8/21/19	3.53	1/9/20	9.84	5/29/20	0.97	10/17/20	5.70	3/7/21	12.9	7/26/21	2.64	12/14/21	20.1
4/28/17	13.8	09/16/17	7.45	2/4/18	22.2	6/25/18	5.56	11/13/18	3.57	4/3/19	11.4	8/22/19	2.32	1/10/20	8.24	5/30/20	n.d.	10/18/20	5.57	3/8/21	16.5	7/27/21	3.39	12/15/21	21.0
4/29/17	13.4	09/17/17	9.75	2/5/18	53.6	6/26/18	6.05	11/14/18	3.17	4/4/19	11.1	8/23/19	4.42	1/11/20	21.1	5/31/20	n.d.	10/19/20	4.62	3/9/21	15.6	7/28/21	4.42	12/16/21	20.3
4/30/17	19.7	09/18/17	10.3	2/6/18	44.4	6/27/18	7.79	11/15/18	3.23	4/5/19	6.96	8/24/19	2.08	1/12/20	16.6	6/1/20	n.d.	10/20/20	4.68	3/10/21	14.3	7/29/21	2.11	12/17/21	20.0
5/1/17	12.4	09/19/17	9.79	2/7/18	41.8	6/28/18	7.33	11/16/18	3.02	4/6/19	14.6	8/25/19	2.49	1/13/20	14.3	6/2/20	n.d.	10/21/20	4.87	3/11/21	15.4	7/30/21	3.05	12/18/21	19.1
5/2/17	13.9	09/20/17	8.63	2/8/18	38.6	6/29/18	2.39	11/17/18	3.18	4/7/19	11.1	8/26/19	1.49	1/14/20	18.4	6/3/20	n.d.	10/22/20	4.68	3/12/21	n.d.	7/31/21	3.57	12/19/21	10.2
5/3/17	15.2	09/21/17	8.64	2/9/18	36.6	6/30/18	7.20	11/18/18	1.05	4/8/19	6.17	8/27/19	3.60	1/15/20	15.4	6/4/20	n.d.	10/23/20	4.76	3/13/21	n.d.	8/1/21	3.01	12/20/21	14.7
5/4/17	4.03	09/22/17	9.75	2/10/18	34.5	7/1/18	5.00	11/19/18	4.26	4/9/19	12.0	8/28/19	3.12	1/16/20	13.8	6/5/20	n.d.	10/24/20	4.93	3/14/21	n.d.	8/2/21	3.26	12/21/21	27.3
5/5/17	27.1	09/23/17	7.38	2/11/18	32.9	7/2/18	4.15	11/20/18	5.67	4/10/19	9.24	8/29/19	5.79	1/17/20	16.0	6/6/20	n.d.	10/25/20	4.58	3/15/21	n.d.	8/3/21	4.24	12/22/21	18.6
5/6/17	21.3	09/24/17	7.79	2/12/18	31.5	7/3/18	4.29	11/21/18	3.82	4/11/19	8.71	8/30/19	0.224	1/18/20	15.2	6/7/20	n.d.	10/26/20	5.08	3/16/21	n.d.	8/4/21	4.14	12/23/21	17.0
5/7/17	18.8	09/25/17	9.32	2/13/18	31.2	7/4/18	4.76	11/22/18	3.84	4/12/19	7.78	8/31/19	1.32	1/19/20	8.06	6/8/20	n.d.	10/27/20	4.94	3/17/21	22.9	8/5/21	3.60	12/24/21	7.00
5/8/17	12.6	09/26/17	12.2	2/14/18	29.8	7/5/18	3.06	11/23/18	3.58	4/13/19	8.06	9/1/19	2.53	1/20/20	7.27	6/9/20	n.d.	10/28/20	4.93	3/18/21	23.5	8/6/21	3.82	12/25/21	24.6
5/9/17	19.9	09/27/17	8.09	2/15/18	29.0	7/6/18	2.98	11/24/18	3.26	4/14/19	8.97	9/2/19	2.86	1/21/20	19.5	6/10/20	n.d.	10/29/20	5.57	3/19/21	16.9	8/7/21	6.83	12/26/21	15.4
5/10/17	15.3	09/28/17	7.84	2/16/18	27.6	7/7/18	4.72	11/25/18	2.76	4/15/19	8.57	9/3/19	1.22	1/22/20	8.41	6/11/20	n.d.	10/30/20	6.17	3/20/21	25.4	8/8/21	4.77	12/27/21	15.4
5/11/17	14.7	09/29/17	8.78	2/17/18	26.9	7/8/18	3.70	11/26/18	3.71	4/16/19	8.16	9/4/19	1.79	1/23/20	20.1	6/12/20	n.d.	10/31/20	6.78	3/21/2021	19.0	8/9/21	3.79	12/28/21	15.2
5/12/17	13.4	09/30/17	8.16	2/18/18	27.0	7/9/18	2.25	11/27/18	3.65	4/17/19	7.90	9/5/19	1.24	1/24/20	14.5	6/13/20	n.d.	11/1/2020	6.79	3/22/2021	21.9	8/10/21	2.91	12/29/21	16.9
5/13/17	14.6	10/01/17	7.90	2/19/18	26.0	7/10/18	2.78	11/28/18	4.31	4/18/19	8.60	9/6/19	1.58	1/25/20	10.6	6/14/20	n.d.	11/2/2020	7.43	3/23/2021	19.7	8/11/21	4.59	12/30/21	17.3
5/14/17	13.7	10/02/17	9.10	2/20/18	27.2	7/11/18	6.43	11/29/18	1.70	4/19/19	6.70	9/7/19	1.07	1/26/20	14.6	6/15/20	n.d.	11/3/2020	6.89	3/24/2021	18.4	8/12/21	3.77	12/31/21	20.0
5/15/17	12.4	10/03/17	8.68	2/21/18	26.1	7/12/18	5.89	11/30/18	3.14	4/20/19	8.19	9/8/19	3.02	1/27/20	11.5	6/16/20	n.d.	11/4/2020	9.41	3/25/2021	17.7	8/13/21	3.89	8/18/22	1.2
5/16/17	12.7	10/04/17	8.76	2/22/18	25.2	7/13/18	5.02	12/1/18	3.09	4/21/19	7.12	9/9/19	4.44	1/28/20	7.67	6/17/20	n.d.	11/5/2020	7.36	3/26/2021	n.d.	8/14/21	3.86		
5/17/17	13.2	10/05/17	12.2	2/23/18	24.5	7/14/18	4.98	12/2/18	1.98	4/22/19	6.03	9/10/19	4.28	1/29/20	14.9	6/18/20	n.d.	11/6/2020	3.69	3/27/2021	n.d.	8/15/21	4.17		
5/18/17	12.6	10/06/17	26.5	2/24/18	24.7	7/15/18	4.49	12/3/18	4.59	4/23/19	6.23	9/11/19	3.11	1/30/20	19.7	6/19/20	n.d.	11/7/2020	10.0	3/28/2021	n.d.	8/16/21	3.62		
5/19/17	13.0	10/07/17	28.2	2/25/18	22.0	7/16/18	5.47	12/4/18	3.97	4/24/19	6.87	9/12/19	1.84	1/31/20	16.1	6/20/20	n.d.	11/8/2020	3.70	3/29/2021	16.8	8/17/21	3.56		
5/20/17	12.5	10/08/17	22.6	2/26/18	24.2	7/17/18	5.51	12/5/18	4.22	4/25/19	7.04	9/13/19	4.19	2/1/20	21.9	6/21/20	n.d.	11/9/2020	9.29	3/30/2021	16.5	8/18/21	4.48		
5/21/17	11.7	10/09/17	33.8	2/27/18	15.2	7/18/18	5.23	12/6/18	3.27	4/26/19	6.86	9/14/19	3.82	2/2/20	15.8	6/22/20	n.d.	11/10/2020	6.76	3/31/2021	16.0	8/19/21	2.81		

Supplementary Table 2 – Results from the temporal campaign carried out at the end of the middle Warnow at Rostock weir.

Date	Q (m^3/s)	EC25 (µS/cm)	pH $_{NBS}$	Temp	O2 (mg/L)	TA (mM)	DIC (mM)	$d^{13}C$-DIC (mUr VPDB)	DOC (mM)	$\delta^{13}C$-DOC (mUr)	PO4	NH4 (µM)	NO3 (µM)	Ca (mM)	K (mM)	Mg (mM)	Na (mM)	SO4 (mM)	Si (µM)	P (µM)	Ba (µM)	Sr (µM)	Fe (µM)	Li (µM)	Mn (µM)	$d^{18}O$-H2O (mUr VSMOW)	$d^{2}H$-H2O (mUr VSMOW)	$d^{34}S$-SO4 (mUr VCDT)	$\delta^{18}O$-SO_4 mUr VSMOW	^{224}Ra (mBq/L)
16/03/17	20.40	n.d.	n.d.	n.d.	n.d.	n.d.	4.00	-10.1	n.d.	n.d.	0.3	n.d.	178	2.62	0.12	0.47	1.30	0.80	149	n.d.	0.44	n.d.	1.5	1.3	0.7	-6.85	-48.6	n.d.	n.d.	n.d.
24/03/17	29.90	n.d.	n.d.	n.d.	n.d.	n.d.	3.83	-10.9	n.d.	n.d.	0.0	n.d.	315	2.65	0.12	0.45	1.28	0.81	148	n.d.	0.47	n.d.	2.0	1.1	0.6	-7.11	-50.2	n.d.	n.d.	n.d.
30/03/17	22.20	637	8.08	10.8	n.d.	3.82	3.85	-10.0	n.d.	n.d.	0.0	n.d.	187	2.53	0.12	0.45	1.24	0.77	110	n.d.	0.43	n.d.	1.3	1.2	0.6	-6.71	-47.7	n.d.	7.3	n.d.
06/04/17	18.60	615	8.03	11.1	n.d.	3.75	3.79	-10.0	n.d.	n.d.	0.0	n.d.	128	2.47	0.12	0.46	1.29	0.74	89	n.d.	0.45	n.d.	1.2	1.2	0.4	-6.59	-47.2	1.2	8.6	n.d.
13/04/17	12.00	658	8.16	10.1	n.d.	3.80	3.80	-9.6	n.d.	n.d.	0.0	n.d.	106	2.45	0.13	0.46	1.34	0.74	88	n.d.	0.44	n.d.	1.1	1.3	0.3	-6.44	-46.6	1.4	7.1	n.d.
20/04/17	18.50	645	8.28	9.6	n.d.	3.97	3.94	-9.4	n.d.	n.d.	n.a.	n.d.	n.a.	2.46	0.13	0.46	1.31	0.74	81	n.d.	0.42	n.d.	1.6	1.3	0.5	-6.41	-46.5	1.8	7.7	n.d.
27/04/17	18.10	646	8.25	9.4	n.d.	3.96	3.94	-9.1	n.d.	n.d.	0.3	n.d.	49	2.43	0.12	0.46	1.34	0.73	64	n.d.	0.41	n.d.	1.2	1.3	0.5	-6.35	-46.1	1.5	6.5	n.d.
04/05/17	4.03	642	8.38	11.6	n.d.	3.83	3.77	-8.7	n.d.	n.d.	0.1	n.d.	29	2.37	0.13	0.46	1.38	0.72	48	n.d.	0.42	n.d.	1.2	1.3	0.2	-6.34	-46.2	1.6	6.4	n.d.
11/05/17	14.70	644	8.09	12.4	n.d.	3.99	4.01	-9.7	n.d.	n.d.	0.2	n.d.	19	2.24	0.12	0.43	1.28	0.68	69	n.d.	0.41	n.d.	0.9	1.2	0.4	-6.54	-47.6	1.9	7.9	n.d.
18/05/17	12.60	640	8.11	17.1	n.d.	3.80	3.80	-9.5	n.d.	n.d.	0.3	n.d.	21	2.32	0.16	0.46	1.37	0.69	62	n.d.	0.44	n.d.	0.7	1.3	0.2	-6.32	-46.4	2.2	7.4	n.d.
26/05/17	10.70	619	8.12	18.7	n.d.	3.71	3.70	-9.7	n.d.	n.d.	0.6	n.d.	21	2.21	0.12	0.45	1.34	0.66	79	n.d.	0.46	n.d.	0.5	1.4	0.1	-6.10	-44.9	2.1	n.d.	n.d.
01/06/17	8.56	621	7.9	19.3	n.d.	3.84	3.90	-10.1	n.d.	n.d.	0.9	10	22	2.17	0.12	0.44	1.35	0.64	110	n.d.	0.46	n.d.	0.6	1.4	0.2	-5.94	-44.2	2	7.3	n.d.
08/06/17	6.74	620	7.79	18.9	n.d.	4.00	4.10	-10.8	n.d.	n.d.	1.8	14	29	2.16	0.14	0.44	1.43	0.62	162	n.d.	0.47	n.d.	1.0	1.4	2.0	-5.82	-43.7	2.3	7.2	n.d.
15/06/17	5.86	615	7.91	19.8	n.d.	3.85	3.90	-10.1	n.d.	n.d.	0.9	5	21	2.13	0.15	0.44	1.43	0.62	162	n.d.	0.46	n.d.	0.6	1.4	0.2	-5.88	-43.6	2.8	7.0	n.d.
22/06/17	5.02	618	7.97	21.4	n.d.	3.87	3.90	-9.9	n.d.	n.d.	0.6	8	3	2.12	0.11	0.44	1.43	0.61	176	n.d.	0.46	n.d.	0.5	1.4	0.1	-5.72	-43.0	3.1	6.2	n.d.
13/07/17	14.80	602	7.69	18.6	n.d.	4.05	4.20	-12.2	n.d.	n.d.	2.1	10	38	2.22	0.13	0.41	1.20	0.60	234	n.d.	0.47	n.d.	3.7	1.2	1.7	-6.10	-44.3	3.2	6.2	n.d.
20/07/17	12.50	606	7.79	19.3	n.d.	4.10	4.20	-11.7	n.d.	n.d.	1.6	7	37	2.22	0.13	0.42	1.24	0.59	221	n.d.	0.45	n.d.	2.1	1.3	0.9	-6.05	-44.4	3.2	7.8	n.d.
17/08/17	12.40	611	7.67	19.4	n.d.	4.24	4.40	-12.4	n.d.	n.d.	1.6	12	46	2.36	0.14	0.47	1.27	0.57	266	n.d.	0.47	n.d.	2.0	1.4	1.8	-5.88	-43.0	3.5	6.5	n.d.
25/08/17	11.10	611	7.74	17.5	n.d.	4.33	4.47	-11.8	n.d.	n.d.	1.5	11	56	2.23	0.13	0.44	1.29	0.56	232	n.d.	0.43	n.d.	1.4	1.4	1.3	-5.94	-43.8	3.3	7.0	n.d.
31/08/17	9.58	640	7.73	19.3	n.d.	4.42	4.55	-11.6	n.d.	n.d.	1.2	0	45	2.34	0.12	0.46	1.38	0.59	232	n.d.	0.45	n.d.	1.1	1.4	1.1	-5.97	-44.1	3.4	6.7	n.d.
07/09/17	9.14	631	7.71	17.5	n.d.	4.37	4.53	-11.3	n.d.	n.d.	1.6	3	41	2.26	0.13	0.46	1.41	0.59	230	n.d.	0.44	n.d.	0.9	1.4	1.1	-5.86	-44.0	3.3	6.5	n.d.
15/09/17	10.40	635	7.84	14.4	n.d.	4.37	4.48	-11.3	n.d.	n.d.	1.8	5	67	2.27	0.13	0.45	1.41	0.59	256	n.d.	0.43	n.d.	1.1	1.4	1.0	-6.05	-44.4	3.3	6.9	n.d.
28/09/17	7.84	641	7.81	14.9	n.d.	4.32	4.44	-10.8	n.d.	n.d.	0.9	2	45	2.32	0.12	0.46	1.42	0.61	239	n.d.	0.44	n.d.	0.9	1.5	0.9	-6.19	-44.7	2.8	6.9	n.d.
05/10/17	12.20	643	7.8	13.6	n.d.	4.39	4.52	-11.2	n.d.	n.d.	1.5	2	48	2.30	0.13	0.45	1.44	0.61	258	n.d.	0.44	n.d.	1.0	1.5	1.2	-6.24	-44.6	2.9	6.4	n.d.
18/10/17	17.90	631	7.8	13	n.d.	4.45	4.58	-12.5	n.d.	n.d.	1.0	2	174	2.52	0.13	0.44	1.05	0.66	250	n.d.	0.46	n.d.	2.4	1.1	1.1	-5.98	-48.7	2.7	6.9	n.d.

25/10/17	24.50	655	7.88	12.5	n.d.	4.21	4.30	-12.3	n.d.	n.d.	1.0	3	138	2.66	0.14	0.47	1.24	0.68	268	n.d.	0.48	n.d.	2.1	1.3	1.1	-6.09	-46.6	2.8	7.4	n.d.
02/11/17	26.20	651	8.03	9.3	n.d.	4.73	4.79	-12.4	n.d.	n.d.	1.2	6	181	2.56	0.13	0.46	1.14	0.63	262	n.d.	0.44	n.d.	2.1	1.2	0.9	-6.18	-46.3	2.7	7.0	n.d.
15/11/17	27.40	662	8.15	5.4	n.d.	4.72	4.75	-12.3	n.d.	n.d.	n.d.	n.d.	n.d.	2.65	0.13	0.46	1.10	0.67	254	n.d.	0.43	n.d.	2.1	1.2	0.8	-6.31	-44.6	2.6	7.5	n.d.
22/11/17	34.90	655	8.2	5.3	n.d.	4.49	4.50	-12.1	n.d.	n.d.	n.d.	n.d.	n.d.	2.60	0.13	0.46	1.14	0.66	253	n.d.	0.42	n.d.	1.7	1.2	0.8	-6.33	-44.3	2.3	7.5	n.d.
06/12/17	26.00	662	8.27	4.2	n.d.	4.71	4.70	-12.0	n.d.	n.d.	n.d.	n.d.	n.d.	2.65	0.12	0.46	1.13	0.67	254	n.d.	0.42	n.d.	1.8	1.2	0.8	-6.49	-45.3	2.3	7.9	n.d.
19/06/18	4.64	625	7.87	23	7.6	4.04	4.10	-10.2	n.d.	n.d.	6.0	12	54	2.11	0.12	0.43	1.35	0.62	162	3.1	0.37	4.4	0.3	1.2	0.4	-5.96	-44.8	2.1	n.d.	n.d.
16/07/18	5.47	647	8.08	21.5	8.6	4.31	4.30	-10.1	n.d.	n.d.	4.4	7	0	2.09	0.12	0.44	1.55	0.61	183	1.8	0.39	4.6	0.3	1.3	0.1	-5.98	-45.4	2.2	n.d.	n.d.
15/08/18	2.79	649	7.68	21.8	3.3	3.77	3.90	-10.3	0.8	-27.7	6.9	16	1	2.12	0.12	0.48	2.01	0.53	262	4.8	0.43	4.9	0.4	1.4	1.3	-5.79	-44.6	3.0	n.d.	n.d.
18/09/18	3.04	649	7.62	17.5	4.6	3.53	3.70	-10.4	0.8	-29.4	n.d.	n.d.	n.d.	2.08	0.14	0.49	2.20	0.61	175	1.6	0.46	5.0	0.2	1.6	0.1	-5.95	-44.9	1.9	n.d.	n.d.
24/10/18	0.79	704	7.42	11.3	9.5	3.30	3.60	-9.4	0.7	-29.7	n.d.	n.d.	n.d.	2.11	0.14	0.53	2.43	0.64	121	0.7	0.43	5.0	0.5	1.5	0.3	-6.36	-46.1	2.7	n.d.	n.d.
26/11/18	3.71	743	8.02	5.4	9.8	4.23	4.30	-10.5	1.0	-29.3	3.1	6	48	2.46	0.16	0.54	2.33	0.67	261	0.8	0.44	5.1	0.7	1.5	1.1	-6.73	-47.8	2.1	n.d.	n.d.
21/12/18	5.00	650	7.61	3.5	9.4	4.02	4.30	-11.0	1.2	-31.4	n.d.	n.d.	n.d.	2.55	0.12	0.49	1.78	0.73	312	2.0	0.45	5.1	1.1	1.4	1.6	-6.82	-48.7	n.d.	n.d.	n.d.
07/01/19	7.50	702	7.50	4	n.d.	3.67	4.00	-10.5	n.d.	n.d.	n.d.	n.d.	n.d.	2.45	0.11	0.47	1.67	0.76	304	1.4	0.44	4.9	0.9	1.3	1.0	-6.56	-46.9	1.3	n.d.	n.d.
11/01/19	12.80	n.d.	7.94	3.7	n.d.	3.71	3.80	-9.7	n.d.	n.d.	n.d.	n.d.	n.d.	2.60	0.13	0.48	1.69	0.79	292	1.4	0.43	4.9	1.2	1.2	1.1	-6.76	-48.6	0.9	n.d.	n.d.
15/01/19	21.20	714	7.77	4.1	n.d.	3.74	3.90	-10.7	n.d.	n.d.	n.d.	n.d.	n.d.	2.61	0.12	0.47	1.66	0.88	284	1.3	0.44	5.0	1.0	1.2	0.9	-6.63	-47.4	1.3	n.d.	n.d.
23/01/19	6.94	710	7.82	1.2	11.7	3.64	3.80	-10.6	n.d.	n.d.	n.d.	n.d.	n.d.	2.55	0.11	0.46	1.58	0.88	284	1.3	0.43	4.8	1.0	1.2	1.1	-6.43	-46.2	0.9	n.d.	n.d.
28/02/19	10.10	715	7.85	5.7	12.9	3.74	3.86	-9.3	n.d.	n.d.	n.d.	n.d.	n.d.	2.67	0.11	0.49	1.62	0.84	168	0.4	0.42	5.0	0.8	1.2	0.8	-6.71	-47.9	0.4	n.d.	n.d.
27/03/19	17.30	680	7.97	8.6	9.5	3.78	3.85	-9.5	0.9	-30.1	n.d.	n.d.	n.d.	2.66	0.11	0.48	1.52	0.87	117	0.5	0.45	5.1	0.9	1.2	0.7	-6.47	-46.8	0.4	n.d.	n.d.
30/04/19	6.89	654	8.3	17.1	n.d.	3.75	3.69	-8.6	1.1	-30.2	0.1	1	4	2.38	0.12	0.49	1.58	0.77	15		0.47	5.2	0.5	1.5	0.6	-6.28	-46.0	1.1	n.d.	n.d.
06/07/19	4.50	651	7.82	20.4	n.d.	3.93	4.01	-9.6	1.1	-28.3	n.d.	n.d.	n.d.	2.29	0.11	0.50	1.72	0.66	113	2.3	0.48	5.3	1.0	1.6	2.5	-5.87	-44.2	3.4	n.d.	n.d.
07/11/19	2.43	655	7.87	21.4	n.d.	3.62	3.67	-9.1	1.1	-29.0	n.d.	n.d.	n.d.	2.10	0.13	0.50	1.86	0.58	272	3.7	0.40	4.4	0.2	1.3	0.2	-5.13	-40.3	5.0	n.d.	n.d.
23/08/2019	4.42	610	n.d.	20.8	n.d.	n.d.	3.63	-9.8	1.3	-29.5	n.d.	n.d.	n.d.	1.96	0.15	0.48	1.90	0.57	418	4.7	0.27		1.5		3.8	-5.55	-42.4	4.4	n.d.	n.d.
09/09/19	4.44	638	7.55	17.7	n.d.	n.d.	3.80	-10.7	1.1	-28.5	n.d.	n.d.	n.d.	1.99	0.14	0.49	1.89	0.55	189	6.4	0.42	4.5	0.7	1.4	1.4	-5.62	-42.4	4.2	n.d.	n.d.
28/10/19	3.66	746	n.d.	12.4	n.d.	n.d.	4.37	-11.9	1.0	-28.9	n.d.	n.d.	n.d.	2.48	0.14	0.49	1.55	0.77	270	1.8	0.48	5.1	1.1	1.4	2.6	-6.64	-47.3	2.9	n.d.	n.d.
12/03/19	11.70	772	7.35	4.5	n.d.	3.70	4.17	-11.4	1.1	-28.9	n.d.	n.d.	n.d.	2.73	0.13	0.56	1.69	0.93	280	1.9	0.43	5.1	1.0	1.4	1.0	-6.79	-49.8	2.1	n.d.	n.d.
19/12/19	12.70	779	7.37	4.6	n.d.	3.81	4.27	-11.4	1.4	-29.0	n.d.	n.d.	n.d.	2.66	0.12	0.50	1.34	0.99	274	1.6	0.44	5.3	1.2	1.3	0.8	-6.85	-50.1	n.d.	n.d.	n.d.
20/01/20	7.27	789	7.48	4.7	n.d.	3.86	4.22	-11.3	1.4	-29.0	3.6	6	262	2.80	0.12	0.51	1.30	1.01	220	1.4	0.41	5.1	0.1	1.3	0.8	-6.71	-48.6	n.d.	n.d.	n.d.
20/02/20	27.10	n.d.	8.02	5.8	n.d.	3.84	3.90	-11.2	1.3	-28.4	37.0	5	430	2.73	0.12	0.48	1.15	0.97	170	1.0	0.39	4.7	0.1	1.5	0.5	-6.80	-48.4	n.d.	n.d.	n.d.
05/04/20	8.57	n.d.	8.45	15.8	n.d.	3.96	3.86	-8.8	1.2	-28.0	n.d.	n.d.	n.d.	2.20	0.11	0.47	1.41	0.83	41	0.9	0.40	4.9	0.2	0.7	0.5	-6.27	-46.8	n.d.	n.d.	n.d.
17/09/20	2.46	675	7.40	16.8	n.d.	3.50	3.80	-10.7	1.7	-28.3	8.4	7	7	2.00	0.14	0.45	1.74	0.58	213	1.4	0.42	4.7	0.7	1.2	1.1	-5.82	-44.7	n.d.	n.d.	n.d.
28/10/20	4.93	676	8.00	11	n.d.	3.91	3.96	-9.6	0.9	-29.0	7.3	1	1	2.15	0.13	0.46	1.56	0.60	181	0.5	0.38	4.8	0.5	1.2	0.1	-6.43	-47.5	n.d.	n.d.	n.d.

25/11/20	5.98	712	7.95	6.6	n.d.	4.16	4.25	-10.8	1.5	-27.5	24.3	25	5	2.34	0.15	0.52	1.99	0.70	286	1.6	0.41	5.0	0.9	1.2	0.8	-6.22	-45.8	n.d.	n.d.	n.d.
21/12/10	7.04	727	7.77	4.9	n.d.	4.22	4.40	-10.7	1.0	-28.9	4.3	14	68	2.43	0.15	0.56	2.07	0.70	296	2.2	0.39	5.1	0.7	1.3	1.0	-6.62	-48.1	n.d.	n.d.	n.d.
29/01/21	15.40	755	7.99	2.2	n.d.	4.13	4.23	-11.2	1.5	-26.8	n.d.	n.d.	n.d.	2.64	0.12	0.46	1.18	0.90	233	1.2	0.38	4.9	1.3	1.0	0.6	-7.12	-51.6	n.d.	n.d.	n.d.
22/02/21	27.30	699	8.02	5.7	n.d.	3.62	3.68	-11.7	2.1	-25.5	n.d.	n.d.	n.d.	2.48	0.13	0.43	1.11	0.81	194	0.9	0.34	4.5	1.5	0.8	0.6	-7.90	-56.7	n.d.	n.d.	1.0
29/03/21	16.80	733	8.06	8.7	n.d.	4.09	4.13	-9.9	2.0	-25.7	n.d.	n.d.	n.d.	2.68	0.14	0.48	1.25	0.88	107	1.5	0.39	5.0	1.1	1.1	0.6	-6.88	-49.8	n.d.	n.d.	1.2
21/04/21	12.50	709	8.41	10.8	n.d.	4.12	4.04	-8.9	n.d.	n.d.	n.d.	n.d.	n.d.	2.50	0.13	0.48	1.35	0.82	36	0.3	0.39	5.0	1.0	1.1	0.3	-6.65	-48.0	n.d.	n.d.	0.7
31/05/21	9.63	681	8.34	16.4	n.d.	4.13	4.05	-9.5	1.7	-26.7	n.d.	n.d.	n.d.	2.42	0.12	0.46	1.32	0.73	51	0.3	0.40	4.9	0.7	1.1	0.1	-6.33	-46.4	n.d.	n.d.	1.5
14/07/21	6.15	n.d.	7.67	23	n.d.	3.58	3.71	-10.5	n.d.	n.d.	n.d.	n.d.	n.d.	2.09	0.16	0.48	1.73	0.58	232	2.2	0.39	4.5	0.7	1.4	0.4	-6.03	-45.9	n.d.	n.d.	0.7
16/08/21	3.62	631	7.35	20.3	n.d.	3.21	3.51	-9.9	1.4	-27.4	n.d.	n.d.	n.d.	1.84	0.13	0.44	1.50	0.55	182	1.9	0.38	4.4	0.4	1.4	0.2	-5.75	-44.8	n.d.	n.d.	0.5
09/06/21	5.48	655	7.47	19.7	n.d.	3.57	3.82	-10.7	1.4	-26.9	n.d.	n.d.	n.d.	2.02	0.15	0.45	1.51	0.58	222	1.0	0.41	4.7	0.2	1.4	0.5	-6.79	-51.0	n.d.	n.d.	0.7
28/10/21	6.97	722	7.42	11.7	n.d.	3.98	4.34	-11.5	1.4	-27.8	n.d.	n.d.	n.d.	2.41	0.14	0.47	1.38	0.66	235	1.1	0.43	5.1	1.3	1.3	0.7	-6.89	-48.1	n.d.	n.d.	n.d.
18/11/21	13.60	700	7.21	8	n.d.	4.55	5.29	-12.4	2.0	-25.9	n.d.	n.d.	n.d.	2.57	0.14	0.48	1.29	0.73	281	1.8	0.43	5.1	1.5	1.2	1.1	-6.97	-49.4	n.d.	n.d.	n.d.
20/12/21	14.70	700	7.49	5.9	n.d.	3.97	4.32	-12.2	1.5	-27.8	n.d.	n.d.	n.d.	2.72	0.13	0.49	1.25	0.79	265	1.4	0.42	5.2	1.6	1.2	0.9	-7.44	-51.7	n.d.	n.d.	n.d.
18/08/21	1.19	721	7.45	24.6	n.d.	n.d.	n.d.	n.d.	0.9	-28.9	n.d.	n.d.	n.d.	2.00	0.13	0.49	1.80	0.55	225	3.2	0.39	5.0	0.3	1.7	0.1	-5.38	-42.2	n.d.	n.d.	n.d.